

# Communications and Control Engineering

---

Springer-Verlag London Ltd.

*Published titles include:*

*Passivity-based Control of Euler-Lagrange Systems*

Romeo Ortega, Antonio Loría, Per Johan Nicklasson and Hebertt Sira-Ramírez

*Stability and Stabilization of Infinite Dimensional Systems with Applications*

Zheng-Hua Luo, Bao-Zhu Guo and Omer Morgul

*Nonsmooth Mechanics (2nd edition)*

Bernard Brogliato

*Nonlinear Control Systems II*

Alberto Isidori

*L<sub>2</sub>-Gain and Passivity Techniques in nonlinear Control*

Arjan van der Schaft

*Control of Linear Systems with Regulation and Input Constraints*

Ali Saberi, Anton A. Stoorvogel and Peddapullaiah Sannuti

*Robust and H $\infty$  Control*

Ben M. Chen

*Computer Controlled Systems*

Efim N. Rosenwasser and Bernhard P. Lampe

*Dissipative Systems Analysis and Control*

Rogelio Lozano, Bernard Brogliato, Olav Egeland and Bernhard Maschke

*Control of Complex and Uncertain Systems*

Stanislav V. Emelyanov and Sergey K. Korovin

*Robust Control Design Using H $\infty$  Methods*

Ian R. Petersen, Valery A. Ugrinovski and Andrey V. Savkin

*Model Reduction for Control System Design*

Goro Obinata and Brian D. O. Anderson

*Control Theory for Linear Systems*

Harry L. Trentelman, Anton Stoorvogel and Malo Hautus

*Functional Adaptive Control*

Simon G. Fabri and Visakan Kadirkamanathan

*Positive 1D and 2D Systems*

Tadeusz Kaczorek

*Identification and Control Using Volterra Models*

F.J. Doyle III, R.K. Pearson and B.A. Ogunnaike

*Non-linear Control for Underactuated Mechanical Systems*

Isabelle Fantoni and Rogelio Lozano

Jürgen Ackermann

In cooperation with Paul Blue, Tilman Bünte, Levent Güvenc,  
Dieter Kaesbauer, Michael Kordt, Michael Muhler  
and Dirk Odenthal

---

# **Robust Control**

**The Parameter Space Approach**

**Second edition**

With 321 Figures



**Springer**

Professor Jürgen Ackermann

Deutsches Zentrum für Luft- und Raumfahrt, Institut für Robotik und Mechatronik,  
Oberpfaffenhofen 82230 Wessling, Germany

*Series Editors*

E.D. Sontag • M. Thoma

ISSN 0178-5354

ISBN 978-1-4471-1099-6 ISBN 978-1-4471-0207-6 (eBook)

DOI 10.1007/978-1-4471-0207-6

British Library Cataloguing in Publication Data

Ackermann, Jürgen

Robust control : the parameter space approach. - 2nd ed. -

(Communications and control engineering)

1. Robust control

I. Title

629.8'312

ISBN 978-1-4471-1099-6

Library of Congress Cataloging-in-Publication Data

Ackermann, J. (Jürgen)

Robust control : the parameter space approach / Jürgen Ackermann.

p. cm. -- (Communications and control engineering)

Includes bibliographical references.

ISBN 978-1-4471-1099-6 (alk. paper)

1. Robust control. I. Title. II. Series.

TJ217.2 .A25 2002

629.8--dc21

2001032821

Apart from any fair dealing for the purposes of research or private study, or criticism or review, as permitted under the Copyright, Designs and Patents Act 1988, this publication may only be reproduced, stored or transmitted, in any form or by any means, with the prior permission in writing of the publishers, or in the case of reprographic reproduction in accordance with the terms of licences issued by the Copyright Licensing Agency. Enquiries concerning reproduction outside those terms should be sent to the publishers.

© Springer-Verlag London 2002

Originally published by Springer-Verlag London Berlin Heidelberg in 2002

Softcover reprint of the hardcover 2nd edition 2002

MATLAB® and SIMULINK® are the registered trademarks of The MathWorks Inc., 3 Apple Hill Drive Natick, MA 01760-2098, U.S.A. <http://www.mathworks.com>

Other registered trademarks used in this book are: BMW, Daimler-Benz, MAN, Airbus.

The use of registered names, trademarks, etc. in this publication does not imply, even in the absence of a specific statement, that such names are exempt from the relevant laws and regulations and therefore free for general use.

The publisher makes no representation, express or implied, with regard to the accuracy of the information contained in this book and cannot accept any legal responsibility or liability for any errors or omissions that may be made.

Typesetting: Camera ready by author

69/3830-543210 Printed on acid-free paper SPIN 10834574

# Preface

Linear control systems with known parameter values are usually described by state space or transfer function models. Deviations from the nominal parameter values are then frequently modelled in an assumed generic structure. Examples are multiplicative perturbations with arbitrary phase and bounded gain or norm bounded perturbations of state space models. The advantage of these approaches is that one can develop generic design procedures and software without restrictions to specific classes of plants.

In many applications, however, more specific knowledge is available on how uncertain real physical parameters (e.g. mass, velocity, friction coefficient, geometry etc.) enter a well-known model structure. Even a large uncertainty of a few such essential parameters can frequently be tolerated by a fixed-gain or gain-scheduled controller, if it is tailored to the structured parameters. If they are embedded, however, in a larger number of generically structured or complex-valued perturbations, then only small admissible parameter uncertainties result. In order to get non-conservative results, we focus on essential parameters entering a known structure. Additionally, high-frequency unstructured model uncertainty and sensor noise are considered by frequency domain specifications on Bode magnitude plots of different sensitivity functions.

The approach of the book is graphics-oriented, and takes advantage of the fact that the engineer nowadays has increasingly powerful computer graphics on his or her desk. Optimization-based approaches are not covered. We believe that optimization should be done at a higher system level where many trade-offs between different specifications for the overall system are required. At the low robust feedback design level, the flexibility for such trade-offs should be preserved, e.g. by admissible solution sets.

In this second edition of *Robust Control*, the material is arranged such that the reader is first introduced to the parameter space approach. Once the limitation to a few uncertain plant parameters or a few free controller parameters in a design step is accepted, the reader is rewarded by easy-to-interpret figures that make design conflicts transparent, and by non-conservative mapping of specifications and parameter ranges. Analysis methods for many uncertain parameters in specifically restricted structures (affine, tree-structured) are postponed to later chapters. New results for the design of PID-controllers and frequency domain specifications are included as well as many new applications in the case study chapters. Compared to the first edition of 1993, the new edition is essentially completely rewritten and augmented by contributions of new coauthors.

## Contents of the Chapters

Chapter 1 introduces an idealized crane example to illustrate analytical state space and transfer function modelling of a plant with uncertain physical parameters  $\mathbf{q}$  bounded by an operating domain  $Q$ . Further, it reviews the notions of robust controllability and observability and shows that for robust observability of the crane a sensor for the rope angle is necessary in addition to a position sensor. The relations between open-loop and closed-loop parametric characteristic polynomials via state and output feedback are established. A parametric Hurwitz-stability analysis for the crane yields a robust transparent linear controller structure with only three free controller parameters  $k_1, k_2, k_3$  for pendulum damping and crab motion stabilization. The crane is a representative for two-mass systems like the inverted pendulum, two coupled vehicles, a robot joint, an aircraft rudder deflection. At the end of Chapter 1, we have a controller structure and a characteristic polynomial  $p(s, \mathbf{q}, \mathbf{k})$  with uncertain plant parameters  $\mathbf{q}$  and undetermined controller parameters  $\mathbf{k}$ . For Chapters 2 to 4 and 8 to 11, this parametric polynomial serves as the primary interface between the engineering problem and the mathematical problem of root locations of parametric polynomials.

Chapter 2 introduces the concepts of critical stability conditions, fictitious boundaries, active boundaries and non-active boundaries, all arising from the last Hurwitz determinant. Also, the distinction between real root boundaries (RRB), complex root boundaries (CRB) and infinite root boundaries (IRB) is introduced. The boundary crossing concept of Frazer and Duncan then leads to the more transparent parameter space approach. The pole placement technique allows a sequential shifting of pole pairs in invariance planes as a strategy element for stepwise improvement of eigenvalue patterns. Next, the case for the parameter space mapping equations being singular, giving rise to singular frequencies, is discussed. The singular frequencies provide boundaries between parameter ranges in which the resulting stability regions are topographically similar. The properties of singular frequencies are exploited for the design of PID-controllers, where for fixed proportional gain the stability regions are convex polygons.

Chapter 3 introduces the basic ideas of the parameter space approach for design and analysis of robust control systems based on eigenvalue specifications. First, some relations between pole and zero locations and time responses are reviewed. The desirable  $\Gamma$ -region for the closed-loop poles is used to define  $\Gamma$ -stability with a boundary  $\partial\Gamma(\alpha), \alpha \in [\alpha^-; \alpha^+]$ . The crane example illustrates that gridding of admissible parameter regions may be useful - although computationally inefficient - for analysis of a given polynomial family. It does not give directions, however, for design steps that improve the system. Design for two controller parameters at a time can be done by mapping  $\partial\Gamma$  for some representative operating conditions, e.g. the vertices of the operating domain  $Q$ . The set of all simultaneously stabilizing regions for the representatives is then the intersection of the stabilizing regions for the representatives. A controller from this intersection is chosen and the resulting closed-loop system is analyzed by mapping  $\Gamma$  into a plant parameter plane (e.g. load mass and rope length of the crane). This analysis shows if the entire operating domain  $Q$  is  $\Gamma$ -stabilized, not only the representatives. Also, a gain-scheduling approach for measured rope length is illustrated. The migration of eigenvalues under continuous controller parameter changes is discussed. It yields a one-to-one correspondence of open-loop and closed-loop eigenvalues as long as

no branching points have been crossed. Finally, a simple example shows that controllability and observability of each plant representative does not guarantee that there exists a simultaneously stabilizing controller. This is a fundamental difference to controller design for a nominal plant.

While the second and third chapters give the motivation for studying the parameter space approach, Chapter 4 deals with the mathematical generation of the mapping equations. First, the boundary of the  $\Gamma$ -stable region is parameterized as  $\partial\Gamma(\alpha)$ ,  $\alpha \in [\alpha^-; \alpha^+]$ , where the scalar  $\alpha$  plays the same role as the frequency  $\omega$  for Hurwitz-stability boundaries. The polynomial  $p(s, \mathbf{q})$  has a root at  $\alpha = \alpha^*$  on  $\partial\Gamma = \sigma(\alpha) + j\omega(\alpha)$  if and only if both the real and the imaginary parts, of  $p(\sigma(\alpha^*) + j\omega(\alpha^*), \mathbf{q})$  vanish for some admissible  $\mathbf{q} \in Q$ . Instead of real and imaginary part two linear combinations thereof are used that can be generated by a simple recursion formula. The resulting equation has the form  $\mathbf{D}(\alpha)\mathbf{a}(\mathbf{q}) = \mathbf{0}$ , where  $\mathbf{D}(\alpha)$  is a  $2 \times (n + 1)$  matrix and  $\mathbf{a}(\mathbf{q})$  is the coefficient vector of the closed-loop characteristic polynomial. If  $\alpha$  is eliminated from these two equations, then a Hurwitz-type algebraic criterion for  $\Gamma$ -stability is obtained. It is very complicated, however. For the parameter space mapping, the two equations are solved, e.g. for  $q_1(\alpha), q_2(\alpha)$  that generate the boundary in the  $(q_1, q_2)$ -plane for a sweep over  $\alpha$ . The concept of singular frequencies is generalized to the boundary  $\partial\Gamma$  and is used for the design of  $\Gamma$ -stabilizing PID-controllers yielding closed-loop poles in a shifted left half plane or in a circle. An example with bilinear coefficient function  $\mathbf{a}(\mathbf{q})$  introduces us to the treatment of non-linear parameter dependencies by the parameter space approach. An example with complicated polynomial coefficient functions shows this particular strength of the parameter space approach. The bilinear example illustrates that for non-linear coefficient functions in  $\mathbf{a}(\mathbf{q})$ , the worst case operating condition is not necessarily on the boundary of the operating domain, but may be an interior point. A Jacobian condition is introduced to identify the interior candidates for the worst case. The resultant method that is used here is described in Appendix A. A short discussion of extensions to higher dimensional parameter spaces concludes the chapter.

Chapter 5 now extends the scope beyond the characteristic polynomial as the interface between engineering systems and their mathematical robustness analysis and design. An introductory example illustrates that  $\Gamma$ -stability does not always imply good gain and phase margins. Therefore,  $\Theta$ -stability is defined to guarantee safety margins for Nyquist plots from the critical point - 1 and from negative-inverse describing functions. Tangent and point conditions yield the boundaries in  $\mathbf{q}$ -space for which  $\Theta$ -boundaries are crossed. Similar conditions arise when a Popov plot does not admit a desired sector for the non-linearity.  $\mathcal{B}$ -stability refers to bounds on Bode magnitude plots. Again, boundaries occur for tangent and point conditions. Mathematically, these boundary conditions lead to two equations  $p_1(\omega, q_1, q_2) = 0, p_2(\omega, q_1, q_2) = 0$  that are similar to the real and imaginary part of a polynomial. Finally, in Chapter 5 the multi-input, multi-output (MIMO) case is reduced to the same type of mapping condition. In particular, the  $H_2$  and  $H_\infty$  conditions are treated.

Chapters 6 and 7 illustrate the combined use of the tools in case studies. Chapter 6 introduces us to the lateral, yaw and roll dynamics of car steering. The essential uncertainty is the lateral force between tire and road. The structure of the mathematical

model allows a robust unilateral decoupling such that the lateral acceleration becomes independent of the yaw rate. In driver assistance systems, control of the lateral acceleration for track following is left to the driver, while the yaw motion is automatically controlled. Automatic car steering systems take over both tasks. The ideal concept of skidding avoidance is based on additional rear wheel steering. If that is not available, then several trade-offs must be made. In rollover avoidance, the uncertain height of the center of gravity poses a robustness problem. Chapter 7 contains three case studies in flight control. The first one directly transfers the above robust decoupling concept to an aircraft in an engine fault situation. Common to both problems is that the yaw disturbance causes large yaw motions followed by overreaction of the driver or pilot. In the case of the aircraft, the robust automatic control system allows a significant weight reduction of the vertical fin. The other two case studies deal with aircraft stabilization and control of the short-period longitudinal mode. First,  $\Gamma$ -specifications are used, then  $B$ -stability is specified and achieved over a large operating domain.

In Chapter 8, the value set approach is presented that is particularly suited to the robustness analysis of polynomials with many uncertain parameters. However, there are restrictions on the kind of coefficient functions that can be handled. A common basis is the Mikhailov plot  $p(j\omega)$  for Hurwitz-stability, which blows up to a family of plots for uncertain  $\mathbf{q} \in Q$ , where the operating domain  $Q$  is a hyperrectangle ( $Q$ -box). This Mikhailov set must contain one stable polynomial and it must not contain the origin of the complex  $p(j\omega)$ -plane. The zero exclusion condition is used in Chapter 8 for proofs of the Kharitonov and edge theorems. The Kharitonov theorem applies to interval polynomials and requires stability of, at most, four extremal polynomials. The edge theorem applies to polynomials with affine coefficient functions and requires stability tests for edges of the  $Q$ -box. An edge may be checked for stability by the Bialas test. Also, the singularity of value sets is analyzed. The construction of Mikhailov sets is done for fixed frequencies, i.e. only the scalar  $\omega$  is gridded and not the higher dimensional  $Q$ -box. For linear coefficient functions, the value set for fixed frequency is a parpolygon (polygon with pairwise parallel edges) and the origin can enter only through the edges. The edge result also holds for  $\Gamma$ -stability. In this case, it is more efficient to plot a root locus for each edge rather than generalizing the Bialas test.

In Chapter 9, the value set approach is applied to non-linear coefficient functions. A warning example at the beginning shows that unstable islands, even isolated unstable points, can occur due to a bilinear term in one of the coefficients. Thus, simple general results, as in the linear case, cannot be expected in the non-linear case. However, useful tools for the computer-aided rendering of value sets are developed. For multilinear coefficient functions, the mapping theorem by Desoer provides a simple sufficient stability condition. It says that the convex hull of the value set is generated by the images of the vertices of the  $Q$ -box. It restricts the frequency band in which the actual value set must be constructed. Necessary and sufficient stability tests for multilinear (and some polynomial) coefficient functions can be performed if the uncertain parameters enter in form of a tree-structure into the characteristic polynomial  $p(s, \mathbf{q})$ , i.e.  $p(s, \mathbf{q})$  may be expressed as a sum of subpolynomials, which in turn may be products of sub-subpolynomials, etc. until basic polynomials are reached. The sequential construction of the value set becomes possible, even for many uncertain parameters, if each uncer-

tain parameter enters only into one of the basic polynomials. If such a tree-structure exists, then it can be exploited both for Hurwitz-stability and for  $\Gamma$ -stability analysis. Tree-structures arise naturally, for example, in modelling of mass-spring-damper systems and they are preserved under feedback. Also, given polynomials may be analyzed for tree-structures. A useful application is the calculation of the “stability profile”, that is, the right hand boundary of the root set.

Chapter 10 introduces the stability radius as a scalar measure of vicinity to instability. Essentially, a ball or box around a test point in parameter space is blown up until it hits the stability boundary. Tsyplkin and Polyak use a frequency-dependent distance function. Also, an algebraic formulation is given for polynomial coefficient functions.

In Chapter 11, the previous results are adapted as far as possible to sampled-data systems. A problem in the exact treatment here arises, because physical parameters enter exponentially into the polynomial coefficients. A good approximation can be achieved, however, by a Poisson series approach.

Appendix A covers some mathematical background material on polynomials, polynomial equations and conic sections. Appendix B gives a short introduction to the software tool PARADISE (PArametric Robustness Analysis and Design Interactive Software Environment). The latest release of the software can be downloaded from [www.robotic.dlr.de/control/paradise](http://www.robotic.dlr.de/control/paradise).

The bibliography shows that many foundations of the methods of robust control have been laid over a long period of time by scientists in Russia and other eastern countries (Bialas, Gantmakher, Kharitonov, Mikhailov, Mitrović, Neimark, Polyak, Popov, Šiljak, Tsyplkin, Vishnegradski and many more). Only in the last decades have these contributions been recognized and further developed in the western literature (Anderson, Barmish, Bartlett, Bhattacharyya, Dasgupta, Desoer, Fam, Hollot, Horowitz, Jury, Mansour, Meditch, Tempo and many more).

## General Remarks

The prerequisite for the reader is an undergraduate course in feedback control systems. We try to keep the mathematics simple. The book is suited for an advanced undergraduate level or for a first graduate level course in robust control. In fact, the material was selected and used for such courses at the University of California, Irvine, at the Technische Universität München and in several short courses. It was also used in continuing education courses at the Carl-Cranz Gesellschaft (CCG), Oberpfaffenhofen, for participants from industry.

For the purpose of such courses, a very restrictive selection had to be made from the large and rapidly growing literature on robust control. Therefore, many important contributions and alternative approaches could not be mentioned. Some cross-references are given in the form of remarks. Remarks also indicate possible generalizations, open problems, and other supplements that are not prerequisites for understanding the following sections. The beginner should ignore all remarks, they are intended for the advanced reader.

In the examples with physical parameters, units are given in brackets, e.g. [m] for meter (to be distinguished from the symbol  $m$  for mass) or [s] for seconds (to be distinguished from the complex variable  $s$  of Laplace transforms). In calculations, the units are omitted. We use the following units:

Physical Variable	Symbol	Unit
Length	$\ell$	meter [m]
Time	$t$	second [s]
Mass	$m$	kilogram [kg]
Moment of inertia	$J$	[kg · m <sup>2</sup> ]
Force	$F$	newton [N] = [kg · m/s <sup>2</sup> ]
Torque	$M$	newton-meter [Nm]
Velocity	$v$	[m/s]
Acceleration	$a$	[m/s <sup>2</sup> ]
Angles	$\alpha, \beta, \dots$	radian [rad]
Frequency	$\omega$	[rad/s]
Flight altitude	$h$	foot [ft] = 0.3048 meter
Mach number	$M$	ratio of $v$ and velocity of sound, dimensionless

### Acknowledgements

The authors like to thank the coauthors of the first edition of this book (1993), who are working in other fields now. Material written by Andrew Bartlett, Wolfgang Sienel and Reinhold Steinhauser has been integrated in the new context. Thanks also to Jessica Laskey for typing part of the manuscript and to Stefan von Dombrowski for his technical support.

Oberpfaffenhofen

June 2002

Jürgen Ackermann

Paul Blue

Tilman Bünte

Levent Güvenç

Dieter Kaesbauer

Michael Kordt

Michael Muhler

Dirk Odenthal

# Contents

<b>1</b>	<b>Parametric Plants and Controllers</b>	<b>1</b>
1.1	State Space Model, Linearization, Eigenvalues . . . . .	2
1.2	The Leverrier-Faddejew Algorithm . . . . .	7
1.3	Transfer Function . . . . .	8
1.4	Robust Controllability, Observability, Feedback Structures . . . . .	12
1.5	Output Feedback, Closed-loop Characteristic Polynomial . . . . .	14
1.6	Hurwitz-stability, Stabilizing Controller Parameters . . . . .	19
1.7	Controller Structures for Partially Known Inputs . . . . .	24
<b>2</b>	<b>Hurwitz-stability Boundary Crossing and Parameter Space Approach</b>	<b>29</b>
2.1	Critical Stability Conditions . . . . .	29
2.2	The Parameter Space Approach . . . . .	33
2.3	Pole Placement . . . . .	37
2.4	Sequential Pole Shifting . . . . .	40
2.5	Singular Frequencies . . . . .	44
2.6	Hurwitz-stability Regions for PID-controllers . . . . .	47
2.7	Hurwitz-stability Regions for a Compensator or Plant Subpolynomial .	56
<b>3</b>	<b>Eigenvalue Specifications</b>	<b>59</b>
3.1	Poles, Zeros and Step Responses . . . . .	59
3.2	Root Sets, Gamma-stability . . . . .	66
3.3	Physical Meaning of Closed-loop Poles . . . . .	73
3.4	Remarks on Existence of Robust Controllers . . . . .	74
3.5	Further Potential of the Parameter Space Approach . . . . .	76
<b>4</b>	<b>Gamma-boundary Mapping into Parameter Space</b>	<b>80</b>
4.1	Algebraic Problem Formulation . . . . .	81
4.2	Parameter Space Mapping . . . . .	81
4.3	Generalized Singular Frequencies . . . . .	90
4.4	Gamma-stable PID-control . . . . .	92
4.5	Non-linear Coefficient Functions . . . . .	96

<b>5 Frequency Domain Analysis and Design</b>	104
5.1 Frequency Loci Specifications (Theta-stability) . . . . .	104
5.2 Mapping of Frequency Loci Margins into Parameter Space . . . . .	121
5.3 Frequency Response Magnitude Specifications (Beta-stability) . . . . .	131
5.4 Mapping of Frequency Response Magnitude Specifications into Parameter Space . . . . .	151
5.5 MIMO Systems . . . . .	158
<b>6 Case Studies in Car Steering</b>	171
6.1 Tires, Braking, and Steering . . . . .	171
6.2 The Two Steering Tasks . . . . .	177
6.3 The Non-linear Single-track Model and its Robust Unilateral Decoupling . . . . .	180
6.4 The Linearized Single-track Model . . . . .	192
6.5 Linear Analysis of Robust Decoupling . . . . .	206
6.6 Skidding Avoidance Based on Robust Decoupling . . . . .	215
6.7 Skidding Avoidance Based on the Disturbance Observer . . . . .	223
6.8 Rollover Avoidance . . . . .	238
6.9 Patents . . . . .	272
6.10 Automatic Car Steering . . . . .	272
<b>7 Case Studies in Flight Control</b>	286
7.1 Aircraft Load Alleviation in case of an Engine Out by Robust Yaw-lateral Decoupling . . . . .	287
7.2 Robust and Fault-tolerant Gamma-stabilization of an F4-E . . . . .	303
7.3 Large Envelope Flight Control of a High Performance Aircraft . . . . .	318
<b>8 Robustness Analysis by Value Sets</b>	334
8.1 Mikhailov Plot . . . . .	334
8.2 Value Sets and Zero Exclusion . . . . .	338
8.3 Interval Polynomials, Kharitonov Theorem . . . . .	341
8.4 Affine Coefficients: Edge Theorem . . . . .	349
8.5 Edge Theorem for Gamma-stability . . . . .	356
8.6 Singularity of Value Sets . . . . .	360
<b>9 Value Sets for Non-linear Coefficient Functions</b>	362
9.1 A Warning Example . . . . .	362
9.2 Desoer Mapping Theorem . . . . .	367
9.3 Tree-structured Value Set Construction . . . . .	370
9.4 Computer-aided Execution of Value Set Operations . . . . .	378
9.5 Tree-structured Transfer Functions . . . . .	382
9.6 The Stability Profile . . . . .	389
9.7 Synopsis of Parametric Robustness Analysis . . . . .	391
<b>10 The Stability Radius</b>	395
10.1 Tsyplkin-Polyak Loci . . . . .	396
10.2 Affine Dependence: The Largest Hypersphere in Parameter Space . . . . .	404

10.3 Polynomial Dependence . . . . .	409
<b>11 Robustness of Sampled-data Control Systems</b>	<b>417</b>
11.1 Plant and Controller Discretization . . . . .	418
11.2 Discrete-time Controllers . . . . .	420
11.3 Eigenvalue Specifications . . . . .	421
11.4 Classical Stability Tests . . . . .	425
11.5 Edge Test . . . . .	437
11.6 Construction of Value Sets . . . . .	439
11.7 Real Radius of Stability . . . . .	440
11.8 Single-loop Feedback Structures . . . . .	440
11.9 Circle Stability . . . . .	444
<b>A Polynomials and Polynomial Equations</b>	<b>448</b>
<b>B PARADISE: Parametric Robustness Analysis and Design Interactive Software Environment</b>	<b>461</b>
<b>Bibliography</b>	<b>465</b>
<b>Index</b>	<b>477</b>

# 1 Parametric Plants and Controllers

A mathematical model for plant dynamics is the basis for analysis and design of control systems. For linear time-invariant systems, we commonly have a state space model of the form

$$\begin{aligned}\dot{\mathbf{x}}(t) &= \mathbf{A}\mathbf{x}(t) + \mathbf{B}\mathbf{u}(t), \\ \mathbf{y}(t) &= \mathbf{C}\mathbf{x}(t),\end{aligned}\tag{1.0.1}$$

with  $\mathbf{u}$  the vector of input signals (manipulated variables), the state vector  $\mathbf{x}$ , and the vector of output signals  $\mathbf{y}$  (performance variables). The output signals are often comprised of those variables that are measured and hence available for feedback.

Another commonly used form of the model can be obtained by the Laplace transformation of (1.0.1)

$$\begin{aligned}s\mathbf{x}(s) - \mathbf{x}(t = 0) &= \mathbf{A}\mathbf{x}(s) + \mathbf{B}\mathbf{u}(s), \\ \mathbf{y}(s) &= \mathbf{C}\mathbf{x}(s).\end{aligned}\tag{1.0.2}$$

Solving for  $\mathbf{x}(s)$  and premultiplying by  $\mathbf{C}$  gives the transformed output vector

$$\mathbf{y}(s) = \mathbf{C}(s\mathbf{I} - \mathbf{A})^{-1}\mathbf{x}(t = 0) + \mathbf{C}(s\mathbf{I} - \mathbf{A})^{-1}\mathbf{B}\mathbf{u}(s)\tag{1.0.3}$$

with the transfer function matrix

$$\mathbf{G}(s) := \mathbf{C}(s\mathbf{I} - \mathbf{A})^{-1}\mathbf{B}.\tag{1.0.4}$$

For zero initial conditions,  $\mathbf{x}(t = 0) = \mathbf{0}$ ,

$$\mathbf{y}(s) = \mathbf{G}(s)\mathbf{u}(s).\tag{1.0.5}$$

*Remark 1.1*

The plant may have a direct throughput term  $\mathbf{D}$ , i.e.  $\mathbf{y}(t) = \mathbf{C}\mathbf{x}(t) + \mathbf{D}\mathbf{u}(t)$  and  $\mathbf{G}(s) := \mathbf{C}(s\mathbf{I} - \mathbf{A})^{-1}\mathbf{B} + \mathbf{D}$ , for example, an accelerometer output  $\mathbf{y}$  of a system with force input  $\mathbf{u}$ . Realistically, however, we would have to include the low-pass dynamics of the force generating motor and we are back to the system (1.0.1) without throughput term.  $\square$

A state space model ( $\mathbf{A}, \mathbf{B}, \mathbf{C}$ ) or a transfer function model  $G(s)$  can be determined by different approaches. The first possibility is called *input-output modelling*. In this approach, the model is obtained from experiments on the plant, which is treated like a *black box*. During the experimentation, the measured signals  $\mathbf{u}(t)$  and  $\mathbf{y}(t)$  are recorded. These data are then processed by identification algorithms to derive a system model. The second approach is called *analytical modelling*. In this approach, the model structure is derived from first principles of physics. A model typically depends on some physical parameters; their values are uncertain between known lower and upper bounds.

In this book the second approach, analytical modelling, is assumed. Its advantage is that the controller can be designed before the plant is fully operational and available for experiments (i.e. cannot be drastically changed). Thus, a “concurrent engineering” of plant and controller becomes feasible. Also, safety-critical experiments with the uncontrolled plant are avoided. For a space vehicle, such experiments would be impossible. Practically, we may combine input-output modelling and analytical modelling, e.g. some submodels of system components may be obtained by experiments with the separated subsystem or by numerical approximation as in finite element models. Other subsystem models can be obtained by analytical modelling. Eventually, all subsystems are integrated in an overall system. Examples of system modelling can be found in [66], [165] and also in case studies in Chapters 6 and 7 of this book.

This chapter begins with an idealized crane example to illustrate analytical state space and transfer function modelling of a system with uncertain physical parameters. Further, it reviews the notions of controllability and observability in the context of uncertain parameters. For the crane example, this leads to a robust feedback structure with two sensors, Figure 1.6. The relations between open-loop and closed-loop characteristic polynomials via state and output feedback are established. A parametric Hurwitz-stability analysis finally yields a robust linear controller structure with three free controller parameters, Figure 1.8. Control system structures for individual requirements regarding the inputs reference signal, plant disturbance and sensor noise are discussed in Section 1.7.

## 1.1 State Space Model, Linearization, Eigenvalues

### *Example 1.2 (Crane)*

Consider the crane in Figure 1.1. The task of the crane or loading bridge is, for example, to load containers into a ship. First, the load mass is only the empty hook. The hook must come to rest above the container. Sometimes, someone helps to damp the swaying pendulum and to fix the hook. In our approach, the placement of the hook above the known position of the container and the damping of the pendulum shall be performed automatically. After lifting the container, it is transported for some distance to the vicinity of the hatch of the ship. This motion can be commanded by feedforward

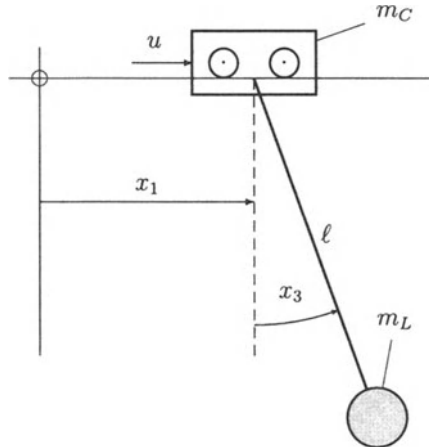


Figure 1.1. Crane

control considering the limited motor force at the crab and safety constraints. Feedback control is needed again in order to position the container above the hatch and to damp the motion. It must be almost at rest before it can be lowered into the ship. In this application, the load mass varies widely between the weight of the empty hook and the maximum load that the crane can carry. Also, the rope length may vary (even more for a construction crane). In contrast, the mass of the crab varies very little (e.g. depending on the weight of the crane operator sitting in the gantry). Many parameters may be uncertain; it is important to look only at the essential ones in control system design. The other ones may be analyzed later.

In common design approaches, a linearized model is used for controller design. It models small motions for positioning the hook with or without the container with sufficient accuracy. It is important that the controller is designed such that the assumptions made in linearization are not violated during the operation of the crane.

The input signal is the force  $u$  that accelerates the crab. The crab mass is  $m_C$ . Further parameters are rope length  $\ell$ , load mass  $m_L$ , and gravity acceleration  $g$ . The position of the crab is  $x_1$  and its velocity  $\dot{x}_1 =: x_2$ , the rope angle is  $x_3$ , and the angular velocity  $\dot{x}_3 =: x_4$ .

The following assumptions are made for simplification of modelling:

- Dynamics and non-linearity of the driving servo motor are neglected. This assumption makes sense only if the controller design guarantees that  $|u|$  and  $|\dot{u}|$  are not excessively large.
- The crab moves along the track without friction.
- The rope has no mass and no elasticity.
- There is no damping of the pendulum (e.g. from air drag).
- The parameters rope length  $\ell$  and load mass  $m_L$  are constant during each operation of the loading bridge.

The two masses of crab and load are coupled by the longitudinal rope force  $F$ . The equations of motion are

$$\text{crab, horizontal} \quad m_C \ddot{x}_1 = u + F \sin x_3,$$

$$\text{load, horizontal} \quad m_L \frac{d^2(x_1 + \ell \sin x_3)}{dt^2} = -F \sin x_3,$$

$$\text{load, vertical} \quad m_L \frac{d^2(\ell \cos x_3)}{dt^2} = -F \cos x_3 + m_L g.$$

Elimination of  $F$  yields

$$\begin{aligned} m_C \ddot{x}_1 + m_L \frac{d^2(x_1 + \ell \sin x_3)}{dt^2} &= u, \\ m_L \frac{d^2(\ell \cos x_3)}{dt^2} \sin x_3 - m_L \frac{d^2(x_1 + \ell \sin x_3)}{dt^2} \cos x_3 &= m_L g \sin x_3, \end{aligned}$$

where

$$\begin{aligned} \frac{d^2(x_1 + \ell \sin x_3)}{dt^2} &= \ddot{x}_1 + \ell \ddot{x}_3 \cos x_3 - \ell \dot{x}_3^2 \sin x_3, \\ \frac{d^2(\ell \cos x_3)}{dt^2} &= -\ell \ddot{x}_3 \sin x_3 - \ell \dot{x}_3^2 \cos x_3, \end{aligned}$$

resulting in the two non-linear second order differential equations

$$\begin{aligned} (m_L + m_C) \ddot{x}_1 + m_L \ell (\ddot{x}_3 \cos x_3 - \dot{x}_3^2 \sin x_3) &= u, \\ m_L \ddot{x}_1 \cos x_3 + m_L \ell \ddot{x}_3 &= -m_L g \sin x_3. \end{aligned} \tag{1.1.1}$$

For deriving a state space description, the scalar differential equations must be solved for the highest derivatives  $\ddot{x}_1$  and  $\ddot{x}_3$ . Rewrite (1.1.1) as

$$\begin{bmatrix} m_L + m_C & m_L \ell \cos x_3 \\ m_L \cos x_3 & m_L \ell \end{bmatrix} \begin{bmatrix} \ddot{x}_1 \\ \ddot{x}_3 \end{bmatrix} = \begin{bmatrix} m_L \ell \dot{x}_3^2 \sin x_3 + u \\ -m_L g \sin x_3 \end{bmatrix}. \tag{1.1.2}$$

The determinant of the matrix on the left hand side is  $m_L \ell (m_C + m_L \sin^2 x_3)$ . It vanishes for  $m_L = 0$  or  $\ell = 0$ . In these two cases, the system degenerates to a second order system because the system has only one degree of freedom of the single mass. It is a standing assumption in all following discussions of crane control that  $m_L > 0$ ,  $m_C > 0$  and  $\ell > 0$ . Then

$$\begin{aligned} \ddot{x}_1 &= f_1(x_3, x_4, u), \\ \ddot{x}_3 &= f_2(x_3, x_4, u), \end{aligned} \tag{1.1.3}$$

with

$$f_1(x_3, x_4, u) := \frac{u + (g \cos x_3 + \ell x_4^2) m_L \sin x_3}{m_C + m_L \sin^2 x_3},$$

$$f_2(x_3, x_4, u) := -\frac{u \cos x_3 + (g + \ell x_4^2 \cos x_3) m_L \sin x_3 + g m_C \sin x_3}{\ell (m_C + m_L \sin^2 x_3)}.$$

With the state vector

$$\mathbf{x} = \begin{bmatrix} x_1 \\ x_2 \\ x_3 \\ x_4 \end{bmatrix} = \begin{bmatrix} x_1 \\ \dot{x}_1 \\ x_3 \\ \dot{x}_3 \end{bmatrix} = \begin{bmatrix} \text{crab position} \\ \text{crab velocity} \\ \text{rope angle} \\ \text{rope angle rate} \end{bmatrix}, \quad (1.1.4)$$

the non-linear state space model is written as

$$\dot{\mathbf{x}} = \mathbf{f}(\mathbf{x}, u) = \begin{bmatrix} x_2 \\ f_1(x_3, x_4, u) \\ x_4 \\ f_2(x_3, x_4, u) \end{bmatrix}. \quad (1.1.5)$$

This state space model can be used for simulations of the crane motion by numerical integration. For this purpose, numerical values for the parameters  $g, \ell, m_L$ , and  $m_C$ , an initial condition for the state  $\mathbf{x}(t = 0)$ , and an input function  $u(t)$  must be chosen.

For controller design, a linearized model is better suited, therefore the non-linear model (1.1.5) is linearized for small deflection angle  $x_3$ , and small angular velocity  $x_4$ . Setting

$$\cos x_3 \approx 1, \sin x_3 \approx x_3, \sin^2 x_3 \approx 0, x_4^2 \approx 0,$$

it is easy to derive the following linear state space model:

$$\dot{\mathbf{x}} = \mathbf{A}\mathbf{x} + \mathbf{b}u,$$

$$\mathbf{A} = \begin{bmatrix} 0 & 1 & 0 & 0 \\ 0 & 0 & a_{23} & 0 \\ 0 & 0 & 0 & 1 \\ 0 & 0 & a_{43} & 0 \end{bmatrix}, \quad \mathbf{b} = \begin{bmatrix} 0 \\ b_2 \\ 0 \\ b_4 \end{bmatrix}, \quad (1.1.6)$$

$$a_{23} = \frac{m_L}{m_C}g, \quad b_2 = \frac{1}{m_C},$$

$$a_{43} = -\frac{(m_L + m_C)g}{m_C\ell}, \quad b_4 = -\frac{1}{m_C\ell}.$$

The characteristic polynomial of  $\mathbf{A}$

$$\begin{aligned} p_A(s) &= \det(s\mathbf{I} - \mathbf{A}) \\ &= s^2(s^2 - a_{43}) \\ &= s^2[s^2 + (1 + m_L/m_C)g/\ell] \end{aligned} \quad (1.1.7)$$

yields the parameter-independent eigenvalues

$$s_{1,2} = 0 \quad (1.1.8)$$

and the parameter-dependent eigenvalues

$$s_{3,4} = \pm j\sqrt{1 + m_L/m_C}\sqrt{g/\ell} \quad (1.1.9)$$

### Notation

In general, we write the open-loop characteristic polynomial as

$$p_0(s) = a_{00} + a_{01}s + \dots + a_{0n-1}s^{n-1} + a_{0n}s^n. \quad (1.1.10)$$

In the evaluation of  $p_A(s) = \det(s\mathbf{I} - \mathbf{A})$ , the polynomial arises in monic form, i.e.  $a_{0n} = 1$ . In parametric representation, it is sometimes convenient, however, to avoid rational coefficient functions like in (1.1.7) and to write the polynomial in the form

$$p_0(s) = \ell m_C p_A(s) = (m_C + m_L)gs^2 + \ell m_C s^4. \quad (1.1.11)$$

□

A polynomial may also be interpreted as a point in its coefficient space, i.e. we write

$$p_0(s) = \mathbf{a}^T \begin{bmatrix} 1 \\ s \\ \vdots \\ s^n \end{bmatrix}, \quad \mathbf{a}^T = [a_{00} \ a_{01} \ \dots \ a_{0n}], \quad (1.1.12)$$

and in the monic case

$$p_0(s) = [\hat{\mathbf{a}}^T \ 1] \begin{bmatrix} 1 \\ s \\ \vdots \\ s^n \end{bmatrix}, \quad \hat{\mathbf{a}}^T = [a_{00} \ a_{01} \ \dots \ a_{0n-1}]. \quad (1.1.13)$$

For uncertain parameters with lower and upper bounds, the following notation is introduced:

$$\begin{aligned} m_L &\in [m_L^-; m_L^+], \\ \ell &\in [\ell^-; \ell^+]. \end{aligned}$$

In a general context, the parameters are called  $q_1, q_2, \dots, q_\ell$  and they are written as a *plant parameter vector*

$$\mathbf{q} = \begin{bmatrix} q_1 \\ q_2 \\ \vdots \\ q_\ell \end{bmatrix}. \quad (1.1.14)$$

The plant parameter vector is bounded by an *operating domain*  $Q$ , which is typically a hyperrectangle

$$Q = \{\mathbf{q} | q_i \in [q_i^-; q_i^+], i = 1, 2, \dots, \ell\}. \quad (1.1.15)$$

Figure 1.2 illustrates the case for  $\ell = 2$ .

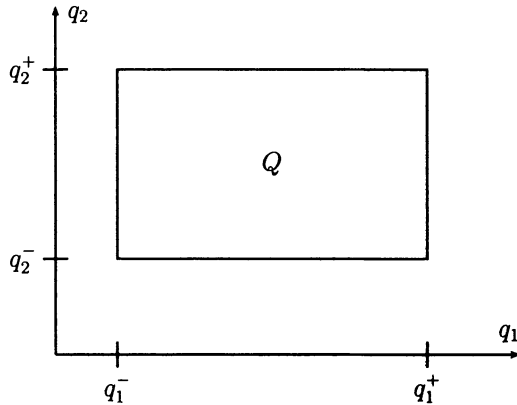


Figure 1.2. The plant parameter vector is bounded by an operating domain, i.e.  $\mathbf{q} \in Q$

The dependency of a state space model on the uncertain constant parameter vector  $\mathbf{q}$  is written in the general form

$$\begin{aligned}\dot{\mathbf{x}}(t) &= \mathbf{A}(\mathbf{q})\mathbf{x}(t) + \mathbf{B}(\mathbf{q})\mathbf{u}(t), \\ \mathbf{y}(t) &= \mathbf{C}(\mathbf{q})\mathbf{x}(t),\end{aligned}\tag{1.1.16}$$

and the notation for the  $\mathbf{q}$ -dependency of a transfer function model is

$$\mathbf{y}(s) = \mathbf{G}(s, \mathbf{q}) \mathbf{u}(s).\tag{1.1.17}$$

The set

$$\mathbf{G}(s, Q) = \{\mathbf{G}(s, \mathbf{q}) \mid \mathbf{q} \in Q\}\tag{1.1.18}$$

is called a *plant family*.

The *open-loop characteristic polynomial family* is defined by

$$P(s, Q) = \det(s\mathbf{I} - \mathbf{A}(\mathbf{q})) = \text{den}(\mathbf{G}(s, \mathbf{q}))\tag{1.1.19}$$

(“den” stands for “denominator of”). For the stability analysis, the closed-loop characteristic polynomial is of interest. It also involves controller parameters  $\mathbf{k}$ , which are here subsumed under the  $\mathbf{q}$ -parameters. The *root set* is denoted by

$$\text{Roots}[P(s, Q)] = \{s \mid p(s, \mathbf{q}) = 0 \text{ for any } \mathbf{q} \in Q\}.\tag{1.1.20}$$

## 1.2 The Leverrier-Faddejew Algorithm

For the calculation of the parametric transfer function matrix

$$\mathbf{G}(s, \mathbf{q}) = \mathbf{C}(\mathbf{q})[s\mathbf{I} - \mathbf{A}(\mathbf{q})]^{-1}\mathbf{B}(\mathbf{q}),\tag{1.2.1}$$

the *Leverrier-Faddejew algorithm* [94] is recommended. It calculates

$$\begin{aligned}(s\mathbf{I} - \mathbf{A})^{-1} &= \frac{\mathbf{D}(s)}{\det(s\mathbf{I} - \mathbf{A})}, \\ \mathbf{D}(s) &= \mathbf{D}_0 + \mathbf{D}_1 s + \dots + \mathbf{D}_{n-1} s^{n-1},\end{aligned}\tag{1.2.2}$$

$$\begin{aligned}a_{0n} &= 1, & \mathbf{D}_{n-1} &= \mathbf{I}, \\ a_{0n-1} &= -\frac{1}{1} \text{ trace } \mathbf{AD}_{n-1}, & \mathbf{D}_{n-2} &= \mathbf{AD}_{n-1} + a_{0n-1}\mathbf{I}, \\ a_{0n-2} &= -\frac{1}{2} \text{ trace } \mathbf{AD}_{n-2}, & \mathbf{D}_{n-3} &= \mathbf{AD}_{n-2} + a_{0n-2}\mathbf{I}, \\ &\vdots & &\vdots \\ a_{01} &= -\frac{1}{n-1} \text{ trace } \mathbf{AD}_1, & \mathbf{D}_0 &= \mathbf{AD}_1 + a_{01}\mathbf{I}, \\ a_{00} &= -\frac{1}{n} \text{ trace } \mathbf{AD}_0, & \mathbf{D}_{-1} &= \mathbf{AD}_0 + a_{00}\mathbf{I} = \mathbf{0}.\end{aligned}$$

The open-loop characteristic polynomial (1.1.10) is in its monic form, i.e.  $a_{0n} = 1$ . The trace of a matrix with elements  $a_{ij}$  is the sum of the elements  $a_{ii}$  in the main diagonal. The last equation  $\mathbf{D}_{-1} = \mathbf{0}$  serves as a check.

### Remark 1.3

The Leverrier-Faddejew algorithm is not recommended for numerical calculations where the checking matrix is not exactly zero and backwards iterations are needed to improve the accuracy. In the symbolic calculations considered here, the checking matrix  $\mathbf{D}_{-1}$  must be exactly zero.

□

## 1.3 Transfer Function

Substitute (1.2.2) into (1.2.1) to obtain the *transfer function matrix*

$$\mathbf{G}(s) = \frac{\mathbf{CD}_0\mathbf{B} + \mathbf{CD}_1\mathbf{Bs} + \dots + \mathbf{CD}_{n-1}\mathbf{Bs}^{n-1}}{\det(s\mathbf{I} - \mathbf{A})}.\tag{1.3.1}$$

Its  $ij$ -th element  $\mathbf{c}_i^T(s\mathbf{I} - \mathbf{A})^{-1}\mathbf{b}_j = n_{ij}(s)/\det(s\mathbf{I} - \mathbf{A})$  is the transfer function from input  $j$  to output  $i$ . It has the numerator degree  $m_{ij} = \deg n_{ij}(s) \leq n - 1$  and the *relative degree* is defined as

$$\varrho_{ij} := n - m_{ij}.\tag{1.3.2}$$

The relative degree cannot be reduced by feedback or feedforward compensation.

The relative degree is directly related to the initial response to a step input. For  $\varrho = 1$ , the step response starts at zero with non-zero slope, for  $\varrho = 2$  the initial slope is zero and the initial second derivative is non-zero. For a root locus, the relative degree of the open-loop system determines the directions of the asymptotes of the root locus branches that go to infinity. They occur under  $180^\circ/\varrho, 3 \cdot 180^\circ/\varrho, 5 \cdot 180^\circ/\varrho \dots$  with respect to the positive (negative) real axis for positive (negative) high-frequency loop-gain.

#### *Example 1.4 (Crane)*

For the vector of transfer functions from  $u$  to the state vector  $\mathbf{x}(s) = \mathbf{g}(s)u(s)$  of the crane, we get

$$\mathbf{g}(s) = (s\mathbf{I} - \mathbf{A})^{-1}\mathbf{b} = \frac{1}{m_C\ell p_A(s)} \begin{bmatrix} s^2\ell + g \\ s(s^2\ell + g) \\ -s^2 \\ -s^3 \end{bmatrix}. \quad (1.3.3)$$

Now consider three output variables: load position  $y_L$ , crab position  $y_C$ , and rope angle  $y_R$ , for which we write the respective transfer functions:

- i. Output load position (horizontal)  $y_L = x_1 + \ell \sin x_3 \approx x_1 + \ell x_3$ ,

$$g_L(s) = [1 \ 0 \ \ell \ 0] \mathbf{g}(s) = \frac{g}{s^2[m_C\ell s^2 + (m_L + m_C)g]}. \quad (1.3.4)$$

Its relative degree is  $\varrho_L = 4$ .

- ii. Output crab position  $y_C = x_1$ ,

$$g_C(s) = [1 \ 0 \ 0 \ 0] \mathbf{g}(s) = \frac{s^2\ell + g}{s^2[m_C\ell s^2 + (m_L + m_C)g]}. \quad (1.3.5)$$

The transfer function has parameter-dependent zeros at  $\pm j\sqrt{g/\ell}$ . The poles and zeros are shown in Figure 1.3. Note that  $\sqrt{1 + m_L/m_C} > 1$ , therefore the zero is closer to the origin than the pole. The relative degree is  $\varrho_C = 2$ .

- iii. Output rope angle  $y_R = x_3$ ,

$$g_R(s) = [0 \ 0 \ 1 \ 0] \mathbf{g}(s) = \frac{-1}{m_C\ell s^2 + (m_L + m_C)g}. \quad (1.3.6)$$

The relative degree is  $\varrho_R = 2$ . It is not changed by the cancellation of the double eigenvalue at  $s = 0$ . The transfer function is second order instead of fourth order. The cancellation occurs because the crab subsystem is not observable from the rope angle  $x_3$ . This can also be seen from the state space model (1.1.6). This

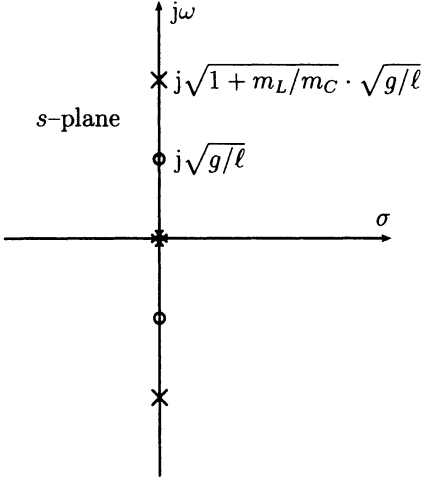


Figure 1.3. Poles and zeros of the transfer function  $g_C(s)$  from force  $u$  to crab position  $x_1$

model has the canonical form for separation of observable and non-observable subsystems as given by Kalman [123] and Gilbert [97]

$$\dot{\mathbf{x}} = \begin{bmatrix} 0 & 1 & | & 0 & 0 \\ 0 & 0 & | & a_{23} & 0 \\ - & - & - & - & - \\ 0^* & 0^* & | & 0 & 1 \\ 0^* & 0^* & | & a_{43} & 0 \end{bmatrix} \mathbf{x} + \begin{bmatrix} 0 \\ b_2 \\ - \\ 0 \\ b_4 \end{bmatrix} u, \quad (1.3.7)$$

$$y_R = \begin{bmatrix} 0^* & 0^* & | & 1 & 0 \end{bmatrix} \mathbf{x}.$$

The zeros with an asterisk are crucial; they indicate that the zero input dynamics of the crab (states  $x_1$  and  $x_2$ ) with arbitrary initial conditions have no influence on the deflection angle  $x_3$ . Physically, this means that the pendulum motion relative to the crab does not depend on the position or (constant) velocity of the crab. The transfer function (1.3.6) describes only the controllable and observable subsystem

$$\begin{bmatrix} \dot{x}_3 \\ \dot{x}_4 \end{bmatrix} = \begin{bmatrix} 0 & 1 \\ a_{43} & 0 \end{bmatrix} \begin{bmatrix} x_3 \\ x_4 \end{bmatrix} + \begin{bmatrix} 0 \\ b_4 \end{bmatrix} u, \quad (1.3.8)$$

$$y_R = \begin{bmatrix} 1 & 0 \end{bmatrix} \begin{bmatrix} x_3 \\ x_4 \end{bmatrix}.$$

Its eigenvalues at  $\pm j\sqrt{1+m_L/m_C}\sqrt{g/\ell}$  can be shifted by feedback of  $x_3$ . The unstable cancelled double eigenvalue at  $s = 0$  cannot be shifted by this feedback.

The model structure (1.3.7) is illustrated by the signal flow diagram in Figure 1.4. We

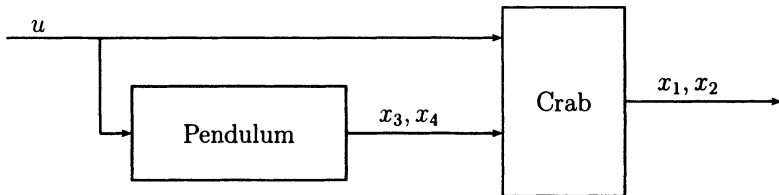


Figure 1.4. Signal flow diagram of the crane

will come back to the loading bridge in later sections. There we will consider that the load mass  $m_L$  and the rope length  $\ell$  are parameters with large uncertainty. The gravitational acceleration is assumed fixed at  $g = 10 \text{ [m} \cdot \text{s}^{-2}\text{]}$ .

In principle, the parameters  $m_L$  and  $\ell$  can be measured before each new operation of the crane. However, this would not be practical. In the context of robust control, the uncertain physical parameters are treated as fixed but unknown quantities for which only lower and upper bounds are known.

□

### Remark 1.5

A particularly simple form of the state space model arises for load coordinates  $x_L = x_1 + \ell x_3$ ,

$$\begin{bmatrix} \dot{y}_L \\ \ddot{y}_L \\ \dot{x}_3 \\ \dot{x}_4 \end{bmatrix} = \begin{bmatrix} 0 & 1 & 0 & 0 \\ 0 & 0 & -g & 0 \\ 0 & 0 & 0 & 1 \\ 0 & 0 & a_{43} & 0 \end{bmatrix} \begin{bmatrix} y_L \\ \dot{y}_L \\ x_3 \\ x_4 \end{bmatrix} + \begin{bmatrix} 0 \\ 0 \\ 0 \\ b_4 \end{bmatrix} u \quad (1.3.9)$$

Its signal flow diagram is shown in Figure 1.5. We do not use it here, because measuring

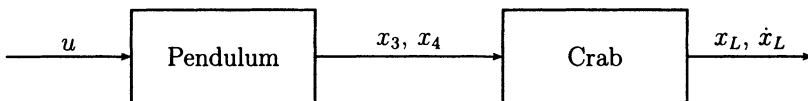


Figure 1.5. Cascade representation of crane

$x_1$  and/or  $\dot{x}_1$  is simpler than measuring  $x_L$  and/or  $\dot{x}_L$ , and the model structure is simple anyway. In Chapter 6 on car steering, we will use such unilateral decoupling structure and exploit exact cancellations as in (1.3.6).

□

## 1.4 Robust Controllability, Observability, Feedback Structures

It is assumed that the reader is familiar with the notions of controllability and observability of linear state space systems [122]; a convenient reference is [120]. In the parameter-dependent case, we are particularly interested in operating conditions  $\mathbf{q}$  for which such properties are lost. We review the controllability and observability conditions and apply them to the crane example.

Consider a plant family in state space notation

$$\begin{aligned}\dot{\mathbf{x}} &= \mathbf{A}(\mathbf{q})\mathbf{x} + \mathbf{B}(\mathbf{q})\mathbf{u}, \\ \mathbf{y} &= \mathbf{C}(\mathbf{q})\mathbf{x},\end{aligned}\tag{1.4.1}$$

with  $\mathbf{q} \in Q$ . The pair  $(\mathbf{A}(\mathbf{q}), \mathbf{B}(\mathbf{q}))$  is *robustly controllable* if

$$\text{rank} [\mathbf{B}(\mathbf{q}) \quad \mathbf{A}(\mathbf{q})\mathbf{B}(\mathbf{q}) \quad \dots \quad \mathbf{A}^{n-1}(\mathbf{q})\mathbf{B}(\mathbf{q})] = n \text{ for all } \mathbf{q} \in Q.\tag{1.4.2}$$

*Example 1.6*

The controllability matrix of the crane is, by (1.1.6),

$$\left[ \mathbf{b} \quad \mathbf{Ab} \quad \mathbf{A}^2\mathbf{b} \quad \mathbf{A}^3\mathbf{b} \right] = \begin{bmatrix} 0 & b_2 & 0 & b_4a_{23} \\ b_2 & 0 & b_4a_{23} & 0 \\ 0 & b_4 & 0 & b_4a_{43} \\ b_4 & 0 & b_4a_{43} & 0 \end{bmatrix}.\tag{1.4.3}$$

(For notational convenience, the dependency of all terms on  $\mathbf{q}$  is not explicitly indicated.) The determinant of the controllability matrix is

$$\det [\mathbf{b} \quad \mathbf{Ab} \quad \mathbf{A}^2\mathbf{b} \quad \mathbf{A}^3\mathbf{b}] = b_4^2(b_2a_{43} - b_4a_{23})^2.\tag{1.4.4}$$

It vanishes for

$$b_4 = -1/m_C\ell = 0,$$

and for

$$b_2a_{43} - b_4a_{23} = -g/m_C\ell = 0.$$

Controllability is lost only under zero gravity. □

The pair  $(\mathbf{C}(\mathbf{q}), \mathbf{A}(\mathbf{q}))$  is *robustly observable* if

$$\text{rank} \begin{bmatrix} \mathbf{C}(\mathbf{q}) \\ \mathbf{C}(\mathbf{q})\mathbf{A}(\mathbf{q}) \\ \vdots \\ \mathbf{C}(\mathbf{q})\mathbf{A}^{n-1}(\mathbf{q}) \end{bmatrix} = n \text{ for all } \mathbf{q} \in Q.\tag{1.4.5}$$

*Example 1.7*

For the crane, let

$$\mathbf{C} = \begin{bmatrix} 0 & 1 & 0 & 0 \\ 0 & 0 & 1 & 0 \\ 0 & 0 & 0 & 1 \end{bmatrix},$$

i.e. all state variables except  $x_1$  are measured.

$$\mathbf{CA} = \begin{bmatrix} 0 & 0 & a_{23} & 0 \\ 0 & 0 & 0 & 1 \\ 0 & 0 & a_{43} & 0 \end{bmatrix}.$$

In  $\mathbf{C}$ ,  $\mathbf{CA}$ , and also for all further  $\mathbf{CA}^i$ ,  $i = 2, 3, \dots$ , the first column is zero, i.e. the plant is not observable. More specifically, the crab position  $x_1$  is not observable and one of the eigenvalues at  $s = 0$  cannot be moved by output feedback  $u = -\mathbf{KCx}$ . For a stabilizing feedback structure, the crab position  $x_1$  must be measured and fed back.

The observability matrix for the crane with output  $y_1 = \mathbf{c}^T \mathbf{x} = [1 \ 0 \ 0 \ 0] \mathbf{x}$  is

$$\begin{bmatrix} \mathbf{c}^T \\ \mathbf{c}^T \mathbf{A} \\ \mathbf{c}^T \mathbf{A}^2 \\ \mathbf{c}^T \mathbf{A}^3 \end{bmatrix} = \begin{bmatrix} 1 & 0 & 0 & 0 \\ 0 & 1 & 0 & 0 \\ 0 & 0 & a_{23} & 0 \\ 0 & 0 & 0 & a_{23} \end{bmatrix}. \quad (1.4.6)$$

As  $m_L \rightarrow 0$ , then  $a_{23} = m_L g / m_C \rightarrow 0$  (see (1.1.6)) and the rank of the matrix drops from 4 to 2 at  $m_L = 0$ . For small  $m_L$ , the system is “almost non-observable”. Physically, this means: for the empty hook case, the horizontal force transmitted from the load to the crab is so small that its effect is hardly recognizable in the measurements of  $x_1$  and  $x_2$ .

For small load mass  $m_L$ , an additional sensor is necessary for damping the pendulum oscillations. Is it better to use a rate sensor for  $x_3$  or an acceleration sensor for  $x_4$ ?

i.  $x_3$

$$\begin{aligned} \mathbf{c}^T &= [0 \ 0 \ 1 \ 0], \\ \mathbf{c}^T \mathbf{A} &= [0 \ 0 \ 0 \ 1]. \end{aligned}$$

Observability is not parameter-dependent.

ii.  $x_4$

$$\begin{aligned} \mathbf{c}^T &= [0 \ 0 \ 0 \ 1], \\ \mathbf{c}^T \mathbf{A} &= [0 \ 0 \ a_{43} \ 1]. \end{aligned}$$

Observability is parameter-dependent. From  $a_{43} = -(m_L + m_C)/g/m_C \ell$ , it follows that observability becomes weak for large rope length  $\ell$ . For small rope length, the feedback of  $x_4$  is useful, however, as will be shown in Example 3.12.

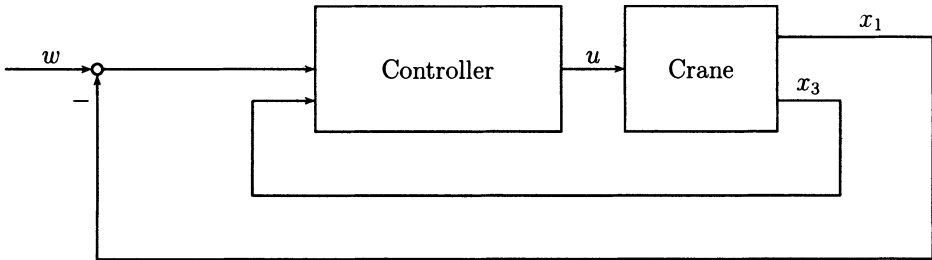


Figure 1.6. Feedback structure for robust controllability and observability

We conclude that feedback of  $x_3$  is better suited for robust control.

Robust controllability and observability is guaranteed by the feedback structure of Figure 1.6. At this point, the controller may still be linear or non-linear (e.g. adaptive). We will restrict the following discussion, however, to linear controllers.

Then, the next question is: what dynamical order of the controller is needed for stabilization? A classical approach would be to choose a second order controller that contains a reduced order observer for reconstructing  $x_2$  and  $x_4$  and state feedback. Such a controller has six parameters: two observer poles and four state feedback gains. These parameters must be chosen such that the sixth order closed-loop system is stable in the entire operating domain of the uncertain parameters. Problems of this approach are i) the mismatch between the actual plant and its nominal model in the observer, such that separation of state observation and pole placement does not hold, and ii) the state feedback design for stabilizing the six uncertain closed-loop eigenvalues is not transparent. In Section 1.6, Hurwitz-stabilization by state and output feedback will be treated. It leads to a simpler transparent controller structure with only three tuning parameters corresponding to three specifications for the closed-loop location of the crab eigenvalues and for the pendulum damping (in other words, the closed-loop natural frequency of the pendulum is not specified).

□

## 1.5 Output Feedback, Closed-loop Characteristic Polynomial

Consider a state space model of a single-input plant family

$$\begin{aligned}\dot{\mathbf{x}} &= \mathbf{A}(\mathbf{q})\mathbf{x} + \mathbf{b}(\mathbf{q})u, \quad \mathbf{q} \in Q, \\ \mathbf{y} &= \mathbf{C}(\mathbf{q})\mathbf{x},\end{aligned}\tag{1.5.1}$$

and the control law

$$u = -\mathbf{k}^T \mathbf{y} + w\tag{1.5.2}$$

(see Figure 1.7). State feedback corresponds to the case  $\mathbf{C}(\mathbf{q}) = \mathbf{I}$ . The closed-loop

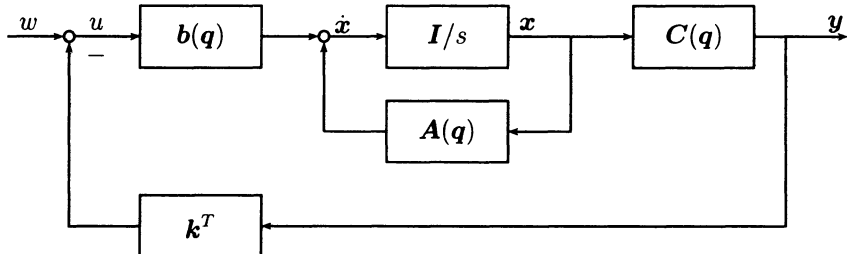


Figure 1.7. Output feedback system

characteristic polynomial is

$$p(s, \mathbf{q}, \mathbf{k}) = \det [s\mathbf{I} - \mathbf{A}(\mathbf{q}) + \mathbf{b}(\mathbf{q})\mathbf{k}^T\mathbf{C}(\mathbf{q})]. \quad (1.5.3)$$

For given  $\mathbf{q}$  and  $\mathbf{k}$ , it is easy to compute the eigenvalues of  $\mathbf{A}(\mathbf{q}) - \mathbf{b}(\mathbf{q})\mathbf{k}^T\mathbf{C}(\mathbf{q})$  numerically. For calculations with general  $\mathbf{q}$  and  $\mathbf{k}$ , a computer algebra program may be used to evaluate  $p(s, \mathbf{q}, \mathbf{k})$ .

It is not practical to evaluate the determinant as in (1.5.3) because multilinear terms ( $k_i k_j, j \neq i$ ) in the elements of  $\mathbf{k}$  occur, which all cancel out, such that  $p(s, \mathbf{q}, \mathbf{k})$  is linear in  $\mathbf{k}$ . Therefore, we first rewrite  $p(s, \mathbf{q}, \mathbf{k})$  in a form that is better suited for the evaluation, also in the case of high system order.

Consider the loop of Figure 1.7 broken at  $u$ . Then the open-loop transfer function from input  $u$  to output  $\mathbf{k}^T \mathbf{y}$  is

$$L(s, \mathbf{q}, \mathbf{k}) = \mathbf{k}^T \mathbf{C}(\mathbf{q}) [\mathbf{sI} - \mathbf{A}(\mathbf{q})]^{-1} \mathbf{b}(\mathbf{q}), \quad (1.5.4)$$

and the closed-loop characteristic polynomial may be written as

$$p(s, \mathbf{q}, \mathbf{k}) = \text{num}(1 + L(s, \mathbf{q}, \mathbf{k})) \quad (1.5.5),$$

("num" stands for "numerator of").

The Leverrier-Faddejew algorithm (1.2.2) yields

$$[\mathbf{sI} - \mathbf{A}(\mathbf{q})]^{-1} = \mathbf{D}(s, \mathbf{q}) / p_0(s, \mathbf{q}), \quad (1.5.6)$$

where

$$p_0(s, \mathbf{q}) = \det[\mathbf{sI} - \mathbf{A}(\mathbf{q})] = a_{00} + a_{01}s + \dots + a_{0n-1}s^{n-1} + s^n \quad (1.5.7)$$

is the open-loop characteristic polynomial. The closed-loop characteristic polynomial (1.5.5) may be written as

$$\begin{aligned} p(s, \mathbf{q}, \mathbf{k}) &= \text{num} \left( 1 + \frac{\mathbf{k}^T \mathbf{C}(\mathbf{q}) \mathbf{D}(s, \mathbf{q}) \mathbf{b}(\mathbf{q})}{p_0(s, \mathbf{q})} \right) \\ &= p_0(s, \mathbf{q}) + \mathbf{k}^T \mathbf{C}(\mathbf{q}) \mathbf{D}(s, \mathbf{q}) \mathbf{b}(\mathbf{q}). \end{aligned} \quad (1.5.8)$$

Thus, the feedback gain  $\mathbf{k}^T$  enters linearly into the coefficients of the closed-loop characteristic polynomial.

The polynomial equation (1.5.8) may also be written in terms of its coefficient vectors in the notation of (1.1.13). The coefficient vector of the monic (i.e.  $a_{0n} = 1$ ) open-loop polynomial  $p_0$  is

$$\hat{\mathbf{a}}_0^T = [a_{00} \ a_{01} \ \dots \ a_{0n-1}], \quad (1.5.9)$$

while for the monic (i.e.  $a_n = 1$ ) closed-loop polynomial  $p$ , the coefficient vector is

$$\hat{\mathbf{a}}^T = [a_0 \ a_1 \ \dots \ a_{n-1}]. \quad (1.5.10)$$

Then (1.5.8) reads

$$\begin{bmatrix} \hat{\mathbf{a}}^T & 1 \end{bmatrix} \begin{bmatrix} 1 \\ s \\ \vdots \\ s^n \end{bmatrix} = \begin{bmatrix} \hat{\mathbf{a}}_0^T & 1 \end{bmatrix} \begin{bmatrix} 1 \\ s \\ \vdots \\ s^n \end{bmatrix} + \mathbf{k}^T \mathbf{C} \begin{bmatrix} \mathbf{D}_0 \mathbf{b} & \mathbf{D}_1 \mathbf{b} & \dots & \mathbf{D}_{n-1} \mathbf{b} \end{bmatrix} \begin{bmatrix} 1 \\ s \\ \vdots \\ s^{n-1} \end{bmatrix}. \quad (1.5.11)$$

By matching the coefficients of equal powers of  $s$ , we get

$$\hat{\mathbf{a}}^T = \hat{\mathbf{a}}_0^T + \mathbf{k}^T \mathbf{W}, \quad (1.5.12)$$

where

$$\mathbf{W} := \mathbf{C} [\mathbf{D}_0 \mathbf{b} \ \mathbf{D}_1 \mathbf{b} \ \dots \ \mathbf{D}_{n-1} \mathbf{b}]. \quad (1.5.13)$$

Equations (1.5.12) and (1.5.13) bring the linear relationship between  $\mathbf{k}$  and the open- and closed-loop polynomials into a compact form, where the symbolic calculations for  $\mathbf{W}$  are done by the Leverrier-Faddejew algorithm.

In the MIMO (multi-input, multi-output) case, the vectors  $\mathbf{k}^T$  and  $\mathbf{b}(\mathbf{q})$  are replaced by matrices  $\mathbf{K}$  and  $\mathbf{B}(\mathbf{q})$  and the characteristic polynomial is

$$\begin{aligned} p(s, \mathbf{q}, \mathbf{K}) &= \det [s\mathbf{I} - \mathbf{A}(\mathbf{q}) + \mathbf{B}(\mathbf{q})\mathbf{K}\mathbf{C}(\mathbf{q})] \\ &= \det [s\mathbf{I} - \mathbf{A}(\mathbf{q}) + \mathbf{b}_1(\mathbf{q})\mathbf{k}_1^T \mathbf{C}(\mathbf{q}) + \dots + \mathbf{b}_m(\mathbf{q})\mathbf{k}_m^T \mathbf{C}(\mathbf{q})], \end{aligned}$$

where  $\mathbf{b}_i(\mathbf{q})$  is the  $i$ -th column of  $\mathbf{B}$  and  $\mathbf{k}_i^T$  is the  $i$ -th row of  $\mathbf{K}$ . Then the closed-loop coefficient vector is

$$\hat{\mathbf{a}}^T = \hat{\mathbf{a}}_0^T + \mathbf{k}_1^T \mathbf{W}_1 + \dots + \mathbf{k}_m^T \mathbf{W}_m. \quad (1.5.14)$$

The matrix  $\mathbf{W}_i$  is calculated from the pair  $(\mathbf{A}, \mathbf{b}_i)$ . It quantifies the eigenvalue-shifting effect of feedback  $u_i = -\mathbf{k}_i^T \mathbf{x}$  to the  $i$ -th input. Eigenvalue shifts of feedback to the other inputs are just superimposed.

In the expansion of this determinant, multilinear terms  $k_{ij}k_{\ell m}$  occur only if  $i \neq \ell$  and  $j \neq m$ . Linearity with respect to the elements of  $\mathbf{K}$  can be preserved by stepwise design, in which in in each design step, feedback from several sensors to one actuator (i.e. elements from one row of  $\mathbf{K}$ ) or feedback from one sensor to several actuators (i.e. elements from one column of  $\mathbf{K}$ ) is assumed.

*Example 1.8 (Crane)*

Consider the motion of the crane (1.1.6) in the neighborhood of an equilibrium point  $\mathbf{x} = [w \ 0 \ 0 \ 0]^T$ , where  $w$  is a constant reference input for the crab position. The reference input  $w$  will be further discussed in Section 1.7.

By (1.1.6), the matrices of the state space model are

$$\mathbf{A} = \begin{bmatrix} 0 & 1 & 0 & 0 \\ 0 & 0 & a_{23} & 0 \\ 0 & 0 & 0 & 1 \\ 0 & 0 & a_{43} & 0 \end{bmatrix}, \quad \mathbf{b} = \begin{bmatrix} 0 \\ b_2 \\ 0 \\ b_4 \end{bmatrix},$$

$$a_{23} = \frac{m_L}{m_C} g, \quad b_2 = \frac{1}{m_C},$$

$$a_{43} = -\frac{(m_L + m_C)g}{m_C \ell}, \quad b_4 = -\frac{1}{m_C \ell},$$

and  $\mathbf{C} = \mathbf{I}$  for state feedback. The Leverrier-Faddejew algorithm yields

$$\begin{aligned} \mathbf{W} &= \begin{bmatrix} \mathbf{D}_0 \mathbf{b} & \mathbf{D}_1 \mathbf{b} & \mathbf{D}_2 \mathbf{b} & \mathbf{D}_3 \mathbf{b} \end{bmatrix} \\ &= \begin{bmatrix} -a_{43}b_2 + a_{23}b_4 & 0 & b_2 & 0 \\ 0 & -a_{43}b_2 + a_{23}b_4 & 0 & b_2 \\ 0 & 0 & b_4 & 0 \\ 0 & 0 & 0 & b_4 \end{bmatrix} \\ &= \begin{bmatrix} g/m_C \ell & 0 & 1/m_C & 0 \\ 0 & g/m_C \ell & 0 & 1/m_C \\ 0 & 0 & -1/m_C \ell & 0 \\ 0 & 0 & 0 & -1/m_C \ell \end{bmatrix} \\ &= \frac{1}{m_C \ell} \begin{bmatrix} g & 0 & \ell & 0 \\ 0 & g & 0 & \ell \\ 0 & 0 & -1 & 0 \\ 0 & 0 & 0 & -1 \end{bmatrix}. \end{aligned} \tag{1.5.15}$$

The crane is controlled by state feedback

$$u = k_1(w - x_1) - k_2x_2 - k_3x_3 - k_4x_4. \tag{1.5.16}$$

The closed-loop characteristic coefficient vector is, by (1.5.12),

$$\begin{aligned}\hat{\mathbf{a}}^T &= \left[ 0 \ 0 \ \frac{(m_L + m_C)g}{m_C\ell} \ 0 \right] \\ &\quad + [k_1 \ k_2 \ k_3 \ k_4] \begin{bmatrix} g & 0 & \ell & 0 \\ 0 & g & 0 & \ell \\ 0 & 0 & -1 & 0 \\ 0 & 0 & 0 & -1 \end{bmatrix} \frac{1}{\ell m_C} \\ &= \frac{1}{\ell m_C} [k_1g \ k_2g \ (m_L + m_C)g + k_1\ell - k_3 \ k_2\ell - k_4].\end{aligned}\tag{1.5.17}$$

For  $\ell > 0$ ,  $m_C > 0$ , we can replace the monic polynomial  $p(s)$  with rational coefficient functions by the non-monic polynomial

$$\begin{aligned}\bar{p}(s) := \ell m_C p(s) &= a_0 + a_1 s + a_2 s^2 + a_3 s^3 + a_4 s^4, \\ a_0 &= k_1 g, \\ a_1 &= k_2 g, \\ a_2 &= (m_L + m_C)g + k_1\ell - k_3, \\ a_3 &= k_2\ell - k_4, \\ a_4 &= \ell m_C.\end{aligned}\tag{1.5.18}$$

Equation (1.5.18) shows how the gains  $k_1$  to  $k_4$  affect the coefficients of the characteristic polynomial and thereby the eigenvalues of the closed loop.

□

### *Remark 1.9*

The uncertain parameter  $m_L$  and the gain  $k_3$  only enter  $a_2$ . Assuming that  $m_L$  can be measured or estimated, the feedback

$$k_3 = k_{30} + m_L g\tag{1.5.19}$$

makes the eigenvalues independent of  $m_L$ . For a measured or estimated rope length  $\ell$ , it is not so easy to see how gain-scheduled feedback improves the robustness with respect to  $\ell$ .

We will come back to gain-scheduled control laws in Section 3.5. Here, we first pursue the more ambitious goal of robust stabilization and control without knowledge of the uncertain parameters  $m_L$  and  $\ell$ .

□

## 1.6 Hurwitz-stability, Stabilizing Controller Parameters

This section reviews the use of algebraic methods for testing the stability of a known polynomial. There are three main originators of algebraic stability tests. The first algebraic test was derived by Hermite [107] in 1856. Partly due to its abstractness, Hermite's paper went unnoticed by most people interested in stability of engineering systems. In 1875, Routh [174] independently presented another algebraic stability test. Unaware of Routh's work, Hurwitz [113] removed the abstraction from Hermite's method and produced a more attractive stability test in 1895. Of the three methods, this section shall present only the Hurwitz method. This method admits the simplest generalization to uncertain polynomials.

Hurwitz has related the stability of an  $n$ -th order polynomial

$$p(s) = a_0 + a_1 s + a_2 s^2 + \cdots + a_n s^n, \quad a_n > 0, \quad (1.6.1)$$

to a set of determinants  $\Delta_i = \det \mathbf{H}_i$ . The determinants come from the following set of  $n$  Hurwitz matrices:

$$\begin{aligned} \mathbf{H}_1 &= \begin{bmatrix} a_{n-1} \end{bmatrix}, \\ \mathbf{H}_2 &= \begin{bmatrix} a_{n-1} & a_{n-3} \\ a_n & a_{n-2} \end{bmatrix}, \\ \mathbf{H}_3 &= \begin{bmatrix} a_{n-1} & a_{n-3} & a_{n-5} \\ a_n & a_{n-2} & a_{n-4} \\ 0 & a_{n-1} & a_{n-3} \end{bmatrix}, \\ &\vdots \end{aligned} \quad (1.6.2)$$

This pattern continues until an  $n \times n$  matrix is obtained. For  $n$  even, this last matrix  $\mathbf{H}_n$  has the form

$$\mathbf{H}_n = \begin{bmatrix} a_{n-1} & a_{n-3} & a_{n-5} & \cdots & a_1 & 0 & 0 & 0 & \cdots & 0 \\ a_n & a_{n-2} & a_{n-4} & \cdots & a_2 & a_0 & 0 & 0 & \cdots & 0 \\ 0 & a_{n-1} & a_{n-3} & \cdots & a_3 & a_1 & 0 & 0 & \cdots & 0 \\ 0 & a_n & a_{n-2} & \cdots & a_4 & a_2 & a_0 & 0 & \cdots & 0 \\ \vdots & & & & & \ddots & & & & \vdots \\ 0 & \cdots & 0 & a_{n-1} & a_{n-3} & a_{n-5} & \cdots & a_3 & a_1 & 0 \\ 0 & \cdots & 0 & a_n & a_{n-2} & a_{n-4} & \cdots & a_4 & a_2 & a_0 \end{bmatrix},$$

while for  $n$  odd, it has the form

$$\mathbf{H}_n = \begin{bmatrix} a_{n-1} & a_{n-3} & a_{n-5} & \cdots & a_0 & 0 & 0 & \cdots & 0 \\ a_n & a_{n-2} & a_{n-4} & \cdots & a_1 & 0 & 0 & \cdots & 0 \\ 0 & a_{n-1} & a_{n-3} & \cdots & a_2 & a_0 & 0 & \cdots & 0 \\ 0 & a_n & a_{n-2} & \cdots & a_3 & a_1 & 0 & \cdots & 0 \\ \vdots & & a_n & a_{n-2} & \ddots & & a_1 & 0 \\ 0 & \cdots & 0 & a_{n-1} & a_{n-3} & a_{n-5} & \cdots & a_2 & a_0 \end{bmatrix}.$$

As an example, if the polynomial is of order  $n = 4$ , the largest Hurwitz matrix is

$$\mathbf{H}_4 = \begin{bmatrix} a_3 & a_1 & 0 & 0 \\ a_4 & a_2 & a_0 & 0 \\ 0 & a_3 & a_1 & 0 \\ 0 & a_4 & a_2 & a_0 \end{bmatrix},$$

while for  $n = 5$ , the largest Hurwitz matrix is

$$\mathbf{H}_5 = \begin{bmatrix} a_4 & a_2 & a_0 & 0 & 0 \\ a_5 & a_3 & a_1 & 0 & 0 \\ 0 & a_4 & a_2 & a_0 & 0 \\ 0 & a_5 & a_3 & a_1 & 0 \\ 0 & 0 & a_4 & a_2 & a_0 \end{bmatrix}.$$

The relation of these matrices to stability is given in the following theorem. No proof shall be provided for this well-known result of Hurwitz.

### Theorem 1.10 (Hurwitz)

An  $n$ -th order polynomial (1.6.1) is stable if and only if

$$\det \mathbf{H}_i > 0 \quad \text{for all } i = 1, 2, \dots, n. \quad (1.6.3)$$

□

Note that, for both  $n$  even and  $n$  odd, it follows from expanding  $\det \mathbf{H}_n$  by its last column that

$$\det \mathbf{H}_n = a_0 \det \mathbf{H}_{n-1}. \quad (1.6.4)$$

Thus, the stability condition (1.6.3) is equivalent to  $\det \mathbf{H}_i > 0$  for  $i = 1, 2, \dots, n - 1$ , and  $a_0 > 0$ .

Given a polynomial with known coefficients  $a_0, a_1, a_2, \dots, a_n$ , it is straightforward to apply the Hurwitz-stability test. The resulting determinants are real numbers that can be easily compared with zero. If the coefficients depend on uncertain parameters,  $a_0(\mathbf{q}), a_1(\mathbf{q}), a_2(\mathbf{q}), \dots, a_n(\mathbf{q})$ , it is still possible to form the Hurwitz determinants symbolically. However, the resulting inequalities are – except for some simple cases like the crane – not very tractable.

A useful necessary condition is the positivity of all coefficients  $a_i$ .

*Theorem 1.11*

A stable polynomial (1.6.1) of degree  $n$  satisfies

$$a_i > 0 \quad \text{for all } i = 0, 1, 2, \dots, n - 1. \quad (1.6.5)$$

□

*Proof*

The proof of this theorem follows from the fact that (1.6.1) is a real polynomial and can be factored as

$$\begin{aligned} p(s) &= a_n \prod_{i=1}^m (s - \sigma_i - j\omega_i)(s - \sigma_i + j\omega_i) \prod_{k=2m+1}^n (s - \sigma_k) \\ &= a_n \prod_{i=1}^m (s^2 - 2\sigma_i s + \sigma_i^2 + \omega_i^2) \prod_{k=2m+1}^n (s - \sigma_k). \end{aligned}$$

where the  $\sigma$ 's and  $\omega$ 's are real numbers. If this polynomial is stable, then the  $\sigma$ 's are all negative. This implies that all the subpolynomials

$$\begin{aligned} s^2 + (-2\sigma_i)s + (\sigma_i^2 + \omega_i^2), \\ s + (-\sigma_k), \end{aligned}$$

have positive coefficients, and hence their product  $p(s)$  must have only positive coefficients.

□

The positive coefficient criteria of Theorem 1.11 can be used to reduce the number of determinant criteria in Theorem 1.10. This simplification is due to Liénard and Chipart [132], for a simpler proof see [94].

*Theorem 1.12 (Liénard, Chipart)*

Necessary and sufficient conditions for a polynomial

$$p(s) = a_0 + a_1 s + \dots + a_n s^n, \quad a_n > 0$$

to be stable can be given in one of the four following forms:

- |     |  |         |
|-----|--|---------|
| LC1 | $a_0 > 0, a_2 > 0, \dots; \Delta_1 > 0, \Delta_3 > 0, \dots,$          | (1.6.6) |
| LC2 | $a_0 > 0, a_2 > 0, \dots; \Delta_2 > 0, \Delta_4 > 0, \dots,$          |         |
| LC3 | $a_0 > 0, a_1 > 0, a_3 > 0, \dots; \Delta_1 > 0, \Delta_3 > 0, \dots,$ |         |
| LC4 | $a_0 > 0, a_1 > 0, a_3 > 0, \dots; \Delta_2 > 0, \Delta_4 > 0, \dots,$ |         |

where  $\Delta_i = \det \mathbf{H}_i$ .

□

*Example 1.13*

For the fourth order example of the crane with  $a_4 = \ell m_C > 0$ , the forms LC1 and LC3 are convenient because only the determinant of a  $3 \times 3$  matrix must be evaluated. With the coefficients of (1.5.18), form LC3 yields

$$\begin{aligned} a_0 &= k_1 g > 0, \\ a_1 &= k_2 g > 0, \\ \Delta_1 = a_3 &= k_2 \ell - k_4 > 0, \\ \Delta_3 = \det \mathbf{H}_3 &= \begin{vmatrix} a_3 & a_1 & 0 \\ a_4 & a_2 & a_0 \\ 0 & a_3 & a_1 \end{vmatrix} > 0. \end{aligned}$$

The evaluation gives

$$\Delta_3 = g[k_2(m_L g - k_3) + k_1 k_4](k_2 \ell - k_4) - k_2 k_4 m_C g^2 > 0. \quad (1.6.7)$$

□

*Remark 1.14*

Form LC1 yields  $a_2 = (m_L + m_C)g + k_1 \ell - k_3 > 0$  instead of  $a_1 = k_2 g > 0$  and the conditions  $a_0 > 0$ ,  $a_3 > 0$ ,  $\Delta_3 > 0$  as above. At first glance, it is surprising that the inequalities  $a_1 > 0$  and  $a_2 > 0$  serve the same purpose in the two forms of stability tests. This puzzle will be solved in Section 2.1 on critical stability conditions.

□

Equation (1.6.7) shows that  $m_L$  and  $k_3$  enter only into the combination  $m_L g - k_3$  as contained in  $a_2$ . Thus, the effect of a variation of the load  $m_L$  on the eigenvalue location can be exactly compensated by an adjustment of  $k_3$ . However, we want to avoid the measurement or estimation of  $m_L$ . Also, we will see later that actuator constraints lead to a solution that leaves the fast system ( $m_L = m_L^+$ ) fast and the slow system ( $m_L = m_L^-$ ) slow, see the open-loop eigenvalues in (1.1.9) and Figure 1.3. Such constraints would not be observed if the same eigenvalues are prescribed for all loads.

The stabilization analysis gives a new insight for the controller structure, that is,  $k_2 > 0$  is required for stabilization. The feedback signal  $x_2 = \dot{x}_1$  must either be measured or generated by controller dynamics, e.g. by low-pass filtered differentiation of  $x_1$  by  $x_2(s) = \frac{s}{1+Ts} x_1(s)$  with a small time constant  $T$ . The time constant is chosen independently of other feedback gains as a trade-off between suppression of measurement noise in  $x_1$  and maintaining the stabilizing effect of the ideal differentiator with  $T = 0$ .

Regarding  $k_3$  and  $k_4$ , interesting special cases of  $\Delta_3$  arise for  $k_4 = 0$ :

$$\Delta_3 = k_2^2 \ell g (m_L g - k_3) > 0, \quad (1.6.8)$$

and for  $k_3 = 0$  and  $k_4 = 0$ :

$$\Delta_3 = k_2^2 l g^2 m_L > 0, \quad (1.6.9)$$

i.e. the output feedback controller

$$k_1 > 0, k_2 > 0, k_3 = 0, k_4 = 0$$

stabilizes all cranes as modelled by (1.1.6). The non-robust observability of  $x_3, x_4$  from  $x_1$  and  $x_2$ , however, indicates that the above controller cannot give sufficient damping to the pendulum in the empty hook case.

For  $k_4$ , there is an upper bound  $k_4 < k_2 \ell$  resulting from  $a_3 > 0$ . Robust stability for small rope length  $\ell$  requires  $k_4 \leq 0$ . For large  $|k_4|$ , the dominating term in  $\Delta_3$  is  $-gk_1k_4^2$ . Thus,  $k_4 = 0$  is a good choice for robust satisfaction of  $\Delta_3 > 0$ . Robustness for small loads then requires  $k_3 < 0$ , i.e. positive feedback of the rope angle. The resulting controller structure is shown in Figure 1.8.

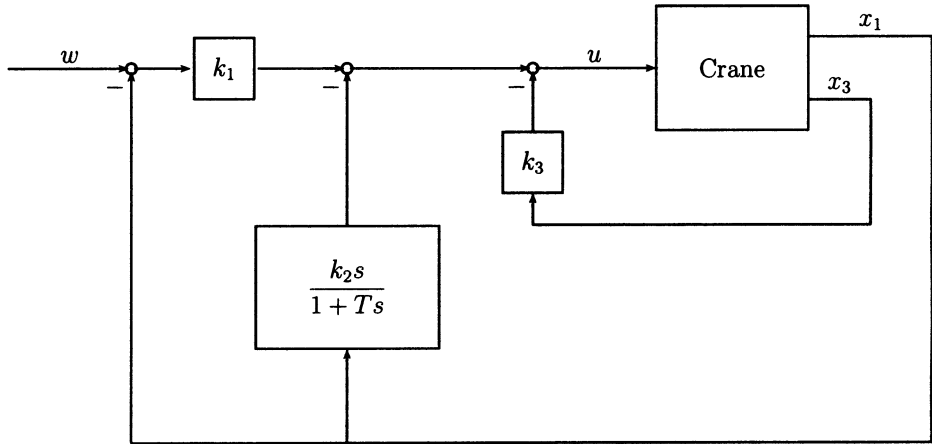


Figure 1.8. Robust controller structure for the crane with  $k_1 > 0, k_2 > 0, k_3 < 0$

The gain  $k_1$  is chosen independently of  $k_2$  and  $k_3$  by a trade-off between fast positioning and a bound on  $|u|$ . For a transport transition from

$$\mathbf{x}(0) = \begin{bmatrix} 0 \\ 0 \\ 0 \\ 0 \end{bmatrix} \quad \text{to} \quad \mathbf{x}(\infty) = \begin{bmatrix} 1 \\ 0 \\ 0 \\ 0 \end{bmatrix},$$

typically the maximum of  $u(t)$  is  $u(0) = k_1$  for a good controller design. The limitation of  $|u(t)|$  will be further discussed in Section 1.7. Also,  $k_1$  should not be so large that the crab eigenvalues approach the pendulum eigenvalues, as this would enforce undesirable fast back and forth motions of the crab. The gain  $k_2$  provides damping for the crab motion and – for medium and large rope lengths – also for the pendulum motion. A negative value of the gain  $k_3$  also provides pendulum damping for small

rope length  $\ell$ . There is a mutual influence between  $k_2$  and  $k_3$  such that these controller parameters should be designed together. Finally,  $T$  is increased beginning from zero, and its influence on the closed-loop eigenvalues is tracked.

The controller structure of Figure 1.8 is:

- i. Lean: only three essential parameters must be tuned.
- ii. Transparent: each controller parameter has a well-defined influence on the crane dynamics as long as the dynamic ranges of the two subsystems are kept separate.
- iii. Robust: also large parameter variations in  $\ell$  and  $m_L$  do not destabilize the system. The low-pass filtered differentiation is not parameter-dependent. This is in contrast to the observer with the problem of a mismatched model.

The closed-loop transfer function is obtained by straightforward calculation as

$$\frac{x_1(s)}{w(s)} = \frac{k_1(s^2\ell + g)(1 + Ts)}{(s^2\ell + g)[(s^2m_C + k_1)(1 + Ts) + k_2s] + s^2(m_Lg - k_3)(1 + Ts)}. \quad (1.6.10)$$

Note that we have not collected the terms in the powers of  $s$  as usual in numerical calculations, because the symbolic expression would get more complicated. For later investigations in Chapter 9, it is even desirable to write the transfer function such that each parameter has only a local influence in one subpolynomial. This leads to a form that resembles continued fractions

$$\frac{x_1(s)}{w(s)} = \frac{1}{1 + \frac{1}{k_1} \left[ s^2m_C + \frac{k_2s}{1 + Ts} + \frac{s^2(m_Lg - k_3)}{s^2\ell + g} \right]}. \quad (1.6.11)$$

Each parameter  $m_C, m_L, \ell, k_1, k_2, k_3$ , and  $T$  enters only once.

### *Remark 1.15*

Feedback structures for other plants can be derived similarly by analyzing the parametric controllability and observability for the worst plant parameters. The crane is typical for two-mass systems as they arise for the inverted pendulum, two coupled vehicles, a robot joint, or an aircraft rudder deflection.  $\square$

## 1.7 Controller Structures for Partially Known Inputs

In Sections 1.4 to 1.6, output feedback structures have been assumed. These structures are convenient for the specification of closed-loop eigenvalue regions as they will be discussed in Chapter 3. No knowledge of the spectrum of input signals is assumed. Then, a good eigenvalue location guarantees that the initial conditions resulting from

previous input signals decay rapidly and well damped to the equilibrium state. If, however, some assumptions on the spectra of reference, disturbance and sensor noise inputs can be made, then the control system may be tailored to specifications in different frequency bands. It is then convenient to assume the controller structure in form of transfer functions. In this section, we will first discuss the model reference approach for the reference input and then feedback structures for disturbance and noise rejection.

Consider the control system of Figure 1.9; the principle is first explained for a nominal plant model  $G(s)$ .  $K(s)$  is the feedback controller and  $F(s)$  is a prefilter.  $G_d(s)$  is a desired transfer function for

$$G_{ry} = \frac{GF}{1 + GK} \quad (1.7.1)$$

(we introduce the notation  $G_{ab}(s)$  for the transfer function from signal  $a$  to signal  $b$ , the complex variable  $s$  is omitted).

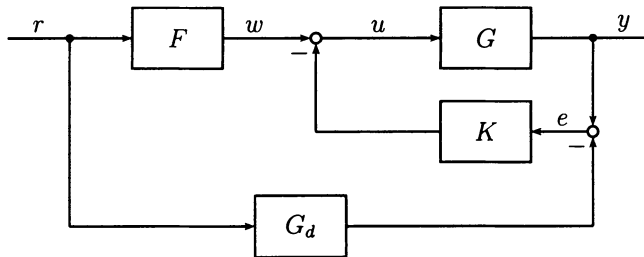


Figure 1.9. Modified twodegree of freedom structure with reference model  $G_d$

The design goal  $G_{ry} = G_d$  can be satisfied only if  $G_d$  satisfies three *feasibility constraints* [185].

- i.  $G_{ry}$  must have at least the same relative degree as the plant  $G$ , otherwise  $F$  would not be realizable.
- ii.  $G_{ry}$  must have at least the same dead time  $e^{-Ts}$  as the plant  $G$ , otherwise  $F$  would not be causal.
- iii.  $G_{ry}$  must contain all zeros of  $G$  in the (closed) right half plane, because the non-minimum phase zeros (including zeros on the imaginary axis) cannot be cancelled.

The design procedure for model reference following then is as follows [111], [128]:

1. Specify a reference transfer function  $G_d$  that meets the feasibility constraints.
2. Choose the prefilter

$$F = G_d/G. \quad (1.7.2)$$

3. The ideal open-loop transfer function

$$G_{ry} = G_d = FG \quad (1.7.3)$$

would be obtained for  $e = 0$ . Then  $K$  has no influence on  $G_{ry}$ .  $K$  is designed to keep  $e$  small; this design step is independent of  $F$  and  $G_d$ .

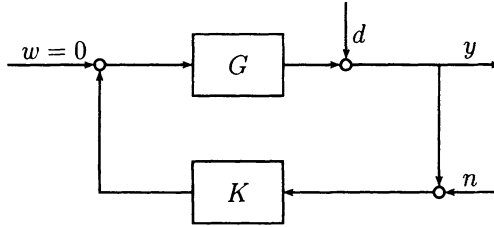


Figure 1.10. Plant disturbance  $d$  and sensor noise  $n$

Now consider  $r \equiv 0$  and a plant disturbance  $d$  at the plant output and sensor noise  $n$  as shown in Figure 1.10. Assume that  $d$  and  $n$  cannot be measured. There is, however, a control system structure specifically suitable for disturbance rejection, see Figure 1.11.

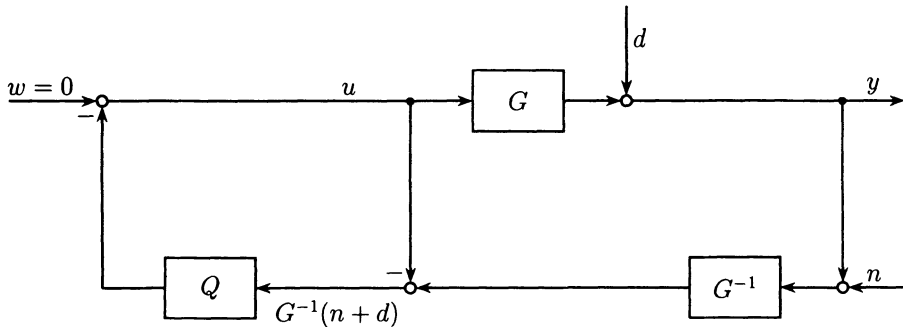


Figure 1.11. Disturbance rejection feedback structure

The inverse  $G^{-1}$  is in general not realizable, but in combination with a filter  $Q$  it can be made realizable.  $Q$  must meet the same feasibility constraints as the reference transfer function  $G_d$  in terms of relative degree, dead time and zeros in the closed right half plane of  $G$ , otherwise the controller transfer function  $QG^{-1}$  would not be realizable and internally stable. Within these constraints,  $Q$  can be chosen by the designer for a trade-off between the influences of  $d$  and  $n$  on  $y$ . In the nominal case, we have

$$y = (1 - Q)d - Qn. \quad (1.7.4)$$

Both  $Q$  and  $1 - Q$  should be small, but the sum of the two terms is 1. This conflict will be dealt with in terms of sensitivity functions and complementary sensitivity functions in Chapter 5. Typically,  $1 - Q$  is made small at low frequencies and  $Q$  is made small at high frequencies. In some applications, the frequency of  $d$  is known such that a disturbance rejection system may be specifically tuned. An example is vibration isolation of a helicopter from the rotor excitation, where the rotor frequency is also controlled.

Another example is the periodic vertical perturbation on a magnetically levitated train from the track that hangs like a garland between its supports. The control system structure of Figure 1.11 will be used in Section 6.7 for skidding avoidance by active car steering, and in Section 7.3 for longitudinal flight control.

So far, we have assumed a nominal plant model  $G$ , such that  $G^{-1}$  in the feedback path is known. Deviations of the real plant  $G$  from its nominal model  $G_n$  with  $G^{-1}$  replaced by  $G_n^{-1}$  in the feedback path may have different origin and appropriate descriptions.

For uncertainty of physical parameters (like  $m_L$ ,  $\ell$ ,  $m_C$  in the crane example), the perturbation structure must be derived by analytical modelling. In Chapter 6, a car steering model with the uncertain parameters velocity, mass, moment of inertia, and road-tire contact will be derived. Only the effects that have been modelled are considered and the order  $n$  of the state space model is fixed.

On the other hand, there are unmodelled uncertainties like neglected actuator and sensor dynamics, neglected details of the plant like flexible structure modes, etc. Here, a standard uncertainty structure with dynamic model uncertainty  $\Delta_m$  may be chosen to describe the deviation of  $G$  from the nominal  $G_n$  in a vague, non-physical sense as an aggregation of several model inaccuracies. Typical standard structures are:

$$\text{Additive perturbation } G = G_n + \Delta_m. \quad (1.7.5)$$

$$\text{Multiplicative perturbation } G = G_n(1 + \Delta_m). \quad (1.7.6)$$

$$\text{Feedback perturbation } G = \frac{G_n}{1 + G_n \Delta_m}. \quad (1.7.7)$$

For the crane example, think of the neglected actuator dynamics as a multiplicative perturbation. Elasticity of the rope may be approximated by an additive perturbation. Typically, the low-frequency control system dynamics are dominated by uncertain physical parameters in a given model structure, and the high-frequency dynamics can only be described by unmodelled dynamic uncertainties  $\Delta_m$ , denoted *non-parametric uncertainty* or *unstructured uncertainty*. A useful assumption that we will apply in Chapter 5 is a frequency response  $\Delta_m(j\omega)$  with bounded magnitude and arbitrary phase.

A combination of the structures of Figure 1.9 and Figure 1.11 is shown in Figure 1.12.

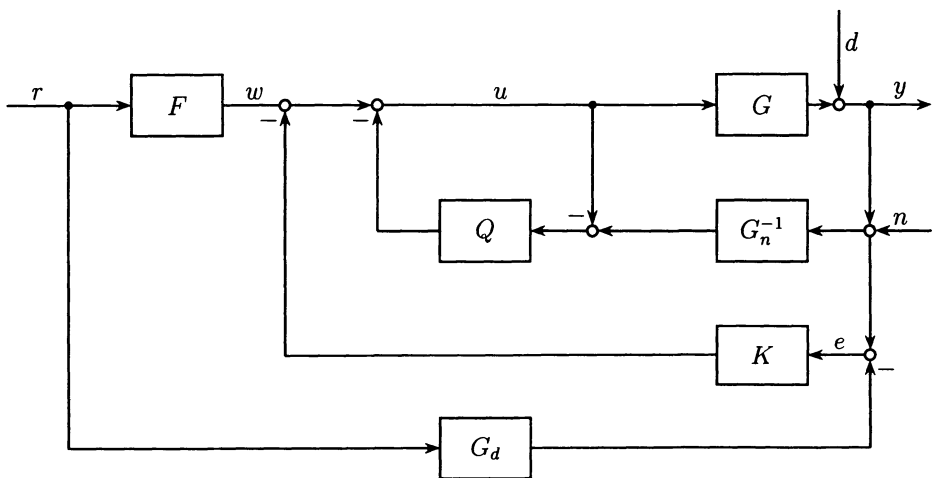


Figure 1.12. Control system structure for separation of design tasks.  $F$  for input  $r$ ,  $Q$  for a tradeoff between inputs  $d$  and  $n$  and  $K$  for robust stabilization,  $G_d$  for model reference dynamics

## 2 Hurwitz-stability Boundary Crossing and Parameter Space Approach

### 2.1 Critical Stability Conditions

The basic idea of *critical stability conditions* is that a starting point in form of a stable characteristic polynomial  $p(s, \mathbf{q})$ ,  $\mathbf{q} = \mathbf{q}_0$  is given. Assume that the (real) coefficients of  $p(s, \mathbf{q})$  are continuous in  $\mathbf{q}$ . Then also the roots of  $p(s, \mathbf{q})$  are continuous in  $\mathbf{q}$ , i.e. they cannot jump from the left half plane to the right half plane without crossing the imaginary axis. The stable neighborhood of  $\mathbf{q}_0$  is bounded by the values of  $\mathbf{q}$ , where for the first time one or more eigenvalues cross the imaginary axis under a continuous variation of  $\mathbf{q}$  starting at  $\mathbf{q}_0$ . Crossing of eigenvalues over the imaginary axis can occur in one of three ways: at  $s = 0$ , at  $s = \infty$  and at  $s = \pm j\omega$ .

An example of an infinite root boundary at  $s = \infty$  is the combination of the crane with an inverted pendulum. Replace the rope by a rod and shift the load mass through  $\ell = 0$  to negative values of  $\ell$ . The eigenvalues at  $s_{3,4} = \pm j\sqrt{1 + m_L/m_C}\sqrt{g/\ell}$  (see (1.1.9)) go to  $\pm j\infty$  and return as a real pair of eigenvalues from  $+\infty$  and  $-\infty$ . The *infinite root boundary* (IRB) is characterized by a degree drop at  $a_n(\mathbf{q}) = 0$ , see (1.1.11).

For the *real root boundary* (RRB) at  $s = 0$  and the *complex root boundary* (CRB) at  $s = \pm j\omega$ , Frazer and Duncan [89] have shown that the critical stability boundary is  $\det \mathbf{H}_n(\mathbf{q}) = 0$ . The result is presented as the following algebraic *boundary crossing theorem*.

*Theorem 2.1 (Frazer, Duncan)*

The family of polynomials

$$P(s, Q) = \{a_0(\mathbf{q}) + a_1(\mathbf{q})s + \dots + a_n(\mathbf{q})s^n \mid \mathbf{q} \in Q\} \quad (2.1.1)$$

with continuous real coefficient functions  $a_i(\mathbf{q})$  is robustly Hurwitz-stable, if and only if:

- i. There exists a stable polynomial  $p(s, \mathbf{q}) \in P(s, Q)$ .
- ii.  $a_n(\mathbf{q}) \neq 0$  for all  $\mathbf{q} \in Q$ .

iii.  $\det \mathbf{H}_n(\mathbf{q}) \neq 0$  for all  $\mathbf{q} \in Q$ .

□

*Proof*

Necessity of the three conditions follows from the Hurwitz- stability condition. To prove sufficiency, it shall be shown that satisfaction of Conditions ii and iii implies that  $P(s, Q)$  does not have roots on the imaginary axis. Consider a polynomial

$$p(s, \mathbf{q}) = a_0(\mathbf{q}) + a_1(\mathbf{q})s + \dots + a_n(\mathbf{q})s^n \quad (2.1.2)$$

with real coefficients. It may be written as

$$p(s, \mathbf{q}) = p_{even}(s^2, \mathbf{q}) + s p_{odd}(s^2, \mathbf{q}),$$

where

$$\begin{aligned} p_{even}(s^2, \mathbf{q}) &= a_0(\mathbf{q}) + a_2(\mathbf{q})s^2 + a_4(\mathbf{q})s^4 + \dots, \\ p_{odd}(s^2, \mathbf{q}) &= a_1(\mathbf{q}) + a_3(\mathbf{q})s^2 + a_5(\mathbf{q})s^4 + \dots. \end{aligned}$$

The polynomial  $p(s, \mathbf{q})$  has a root at  $s = \pm j\omega$  if and only if both the real and the imaginary part of

$$p(\pm j\omega, \mathbf{q}) = p_{even}(-\omega^2, \mathbf{q}) \pm j\omega p_{odd}(-\omega^2, \mathbf{q}) \quad (2.1.3)$$

vanish. Note that  $s = 0$  is a root of  $s p_{odd}(s^2, \mathbf{q})$  resulting in the RRB at  $a_0(\mathbf{q}) = 0$ . For  $s \neq 0$ , the common root condition for  $p_{even}(s^2, \mathbf{q})$  and  $p_{odd}(s^2, \mathbf{q})$  is written in terms of a new complex variable  $v := s^2$

$$\begin{aligned} p_{even}(v) &= a_0(\mathbf{q}) + a_2(\mathbf{q})v + a_4(\mathbf{q})v^2 + \dots = 0, \\ p_{odd}(v) &= a_1(\mathbf{q}) + a_3(\mathbf{q})v + a_5(\mathbf{q})v^2 + \dots = 0. \end{aligned} \quad (2.1.4)$$

These two polynomials share a root if and only if their resultant matrix has a zero determinant (see Appendix A). If  $n$  is even, then the  $n \times n$  resultant matrix is

$$\mathbf{R}(\mathbf{q}) = \begin{bmatrix} a_{n-1} & a_{n-3} & a_{n-5} & \cdots & a_1 & 0 & 0 & 0 & \cdots & 0 \\ 0 & a_{n-1} & a_{n-3} & \cdots & a_3 & a_1 & 0 & 0 & \cdots & 0 \\ \vdots & & & & & & \ddots & & & \vdots \\ 0 & \cdots & 0 & a_{n-1} & a_{n-3} & a_{n-5} & \cdots & a_3 & a_1 & 0 \\ a_n & a_{n-2} & a_{n-4} & \cdots & a_2 & a_0 & 0 & 0 & \cdots & 0 \\ 0 & a_n & a_{n-2} & \cdots & a_4 & a_2 & a_0 & 0 & \cdots & 0 \\ \vdots & & & & & & \ddots & & & \vdots \\ 0 & \cdots & 0 & a_n & a_{n-2} & a_{n-4} & \cdots & a_4 & a_2 & a_0 \end{bmatrix}, \quad (2.1.5)$$

where the dependence of the coefficients on  $\mathbf{q}$  has been omitted for brevity. By interchanging rows, it is possible to transform  $\mathbf{R}(\mathbf{q})$  into the Hurwitz matrix

$\mathbf{H}_n(\mathbf{q})$ . (The relation of  $\mathbf{R}(\mathbf{q})$  and  $\mathbf{H}_n(\mathbf{q})$  holds both for  $n$  even and for  $n$  odd.) This relationship implies that

$$\det \mathbf{R}(\mathbf{q}) = \pm \det \mathbf{H}_n(\mathbf{q}). \quad (2.1.6)$$

By Condition 3 of the theorem,  $\det \mathbf{H}_n(\mathbf{q}) \neq 0$  so the determinant of the resultant matrix is also non-zero. Therefore,

$$p(j\omega, \mathbf{q}) \neq 0 \quad \text{for all } \omega. \quad (2.1.7)$$

This implies that no  $p(s) \in P(s, Q)$  has a root on the  $j\omega$ -axis.

□

### Theorem 2.2

Note that by  $\det \mathbf{H}_n = a_0 \det \mathbf{H}_{n-1}$ , the three conditions of Theorem 2.1 may be replaced by the following four conditions:

- i. There exists a stable polynomial  $p(s, \mathbf{q}) \in P(s, Q)$ .
- ii.  $a_n(\mathbf{q}) \neq 0$  for all  $\mathbf{q} \in Q$ .
- iii.  $a_0(\mathbf{q}) \neq 0$  for all  $\mathbf{q} \in Q$ .
- iv.  $\det \mathbf{H}_{n-1}(\mathbf{q}) \neq 0$  for all  $\mathbf{q} \in Q$ .

□

### Fictitious and Non-active Boundaries

A relationship between  $\det \mathbf{H}_{n-1}$  and the roots of  $p(s)$  is given by *Orlando's formula* [164], [94]. Given an  $n$ -th order polynomial in factorized form

$$p(s) = a_n \prod_{i=1}^n (s - s_i), \quad s_i = \sigma_i + j\omega_i. \quad (2.1.8)$$

Orlando's formula relates  $\det \mathbf{H}_{n-1}$  to the polynomial's roots as follows:

$$\det \mathbf{H}_{n-1} = (-1)^{n(n+1)/2} a_n^{n-1} \prod_{\substack{i,k=1 \\ i < k}}^n (s_i + s_k). \quad (2.1.9)$$

If the polynomial has a pair of roots on the imaginary axis at  $\sigma_1 = \sigma_2 = 0, \omega_1 = -\omega_2$ , then the product term  $s_1 + s_2$  is zero and hence  $\det \mathbf{H}_{n-1}$  also equals zero.

The condition  $\det \mathbf{H}_{n-1} = 0$  is also satisfied for a real symmetric pair  $\sigma_1 = -\sigma_2, \omega_1 = \omega_2 = 0$  or for two complex and symmetric pairs  $s_{1/2} = \sigma_1 \pm j\omega_1, s_{3,4} = -\sigma_1 \pm j\omega_1$ . Thus, the condition  $\det \mathbf{H}_{n-1}(\mathbf{q}) = 0$  not only generates the boundary in  $\mathbf{q}$ -space, where

a root on the imaginary axis occurs, but also *fictitious boundaries* at complex frequencies  $\omega$ . They cannot, however, intersect the stable neighborhood of  $\mathbf{q}_0$ , because one or more eigenvalues have to cross the imaginary axis first before reaching a symmetric pattern with respect to the imaginary axis with unstable eigenvalues.

The condition  $\det \mathbf{H}_n(\mathbf{q}) = 0$  is also satisfied for a polynomial with unstable roots plus a pair of roots on the imaginary axis. This situation gives rise to a *non-active boundary*.

### Example 2.3

For the crane example, let  $m_C = 5$ ,  $m_L = 5$ ,  $\ell = 2$ ,  $k_1 = 1$ ,  $k_4 = 2$ . Find the set of stabilizing  $k_2$ ,  $k_3$ . The characteristic polynomial of (1.5.18) has the coefficients

$$\begin{aligned} a_0 &= 10, \\ a_1 &= 10k_2, \\ a_2 &= 102 - k_3, \\ a_3 &= 2k_2 - 2, \\ a_4 &= 10. \end{aligned}$$

The Hurwitz determinant  $\Delta_3 = \det \mathbf{H}_3$  is

$$\begin{aligned} \Delta_3 &= a_1 a_2 a_3 - a_0 a_3^2 - a_4 a_1^2 \\ &= 20 [50k_2^2 - 98k_2 - 2 - k_3 k_2(k_2 - 1)]. \end{aligned}$$

$\Delta_3$  vanishes for

$$k_3 = \frac{50k_2^2 - 98k_2 - 2}{k_2(k_2 - 1)}.$$

This boundary is plotted in Figure 2.1. It consists of three branches that divide the plane into tree regions with  $\Delta_3 > 0$ , and one complementary region with  $\Delta_3 < 0$ . For a test point on the upper branch, the polynomial has a symmetric real pair of roots; this is a fictitious boundary. For a test point on the left branch, the polynomial has an imaginary pair of roots at  $\pm j\omega$ ,  $0 < \omega < \sqrt{5}$  and two unstable roots; this is a non-active boundary. Only the right branch is an active boundary corresponding to two stable roots and one pair on the imaginary axis at  $\pm j\omega$ ,  $\omega > \sqrt{5}$ . The real root boundary (RRB)  $a_0 = k_1 g = 10 > 0$  and the infinite root boundary (IRB)  $a_4 = \ell m_C = 10 > 0$  do not exist in this example.

The example also gives an explanation for the puzzle on the different Liénard-Chipart conditions in Remark 1.14. Both LC1 and LC3 require  $a_0 > 0$  (satisfied everywhere) and  $a_3 > 0$ , i.e.  $k_2 > 1$ , which rules out the left and the upper region with  $\Delta_3 > 0$ . The additional conditions from LC1 ( $a_2 > 0 \Rightarrow k_3 < 102$ ), and LC3 ( $a_1 > 0 \Rightarrow k_2 > 0$ ) are non-active in this example.

The result of the boundary crossing theorem may also be illustrated by Figure 2.1. If a stable starting point  $p(s, \mathbf{q}_0)$  is chosen, e.g.  $k_2 = 3$ ,  $k_3 = 0$ , then the first crossing of the imaginary axis under continuous variation of  $k_2$  and  $k_3$  occurs on the right lower

branch of the curve  $\Delta_3 = 0$ . The other three regions do not contain a stable starting point.  $\square$

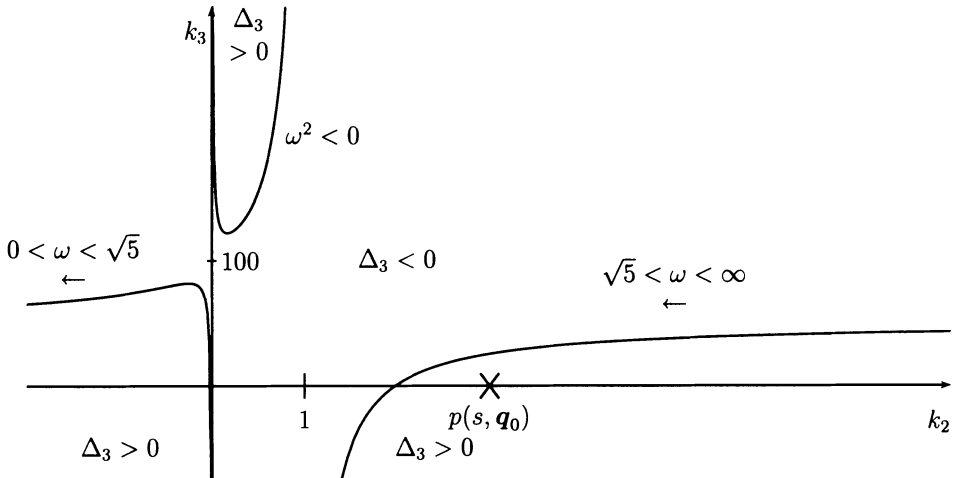


Figure 2.1. The boundary  $\Delta_3 = 0$  for the crane example

## 2.2 The Parameter Space Approach

A drawback of the algebraic boundary crossing approach is that the condition  $\Delta_{n-1}(\mathbf{q}) = \det \mathbf{H}_{n-1}(\mathbf{q}) = 0$  for large  $n$  leads to complicated symbolic expressions, even for simple dependence of the coefficients  $a_i$  on  $\mathbf{q}$ . A second drawback is that the above conditions also generate fictitious boundaries. The reason is that the real frequency  $\omega$  has been eliminated from the two equations (see (2.1.3))

$$\begin{aligned}\operatorname{Re} p(j\omega, \mathbf{q}) &= a_0(\mathbf{q}) - a_2(\mathbf{q})\omega^2 + a_4(\mathbf{q})\omega^4 - \dots = 0, \\ \operatorname{Im} p(j\omega, \mathbf{q}) &= \omega [a_1(\mathbf{q}) - a_3(\mathbf{q})\omega^2 + a_5(\mathbf{q})\omega^4 - \dots] = 0\end{aligned}\quad (2.2.1)$$

by the resultant condition  $\det \mathbf{R}(\mathbf{q}) = \pm \det \mathbf{H}_n(\mathbf{q})$ . Therefore, complex values for  $\omega$  are also included in the boundary  $\det \mathbf{H}_n(\mathbf{q}) = 0$ .

The basic idea of the parameter space approach is not to eliminate  $\omega$ , but to leave it as a parameter that is restricted to real non-negative values. The stability boundaries in a two-dimensional slice through the  $\mathbf{q}$ -space are calculated by a sweep over  $\omega$ .

*Example 2.4*

In the previous crane example, the two equations (2.2.1) are

$$\begin{aligned}\operatorname{Re} p(j\omega, k_2, k_3) &= 10 - (102 - k_3)\omega^2 + 10\omega^4 = 0, \\ \operatorname{Im} p(j\omega, k_2, k_3) &= \omega [10k_2 - (2k_2 - 2)\omega^2] = 0.\end{aligned}$$

The equations are solved for

$$\begin{aligned}k_2(\omega^2) &= \frac{-\omega^2}{5 - \omega^2}, \\ k_3(\omega^2) &= \frac{-10 + 102\omega^2 - 10\omega^4}{\omega^2}.\end{aligned}$$

For a sweep over real values of  $\omega$ , only the two lower branches of  $\Delta_3(k_2, k_3) = 0$  in Figure 2.1 are generated in a parameterized form. The fictitious branch of Figure 2.1 is not generated by real  $\omega$  values. Figure 2.2 shows the two lower branches with the parameter  $\omega$ . In the lower left region, there does not exist a stable polynomial, and Condition 1 of Theorem 2.1 is violated.

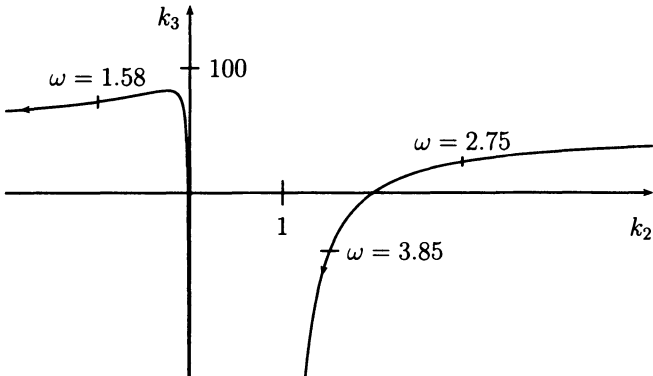


Figure 2.2. Parameterized complex root boundary for the example of Figure 2.1

□

The previous example was particularly simple, because only the CRB was active. Therefore, we now look at an example where the RRB is also active.

*Example 2.5*

In the crane example, let  $m_C = 5$ ,  $m_L = 5$ ,  $\ell = 2$ ,  $k_3 = 10$ ,  $k_4 = 1$ . Find the stable region in the  $(k_1, k_2)$ -plane. The characteristic polynomial of (1.5.14) has the coefficients

$$a_0 = 10k_1,$$

$$\begin{aligned} a_1 &= 10k_2, \\ a_2 &= 90 + 2k_1, \\ a_3 &= 2k_2 - 1, \\ a_4 &= 10. \end{aligned}$$

The equations for the real and imaginary parts read as

$$\begin{aligned} \operatorname{Re} p(j\omega, k_1, k_2) &= 10k_1 - (90 + 2k_1)\omega^2 + 10\omega^4 = 0, \\ \operatorname{Im} p(j\omega, k_1, k_2) &= \omega [10k_2 - (2k_2 - 1)\omega^2] = 0. \end{aligned} \quad (2.2.2)$$

For  $\omega = 0$ , the equation for the imaginary part is always satisfied and the corresponding RRB is  $k_1 = 0$ . The CRB is described by

$$\begin{aligned} k_1(\omega^2) &= \frac{5\omega^2(\omega^2 - 9)}{\omega^2 - 5}, \\ k_2(\omega^2) &= \frac{\omega^2}{2(\omega^2 - 5)}. \end{aligned}$$

Figure 2.3 shows the parametric stability boundary in the  $(k_1, k_2)$ -plane. For  $k_1 = 0$ ,

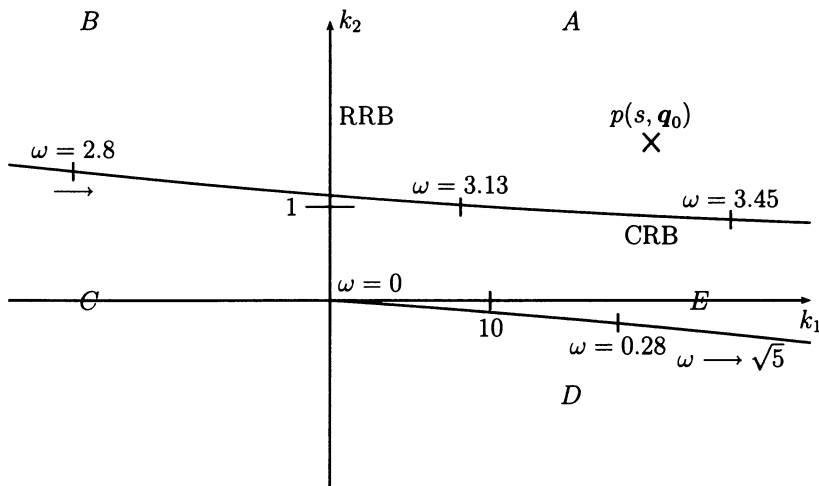


Figure 2.3. At  $\omega = 0$  the CRB branches off from the RRB

there is a real root at  $s = 0$ . If also  $k_2 = 0$ , then this becomes a double root at  $s = 0$ . This is the point, where the CRB branches off from the RRB. The CRB passes through infinity at  $\omega = \sqrt{5}$  and intersects the RRB a second time for  $\omega = 3$  at  $k_1 = 0$ ,  $k_2 = 1.125$ .

Starting from a stable  $p(s, q_0)$ , e.g. at  $k_1 = 20$ ,  $k_2 = 2$ , a continuous variation of  $k_1$  and  $k_2$  brings either a real root to the active part of the RRB for  $k_2 > 1.125$  or a complex pair to the active part of the CRB for  $k_1 > 0$  (i.e.  $\omega > 3$ ). The boundaries decompose the  $(k_1, k_2)$ -plane into five regions, designated as  $A \dots E$  in Figure 2.3.  $A$  is

the only stable region.  $B$  has an unstable real root,  $C$  has three roots in the right half plane,  $D$  has four unstable eigenvalues, and  $E$  has two of them.  $\square$

The boundary crossing concept may now be formulated as:

*Theorem 2.6 (boundary crossing)*

The family of polynomials  $P(s, Q)$  is robustly stable, if and only if:

- i. There exists a stable polynomial  $p(s, \mathbf{q}) \in P(s, Q)$ .
- ii.  $j\omega \notin \text{Roots}[P(s, Q)]$  for all  $\omega \geq 0$ .

( $\text{Roots}[P(s, Q)]$  denotes the set of all roots of  $p(s, \mathbf{q})$  for all  $\mathbf{q} \in Q$ .)

$\square$

The idea of a graphical representation of stability regions in a plane goes back to Vishnegradsky [199]. In 1876, he studied the stability of Watt's flyball governor for the steam engine. He analyzed the effect of the two middle coefficients of a third degree characteristic polynomial. Neimark [156] generalized this approach to  $n$ -th degree polynomials depending linearly on two parameters and called it  $D$ -decomposition, because the parameter plane is decomposed into regions with a fixed number of stable roots. Mitrović [149] extended the parameter space method to other eigenvalue regions than the left half plane, thereby relating controller parameters to step response specifications. Several further results and references along this line are reported in Šiljak's book [200]. In 1980, the first author [2] used the parameter space approach for the design of robust controllers, that meet eigenvalue specifications simultaneously for several plant representatives (operating points or nominal and faulted sensor situations). The solution is the intersection of the admissible controller parameter sets for the individual representatives. A pragmatic design approach is, for example, to find a robust controller that simultaneously satisfies eigenvalue specifications for the four vertices of the operating domain  $Q$  in Figure 1.2. In an analysis step, the eigenvalue boundaries are then mapped onto the  $(q_1, q_2)$ -plane in order to check if the entire continuum of  $Q$  meets the eigenvalue specifications. If necessary, the design step must be repeated with additional representatives of  $Q$ . The attitude may be described as: be an optimist in design and a pessimist in analysis!

Historically, paper-and-pencil graphic methods have a long tradition. The use of computers shifted the attention towards numeric optimization methods. This typically required the formulation of all trade-offs in a scalar performance criterion. Engineers continued, however, to visualize results in parameter spaces, because a figure tells more than an "optimal" point. Also, the optimization at the low level of controller design leaves no chance for a trade-off with requirements from other fields dealing with dynamics, e.g. structural dynamics, fluid dynamics, flight mechanics, multi-body dynamics. In a concurrent engineering design process, optimization should be used on a high level of system performance. Ideally, the individual fields should provide sets of admissible solutions that satisfy the respective specifications. Today, graphic methods are easily

computerized because graphical interfaces support the problem formulation and symbolic computer programs (MATHEMATICA, MAPLE, etc.) take care of the generation of mapping equations and producing the figures. And we can take advantage of the fact that engineers have computers with rapidly growing 2D and 3D graphic capabilities on their desk. Also, the use of colors opens new possibilities for color coding. Thus, the design engineer can fully concentrate on the interpretation of figures and on decisions for the next step in design or analysis. In this sense, the parameter space method is a very useful tool for the control engineer, but not an automatic design procedure that replaces her or him. Also, it is not meant to replace other useful tools.

## 2.3 Pole Placement

In Examples 2.4 and 2.5, the 2D-subspace for representing results was determined by fixing all but two controller parameters. A very useful alternative is to fix all but two eigenvalues in a design step. The design process then consists of sequential pole shifting steps. This approach becomes feasible by combination of parameter space and pole placement methods as will be explained in Sections 2.3 and 2.4. First, the pole placement approach is formulated in a convenient way, where the closed-loop characteristic polynomial is specified in factorized form.

In 1960, Kalman [122] introduced the definition of controllability and observability and tests for these properties. The concept of placing the poles of a single-input system in feedback canonical form appeared in [173]. The relation “controllability implies pole assignability” for a single-input system was published in [45]. It was further formalized by transformation to feedback canonical form in [123]. Another line of research places the closed-loop poles without the need for a transformation to a canonical form. For the single-input case, this was achieved in [44]. A particularly simple solution that directly allows sequential pole shifting is Ackermann’s formula [1].

Consider a single-input plant

$$\dot{\mathbf{x}} = \mathbf{A}\mathbf{x} + \mathbf{b}u \quad (2.3.1)$$

and assume controllability, i.e.

$$\det[\mathbf{b} \ \mathbf{Ab} \ \mathbf{A}^2\mathbf{b} \ \dots \ \mathbf{A}^{n-1}\mathbf{b}] \neq 0. \quad (2.3.2)$$

Pole assignment by state feedback

$$u = -\mathbf{k}^T \mathbf{x} \quad (2.3.3)$$

is the solution of

$$\det(s\mathbf{I} - \mathbf{A} + \mathbf{b}\mathbf{k}^T) = p(s) \quad (2.3.4)$$

for the elements of  $\mathbf{k}^T$ . By matching coefficients of the powers in  $s$  with

$$p(s) = a_0 + a_1 s + \dots + a_{n-1} s^{n-1} + s^n, \quad (2.3.5)$$

there are  $n$  equations in  $n$  unknowns of  $\mathbf{k}^T$ . These equations have a unique solution, if and only if the pair  $(\mathbf{A}, \mathbf{b})$  is controllable.

*Theorem 2.7 (Ackermann)*

The solution of  $\det(s\mathbf{I} - \mathbf{A} + \mathbf{b}\mathbf{k}^T) = p(s)$  with  $(\mathbf{A}, \mathbf{b})$  controllable is

$$\begin{aligned}\mathbf{k}^T &= \mathbf{e}^T p(\mathbf{A}), \\ \mathbf{e}^T &= [0 \dots 0 1] [\mathbf{b} \ \mathbf{Ab} \ \mathbf{A}^2\mathbf{b} \ \dots \ \mathbf{A}^{n-1}\mathbf{b}]^{-1}.\end{aligned}\tag{2.3.6}$$

□

The  $n$ -vector  $\mathbf{e}^T$  is the last row of the inverted controllability matrix and  $p(\mathbf{A})$  is the matrix polynomial that is obtained by replacing the powers of  $s$  by the powers of  $\mathbf{A}$ , i.e.  $s^0 \rightarrow \mathbf{A}^0 = \mathbf{I}$ ,  $s^1 \rightarrow \mathbf{A}^1$ , etc.

*Proof*

Let  $\mathbf{F} = \mathbf{A} - \mathbf{b}\mathbf{k}^T$ , expand  $\mathbf{F}^k$  into expressions of the form  $\mathbf{A}^k$  and  $\mathbf{A}^i\mathbf{b}\mathbf{k}^T\mathbf{F}^j$ ,  $i + j = k - 1$ , and evaluate  $p(\mathbf{F}) = a_0\mathbf{F}^0 + a_1\mathbf{F}^1 + \dots + a_{n-1}\mathbf{F}^{n-1} + \mathbf{F}^n$ .

$$\begin{array}{lcl} \mathbf{F}^0 = \mathbf{A}^0 \quad (= \mathbf{I}) & & \times a_0 \\ \mathbf{F}^1 = \mathbf{A}^1 - \mathbf{b}\mathbf{k}^T & & \times a_1 \\ \mathbf{F}^2 = \mathbf{A}^2 - \mathbf{Ab}\mathbf{k}^T - \mathbf{b}\mathbf{k}^T\mathbf{F} & & \times a_2 \\ \vdots & & \vdots \\ \mathbf{F}^n = \mathbf{A}^n - \mathbf{A}^{n-1}\mathbf{b}\mathbf{k}^T - \mathbf{A}^{n-2}\mathbf{b}\mathbf{k}^T\mathbf{F} - \dots - \mathbf{b}\mathbf{k}^T\mathbf{F}^{n-1} & & \times 1 \end{array}$$

$$p(\mathbf{F}) = p(\mathbf{A}) - [\mathbf{b} \ \mathbf{Ab} \ \dots \ \mathbf{A}^{n-1}\mathbf{b}] \begin{bmatrix} \vdots \\ \mathbf{k}^T \end{bmatrix}. \tag{2.3.7}$$

The polynomial  $p(s) = \det(s\mathbf{I} - \mathbf{F})$  is the characteristic polynomial that shall be given to  $\mathbf{F}$ . Therefore, by the Cayley-Hamilton theorem [94],  $p(\mathbf{F}) = 0$ . Now  $\begin{bmatrix} \vdots \\ \mathbf{k}^T \end{bmatrix} = [\mathbf{b} \ \mathbf{Ab} \ \dots \ \mathbf{A}^{n-1}\mathbf{b}]^{-1} p(\mathbf{A})$ . From the last row of this equation follows

$$\mathbf{k}^T = \mathbf{e}^T p(\mathbf{A}), \tag{2.3.8}$$

where  $\mathbf{e}^T = [0 \dots 0 1] [\mathbf{b} \ \mathbf{Ab} \ \dots \ \mathbf{A}^{n-1}\mathbf{b}]^{-1}$  is the last row of the inverted controllability matrix.

□

Note that Equation (2.3.6) may be written as

$$\mathbf{k}^T = \mathbf{e}^T(a_0\mathbf{I} + a_1\mathbf{A} + \cdots + a_{n-1}\mathbf{A}^{n-1} + \mathbf{A}^n) = [\hat{\mathbf{a}} \ 1] \ \mathbf{E}. \quad (2.3.9)$$

The matrix

$$\mathbf{E} = \begin{bmatrix} \mathbf{e}^T \\ \mathbf{e}^T \mathbf{A} \\ \vdots \\ \mathbf{e}^T \mathbf{A}^n \end{bmatrix} \quad (2.3.10)$$

is called the *pole placement matrix*. The form (2.3.9) illustrates that it is not necessary to evaluate  $p(\mathbf{A})$  by calculations with  $n^2$ -matrices. The calculation of  $\mathbf{E}$  only requires operations on  $n$ -vectors. For the numerical calculation of  $\mathbf{E}$ , see [4], [13].

Note also that  $p(s)$  may be given in factorized form as

$$p(s) = \begin{cases} \prod_{i=1}^{n/2} (s^2 + b_i s + c_i) & \text{for } n \text{ even,} \\ (s+d) \prod_{i=1}^{(n-1)/2} (s^2 + b_i s + c_i) & \text{for } n \text{ odd,} \end{cases} \quad (2.3.11)$$

rather than in the multiplied form (2.3.6). The closed-loop system is then stable if and only if all  $b_i, c_i$  and  $d$  are positive. This is a characterization of all stabilizing state feedback gains  $\mathbf{k}$  in equation (2.3.6).

While the factorization of  $p(s)$  can be performed only numerically, the opposite step of finding the polynomial from its roots by (2.3.11) can be performed symbolically and is therefore particularly suited to parametric systems.

### Remark 2.8

Equation (2.3.6) is related with (1.5.12), i.e.

$$\hat{\mathbf{a}}^T = \hat{\mathbf{a}}_0^T + \mathbf{k}^T \mathbf{W} \quad (2.3.12)$$

for output feedback. In the special case of full state feedback,  $\mathbf{W}$  is non-singular for a controllable system, and

$$\mathbf{k}^T = (\hat{\mathbf{a}}^T - \hat{\mathbf{a}}_0^T) \mathbf{W}^{-1}. \quad (2.3.13)$$

Small gains can be expected for small changes in the coefficients of the characteristic polynomial from  $\hat{\mathbf{a}}_0$  to  $\hat{\mathbf{a}}$ . However, roots may be very sensitive to coefficient changes. Therefore, we will look at shifting only one pair of eigenvalues in the next section rather than changing coefficient vectors.

The connection between Equations (2.3.6) and (2.3.12) is established by substitution of  $\hat{\mathbf{a}}^T$  into (2.3.9).

$$\mathbf{k}^T = [\hat{\mathbf{a}}_0^T + \mathbf{k}^T \mathbf{W} \ 1] \ \mathbf{E},$$

where by Cayley-Hamilton  $[\hat{\mathbf{a}}_0^T \ 1] \ \mathbf{E} = 0$ , i.e.

$$\mathbf{W} = \begin{bmatrix} \mathbf{e}^T \\ \mathbf{e}^T \mathbf{A} \\ \vdots \\ \mathbf{e}^T \mathbf{A}^{n-1} \end{bmatrix}^{-1} \quad (2.3.14)$$

for a controllable system. For non-controllable systems, only the singular  $\mathbf{W}$  exists, but not its inverse.

□

## 2.4 Sequential Pole Shifting

Consider a stepwise design procedure in which in each step  $n - 2$  eigenvalues are fixed, and only two eigenvalues are shifted by state feedback  $\mathbf{k}^T$ . In the first step, the characteristic polynomial of  $\mathbf{A}$  is factorized as

$$\det(s\mathbf{I} - \mathbf{A}) = h(s)(d_0 + d_1 s + d_2 s^2). \quad (2.4.1)$$

The roots of  $d_0 + d_1 s + d_2 s^2$  are selected for shifting in the first design step, the polynomial  $h(s) = h_0 + h_1 s + \dots + h_{n-3} s^{n-3} + s^{n-2}$  shall be invariant under state feedback, i.e.

$$\det(s\mathbf{I} - \mathbf{A} + \mathbf{b}\mathbf{k}^T) = h(s)(t_0 + t_1 s + s^2). \quad (2.4.2)$$

The shift is denoted by

$$(t_0 - d_0) + (t_1 - d_1)s =: \kappa_a + \kappa_b s.$$

It may be visualized in the  $(\kappa_a, \kappa_b)$ -plane. How is a point in this plane related with the full state feedback vector  $\mathbf{k}^T$ ? The answer follows immediately from (2.3.6):

$$\mathbf{k}^T = \mathbf{e}^T p(\mathbf{A}) = \mathbf{e}^T h(\mathbf{A})(t_0 \mathbf{I} + t_1 \mathbf{A} + \mathbf{A}^2).$$

$$\text{Let } \mathbf{e}_h^T := \mathbf{e}^T h(\mathbf{A}) = [\hat{\mathbf{h}} \ 1] \begin{bmatrix} \mathbf{e}^T \\ \mathbf{e}^T \mathbf{A} \\ \vdots \\ \mathbf{e}^T \mathbf{A}^{n-2} \end{bmatrix}, \quad (2.4.3)$$

$$\mathbf{k}^T = \mathbf{e}_h^T (t_0 \mathbf{I} + t_1 \mathbf{A} + \mathbf{A}^2). \quad (2.4.4)$$

No shift ( $t_0 = d_0$ ,  $t_1 = d_1$ ) yields

$$0 = \mathbf{e}_h^T (d_0 \mathbf{I} + d_1 \mathbf{A} + \mathbf{A}^2). \quad (2.4.5)$$

The difference of Equations (2.4.4) and (2.4.5) is

$$\begin{aligned} \mathbf{k}^T &= \mathbf{e}_h^T [(t_0 - d_0)\mathbf{I} + (t_1 - d_1)\mathbf{A}] \\ &= [\kappa_a \ \kappa_b] \begin{bmatrix} \mathbf{e}_h^T \\ \mathbf{e}_h^T \mathbf{A} \end{bmatrix} = [\kappa_a \ \kappa_b] \begin{bmatrix} h_0 & h_1 & \dots & h_{n-2} & 0 \\ 0 & h_0 & \dots & h_{n-3} & h_{n-2} \end{bmatrix} \begin{bmatrix} \mathbf{e}^T \\ \mathbf{e}^T \mathbf{A} \\ \vdots \\ \mathbf{e}^T \mathbf{A}^{n-1} \end{bmatrix}. \end{aligned} \quad (2.4.6)$$

The  $(\kappa_a, \kappa_b)$ -plane is a linear subspace of the  $\mathbf{k}$ -space. It is called the *invariance plane*. It is spanned by the vectors  $\mathbf{e}_h^T$  and  $\mathbf{e}_h^T \mathbf{A}$  and its coordinates are  $\kappa_a = t_0 - d_0$ ,  $\kappa_b = t_1 - d_1$ .

*Remark 2.9*

An alternative interpretation of the  $h$ -invariant subspace is that the  $n - 2$  roots of  $h(s)$  are non-observable from the output  $\mathbf{k}^T \mathbf{x}$ .  $\square$

For the new system  $(\mathbf{F}, \mathbf{b}) = (\mathbf{A} - \mathbf{b}\mathbf{k}^T, \mathbf{b})$ , again only two eigenvalues are shifted. A new invariant polynomial

$$\bar{h}(s) = \bar{h}_0 + \bar{h}_1 s + \cdots + \bar{h}_{n-3} s^{n-3} + s^{n-2}$$

is chosen for  $n - 2$  eigenvalues of  $\mathbf{F}$  and

$$\mathbf{e}_h^T = [\hat{\mathbf{h}}^T \ 1] \begin{bmatrix} \mathbf{e}_F^T \\ \mathbf{e}_F^T \mathbf{F} \\ \vdots \\ \mathbf{e}_F^T \mathbf{F}^{n-2} \end{bmatrix}. \quad (2.4.7)$$

No new calculation of the pole placement matrix is necessary, because its first  $n$  rows are invariant under state feedback. The vectors  $\mathbf{e}^T$  and  $\mathbf{e}_F^T$  are, by definition, the last row of the respective inverse controllability matrices, i.e.

$$\mathbf{e}^T [\mathbf{b} \ \mathbf{Ab} \ \dots \ \mathbf{A}^{n-1} \mathbf{b}] = [0 \ \dots \ 0 \ 1], \quad (2.4.8)$$

$$\mathbf{e}_F^T [\mathbf{b} \ (\mathbf{A} - \mathbf{b}\mathbf{k}^T)\mathbf{b} \ \dots \ (\mathbf{A} - \mathbf{b}\mathbf{k}^T)^{n-1} \mathbf{b}] = [0 \ \dots \ 0 \ 1]. \quad (2.4.9)$$

Substituting the first column of (2.4.9), i.e.  $\mathbf{e}_F^T \mathbf{b} = 0$  into the second one yields

$$\mathbf{e}_F^T (\mathbf{A} - \mathbf{b}\mathbf{k}^T) \mathbf{b} = \mathbf{e}_F^T \mathbf{Ab} = 0.$$

The third column is

$$\mathbf{e}_F^T (\mathbf{A} - \mathbf{b}\mathbf{k}^T) (\mathbf{A} - \mathbf{b}\mathbf{k}^T) \mathbf{b} = \mathbf{e}_F^T \mathbf{A}^2 \mathbf{b} = 0,$$

and so on until

$$\mathbf{e}_F^T [\mathbf{b} \ \mathbf{Ab} \ \dots \ \mathbf{A}^{n-1} \mathbf{b}] = [0 \ \dots \ 0 \ 1] \quad (2.4.10)$$

is obtained, and by comparison with (2.4.8),

$$\mathbf{e}_F^T = \mathbf{e}^T \quad \text{for all } \mathbf{k}^T. \quad (2.4.11)$$

The pole placement matrices  $\mathbf{E}$  and  $\mathbf{E}_F$  of the two pairs  $(\mathbf{A}, \mathbf{b})$  and  $(\mathbf{F}, \mathbf{b}) = (\mathbf{A} - \mathbf{b}\mathbf{k}^T, \mathbf{b})$  are related by

$$\mathbf{E}_F = \mathbf{E} - \begin{bmatrix} 0 \\ \vdots \\ 0 \\ \mathbf{k}^T \end{bmatrix}. \quad (2.4.12)$$

Therefore, (2.4.7) may be written as

$$\mathbf{e}_h^T = [\hat{\mathbf{h}}^T \ 1] \begin{bmatrix} \mathbf{e}^T \\ \mathbf{e}^T \mathbf{A} \\ \vdots \\ \mathbf{e}^T \mathbf{A}^{n-2} \end{bmatrix}. \quad (2.4.13)$$

The above results for sequential pole shifting are summarized in the following:

### Recipe

#### 1. Calculate

$$\bar{\mathbf{E}} = \begin{bmatrix} \mathbf{e}^T \\ \mathbf{e}^T \mathbf{A} \\ \vdots \\ \mathbf{e}^T \mathbf{A}^{n-1} \end{bmatrix}, \quad \mathbf{e}^T = [0 \ \dots \ 0 \ 1] [\mathbf{b} \ \mathbf{Ab} \ \dots \ \mathbf{A}^{n-1}\mathbf{b}]^{-1}.$$

#### 2. Factorize $\det(s\mathbf{I} - \mathbf{A}) = \prod_{i=1}^n (s - s_i)$ .

##### 3.1. Select two eigenvalues, say $s_1$ and $s_2$ , for shifting in the first design step.

##### 4.1. Determine the coefficient vector $\hat{\mathbf{h}}^T$ of the invariant polynomial $h(s) = \prod_{i=3}^n (s - s_i)$ and calculate $\mathbf{e}_h^T = \hat{\mathbf{h}}^T \bar{\mathbf{E}}$ .

##### 5.1. Choose a state feedback

$$\mathbf{k}^T = [\kappa_a \ \kappa_b] \begin{bmatrix} \mathbf{e}_h^T \\ \mathbf{e}_h^T \mathbf{A} \end{bmatrix} = [\kappa_a \ \kappa_b] \begin{bmatrix} \hat{\mathbf{h}}^T & 0 \\ 0 & \hat{\mathbf{h}}^T \end{bmatrix} \bar{\mathbf{E}} \quad (2.4.14)$$

in the  $(\kappa_a, \kappa_b)$ -invariance-plane that shifts  $s_1, s_2$  to  $s_1^*, s_2^*$ .

##### 3.2. If necessary, repeat step 3.1; select, for example, $s_3$ and $s_4$ .

##### 4.2. Repeat step 4.1 with $h(s) = \prod_{i=1}^2 (s - s_i^*) \prod_{i=5}^n (s - s_i)$ .

##### 5.2. Repeat step 5.1 and shift $s_3, s_4$ to $s_3^*, s_4^*$ etc.

For shifting a single real eigenvalue,  $h(s)$  is of degree  $n - 1$  and  $\bar{\mathbf{E}}$  is augmented by a last row  $\mathbf{e}^T \mathbf{A}^n$ .

### Example 2.10

Consider the crane with parameters  $\ell = 12$ ,  $m_L = 1500$ ,  $m_C = 1000$ . The state space representation is given by (1.1.6)

$$\dot{\mathbf{x}} = \begin{bmatrix} 0 & 1 & 0 & 0 \\ 0 & 0 & 15 & 0 \\ 0 & 0 & 0 & 1 \\ 0 & 0 & -25/12 & 0 \end{bmatrix} \mathbf{x} - \begin{bmatrix} 0 \\ 1/1000 \\ 0 \\ -1/-12000 \end{bmatrix} u,$$

and the open-loop characteristic polynomial is

$$p(s) = \left(\frac{25}{12} + s^2\right)s^2.$$

The open-loop system has a double pole at the origin,  $d(s) = s^2$ , and a complex conjugate pole pair on the  $j\omega$ -axis,  $h(s) = 25/12 + s^2$ . Choose an invariance plane in

which only the double pole at the origin is shifted to the roots of  $t_0 + t_1 s + s^2$ . By (2.4.14), the feedback vector is

$$\mathbf{k}_1^T = [t_0 \ t_1] \begin{bmatrix} 2500 & 0 & 18000 & 0 \\ 0 & 2500 & 0 & 18000 \end{bmatrix}.$$

The pole pair is shifted by  $t_0 > 0$ ,  $t_1 > 0$ , let, for example,  $t_0 = 0.1$ ,  $t_1 = 0.6$ , then

$$\mathbf{k}_1^T = [250 \ 1500 \ 1800 \ 10800].$$

In a second step, the roots of  $\bar{h}(s) = 0.1 + 0.6s + s^2$  are kept invariant, and the roots of  $d(s) = 25/12 + s^2$  are shifted to the roots of a new  $\bar{t}(s) = \bar{t}_0 + \bar{t}_1 s + s^2$ , i.e.  $\kappa_c = \bar{t}_0 - d_0 = \bar{t}_0 - 25/12$ ,  $\kappa_d = \bar{t}_1 - d_1 = \bar{t}_1$ . The resulting feedback vector is

$$\mathbf{k}_2^T = [\kappa_c \ \kappa_d] \begin{bmatrix} 120 & 720 & -10560 & 8640 \\ 0 & 120 & -7200 & -19560 \end{bmatrix}.$$

The total state feedback gain is  $\mathbf{k} = \mathbf{k}_1 + \mathbf{k}_2 = [k_1 \ k_2 \ k_3 \ k_4]^T$ , with

$$\begin{aligned} k_1 &= 250 + 120\kappa_c, \\ k_2 &= 1500 + 720\kappa_c + 120\kappa_d, \\ k_3 &= 1800 - 10560\kappa_c - 7200\kappa_d, \\ k_4 &= 10800 + 8640\kappa_c - 10560\kappa_d. \end{aligned}$$

The system is stable for  $\bar{t}_0 > 0$ ,  $\bar{t}_1 > 0$ , i.e.  $\kappa_c > -\frac{25}{12}$ ,  $\kappa_d > 0$ .

A practically useful choice of  $\kappa_c$ ,  $\kappa_d$  from the stable region is one for which we do not have to feed back the rope angle rate, i.e.

$$k_4 = 10800 + 8640\kappa_c - 10560\kappa_d = 0.$$

The line  $k_4 = 0$  is shown in the  $(\kappa_c, \kappa_d)$ -plane of Figure 2.4.

### Remark 2.11

Figure 2.4 also contains the image of a more restrictive boundary than Hurwitz-stability. Such “ $\Gamma$ -stability” will be treated in Chapter 3. The chosen boundary is the left branch of the hyperbola  $\omega^2 = 4\sigma^2 - 0.25$ . The point  $\kappa^{(2)}$  is chosen such that not only Hurwitz-stability is given, but also  $\Gamma$ -stability in the sense that all poles are on the left side of the above hyperbola.

□

We choose  $\kappa_c = 0.83$ ,  $\kappa_d = 1.7$  on the line  $k_4 = 0$ , then the second pair of roots moves from the imaginary axis to the root of  $r(s) = \kappa_c + 25/12 + \kappa_d s + s^2 = 2.91 + 1.7s + s^2$ , and the total feedback vector is  $\mathbf{k}^T = [349 \ 2300 \ -19181 \ 0]$ .

□

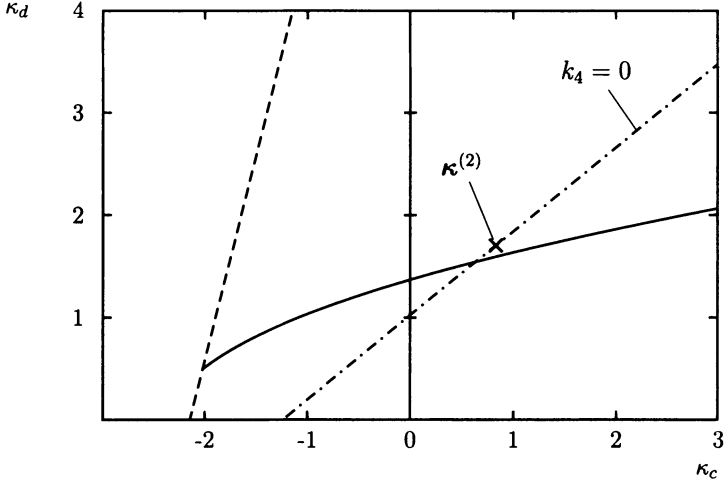


Figure 2.4. Invariance plane for the second design step. Feedback of the angular velocity  $x_4$  is avoided on the line  $k_4 = 0$

At this point, the reader may wonder why both pole shifts are not executed in one shot. However, in the simultaneous stabilization of several operating points, it turns out that sequential pole shifting is a very useful tool because it allows sequential graphical design steps in 2D-subspaces. In fact, the idea of sequential pole shifting originated from the application example of a track-guided bus [32], see Section 6.9.

## 2.5 Singular Frequencies

In the previous examples, a continuum of frequencies contributed to the CRB (see, for example, Figure 2.2) There are, however, special cases, where a singular frequency generates an entire branch of the stability boundary. Consider a polynomial that depends linearly on two uncertain real parameters  $q_1$  and  $q_2$  (these may be plant or controller parameters). It may be written as

$$p(s, q_1, q_2) = p_0(s) + q_1 p_1(s) + q_2 p_2(s), \quad (2.5.1)$$

where  $p_0(s), p_1(s), p_2(s)$  are known polynomials. For  $s = j\omega$ , their real and imaginary parts are

$$\begin{aligned} p_0(j\omega) &= R_0(\omega) + jI_0(\omega), \\ p_1(j\omega) &= R_1(\omega) + jI_1(\omega), \\ p_2(j\omega) &= R_2(\omega) + jI_2(\omega), \end{aligned} \quad (2.5.2)$$

and the real and imaginary parts of

$$p(j\omega, q_1, q_2) = R_p(\omega, q_1, q_2) + jI_p(\omega, q_1, q_2) \quad (2.5.3)$$

are zero for

$$\begin{aligned} R_p(\omega, q_1, q_2) &= R_0(\omega) + q_1 R_1(\omega) + q_2 R_2(\omega) = 0, \\ I_p(\omega, q_1, q_2) &= I_0(\omega) + q_1 I_1(\omega) + q_2 I_2(\omega) = 0. \end{aligned}$$

In matrix notation,

$$\begin{bmatrix} R_1(\omega) & R_2(\omega) \\ I_1(\omega) & I_2(\omega) \end{bmatrix} \begin{bmatrix} q_1 \\ q_2 \end{bmatrix} + \begin{bmatrix} R_0(\omega) \\ I_0(\omega) \end{bmatrix} = \begin{bmatrix} 0 \\ 0 \end{bmatrix}. \quad (2.5.4)$$

A singularity occurs at a frequency  $\omega$  for which the determinant of the matrix in (2.5.4) vanishes, i.e.

$$R_1(\omega)I_2(\omega) - R_2(\omega)I_1(\omega) = 0. \quad (2.5.5)$$

In this case, the two straight lines represented by (2.5.4) are parallel in the  $(q_1, q_2)$ -plane, i.e. a solution exists only if the two lines become identical, i.e. if also

$$R_1(\omega)I_0(\omega) - R_0(\omega)I_1(\omega) = 0. \quad (2.5.6)$$

Real frequencies  $\omega = \omega_k$  that satisfy both Equations (2.5.5) and (2.5.6) are called *singular frequencies*. At such a singular frequency, the solution in the  $(q_1, q_2)$ -plane is not just an intersection point (like for non-singular frequencies) but an entire straight line. We will exploit this fact for the design of robust PID-controllers in Section 2.6.

The real parts  $R_0, R_1, R_2$  are polynomials in  $\omega^2$ , hence  $R(\omega) = \bar{R}(\omega^2)$ . The imaginary parts  $I_0, I_1, I_2$  have the form  $I(\omega) = \omega \bar{I}(\omega^2)$ . The case  $\omega = 0$  yields the RRB. For the CRB with  $\omega \neq 0$ , divide (2.5.5) and (2.5.6) by  $\omega$  to get

$$d(\omega^2) = \bar{R}_1(\omega^2)\bar{I}_2(\omega^2) - \bar{R}_2(\omega^2)\bar{I}_1(\omega^2) = 0, \quad (2.5.7)$$

$$d_1(\omega^2) = \bar{R}_1(\omega^2)\bar{I}_0(\omega^2) - \bar{R}_0(\omega^2)\bar{I}_1(\omega^2) = 0. \quad (2.5.8)$$

The real positive solutions  $\omega_i^2$  of  $d(\omega^2) = 0$  yield real frequencies  $\omega_i$  that are candidates for singular frequencies. Substitute  $\omega_i$  in  $d_1(\omega^2) = 0$ , i.e.

$$d_1(\omega_i^2) = \bar{R}_1(\omega_i^2)\bar{I}_0(\omega_i^2) - \bar{R}_0(\omega_i^2)\bar{I}_1(\omega_i^2) = 0 \quad (2.5.9)$$

If this condition is satisfied, then  $\omega_i$  is a singular frequency.

### Remark 2.12

The equations  $d_1 = \bar{R}_1\bar{I}_0 - \bar{R}_0\bar{I}_1 = 0$  and  $d_2 = \bar{R}_2\bar{I}_0 - \bar{R}_0\bar{I}_2 = 0$  are linearly dependent by construction and it does not matter which one is used. The only exception is the trivial case  $d_1(\omega^2) \equiv 0$ , then  $d_2(\omega^2) = 0$  must be used.

□

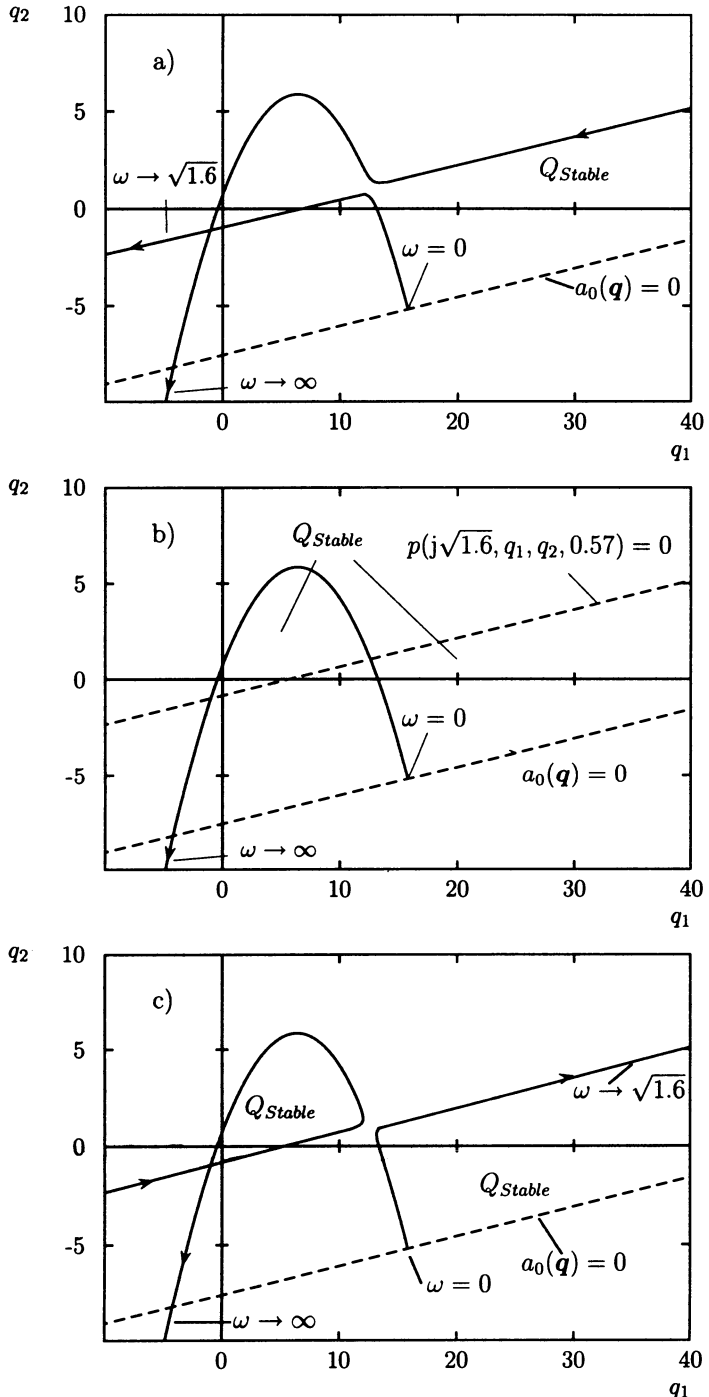


Figure 2.5. Three stability regions in the  $(q_1, q_2)$ -plane. a)  $q_3 = 0.56$ , connected, b)  $q_3 = 0.57$ , singular case, c)  $q_3 = 0.58$ , disjoint

*Example 2.13*

Consider the uncertain polynomial

$$p(s, \mathbf{q}) = (14 - 0.3q_1 + 2q_2 + 2q_3) + (10 + 2q_1 + 8q_2)s + 10s^2 + 2(1 + q_1)s^3 + s^4.$$

Plot the stable region  $Q_{stable}$  in the  $(q_1, q_2)$ -plane for fixed  $q_3$ .

The RRB for  $\omega = 0$  is

$$a_0(\mathbf{q}) = -0.3q_1 + 2q_2 + (14 + 2q_3) = 0.$$

Equation (2.5.7) reads  $d(\omega^2) = -1.6 + \omega^2 = 0$ . The candidate frequency  $\omega = \sqrt{1.6}$  is substituted in (2.5.8):

$$d_1(1.6) = -1.368 + 2.4q_3 = 0.$$

This equation yields  $q_3 = 0.57$  as the only possibility that  $\omega = \sqrt{1.6}$  is a singular frequency.

The complex root boundary for all frequencies follows from (2.5.4), with the second row divided by  $\omega$ :

$$\begin{bmatrix} q_1 \\ q_2 \end{bmatrix} = - \begin{bmatrix} -0.3 & 2 \\ 2 - 2\omega^2 & 8 \end{bmatrix}^{-1} \begin{bmatrix} (14 + 2q_3) - 10\omega^2 + \omega^4 \\ 10 - 2\omega^2 \end{bmatrix},$$

$$q_1(\omega^2, q_3) = -5 \frac{2\omega^4 - 19\omega^2 + 23 + 4q_3}{5\omega^2 - 8},$$

$$q_2(\omega^2, q_3) = -\frac{1}{4} \frac{10\omega^6 - 110\omega^4 + (243 + 20q_3)\omega^2 - 155 - 20q_3}{5\omega^2 - 8}.$$

Figure 2.5 shows the three cases with a)  $q_3 = 0.56$ , b)  $q_3 = 0.57$ , and c)  $q_3 = 0.58$ . The asymptote for  $\omega = \sqrt{1.6}$  is approached in opposite directions in the cases a) and c). In case b), it is a singular boundary. Obviously, the topology in the  $(q_1, q_2)$ -plane changes at  $q_3 = 0.57$  from a simply connected stability region to two disjoint stable regions.  $\square$

## 2.6 Hurwitz-stability Regions for PID-controllers

In the previous section, the occurrence of singular frequencies appeared as a very special case. In this section, it will be shown, that singular frequencies occur in PID-control systems and can be exploited for their design. Consider the PID-control system in Figure 2.6.  $G_i(s)$ ,  $i = 1, 2, \dots, N$  is a finite family of plant models for  $N$  representative operating conditions. The problem is to design a robust PID-controller

$$\text{PID}(s) = \frac{K_I + K_P s + K_D s^2}{s(1 + T_R s)} \quad (2.6.1)$$

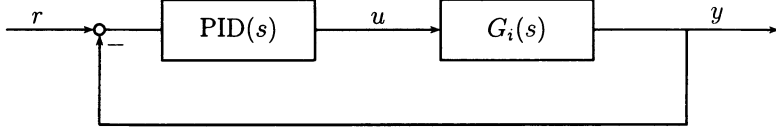


Figure 2.6. PID-control system

that simultaneously stabilizes all  $N$  members of the plant family. A small time constant  $T_R$  is introduced for realizability of the PID-controller.  $T_R = 0$  may be assumed for the design of the essential parameters  $K_I$ ,  $K_P$  and  $K_D$ . In order to allow for trade-offs with other design specifications, e.g. in the frequency domain, it is of interest to calculate the set of all simultaneously stabilizing PID-controllers. This set can be visualized in a tomographic rendering, e.g. by representing the stable region in a  $(K_P, K_D)$ -plane for a grid of  $K_I$ -values. In this plane, the stable region is non-convex and bounded by curves, which may be calculated, for example, by the software tool PARADISE, see Appendix B. In each plane, the intersection of the admissible sets for the  $N$  operating conditions is determined in order to find the set of simultaneous stabilizers.

The above process is considerably simplified by a recent result of Bhattacharyya, Ho and Datta [108], [71]. They have shown that for fixed  $K_P$  the Hurwitz-stable region in the  $(K_D, K_I)$ -plane consists of convex polygons. Thus, also the intersection for several operating conditions consists of convex polygons, and a tomographic rendering for a grid on  $K_P$  yields a visualization of the set of all simultaneously stabilizing PID-controllers. The above authors assume  $T_R = 0$  and use a modified Hermite-Biehler theorem for the proof. An alternative proof was given by Munro and Soylemez [155] by calculating the real axis intersections of the Nyquist plot. In this section, the parameter space approach is applied to the problem.

The theory will be first developed for one operating condition

$$\begin{aligned} A(s) &= \text{num } G(s) = a_0 + a_1 s + \dots + a_k s^k, \quad a_k \neq 0 \\ B(s) &= s(1 + T_R s) \text{ den } G(s) = b_0 + b_1 s + \dots + b_m s^m, \quad b_m \neq 0. \end{aligned}$$

The characteristic polynomial of the PID-control system in Figure 2.6 has the structure

$$P(s, K_I, K_P, K_D) = A(s)(K_I + K_P s + K_D s^2) + B(s). \quad (2.6.2)$$

(The following derivation also holds for  $b_0 \neq 0$ .) The polynomial (2.6.2) has a root at  $s = j\omega$  if and only if:

$$\begin{aligned} R_P &= \text{Re } P(j\omega, K_I, K_P, K_D) = 0, \quad \text{and} \\ I_P &= \text{Im } P(j\omega, K_I, K_P, K_D) = 0. \end{aligned} \quad (2.6.3)$$

For the separation of real and imaginary parts, write

$$A(j\omega) = R_A + jI_A,$$

$$B(j\omega) = R_B + jI_B.$$

Then for fixed  $K_P$ , Equation (2.6.3) may be written as

$$\begin{bmatrix} R_P \\ I_P \end{bmatrix} = \begin{bmatrix} R_A & -R_A\omega^2 \\ I_A & -I_A\omega^2 \end{bmatrix} \begin{bmatrix} K_I \\ K_D \end{bmatrix} + \begin{bmatrix} -K_P I_A \omega + R_B \\ K_P R_A \omega + I_B \end{bmatrix} = \begin{bmatrix} 0 \\ 0 \end{bmatrix}. \quad (2.6.4)$$

Note that the matrix multiplying  $[K_I \ K_D]^T$  is always singular, i.e. geometrically (2.6.4) represents the intersection of two parallel lines. A solution exists, if and only if the parallels are identical, i.e. for real frequencies  $\omega_k$  such that

$$\begin{aligned} g(\omega) &= \det \begin{bmatrix} R_A & -K_P I_A \omega + R_B \\ I_A & K_P R_A \omega + I_B \end{bmatrix} \\ &= R_A(K_P R_A \omega + I_B) + I_A(K_P I_A \omega - R_B) \\ &= \omega K_P(R_A^2 + I_A^2) + R_A I_B - I_A R_B = 0. \end{aligned} \quad (2.6.5)$$

It is easily verified that  $g(\omega)$  is  $\omega$  times a polynomial  $\bar{g}$  in  $\omega^2$ , i.e.  $g(\omega) = \omega \bar{g}(\omega^2)$  and  $\omega_0 = 0$  is always a solution of  $g(\omega) = 0$ . The degree of the remaining polynomial  $\bar{g}(\omega^2)$  results from the highest degree of the product terms in (2.6.5). Only its positive real solutions  $\omega_k^2$  lead to real frequencies  $\omega_k$ . The solutions  $\omega_k$  ( $k = 0, 1, 2 \dots K$ ) are *singular frequencies*.

The interpretation of (2.6.5) is that the root set of  $P(s, q_0, q_2)$  (e.g.  $q_0 = K_I, q_2 = K_D$ ) can cross the imaginary axis only through the “holes” at the singular frequencies  $\omega_k$ .

### Example 2.14

$$P(s) = (s - 1)(q_0 + q_2 s^2) + s^2 + s + 1,$$

$$\begin{aligned} q_0 &\in [-2; 0.1], \\ q_2 &\in [0.1; 0.7]. \end{aligned}$$

Figure 2.7 shows the two-parametric root set generated by gridding  $q_0$  and  $q_2$ . It can cross the imaginary axis only through the hole  $\omega_1 = \sqrt{2}$ .  $\square$

### Remark 2.15

This example also serves as a warning that gridding of  $\omega$  will miss the value  $\omega_1 = \sqrt{2}$ .  $\square$

Starting from a stable polynomial (2.6.2), there are three possibilities of how a root can cross over the imaginary axis by variation of  $K_I$  and  $K_D$ .

- a) A real root crosses at  $s = 0$ . For  $\omega = 0$ , we have  $I_P = 0$  and the real root boundary (RRB) is obtained from

$$R_P(\omega = 0) = a_0 K_I + b_0 = 0$$

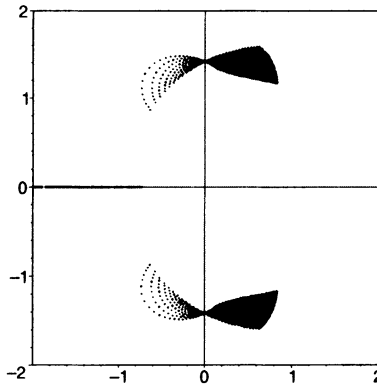


Figure 2.7. The root set can cross the imaginary axis only at the hole  $\omega_1 = \sqrt{2}$

The RRB is

$$K_I = -b_0/a_0. \quad (2.6.6)$$

- b) A real root crosses at  $s = \infty$ . This infinite root boundary (IRB) is characterized by  $p_n = 0$  in  $P(s) = p_0 + p_1s + \dots + p_ns^n$ .

$$p_n = \begin{cases} a_k K_D & \text{for } m < k+2 \\ a_k K_D + b_m & \text{for } m = k+2 \\ b_m & \text{for } m > k+2 \end{cases}.$$

In the  $(K_D, K_I)$ -plane, the IRB is

$$K_D = \begin{cases} 0 & \text{for } m < k+2 \\ -b_m/a_k & \text{for } m = k+2 \\ \text{no boundary} & \text{for } m > k+2 \end{cases}. \quad (2.6.7)$$

- c) A conjugate pair of roots crosses at one of the non-zero singular frequencies  $\omega_k$ . These complex root boundaries (CRB) are obtained by substitution of  $\omega_k$  into the first row of (2.6.4) (assuming  $R_A \neq 0$ ) or second row (assuming  $I_A \neq 0$ ). The first row becomes

$$K_I - K_D \omega_k^2 = -[R_B(\omega_k) - I_A(\omega_k) \omega_k K_P]/R_A(\omega_k). \quad (2.6.8)$$

In the  $(K_D, K_I)$ -plane, these are straight lines with positive slopes  $\omega_k^2$ , one line for each singular frequency.

In summary: in the  $(K_D, K_I)$ -plane for fixed  $K_P$ , roots cross over the imaginary axis:

- i. On the line  $K_I = -b_0/a_0$  with slope zero (RRB,  $\omega_0 = 0$ ).
- ii. On the lines of Equation (2.6.8) with positive slope (CRB,  $\omega = \omega_k$ ,  $k = 1, 2, \dots, K$ ).

iii. Possibly on the boundary for  $K_D$  of (2.6.7) with infinite slope (IRB,  $\omega = \infty$ ).

These straight lines form convex polygons (also infinity may be a vertex), where neighboring polygons correspond to a different number of poles in the left half plane.

There remains the task of identifying the stable polygons. One possibility is to check one point in each polygon in order to find the stable ones.

*Example 2.16*

$$P(s, K_I, K_P, K_D) = (s - 1)(K_I + K_P s + K_D s^2) + 2s + 1.$$

For  $K_P = 1$ , the example is identical to Example 2.14.

i. RRB for  $\omega_0 = 0$ :

$$K_I = -b_0/a_0 = 1.$$

ii. CRB for  $\omega_1 = \sqrt{2}$ :

$$K_I = 2K_D - 1, \text{ slope } \omega_1^2 = 2.$$

iii. IRB for  $\omega_\infty = \infty$ :

$$K_D = 0.$$

The three boundaries are shown in Figure 2.8 together with a stable test point in the triangle.  $\square$

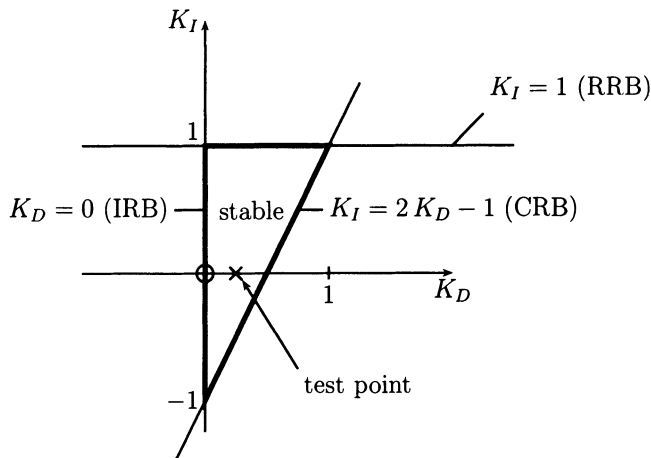


Figure 2.8. A test point  $K_I = 0$ ,  $K_D = 0.25$  is stable, i.e. the triangle is stable

Another possibility to find the stable polygons is to find the intersections of all lines, bisect each boundary segment and divide the polynomial by the known elementary factor of the line. If the remainder polynomial is stable, then the segment is an active part of the boundary, i.e. it divides a stable polygon from one with one or more roots in the right half plane. This second approach is more suited to an automated computer test, in particular if several singular frequencies occur, like in the following example.

*Example 2.17*

$$\begin{aligned} A(s) &= -s^4 - 7s^3 - 2s + 1, \\ B(s) &= s(s+1)(s+2)(s+3)(s+4)(s^2+s+1). \end{aligned}$$

Find the stable region in the  $(K_D, K_I)$ -plane for  $K_P = -4.4$ .

RRB:  $K_I = -b_0/a_0 = 0$ .

IRB does not exist, because  $p_n = b_6 = 1$ .

CRB:

$$\begin{aligned} d(\omega^2) &= \omega^{10} + (31 + K_P)\omega^8 + (-579 + 49K_P)\omega^6 \\ &\quad + (730 - 30K_P)\omega^4 + (-257 + 4K_P)\omega^2 + 24 + K_P = 0. \end{aligned}$$

One root with  $\omega^2 < 0$  does not lead to a singular frequency. The other  $\omega_k$  and corresponding stability boundaries for  $K_P = -4.4$  are

$$\begin{aligned} \omega_1 &= 0.316, \quad K_I = 0.01K_D + 7.09, \\ \omega_2 &= 0.695, \quad K_I = 0.48K_D + 15.5, \\ \omega_3 &= 0.730, \quad K_I = 0.53K_D + 14.1, \\ \omega_4 &= 4.13, \quad K_I = 17.1K_D - 67.0. \end{aligned}$$

Figure 2.9 shows the five boundary lines. The reduction to the active segments by bisection and division is shown in Figure 2.10.

The idea of a tomographic representation of all stabilizing PID-controllers, by gridding  $K_P$ , is illustrated in Figure 2.11. The figure shows that the two stable regions of Figure 2.10 are simply connected in 3D space. The cross-section of Figure 2.10 is enhanced.  $\square$

In order to decide on the  $K_P$  intervals for which stabilizing polygons exist in the  $(K_D, K_I)$ -plane, it is useful and simple to replace the factorization of (2.6.5), i.e.

$$\omega K_P [R_A^2(\omega) + I_A^2(\omega)] + R_A(\omega)I_B(\omega) - I_A(\omega)R_B(\omega) = 0 \quad (2.6.9)$$

for  $\omega_K(K_P)$  by the evaluation of the inverse function  $K_P(\omega_K)$  from

$$K_P(\omega) = \frac{I_A(\omega)R_B(\omega) - R_A(\omega)I_B(\omega)}{\omega[R_A^2(\omega) + I_A^2(\omega)]}. \quad (2.6.10)$$

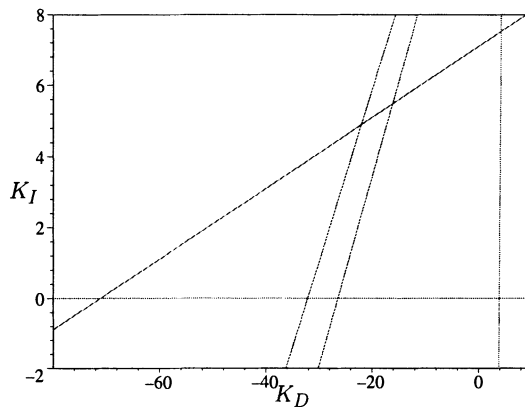


Figure 2.9. Five boundary lines in  $(K_D, K_I)$ -plane for  $K_P = -4.4$

### Example 2.18

For Example 2.18  $K_P(\omega)$  is plotted in Figure 2.12. For fixed  $K_P = -4.4$ , the  $\omega_K$  can be read off from the graph, e.g.  $\omega_1 = 0.3156$ ,  $\omega_2 = 0.695$ ,  $\omega_3 = 0.730$ ,  $\omega_4 = 4.13$ .

For  $\omega \rightarrow 0$ , the CRB with  $K_P = -24$  approaches the real root boundary. At the minimum  $\omega_2 = \omega_3 = 0.712$ ,  $K_P = -4.51$ , two singular frequencies merge into one and two boundaries disappear. Figure 2.13 shows the slice for  $K_P = -4.51$ , which is closely neighboring the slice in Figure 2.10 for  $K_P = -4.4$ .

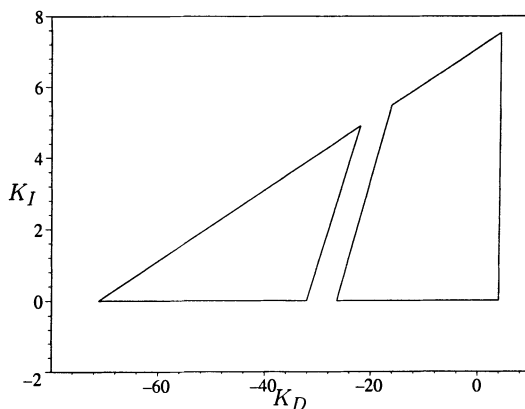


Figure 2.10. The active parts of the stability boundary form two stable convex polygons

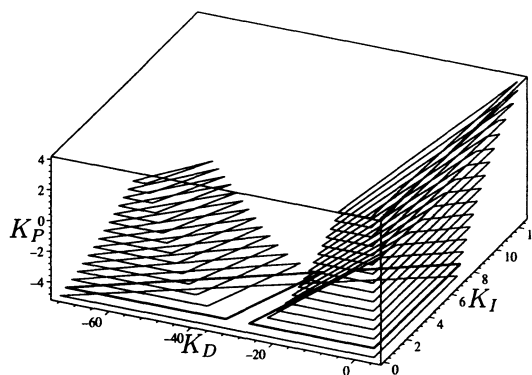


Figure 2.11. The set of all stabilizing PID-controllers

From the maxima and minima of the graph, the following  $K_P$ -intervals are obtained:

$K_P < -24$		no real $\omega_k$
$-24 < K_P < -4.51$	(minimum)	triangle
$-4.51 < K_P < 3.99$	(first maximum)	two polygons
$3.99 < K_P < 6.15$	(second maximum)	triangle
$6.15 < K_P$		no real $\omega_k$

□

The design of simultaneous PID-stabilizers for an infinite plant family  $G(s, \mathbf{q})$ ,  $\mathbf{q} \in Q$  proceeds in three steps:

1. Choose representatives  $\mathbf{q}^{(i)}$ ,  $i = 1, 2 \dots N$ , typically the vertices of the  $Q$ -box. The result is a *finite plant family*.

$$G_i(s) = G(s, \mathbf{q}^{(i)}), i = 1, 2 \dots N. \quad (2.6.11)$$

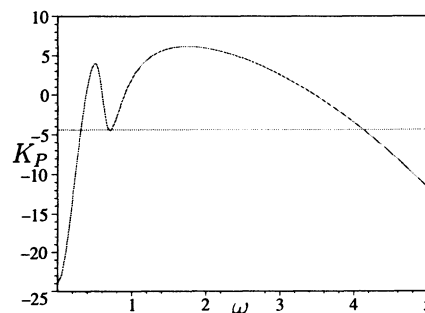
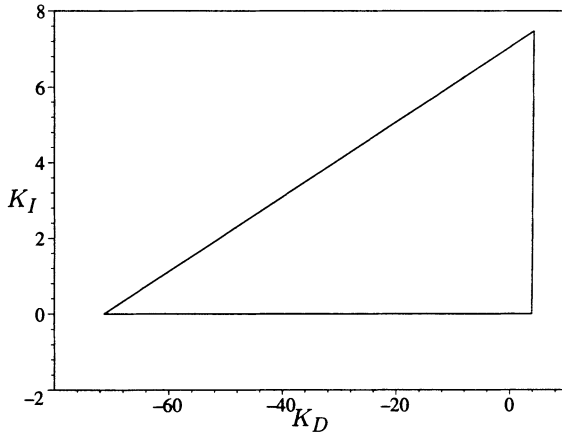


Figure 2.12.  $K_P$  as function of  $\omega$

Figure 2.13. Slice for  $K_P = -4.51$ .

For each  $i$ , the set of all stabilizing controllers is determined.

2. For the system in Figure 2.6 find a PID-controller that stabilizes the loop for all representatives. For each gridded value of  $K_P$ , the set of all such controllers is the intersection of the convex polygons for the individual representatives, i.e. a convex polygon. Choose a centrally located point for the controller.
3. Do a robustness analysis for the continuum of the parameters  $\mathbf{q} \in Q$ . This procedure is easy for two uncertain parameters, as will be shown in the following example. Additional parameters must be gridded, see Figure 2.11. If there is an unstable subregion in  $Q$ , choose additional representatives that were unstable in the first design iteration and go back to step 1.

#### *Example 2.19 ([71])*

Consider the continuous plant family

$$G(s, K, T) = \frac{K}{(1 + Ts)^8}, \quad K \in [0.5; 2], \quad T \in [0.5; 1.5].$$

Choose the four vertices of the  $Q$ -box as representatives. Figure 2.14 shows the four stabilizing triangles in a  $(K_D, K_I)$ -plane for  $K_P = 0.35$ . In their intersection, the centrally located point  $K_D = 0.50$ ,  $K_I = 0.05$  is chosen. For the robustness analysis, the controller is now fixed and the stability region in the plane of plant parameters  $T$  and  $K$  is determined. The mathematical details of mapping the imaginary axis (or other boundaries in the  $s$ -plane) into a parameter plane will be treated in Chapter 4, in Example 4.19. Returning to the present example, the result is Figure 2.15. It shows that not only the four vertices of the  $Q$ -box are stable, but the entire continuum of parameter values in  $Q$  is stable.  $\square$

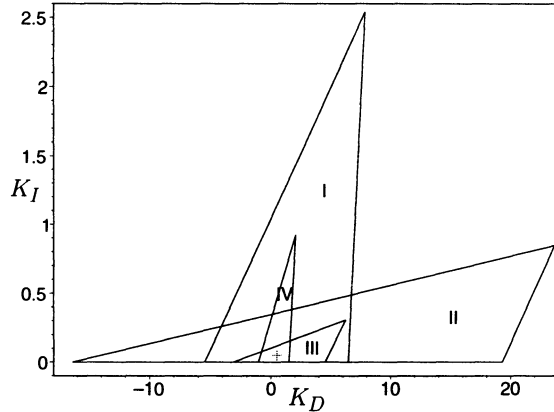


Figure 2.14. Simultaneous stabilizers in the plane  $K_P = 0.35$  in the intersection of four triangles for the vertices of the  $Q$ -box

## 2.7 Hurwitz-stability Regions for a Compensator or Plant Subpolynomial

A generalization of the characteristic polynomial (2.6.2) is

$$p(s, \mathbf{q}) = A(s)Q(s) + B(s), \quad (2.7.1)$$

where  $Q(s) = q_0 + q_1 s + \dots + q_\ell s^\ell$  is a numerator or denominator polynomial of the controller (for design) or of the plant (for robustness analysis). In this section, the PID results of Section 2.6 will be generalized to a fixed even or odd part of  $Q(j\omega)$ .

For  $s = j\omega$ , all polynomials are split into their real and imaginary parts, i.e. (omitting the arguments)

$$p(j\omega, \mathbf{q}) = R_P + jI_P = (R_A + jI_A)(R_Q + jI_Q) + (R_B + jI_B). \quad (2.7.2)$$

The polynomial  $p(s, \mathbf{q})$  has a root at  $s = j\omega$  on the imaginary axis if and only if  $R_P = 0$  and  $I_P = 0$ .

$$\begin{bmatrix} R_P \\ I_P \end{bmatrix} = \begin{bmatrix} R_A R_Q - I_A I_Q + R_B \\ I_A R_Q + R_A I_Q + I_B \end{bmatrix} = \begin{bmatrix} 0 \\ 0 \end{bmatrix}. \quad (2.7.3)$$

With the detailed notation

$$\begin{aligned} R_Q &= q_0 - q_2 \omega^2 + q_4 \omega^4 \mp \dots, \\ I_Q &= q_1 \omega - q_3 \omega^3 + q_5 \omega^5 \mp \dots, \end{aligned}$$

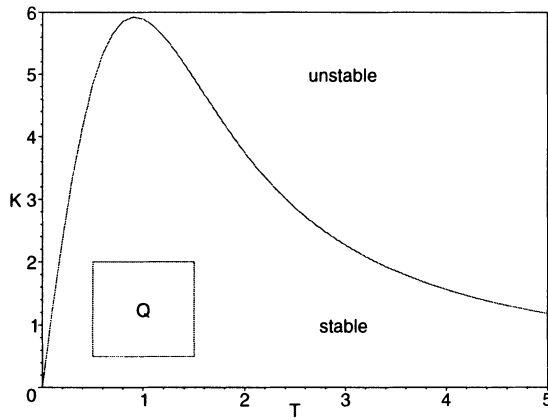


Figure 2.15. The simultaneously stabilizing PID controller not only stabilizes the representatives (vertices of  $Q$ ) but the continuum  $Q$  of operating conditions

Equation (2.7.3) becomes

$$\begin{bmatrix} R_P \\ I_P \end{bmatrix} = \begin{bmatrix} R_A & -\omega^2 R_A & \omega^4 R_A & \dots \\ I_A & -\omega^2 I_A & \omega^4 I_A & \dots \end{bmatrix} \begin{bmatrix} q_0 \\ q_2 \\ q_4 \\ \vdots \end{bmatrix} + \omega \begin{bmatrix} -I_A & \omega^2 I_A & -\omega^4 I_A & \dots \\ R_A & -\omega^2 R_A & \omega^4 R_A & \dots \end{bmatrix} \begin{bmatrix} q_1 \\ q_3 \\ q_5 \\ \vdots \end{bmatrix} + \begin{bmatrix} R_B \\ I_B \end{bmatrix} = \begin{bmatrix} 0 \\ 0 \end{bmatrix}. \quad (2.7.4)$$

Obviously, both matrices in Equation (2.7.4) have rank 1. (The trivial case  $A(s) \equiv 0$  is excluded here.) For fixed  $I_Q$ , Equation (2.7.4) represents two parallel hyperplanes in the parameter space with coordinates  $q_0, q_2, q_4, \dots$ . The two hyperplanes become identical at real frequencies  $\omega$ , for which

$$\begin{aligned} g_R(\omega) &= \det \begin{bmatrix} R_A & R_B - I_A I_Q \\ I_A & I_B + R_A I_Q \end{bmatrix} \\ &= R_A(I_B + R_A I_Q) - I_A(R_B - I_A I_Q) \\ &= (R_A^2 + I_A^2)I_Q + R_A I_B - I_A R_B = 0. \end{aligned} \quad (2.7.5)$$

It is easily verified that  $g_R(\omega)$  is  $\omega$  times a polynomial in  $\omega^2$ . Its degree results from the highest degree in  $\omega^2$  occurring among the products  $R_A I_B$ ,  $R_A^2 I_Q$ ,  $I_A R_B$  and  $I_A^2 R_Q$ .  $\omega_0^* = 0$  is always a solution. Further solutions are the positive real roots in  $\omega^2$  that result in a real frequency  $\omega$ . These real solutions  $\omega_k$ , ( $k = 0, 1, 2, \dots, K$ ) are the singular frequencies.

*Remark 2.20*

A dual result is obtained by fixing  $R_Q$ . The singular frequencies are then the real roots of

$$\begin{aligned} g_I(\omega) &= -I_A(I_B + I_A R_Q) - R_A(R_B + R_A R_Q) \\ &= -(I_A^2 + R_A^2)R_Q - I_A I_B - R_A R_B = 0, \end{aligned} \quad (2.7.6)$$

which is a polynomial in  $\omega^2$ .

□

The stability boundaries are

a) RRB

$$q_0 = -b_0/a_0. \quad (2.7.7)$$

b) CRB

For the singular frequencies  $\omega_k$ , the first row of (2.7.4) becomes

$$R_P(\omega_k) = R_A(\omega_k)R_Q(\omega_k) - I_A(\omega_k)I_Q(\omega_k) + R_B(\omega_k) = 0,$$

$$R_Q(\omega_k) = \frac{[I_A(\omega_k)I_Q(\omega_k) - R_B(\omega_k)]}{R_A(\omega_k)} , k = 1, 2, \dots, K. \quad (2.7.8)$$

For fixed  $I_Q$ , Equation (2.7.8) represents  $K$  hyperplanes in the parameter space of  $R_Q$ -coefficients.

c) IRB

In the  $R_Q$ -space, the IRB is

$$q_\ell = \begin{cases} 0 & \text{for } m < k + \ell \\ -b_m/a_k & \text{for } m = k + \ell \\ \text{no boundary} & \text{for } m > k + \ell \end{cases}. \quad (2.7.9)$$

Based on the two dual results, it should be possible to develop a design procedure for a compensator polynomial  $Q(s)$  by alternating design steps on the even and odd part of  $Q(s)$ .

# 3 Eigenvalue Specifications

In Chapter 2, we were primarily concerned with Hurwitz-stabilization and Hurwitz-stability analysis of feedback systems with uncertain parameters. In this third chapter, the parameter space approach is extended to Gamma-stability, i.e. the left half  $s$ -plane for Hurwitz-stability is replaced by other regions  $\Gamma$  that guarantee, for example, some damping or negative real part for all eigenvalues. A linear system is called  $\Gamma$ -stable if all roots of its characteristic polynomial are located in a specified region  $\Gamma$  in the  $s$ -plane. This is an indirect approach to meet *time-domain specifications*. A direct approach would require simulations of responses of several state variables and actuator signals of the closed-loop system to typical reference inputs and disturbances. Such numerical solutions with a more detailed model including plant and actuator non-linearities are frequently necessary in a final analysis of the control system before its hardware and software implementation. For systems with uncertain parameters, then gridding of the operating domain (see Figure 1.2) is unavoidable. Such a detailed analysis would not be practical in design iterations. Therefore, we work in the design process with simple linearized plant models in order to understand and accommodate the influence of uncertain parameters without brute-force gridding. In this context it is important to know some elementary relations between eigenvalue locations and time responses, where the step responses are of primary interest.

## 3.1 Poles, Zeros and Step Responses

The performance of control systems is frequently evaluated by typical responses to reference and disturbance inputs. Examples are:

- Transport of a load by a crane, where the initial and final values of the rope angle and its rate and also of the crab velocity are zero.
- Transition of a vehicle from a straight track into a curve.
- Rapid increase of the crosswind acting on a car.
- Transition of an aircraft to a higher altitude.

Undesirable properties of a response and appropriate countermeasures are:

- i. There are oscillations that do not decay fast enough and cause excessive overshoot. The frequency  $\omega^* = 2\pi/T$  is determined from the period  $T$  of the undesired oscillation. In a distance  $\omega^*$  from the origin of the  $s$ -plane, there is a complex pair of eigenvalues with insufficient damping. Improvement of this damping has priority in the next design step. Note, however, that excessive overshoot may also be caused by poles placed further away from the origin than a zero of the plant transfer function, see Figure 3.4.
- ii. The response is “sluggish”, it creeps towards the stationary value. A negative real eigenvalue is too close to the origin and must be moved to the left in the next design step.
- iii. There is undesired high-frequency content in the actuator signal. Countermeasures are reduction of the feedback bandwidth, increase of the relative degree of the controller, and shifting far left eigenvalues closer to the origin on a circle with radius  $\omega_b$  such that the absolute value of the frequency response drops rapidly for frequencies  $\omega > \omega_b$ . In sampled-data systems, frequently the anti-aliasing filter is a cure.

For the single-input single-output plant, some further aspects of pole shifting must be observed:

- iv. If the closed-loop eigenvalues are shifted too close to open-loop zeros, then large loop gains may result as can be seen from the root locus. High-loop gains are undesirable for our examples of mechanical systems in view of the limited actuator forces and amplification of sensor noise. If, however, open-loop poles are located nearby zeros such that an almost cancellation occurs, then they have only minor effect on responses.
- v. If the open loop has a relative degree of two or more (this is a common case), then the center of all eigenvalues of plant and compensator cannot be shifted. In this case, the coefficient  $a_{m-1}$  in a polynomial  $\prod_{i=1}^m (s - s_i) = a_0 + \dots + a_{m-1}s^{m-1} + s^m$  is determined by the plant and compensator poles only and not by any zeros. The coefficient represents the center of the  $s_i$  by  $a_{m-1} = -\sum_{i=1}^m s_i$ . If some eigenvalues must be shifted to the left, then necessarily other eigenvalues migrate to the right. In this case, the compensator poles must be chosen sufficiently far left, such that the plant poles can be shifted to the left.
- vi. Pole-zero cancellations outside the desired closed-loop eigenvalue region  $\Gamma$  should be avoided. From the frequency domain point of view, they may still look acceptable for a specific transfer function, but there may be a disturbance or initial condition that excites the subsystem with the undesired response. The control system should be “internally  $\Gamma$ -stable”, i.e. the transfer functions from each possible input to each signal inside the feedback loop should have all their poles in the region  $\Gamma$ .

In the following paragraphs, we recapitulate some simple relationships between time responses and eigenvalue locations for second and third order systems. Such relationships are useful if a “dominant behavior” similar to such simple systems is desired.

If all eigenvalues are located to the left of a parallel to the imaginary axis of the  $s$ -plane at  $\sigma = -a$ , then all solution terms decay at least like  $e^{-at}$ . Figure 3.1 shows two examples:  $y_1$  and  $y_2$  have the same negative real part  $\sigma = -a$  of the eigenvalues.

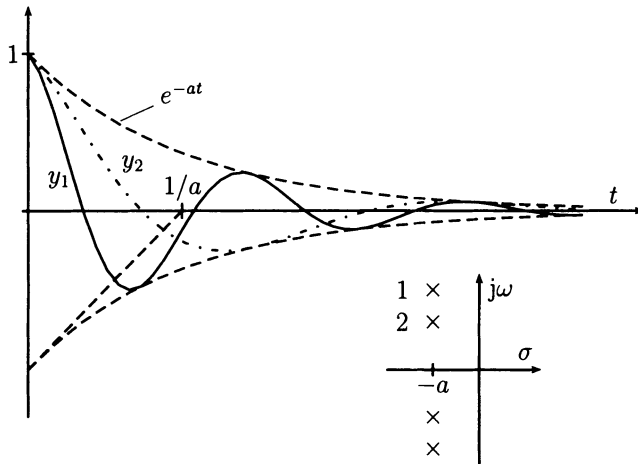


Figure 3.1. Two solution terms with the same negative real part  $\sigma = -a$  of the eigenvalues

Terms of the type  $y_1$  are, however, undesirable because more overshoot and larger oscillations occur inside the envelope  $\pm e^{-at}$  than for  $y_2$  with a lower frequency  $\omega_2$ . The high-frequency eigenvalues should be located further to the left in the  $s$ -plane. Therefore, a minimum value of the damping  $D$  is required. A complex conjugate pair of eigenvalues  $\sigma_i \pm j\omega_i$  may be written as a second order factor of the closed-loop characteristic polynomial

$$p_i(s) = (s - \sigma_i - j\omega_i)(s - \sigma_i + j\omega_i) = s^2 - 2\sigma_i s + \sigma_i^2 + \omega_i^2 = s^2 + 2D\omega_0 s + \omega_0^2.$$

The distance of the eigenvalues from the origin is the natural frequency  $\omega_0 = \sqrt{\sigma_i^2 + \omega_i^2}$ , and  $D = -\sigma_i/\omega_0$  is the damping. The inverse relation for the real part  $\sigma_i$  and the imaginary part  $\omega_i$  of the eigenvalue is  $\sigma_i = -D\omega_0$ ,  $\omega_i = \omega_0\sqrt{1 - D^2}$ . Figure 3.2 illustrates these relations in the  $s$ -plane. A damping value  $D$  corresponds to an angle  $\alpha$  with respect to the imaginary axis, where

$$D = \sin \alpha. \quad (3.1.1)$$

The corresponding solution term in the time-domain is

$$y_i(t) = A e^{-D\omega_0 t} \cos(\sqrt{1 - D^2}\omega_0 t + \varphi) \quad \text{for } |D| < 1. \quad (3.1.2)$$

Amplitude  $A$  and phase angle  $\varphi$  depend on input and initial conditions. Natural frequency  $\omega_0$  and time  $t$  appear only as product  $\omega_0 t$ , i.e.  $\omega_0$  may be considered as a scaling factor for the time.

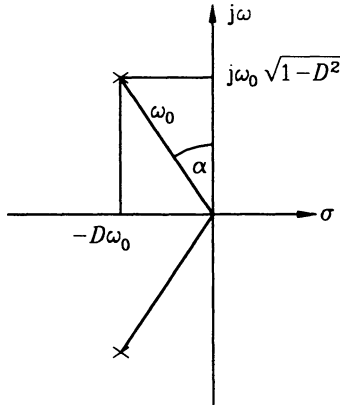


Figure 3.2. Natural frequency  $\omega_0$  and damping  $D$  of a complex conjugate pair of poles

### Example 3.1

As an example, consider the step responses of the system

$$g(s) = \frac{1}{1 + 2Ds/\omega_0 + s^2/\omega_0^2} \quad (3.1.3)$$

for different damping values. For  $u(s) = 1/s$ , and  $y(s) = g(s)u(s)$ , we have

$$y(s) = \frac{1}{(s^2/\omega_0^2 + 2Ds/\omega_0 + 1)s} = \frac{1}{s} - \frac{(s + D\omega_0) + D\omega_0}{(s + D\omega_0)^2 + (1 - D^2)\omega_0^2}.$$

The inverse Laplace transform is

$$y(t) = 1 - e^{-D\omega_0 t} \left[ \cos(\sqrt{1 - D^2}\omega_0 t) + \frac{D}{\sqrt{1 - D^2}} \sin(\sqrt{1 - D^2}\omega_0 t) \right]. \quad (3.1.4)$$

The responses for  $D = 0.5$ ,  $D = 1/\sqrt{2}$ , and  $D = 0.9$  are shown in Figure 3.3 for the scaled time  $\omega_0 t$ . The step response for  $D = 1/\sqrt{2} \approx 0.7$  is considered as particularly favorable. Its maximum overshoot of 4.3% occurs at  $\omega_0 t = 4.4$ . The value  $D = 1/\sqrt{2}$  is characterized by the fact that the magnitude of the frequency response  $|g(j\omega)|$  has a maximum only for smaller damping; the resonance frequency is  $\omega_0 = \sqrt{1 - 2D^2}$ . For larger damping no resonance occurs. In Figure 3.2 we have  $\alpha = 45^\circ$  for the damping value  $D = 1/\sqrt{2}$ .  $\square$

### Example 3.2

Next, we assume a zero at  $s = -b\omega_0$ .

$$g(s) = \frac{(1 + s/(b\omega_0))}{1 + 2Ds/\omega_0 + s^2/\omega_0^2}. \quad (3.1.5)$$

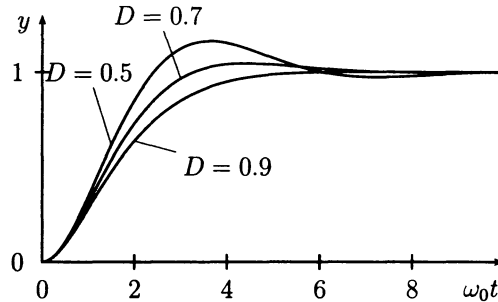
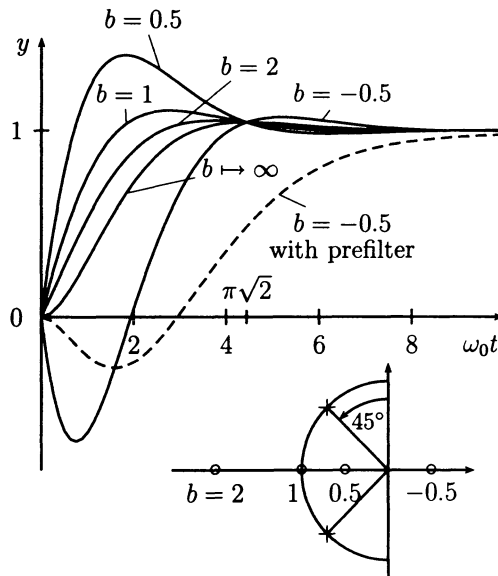


Figure 3.3. Step responses of the system (3.1.3)

The step response is

$$y(t) = 1 - e^{-D\omega_0 t} \left[ \cos(\sqrt{1-D^2}\omega_0 t) + \frac{D-1/b}{\sqrt{1-D^2}} \sin(\sqrt{1-D^2}\omega_0 t) \right]. \quad (3.1.6)$$

Again,  $\omega_0 t$  can be introduced as scaled time. For  $D = 1/\sqrt{2}$  and some values of  $b$ , the

Figure 3.4. Step response of the system (3.1.5) for different zero locations  $b$ 

pole zero locations and the step responses are shown in Figure 3.4.

All curves are focused at  $\omega_0 t = \pi\sqrt{2} = 4.44$ , because here the sine term in (3.1.6) vanishes and that is the only term which contains the varying  $b$ . The curve for  $b \rightarrow \infty$

is identical to the center curve of Figure 3.3. It is the only one with relative degree two such that the step response begins with slope zero by the initial value theorem of Laplace transforms. A zero for  $b = 2$  does not change the response significantly. Even for  $b = 1$  the response is acceptable, but if the zero is closer to the origin than the poles, then a large overshoot occurs (40.7 % for  $b = 0.5$ ). It could be removed in the step response by cancellation of the zero at  $s = -0.5$ . If we want to avoid this cancellation, then the distance  $\omega_0$  of the eigenvalues from the origin must be reduced, i.e. for a fixed zero location at  $s = -b\omega_0$ ,  $b$  is increased and  $\omega_0$  is reduced.

For negative  $b$ , the system has non-minimum phase behavior; the step response starts in the negative direction. Cancellation is impossible here, because it would give the system an unstable eigenvalue. The unfavorable undershoot can be reduced by cancelling the mirror image of the zero by a compensator  $1/(1 - s/(b\omega_0))$ . In the example, it is  $0.5/(s + 0.5)$ . The step response with this compensator is shown in dashed lines in Figure 3.4; it is significantly slower.  $\square$

### *Example 3.3*

Next, the mutual influence of poles will be studied. Extend the system (3.1.5) by a low-pass filter with a pole at  $s = -a\omega_0$ , i.e.

$$g(s) = \frac{1}{(1 + 2Ds/\omega_0 + s^2/\omega_0^2)(1 + s/(a\omega_0))}. \quad (3.1.7)$$

The step response is

$$\begin{aligned} y(t) &= 1 - \frac{1}{a^2 - 2aD + 1} \{ e^{-a\omega_0 t} + \\ &\quad e^{-D\omega_0 t} [a(a - 2D) \cos(\sqrt{1 - D^2}\omega_0 t) + \frac{a(1 + aD - 2D^2)}{\sqrt{1 - D^2}} \sin(\sqrt{1 - D^2}\omega_0 t)] \}. \end{aligned} \quad (3.1.8)$$

Now, a smaller damping may be chosen because the additional pole counteracts a resonance in the frequency response. The chosen value is  $D = 0.5$  such that the third order Butterworth filter is contained as a special case with  $a = 1$ . For  $a \rightarrow \infty$ , i.e. without the additional pole the response is identical to the curve for  $D = 0.5$  from Figure 3.3. Figure 3.5 shows some typical step responses. The pole for  $a = 2$  has little influence. For  $a = 1$ , the overshoot is reduced from 15.5 % to 8.1 % and for  $a = 0.5$  there is no overshoot. The solution gets slower as the real pole migrates to the right. Finally, the real pole dominates and the complex poles show their influence only in the beginning of the step response. The later response is “sluggish”.  $\square$

### *Summary*

The question of when the step response of a robustly stable system approaches its steady state value depends only on the dominant poles with the smallest distance from the origin  $s = 0$ . Further left and more remote poles and zeros (more than twice the

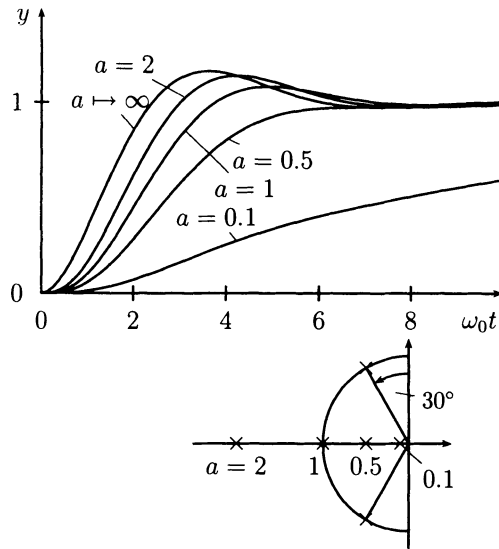


Figure 3.5. Influence of a pole at  $s = -a$  on the step response

distance) have an influence only on the initial part of the step response; the corresponding time response terms have died out before the entire solution approaches its steady state value. They may have strong influence on the initial actuator signal magnitude. Zeros in the left half plane have a similar effect as reduced damping. Their influence can be reduced by cancellation in a prefilter or by a compensator in the closed loop.

The unfavorable influence of right half plane zeros can be modified but not removed.

It is recommended to place several closed-loop poles at about the same distance from the origin. If more poles on this radius contribute to the dominant behavior, then a small lowest damping is acceptable.

#### *Remark 3.4*

The step response is taken as a reference in the preceding discussion. It resulted in the “ideal” damping of  $D = 1/\sqrt{2}$ , see Figure 3.3. There are applications where much smaller damping is acceptable, because typical input signals are milder than a step. Take, for example, a car at maximum speed. It may have a damping of only 0.3 or 0.4 in the yaw motion, but the driver will turn the steering wheel only softly and not stepwise. Similarly, military specifications for aircraft require only 0.35 minimum damping in the short-period longitudinal mode. On the other hand, there are applications where no overshoot at all is allowed (e.g. an aperiodic solution with  $D > 1$  or the response for  $a = 0.5$  in Figure 3.5). An example is the increase of thrust to 100 % for an aircraft engine. Here, the materials reach their temperature limits, and

overshoot of the temperature would reduce the lifetime of some parts of the engine.  $\square$

## 3.2 Root Sets, Gamma-stability

For control systems with uncertain plant parameters, it is a brute-force analysis approach to grid the operating domain  $Q$  and to calculate and plot all closed-loop eigenvalues for the grid points. For stability, this root set must be located in the left half plane.

*Example 3.5*

Consider the crane with fixed parameter  $m_C = 1000$  and uncertain parameters  $m_L \in [1000; 2000]$ ,  $\ell \in [8; 16]$ . For the nominal case  $m_L = 1500$ ,  $\ell = 12$ ; the output feedback controller

$$u = -K [500 \quad 2191 \quad -4299 \quad 0] x, \quad K = 1 \quad (3.2.1)$$

shifts the eigenvalues to  $s_{1,2} = -0.59 \pm 1.06j$ ,  $s_{3,4} = -0.51 \pm 0.16j$ .

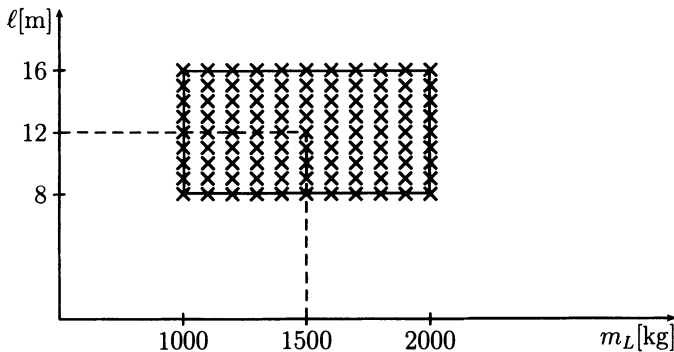


Figure 3.6. An  $11 \times 9$  grid over the operating domain  $Q$

The operating domain  $Q$  of Figure 3.6 is now gridded in order to find the root set of Figure 3.7 by numerical factorization.  $\square$

The main difficulty in carrying out a stability analysis by root set construction is large computation time. An algorithm to find the roots of a single polynomial of reasonably low order is not particularly time-consuming. Generally, repetition of the algorithm up to a few thousand times for a one or two parameter root set is acceptably brief. Now, consider the general case of  $\ell$  parameters. If an  $N$  point grid were used for each parameter, the root finding algorithm would need to be repeated  $N^\ell$  times. No

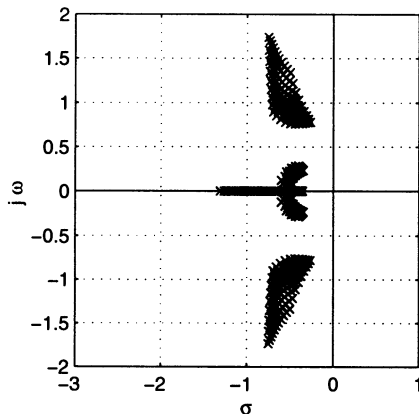


Figure 3.7. Root set for the grid points of Figure 3.6

matter how fast the computer is, it is easy to select fairly small values of  $\ell$  and  $N$  that would make the root computations last hours, weeks, even years. Motivated by these limits, we will look at alternative, potentially more efficient stability analysis methods in the parameter space. These methods are based on the boundary crossing concept that we have introduced for Hurwitz-stability already in Chapter 2. For this purpose,  $\Gamma$ -stability is defined here.

#### *Definition 3.6*

A polynomial  $p(s) = (s - s_1)(s - s_2) \dots (s - s_n)$  is called  $\Gamma$ -stable if all  $s_i \in \Gamma$ . The region  $\Gamma$  has a boundary  $\partial\Gamma$  that consists of one or more contours in the  $s$ -plane such that the membership  $s_i \in \Gamma$  is well defined.  $\square$

The boundary crossing theorem (Theorem 2.1) can be immediately generalized to other pole regions. Only minor modifications have to be made.

#### *Theorem 3.7 (boundary crossing theorem for pole regions $\Gamma$ )*

The family of polynomials  $P(s, Q)$  is robustly  $\Gamma$ -stable, if and only if:

- i. There exists a  $\Gamma$ -stable polynomial  $p(s) \in P(s, Q)$ .
- ii.  $\sigma(\alpha) + j\omega(\alpha) \notin \text{Roots}[P(s, Q)]$  for all  $\alpha \in [\alpha^- ; \alpha^+]$ .

$\square$

In Example 3.1, the controller was designed by pole placement for a nominal plant in the center of the  $Q$ -box. Pole placement for single-input systems is primarily attractive as a synthesis method, because it yields a unique solution for state feedback or for the compensator. This supposed advantage in the synthesis procedure, however, turns into

a disadvantage for uncertain parameters; a unique solution does not allow any flexibility: if plant parameters change and the same pole locations are prescribed, then also the controller must be changed. The preceding discussion on eigenvalue specifications has shown that a precise assignment of all eigenvalues is more than what actually follows from the time-domain design specifications. For uncertain parameters, it is a reasonable requirement that all eigenvalues are located in a specified region  $\Gamma$  in the  $s$ -plane and must remain in this region under all admissible parameter variations. We call this approach *pole region assignment*.

Figure 3.8 shows a pole region  $\Gamma$ . Its bandwidth is bounded by a circular arc and its damping by a hyperbola that guarantees damping according to the asymptotes, and its real part is bounded by the apex of the hyperbola.

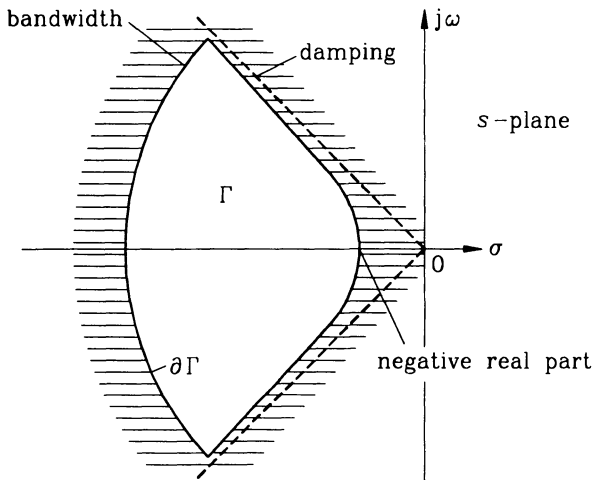


Figure 3.8. Specification of a pole region  $\Gamma$  that guarantees damping, negative real part and bandwidth limitation

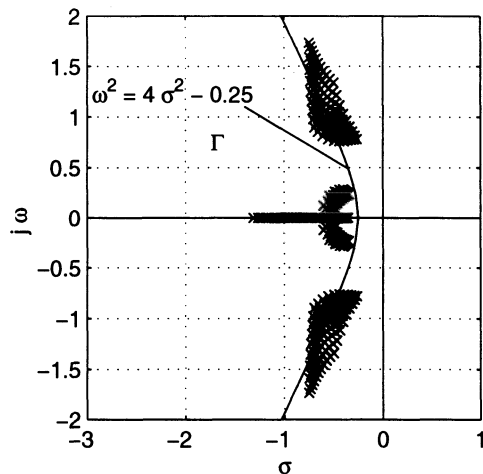
### Example 3.8

For the control system of Example 3.8, choose the left branch of the hyperbola  $\omega^2 = 4\sigma^2 - 0.25$  as the  $\Gamma$ -stability boundary. It passes through the nominal poles at  $s_{1,2} = -0.59 \pm 1.06j$  and is shown in Figure 3.9.

It is now reasonable to modify the controller (3.2.1) such that the root set becomes  $\Gamma$ -stable without overdamping it. A trial-and-error approach would be time-consuming here. We use this example to show a systematic approach by mapping the hyperbola:

- i. to a  $(k_2, k_3)$ -plane for simultaneous design of a fixed gain controller, and
- ii. to an  $(m_L, \ell)$ -plane for analysis,
- iii. to an  $(\ell, k_4)$ -plane for gain-scheduling design in Section 3.5.

The mathematical details of mapping a boundary  $\partial\Gamma$  will be given in Chapter 4. The present example should motivate the approach.

Figure 3.9.  $\Gamma$ -stability specified by a hyperbola

Consider the vertex  $m_L = 1000$ ,  $\ell = 8$  of the operating domain  $Q$  and the controller

$$u = -[500 \ k_2 \ k_3 \ 0] \ x. \quad (3.2.2)$$

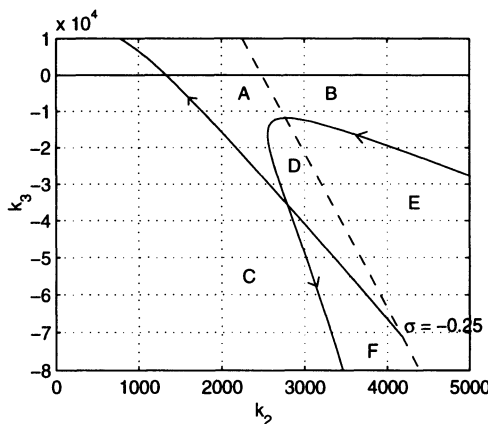


Figure 3.10. On the boundary lines there are closed-loop eigenvalues on the hyperbola

The boundary  $\omega^2 = 4\sigma^2 - 0.25$  with parameter  $\sigma$  is mapped into the  $(k_2, k_3)$ -plane in Figure 3.10. There is an RRB for  $\sigma = -0.25$  (dashed line). The CRB branches off the RRB at a double root at  $\sigma = -0.25$ , goes through infinity for  $\sigma = -0.548$ , intersects the RRB and itself, and goes to infinity again. The boundaries decompose the  $(k_2, k_3)$ -plane into six regions  $A$  to  $F$ . Only region  $D$  is  $\Gamma$ -stable and Figure 3.10 is

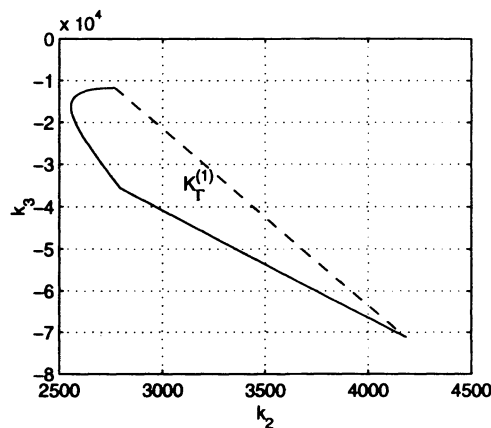


Figure 3.11. Active boundaries from Figure 3.10

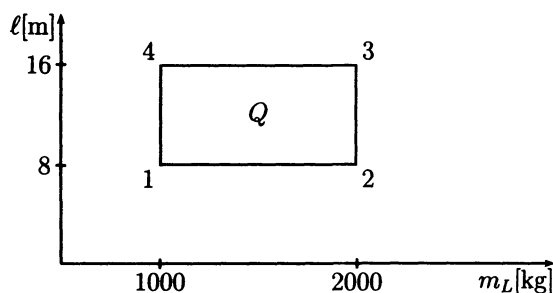


Figure 3.12. The operating domain and four representatives

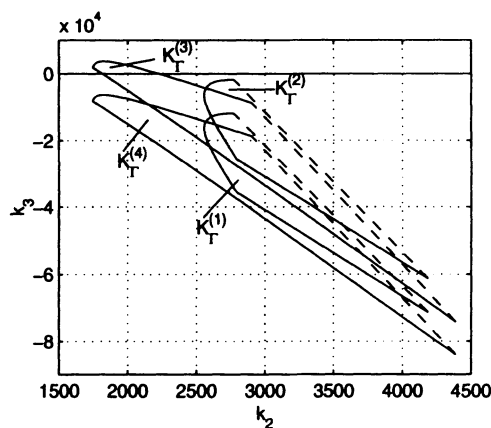


Figure 3.13.  $\Gamma$ -stabilization of the four vertices of  $Q$

reduced to the active boundaries in Figure 3.11.  $K_{\Gamma}^{(1)}$  is the set of all controllers (3.2.2) that  $\Gamma$ -stabilize the crane for the operating condition  $m_L = 1000$ ,  $\ell = 8$ .

For a simultaneous  $\Gamma$ -stabilization of the four vertices of  $Q$  as shown in Figure 3.12, the procedure is repeated for the vertices 2, 3, and 4 and the active boundaries are plotted together in Figure 3.13. Obviously, the four vertices are simultaneously  $\Gamma$ -stabilized by all controllers in the intersection of the four regions  $K_{\Gamma}^{(1)}$  to  $K_{\Gamma}^{(4)}$  in Figure 3.13. Again, only the active boundaries of the intersection are relevant, they are shown in Figure 3.14. For this set of controllers, it turns out that only the operating conditions two and four contribute to the active boundary.

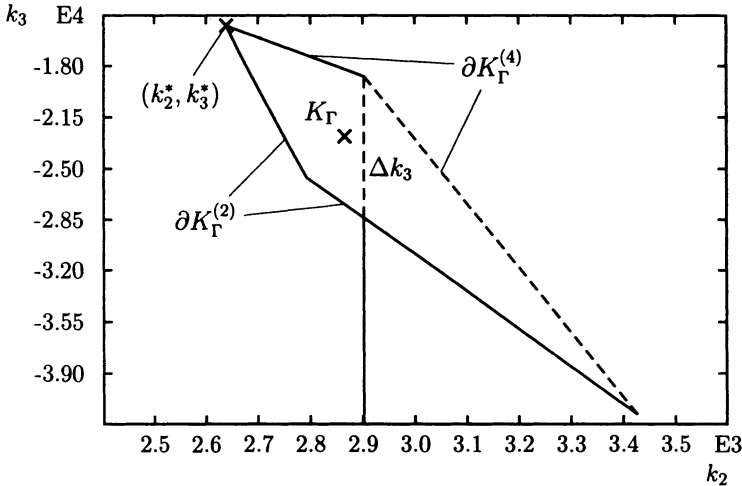


Figure 3.14. Intersection of the four regions of Figure 3.5

Two candidate controllers

$$u = -[500 \quad 2639 \quad -15255 \quad 0] \ x \quad (3.2.3)$$

and

$$u = -[500 \quad 2865 \quad -22800 \quad 0] \ x \quad (3.2.4)$$

have been marked. The first one minimizes  $k_2^2 + k_3^2$ ; it is *fragile*, however, in the sense that all variations in  $k_2^*$  or in  $k_3^*$  lead to a loss of  $\Gamma$ -stability. Therefore, the more central second controller will be used and further analyzed. It has  $\Gamma$ -stability margins in all directions.

Note that the relation between  $m_L$  and  $k_3$  is very simple, according to (1.5.18) both parameters enter only into  $a_2 = (m_L + m_C)g + k_1\ell - k_3$ . The  $\Gamma$  stable variations in the two parameters are related by  $\Delta k_3 = 10\Delta m_L$  with  $\Delta m_L = m_L^+ - m_L^-$ . Therefore, Figure 3.14 allows a graphical optimization. The largest  $\Gamma$ -stable variation  $\Delta k_3 = 9680$ , corresponding to  $\Delta m_L = 968$  [kg] is obtained for  $k_2 = 2900$ . The  $\Delta m_L$  interval may then be shifted by  $k_3$ . For example, for  $m_L \in [0; 1000]$ ,  $\ell \in [8; 16]$ , the output feedback controller ( $k_1 = 500$ ,  $k_4 = 0$ ) is

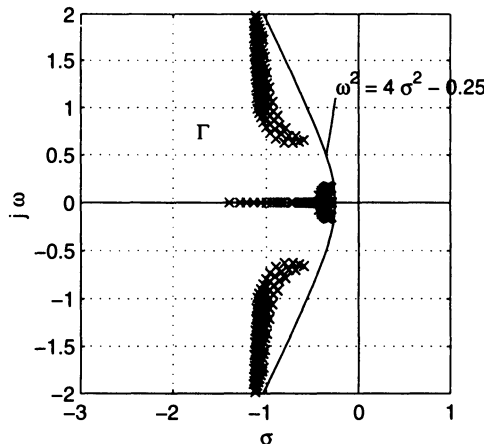


Figure 3.15. Root set for the controller (3.2.4)

$$u = -[500 \ 2900 \ -32000 \ 0] \ x. \quad (3.2.5)$$

So far, we can only be sure that the four vertices of the  $Q$ -box, Figure 3.12, are  $\Gamma$ -stable. A robustness analysis must now show if this still holds for all operating points in  $Q$ . The result of a gridding analysis is shown in Figure 3.15.

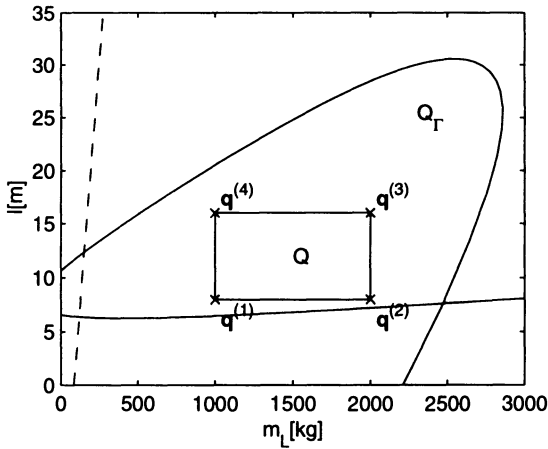


Figure 3.16. Robustness analysis in the  $(m_L, \ell)$ -plane

A more elegant and reliable robustness analysis is, however, to map the  $\Gamma$ -stability boundary  $\partial\Gamma$  into the  $(m_L, \ell)$ -plane as shown in Figure 3.16. In this example, the  $\Gamma$ -stable region  $Q_\Gamma$  is convex. Therefore, the simultaneous  $\Gamma$ -stabilization of the four vertices of  $Q$  also  $\Gamma$ -stabilizes the entire continuum of operating conditions in  $Q$ . Note,

however, that stability regions in parameter planes are not convex in general such that the robustness analysis is non-trivial. This is, in particular, true for non-linear dependence of the polynomial coefficients on the physical plant parameters, see Section 4.5.  $\square$

### 3.3 Physical Meaning of Closed-loop Poles

For a controllable and observable nominal plant, the eigenvalues can be placed arbitrarily by feedback of measured states or reconstructed states from an observer. If this process is executed in one shot (or two shots by the separation principle), then the idea of relating the physical meaning of open-loop and closed-loop poles is lost. We may assign the same set of eigenvalues (with different time scaling) to a power plant, an aircraft or a distillation column. The pilot, however, likes to recognize the familiar Dutch roll or short-period longitudinal mode in the behavior of the controlled aircraft. Otherwise, it does not “feel like an aircraft”. Therefore, it is of interest to relate the closed-loop poles one-to-one or pair-to-pair to the open-loop poles.

*Example 3.9*

In the crane controller (3.2.1), let the loop-gain  $K$  grow continuously from zero (open loop) to one (the analyzed control system). The result of this eigenvalue tracing is illustrated by the root locus of Figure 3.17. The higher frequency closed-loop poles can be associated uniquely with the pendulum and the lower frequency eigenvalues with the crab. This one-to-one relationship also holds for the neighborhood of the nominal case as defined by the uncertain parameter intervals, see Figure 3.7.

When is this one-to-one relationship destroyed? The answer is: as soon as we cross a *branching point* of the root locus. As an example, take the controller

$$u = -K [500 \ 0 \ 15 \ 508 \ 0] x \quad (3.3.1)$$

for the crane of Example 3.1. For  $K = 1$ , it yields a double imaginary root at  $\pm j0.803$ . If  $K$  is increased beyond 1, then it becomes impossible to distinguish between crab and pendulum eigenvalues. It is possible, for example, to design a bad pole placement controller that lets the crab oscillate faster than the pendulum and thereby wastes actuator energy.  $\square$

A branching point of a polynomial  $p(s)$  is characterized by the property

$$\begin{aligned} p(s) &= 0 \quad \text{and} \\ \frac{dp(s)}{ds} &= 0. \end{aligned} \quad (3.3.2)$$

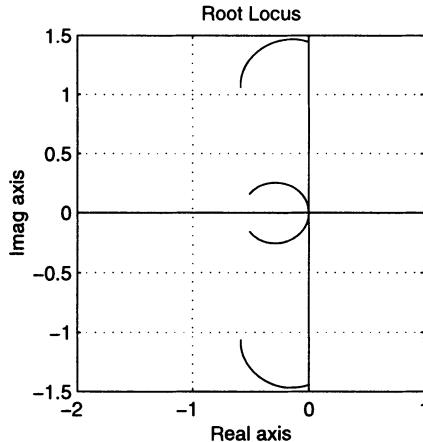


Figure 3.17. Eigenvalue tracing for continuously growing loop gain

A desirable feature of control systems is their transparency, that means we try to avoid crossing branching points. If the polynomial depends on two uncertain parameters, i.e.  $p(s, q_1, q_2)$ , then the two equations in (3.3.2) may be mapped into the  $(q_1, q_2)$ -plane, and the design path should not cross these lines. The parameter space approach allows us to trace the effect of continuous variations of controller gains starting from the open loop with controller gain zero.

### 3.4 Remarks on Existence of Robust Controllers

For systems with nominal parameter values, there are well-known necessary and sufficient conditions for pole placement design. A sufficient condition is that the plant is controllable and observable. Then, an observer with arbitrary stable poles can reconstruct all state-variables. By the separation theorem, it may be combined with pole placement by state feedback without changing the individually assigned observer and feedback poles. In a more detailed analysis, the controllability and observability of individual eigenvalues is considered. It may be checked by the Hautus test [104], [105].

*Theorem 3.10 (Hautus)*

An eigenvalue  $s_i$  of a system  $\dot{\mathbf{x}} = \mathbf{A}\mathbf{x} + \mathbf{B}\mathbf{u}$  is controllable, if and only if rank  $[\mathbf{A} - s_i\mathbf{I} \quad \mathbf{B}] = n$ . An eigenvalue  $s_i$  of a system  $\dot{\mathbf{x}} = \mathbf{A}\mathbf{x}$ ,  $\mathbf{y} = \mathbf{C}\mathbf{x}$  is observable, if and only if rank  $\begin{bmatrix} \mathbf{A} - s_i\mathbf{I} \\ \mathbf{C} \end{bmatrix} = n$ .

□

An eigenvalue can be shifted by feedback from  $\mathbf{y}$  to  $\mathbf{u}$ , if and only if it is controllable and observable. Obviously, a necessary and sufficient condition for  $\Gamma$ -stabilization is that all open-loop eigenvalues outside  $\Gamma$  must be controllable and observable.

A fundamental difference between the classical stabilization problem for a fixed plant and the robust stabilization of a plant family  $G(s, Q)$  is illustrated in the following example.

### Example 3.11

Consider the finite plant family

$$g^{(1)}(s) = \frac{1}{s-1}, \quad g^{(2)}(s) = \frac{-1}{s-1}. \quad (3.4.1)$$

The unstable pole at  $s = 1$  is controllable and observable, because there are no cancellations and the numerator is non-zero. However, the two plants cannot be simultaneously stabilized by a common linear controller.

First, assume proportional feedback  $c(s) = k$ . Obviously,  $g^{(1)}(s)$  can be stabilized by  $k > 1$  and  $g^{(2)}(s)$  can be stabilized by  $k < -1$ , but there is no  $k$  that stabilizes both plants simultaneously. If we assume a compensator  $c(s) = (c_0 + c_1 s + \dots + c_m s^m)/(d_0 + d_1 s + \dots + d_m s^m)$  and write the plant family as  $g(s, q) = q/(s-1)$ ,  $q \in \{1, -1\}$ , then the coefficients of the closed-loop characteristic polynomial are

$$\begin{aligned} a_0 &= c_0 q - d_0, \\ a_1 &= c_1 q + d_0 - d_1, \\ &\vdots \\ a_m &= c_m q + d_{m-1} - d_m, \\ a_{m+1} &= d_m. \end{aligned}$$

Now, the necessary stability conditions  $a_i > 0$ ,  $i = 0, 1, \dots, m$ , imply  $d_i < 0$ ,  $i = 0, 1, \dots, m$ , but  $d_m < 0$  contradicts the necessary stability condition  $a_{m+1} > 0$ . Thus, the two plants (3.4.1) cannot be simultaneously stabilized by any linear compensator.

An explanation is, that the two plants with gains 1 and -1 are on different sides of the case num  $g = 0$ , where an unstable eigenvalue becomes uncontrollable/unobservable. It is generally recommended to check first that in the operating domain  $Q$  there is no loss of controllability or observability of  $\Gamma$ -unstable eigenvalues before a feedback structure is chosen and a search for good parameter values in it is started.

□

The example gives rise to a fundamental question of robust control: given a plant family  $G(s, Q)$ , does there exist a fixed compensator  $c(s)$  that stabilizes the plant family? What is the order of  $c(s)$ ?

Unfortunately, an answer to this question exists only for very simple systems, e.g. for a first order uncertain system [175]. Thus, in a scientific sense, it is premature to synthesize a robust compensator  $c(s)$ . On the other hand, there are many control systems in operation that show remarkable robustness with respect to uncertainty in the parameters  $q$ . There is a practical need to analyze and design such control systems and to provide algorithms and software tools for this purpose. In summary: the design of a robust controller is more of an art than a science.

### 3.5 Further Potential of the Parameter Space Approach

The concept of mapping  $\Gamma$ -regions from the  $s$ -plane into regions in a parameter plane may be extended to more informative displays, to the design of gain-scheduling controllers, and for more than two parameters. The following examples indicate some of the potential for further developments of the methods and software tools.

#### *Grey-tone or Color Coding*

In Figure 3.14, it was easy to choose the centrally located point (3.2.4) from the admissible set of controllers  $K_\Gamma$ . A more detailed discussion on the choice of a controller from the admissible set is done in Section 7.2 for a flight control example. In Figures 7.19–7.24, fault tolerance is the criterion; in Figure 7.15, specifications are tightened in order to reduce the admissible solution set. Such stepwise tightening of specifications is supported by grey-tone coding.

As an example, take the region of Figure 3.11. It is the image of the  $\Gamma$ -stable region to the left of the left branch of the hyperbola  $\omega^2 = 4\sigma^2 - 0.25$ . This hyperbola is now embedded into a family of hyperbolas and the spaces in between are coded by grey tones from black (= forbidden) to white (good). Figure 3.18 shows the  $\Gamma$ -stability grades and their images.

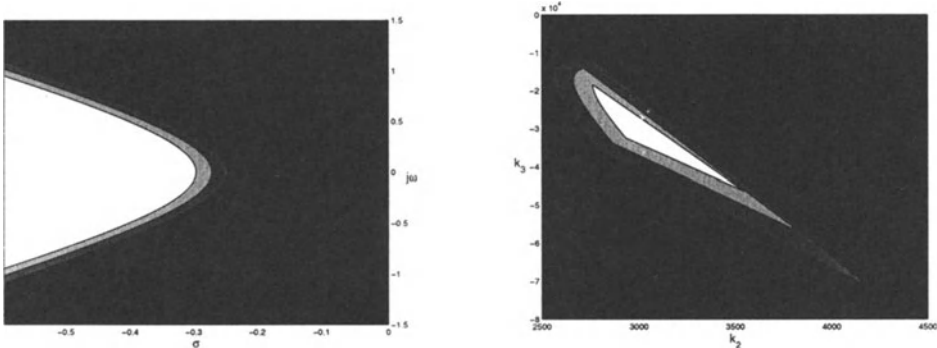


Figure 3.18. Grey-tone coding of  $\Gamma$ -stability grades and their images

Since we are interested in intersections, it is recommended to have the admissible region white on white paper printouts. It is then further reduced by other operating conditions like in Figure 3.13 or additional criteria like in Figures 5.26 and 5.46.

On the computer screen, grey tones may be replaced by colors (e.g. red = forbidden, yellow = possible, green = good). For example, frequency domain performance grades may be color coded and overlayed to  $\Gamma$ -stability regions in order to visualize where eigenvalue and frequency domain criteria are in agreement and where they are in conflict, see Chapter 5.

### Gain-scheduling Design

In the crane example, we have used the  $(k_2, k_3)$ -plane (Figure 3.14) for the design of a robust fixed-gain controller and the  $(m_L, \ell)$ -plane (Figure 3.16) for the robustness analysis. A third possibility arises if an uncertain parameter is measured and used for scheduling a gain.

#### Example 3.12

In the crane example, let  $m_C = 1000$ ,  $m_L = 1500$ ,  $k_1 = 500$ ,  $k_2 = 2865$ ,  $k_3 = -22\,800$  and find a gain-scheduling controller  $k_4(\ell)$  that complies with the  $\Gamma$ -stability specifications postulated in Figure 3.9 even at very low rope lengths  $\ell$ . This is of practical interest for a construction crane operating on the top floor of a building under construction. The assumption here is that the rope length can be measured (e.g. from the rotation of the rope drum) and used to schedule the feedback  $k_4$  of the rope angle rate. (The rope angle rate can be obtained by forming the derivative of the measured rope angle by means of a suitable filter.) Figure 3.19 shows the mapping of  $\Gamma$ -stability into the  $(\ell, k_4)$ -plane for two different values of  $m_L$  ( $m_L = 1000$  with grey line color and

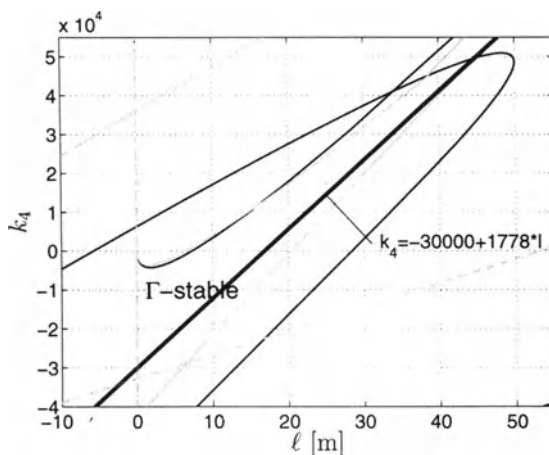


Figure 3.19. Gain scheduling of  $k_4(\ell)$  for the crane

$m_L = 2000$  with black line color). The bold line in the  $\Gamma$ -stable region represents the gain-scheduling  $k_4(\ell) = -30\,000 + 1778 \ell$ , which is adopted here. So the gain-scheduled feedback system is  $\Gamma$ -stable for a much larger interval of  $\ell$ , which is also recognizable in the corresponding parameter space plot shown in Figure 3.20.  $\square$

Gain-scheduling design in a  $(q, k)$ -plane shows that the interpolation between linear controllers is quite arbitrary and may therefore be done as a linear interpolation (as in the crane example) or by a simple polynomial. For the practical implementation, this

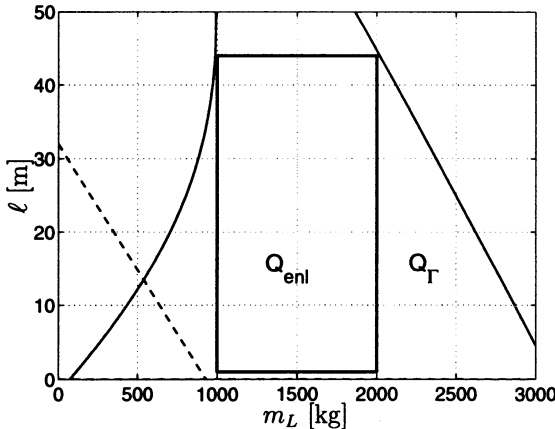


Figure 3.20. An enlarged operating domain (in terms of  $\ell$ ) becomes feasible by gain-scheduling according to Figure 3.19

approach is more useful than other interpolations, e.g. based on poles/zeros or state space models.

### More than Two Parameters

So far, we have shown that the parameter space approach is a very intuitive tool, as long as the user accepts the limitation of two parameters at a time. Design with more than two controller parameters can be broken down to sequential steps with two parameters in each step, as shown in Section 2.4 on sequential pole shifting.

Tomographic renderings for a third gridded parameter have been used for PID-controller design in Figure 2.11. An early contribution to 3D renderings of stability regions was given in [170]. In the meantime, much software has been developed to visualize the 3D world on a 2D screen. Motion of objects or point of view and light sources, stereoscopic vision, moving 2D slices under the control of a joystick and color coding may also be exploited to visualize 3D  $\Gamma$ -stability regions and their intersections for the purpose of design. The  $\Gamma$ -stable regions may thus be explored interactively. This approach may be extended to more than three parameters. Then, however, the user needs some help with navigation in higherdimensional spaces. Slices are best suited for looking at intersections of sets as they occur in simultaneous design for several representative operating conditions. The human user is very good and fast at recognizing intersections of 2D-sets, even in cases where a lot of computation would be needed to calculate the intersection.

For robustness analysis for a given  $Q$ -box, a third and further parameters may be gridded and all planes are projected onto one plane. The projection of  $Q$ -box is a rectangle and for robust  $\Gamma$ -stability it must be avoided by all projected  $\Gamma$ -stability boundaries.

*Example 3.13*

As an example, consider the robustness analysis for a crane. In Figure 3.16, the  $\Gamma$ -stable region was shown for a crab mass  $m_C = 1000$ . It enters into the characteristic polynomial (1.5.18) via  $a_2 = (m_L + m_C)g + k_1\ell - k_3$  (linearly) and via  $a_4 = \ell m_C$  (bilinearly). In Figure 3.21,  $m_C$  is gridded in the interval  $m_C \in [800; 1200]$ . All curves must avoid the operating domain  $Q$  for robust stability with respect to  $m_C$ .

□

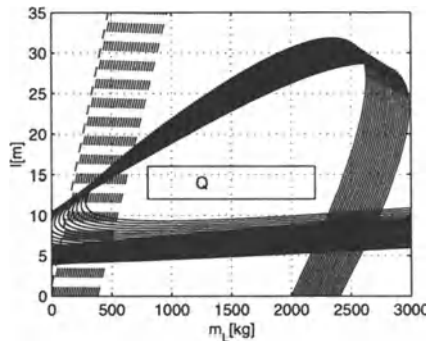


Figure 3.21.  $\Gamma$ -stability boundaries by gridding  $m_C$  which enters together with  $\ell$  bilinearly into the characteristic polynomial

Similarly, a fourth (or fifth, etc.) parameter may be gridded and all boundaries are projected to a  $(q_1, q_2)$ -plane where  $q_1$  and  $q_2$  are treated continuously. Also, any other pair of two parameters may be treated continuously by choosing the appropriate projection plane.

Alternative methods for dealing with a larger number of parameters in robustness analysis of polynomials with specially simple coefficient functions  $\mathbf{a}(\mathbf{q})$  will be treated in Chapters 8 and 9.

## 4 Gamma-boundary Mapping into Parameter Space

Chapter 3 has provided the motivation for mapping boundaries  $\partial\Gamma$  of  $\Gamma$ -stability regions into various planes of two real parameters. In Figure 3.10, a hyperbola was mapped into a plane of two gains for design. In Figure 3.16, the same hyperbola was mapped into a plane of two plant parameters for robustness analysis, and in Figure 3.19 it was mapped into a plane of one measurable plant parameter and one gain for design of a gain-scheduling system.

The mathematical formalism for these three mappings is exactly the same, although the interpretation and use of the resulting  $\Gamma$ -stable regions is quite different in the three cases. This chapter deals with the mathematical formalism and we call all (real) parameters  $q_i$ , independent of their meaning as plant parameters or controller parameters. For  $\ell$  parameters,  $i = 1, 2, \dots, \ell$ , the parameter space or  $\mathbf{q}$ -space is  $\ell$ -dimensional. The decision of how we choose a two-dimensional linear or affine subspace for graphical representation in a parameter plane may be taken later after we have derived the general equations for mapping into the  $\mathbf{q}$ -space.

An eigenvalue region  $\Gamma$  is characterized by the equation of the boundary  $\partial\Gamma$ . In the case of the left half plane, the boundary is described by

$$\partial\Gamma := \{s \mid s = j\omega, 0 \leq \omega < \infty\}. \quad (4.0.1)$$

The restriction to non-negative  $\omega$  is made because polynomials with real coefficients are assumed. Hence, for each complex eigenvalue, also a conjugate complex eigenvalue exists. Therefore, in general the  $\Gamma$ -root regions should be chosen to be symmetric with respect to the real axis. The boundary  $\partial\Gamma$  of the desired root region  $\Gamma$  can be described by

$$\partial\Gamma := \{s \mid s = \sigma(\alpha) + j\omega(\alpha), \alpha \in [\alpha^-; \alpha^+]\}. \quad (4.0.2)$$

The lower and upper bounds  $\alpha^-$  and  $\alpha^+$  may also be  $+\infty$  or  $-\infty$ . The scalar parameter  $\alpha$  is called the *generalized frequency*. For generalizing the results on Hurwitz-stability to  $\Gamma$ -stability,  $s = j\omega$  has to be replaced by  $s = \sigma(\alpha) + j\omega(\alpha)$  and  $s = 0$  by  $s = a$  where  $a$  is an intersection point of  $\partial\Gamma$  with the real axis.

Assume that the real functions  $\sigma(\alpha)$  and  $\omega(\alpha)$ , or implicit descriptions by  $f[\sigma(\alpha), \omega(\alpha)] = 0$ , are polynomials or simple trigonometric functions. By choosing polynomials of degree less or equal to two, root regions can be described, which are

bounded by conic sections, i.e. straight lines, circles, ellipses, hyperbolas and parabolas. For most applications, it suffices to compose the boundary  $\partial\Gamma$  from segments of conic sections.

## 4.1 Algebraic Problem Formulation

For Hurwitz-stability of a polynomial  $p(s, \mathbf{q})$  with real coefficients  $a_i(\mathbf{q})$ , continuous in  $\mathbf{q}$ , the three hypersurfaces

$$\text{CRB: } \operatorname{Re} p(j\omega, \mathbf{q}) = 0, \quad \operatorname{Im} p(j\omega, \mathbf{q}) = 0, \quad (4.1.1)$$

$$\text{RRB: } a_0(\mathbf{q}) = 0, \quad (4.1.2)$$

$$\text{IRB: } a_n(\mathbf{q}) = 0, \quad (4.1.3)$$

represent the boundary surfaces around a nominal point  $\mathbf{q}^0$ , which corresponds to a stable polynomial. Eliminating  $\omega$  from the two equations (4.1.1) gives the last but one Hurwitz determinant  $\Delta_{n-1}$ , see Theorem 2.2.

The extension to other pole regions  $\Gamma$  is straightforward. Instead of  $s = j\omega$  in (4.1.1), now  $s = \sigma(\alpha) + j\omega(\alpha)$  is substituted. Compared to Hurwitz-stability, there are only minor differences. The resulting equations are more complicated depending on the complexity of the functions  $\sigma = \sigma(\alpha)$ ,  $\omega = \omega(\alpha)$ , which describe the boundary of  $\Gamma$ . Eliminating  $\alpha$  by means of the resultant method (see Appendix A) gives the analog to the last but one Hurwitz determinant, that is,

$$\operatorname{Res}_\alpha \left( \operatorname{Re} p[\sigma(\alpha) + j\omega(\alpha), \mathbf{q}], \operatorname{Im} p[\sigma(\alpha) + j\omega(\alpha), \mathbf{q}] \right) = 0. \quad (4.1.4)$$

The restriction to a real interval  $\alpha \in [\alpha^-; \alpha^+]$  is lost by the elimination of  $\alpha$ . Therefore, fictitious boundaries are not only generated by complex values of  $\alpha$ , but also by real  $\alpha$ -values outside the above interval. For the example of the hyperbola in Figure 3.8, the symmetric branch in the right half plane would generate a fictitious boundary as well as the extension of the hyperbola beyond the bandwidth circle. Also, the bandwidth circle would be mapped as an entire circle. Therefore, a piecewise definition of  $\partial\Gamma$  becomes impractical. We do not pursue the algebraic approach, because in the case of  $\Gamma$ -stability there are even more good reasons to prefer the parameter space approach.

## 4.2 Parameter Space Mapping

A real root boundary (RRB) arises for each real axis intersection of  $\partial\Gamma$ . Such intersection at  $s = \sigma_0$  is mapped into  $\mathbf{q}$ -space by

$$p(\sigma_0, \mathbf{q}) = 0. \quad (4.2.1)$$

Similarly, an infinite root boundary (IRB) may result from

$$\lim_{\alpha \rightarrow \infty} p(\sigma(\alpha) + j\omega(\alpha), \mathbf{q}) = 0. \quad (4.2.2)$$

The mapping of the complex root boundary (CRB) into the set of all parameter vectors  $\mathbf{q}$  that yield a root pair at  $s = \sigma(\alpha) + j\omega(\alpha)$ , i.e.

$$Q_{CRB}(\alpha) := \{ \mathbf{q} \mid p(\sigma(\alpha) + j\omega(\alpha), \mathbf{q}) = 0, \alpha \in [\alpha^-; \alpha^+] \} \quad (4.2.3)$$

is formulated in the following theorem [23].

*Theorem 4.1 (CRB Mapping, Ackermann, Kaesbauer)*

Consider a polynomial family  $p(s, \mathbf{q}) = [1 s \dots s^n] \mathbf{a}(\mathbf{q})$  with real continuous coefficient function  $\mathbf{a}(\mathbf{q})$ .

Now,  $\mathbf{q} \in Q_{CRB}(\alpha)$  if and only if

$$\begin{bmatrix} d_0(\alpha) & d_1(\alpha) & \dots & d_n(\alpha) \\ 0 & d_0(\alpha) & \dots & d_{n-1}(\alpha) \end{bmatrix} \mathbf{a}(\mathbf{q}) = \begin{bmatrix} 0 \\ 0 \end{bmatrix} \quad (4.2.4)$$

for some  $\alpha \in [\alpha^-; \alpha^+]$ , where

$$\begin{aligned} d_0(\alpha) &= 1, \\ d_1(\alpha) &= 2\sigma(\alpha), \\ d_{i+1}(\alpha) &= 2\sigma(\alpha)d_i(\alpha) - [\sigma^2(\alpha) + \omega^2(\alpha)]d_{i-1}(\alpha), \quad i = 1, 2, \dots, n-1. \end{aligned} \quad (4.2.5)$$

□

*Proof*

Consider the polynomial  $p(s, \mathbf{q})$  for fixed  $\mathbf{q} = \mathbf{q}^*$ . It has a complex conjugate pair of roots on  $\partial\Gamma$  at  $\sigma(\alpha) \pm j\omega(\alpha)$ , if and only if

$$p(s, \mathbf{q}^*) = [\sigma^2(\alpha) + \omega^2(\alpha) - 2\sigma(\alpha)s + s^2] r(s, \mathbf{q}^*), \quad (4.2.6)$$

where

$$r(s, \mathbf{q}^*) = r_0 + r_1 s + r_{n-2} s^{n-2} = [1 s \dots s^{n-2}] \mathbf{r} \quad (4.2.7)$$

is an arbitrary polynomial of degree  $n-2$  with real coefficients. Equivalently (omitting the dependence of  $\sigma$  and  $\omega$  on  $\alpha$  for notational convenience),

$$\mathbf{a}(\mathbf{q}^*) = \begin{bmatrix} 1 & -2\sigma & \sigma^2 + \omega^2 & 0 & \dots & 0 \\ 0 & 1 & -2\sigma & . & & \\ 0 & 0 & 1 & . & . & 0 \\ & & & . & . & \sigma^2 + \omega^2 \\ & & & & . & -2\sigma \\ 0 & & & & & 1 \end{bmatrix} \begin{bmatrix} 0 \\ 0 \\ r_0 \\ . \\ . \\ r_{n-2} \end{bmatrix}. \quad (4.2.8)$$

The matrix in (4.2.8) is triangular with identical elements on the diagonals. Therefore, its inverse  $\hat{\mathbf{D}}$  has the same structure. The entries  $d_i$  of  $\hat{\mathbf{D}}$  are determined from

$$\begin{bmatrix} d_0 & d_1 & \dots & d_n \\ 0 & d_0 & \dots & \\ \vdots & \ddots & d_1 & \\ & & d_0 & \end{bmatrix} \begin{bmatrix} 1 & -2\sigma & \sigma^2 + \omega^2 & 0 & \dots & 0 \\ 0 & 1 & -2\sigma & \dots & & \\ 0 & 0 & 1 & \dots & & 0 \\ 0 & & & \dots & & \sigma^2 + \omega^2 \\ 0 & & & & & -2\sigma \\ & & & & & 1 \end{bmatrix} = \mathbf{I}, \quad (4.2.9)$$

which implies

$$\begin{aligned} d_0 &= 1, \\ -2\sigma d_0 + d_1 &= 0, \\ (\sigma^2 + \omega^2)d_0 - 2\sigma d_1 + d_2 &= 0, \\ &\vdots \\ (\sigma^2 + \omega^2)d_{n-2} - 2\sigma d_{n-1} + d_n &= 0, \end{aligned}$$

and solving for  $d_i$  yields

$$\begin{aligned} d_0 &= 1, \\ d_1 &= 2\sigma, \\ d_2 &= 2\sigma d_1 - (\sigma^2 + \omega^2)d_0, \\ &\vdots \\ d_n &= 2\sigma d_{n-1} - (\sigma^2 + \omega^2)d_{n-2}. \end{aligned}$$

By premultiplying (4.2.8) by  $\hat{\mathbf{D}}$ , it can be concluded that  $p(s(\alpha), \mathbf{q}^*) = 0$  if and only if

$$\begin{bmatrix} d_0 & d_1 & \dots & d_n \\ 0 & d_0 & & \\ \vdots & & \ddots & d_1 \\ 0 & & 0 & d_0 \end{bmatrix} \mathbf{a}(\mathbf{q}^*) = \begin{bmatrix} 0 \\ 0 \\ \vdots \\ r_0 \\ \vdots \\ r_{n-2} \end{bmatrix}. \quad (4.2.10)$$

The last  $n - 1$  rows of (4.2.10) have an undetermined right hand side because the remainder polynomial  $r(s, \mathbf{q}^*)$  is arbitrary. In other words, whatever the left hand side requires, the equation is satisfied by the appropriate choice of  $r_i$ . There only remain the first two rows. Hence, it can be concluded that  $\mathbf{q}^* \in Q_{CRB}(\alpha)$  if and only if

$$\begin{bmatrix} d_0(\alpha) & d_1(\alpha) & \dots & d_n(\alpha) \\ 0 & d_0(\alpha) & \dots & d_{n-1}(\alpha) \end{bmatrix} \mathbf{a}(\mathbf{q}^*) = \begin{bmatrix} 0 \\ 0 \end{bmatrix}. \quad (4.2.11)$$

The fixed value  $\mathbf{q}^*$  may be replaced by the general vector  $\mathbf{q}$  to obtain (4.2.4). Thus, the proof of the theorem is complete.

□

For short notation, Equation (4.2.4) is written as

$$\mathbf{D}(\alpha) \mathbf{a}(\mathbf{q}) = \mathbf{0}. \quad (4.2.12)$$

This formulation clearly separates the  $\Gamma$ -boundary description by  $\mathbf{D}(\alpha)$  from the  $\mathbf{q}$ -parameter-dependent coefficient vector  $\mathbf{a}(\mathbf{q})$ . In the parameter space approach, the scalar parameter  $\alpha$  is gridded and the complexity of (4.2.12) depends on the *coefficient function*  $\mathbf{a}(\mathbf{q})$ . If it is linear, then the edge theorem (see Chapter 8) offers an interesting alternative, also for more parameters. If the coefficient function is multilinear or polynomial, however, then the parameter space approach is superior.

The polynomial  $p(s, \mathbf{q})$  has a complex conjugate pair of roots on  $\partial\Gamma$ , if and only if there exists an  $\alpha \in [\alpha^-; \alpha^+]$  such that (4.2.4) holds. In other words, in analogy to the  $\omega$ -sweep over the imaginary axis in the robust stability test of Chapter 2, an  $\alpha$ -sweep along all branches or segments of  $\partial\Gamma$  must be made. For each  $\alpha$ , the set  $Q_{CRB}(\alpha)$  can be calculated from (4.2.4).

#### *Example 4.2*

Let  $\partial\Gamma$  be the imaginary axis, i.e.  $\sigma = 0$ , choose the parametrization  $\alpha = \omega^2$ ,  $\alpha \in [0; \infty)$ .

$$\begin{aligned} d_0 &= 1, \\ d_1 &= 0, \\ d_{i+1} &= -\alpha d_{i-1}, \\ \left[ \begin{array}{cccccc} 1 & 0 & -\alpha & 0 & \alpha^2 & \dots \\ 0 & 1 & 0 & -\alpha & 0 & \dots \end{array} \right] \mathbf{a}(\mathbf{q}) &= \left[ \begin{array}{c} 0 \\ 0 \end{array} \right]. \end{aligned} \quad (4.2.13)$$

□

#### *Example 4.3*

Let  $\partial\Gamma$  be parallel to the imaginary axis at  $\sigma = \sigma_0$ .

$$\begin{aligned} d_0 &= 1, \\ d_1 &= 2\sigma_0, \\ d_{i+1} &= 2\sigma_0 d_i - (\sigma_0^2 + \omega^2) d_{i-1}. \end{aligned}$$

Again,  $\alpha = \omega^2$  is chosen.

$$\left[ \begin{array}{cccccc} 1 & 2\sigma & 3\sigma_0^2 - \alpha & 4\sigma_0(\sigma_0^2 - \alpha) & \dots \\ 0 & 1 & 2\sigma & 3\sigma_0^2 - \alpha & \dots \end{array} \right] \mathbf{a}(\mathbf{q}) = \left[ \begin{array}{c} 0 \\ 0 \end{array} \right]. \quad (4.2.14)$$

□

*Example 4.4*

Let  $\partial\Gamma$  be a line of constant damping  $D$ , see Figure 3.2, with  $\omega^2 = \sigma^2(1 - D^2)/D^2$ . Choose the parametrization  $\alpha = \sigma$ ,  $\alpha \in [0; -\infty)$ .

$$\begin{aligned} d_0 &= 1, \\ d_1 &= 2\alpha, \\ d_{i+1} &= 2\alpha d_i - (\alpha^2/D^2)d_{i-1}, \end{aligned}$$

$$\begin{bmatrix} 1 & 2\alpha & \alpha^2(4 - 1/D^2) & 4\alpha^3(2 - 1/D^2) & \dots \\ 0 & 1 & 2\alpha & \alpha^2(4 - 1/D^2) & \dots \end{bmatrix} \mathbf{a}(\mathbf{q}) = \begin{bmatrix} 0 \\ 0 \end{bmatrix}. \quad (4.2.15)$$

□

*Example 4.5*

Let  $\partial\Gamma$  be the left branch of the hyperbola

$$\left(\frac{\sigma}{a}\right)^2 - \left(\frac{\omega}{b}\right)^2 = 1, \quad \sigma \in [-a; -\infty). \quad (4.2.16)$$

The hyperbola is shown in Figure 4.1. This hyperbola ensures a minimum damping

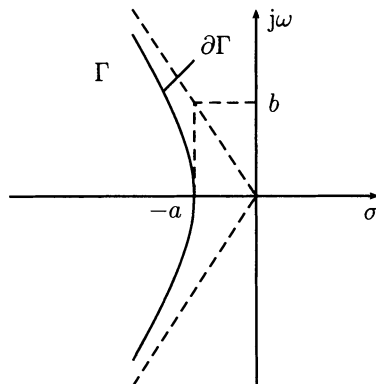


Figure 4.1. A hyperbola combines constraints on damping and real parts of the eigenvalues

of  $D = \frac{a}{\sqrt{a^2 + b^2}}$ , corresponding to the asymptotes, and a maximal real part of the eigenvalues of  $\sigma = -a$ .

The parametrization is  $\alpha = \sigma$ ,  $\alpha \in [-a; -\infty)$ .

From (4.2.16),

$$\omega^2 = b^2 \left( \left(\frac{\sigma}{a}\right)^2 - 1 \right),$$

$$\begin{aligned} d_0 &= 1, \\ d_1 &= 2\alpha, \\ d_{i+1} &= 2\alpha d_i - [\alpha^2(1 + (b/a)^2)b^2] d_{i-1}, \end{aligned}$$

$$\left[ \begin{array}{cccc} 1 & 2\alpha & \alpha^2(3 - (b/a)^2) - b^2 & \dots \\ 0 & 1 & 2\alpha & \dots \end{array} \right] \mathbf{a}(\mathbf{q}) = \left[ \begin{array}{c} 0 \\ 0 \end{array} \right]. \quad (4.2.17)$$

□

*Example 4.6*

Let  $\partial\Gamma$  be a circle with center  $s = 0$  and radius  $R$ , i.e.  $\sigma^2 + \omega^2 = R^2$ . Choose  $\alpha = \sigma$ ,  $\alpha \in [-R ; R]$ .

$$\begin{aligned} d_0 &= 1, \\ d_1 &= 2\alpha, \\ d_{i+1} &= 2\alpha d_i - R^2 d_{i-1}, \\ \left[ \begin{array}{cccc} 1 & 2\alpha & 4\alpha^2 - R^2 & 4\alpha(2\alpha^2 - R^2) & \dots \\ 0 & 1 & 2\alpha & 4\alpha^2 - R^2 & \dots \end{array} \right] \mathbf{a}(\mathbf{q}) = \left[ \begin{array}{c} 0 \\ 0 \end{array} \right]. \end{aligned} \quad (4.2.18)$$

RRB's occur for  $\alpha = -R$  and  $\alpha = R$ . There is no IRB, because  $\Gamma$  is finite.

□

*Remark 4.7*

Equation (4.2.18) may be further simplified in terms of the powers of  $\alpha$ , see Chapter 11. Since  $\alpha$  is gridded anyway, the effect on computing time is not dramatic. □

*Example 4.8*

The  $\Gamma$ -stability region of Figure 3.8 can be composed from the hyperbola equation (4.2.17) and the circle equation (4.2.18).

The circle and the hyperbola intersect for a real value  $\sigma_1 = -\sqrt{\frac{a^2(R^2 + b^2)}{a^2 + b^2}}$ .

Thus, (4.2.18) applies for  $\alpha \in [-R ; \sigma_1]$  and (4.2.17) for  $\alpha \in [\sigma_1 ; -a]$ . There are two RRB's at  $\alpha = -R$  and  $\alpha = -a$ . There is no IRB because  $\Gamma$  is finite. □

In the last example, the  $\Gamma$ -region was defined as an intersection of two regions. Also, a union of regions can be useful. If the union consists of disjoint sets, then it must also be specified how many roots are located in each disjoint set. A practical use of a union of sets is the following. Assume you have designed a controller for a nominal plant model, i.e. you know the nominal location of all closed-loop eigenvalues. If the uncertain parameters vary, you want to keep the eigenvalues in some well-defined neighborhood of their nominal locations.

*Example 4.9*

Assume that the nominal polynomial closed-loop characteristic in factorized form is

$$p(s) = (4 + 2s + s^2)(2 + s)(5 + s)(8 + s)(72 + 12s + s^2).$$

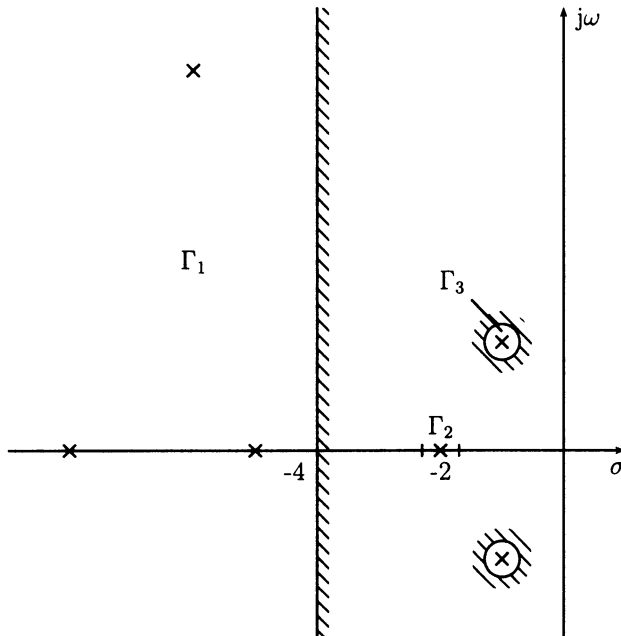


Figure 4.2. Several components may constitute a  $\Gamma$ -stability region

The roots are shown in Figure 4.2, they represent a dominant Butterworth pole configuration in a distance 2 from the origin and some eigenvalues that are located further to the left.  $\Gamma$ -stability is now defined by the admissible migration of individual eigenvalues or groups of eigenvalues. Take, for example, a circle of radius 0.3 around the eigenvalues at  $s_{1,2} = -1 + j\sqrt{3}$ . Then it is important to also keep the real eigenvalue at  $s = -2$  in the interval  $\sigma \in [-2.3 ; -1.7]$ , otherwise the low damping  $D = 0.5$  of the two eigenvalues  $s_{1,2}$  yields too much overshoot of the step response, see Figure 3.5. It is not necessary to care about the other eigenvalues as long as they do not interfere with the dominant behavior. Therefore, the requirement is that their real part must remain less than  $\sigma_1 = -4$ . The disjoint parts  $\partial\Gamma_1$ ,  $\partial\Gamma_2$ , and  $\partial\Gamma_3$  of the boundary are shown in Figure 4.2. Note that the real axis interval contains only one real root; therefore,  $\partial\Gamma_2$  consists only of the real root boundaries at  $\sigma_2 = -2.3$  and  $\sigma_3 = -1.7$ . The left region  $\Gamma_1$  has a real root boundary at  $\sigma_1 = -4$  and its complex root boundary is  $s = -4 + j\omega$ ,  $\omega \geq 0$ . The circle around the dominant complex poles is described by

$$\partial\Gamma_3 = \{s \mid s = -1 + 0.3 \cos \alpha + j(\sqrt{3} + 0.3 \sin \alpha), \alpha \in [0 ; 2\pi]\}. \quad (4.2.19)$$

□

*Example 4.10*

For sampled-data systems (see Chapter 11), the constant damping lines  $\sigma = c\omega$ , ( $c = -D/\sqrt{1 - D^2}$ ,  $D$  = damping) are mapped via  $z = e^{sT} = e^{\sigma T} e^{j\omega T} = e^{c\omega T} e^{j\omega T}$  into the  $z$ -plane.

Choose a parametrization by polar coordinates  $\alpha = \omega T$ ,  $\alpha \in [-\pi ; 0]$ . Then the real and imaginary parts of  $z = \tau + j\eta$  are  $\tau = e^{c\alpha} \cos \alpha$  and  $\eta = e^{c\alpha} \sin \alpha$ . They now play the role of  $\sigma$  and  $\omega$  in (4.2.5).

$$\begin{aligned} d_0 &= 1, \\ d_1 &= 2\tau = 2e^{c\alpha} \cos \alpha, \\ d_{i+1} &= 2\tau d_i - (\tau^2 + \omega^2) d_{i-1} \\ &= 2e^{c\alpha} \cos \alpha d_i - e^{2c\alpha} d_{i-1}. \end{aligned} \tag{4.2.20}$$

This is an example where the algebraic (Hurwitz-like) approach fails. The boundary mapping, however, is not particularly difficult. The RRB's are  $p(1, \mathbf{q}) = 0$  and  $p(-e^{c\pi}, \mathbf{q}) = 0$ . There is no IRB.  $\square$

*Example 4.11*

In Example 4.9 there was a real axis segment  $\sigma \in [\sigma^-, \sigma^+]$  with only one root, and the two RRB's  $p(\sigma^-, \mathbf{q}) = 0$  and  $p(\sigma^+, \mathbf{q}) = 0$ . If there are more roots in the segment, then they can also leave it through a double root into imaginary direction (aperiodicity constraint). A polynomial  $p(s)$  has a double root at  $s = s^*$ , if and only if  $p(s^*) = 0$  and  $p'(s^*) = 0$ , where  $p'(s) = dp(s)/ds$ . Therefore, (4.1.1) has to be replaced by

$$p(\alpha, \mathbf{q}) = 0, \quad p'(\alpha, \mathbf{q}) = 0. \tag{4.2.21}$$

The resultant with respect to  $p(s)$  and  $p'(s)$  is called the *discriminant* of  $p(s)$ .  $\square$

*Remark 4.12*

A related boundary representation was derived by Šiljak [200]. Instead of the starting point (4.2.6), he uses the real and imaginary part of  $p[\sigma(\alpha) + j\omega(\alpha)]$ . The  $k$ -th power of  $s$  is expressed by  $[s(\alpha)]^k = [\sigma(\alpha) + j\omega(\alpha)]^k = X_k(\alpha) + jY_k(\alpha)$ . Then

$$\begin{aligned} p[\sigma(\alpha) + j\omega(\alpha)] &= \operatorname{Re} p(X_1(\alpha) + jY_1(\alpha)) + j \operatorname{Im} p(X_1(\alpha) + jY_1(\alpha)) \\ &= \sum_{k=0}^n a_k X_k(\alpha) + j \sum_{k=0}^n b_k Y_k(\alpha) = 0. \end{aligned} \tag{4.2.22}$$

The advantage of the form (4.2.4) is that only one recursion for  $d_k$  is needed instead of two recursions for  $X_k$  and  $Y_k$ . The two equations for real and imaginary parts are

related to (4.2.4) by

$$\begin{bmatrix} \text{Re } p[\sigma(\alpha) + j\omega(\alpha)] \\ \text{Im } p[\sigma(\alpha) + j\omega(\alpha)] \end{bmatrix} = \begin{bmatrix} 1 & -\sigma(\alpha) \\ 0 & \omega(\alpha) \end{bmatrix} \begin{bmatrix} d_0(\alpha) & d_1(\alpha) & \dots & d_n(\alpha) \\ 0 & d_0(\alpha) & \dots & d_{n-1}(\alpha) \end{bmatrix} \mathbf{a}(\mathbf{q}). \quad (4.2.23)$$

□

The toolbox PARADISE (see Appendix B) contains a  $\Gamma$ -editor [27]. The user composes the  $\Gamma$ -region from standard elements by a graphical user interface or specifies it numerically. The  $\Gamma$ -editor then generates  $D(\alpha)$  for (4.2.12). The second ingredient  $\mathbf{a}(\mathbf{q})$  for (4.2.12) is provided by symbolic generation of the closed-loop characteristic polynomial, i.e.  $\mathbf{a}(\mathbf{q})$ , for example, from a SIMULINK model. This completes the mapping into the  $\ell$ -dimensional  $\mathbf{q}$ -space.

### Example 4.13

For the crane example, choose the hyperbola  $\omega^2 = 4\sigma^2 - 0.25$ , i.e.  $\left(\frac{\sigma}{0.25}\right)^2 - \left(\frac{\omega}{0.5}\right)^2 = 1$ ,  $a = 0.25$ ,  $b = 0.5$ . Equation (4.2.5) becomes

$$\begin{aligned} d_0(\sigma) &= 1, \\ d_1(\sigma) &= 2\sigma, \\ d_2(\sigma) &= 0.25 - \sigma^2, \\ d_3(\sigma) &= \sigma - 12\sigma^3, \\ d_4(\sigma) &= 0.0625 + 0.5\sigma^2 - 19\sigma^4, \end{aligned}$$

and the CRB-mapping equation is

$$\mathbf{D}(\sigma)\mathbf{a}(\mathbf{q}) = \begin{bmatrix} d_0(\sigma) & d_1(\sigma) & d_2(\sigma) & d_3(\sigma) & d_4(\sigma) \\ 0 & d_0(\sigma) & d_1(\sigma) & d_2(\sigma) & d_3(\sigma) \end{bmatrix} \mathbf{a}(\mathbf{q}) = \begin{bmatrix} 0 \\ 0 \end{bmatrix}.$$

The coefficient vector is, by (1.5.8),

$$\mathbf{a}(m_L, m_C, \ell, k_1, k_2, k_3, k_4) = \begin{bmatrix} k_1 g \\ k_2 g \\ (m_L + m_C)g + k_1 \ell - k_3 \\ k_2 \ell - k_4 \\ \ell m_C \end{bmatrix}.$$

All plots for the crane in Chapter 3 are generated from  $\mathbf{D}(\sigma)\mathbf{a}(\mathbf{q}) = \mathbf{0}$  by fixing five of the seven parameters. The two free parameters are  $k_2, k_3$  for design,  $m_L, \ell$  for robustness analysis and  $\ell, k_4$  for gain-scheduling. In each case, the resulting equations are linear in the parameters. They would be bilinear, however, for combining  $\ell$  with  $k_1, k_2$  or  $m_C$ .

□

For the visualization of the result, the user specifies an interesting subspace of the  $\mathbf{q}$ -space. In the case of robustness analysis, the choice of two plant parameters  $q_i, q_j$  is a natural one. Further plant parameters may be gridded and projected, as in Figure 3.21, or they are assigned to a joystick such that the user can move them back and forth in order to explore the higher dimensional stability region. For design, two gains  $k_i, k_j$  in one design step are appropriate, but also a linear subspace at some odd angle may be useful, like in the invariance planes of Section 2.4. Again, further gains or eigenvalues may be assigned to a joystick.

In gain-scheduling design, it may be of interest to schedule two gains by the same measured parameter. If the 3D-stability region (with the  $\Gamma$ -unstable region non-transparent) can be rotated such that it is possible to peek through it, then this line of sight describes a linear gain-scheduling control law.

In all cases, it is important that the symbolic calculations for  $D(\alpha)\mathbf{a}(\mathbf{q})$  are done beforehand, such that the remaining numeric calculations can be executed online.

An interesting application is also a comparison of three controller candidates  $\mathbf{k}^{(1)}, \mathbf{k}^{(2)}$  and  $\mathbf{k}^{(3)}$  (one of them may be the open loop  $\mathbf{k}^{(1)} = \mathbf{0}$ ) as they are obtained by different design approaches. The three points define an affine subspace

$$\gamma_1 \mathbf{k}^{(1)} + \gamma_2 \mathbf{k}^{(2)} + \gamma_3 \mathbf{k}^{(3)}, \quad \gamma_1 + \gamma_2 + \gamma_3 = 1 \quad (4.2.24)$$

for visualizing  $\Gamma$ -stable regions that help in the decision on a trade-off.

### 4.3 Generalized Singular Frequencies

In Section 2.5, the concept of singular frequencies  $\omega_k$  on the imaginary axis of the  $s$ -plane was introduced. It is generalized now to singular frequencies  $\alpha_k$  on the  $\Gamma$ -stability boundary  $s = \sigma(\alpha) + j\omega(\alpha)$ ,  $\alpha \in [\alpha^-; \alpha^+]$ .

Consider again the polynomial (2.5.1) with linear dependency on  $q_1$  and  $q_2$ , i.e.

$$p(s, q_1, q_2) = p_0(s) + q_1 p_1(s) + q_2 p_2(s). \quad (4.3.1)$$

Let  $s = \sigma(\alpha) + j\omega(\alpha)$  and determine the two equations (4.2.4) for the chosen  $\Gamma$ -stability boundary. Substitute the coefficient vector

$$\mathbf{a}(q_1, q_2) = \mathbf{a}_0 + q_1 \mathbf{a}_1 + q_2 \mathbf{a}_2 \quad (4.3.2)$$

to obtain two linear equations in  $q_1$  and  $q_2$  of the form

$$\begin{bmatrix} c_{11}(\alpha) & c_{12}(\alpha) \\ c_{21}(\alpha) & c_{22}(\alpha) \end{bmatrix} \begin{bmatrix} q_1 \\ q_2 \end{bmatrix} + \begin{bmatrix} c_{10}(\alpha) \\ c_{20}(\alpha) \end{bmatrix} = \begin{bmatrix} 0 \\ 0 \end{bmatrix}. \quad (4.3.3)$$

Again, a generalized singular frequency  $\alpha = \alpha_k$  is defined by the condition

$$\text{rank} \begin{bmatrix} c_{11}(\alpha) & c_{12}(\alpha) & c_{10}(\alpha) \\ c_{21}(\alpha) & c_{22}(\alpha) & c_{20}(\alpha) \end{bmatrix} = 1. \quad (4.3.4)$$

*Example 4.14*

Continue Example 4.13 with the fixed parameters  $m_C = 1000$ ,  $m_L = 1000$ ,  $k_1 = 500$ ,  $k_4 = 0$ . The  $\Gamma$ -stability boundary is  $\omega^2 = 4\sigma^2 - 0.25$ ,  $\sigma \leq -0.25$ . Equation (4.2.4) with  $\alpha = \sigma$  becomes

$$\begin{bmatrix} 1 & 2\sigma & 0.25 - \sigma^2 & \sigma - 12\sigma^3 & 0.0625 + 0.5\sigma^2 - 19\sigma^4 \\ 0 & 1 & 2\sigma & 0.25 - \sigma^2 & \sigma - 12\sigma^3 \end{bmatrix} \begin{bmatrix} 5000 \\ 10k_2 \\ 20000 + 500\ell - k_3 \\ k_2\ell \\ 1000\ell \end{bmatrix} = \begin{bmatrix} 0 \\ 0 \end{bmatrix},$$

$$\begin{bmatrix} (20 + \ell)\sigma - 12\ell\sigma^3 & -0.25 + \sigma^2 \\ 10 + 0.25\ell - \ell\sigma^2 & -2\sigma \end{bmatrix} \begin{bmatrix} k_2 \\ k_3 \end{bmatrix} + \begin{bmatrix} 10000 + 187.5\ell - 20000\sigma^2 - 19000\ell\sigma^4 \\ (40000 + 20000\ell)\sigma - 12000\ell\sigma^3 \end{bmatrix} = \begin{bmatrix} 0 \\ 0 \end{bmatrix}. \quad (4.3.5)$$

Is there a rope length  $\ell$ , for which a generalized singular frequency  $\sigma_1$  on  $\partial\Gamma$  occurs?

Candidates for  $\sigma_1$  are the roots of the determinant

$$\begin{aligned} d(\sigma^2) &= [(20 + \ell)\sigma - 12\ell\sigma^3](-2\sigma) - (10 + 0.25\ell - \ell\sigma^2)(-0.25 + \sigma^2) \\ &= 2.5 + 0.0625\ell + (-50 - 2.5\ell)\sigma^2 + 25\ell\sigma^4 = 0. \end{aligned}$$

The solutions of this quadratic equation in  $\sigma^2$  are  $\sigma_1^2 = \frac{2}{\ell} + 0.05$  and  $\sigma_2^2 = 0.05$ . In the range of  $\sigma \leq -0.25$ , the value  $\sigma_2 = \pm\sqrt{0.05}$  is ruled out, and  $\sigma_1 = -\sqrt{\frac{2}{\ell} + 0.05} \leq -0.25$  is possible for  $\ell \leq 160$ . The second condition for satisfying (4.3.4) is for  $\sigma_1^2 = \frac{2}{\ell} + 0.05$

$$\begin{aligned} &\left| \begin{array}{cc} -0.25 + \sigma_1^2 & 10000 + 187.5\ell - 20000\sigma_1^2 - 19000\ell\sigma_1^4 \\ -2 & 40000 + 2000\ell - 12000\ell\sigma_1^2 \end{array} \right| \\ &= \left| \begin{array}{cc} -0.2 + 2/\ell & 140\ell + 5200 - 116000/\ell \\ -2 & 1400\ell + 16000 \end{array} \right| \\ &= \frac{1}{\ell} (-0.2\ell + 2)(1400\ell + 16000) + 2(140\ell^2 + 5200\ell - 116000) \\ &= \frac{1000}{\ell} (\ell - 20) = 0. \end{aligned}$$

The answer to the above question is: yes,  $\ell = 20$ , the corresponding  $\sigma$ -value is  $\sigma_1 = -\sqrt{0.15}$ , i.e. the roots can cross  $\partial\Gamma$  only at  $s = -\sqrt{0.15} \pm j\sqrt{0.35}$ .

The example illustrates that non-generic situations in a world of nominal parameters (the probability of hitting exactly  $\ell = 20$  is zero) become likely events in the world of interval parameters.

For all  $\ell \neq 20$ , Equation (4.3.5) is solved for

$$\begin{aligned} k_2(\sigma, \ell) &= \frac{1000\sigma[10 - 2\ell(0.25 - 5\sigma^2)^2]}{(0.25 - 5\sigma^2)[10 + \ell(0.25 - 5\sigma^2)]}, \\ k_3(\sigma, \ell) &= 2\sigma\ell k_2(\sigma, \ell) + 1000 \left[ \frac{5}{0.25 - 5\sigma^2} + 20 + \ell(0.75 - \sigma^2) \right]. \end{aligned}$$

The RRB at  $\sigma = -0.25$  is the straight line

$$k_3(\ell) = -(40 + 0.25\ell)k_2 + (10000 + 562.5\ell).$$

The  $\Gamma$ -stability boundaries for a)  $\ell = 19$ , b)  $\ell = 20$ , and c)  $\ell = 21$  are plotted in Figure 4.3. Like in Figure 2.5 two regions ( $A, F$ ) that are disjoint for  $\ell < 20$  become connected for  $\ell > 20$ . In this case, the two regions are unstable. The stable region  $D$  does not change much by variations of  $\ell$  around 20.

□

## 4.4 Gamma-stable PID-control

In Section 2.6, it was shown that Hurwitz-stable regions in a  $(K_D, K_I)$ -plane of a PID-controller (i.e. for fixed  $K_P$ ) are convex polygons. Does this polygon property also hold for other regions of  $\Gamma$ -stability? A complete characterization of all  $\Gamma$ -stability regions with the above property will be given in this section. The polynomial

$$P(s, K_I, K_P, K_D) = A(s)(K_I + K_P s + K_D s^2) + B(s) \quad (4.4.1)$$

has a root at  $\sigma + j\omega$  if and only if

$$\begin{aligned} R_P &= \operatorname{Re} P(\sigma + j\omega, K_I, K_P, K_D) = 0, \text{ and} \\ I_P &= \operatorname{Im} P(\sigma + j\omega, K_I, K_P, K_D) = 0. \end{aligned} \quad (4.4.2)$$

For the separation of real and imaginary parts, write

$$A(\sigma + j\omega) = R_A + jI_A,$$

$$B(\sigma + j\omega) = R_B + jI_B.$$

Then

$$\begin{aligned} \begin{bmatrix} R_P \\ I_P \end{bmatrix} &= \begin{bmatrix} R_A & R_A\sigma - I_A\omega & R_A(\sigma^2 - \omega^2) - 2I_A\sigma\omega \\ I_A & I_A\sigma + R_A\omega & I_A(\sigma^2 - \omega^2) + 2R_A\sigma\omega \end{bmatrix} \begin{bmatrix} K_I \\ K_P \\ K_D \end{bmatrix} \\ &+ \begin{bmatrix} R_B \\ I_B \end{bmatrix} = \begin{bmatrix} 0 \\ 0 \end{bmatrix}. \end{aligned} \quad (4.4.3)$$

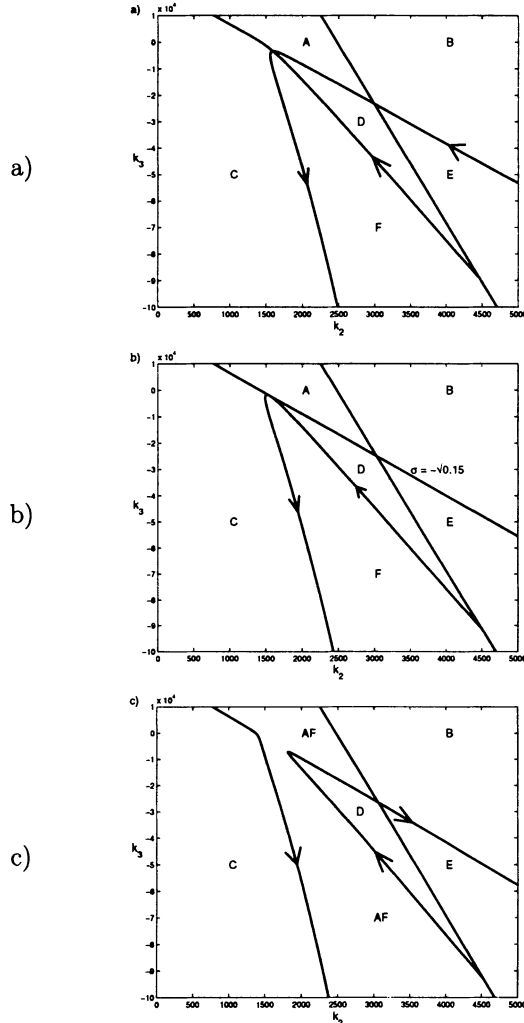


Figure 4.3. a)  $\ell = 19$ , b)  $\ell = 20$ , c)  $\ell = 21$ . In the neighborhood of the singular rope length  $\ell = 20$ , the curves change direction of approach to the asymptote. For  $\ell = 20$ ,  $\sigma = -\sqrt{0.15}$ , a singular boundary in form of a tangent occurs instead of the asymptote

In [71] a coordinate transformation is introduced in order to treat  $\Gamma$ -stability for the half plane to the left of a parallel to the imaginary axis at  $s = \sigma_0$ . This idea is generalized here in order to answer the question: which other  $\Gamma$ -stability regions yield the same nice geometric properties as the left half plane? The answer follows from Equation (4.4.3) by introducing a linear coordinate transformation

$$\begin{aligned} K_I &= t_{11}r_0 + t_{12}r_1 + t_{13}r_2, \\ K_P &= t_{21}r_0 + t_{22}r_1 + t_{23}r_2, \\ K_D &= t_{31}r_0 + t_{32}r_1 + t_{33}r_2. \end{aligned} \quad (4.4.4)$$

Choose  $r_1$  as the fixed parameter (other choices only lead to index permutations). Then Equation (4.4.3) for  $R_P = 0, I_P = 0$  read

$$\begin{bmatrix} R_A & R_A\sigma - I_A\omega & R_A(\sigma^2 - \omega^2) - 2I_A\sigma\omega \\ I_A & I_A\sigma + R_A\omega & I_A(\sigma^2 - \omega^2) + 2R_A\sigma\omega \end{bmatrix} \begin{bmatrix} t_{11} & t_{13} \\ t_{21} & t_{23} \\ t_{31} & t_{33} \end{bmatrix} \begin{bmatrix} r_0 \\ r_2 \end{bmatrix} \quad (4.4.5)$$

$$+ \begin{bmatrix} R_B + r_1\{t_{12}R_A + t_{22}(R_A\sigma - I_A\omega) + t_{32}[R_A(\sigma^2 - \omega^2) - 2I_A\sigma\omega]\} \\ I_B + r_1\{t_{12}I_A + t_{22}(I_A\sigma - R_A\omega) + t_{32}[I_A(\sigma^2 - \omega^2) + 2R_A\sigma\omega]\} \end{bmatrix} = \begin{bmatrix} 0 \\ 0 \end{bmatrix}.$$

The  $2 \times 2$ -matrix multiplying  $[r_0 \ r_2]^T$  is analyzed for singularity.

$$J = \det \begin{bmatrix} \begin{bmatrix} R_A & R_A\sigma - I_A\omega & R_A(\sigma^2 - \omega^2) - 2I_A\sigma\omega \\ I_A & I_A\sigma + R_A\omega & I_A(\sigma^2 - \omega^2) + 2R_A\sigma\omega \end{bmatrix} \begin{bmatrix} t_{11} & t_{13} \\ t_{21} & t_{23} \\ t_{31} & t_{33} \end{bmatrix} \end{bmatrix}. \quad (4.4.6)$$

$J$  can be symbolically factorized into an  $A$ -dependent term, a factor  $\omega$ , and a factor that only depends on the transformation but not on  $A$ .

$$J = (R_A^2 + I_A^2)\omega[a(\sigma^2 + \omega^2) + 2b\sigma + c], \quad (4.4.7)$$

$$a = t_{21}t_{33} + t_{23}t_{31},$$

$$b = t_{11}t_{33} + t_{13}t_{31},$$

$$c = t_{11}t_{23} + t_{21}t_{13}.$$

$J$  vanishes for the RRB at  $\omega = 0$  and for

$$a(\sigma^2 + \omega^2) + 2b\sigma + c = 0. \quad (4.4.8)$$

For  $a = 0$ , Equation (4.4.8) represents a parallel to the imaginary axis at

$$\sigma_0 = -c/2b. \quad (4.4.9)$$

The only other possibility is  $a \neq 0$ , leading to the circle

$$(\sigma + b/a)^2 + \omega^2 = c/a - (b/a)^2, \quad (4.4.10)$$

with center  $m = -b/a$  and radius  $r = \sqrt{c/a - (b/a)^2}$ .

Such circles are useful for bandwidth limitation in the  $s$ -plane and for stability and performance analysis of discrete-time systems in the  $z$ -plane.

Note that the transformation matrices are not unique. Simple forms are

$$\mathbf{T} = \begin{bmatrix} 1 & 0 & 0 \\ 0 & 1 & -2\sigma_0 \\ 0 & 0 & 1 \end{bmatrix} \text{ for } \sigma_0\text{-stability,} \quad (4.4.11)$$

$$\mathbf{T} = \begin{bmatrix} r^2 - m^2 & 1 & -m \\ 0 & 0 & 1 \\ 1 & 0 & 0 \end{bmatrix} \text{ for circle-stability.} \quad (4.4.12)$$

An alternative to the linear transformation (4.4.4) is a conformal mapping that maps the  $\Gamma$ -region onto the left half plane.

For the shifted half plane, substitute

$$s = v + \sigma_0. \quad (4.4.13)$$

The original polynomial is  $\sigma_0$ -stable if and only if the transformed polynomial

$$\begin{aligned} P'(v) &= P(v + \sigma_0) = A(v + \sigma_0)[K_I + K_P(v + \sigma_0) + K_D(v + \sigma_0)^2] + B(v + \sigma_0) \\ &= A(v + \sigma_0)[(K_I + K_P\sigma_0 + K_D\sigma_0^2) + (K_P + 2K_D\sigma_0)v + K_Dv^2] \\ &\quad + B(v + \sigma_0) \end{aligned} \quad (4.4.14)$$

is Hurwitz-stable. Introduce the transformed PID parameters

$$K'_I = K_I + \sigma_0 K_P + \sigma_0^2 K_D, \quad K'_P = K_P + 2\sigma_0 K_D, \quad K'_D = K_D. \quad (4.4.15)$$

Then for fixed  $K'_P$ , convex polygons in the  $(K'_D, K'_I)$ -plane are obtained as described in Section 2.6. Also, the intersection for several representative operating conditions is done in this plane. By gridding  $K'_P$ , the tomographic rendering of all simultaneously  $\sigma_0$ -stabilizing PID-controllers is obtained. A (centrally located) controller  $K'_I, K'_P, K'_D$  is chosen and transformed back to the PID-controller parameters

$$K_I = K'_I - \sigma_0 K'_P + \sigma_0^2 K'_D, \quad K_P = K'_P - 2\sigma_0 K'_D, \quad K_D = K'_D. \quad (4.4.16)$$

Also, a circle with real center and real axis intersections at  $\sigma_L$  and  $\sigma_R$ , Figure 4.4, can be mapped into the left half  $v$ -plane by the bilinear transformation

$$s = \frac{v\sigma_R - \sigma_L}{v - 1}, \quad v = \frac{s - \sigma_L}{s - \sigma_R}. \quad (4.4.17)$$

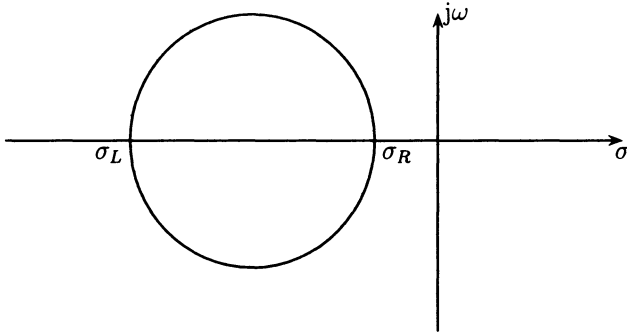


Figure 4.4. The circle is mapped to the left half plane

As shown by (4.4.8), these are the only two examples for which the convex stable polygon property holds for a space of the same dimension as given by the degree of  $P(s, \mathbf{q})$ . If we allow also a non-linear transformation

$$s = \frac{v^2 + b_1 v + b_0}{v^2 + a_1 v + a_0}, \quad (4.4.18)$$

then a large class of eigenvalue regions can be treated, which includes, for example, all conic section boundaries [187]. The price is, however, that the transformed polynomial in  $v$  has twice the degree of  $P(s, \mathbf{q})$ .

## 4.5 Non-linear Coefficient Functions

A particular strength of the parameter space approach in comparison to most other methods of robust control is that the two parameters, for which  $\Gamma$ -stability regions are plotted, may also enter in a multilinear or polynomial fashion into the coefficient vector  $\mathbf{a}(\mathbf{q})$  of the closed-loop characteristic polynomial. This will be illustrated first for a bilinear example.

### *Example 4.15*

Consider Hurwitz-stability of the uncertain polynomial

$$p(s, \mathbf{q}) = (2.04 + 6q_1 + 6q_2 + 2q_1 q_2) + (2 + q_1 + q_2)s + (2 + q_1 + q_2)s^2 + s^3.$$

The equations of the real and imaginary part of  $p(j\omega, \mathbf{q})$  are

$$\begin{aligned} (2.04 + 6q_1 + 6q_2 + 2q_1 q_2) - (2 + q_1 + q_2)\omega^2 &= 0, \\ \omega [(2 + q_1 + q_2) - \omega^2] &= 0. \end{aligned}$$

The RRB for  $\omega = 0$  is the hyperbola

$$2.04 + 6q_1 + 6q_2 + 2q_1 q_2 = 0.$$

Substituting  $q_2 = -q_1 - 2 + \omega^2$  from the imaginary part into the real part gives

$$2q_1^2 + (4 - 2\omega^2)q_1 + \omega^4 - 6\omega^2 + 9.96 = 0.$$

The solution to this quadratic equation is  $q_1 = -(1 - 0.5\omega^2) \pm \sqrt{-3.98 + 2\omega^2 - 0.25\omega^4}$ . The interval of real  $q_1$  is bounded by the roots of

$$\omega^4 - 8\omega^2 + 15.92 = 0,$$

i.e.  $\omega^2 = (20 \pm \sqrt{2})/5$ , and real  $q_1$  occurs in the frequency interval  $\omega^2 \in [(20 - \sqrt{2})/5 ; (20 + \sqrt{2})/5] \approx [3.71 ; 4.28]$ ,  $\omega \in [1.93 ; 2.07]$ . At the  $\omega^2$ -boundary, we have

$$\begin{aligned} q_1 &= -(1 - 0.5\omega^2) = 1 \pm \sqrt{2}/10, \\ \text{and } q_2 &= -q_1 - 2 + \omega^2 = 1 \pm \sqrt{2}/10. \end{aligned}$$

For  $\omega = 1.93$ , the point  $q_1 = 0.86$ ,  $q_2 = 0.86$  is obtained and for  $\omega = 2.07$  the result is  $q_1 = 1.14$ ,  $q_2 = 1.14$ . Correspondingly, the two solutions  $q_1(\omega^2)$  and the associated values  $q_2 = -q_1 - 2 + \omega^2$  are calculated for frequencies in the admissible interval. Figure 4.5 shows the circular stability boundary. The center  $q_1 = 1$ ,  $q_2 = 1$  yields the unstable polynomial  $16.04 + 4s + 4s^2 + s^3$ , thus the system is unstable inside the circle.  $\square$

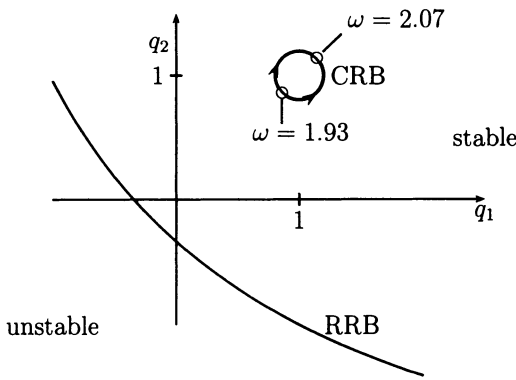


Figure 4.5. The polynomial is unstable inside the circle

#### Remark 4.16

For the calculation of the CRB, it is tempting to eliminate  $\omega^2$  from the equations for the real and imaginary parts, yielding

$$(q_1 - 1)^2 + (q_2 - 1)^2 = 0.2^2,$$

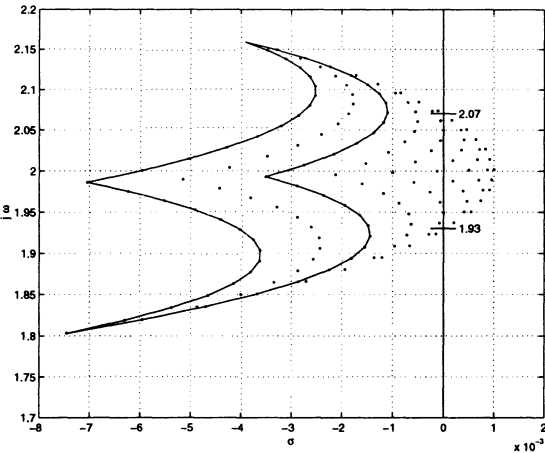


Figure 4.6. Root set of Example 4.14. The edges of the  $Q$ -box are stable, but some interior points are unstable

i.e. the equation of a circle with center  $q_1 = 1, q_2 = 1$  and radius 0.2. (This is, in fact, how the example was constructed.) But for higher degree polynomials, this algebraic approach leads to very complicated expressions for  $\det \mathbf{H}_{n-1} = 0$ , see Section 2.1.

□

Choose  $Q$  by  $q_1 \in [0.6; 1.3], q_2 \in [0.7; 1.4]$ , this operating domain encloses the unstable circle. Plot the root set for a  $15 \times 15$  grid. Figure 4.6 shows the part of the root set near the crossover of the imaginary axis. There is also a third real root, which is stable for all grid points. The solid lines are the images of the edges of  $Q$ ; they are stable.

In the frequency interval  $\omega \in [1.93; 2.07]$ , the root set crosses the imaginary axis. Note that these boundary frequencies are independent of the chosen  $Q$ -box.

It will be shown in Section 8.4 that an unstable island as in Figure 4.5 cannot occur if the coefficients of the characteristic polynomial depend linearly on the uncertain parameters. Then, a  $\Gamma$ -instability inside  $Q$  will also show up on the edges of  $Q$ . It is the bilinear term  $q_1 q_2$  in  $a_0$  that destroys this nice property.

## Singular Frequencies

In Section 2.5, we have introduced the notion of *singular frequencies* for polynomials with linear parameter dependence. It is now generalized to the case of non-linear parameter dependence. Consider a root that moves in the root set in Figure 4.6. When it reaches the right hand boundary of this set, it must return. Finding such extremum means that a derivative becomes zero. In the case of two independent variables, i.e.  $\text{Re } p(j\omega, q_1, q_2)$  and  $\text{Im } p(j\omega, q_1, q_2)$  this derivative is the Jacobian matrix

$$\mathbf{J}(\omega, q_1, q_2) = \begin{bmatrix} \frac{\partial \operatorname{Re} p}{\partial q_1} & \frac{\partial \operatorname{Re} p}{\partial q_2} \\ \frac{\partial \operatorname{Im} p}{\partial q_1} & \frac{\partial \operatorname{Im} p}{\partial q_2} \end{bmatrix} \quad (4.5.1)$$

and the extremum condition is

$$\det \mathbf{J}(\omega, q_1, q_2) = 0. \quad (4.5.2)$$

### Example 4.17

For Example 4.15, the Jacobian is

$$\mathbf{J}(\omega, q_1, q_2) = \begin{bmatrix} 6 + 2q_2 - \omega^2 & 6 + 2q_1 - \omega^2 \\ \omega & \omega \end{bmatrix},$$

$$\det \mathbf{J}(\omega, q_1, q_2) = 2\omega(q_2 - q_1) = 0.$$

The case  $\omega = 0$  is the RRB. The other factor gives  $q_1 = q_2$ , which is  $\omega$ -independent in this simple example. Therefore, the envelope of the root set of Figure 4.6 can be calculated from the edges of  $Q$  and the segment of the line  $q_2 = q_1$  that is contained in  $Q$ . For  $q_1 = q_2$ , the polynomial becomes

$$p(s, q_1) = (2.04 + 12q_1 + 2q_1^2) + 2(1 + q_1)s + 2(1 + q_1)s^2 + s^3.$$

The boundary generating  $q$ 's and their image in the  $s$ -plane are shown in Figure 4.7. The dense gridding of  $Q$  is avoided in this approach.

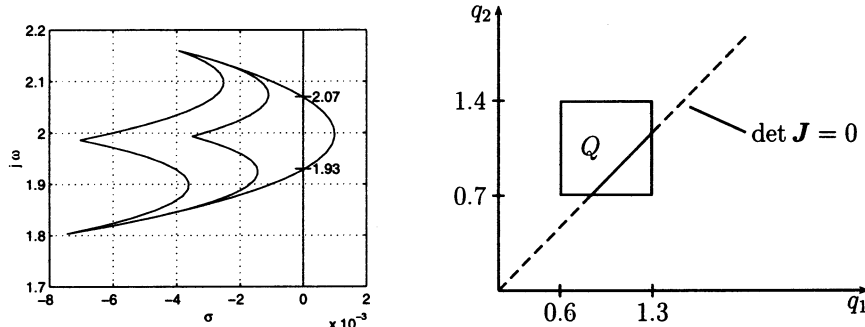


Figure 4.7. The image of points on  $\mathbf{J} = 0$  inside  $Q$  is the right hand boundary of the root set

□

For  $\ell$  uncertain parameters, the Jacobian is a rectangular matrix

$$\mathbf{J}(\omega, \mathbf{q}) = \begin{bmatrix} \frac{\partial \operatorname{Re} p}{\partial q_1} & \dots & \frac{\partial \operatorname{Re} p}{\partial q_\ell} \\ \frac{\partial \operatorname{Im} p}{\partial q_1} & \dots & \frac{\partial \operatorname{Im} p}{\partial q_\ell} \end{bmatrix} \quad (4.5.3)$$

and the extremum condition is

$$\operatorname{rank} \mathbf{J}(\omega, \mathbf{q}) < 2. \quad (4.5.4)$$

The test of this rank condition involves  $\ell - 1$  determinant conditions on  $2 \times 2$  submatrices of  $\mathbf{J}$ .

With these preparations we can now give a general definition of singular frequencies.

#### *Definition 4.18*

The non-negative frequency  $\omega_s$  is a *singular frequency* of the uncertain polynomial  $p(s, \mathbf{q})$  if there exists a  $\mathbf{q}^0 \in \mathbb{R}^\ell$  such that the three conditions

$$\begin{aligned} \operatorname{Re} p(j\omega_s, \mathbf{q}^0) &= 0, \\ \operatorname{Im} p(j\omega_s, \mathbf{q}^0) &= 0, \\ \operatorname{rank} \mathbf{J}(\omega_s, \mathbf{q}^0) &< 2, \end{aligned} \quad (4.5.5)$$

are simultaneously satisfied.  $\square$

Note that  $\omega = 0$  always satisfies the rank condition and makes  $\operatorname{Im} p = 0$ , thus the RRB  $a_0(\mathbf{q}) = 0$  is a singular frequency. The notion of singular frequencies is not standard in the literature; the concept has been used, however, by several authors, e.g. [75], [200], [201].

In the above example, the Jacobian is linear in  $q_1$  and  $q_2$  and can be treated easily. In general,  $\mathbf{J}(\omega, \mathbf{q})$  is non-linear in  $\mathbf{q}$  and also  $\omega$ -dependent. Then the calculation of the additional rank condition in (4.5.4) and finding the simultaneous solutions of the three equations in (4.5.4), for example, by the resultant method of Appendix A, is quite involved. In this case, gridding of the  $Q$ -box may be more practical.

If the coefficients  $\mathbf{a}(\mathbf{q})$  depend polynomially on the uncertain parameters, then (4.2.4) may be written as

$$f = f_0(q_2) + f_1(q_2)q_1 + \dots + f_k(q_2)q_1^k = 0, \quad (4.5.6)$$

$$g = g_0(q_2) + g_1(q_2)q_1 + \dots + g_m(q_2)q_1^m = 0. \quad (4.5.7)$$

$f_i$  and  $g_i$  are polynomials in  $q_2$  and continuous functions of  $\alpha$ . (4.5.6) and (4.5.7) describe the intersection of two algebraic curves in the  $(q_1, q_2)$ -plane. These solution pairs  $(q_1, q_2)$  can be calculated either with the resultant method, see Appendix A, or by construction of a Gröbner basis.

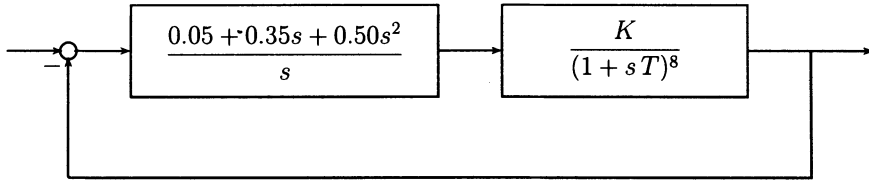


Figure 4.8. Robustness analysis for uncertain K and T

*Example 4.19*

In Example 2.19 we have designed a PID-controller for a plant with non-linear parameter dependency. Then a robustness analysis for the loop of Figure 4.8 is necessary.

The characteristic polynomial is

$$\begin{aligned} p(s, K, T) = & K(0.05 + 0.35s + 0.50s^2) \\ & + s(1 + 8Ts + 28Ts^2s^2 + 56T^3s^3 + 70T^4s^4 \\ & + 56T^5s^5 + 28T^6s^6 + 8T^7s^7 + T^8s^8). \end{aligned}$$

Let  $s = j\omega$ , then the equations  $\text{Re } p(j\omega, K, T) = 0$  and  $\text{Im } p(j\omega, K, T) = 0$  have the Jacobian

$$\begin{aligned} J(\omega, K, T) &= \begin{bmatrix} \frac{\partial \text{Re } p}{\partial K} & \frac{\partial \text{Re } p}{\partial T} \\ \frac{\partial \text{Im } p}{\partial K} & \frac{\partial \text{Im } p}{\partial T} \end{bmatrix} \\ &= \begin{bmatrix} 1/20 - 1/2\omega^2 & -8\omega^2 + 168\omega^4T^2 - 280\omega^6T^4 + 56\omega^8T^6 \\ 7/20\omega & -56\omega^3T + 280\omega^5T^3 - 168\omega^7T^5 + 8\omega^9T^7 \end{bmatrix}. \end{aligned}$$

The resulting boundary in the  $(T, K)$ -plane was shown already in Figure 2.15.  $\square$

*Example 4.20*

Consider the polynomial  $p(s, q_1, q_2) = \sum_{i=0}^8 a_i s^i$  with

$$a_0 = 453 \cdot 10^6 q_1^2,$$

$$a_1 = 528 \cdot 10^6 q_1^2 + 3640 \cdot 10^6 q_1,$$

$$a_2 = 5.72 \cdot 10^6 q_2 q_1^2 + 113 \cdot 10^6 q_1^2 + 4250 \cdot 10^6 q_1,$$

$$a_3 = 6.93 \cdot 10^6 q_2 q_1^2 + 911 \cdot 10^6 q_1 + 4220 \cdot 10^6,$$

$$\begin{aligned}
a_4 &= 1.45 \cdot 10^6 q_2 q_1^2 + 16.8 \cdot 10^6 q_2 q_1 + 338 \cdot 10^6, \\
a_5 &= 15.6 \cdot 10^3 q_2^2 q_1^2 + 840 q_2 q_1^2 + 1.35 \cdot 10^6 q_2 q_1 + 13.5 \cdot 10^6, \\
a_6 &= 1.25 \cdot 10^3 q_2^2 q_1^2 + 16.8 q_2 q_1^2 + 53.9 \cdot 10^3 q_2 q_1 + 270 \cdot 10^3, \\
a_7 &= 50 q_2^2 q_1^2 + 1080 q_2 q_1, \\
a_8 &= q_2^2 q_1^2.
\end{aligned}$$

This problem comes from the robustness analysis of a track-guided bus, where  $q_1$  is the velocity and  $q_2$  is the quotient of mass and friction coefficient. The technical background will be described in Section 6.8.

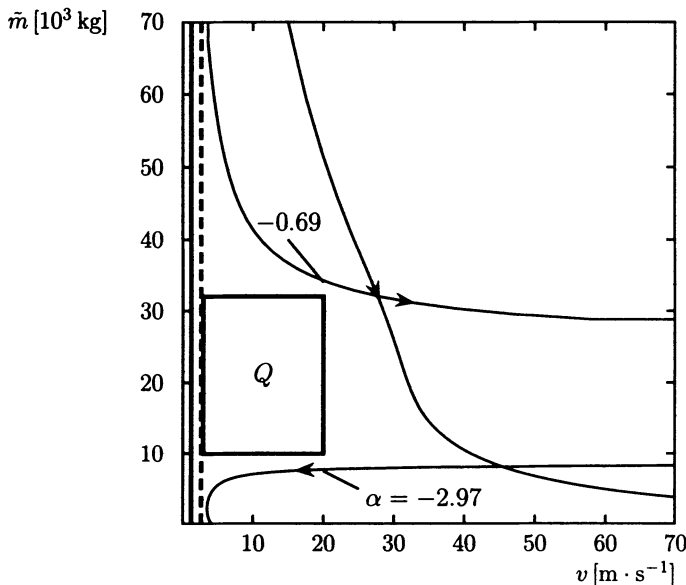


Figure 4.9. The track-guided bus is robustly  $\Gamma$ -stable in the operating domain  $Q$

The closed-loop poles should be located to the left of the left branch of the hyperbola

$$\left(\frac{\sigma}{0.35}\right)^2 - \left(\frac{\omega}{1.75}\right)^2 = 1. \quad (4.5.8)$$

The real root boundary for  $\sigma = -0.35$  is described by

$$\begin{aligned}
p(-0.35, q_1, q_2) &= \\
-79.66(q_1^2 q_2^2 - 5339 q_1^2 q_2 - 3077 q_1 q_2 - 3540213 q_1^2 + 9946676 q_1 + 22088293) &= 0.
\end{aligned} \quad (4.5.9)$$

This curve can be plotted by gridding one of the parameters, say  $q_2$ , and solving the remaining quadratic equation in  $q_1$ .

The complex root boundary  $\partial\Gamma$  is parameterized by  $\sigma(\alpha) = \alpha$ ,  $\omega^2(\alpha) = 25\alpha^2 - 1.75^2$ ,  $\alpha \in (-\infty; -0.35]$ . The coefficients  $d_i$  in the boundary representation (4.2.4) are

given by

$$d_0(\alpha) = 1, \quad (4.5.10)$$

$$d_1(\alpha) = 2\alpha, \quad (4.5.11)$$

$$d_{i+1}(\alpha) = 2\alpha d_i(\alpha) - (26\alpha^2 - 3.0625) d_{i-1}(\alpha). \quad (4.5.12)$$

Substituting the  $d_i$  and  $\mathbf{a}(\mathbf{q})$  into (4.2.4) and collecting terms with the same power of  $q_1$ , the following form is obtained:

$$f_{00}(\alpha) + [f_{10}(\alpha) + f_{11}(\alpha)q_2]q_1 + [f_{20} + f_{21}(\alpha)q_2 + f_{22}(\alpha)q_2^2]q_1^2 = 0, \quad (4.5.13)$$

$$g_{00}(\alpha) + [g_{10}(\alpha) + g_{11}(\alpha)q_2]q_1 + [g_{20} + g_{21}(\alpha)q_2 + g_{22}(\alpha)q_2^2]q_1^2 = 0. \quad (4.5.14)$$

The resultant has the form

$$\text{Res}_{q_1}(\alpha, q_2) = h_0(\alpha) + h_1(\alpha)q_2 + h_2(\alpha)q_2^2 + h_3(\alpha)q_2^3 + h_4(\alpha)q_2^4 = 0. \quad (4.5.15)$$

If all its roots are complex for a given  $\alpha = \alpha^*$ , then there exists no real pair  $(q_1, q_2)$  for which the closed loop has an eigenvalue at  $\sigma(\alpha^*) + j\omega(\alpha^*)$ . On the other hand, if there are real solutions  $q_2^{(i)}(\alpha^*)$ , then the corresponding  $q_1^{(i)}(\alpha^*)$  is given by the roots of the greatest common divisor of (4.4.13) and (4.4.14). In this example, the  $q_1^{(i)}(\alpha^*)$  corresponding to  $q_2^{(i)}(\alpha^*)$  can be expressed immediately by the coefficients  $f_{ij}$  and  $g_{ij}$ , omitting the argument  $\alpha$  (see Appendix A):

$$q_1 = - \begin{vmatrix} f_{20} + f_{21}q_2 + f_{22}q_2^2 & f_{10} + f_{11}q_1 \\ g_{20} + g_{21}q_2 + g_{22}q_2^2 & g_{10} + g_{11}q_1 \end{vmatrix} : \begin{vmatrix} f_{20} + f_{21}q_2 + f_{22}q_2^2 & f_{00} \\ g_{20} + g_{21}q_2 + g_{22}q_2^2 & g_{00} \end{vmatrix}. \quad (4.5.16)$$

It turns out that the polynomial (4.5.15) has two real roots so that the complex root boundary consists of two branches. In Figure 4.9 the root boundaries are plotted in the interesting domain of the parameters velocity ( $v = q_1$ ) and virtual mass ( $\tilde{m} = q_2$ ). The real root boundary is the dashed line, the complex root boundary is the solid line. Assuming the operating domain is given by  $q_1 \in [3 ; 20]$  and  $q_2 \in [9.9 ; 32]$ , then the track-guided bus is robustly  $\Gamma$ -stable.

□

# 5 Frequency Domain Analysis and Design

In the previous chapters, all specifications were restricted to the eigenvalue domain. With respect to the closed-loop transfer functions, their denominator  $p(s, \mathbf{q}, \mathbf{k})$  was considered. Now, the effect of the numerators will also be taken into account. The aim of this chapter is to combine a variety of frequency domain criteria with the parameter space approach. The sequence of the chapters thus follows the historic evolution of the parameter space technique. It was initially developed for mapping of  $\Gamma$ -stability boundaries into parameter space. However, it is obvious that complete design and analysis of control systems requires consideration of more criteria beyond mere eigenvalue specifications. This chapter distinguishes between two types of frequency domain specifications, which will be made accessible for parameter space mapping:

- *Frequency loci specifications*

The most common locus used for linear control system analysis in frequency domain is the Nyquist plot. Moreover, there are non-linear stability criteria that refer to frequency loci, like the dual locus method, which uses describing functions as an approximation for non-linear elements, and the Popov criterion which is used for proving absolute stability in the presence of sector non-linearities.

- *Frequency magnitude criteria*

Frequency domain magnitude specifications put bounds on the magnitude frequency response of specific transfer functions or sensitivity functions. Thus, tracking quality, noise and disturbance rejection, and robustness against unstructured uncertainty (e.g. unmodelled dynamics) can be addressed. Using these criteria with the parameter space technique provides the possibility of combining the advantages of non-conservative mapping of inequalities into parameter space with knowledge and experience in the field of frequency domain control design (e.g.  $H_\infty$ -loop shaping) and analysis (e.g.  $\mu$ -analysis).

## 5.1 Frequency Loci Specifications (Theta-stability)

In this section, a number of frequency loci type of specifications is introduced before  $\Theta$ -stability [63],[64] is defined as a generalization.

## Nyquist Plot-related Specifications

The following example illustrates that it may not be sufficient to consider only eigenvalue specifications.

### Example 5.1

Consider the uncertain single-input single-output (SISO) system with open-loop transfer function

$$L(s, \mathbf{q}) = \frac{y(s)}{e(s)} = \frac{-q_1(5q_2 s - 8)}{5s^2 + 5(q_2 + 2)s + 2}. \quad (5.1.1)$$

It depends on the uncertain parameter vector  $\mathbf{q} = [q_1, q_2]^T$ . Assuming unity feedback  $e = w - y$  according to Figure 5.1, the closed-loop transfer function is

$$T(s, \mathbf{q}) = \frac{y(s)}{w(s)} = \frac{-q_1(5q_2 s - 8)}{5s^2 + 5(2 + (1 - q_1)q_2)s + 2 + 8q_1}. \quad (5.1.2)$$

At first, an eigenvalue specification in terms of an admissible region  $\Gamma$  is formulated: all

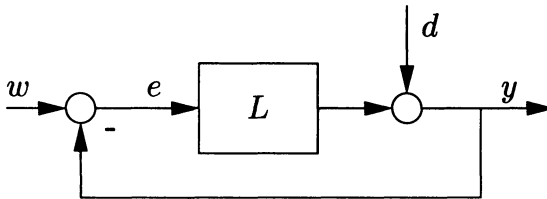


Figure 5.1. SISO system feedback structure

eigenvalues of  $T(s, \mathbf{q})$  are required to be in the region to the left of the hyperbola being displayed in Figure 5.2. By mapping the  $\Gamma$ -stability boundaries into the  $(q_1, q_2)$ -plane, the  $\Gamma$ -stability region  $Q_\Gamma$  in Figure 5.3 is obtained.

In the sequel, the effect of variations of  $q_2$  is investigated, while  $q_1 = 1$  is assumed. Now the characteristic polynomial (denominator of  $T(s, \mathbf{q})$  in (5.1.2)) does not depend on  $q_2$  anymore. The closed-loop poles are  $s_{1,2} = -1 \pm j$ , thus the system is  $\Gamma$ -stable for all values of  $q_2$ . However, the Nyquist plot  $G(j\omega, \mathbf{q}) = L(j\omega, \mathbf{q})$  according to (5.1.1) still depends on  $q_2$ . The positive frequency branches ( $\omega \geq 0$ ) of the Nyquist plots are displayed in Figure 5.4 and Figure 5.5 for values  $q_2 = 1$  and  $q_2 = 10$ , respectively. Neither of the frequency responses encircle the critical point  $-1$ , so the corresponding closed-loop systems are both stable. However, if gain and phase margins of the Nyquist plots are considered, the situation turns out to be completely different for the two different  $q_2$  parameter values.

Now, as an additional specification, it is postulated that the Nyquist plot must be completely contained in the region  $\Theta$ , which is displayed in Figure 5.4 and Figure 5.5. In other words, the Nyquist plot must avoid the region  $\bar{\Theta}$ , which is the complement of  $\Theta$ . (The region  $\bar{\Theta}$  continues towards  $-\infty$  beyond the left edge of the diagrams.) This

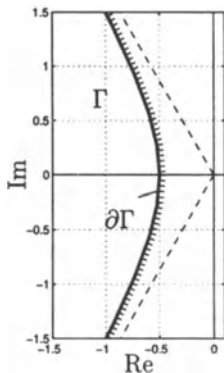


Figure 5.2. Definition of a  $\Gamma$ -region in the eigenvalue plane

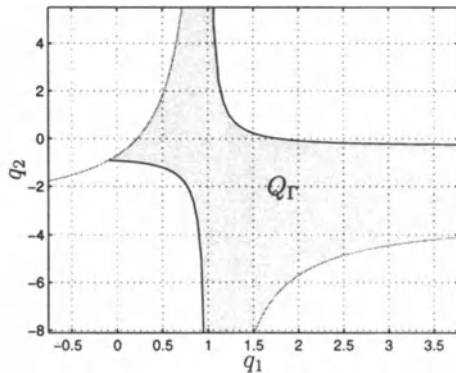


Figure 5.3. Mapped  $\Gamma$ -stable region  $Q_\Gamma$  of  $T(s, q)$  in parameter space

implies that the locus must not intersect the boundary  $\partial\Theta$ . At first, this specification guarantees Hurwitz-stability for the closed loop, if the open loop is stable (i.e.  $q_2 > -2$ ) according to the Nyquist-stability criterion. Moreover, it warrants a phase margin of  $\pi/4$  and a gain margin of 2. The Nyquist plot for  $q_2 = 1$  satisfies this new specification. However, for  $q_2 = 10$ , it does not.  $\square$

If the new criterion is to be included in robustness considerations, the question is: for

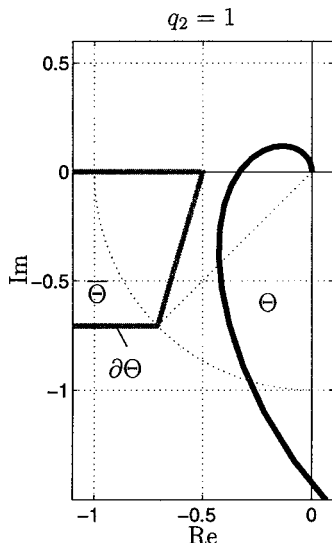


Figure 5.4. Nyquist plot for  $q_1 = 1$ ,  $q_2 = 1$  avoids the forbidden region  $\bar{\Theta}$

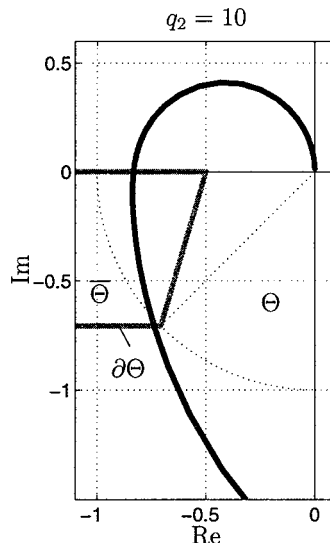


Figure 5.5. Nyquist plot for  $q_1 = 1$ ,  $q_2 = 10$  intersects the forbidden region  $\bar{\Theta}$

which parameter values of  $\mathbf{q}$  does the open loop comply with the postulated properties regarding the shape of the Nyquist plot? This question will be answered in this section for:

- Frequency loci of rational functions of the frequency  $\omega$ , where the coefficients of the rational functions depend polynomially on the parameters  $q_i$ .
- Almost arbitrary shapes of the region  $\Theta$  in the complex plane in which the locus must be contained. This type of specification is denoted  $\Theta$ -*stability* and is analogous to the notion of  $\Gamma$ -stability in the eigenvalue plane.

The suggested specifications will be mapped using the parameter space approach. This provides the possibility of including various locus criteria for the synthesis and analysis of parametric control systems. In particular, it creates the option of robustness analysis of systems w.r.t. non-linear locus criteria like the dual locus method and the Popov criterion. The foundations of this method have been developed and demonstrated by the challenge of practical problems [62],[16].

Over the next pages, the foundations of two non-linear frequency locus criteria are recapitulated, which can be applied to non-linear systems. If the reader is familiar with the dual locus method and the Popov criterion, then he or she may directly proceed to the introduction of  $\Theta$ -stability.

### Describing Functions and Dual Locus Method

Limit cycles are periodic oscillations performed by non-linear systems. Without external input signals, the oscillations sustain with a certain frequency and amplitude. Since in many cases they are not desired, criteria that enable non-linear stability analysis are useful. One approximation method, that can be applied for analyzing the existence and properties of limit cycles for a class of non-linear systems is the *dual locus method* [95],[200]. This method requires several assumptions. The first assumption is that it is feasible to represent the open-loop system as a series connection of a single non-

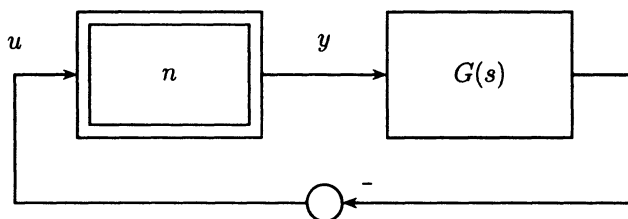


Figure 5.6. Single loop non-linear system

linearity  $n$  and the remaining linear part. In the sequel, the linear part is represented by its frequency response  $G(j\omega)$ . Therefore, the (control) system consists of a single loop as depicted in Figure 5.6.

The analysis of limit cycles starts with the assumption that the system is in the state of a sustained oscillation. Another assumption is necessary for the application of the dual locus method: the linear part  $G(j\omega)$  needs to have distinct low-pass properties in the frequency range of the considered oscillation and at higher frequencies. As a rule of thumb, a drop of  $-40$  dB/decade is required. Then it is reasonable to assume that the signal  $u$ , which is present at the input of the non-linearity, is sinusoidal. This holds since it is equal (except for the sign) to the output signal of the linear part. Since the higher harmonics are attenuated by the low-pass effect of  $G(j\omega)$ , the output of the non-linearity can be approximated by its first harmonic.

Thus, the consideration of the non-linearity can be restricted to its transmission of sinusoidal input signals, and a linear approximation of the non-linear system can be obtained. This approach is called *harmonic linearization*. A *describing function* is defined as the frequency response from a sinusoidal input signal

$$u = A \sin \omega t \quad (5.1.3)$$

to the first harmonic  $y_g$  of the output signal  $y$ , i.e.

$$N(\omega, A) = \frac{y_g(\omega)}{u(\omega)}. \quad (5.1.4)$$

For static characteristics, the describing function depends only on the input amplitude  $A$ , because input and first harmonic of the output are in phase and  $N(A)$  is real. The describing function may also be applied to non-linear elements that produce a frequency- and amplitude-dependent phase shift. Then the describing function  $N(\omega, A)$  is complex. For some elementary non-linearities, the describing functions can be derived analytically [200] by Fourier series expansion of the periodic signal  $y$ .

If the system shown in Figure 5.6 is in a sustained oscillation and the above-mentioned assumptions hold, then the transmission properties of the non-linearity can be approximated by its describing function. This leads to the condition

$$N(\omega, A) G(j\omega) = -1 \quad \text{or} \quad G(j\omega) = \frac{-1}{N(\omega, A)}, \quad (5.1.5)$$

which is denoted *harmonic balance*. If this equation holds for a pair  $(\omega, A)$ , then the system is capable of performing an oscillation with this frequency and amplitude. The representation on the right hand side in (5.1.5) provides the foundation for the graphical dual locus method: limit cycles are possible if there are intersection points between the locus  $G(j\omega)$  of the linear part and the locus of the negative-inverse describing function  $-1/N(\omega, A)$ . From the parameterization of both loci at the intersection, the values of  $\omega$  and  $A$  can be determined as properties of the corresponding limit cycle. Whether the limit cycle is stable (i.e. persists after a perturbation) or unstable may also be determined. In the latter case, the oscillation either decays or, after some time, turns into another limit cycle with different frequency and/or amplitude or the amplitude goes to infinity. For determination of the limit cycle's stability, the locus of  $G(j\omega)$  is pursued in the direction of increasing frequency in the vicinity of the intersection point with the locus of the negative-inverse describing function  $-1/N(\omega, A)$ . If the left hand side of  $-1/N(\omega, A)$  corresponds to higher input amplitudes than on the right hand side

of the intersection point, then the limit cycle is stable. Otherwise, it is not stable. In the example depicted in Figure 5.7, the lower of the two intersection points is stable according to the criterion just mentioned. The upper intersection point corresponds to an unstable limit cycle. Note that the stability of limit cycles has nothing to do with

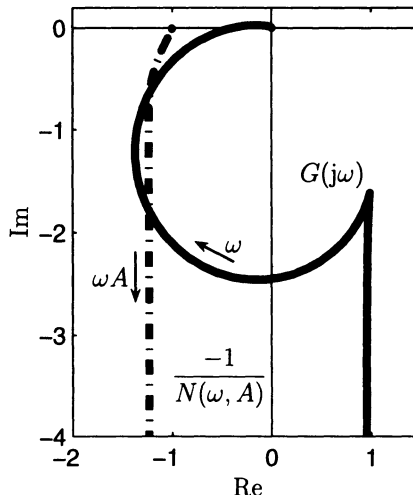


Figure 5.7. Determining the stability of limit cycles

the stability of the respective system. The goal of applying the dual locus method in the context of this book is to provide a means for robustness analysis w.r.t. non-existence of both stable and unstable limit cycles. The parameter space method can be applied to determine stability regions where no intersections of the two loci exist. However, it has to be kept in mind that an approximation is used and, consequently, the results are not exact. In particular, the low-pass property has to be checked separately for the stability regions obtained to investigate the reliability of the results. The notion of  $\Theta$ -stability here refers to the requirement that the locus  $G(j\omega)$  of the linear part does not intersect the locus of the negative-inverse describing function.

### *Remark 5.2*

Note that the existence of intersection points between the two loci does not necessarily mean that the corresponding system will perform limit cycles. The system will not perform limit cycles if its state does not leave the region of attraction of an asymptotically stable equilibrium state. The region of attraction cannot be determined by the dual locus method. If this is the aim, then, e.g. Lyapunov theory can be applied. We understand the specification established here in the way that no limit cycles may occur (independent of the initial system state).  $\square$

For the analysis of limit cycles by means of the dual locus method, it is prerequisite to obtain the describing function of the non-linearity involved. For that purpose, the describing functions of two elementary non-linearities are now derived as examples. For a detailed description of describing functions and their derivation, see [200].

*Example 5.3 (describing function of a saturation)*

With a saturation (also denoted *limiter*), the absolute value of its output signal is limited to  $r_s$ :

$$y = \begin{cases} u & \text{if } |u| \leq r_s \\ r_s \operatorname{sign}(u) & \text{if } |u| > r_s \end{cases} \quad (5.1.6)$$

The symmetric characteristic curve is linear until the saturation value is reached. For the sake of simplicity, unity slope about zero is assumed. The symbol for a saturation is

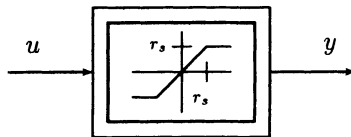


Figure 5.8. Block diagram of a limiter

shown in Figure 5.8. For derivation of the describing function, the saturation is excited with sinusoidal input signals (5.1.3) of various amplitudes  $A$ . Figure 5.9 shows the input signals and the corresponding saturated outputs (dashed line style). If  $A \leq r_s$ , then the output is equal to the input and the describing function value is equal to 1. The more the input amplitude  $A$  exceeds the saturation value  $r_s$ , the more of the input signal gets truncated, which causes the amplitude of the output's first harmonic to decrease. Thus, the gain of the describing function continuously decays with increasing  $A/r_s > 1$ . Since there is no phase shift between input and output, the describing function of the saturation is real. It does not depend on the frequency. In [200], an analytical expression is provided:

$$N_s(A) = \begin{cases} 1 & \text{if } A \leq r_s \\ \frac{2}{\pi} \left( \arcsin\left(\frac{r_s}{A}\right) + \frac{r_s}{A} \sqrt{1 - \left(\frac{r_s}{A}\right)^2} \right) & \text{if } A > r_s. \end{cases} \quad (5.1.7)$$

Figure 5.10 shows the locus of  $N_s(A)$ . It starts with  $A \leq r_s$  at 1 and tends to zero along the real axis for  $A/r_s \rightarrow \infty$ . The negative-inverse describing function  $-1/N_s(A)$  starts at  $-1$  and tends towards  $-\infty$ .  $\square$

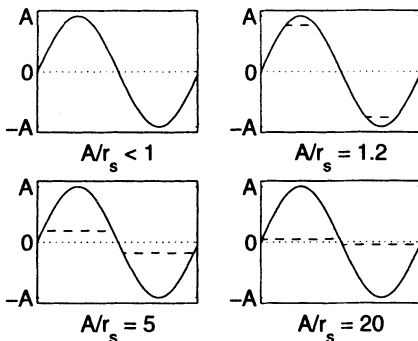


Figure 5.9. Sinusoidal input signals (solid line style) with various amplitudes and respective saturation time responses (dashed)

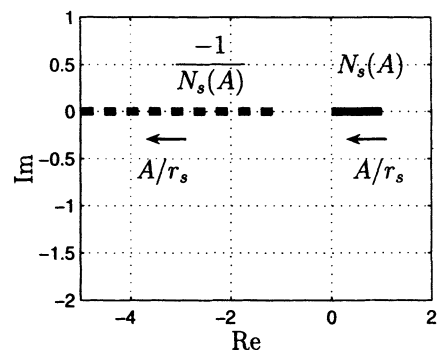


Figure 5.10. Loci of the saturation describing function  $N_s(A)$  and its negative-inverse  $-1/N_s(A)$

#### *Example 5.4 (describing function of a rate limiter)*

The effect of a rate limiter is to limit the absolute value of the derivative  $\dot{y}$  of a signal  $y$ , i.e.

$$\dot{y} = R \operatorname{sign}(u - y). \quad (5.1.8)$$

This dynamic non-linearity is not representable by a static characteristic. Nevertheless, a describing function can be derived. Figure 5.11 shows an ideal realization of the

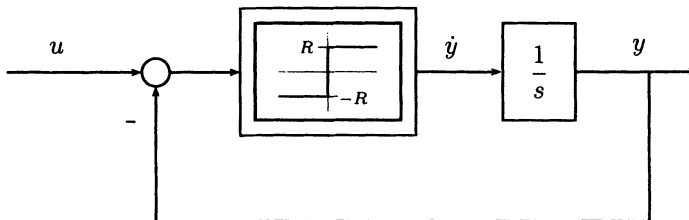


Figure 5.11. Block diagram of a rate limiter

rate limiter. It consists of a closed loop featuring an integrator and a symmetric two point switch (output value  $-R$  or  $R$  respectively). The derivative  $\dot{y}$  of the rate limiter output signal  $y$  is present at the output of the two point switch and thus its absolute value cannot exceed  $R$ . On the other hand, with a constant input  $u$  the two point switch perpetually chatters between  $-R$  and  $R$  and thus retains  $y$  at the input value  $u$ . In Figure 5.12, some time responses of the rate limiter are shown. Various sinusoidal input signals are applied with different frequency  $\omega$  and amplitude  $A$ . The shape of the output signal in relation to the input signal only depends on the ratio  $\omega A/R$ . Therefore, the describing function only depends on this composed parameter. The steady state oscillation may be categorized into three ranges [80] depending on the value of  $\omega A/R$ :

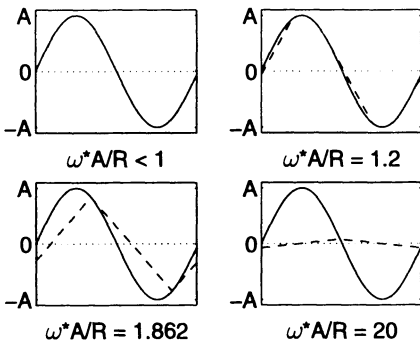


Figure 5.12. Sinusoidal input signals (solid line style) at various values of  $\omega A/R$  and respective rate limiter time responses (dashed)

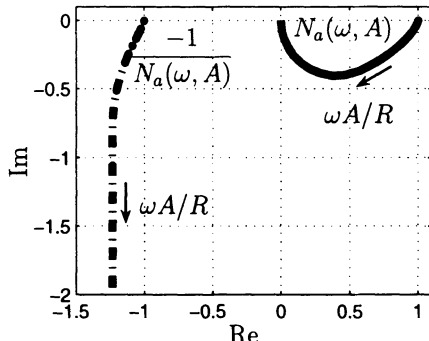


Figure 5.13. Loci of the rate limiter describing function  $N_a(\omega, A)$  and its negative-inverse  $-1/N_a(\omega, A)$

- Range I: if  $\omega A/R \leq 1$ , then the rate limiter does not change the signal ( $y = u$ ). Consequently, in range I the describing function value is 1.
- Range III: if  $\omega A/R \geq \sqrt{(\pi/2)^2 + 1} \approx 1.862$ , then the output signal  $y$  is a “triangular function” of time with maximum rate of change. Only at the reversal points is the output equal to the input. In range III, an analytic expression for the describing function can be derived [80]:

$$N_a(\omega, A) = \frac{4R}{\pi\omega A} e^{-j \arccos\left(\frac{\pi R}{2\omega A}\right)}. \quad (5.1.9)$$

- Range II: between range I and range III, there is a transition range where the rate of change of the input signal is only partly greater than the maximum rate  $R$ , which the rate limiter permits. The output signal  $y$  matches the input signal only if  $|u| < R$ , otherwise it follows the input signal at maximum rate of change  $R$ . In this transition range, sophisticated mathematical effort would be needed to derive an analytical describing function. Alternatively, the determination of  $N_a(\omega, A)$  may be done numerically for range II. The Fourier coefficient of the first harmonic of the output signal is computed by numeric integration. For a grid of values of  $\omega A/R$  in the interval  $[1; 1.862]$ , the gain and phase of the output signal's first harmonic are put in relation to the input signal. Note that this procedure can be generically applied to other non-linearities, if no convenient analytic representation of their describing functions is available.

Figure 5.13 shows both the locus and negative-inverse locus of  $N_a(\omega, A)$ . In contrast to the saturation, a phase shift occurs as soon as the rate limiter gets activated. In the limit case ( $\omega A/R \rightarrow \infty$ ), the phase shift is  $-\pi/2$ . For large values of  $\omega A/R$ , the amplitude of the output signal drops towards zero. Therefore, the locus of the describing function  $N_a(\omega, A)$  ends at the origin of the complex plane, with the imaginary axis as an asymptote. Note that (5.1.9) is a parameterized representation of a circle

in the complex plane (radius  $4/\pi^2$ , center  $(0, 4/\pi^2)$ ). In range III this is the locus of the rate limiter describing function. If the locus of its negative-inverse  $-1/N_a(\omega, A)$  is plotted, this circle becomes mapped to a straight line, which is parallel to the imaginary axis. This straight line's real part is  $-\pi^2/8 \approx -1.234$ . The maximum imaginary part of the range III section of  $-1/N_a(\omega, A)$  is  $-\pi/4 \approx -0.785$ , which corresponds to  $\omega A/R = \sqrt{(\pi/2)^2 + 1}$ . There, the transition range (range II) begins, which ends at the point  $-1$ . The latter represents range I. Figure 5.22 shows how the negative-inverse describing function locus of the rate limiter can be well approximated by three sections formed by segments of diverse conic sections. This is a suitable representation for the application of the parameter space method, which will be explained in Section 5.2.  $\square$

With the dual locus method and the Popov criterion (which will be explained next) non-linear systems can be analyzed for the existence of limit cycles or absolute stability, respectively. Note that with the describing function approach, we assume that the parametric uncertainty only affects the frequency locus representing the linear system part, the non-linearity is assumed certain. With the Popov criterion, however, some uncertainty of a considered non-linear characteristic is allowed in terms of the sector in which it resides.

### Popov Criterion

In this section, we consider the feedback loop of the system

$$\begin{aligned} u(s) &= -G(s), \quad y(s) \\ y &= f(u), \end{aligned} \tag{5.1.10}$$

which is shown in Figure 5.14. Let us first assume that the rational transfer function

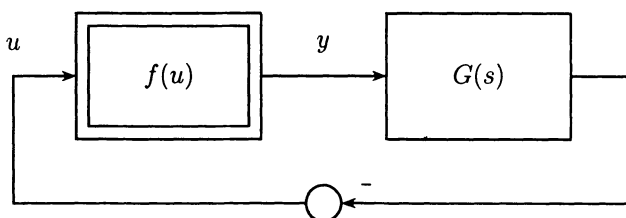


Figure 5.14. Non-linear function in the feedback loop

$G(s)$  is known. However, the function  $f$  is considered uncertain; it is assumed to be continuous and to belong to the class of functions

$$\mathcal{F}_k := \{f(u) \mid f(0) = 0, 0 \leq uf(u) \leq ku^2\}, \quad 0 < k < \infty. \tag{5.1.11}$$

That means it is only known that the graph of  $f$  is within a sector  $[0 ; k]$ , limited by the abscissa and by the line

$$f(u) = k u. \quad (5.1.12)$$

We call this sector the  $k$ -sector, with notation  $[0 ; k]$ . In the  $k$ -sector, the graph of the continuous function  $f$  can be arbitrary, see Figure 5.15. If for a given transfer function  $G(s)$ , the above non-linear closed-loop system is globally asymptotically stable, then it is called *absolutely stable* in the sector  $[0 ; k]$ . A classical result for absolute stability is the sufficient *Popov criterion* [168],[200],[198]:

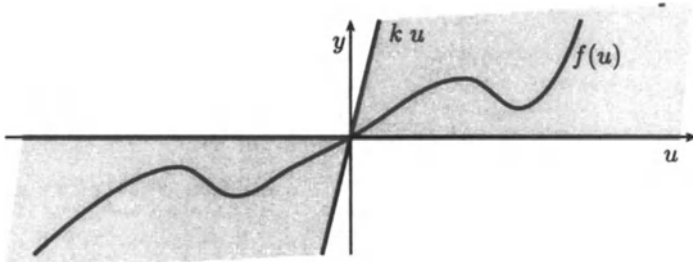


Figure 5.15. Sector of non-linearity

### Theorem 5.5 (Popov)

For  $f$  a continuous function in the class  $\mathcal{F}_k$  of (5.1.11) and  $G(s)$  a strictly proper rational transfer function with all poles in the open left half complex plane, the feedback loop of Figure 5.14 is absolutely stable, if there exists a  $\zeta \in \mathbb{R}$  such that the inequality

$$1/k + \operatorname{Re} \{(1 + j\omega\zeta)G(j\omega)\} > 0, \quad \forall \omega \geq 0 \quad (5.1.13)$$

holds.

□

The classical Popov criterion represents a strong robustness result, since  $f$  is assumed to be an uncertain continuous function within a sector  $[0 ; k]$ .

If  $G(s)$  is unstable, then the Popov criterion obviously cannot hold for any  $k > 0$  because the zero function ( $f(u) = 0, \forall u \in \mathbb{R}$ ) is in  $\mathcal{F}_k$ . However, we can now ask for a sector  $[k_1 ; k_2]$  for which absolute stability can be proven. For instance, in [200],[198] it is shown that this more general problem can be transformed to the canonical problem given above: if the open-loop transfer function  $G(s)$  of Figure 5.14 is unstable, but can be stabilized by a constant negative feedback with gain  $\rho > 0$ , then replace in the Popov criterion above the transfer function  $G(s)$  by  $\tilde{G}(s) = G(s)/(1 + \rho G(s))$  and the non-linear function  $f(u)$  by  $\tilde{f}(u) = f(u) - \rho u$ , see Figure 5.16. It is obvious that the two paths involving  $\rho$  cancel each other. If application of the Popov criterion to the

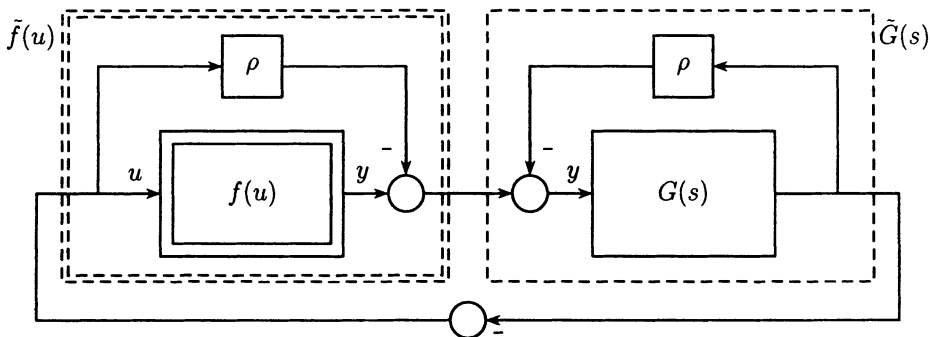


Figure 5.16. Transformation to the standard form

transformed system yields a sector  $[0; k]$  for  $\tilde{f}$ , then the original system is absolutely stable in the sector  $[\rho; k + \rho]$ .

Values for  $k$  guaranteeing absolute stability can easily be determined graphically by means of the *Popov plot*

$$G_p(j\omega) := \operatorname{Re} G(j\omega) + j\omega \operatorname{Im} G(j\omega), \quad \omega \geq 0 \quad (5.1.14)$$

of the stable transfer function  $G(s)$ . Consider any straight line  $y = (1/\zeta)(x + 1/k)$  in the  $(x, y)$ -plane with  $k > 0$ , intersecting the negative  $x$ -axis at  $-1/k$  and with a slope of  $1/\zeta$ . For all points on the right hand side of this line, we have  $1/k + x - \zeta y > 0$ . Let  $x = \operatorname{Re} G(j\omega)$ ,  $y = \omega \operatorname{Im} G(j\omega)$ , then

$$1/k + \operatorname{Re} G(j\omega) - \zeta \omega \operatorname{Im} G(j\omega) > 0 \quad (5.1.15)$$

for all  $\omega \geq 0$ , if the Popov plot  $G_p(j\omega) := \operatorname{Re} G(j\omega) + j\omega \operatorname{Im} G(j\omega)$  lies on the right hand side of the above line. But (5.1.15) is identical to the expression (5.1.13), so we have the following result: any straight line in the complex plane crossing the negative real axis at the point  $z < 0$ , and with the property that the Popov plot lies totally on its right hand side, yields  $k = -1/z$  for a sector  $[0; k]$  of absolute stability. For such a  $k$  and with  $1/\zeta$  as the slope of the corresponding Popov-line the Popov criterion (5.1.13) is satisfied.

With the Popov plot, we can easily find the maximal value of  $k$  with absolute stability. It follows from the tangent Popov-line as illustrated by Figure 5.17. The sector with maximal value of  $k$  is called the *Popov-sector*. For instance,  $\bar{k} = -1/\bar{z}$  determines the Popov-sector for a  $G(s)$  with the Popov plot of Figure 5.17 (with the corresponding slope  $1/\bar{\zeta} = \tan(\bar{\alpha})$  of the line). But note that the Popov criterion is a sufficient condition. Therefore, we cannot exclude in general conservative results, i.e. the possibility that for absolute stability a greater sector than the Popov-sector exists.

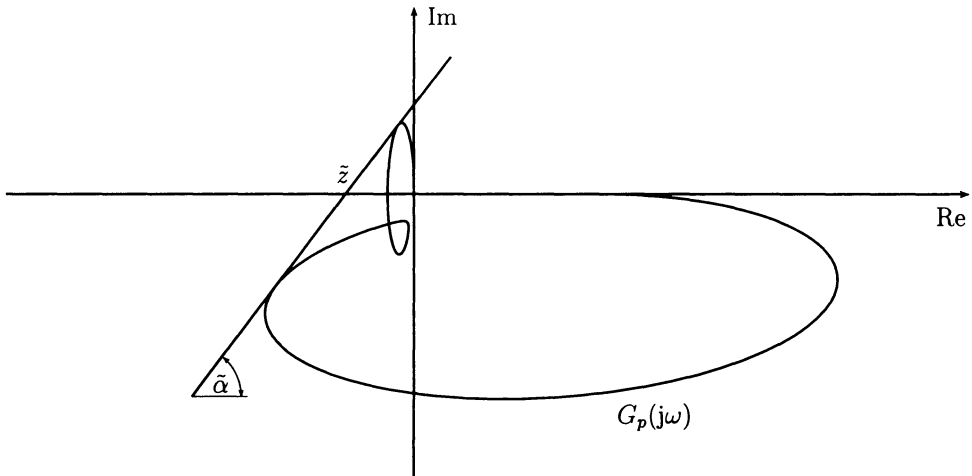


Figure 5.17. Absolute stability and Popov-sector

*Remark 5.6*

A good hypothesis for testing is the so-called *Aizerman Conjecture*. It relates the Popov-sector with the Nyquist-sector corresponding to the interval of stable linear gains. The latter is obtained from the intersections of the Nyquist plot with the negative real axis. In view of (5.1.14), these intersections are identical to those of the Popov plot. A situation that frequently arises is shown in the Popov plot of Figure 5.18. Here,

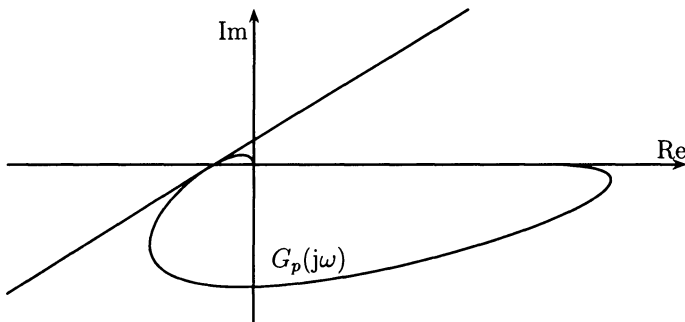


Figure 5.18. An example for identical Nyquist- and Popov-sectors

the tangent to the Popov plot in its leftmost real axis intersection is a feasible line for satisfaction of the Popov criterion, i.e. the Popov-sector and the Nyquist-sector have the same upper bound which in this case is obviously both necessary and sufficient for absolute stability.

Note that Aizerman's conjecture does not hold for the Popov plot shown in Figure 5.17.  $\square$

*Remark 5.7*

A family of Popov plots  $g_p(j\omega, \mathbf{q})$ ,  $\mathbf{q} \in Q$  results in a family of tangent Popov-lines. The leftmost real axis intersection of all tangent Popov-lines yields  $-1/k^+$  (i.e. the

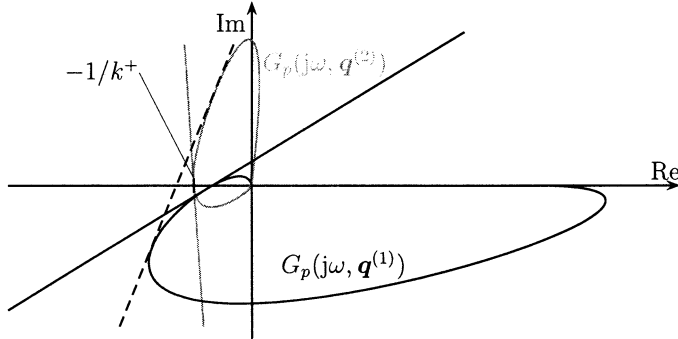


Figure 5.19. Different Popov-lines apply to different members of a Popov plot family

maximal common Popov-sector  $[0, k^+]$ ), see Figure 5.19. Note that this  $k^+$  is greater or equal to the  $k$  resulting from a common Popov-line (dashed line in Figure 5.19) for the family  $G_p(j\omega, \mathbf{q})$ ,  $\mathbf{q} \in Q$ .  $\square$

### $\Theta$ -stability

Analogous to the definition of  $\Gamma$ -stability for eigenvalues is the notion of  $\Theta$ -stability for frequency loci, which will now be defined. The following depiction is made with a Nyquist plot (see Figure 5.20). However, all statements can analogously be applied to other frequency loci (e.g. the Popov plot). Only the locus branch with positive frequency ( $\omega \geq 0$ ) is considered.

With the example shown in Figure 5.4, the  $\Theta$ -definition specified that the region  $\bar{\Theta}$  is to be avoided by the Nyquist plot. In Figure 5.20, another practically relevant example for Nyquist diagrams is shown. Here, the admissible region  $\Theta$  is the exterior of a circle centered at the critical point. The non-zero radius of this circle guarantees some Nyquist-stability margin.

### *Definition 5.8*

Let  $\Theta$  be an open region of the complex plane. The boundary of this region is

$$\partial\Theta = \{x + jy \mid F_{\partial\Theta}(x, y) = 0\}. \quad (5.1.16)$$

The complement of  $\Theta$  is denoted  $\bar{\Theta}$ . Since  $\Theta$  is open,  $\partial\Theta \subset \bar{\Theta}$ . The frequency locus  $G(j\omega, \mathbf{q}_0)$  is defined to be  $\Theta$ -stable, if

$$G(j\omega, \mathbf{q}_0) \subset \Theta, \quad \forall \omega \geq 0, \quad (5.1.17)$$

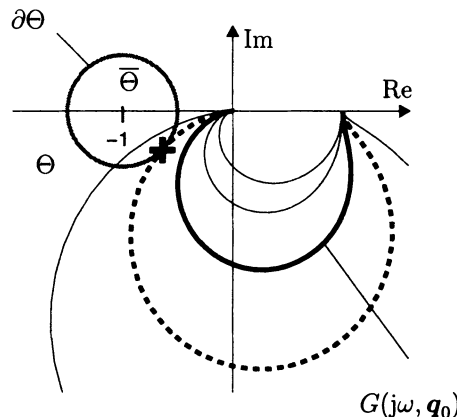


Figure 5.20. Example of a  $\Theta$ -stability definition in the Nyquist diagram

i.e. if the locus resides completely within  $\Theta$ . The frequency locus  $G(j\omega, \mathbf{q}_0)$  with  $\omega \geq 0$  is defined as  $\Theta$ -limit-stable, if  $G(j\omega, \mathbf{q}_0)$  is  $\Theta$ -stable except for the points of contact with the boundary  $\partial\Theta$ .  $\square$

### Robust $\Theta$ -stability

Analogous to robust  $\Gamma$ -stability is robust  $\Theta$ -stability, which is defined: a system is robustly  $\Theta$ -stable in the operating domain  $Q$ , if for all operating points  $\mathbf{q} \in Q$  the frequency locus  $G(j\omega, \mathbf{q})$  of the respective system is  $\Theta$ -stable. For the sake of linguistic simplicity, the notion of  $\Theta$ -stability is also applied to a parameter vector  $\mathbf{q}^*$ , for which  $G(j\omega, \mathbf{q}^*)$  is  $\Theta$ -stable.

Assume  $\mathbf{q}_0$  is a  $\Theta$ -stable operating point, i.e. the locus  $G(j\omega, \mathbf{q}_0)$  avoids the forbidden region  $\overline{\Theta}$ . Now we are interested in the set of all possible continuous variations  $\mathbf{q}$  of  $\mathbf{q}_0$  such that the locus  $G(j\omega, \mathbf{q})$  does not lose the property of  $\Theta$ -stability. If the continuous variation is started with a different  $\Theta$ -stable operating point  $\mathbf{q}_1$ , then possibly a different set of  $\Theta$ -stable  $\mathbf{q}$ -values is obtained. This set consequently does not cohere with the first set. The union of all existing subsets of this kind is called the  $\Theta$ -stability region  $Q_\Theta$ :

### Definition 5.9

The  $\Theta$ -stable region in the  $\mathbf{q}$ -space is defined as

$$Q_\Theta = \{ \mathbf{q} \mid G(j\omega, \mathbf{q}) \subset \Theta, \forall \omega \in \mathbb{R}_0^+ \}. \quad (5.1.18)$$

$\square$

Figure 5.20 shows a nominal  $\Theta$ -stable locus  $G(j\omega, \mathbf{q}_0)$  (bold line style) and a family of loci  $G(j\omega, \mathbf{q})$  (normal line style) with varying parameters  $\mathbf{q}$ . For certain values of  $\mathbf{q}$  the locus  $G(j\omega, \mathbf{q})$  becomes  $\Theta$ -limit-stable (dashed), where the locus is tangent to the boundary  $\partial\Theta$  of the forbidden region  $\bar{\Theta}$ . The point of contact is indicated by “+”. The special situation where  $G(j\omega, \mathbf{q})$  becomes  $\Theta$ -limit-stable will be used in Section 5.2 to establish mathematical conditions for mapping  $\Theta$ -stability boundaries into parameter space. This is analogous to  $\Gamma$ -stability boundary mapping. In Section 2.2 and Section 4.2, the condition that eigenvalues are exactly located on  $\partial\Gamma$  provides the equations to be solved for the determination of  $\Gamma$ -stability boundaries in parameter space.

### Representation of the $\Theta$ -stability Boundary

Before mapping frequency loci margins, the specific  $\Theta$ -stability definition has to be made by fixing the admissible region  $\Theta$  and thereby also fixing its forbidden complement  $\bar{\Theta}$ . In the sequel, it is assumed that  $\Theta$  is defined by establishing adequate boundaries  $\partial\Theta$  of  $\Theta$  in terms of mathematical curve equations  $F_{\partial\Theta}(x, y) = 0$ . It is further assumed that the boundary is put together from piecewise smooth boundary sections. (This way of forming  $\partial\Theta$  is very similar to the way  $\Gamma$ -boundaries were composed in Section 3.2.) The transition points where the boundary sections border on each other in a non-smooth but continuous way are denoted *junctions*  $z_{i,j}$ . For illustration, Figure 5.21 refers to the example shown in Figure 5.4 and Figure 5.5. As will be discussed later, for the

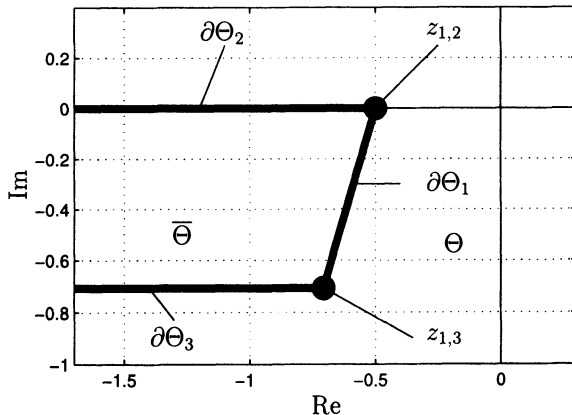


Figure 5.21. Complete definition  $\partial\Theta$  for the example

mathematical effort, it is very advantageous to compound the boundary from segments of conic sections (i.e. straight lines, circles, ellipses, hyperbolas and parabolas). In this way, a good approximation of practically relevant  $\Theta$ -stability region boundaries can be constructed. See Figure 5.21 as an example for a compound boundary.

The complete compound boundary  $\partial\Theta$  according to (5.1.16) is formed by the col-

lectivity of its sections:

$$F_{\partial\Theta}(x, y) = \begin{cases} F_{\partial\Theta_1}(x, y), & \text{if } x + jy \in C_{\partial\Theta_1}(x, y) \\ F_{\partial\Theta_2}(x, y), & \text{if } x + jy \in C_{\partial\Theta_2}(x, y) \\ \vdots & \end{cases}, \quad (5.1.19)$$

where  $C_{\partial\Theta_i}$  is a region in the complex plane in which the respective function  $F_{\partial\Theta_i}$  is defined. The upper horizontal boundary segment in Figure 5.21, for instance, is characterized by  $F_{\partial\Theta_2} = y = 0$  and  $C_{\partial\Theta_2} = \{x + jy \mid x \leq -0.5\}$ .

*Example 5.10 (approximation of the negative-inverse locus of the rate limiter describing function by segments of conic sections)*

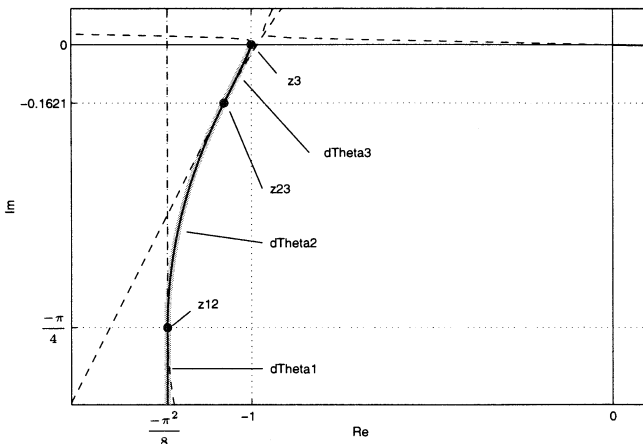


Figure 5.22. Approximation of rate limiter negative-inverse describing function by conic section segments

Conic sections are second order curves, which can be represented in the  $(x, y)$ -plane in the following form:

$$F_{\partial\Theta_i}(x, y) = a_{11}^{(i)}x^2 + 2a_{12}^{(i)}xy + a_{22}^{(i)}y^2 + 2a_{10}^{(i)}x + 2a_{20}^{(i)}y + a_{00}^{(i)} = 0 \quad (5.1.20)$$

As illustrated by Figure 5.22, the locus of the negative-inverse describing function of a rate limiter (see p. 112) can be piecewisely approximated by three segments of conic sections:

- i. Straight line:

$$F_{\partial\Theta_1}(x, y) : a_{11}^{(1)} = a_{12}^{(1)} = a_{22}^{(1)} = a_{20}^{(1)} = 0, a_{10}^{(1)} = 1/2, a_{00}^{(1)} = \frac{\pi^2}{8},$$

$$C_{\partial\Theta_1}(x, y) = \left\{ x + jy \mid y \leq -\frac{\pi}{4} \right\}.$$

ii. Parabola:

$$\begin{aligned} F_{\partial\Theta_2}(x, y) : \quad & a_{11}^{(2)} = a_{12}^{(2)} = 0, \quad a_{10}^{(2)} = -1/2, \\ & a_{22}^{(2)} = a, \quad a_{20}^{(2)} = \frac{a\pi}{4}, \quad a_{00}^{(2)} = \frac{\pi^2}{16}(a-2), \text{ with } a = 0.405424, \\ C_{\partial\Theta_2}(x, y) = & \left\{ x + jy \mid -\frac{\pi}{4} < y \leq -0.1621 \right\}. \end{aligned}$$

iii. Hyperbola:

$$\begin{aligned} F_{\partial\Theta_3}(x, y) : \quad & a_{11}^{(3)} = -14.7846, \quad a_{12}^{(3)} = -370.3541, \quad a_{22}^{(3)} = 381.350, \\ & a_{20}^{(3)} = -371.403, \quad a_{00}^{(3)} = 0, \quad a_{10}^{(3)} = \frac{a_{11}^{(3)} + a_{00}^{(3)}}{2} = -7.39229, \\ C_{\partial\Theta_3}(x, y) = & \{x + jy \mid 0.1621 < y \leq 0\}. \end{aligned}$$

The dashed lines in Figure 5.22 show the idle continuation of the conic sections beyond the segments, which are used for the locus approximation.  $\square$

## 5.2 Mapping of Frequency Loci Margins into Parameter Space

### Representation of the Frequency Locus

We consider the family of uncertain frequency loci

$$G(j\omega, \mathbf{q}) = \frac{N_G(j\omega, \mathbf{q})}{D_G(j\omega, \mathbf{q})} = \frac{\sum_{i=0}^m a_i(\mathbf{q})(j\omega)^i}{\sum_{i=0}^n b_i(\mathbf{q})(j\omega)^i}, \quad \mathbf{q} \in Q \quad (5.2.1)$$

with  $m \leq n$ . This covers Nyquist plots of proper open-loop transfer functions and Popov plots of strictly proper linear part transfer functions, respectively. Moreover, it is assumed that the coefficients  $a_i(\mathbf{q}), b_i(\mathbf{q})$  are real, and depend polynomially on the  $\ell$  elements of the parameter vector  $\mathbf{q}$ . (This includes the simpler cases of interval coefficients as well as affine and multilinear coefficient functions.) For the sake of simplicity, the real and imaginary parts of the loci are represented according to

$$G(j\omega, \mathbf{q}) = R_G(\omega, \mathbf{q}) + jI_G(\omega, \mathbf{q}). \quad (5.2.2)$$

The goal of applying the parameter space method is to display the regions in a plane of parameters  $\mathbf{q}$ , where  $G(j\omega, \mathbf{q})$  is  $\Theta$ -stable. In particular, this means determination of the boundaries of the  $\Theta$ -stability regions. Analogous with  $\Gamma$ -stability, here for mapping into the  $(q_1, q_2)$ -plane, the parameter space method complies with the following perception: if (after starting from a  $\Theta$ -stable point  $(q_{1,0}, q_{2,0})$ ) a boundary curve in the

parameter plane is crossed due to continuous parameter variations, then this means that the system becomes  $\Theta$ -unstable. Thus, for mapping  $\Theta$ -stability margins into parameter space, the values of  $\mathbf{q}$  for which the frequency locus  $G(j\omega, \mathbf{q})$  changes from  $\Theta$ -stable to  $\Theta$ -unstable need to be determined.

As with  $\Gamma$ -stability in Chapter 2, critical  $\Theta$ -stability conditions will now be established. Therefore, it is assumed that the frequency locus is continuous in  $\mathbf{q}$ , i.e. continuous changes in the parameters result in continuous changes of the locus (except for values of  $\mathbf{q}$ , for which  $D_G(j\omega, \mathbf{q}) = 0$ ). This analogy with Frazer and Duncan's boundary crossing theorem to frequency loci is not proven here since it follows analogously from the assumed coefficient structure (see (5.2.1)). However, the case where  $G(s, \mathbf{q})$  has poles on the imaginary axis must be specially considered.

### *Definition of Critical $\Theta$ -stability Conditions*

*Critical  $\Theta$ -stability condition* here denotes a geometrically interpretable condition under which a frequency locus  $G(j\omega, \mathbf{q})$  potentially changes from  $\Theta$ -stable to  $\Theta$ -unstable with variation of  $\mathbf{q}$ . Depending on both the specific definition of  $\Theta$  and the properties of the considered locus, various critical conditions may come into play. Which of the critical conditions he or she considers is left to the control engineer. Any previous knowledge concerning properties of the system (e.g. the order, relative degree, etc.) may be taken into account and additional critical conditions may be established according to requirements. The following is a compilation of some critical  $\Theta$ -stability conditions that are reasonable and practical:

a) *The point condition*

$G(j\omega, \mathbf{q})$  runs through a junction or closing point (see below) of the boundary  $\partial\Theta$ .

b) *The tangent condition*

$G(j\omega, \mathbf{q})$  tangentially touches a smooth section of the boundary  $\partial\Theta$ . (The dashed locus in Figure 5.20 complies with this case. The point of contact is indicated by “+”.)

c) *Frequency endpoint condition*

$G(j\omega, \mathbf{q})$  starts (i.e.  $\omega = 0$ ) or ends (i.e.  $\omega \rightarrow \infty$ ) on  $\partial\Theta$ .

d) *The infinite locus magnitude condition*

$G(s, \mathbf{q})$  has poles on the imaginary axis. At the corresponding frequencies, the frequency locus  $G(j\omega, \mathbf{q})$  tends to infinitely high magnitudes. On the  $\Theta$ -stable side of this critical condition, the frequency locus completely resides in  $\Theta$ . On the other side, intersections with  $\partial\Theta$  occur. This case is only relevant if  $\overline{\Theta}$  extends to infinity, like in Figure 5.21.

These geometric conditions are easily translatable into mathematical equations, which allow the mapping of  $\Theta$ -stability boundaries into parameter space. Before the mapping is explained in detail for each critical condition, the treatment of compound and closing boundaries is illustrated.

### How to Treat Compound and Closing $\Theta$ -boundaries

We assume that the boundary  $\partial\Theta$  is given in the form as represented by (5.1.19). A reasonable procedure for mapping boundaries of this kind into parameter space takes into account the following:

- For each boundary section  $\partial\Theta_i$ , an appropriate tangent condition is established and mapped. A circumstance that has to be considered is illustrated by means of the tangent condition for  $\partial\Theta_2$  in Figure 5.21: the mapping of the boundary equation  $F_{\partial\Theta_2} = y = 0$  also yields solutions that belong to  $x > -0.5$ . The function  $F_{\partial\Theta_2}(x, y)$ , however, is defined only for values of  $x + jy$  that are contained in the definition region  $C_{\partial\Theta_2}$ . Consequently, the *relevance* of each solution  $(q, \omega, x, y)$  resulting from the tangent condition needs to be checked. If  $x + jy \in C_{\partial\Theta_2} = \{x + jy \mid x \leq -0.5\}$ , then the corresponding solution is *relevant*, otherwise it is denoted *fictitious*. For mapping, the fictitious solutions are skipped since they do not contribute to the stability boundaries in parameter space.
- As with the tangent condition, the relevance of solutions corresponding to a frequency endpoint condition has to be checked, and fictitious solutions must be skipped when mapping.
- In general, at a junction, the slope of the boundary  $\partial\Theta$  is not continuous. Thus, for each junction, a separate point condition needs to be pursued. The mapping of the point condition  $z_{i,j}$  provides a continuous transition between the tangent conditions, which belong to the neighboring boundary sections  $\partial\Theta_i$  and  $\partial\Theta_j$ .
- With the dual locus method,  $\Theta$ -definitions are reasonable, where  $\bar{\Theta}$ , i.e. the forbidden complement of  $\Theta$ , is not a region but a non-closed curve (not enclosing any area), see  $-1/N_s(A)$  in Figure 5.10 and  $-1/N_a(\omega, A)$  in Figure 5.13 as examples. In this case, the boundary of  $\partial\Theta$  is identical to  $\bar{\Theta}$ . The boundary curve may close amidst the complex plane like with the locus of the negative-inverse describing function of a saturation. For such a closing point, a point condition also needs to be established.

### Mapping Critical $\Theta$ -stability Conditions

#### a) Mapping the point condition

The goal of mapping the point condition is to show the set of parameter vectors  $q$  in parameter space for which the frequency locus  $G(j\omega, q)$  contains the point  $z^* = x^* + jy^* \in \mathbb{C}$ :

$$Q_{z^*} = \{ q \in \mathbb{R}^2 \mid G(j\omega, q) = z^*, \quad \omega \in \mathbb{R}_0^+ \}. \quad (5.2.3)$$

The equation  $G(j\omega, q) = z^*$ , using (5.2.1), yields

$$p(j\omega, q, z^*) = N_G(j\omega, q) - z^* D_G(j\omega, q) = 0. \quad (5.2.4)$$

*Remark 5.11*

Note the case that  $G(j\omega, \mathbf{q})$  represents a SISO Nyquist plot and  $z^*$  is chosen to be the critical point ( $z^* = -1$ ). Then, in the Laplace domain,  $p(s, \mathbf{q}, z^*)$  is the characteristic polynomial of the closed loop. For all  $\mathbf{q}$ , for which (5.2.4) is true, at least one root of  $p(s, \mathbf{q}, z^*)$  is located on the imaginary axis. The point condition with  $z^* = -1$  in this case is equivalent to the condition that the closed loop has poles on the imaginary axis. Thus, it may be used as an alternative to the method described in Section 2.1 for mapping Hurwitz-stability boundaries.  $\square$

The first step to accomplish the mapping is to establish the equations that represent the point condition. At the frequency  $\omega$  where  $G(j\omega)$  runs through the point  $z^* = x^* + jy^*$ , the real and imaginary parts of  $G(j\omega)$  and  $z^*$  have to be identical:

$$\begin{aligned} R_G(\omega, \mathbf{q}) &= x^*, \\ I_G(\omega, \mathbf{q}) &= y^*. \end{aligned} \quad (5.2.5)$$

Usually, the solution of these equations is mapped into a two-dimensional cross-section of the parameter space, i.e. into a plane of two parameters  $q_1$  and  $q_2$ . The remaining parameters, therefore, are set constant, or gridded where appropriate. Including the frequency, there are three unknowns ( $q_1$ ,  $q_2$ , and  $\omega$ ) and two real equations (5.2.5). The subset  $Q_{z^*}$  of the parameter space, for which (5.2.3) is true, is represented by curves in the  $q_1, q_2$ -plane. These curves are parameterized with the frequency  $\omega$ . Solving (5.2.5) may be realized in the following way: (5.2.5) is transformed into

$$\begin{aligned} p_1(\omega, q_1, q_2) &= 0, \\ p_2(\omega, q_1, q_2) &= 0, \end{aligned} \quad (5.2.6)$$

with two polynomials  $p_1$  and  $p_2$ . These two equations are of the form of (A.1). Therefore, the mapping for rendering the graphical display of (5.2.6) can be performed as generically described in Appendix A.

*Example 5.12*

For illustration, Example 5.1 is continued here: the point conditions for  $z_{1,2} = -1/2$  and  $z_{1,3} = e^{j5/4\pi}$  from Figure 5.21 are mapped. For the open-loop transfer function (5.1.1), the real and imaginary part of the Nyquist plot can be determined after replacing  $s$  by  $j\omega$ :

$$R_G(\omega, q_1, q_2) = \frac{16 q_1 - 5 q_1 (8 + 10 q_2 + 5 q_2^2) \omega^2}{4 + 5 (16 + 20 q_2 + 5 q_2^2) \omega^2 + 25 \omega^4}, \quad (5.2.7)$$

$$I_G(\omega, q_1, q_2) = \frac{-10 q_1 (8 + 5 q_2) \omega + 25 q_1 q_2 \omega^3}{4 + 5 (16 + 20 q_2 + 5 q_2^2) \omega^2 + 25 \omega^4}. \quad (5.2.8)$$

For the point condition at  $z_{1,2} = -1/2$ , i.e.  $x^* = -1/2$ ,  $y^* = 0$ , the polynomials  $p_1$  and  $p_2$  corresponding to (5.2.6) are

$$\begin{aligned} p_1 &= -5 (-16 - 20 q_2 - 5 q_2^2 + 2 q_1 (8 + 10 q_2 + 5 q_2^2)) \omega^2 \\ &\quad + 4 + 32 q_1 + 25 \omega^4, \\ p_2 &= 5 q_1 \omega (-16 - 10 q_2 + 5 q_2 \omega^2). \end{aligned} \quad (5.2.9)$$

Multiple solutions exist, which can be found by looking at the various combinations of factors of these polynomials separately:

- For  $\omega = 0$ , the polynomial  $p_2$  is always zero and  $p_1 = 4 + 32 q_1 = 0$  yields  $q_1 = -1/8$ .
- For  $q_1 = 0$ , the polynomial  $p_2$  is always zero, but  $p_1 = 0$  does not yield real solutions for  $q_2$ .
- For the last factor combination, simplification of the equations is obtained through substituting  $\omega^2$  by  $\alpha$ . The resultant (eliminating  $q_1$ ) is

$$(16 + (10 - 5 \alpha) q_2) (4 + 80 \alpha + 25 \alpha^2 + 100 \alpha q_2 + 25 \alpha q_2^2) = 0. \quad (5.2.10)$$

The first factor solution is  $q_2 = 16/(5(-2 + \alpha))$ . Back substituting and solving  $p_1$  for  $q_1$  then yields  $q_1 = (5\alpha - 2)/16$ . (This is a parameterized representation of the hyperbola  $2q_1 q_2 - q_2 - 2 = 0$  with  $q_1 \geq -1/8$  for  $\alpha \geq 0$ .) For plotting this curve in the  $(q_1, q_2)$ -plane,  $\alpha$  runs from zero to infinity. The second factor solutions for  $q_2$  are not relevant, since they are not real for  $\alpha > 0$ .

The boundaries are displayed in Figure 5.23.

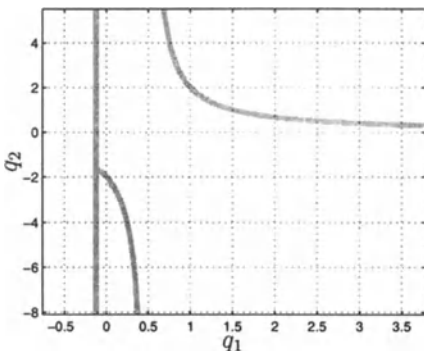


Figure 5.23. Point condition for  $z_{1,2} = -1/2$

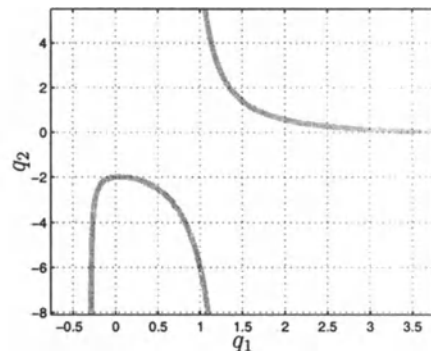


Figure 5.24. Point condition for  $z_{1,3} = e^{j5/4\pi}$

The boundaries of the point condition for  $z^* = e^{j5/4\pi}$  are shown in Figure 5.24.  $\square$

*b) Mapping the tangent condition*

The goal of mapping the tangent condition is to show, in parameter space, the set of parameter vectors  $\mathbf{q}$  for which the frequency locus  $G(j\omega, \mathbf{q})$  tangentially touches a smooth section of the boundary  $\partial\Theta$ . This situation is illustrated by the dashed locus in Figure 5.20. The tangent condition is made up of two subconditions. The first is that the curves  $G(j\omega, \mathbf{q})$  and  $\partial\Theta$  share the common point of contact, which may be expressed by substituting  $x = R_G(\omega, \mathbf{q})$  and  $y = I_G(\omega, \mathbf{q})$  from (5.2.2) into the definition of the respective boundary section (5.1.16):

$$F_{\partial\Theta_i}(R_G(\omega, \mathbf{q}), I_G(\omega, \mathbf{q})) = 0. \quad (5.2.11)$$

Second, matching the tangent condition means equality of the slopes of both the boundary  $\partial\Theta$  and the locus  $G(j\omega, \mathbf{q})$  at the point of contact:

$$\frac{\partial}{\partial\omega} F_{\partial\Theta_i}(R_G(\omega, \mathbf{q}), I_G(\omega, \mathbf{q})) = 0. \quad (5.2.12)$$

With all boundary sections, the tangent condition for mapping into a  $q_1, q_2$ -plane can be transformed into a set of two polynomial equations that match the generic form of (5.2.6):

$$\begin{aligned} p_1(\omega, q_1, q_2) &= \text{num}(F_{\partial\Theta_i}(R_G(\omega, q_1, q_2), I_G(\omega, q_1, q_2))) = 0, \\ p_2(\omega, q_1, q_2) &= \frac{\partial}{\partial\omega} p_1(\omega, q_1, q_2) = 0. \end{aligned} \quad (5.2.13)$$

Thus, the mapping can be performed as generically described in Appendix A.

*Example 5.13*

Again, Example 5.1 is used for illustrating the tangent condition: the slanted straight line  $\partial\Theta_1$ , as a part of the boundary  $\partial\Theta$  shown in Figure 5.21, may be represented as

$$\begin{aligned} F_{\partial\Theta_1}(x, y) &= 2x + (\sqrt{2} - 2)y + 1 = 0, \\ C_{\partial\Theta_1}(x, y) &= \{x + jy \mid -1/\sqrt{2} \leq x \leq -1/2\}. \end{aligned} \quad (5.2.14)$$

With  $x = R_G(\omega, q_1, q_2)$  and  $y = I_G(\omega, q_1, q_2)$  substituted from (5.2.7) and (5.2.8) in (5.2.14), the equations (5.2.13) look like

$$\begin{aligned} p_1(\omega, q_1, q_2) &= 4 + 32q_1 - 20(1/\sqrt{2} - 1)q_1(8 + 5q_2)\omega \\ &\quad + 5(4(1 - q_1)(4 + 5q_2) + 5(1 - 2q_1)q_2^2)\omega^2 \\ &\quad + 50(1/\sqrt{2} - 1)q_1q_2\omega^3 + 25\omega^4 \\ &= 0, \end{aligned} \quad (5.2.15)$$

$$\begin{aligned}
p_2(\omega, q_1, q_2) &= -2 (1/\sqrt{2} - 1) q_1 (8 + 5q_2) \\
&\quad + (4(1 - q_1)(4 + 5q_2) + (5 - 10q_1)q_2^2) \omega \\
&\quad + 15q_1 q_2 (1/\sqrt{2} - 1) \omega^2 + 10\omega^3 \\
&= 0.
\end{aligned} \tag{5.2.16}$$

The resultant obtained by elimination of  $q_1$  is

$$\begin{aligned}
\text{res}_{q_1}(p_1, p_2) &= 8 (1/\sqrt{2} - 1) (8 + 5q_2) + (8(6 + 5q_2)(12 + 5q_2)) \omega \\
&\quad - 10 (1/\sqrt{2} - 1) (128 + 246q_2 + 140q_2^2 + 25q_2^3) \omega^2 \\
&\quad + 320\omega^3 \\
&\quad - 25 (1/\sqrt{2} - 1) (48 + 46q_2 + 20q_2^2 + 5q_2^3) \omega^4 \\
&\quad - 50 (8 + 10q_2 + 5q_2^2) \omega^5 + 125 (1/\sqrt{2} - 1) q_2 \omega^6 \\
&= 0.
\end{aligned} \tag{5.2.17}$$

With these equations, the mapping into the  $q_1, q_2$ -plane can be done: the frequency  $\omega$  is gridded. Then, for all real solutions of  $q_2$  obtained by (5.2.17) for one value of  $\omega$ , one corresponding solution for  $q_1$  can be determined from solving either (5.2.15) or (5.2.16) for  $q_1$ . This approach provides the boundary curves in the  $q_1, q_2$ -plane. Note that real solutions do not necessarily exist for each frequency  $\omega$ . The particular frequencies where the number of solutions changes may be determined from the discriminant of (5.2.17), see Appendix A. In this example, the positive real discriminant frequencies are  $\omega_d \in \{0, 0.632456, 0.684375, 1.63691\}$ .

The tangent condition for the entire straight line  $2x + (\sqrt{2} - 2)y + 1 = 0$  is shown in Figure 5.25 with gray lines. However, not the entire straight line is relevant. Regarding the additional constraint  $-1/\sqrt{2} \leq x \leq -1/2$ , the relevant tangent condition is plotted in bold black line style. The distinction between relevant and fictitious parts of the boundary can be done in the following way: assume the real triple  $(\omega^*, q_1^*, q_2^*)$  is a solution of (5.2.15), (5.2.16). If

$$R_G(\omega^*, q_1^*, q_2^*) + jI_G(\omega^*, q_1^*, q_2^*) \in C_{\partial\Theta_1}(x, y) = \left\{ x + jy \mid -1/\sqrt{2} \leq x \leq -1/2 \right\} \tag{5.2.18}$$

with  $R_G$  from (5.2.7) and  $I_G$  from (5.2.8) holds, then  $(\omega^*, q_1^*, q_2^*)$  contributes to the mapping of the  $\Theta$ -stability boundary, otherwise it is discarded since it is fictitious. Note that in this specific example the relevance of the solution can be checked by means of the simpler expression  $-1/\sqrt{2} \leq R_G(\omega^*, q_1^*, q_2^*) \leq -1/2$ .

The tangent conditions for the two horizontal straight line segments  $\partial\Theta_2$  and  $\partial\Theta_3$  in Figure 5.21 are mapped analogously.  $\square$

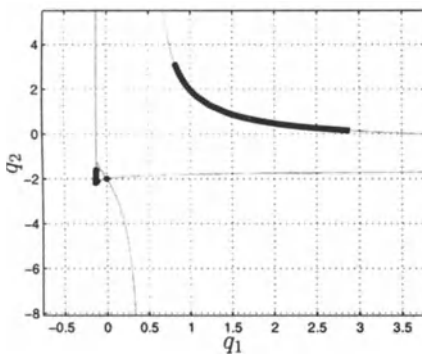
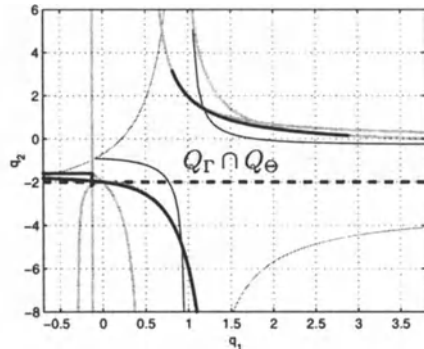


Figure 5.25. Tangent condition

Figure 5.26. Boundaries and stability region  $Q_\Gamma \cap Q_\Theta$  for simultaneous  $\Gamma$ - and  $\Theta$ -stability

c) *Mapping of frequency endpoint conditions*

Frequency endpoint conditions deal with the situation that  $G(j\omega, \mathbf{q})$  starts (i.e.  $\omega = 0$ ) or ends (i.e.  $\omega \rightarrow \infty$ ) on  $\partial\Theta$ . Let  $\omega^*$  denote the considered endpoint frequency. The mapping equations are established in a straightforward manner by postulating both real part and imaginary part equality of the  $\Theta$ -stability boundary  $\partial\Theta$  and the frequency locus  $G(j\omega, \mathbf{q})$  at the respective frequency  $\omega^*$ :

$$F_{\partial\Theta_i}(R_G(\omega^*, \mathbf{q}), I_G(\omega^*, \mathbf{q})) = 0. \quad (5.2.19)$$

Taking the numerator of  $F_{\partial\Theta_i}$  results in one single polynomial equation:

$$p_1(\mathbf{q}) = 0. \quad (5.2.20)$$

For display in a  $(q_1, q_2)$ -plane, even explicit solutions  $q_1 = f_1(q_2)$  or  $q_2 = f_2(q_1)$  may exist. Otherwise, gridding of one of the parameters may yield numeric solutions. As with the tangent condition, the relevance of the solutions has to be checked and fictitious solutions must be skipped during mapping.

*Example 5.14*

For Example 5.1, the only endpoint frequency is  $\omega = 0$ . It applies along the boundary section  $\partial\Theta_2$ . For all  $q_1 \leq -1/8$ , the locus of  $G(j\omega, q_1, q_2)$  starts on  $\partial\Theta_2$ . At the limit of  $C_{\partial\Theta_2}$  (i.e. at  $x = -1/2$ ), the locus of  $G(j\omega, -1/8, q_2)$  starts at the junction  $z_{1,2} = -1/2$ . The solution  $q_1 = -1/8$  has already been determined as a solution of the corresponding point condition.  $\square$

d) *Mapping the infinite locus magnitude condition*

If  $\overline{\Theta}$  extends to infinity in any direction of the complex plane, then this condition needs to be considered. However, it is recommended that this condition is checked in any

case for verification of the mapping results of the previous conditions. For instance, in (5.2.11) or in (5.2.19) the expression 0/0 may occur, which is not taken into account when only considering the respective numerator. The parameter values for which both the corresponding critical  $\Theta$ -stability condition and the infinite locus condition apply may subsequently be treated. The mathematical equations may be derived from the Hurwitz-stability boundary for  $G(s, \mathbf{q})$ .

### *Example 5.15*

For Example 5.1,  $q_2 = -2$  is the boundary for the infinite locus magnitude condition, which can be directly seen from the denominator of  $G(s, \mathbf{q}) = L(s, \mathbf{q})$  in (5.1.1).  $\square$

## *Multiple Criteria Mapping*

An advantage of the parameter space method is that parameter values for which multiple criteria are satisfied may be determined from forming the intersection of the respective stability regions. For Example 5.1, the  $\Gamma$ -stability boundaries (Figure 5.3) plus both point conditions (Figure 5.23, Figure 5.24) and the tangent condition (Figure 5.25) are displayed together in Figure 5.26. Here, all fictitious boundary parts were skipped. The dashed line represents the infinite locus magnitude condition. For all parameter values  $\mathbf{q}$  in the shaded stability region  $Q_\Gamma \cap Q_\Theta$ , both  $\Gamma$ -stability (as defined in Figure 5.2) and  $\Theta$ -stability (as defined in Figure 5.21) are satisfied.

## *Absolute Stability $\Theta$ -margins for the Crane Example*

### *Example 5.16*

The Popov criterion is used to check robust absolute stability of the crane with output feedback:  $k_1 = 500$ ,  $k_2 = 2865$ ,  $k_3 = -22\,800$ ,  $k_4 = 0$ ,  $g = 10$ ,  $m_C = 1000$  (see Example 3.8 with (3.2.4)). The open-loop transfer function is

$$G(s, m_L, \ell) = \frac{1000 + 5730 s + (4560 + 100 \ell) s^2 + 573 \ell s^3}{2 s^2 (1000 + m_L + 100 \ell s^2)}. \quad (5.2.21)$$

The absolute value of the input to the crane (i.e. the propelling force of the crab) is now considered physically limited to  $|y| \leq 2000$  [N]. A corresponding saturation characteristic curve is shown in Figure 5.27. This non-linearity can be considered a sector limited characteristic as introduced with Figure 5.15. The sector assigned to the characteristic is  $[\rho, k + \rho]$  with  $\rho = 0.07$  and  $k = 1$ . The lower sector needs to be greater than zero since zero controller gain does not stabilize the undamped poles of the crane. The fact that the saturation characteristic leaves the assigned sector for  $|u| = |[k_1, k_2, k_3, k_4] \cdot \mathbf{x}| > 28\,571$  can be neglected since no realistic state of the crane

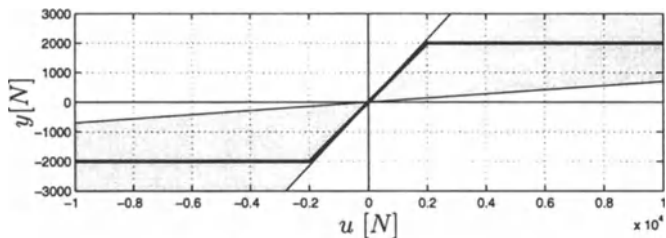


Figure 5.27. Saturation of the crane input (i.e. crab acceleration)

produces any bigger absolute value of the controller output than 28 571. The system is transformed to standard form as described in the context of Figure 5.16. The open-loop linear part of the transformed system is

$$\tilde{G}(s, m_L, \ell) = \frac{1000 + 5730 s + (4560 + 100 \ell) s^2 + 573 \ell s^3}{1000 \rho + 5730 \rho s + a_2 s^2 + 573 \rho \ell s^3 + 200 \ell s^4}, \quad (5.2.22)$$

with  $a_2 = 2000 + 4560 \rho + 100 \rho \ell + 2 m_L$ .

The  $\Theta$ -stability region to be defined before mapping it into the parameter space is

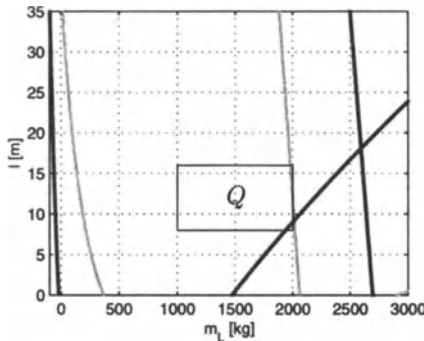


Figure 5.28.  $\Theta$ -stability region of the crane for two Popov-line slopes (gray: 1.8, black: 0.8)

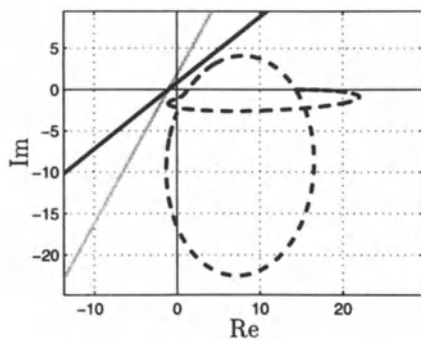


Figure 5.29. The Popov plot (dashed line) of the transformed system for  $m_L = 1500$ ,  $\ell = 12$  lies entirely to the right hand side of the two Popov-lines with slopes 0.8 (gray) and 1.8 (black)

the region to the right hand side of the Popov-line, which intersects the real axis at  $-1/k = -1$ . The slope of the Popov-line may be chosen arbitrarily, however, it will affect the result in terms of the obtained  $\Theta$ -stable region. Figure 5.28 shows the  $\Theta$ -stable boundaries for two different slopes of the Popov-line. The center ( $m_L = 1500$  and  $\ell = 12$ ) of the operating domain  $Q$  turns out to be  $\Theta$ -stable in both cases. The corresponding Popov plot resides entirely to the right hand side of both Popov-lines, see Figure 5.29. However, a little bit of the operating domain is cut off at different

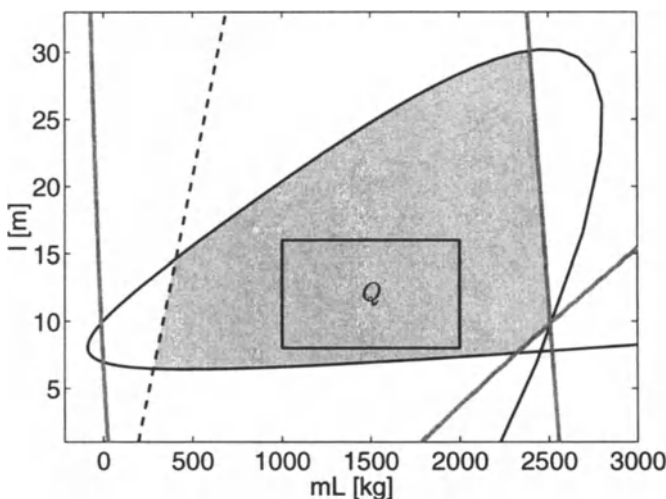


Figure 5.30. Stability region of the crane for simultaneous  $\Gamma$ - and  $\Theta$ -(absolute) stability (compare to Fig. 3.16)

vertices by the stability boundaries. For the specific example, the results shown in Figure 5.28 and Figure 5.29 suggest trying of an intermediate value for the Popov-line slope. With a slope of 0.95, the  $\Theta$ -stability-region shown in Figure 5.30 is obtained. Also, the  $\Gamma$ -stability region from Fig. 3.16 is included. The entire operating domain is contained in the intersection of the  $\Gamma$ - and the  $\Theta$ -stability regions.  $\square$

In the above example, it was possible to choose a common Popov-line in order to prove robust absolute stability for the entire operating domain  $Q$ . Nevertheless, Figure 5.28 also proves absolute stability by means of two Popov-lines with different slopes. The system is absolutely stable if the Popov plot resides to the right hand side of a Popov-line with *arbitrary* slope. Thus, the overall  $\Theta$ -stability region is formed by the union of all  $\Theta$ -stability regions that are obtainable at different Popov-line slopes. In practice, the procedure for computing  $\Theta$ -stability boundaries can be repeated with some exemplary Popov-line slopes. The result will provide at least a good approximation of the attainable absolute stability region in parameter space.

### 5.3 Frequency Response Magnitude Specifications (Beta-stability)

The parameter space approach has been proven to be a very useful control design tool in a number of applications involving parametric linear systems. This is due in part to

the non-conservative treatment of uncertain parameters, the simplicity of the resulting controller, and the transparency provided by the design method.

On the other hand,  $H_\infty$ -based techniques do facilitate the design and analysis of controllers for systems with both parametric and unstructured uncertainty subject to Frequency Response Magnitude (FRM) specifications. However, even for very simple systems, these methods often result in complex controllers that provide conservative results, which is due in part to the conservative treatment of parametric uncertainty.

In this section, typical frequency domain specifications used to ensure a number of closed-loop characteristics (e.g. disturbance attenuation, noise rejection, reference tracking, model matching, robust stability w.r.t. structured (parametric) and unstructured uncertainty) are reviewed to motivate the use of frequency response magnitude (FRM) specifications. Then, the notion of  $\mathcal{B}$ -stability is formally defined to enable the treatment of FRM specifications in the parameter space framework.  $\mathcal{B}$ -stability is analogous to  $\Gamma$ -stability and defines acceptable and unacceptable frequency response magnitudes just as  $\Gamma$ -stability defined acceptable and unacceptable closed-loop pole locations. Using the concept of  $\mathcal{B}$ -stability, the parameter space approach can be used to design controllers that provide desired closed-loop characteristics stated in terms of FRM specifications. Some elementary examples are provided in Section 5.3 and Section 5.4 to demonstrate the concept of using FRM specifications in parameter space. In Sections 6.7, 6.8, and 7.3, case studies in vehicle dynamics and flight control are presented that demonstrate these concepts in “real-world” control design problems.

### *Remark 5.17*

In this section, only SISO FRM specifications are considered. While any number of these SISO specifications can be considered simultaneously, in some cases it is more desirable to consider MIMO FRM specifications, as presented in Section 5.5.  $\square$

### *Remark 5.18*

SISO FRM specifications are often given in terms of the  $\infty$ -norm of transfer functions, where the  $\infty$ -norm of the transfer function  $G(s)$  is given by

$$\|G(s)\|_\infty = \sup_{\omega \in \mathbb{R}_0^+} |G(j\omega)|. \quad (5.3.1)$$

The  $\infty$ -norm of  $G(s)$  is the peak value of its FRM plot (i.e. Bode magnitude plot). It is also the distance in the complex plane from the origin to the farthest point on the Nyquist plot of  $G(j\omega)$ .  $\square$

Before presenting the general discussion on frequency domain specifications, Example 5.1 will be revisited to introduce the concept of FRM specifications.

*Example 5.19*

Consider the parametric single-loop unity feedback system in Figure 5.1 with parametric open-loop transfer function  $L(s, \mathbf{q})$  defined by (5.1.1). Here, both the reference input  $w$  and the disturbance  $d$  are considered. Thus, in addition to reference tracking performance, disturbance attenuation qualities of the closed-loop system can also be addressed. Therefore, we consider the two closed-loop transfer functions

$$T(s, \mathbf{q}) = \frac{y(s)}{w(s)} = \frac{q_1(-5q_2s + 8)}{5s^2 + (10 + 5q_2 - 5q_1q_2)s + 2 + 8q_1}, \quad (5.3.2)$$

$$S(s, \mathbf{q}) = \frac{y(s)}{d(s)} = \frac{5s^2 + (5q_2 + 10)s + 2}{5s^2 + (10 + 5q_2 - 5q_1q_2)s + 2 + 8q_1}, \quad (5.3.3)$$

i.e. the tracking transfer function  $T$  and the disturbance transfer function  $S$ , also denoted complementary sensitivity function and sensitivity function, respectively. A detailed description of the sensitivity functions will be given later in this section.

As in Example 5.1, the effect of variations of  $q_2$  is investigated while  $q_1 = 1$  is assumed. For this value of  $q_1$ , the characteristic polynomial is robustly stable for all values of  $q_2$ , in fact it does not depend on  $q_2$ . However, variations in  $q_2$  affect the zeros of the closed-loop system and thus also the tracking and disturbance transfer functions  $T$  and  $S$ . The Bode magnitude (i.e. FRM) plots of  $S$  and  $T$  are shown in Figure 5.31 for values  $q_2 = 1$  and  $q_2 = 5$  respectively.

For interpretation of the Bode magnitude plots in Figure 5.31, it is useful to consider three frequency ranges:

- i. *Low-frequency range*: the low-frequency range ( $\omega \rightarrow 0$ ) determines the steady state behavior of the closed-loop system. Here, the steady state values of  $S$  and  $T$  are given by

$$\lim_{s \rightarrow 0} T(s, \mathbf{q}) = \frac{8q_1}{2 + 8q_1} \quad \text{and} \quad \lim_{s \rightarrow 0} S(s, \mathbf{q}) = \frac{2}{2 + 8q_1},$$

and do not depend on  $q_2$  and thus, the steady state behavior does not depend on  $q_2$ . However, this shows that the steady state error ( $\lim_{t \rightarrow \infty} e(t)$ ) will not be zero, since  $T(0) \neq 1$  and  $S(0) \neq 0$ .

- ii. *High-frequency range*: the high-frequency range determines the immediate responsiveness of the closed-loop system, which may be characterized by the direct transmission values

$$\lim_{s \rightarrow \infty} T(s, \mathbf{q}) = 0 \quad \text{and} \quad \lim_{s \rightarrow \infty} S(s, \mathbf{q}) = 1.$$

These values differ from 0 and 1, respectively, only for systems where the open-loop transfer function  $L$  is of relative degree 0.

- iii. *Intermediate frequency range*: the intermediate frequency range determines the dynamic behavior of the system. Although  $S$  and  $T$  are stable transfer functions, their magnitude plots vary largely with  $q_2$  within this frequency range.

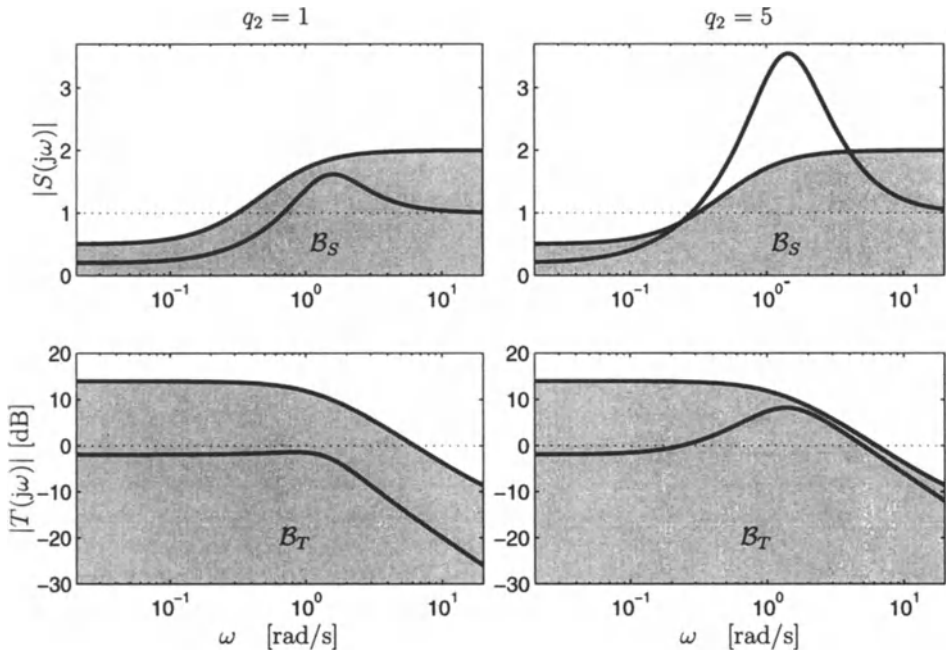


Figure 5.31. Bode magnitude plot of sensitivity function  $S$  (top) and complementary sensitivity function  $T$  (bottom) for  $q_1 = 1$ ,  $q_2 = 1$  (left) and  $q_1 = 1$ ,  $q_2 = 5$  (right). The desired regions  $\mathcal{B}_S$  and  $\mathcal{B}_T$  are shaded in gray

In Example 5.1,  $\Gamma$ - and  $\Theta$ -specifications were considered. Here, two new specifications ( $\mathcal{B}$ -specifications) with regard to the FRM plots of  $S$  and  $T$  are introduced. Namely, the FRM plots of  $S$  and  $T$  shall reside within the desired regions  $\mathcal{B}_S$  and  $\mathcal{B}_T$  shown in Figure 5.31. Both specifications are satisfied for  $q_2 = 1$ . However, for  $q_2 = 5$  the sensitivity specification is violated (i.e. the FRM of  $S$  does not reside in the desired  $\mathcal{B}_S$  region). Then, if the FRM specifications on  $S$  and  $T$  are to be included in a parameter space robustness analysis, the task is to determine the parameter values of  $q_1$  and  $q_2$  for which both FRM specifications are satisfied. This task will be addressed fully in Section 5.4.

□

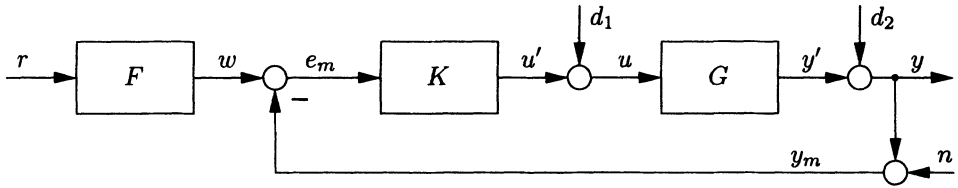
### Basics of Frequency Domain Feedback Control

Before showing how frequency response magnitude specifications can be incorporated into the parameter space approach, some basics of frequency domain feedback control are reviewed. For a more detailed description of feedback control theory with frequency response magnitude specifications, the reader is referred to [79] and [203],[137],[171],[38].

*Remark 5.20*

Since we are working in the frequency domain, all variables (both signals and transfer functions) are functions of the Laplace variable  $s$ . For the sake of simplicity, in the sequel,  $s$  is being suppressed in most instances.  $\square$

The following discussion considers the standard single-loop feedback system in Figure 5.32, which serves as a generic structure for many control systems. However, all of the following can be easily extended to arbitrary feedback systems. The open-loop



$y$	controlled signal	$d_1$	(plant) input external signal
$y_m$	measured controlled signal	$d_2$	(plant) output disturbance
$u$	actuating signal	$y'$	plant output
$e$	tracking error ( $e = w - y$ )	$u'$	controller output
$e_m$	measured tracking error ( $e_m = w - y_m$ )	$u$	control signal
$r$	reference input	$n$	sensor noise
		$w$	filtered reference input

Figure 5.32. Standard single-loop feedback system

transfer function for the standard loop is defined as

$$L = K G, \quad (5.3.4)$$

and the characteristic polynomial of the closed-loop is

$$p = \text{num}(1 + K G). \quad (5.3.5)$$

The transfer function from the reference input  $r$  to the controlled signal  $y$ , i.e.

$$H = \frac{F K G}{1 + K G} \quad (5.3.6)$$

denotes the tracking transfer function, often referred to as the *model regulator transfer function*.

The two basic design steps are:

- i. *Feedback step*: design the controller  $K$  such that the input and output disturbances  $d_1$  and  $d_2$  are attenuated, the sensor noise  $n$  is rejected, and the filtered reference signal  $w$  is tracked.
- ii. *Feedforward step*: design the prefilter  $F$  such that the tracking performance with regard to the reference signal  $r$  matches a desired transfer function  $G_d$  (“model matching”, see also Figure 5.33).

The first design step (i.e. the feedback step) is the primary focus in the sequel. Therefore, except when otherwise stated,  $F = 1$  ( $w = r$ ) is assumed. The input/output relation between all external inputs  $w$ ,  $d_1$ ,  $d_2$ , and  $n$  and all signals of interest, i.e. tracking error  $e$ , control signal  $u$  and controlled signal  $y$  is given by

$$\underbrace{\begin{bmatrix} e \\ u \\ y \end{bmatrix}}_{\mathbf{z}} = \underbrace{\begin{bmatrix} S & T & -S_G & -S \\ S_K & -S_K & S & -S_K \\ T & -T & S_G & S \end{bmatrix}}_{\mathbf{R}} \cdot \underbrace{\begin{bmatrix} w \\ n \\ d_1 \\ d_2 \end{bmatrix}}_{\mathbf{w}}, \quad (5.3.7)$$

where  $\mathbf{w}$  is the vector of external input signals, and  $\mathbf{z}$  is the vector of internal signals to be used to evaluate internal stability and performance of the closed-loop system. The elements of the transfer matrix  $\mathbf{R}$  are the four sensitivity functions  $S$ ,  $T$ ,  $S_G$ , and  $S_K$  defined as:

- *Sensitivity function*:

$$S = \frac{1}{1 + KG} = \frac{1}{1 + L} \quad (5.3.8)$$

$S$  describes the sensitivity of the closed-loop system w.r.t. output disturbances and changes in the filtered reference signal.

- *Complementary sensitivity function*:

$$T = \frac{KG}{1 + KG} = KG S = 1 - S. \quad (5.3.9)$$

$T$  describes the influence of measurement noise on the controlled signal and the tracking error, as well as the response of the controlled signal to changes in the filtered reference signal.

- *Input sensitivity function*:

$$S_K = \frac{K}{1 + KG} = K S. \quad (5.3.10)$$

$S_K$  describes the influence of the filtered reference signal, measurement noise, and the output disturbance on the control signal.

- *Output sensitivity function:*

$$S_G = \frac{G}{1 + K G} = G S. \quad (5.3.11)$$

$S_G$  describes the sensitivity of the closed-loop system w.r.t. external input signals  $d_1$ , i.e. the effect of  $d_1$  on  $y$  and  $e$ .

These four sensitivity functions (i.e.  $S$ ,  $T$ ,  $S_G$ ,  $S_K$ ) along with the characteristic polynomial  $p$  and the model regulator transfer function  $H$  can be used to thoroughly evaluate the stability and performance of the nominal closed-loop system in Figure 5.32 as well as that of the uncertain closed-loop system in Figure 5.39. In the discussion to follow, investigating the stability and performance of closed-loop systems is divided into the following four categories:

- *Nominal stability:* stability with no model uncertainty.
- *Nominal performance:* performance with no model uncertainty.
- *Robust stability:* stability with model uncertainty.
- *Robust performance:* stability and performance with model uncertainty.

### Nominal Stability

First, the internal stability of the nominal closed-loop system must be verified. The standard feedback loop in Figure 5.32 is internally stable, if all internal signals fade to zero after the external signals  $w$ ,  $d_1$ ,  $d_2$  and  $n$  have vanished. A necessary and sufficient condition for internal stability of the standard feedback loop is [79]:

#### Theorem 5.21 (internal stability)

The standard feedback loop is internally stable, if and only if:

- All roots of  $p = \text{num}(1 + K G)$  are located in the left eigenvalue half plane  $\text{Re}(s) < 0$ .
- There is no pole-zero cancellation in  $\text{Re}(s) \geq 0$  while forming the product  $K G$ .

□

#### Remark 5.22

The notion of internal stability can be extended to  $\Gamma$ -stability, which was defined in Chapter 3. The standard feedback loop is internally  $\Gamma$ -stable, if and only if:

- All roots of  $p = \text{num}(1 + K G)$  are located in the desired  $\Gamma$ -region.
- There is no pole-zero cancellation outside  $\Gamma$  in the product  $K G$ .

□

## Nominal Performance

Next, the performance of the nominal closed-loop in Figure 5.32 will be investigated. A number of closed-loop performance characteristics (e.g. *tracking performance*, *disturbance attenuation*, *noise rejection*, *required control input* and *model matching*) can be evaluated by examining the magnitudes of the individual frequency responses (i.e. FRMs) of the transfer matrix  $\mathbf{R}$  (i.e. the four sensitivity functions) as described below. Insight regarding the desired magnitudes of these sensitivity functions can be obtained by observing the effect that the external inputs  $w$  have on the internal signals  $z$ . Of particular interest is the effect of the external inputs on the tracking error,

$$e = w - y \quad (5.3.12)$$

$$= Sw + Tn - S_G d_1 - S d_2, \quad (5.3.13)$$

as this provides information regarding the magnitudes required for three of the sensitivity functions in order to achieve good performance. Since the FRMs of these transfer function are frequency-dependent, further insight can be gained by considering the frequency range of the external input signals. Typically, reference and disturbance inputs are low-frequency signals, while sensor noise generally occurs at high frequency.

- i. *Tracking*: in order to have good tracking performance in the frequency range  $[0; \omega_S]$ , changes in the filtered reference signal  $w$  can only have a small effect on the tracking error  $e$  (5.3.12), which requires

$$|S(j\omega)| \ll 1 \quad \text{for } 0 \leq \omega \leq \omega_S. \quad (5.3.14)$$

- ii. *Disturbance attenuation*: if inequality (5.3.14) is satisfied, then output disturbances  $d_2$  are also attenuated (i.e. don't have a significant effect on the tracking error) in the frequency range  $[0; \omega_S]$ . Input disturbances  $d_1$  are attenuated in the frequency range  $[0; \omega_S]$  if

$$|S_G(j\omega)| \ll 1 \quad \text{for } 0 \leq \omega \leq \omega_S. \quad (5.3.15)$$

- iii. *Noise rejection*: the effect of noise on the tracking error can be rejected to a great extent in the frequency range  $[\omega_T; \infty)$  if

$$|T(j\omega)| \ll 1 \quad \text{for } \omega_T \leq \omega < \infty. \quad (5.3.16)$$

- iv. *Required control input*: since all actuators have performance limits, it is often necessary to ensure that these limits are not exceeded. The control signal (i.e. actuator command) is limited within the actuator bandwidth  $[0; \omega_{act}]$  if

$$|S_K(j\omega)| \text{ is small for } 0 \leq \omega < \omega_{act}. \quad (5.3.17)$$

- v. *Model matching*: the model matching performance also depends on the prefilter  $F$  used to generate the filtered reference signal  $w$  (i.e.  $w = Fr$ ). If  $G_d$  is the desired transfer function that the closed-loop system in Figure 5.33 is to track, then the model matching error is

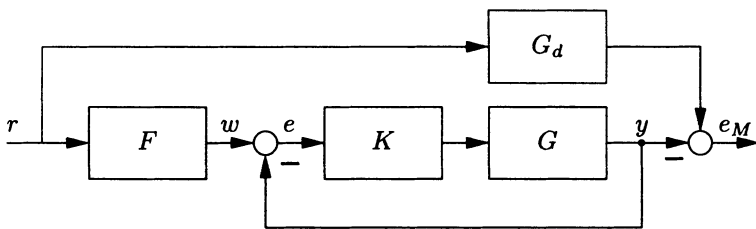


Figure 5.33. Model matching error

$$e_M = (G_d - H)r = E r , \quad (5.3.18)$$

where

$$E = G_d - H . \quad (5.3.19)$$

The desired matching performance is achieved in the frequency range  $[0; \omega_M]$  if

$$|E(j\omega)| \text{ is small for } \omega \in [0; \omega_M] . \quad (5.3.20)$$

### Remark 5.23

In order for the model matching error  $e_M$  defined by (5.3.18) to be small,  $|E(j\omega)|$  must be small, which means that  $G_d$  must be a feasible closed-loop transfer function. That is, by a proper choice of  $K$  and  $F$  it must be possible that the model regulator transfer function  $H$  defined by (5.3.6) approximately matches  $G_d$ , see Section 1.7.  $\square$

As briefly discussed above, a number of performance specifications can be stated in terms of keeping the FRMs of various transfer functions small in certain frequency ranges. While all of the specifications outlined may be of interest, for standard control problems we are especially interested in the magnitude specifications on  $S$  and  $T$ , and specifically in ensuring that  $|S(j\omega)| \ll 1$  for small frequencies and  $|T(j\omega)| \ll 1$  for high frequencies. More specific details regarding the desired magnitude or  $T$  will be given later in this section, but for now we will focus on  $S$ . Magnitude specifications on  $S$ , often referred to as nominal performance criteria in SISO  $H_\infty$  control theory, can be used to formulate three design goals concerning the steady state error, the stability margin, and the transition frequency. Specifically, the maximum steady state error can be limited to  $S(0) < l_g$ , the high-frequency disturbance amplification can be limited to  $|S(j\omega)| < h_g$ , and the transition frequency  $\omega_t$  for which  $|S(j\omega_t)| = 1$  (i.e. the frequency at which disturbances become amplified instead of attenuated) can be limited to  $\omega_t \geq \omega_S$  if

$$|S(j\omega)| < \partial \mathcal{B}_S(\omega) , \quad (5.3.21)$$

where the magnitude specification, given by the frequency-dependent bound  $\partial\mathcal{B}_S$ , can either be represented piecewisely by straight line segments, e.g.

$$\partial\mathcal{B}_S(\omega) = \begin{cases} l_g & \forall \omega \in [0; \omega_S] \\ h_g & \forall \omega \in (\omega_S; \infty) \end{cases}, \quad (5.3.22)$$

or by the magnitude of a transfer function, e.g.

$$\partial\mathcal{B}_S(\omega) = |B(j\omega)|, \quad \text{where } B(s) = h_g \frac{s + \omega_S l_g}{s + \omega_S h_g}. \quad (5.3.23)$$

These typical magnitude bounds on  $S$  are demonstrated in the following example.

*Remark 5.24*

The disturbance amplification specification  $|S(j\omega)| < h_g$  also determines a lower bound for the Nyquist-stability margin  $\rho_S$ , which is defined as the minimum spacing between the Nyquist locus and critical point  $(-1, 0)$ , i.e. by the relation

$$\begin{aligned} \rho_S &= \inf_{\omega \in [0, \infty)} |1 + L(j\omega)| \\ &= \|S(j\omega)\|_\infty^{-1}. \end{aligned} \quad (5.3.24)$$

Thus, if  $|S(j\omega)| < h_g$ , the Nyquist-stability margin must satisfy

$$\rho_S > 1/h_g. \quad (5.3.25)$$

□

*Example 5.25 (nominal performance)*

Let the open-loop transfer function be given by

$$L(s) = k \frac{\omega_0^2}{s^2 + 2D\omega_0 s + \omega_0^2}, \quad (5.3.26)$$

where  $k = 1$ ,  $D = 0.3$ ,  $\omega_0 = 6\pi$ . The two diagrams in Figure 5.34 show the Bode magnitude plots of the corresponding sensitivity function  $S$ , together with the magnitude bounds  $\partial\mathcal{B}_S(\omega)$  corresponding to (5.3.23) and (5.3.22). The permissible steady state error is  $l_g = 0.6$  and the permissible high frequency disturbance amplification is  $h_g = 1.9$ . The required minimum transition frequency is  $\omega_S = 2\pi$ . The magnitude plot of  $S$  remains below  $\partial\mathcal{B}_S(\omega)$  in both cases, i.e. the specifications are satisfied. □

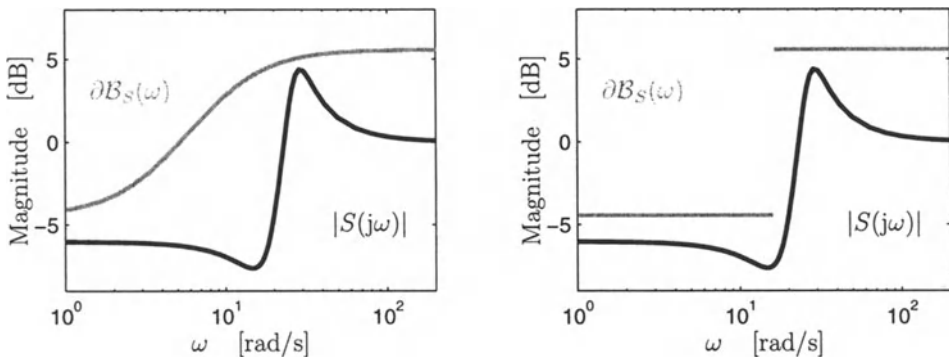


Figure 5.34. Graphic interpretation of the requirements on the sensitivity function in the Bode magnitude diagram

### Modelling Uncertainty

Before addressing the issues of robust stability and robust performance, a brief discussion of uncertainty modelling will be given. Model uncertainty can be represented in two distinctly different forms, parametric uncertainty and unstructured uncertainty. Parametric uncertainty typically arises from a physical model that has uncertain or changing parameters. On the other hand, unstructured uncertainty is typically used to account for neglected or unmodelled dynamics (e.g. flexible body modes, actuator dynamics, sensor dynamics), and both magnitude and phase are considered to be uncertain.

#### Parametric Uncertainty

In the case of parametric uncertainty, the plant is represented by a parametric transfer function  $G(s, \mathbf{q})$  (5.2.1). When the family of transfer functions  $G(s, \mathbf{q})$  (5.2.1) is substituted for  $G(s)$  in the standard feedback loop in Figure 5.32, the corresponding sensitivity functions also become a family of transfer functions that depend on the plant parameters  $\mathbf{q}$ . Furthermore, if the controller  $K$  is parameterized, then the sensitivity functions also depend on the controller parameters  $\mathbf{k}$ .

#### Unstructured Uncertainty

There are a number of models used in robust control design to account for unstructured uncertainty, the most common of which is the multiplicative perturbation model, which can be used to capture a wide variety of model uncertainty including unmodelled dynamics as well as parameter variations. The multiplicative perturbation model corresponding to Figure 5.35 is described by

$$\tilde{G}(s) = (1 + W_\Delta(s)\Delta(s))G(s) . \quad (5.3.27)$$

$\Delta(s)$  is the multiplicative perturbation and is assumed to satisfy  $\|\Delta(s)\|_\infty \leq 1$ . The phase  $\angle\Delta(j\omega)$  is considered arbitrary. The weighting function  $|W_\Delta(j\omega)|$  scales  $\Delta(s)$  to

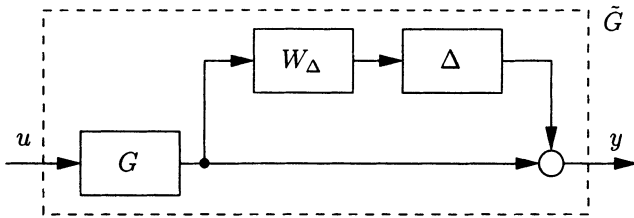


Figure 5.35. Plant with multiplicative perturbation

account for the frequency-dependent magnitude of the uncertainty, where it is assumed that the model uncertainty is less than  $\pm|W_\Delta(j\omega)|$ .

A typical weighting function magnitude plot is shown in Figure 5.36.

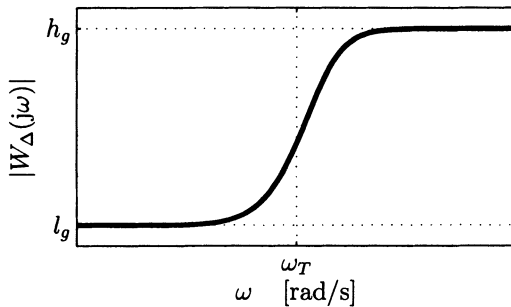


Figure 5.36. Typical weighting function magnitude plot for a multiplicative perturbation model

As shown in Figure 5.36,  $|W_\Delta(j\omega)|$  is typically small (i.e.  $|W_\Delta(j\omega)| = l_g$ ) at low frequencies where  $G(s)$  accurately represents the system, and large (i.e.  $|W_\Delta(j\omega)| = h_g$ ) at high frequencies  $\omega \gg \omega_T$  where the influence of unmodelled dynamics may be significant. The frequency  $\omega_T$  indicates the transition frequency where the model  $G(s)$  becomes unreliable. Typical weighting functions with which the above-mentioned requirements may be realized, i.e.  $\lim_{\omega \rightarrow 0} |W_\Delta(j\omega)| = l_g$  and  $\lim_{\omega \rightarrow \infty} |W_\Delta(j\omega)| = h_g$ , are:

$$|W_\Delta(j\omega)| = \left| h_g \frac{j\omega + \omega_T l_g}{j\omega + \omega_T h_g} \right|, \quad (5.3.28)$$

or

$$|W_\Delta(j\omega)| = \begin{cases} l_g & \forall \omega \in [0; \omega_T] \\ h_g & \forall \omega \in (\omega_T; \infty) \end{cases}. \quad (5.3.29)$$

*Remark 5.26*

The transition frequency  $\omega_T$  may be considered closely related to the desired *bandwidth*  $\omega_B$  of the closed-loop system. The latter is defined as the frequency for which the magnitude of  $T(s)/T(0)$  falls below the  $-3$  dB-line, i.e. for which

$$|T(j\omega_B)/T(0)| = 1/\sqrt{2}. \quad (5.3.30)$$

□

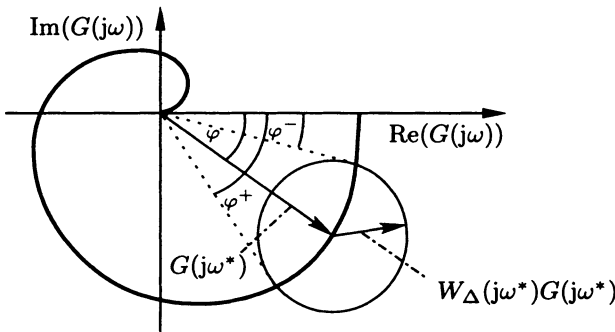


Figure 5.37. Frequency locus of the multiplicative perturbation model

Figure 5.37 shows the frequency locus of the multiplicative perturbation model. For a fixed frequency  $\omega^*$ , a disk centered at  $G(j\omega^*)$  with frequency weighted radius  $|W_\Delta(j\omega^*)G(j\omega^*)|$  is plotted. The multiplicative model  $\tilde{G}(s)$  represents the family of transfer functions for which the locus  $\tilde{G}(j\omega)$  remains within the disk for the respective frequency  $\omega$ . The phase of  $\tilde{G}(j\omega^*)$  is uncertain within the range  $\varphi^- < \tilde{\varphi} < \varphi^+$ .

*Remark 5.27*

In addition to the multiplicative perturbation model, three other uncertainty models are commonly used in frequency domain feedback control theory to incorporate structured and unstructured uncertainty information into robust controller design, namely:

- The additive uncertainty model (left plot in Figure 5.38),

$$\tilde{G} = G + \Delta W_\Delta. \quad (5.3.31)$$

- The two feedback perturbation models (middle and right plot in Figure 5.38),

$$\tilde{G} = \frac{G}{1 + \Delta W_\Delta}, \quad (5.3.32)$$

$$\tilde{G} = \frac{G}{1 + \Delta W_\Delta G}. \quad (5.3.33)$$

Examples for these unstructured uncertainty models can be found e.g. in [38].

□

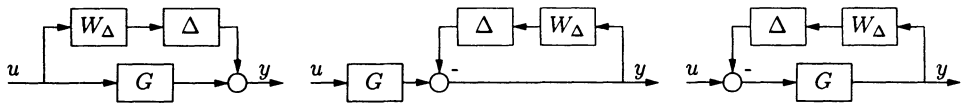


Figure 5.38. Common uncertainty models

## Robust Stability

Theorem 5.21 describes a necessary and sufficient condition for internal stability of the control loop in Figure 5.32, assuming a nominal plant model  $G$ . However, if the nominal model is replaced with a parametric model  $G(\mathbf{q})$ , unstructured uncertainty model  $\tilde{G}$ , or a parametric model with unstructured uncertainty  $\tilde{G}(\mathbf{q})$ , appropriate robust stability conditions must be considered.

### Robust Stability for Parametric Uncertainty

Robust stability in the presence of parametric uncertainty is discussed in detail in Chapter 2.

### Robust Stability for Unstructured Uncertainty

We will now focus on the effect of unstructured uncertainty on the robust stability condition. Figure 5.39 depicts the standard feedback loop with a multiplicative perturbation corresponding to (5.3.27). External input signals are not considered. Assuming the non-perturbed closed-loop system (i.e.  $\Delta(s) = 0$ ) is internally stable, a necessary and sufficient condition for robust stability of the perturbed system is [79]:

#### Theorem 5.28 (robust stability)

The uncertain closed loop in Figure 5.39 is robustly stable for all  $\Delta$  such that  $\|\Delta(s)\|_\infty \leq 1$ , if and only if

$$\|W_\Delta(s) T(s)\|_\infty < 1. \quad (5.3.34)$$

□

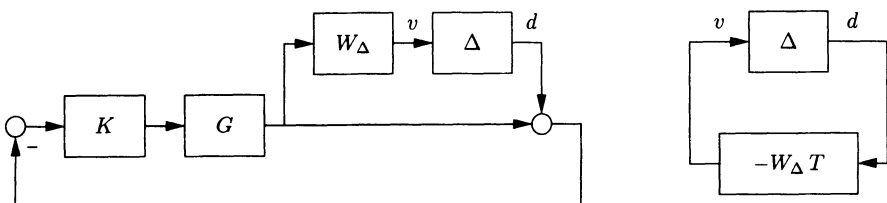


Figure 5.39. Application of the small-gain theorem to the standard feedback loop with a multiplicative perturbation

For a simple interpretation of condition (5.3.34), consider the closed-loop system shown on the left side of Figure 5.39, and note that the transfer function from  $d$  to  $v$  is given by

$$\frac{v}{d} = -W_\Delta T . \quad (5.3.35)$$

Then, it is clear that the system in 2-block form on the right side of Figure 5.39 is equivalent to the system on the left w.r.t. the signals  $d$  and  $v$ . The small-gain theorem [203] can be easily applied to this 2-block structure to obtain (5.3.34) in Theorem 5.28.

Table 5.1 lists the robust stability conditions for the four uncertainty models corresponding to Figure 5.35 and Figure 5.38 [79].

Table 5.1. Robust stability conditions for unstructured uncertainty models

a) multiplicative perturbation	$\ W_\Delta(s)T(s)\ _\infty < 1$
b) additive perturbation	$\ W_\Delta(s)S_K(s)\ _\infty < 1$
c) feedback perturbation	$\ W_\Delta(s)S(s)\ _\infty < 1$
d) feedback perturbation	$\ W_\Delta(s)S_G(s)\ _\infty < 1$

### Example 5.29 (robust stability)

The control loop in Example 5.25 will be revisited to investigate its robust stability subject to a multiplicative perturbation model (i.e. unstructured uncertainty). The open-loop transfer function is given by (5.3.26). For frequencies  $\omega \ll 12\pi$  [rad/s], the (unstructured) model error is assumed to be smaller than 10 % (i.e.  $|W_\Delta(j\omega)| = 0.1$ ), and for frequencies  $\omega \gg 12\pi$  [rad/s] it is assumed that the model error does not exceed 200 % (i.e.  $|W_\Delta(j\omega)| = 2$ ). The uncertainty is assumed to transition continuously from its low- to high-frequency magnitude with a transition frequency of  $12\pi$  [rad/s]. A weighting function that satisfies these specifications is

$$W_\Delta(s) = 2 \frac{s + 2\pi \cdot 6 \cdot 0.1}{s + 2\pi \cdot 6 \cdot 2} . \quad (5.3.36)$$

Figure 5.40 shows the graphical interpretation of the robust stability criterion in a Bode- and Nyquist-diagram. The magnitude of the complementary sensitivity function resides below the magnitude plot of the inverted weighting function, i.e.  $|T(j\omega)| < |W_\Delta(j\omega)|^{-1} \forall \omega$ , as shown in the left plot of Figure 5.40. Hence, (5.3.34) is satisfied and the closed-loop system is robustly stable w.r.t. the assumed multiplicative uncertainty model. The right plot in Figure 5.40 shows an interpretation of the robust stability condition  $|W_\Delta(j\omega)T(j\omega)| < 1$  in the Nyquist-diagram. From (5.3.9) and (5.3.4), it follows that

$$|W_\Delta(j\omega) L(j\omega)| < |1 + L(j\omega)|, \quad \forall \omega \in [0; \infty) . \quad (5.3.37)$$

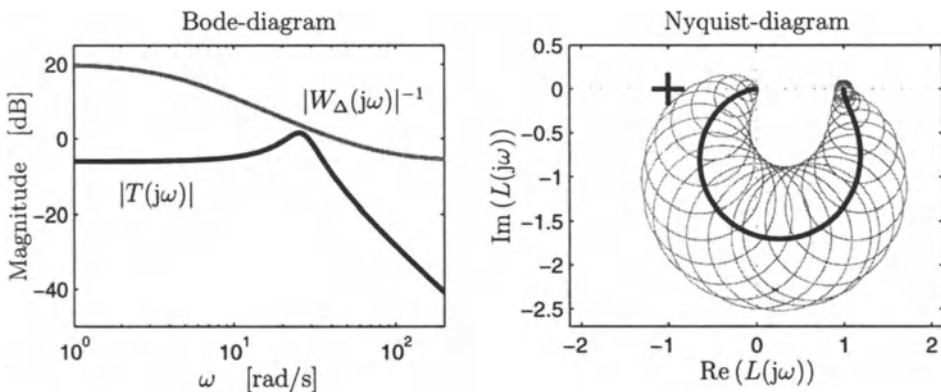


Figure 5.40. “Robust stability” in Bode- and Nyquist-diagram

This inequality means that the closed-loop system is robustly stable if at all frequencies  $\omega$  the point  $(-1, 0)$  lies outside the disk centered at  $L(j\omega)$  with radius  $|W_\Delta(j\omega)L(j\omega)|$ .  $\square$

### *Robust Stability for Mixed Parametric and Unstructured Uncertainty*

For a system with mixed parametric and multiplicative uncertainty (i.e. the closed-loop system represented in Figure 5.39, with  $G$  replaced by  $G(\mathbf{q})$ ), the robust stability criterion is formulated by merging the robust Hurwitz-stability condition and the robust stability condition (5.3.34) to obtain:

#### *Theorem 5.30*

The uncertain closed-loop in Figure 5.39, where  $G = G(s, \mathbf{q})$ , is robustly stable for all  $\mathbf{q} \in Q$  and all  $\Delta$  such that  $\|\Delta(s)\|_\infty \leq 1$ , if and only if

$$\|W_\Delta(s)T(s, \mathbf{q})\|_\infty < 1, \quad \forall \mathbf{q} \in Q. \quad (5.3.38)$$

$\square$

### *Robust Performance*

In general, robust performance means that some performance specifications (e.g. eigenvalue specifications (Chapter 3), frequency loci specifications (Section 5.1), frequency magnitude specifications (this section)) are satisfied robustly w.r.t. parametric and/or unstructured uncertainty. Therefore, there are a large number of conceivable criteria for robust performance.

In this section, we will consider the robust performance criterion expressed in terms of FRM specifications, and commonly used in  $H_\infty$  control theory [79]. Consider Figure 5.41 where the plant  $G$  is perturbed by a multiplicative perturbation according to (5.3.27). In addition to ensuring robust stability w.r.t. the multiplicative uncertainty,

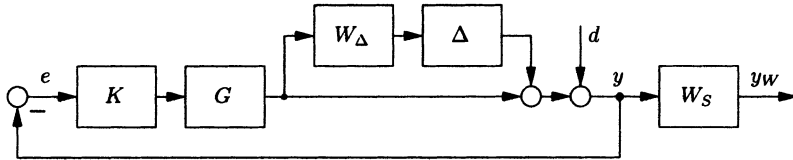


Figure 5.41. Weighted controller structure

we would like to achieve good disturbance attenuation properties for the perturbed system, and therefore introduce a weighting function  $W_S$ , whose inverse is an upper bound on the perturbed sensitivity function  $\tilde{S}$ , i.e.

$$|\tilde{S}(j\omega)| < \partial \mathcal{B}_S(\omega) = |W_S(j\omega)|^{-1}, \quad (5.3.39)$$

or equivalently,

$$\|W_S(j\omega)\tilde{S}(j\omega)\|_\infty < 1, \quad (5.3.40)$$

where

$$\tilde{S}(s) = \frac{1}{1 + K(s)G(s)(1 + W_\Delta(s)\Delta(s))}.$$

From (5.3.39) or (5.3.40), the following robust performance condition may be derived [79]:

$$|W_\Delta(j\omega)T(j\omega)| + |W_S(j\omega)S(j\omega)| < 1, \quad \forall \omega \in [0; \infty). \quad (5.3.41)$$

If  $G$  in Figure 5.41 also depends on uncertain plant parameters  $q \in Q$ , then the robust performance specification is extended to

$$|W_\Delta(j\omega)T(j\omega, q)| + |W_S(j\omega)S(j\omega, q)| < 1, \quad \forall \omega \in [0; \infty), \quad \forall q \in Q. \quad (5.3.42)$$

### *Limiting Factors of Attainable Performance*

In the preceding discussion, stability and performance specifications in terms of the FRMs of various transfer functions were reviewed. However, some of the desired stability and performance specifications are conflicting and require compromises. To provide some insight regarding the compromises that must be made, some of the limiting factors of the attainable closed-loop performance are reviewed here. These limitations are due to the relation of the sensitivity functions and the pole-zero locations of the open-loop transfer function as well as its relative degree.

An algebraic constraint for the performance of the closed-loop system is the relation between the sensitivity and the complementary sensitivity function:

$$S + T = 1, \quad (5.3.43)$$

which requires

$$|S(j\omega)| + |T(j\omega)| \geq 1. \quad (5.3.44)$$

Therefore, it is not possible to have arbitrarily good tracking and noise rejection, (i.e. cannot have both  $|S(j\omega)| \ll 1$  and  $|T(j\omega)| \ll 1$ ) at a given frequency.

Furthermore, increasing demands on the magnitude of  $S$  (i.e. making  $|S(j\omega)| \ll 1$ ) at low frequencies results in magnitude amplification at high frequencies. This effect is termed the *waterbed effect* and implies a reduction of the Nyquist-stability margin  $\rho_S$  corresponding to (5.3.24). For systems with relative degree of at least two, the waterbed effect can be quantified by *Bode's integral theorem*, often referred to as the *area formula*, which is [90],[55]

$$\int_0^{\infty} \log |S(j\omega)| d\omega = \pi \log e^{\sum_i \operatorname{Re}(s_i)}. \quad (5.3.45)$$

In (5.3.45),  $\{s_i\}$  is the set of unstable poles of the open-loop transfer function. The integral of the logarithmic magnitude of the sensitivity function is a constant and does not depend on the controller parameters. If all poles of  $L$  are stable, then the right hand side of (5.3.45) equals zero [55]. In this case, the area below  $\log |S(j\omega)| = 0$ , termed the negative area, equals the positive area, which is above  $\log |S(j\omega)| = 0$  as shown in Figure 5.42. This clearly shows that disturbance attenuation in some

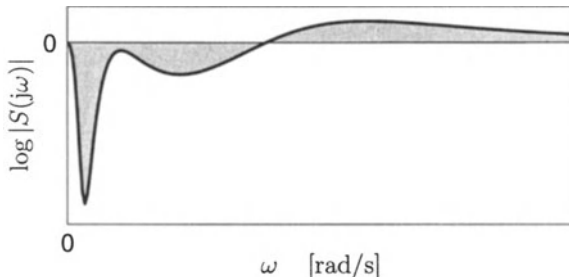


Figure 5.42. Graphic interpretation of Bode's integral theorem

frequency range must be accompanied by disturbance amplification in another frequency range. If  $L$  has unstable poles, the right hand side of (5.3.45) equals a positive number that depends on the number and magnitude of the unstable poles. Then, the ratio of disturbance attenuation and amplification (i.e. the ratio of negative and positive area) decreases, which means that either less disturbance attenuation can be achieved or greater disturbance amplification must occur at some frequencies.

### Quantification of Frequency Response Magnitude Specifications

A number of FRM specifications were reviewed to show that they provide a convenient way of rating the stability and performance of both nominal and uncertain systems, and

to motivate incorporating FRM specifications into the framework of parameter space. All of these specifications result in ensuring that the FRM of a transfer function (i.e. sensitivity functions  $S$ ,  $T$ ,  $S_G$  and  $S_K$ , model regulator and model matching transfer functions  $H$  and  $E$ ) is less than a bound specification as summarized here:

$$\left. \begin{array}{l} |S(j\omega)| < \partial\mathcal{B}_S(\omega) \\ |T(j\omega)| < \partial\mathcal{B}_T(\omega) \\ |S_K(j\omega)| < \partial\mathcal{B}_{S_K}(\omega) \\ |S_G(j\omega)| < \partial\mathcal{B}_{S_G}(\omega) \\ |H(j\omega)| < \partial\mathcal{B}_H(\omega) \\ |E(j\omega)| < \partial\mathcal{B}_E(\omega) \end{array} \right\} \forall\omega \in [\omega^-; \omega^+]. \quad (5.3.46)$$

By choosing appropriate bounds, as shown in the preceding review, these specifications can be used to guarantee a number of performance criteria (e.g. tracking, disturbance attenuation, noise rejection, model matching) and to guarantee robustness for both parametric and unstructured uncertainty. The specifications can be formulated for different frequency ranges  $[\omega^-, \omega^+]$  as appropriate to meet design requirements and to make compromises between the limitations in attainable performance.

### Beta-stability

The definition of  $\mathcal{B}$ -stability is analogous to  $\Gamma$ - and  $\Theta$ -stability considered in Chapter 4 and Section 5.1, respectively.

As discussed previously in this section, stability and performance specifications may be clearly represented by magnitude bounds on the four sensitivity functions  $S$ ,  $T$ ,  $S_G$  and  $S_K$  and on the model regulator and model matching transfer functions  $H$  and  $E$ , or, more generally, by magnitude bounds on an arbitrary transfer function  $M$ . Now, a transfer function is considered to be  $\mathcal{B}$ -stable if its frequency response magnitude (FRM) lies within a desired region in the FRM-plane referred to as  $\mathcal{B}$ . The region  $\mathcal{B}$  is bounded by the  $\mathcal{B}$ -boundary

$$\partial\mathcal{B}(\omega) = |B(j\omega)|, \quad \forall\omega \in [\omega^-; \omega^+]. \quad (5.3.47)$$

Here, for the sake of simplicity, the bound  $\partial\mathcal{B}$  is assumed to be the FRM of  $B(s)$ , where  $B(s)$  is assumed to be a rational transfer function in  $s$  with real coefficients. However,  $\partial\mathcal{B}$  could be a piecewise curve in the FRM-plane composed of multiple, not necessarily continuous, segments. Assuming non-negative real frequencies  $\omega$ , the upper and lower bounds  $\omega^+$  and  $\omega^-$  may take on values between 0 and  $\infty$ . Fig. 5.43 shows some examples of  $\mathcal{B}$ -stability regions for various  $\mathcal{B}$ -specifications.

The notion of  $\mathcal{B}$ -stability can be applied to both LTI systems and parametric LTI systems. For the LTI case, a nominal transfer function  $G(s)$  is called  $\mathcal{B}$ -stable in the interval  $[\omega^-; \omega^+]$ , if

$$|G(j\omega)| \subset \mathcal{B}, \quad \forall\omega \in [\omega^-; \omega^+], \quad (5.3.48)$$

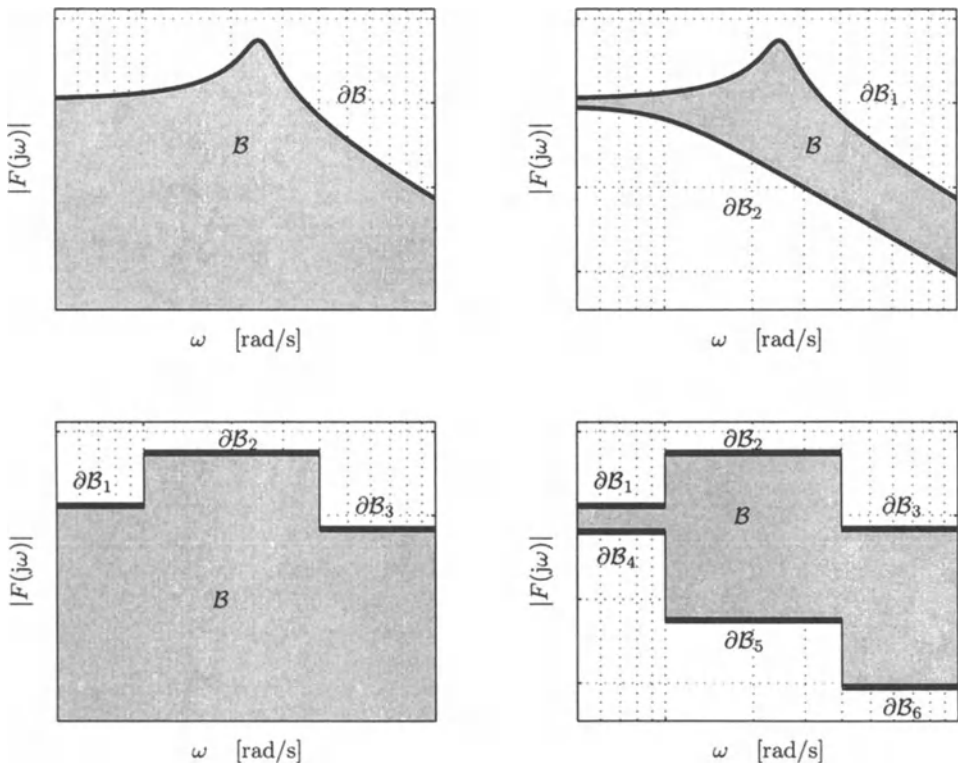


Figure 5.43. Representation of various  $\mathcal{B}$ -stability regions in the FRM plane

with  $\omega^- \in \mathbb{R}_0^+$ ,  $\omega^+ \in \mathbb{R}_0^+$ .

In the case of a parametric LTI system with varying or uncertain parameters  $\mathbf{q}$ , where  $\mathbf{q}$  is included in a predefined operating domain  $Q$ , the family of transfer functions  $\mathcal{G}(j\omega, Q)$  defined by (5.2.1) is called  $\mathcal{B}$ -stable if

$$\mathcal{G}(j\omega, Q) \subset \mathcal{B} \quad \forall \omega \in [\omega^-; \omega^+]. \quad (5.3.49)$$

### *Application of $\mathcal{B}$ -stability*

The notion of  $\mathcal{B}$ -stability can be applied to both robustness analysis and robust controller design.

- i. *Analysis:* for robustness analysis, the task is to determine the parameter set  $Q_{\mathcal{B}}$  for which robust  $\mathcal{B}$ -stability is satisfied. This set is defined by:

*Definition 5.31*

$$Q_B = \{ \mathbf{q} \mid |G(j\omega, \mathbf{q})| \subset \mathcal{B}, \forall \omega \in [\omega^-; \omega^+] \}. \quad (5.3.50)$$

□

If the operating domain  $Q$  is included in  $Q_B$ , i.e.  $Q \subseteq Q_B$ , then the family of transfer functions  $\mathcal{G}(j\omega, Q)$  is robustly  $\mathcal{B}$ -stable.

- ii. *Design:* for robust controller design, the task is to determine the set of controller parameters  $K_B$  such that for all controller parameters  $\mathbf{k} \in K_B$  and for a predefined operating domain  $Q$  the family of closed-loop transfer functions  $\mathcal{G}(j\omega, Q, K_B)$  is  $\mathcal{B}$ -stable. This set is defined by:

*Definition 5.32*

$$K_B = \{ \mathbf{k} \mid |\mathcal{G}(j\omega, Q, \mathbf{k})| \subset \mathcal{B}, \forall \omega \in [\omega^-; \omega^+] \} \quad (5.3.51)$$

□

Thereby, in a first design step,  $K_B$  is determined assuming a multi-model approach, meaning that only a finite number of operating points (representatives) are considered, e.g. the vertices of  $Q$ . Then, after having selected a controller  $\mathbf{k} \in K_B$  in a subsequent analysis step, the set  $Q_B$  is determined. If  $Q \subseteq Q_B$ , then robust  $\mathcal{B}$ -stability is satisfied for all  $\mathbf{q} \in Q$ .

In the sequel, we do not distinguish between analysis and design since the mathematics are the same. Therefore, except when otherwise stated, the parameter vector  $\mathbf{q}$  applies for both controller and plant parameters.

## 5.4 Mapping of Frequency Response Magnitude Specifications into Parameter Space

In this section, the mathematical equations required to map the FRM specifications of the previous section into parameter space are developed. This development is motivated by the mean value theorem [61]. Consider the magnitude of a continuous transfer function  $G(j\omega, q_1)$  at a fixed frequency  $\omega = \omega^*$  given by

$$g(q_1) = |G(j\omega^*, q_1)|, \quad (5.4.1)$$

where  $q_1 \in \mathbb{R}$ . The mean value theorem of continuous functions states that the function  $g(q_1)$ , being continuous in the interval  $[a; b]$  with  $g(a) \neq g(b)$ , takes on all values in-between  $g(a)$  and  $g(b)$ . Now, let  $g(a) < |B(j\omega^*)| < g(b)$ , where  $|B(j\omega^*)|$  represents an

FRM boundary (e.g. separating a desired region from an undesired region). Then, for continuous variation of  $q_1$  between  $a$  and  $b$ , the boundary  $|B(j\omega^*)|$  is crossed.

From this consideration, the boundary crossing theorem for frequency response magnitude specifications may be derived [159]:

*Theorem 5.33*

The set of transfer functions

$$\mathcal{G}(j\omega, Q_B) = \{G(j\omega, \mathbf{q}) \mid \mathbf{q} \in Q_B\} \quad (5.4.2)$$

is  $\mathcal{B}$ -stable if and only if:

1. There exists a  $\mathcal{B}$ -stable transfer function  $G(j\omega) \in \mathcal{G}(j\omega, Q_B)$ .
2.  $|\mathcal{G}(j\omega, Q_B)| \neq \partial\mathcal{B}$  for all  $\omega \in [\omega^-, \omega^+]$ .

□

Theorem 5.33 states that starting from a  $\mathcal{B}$ -stable transfer function  $G(j\omega, \mathbf{q}_0)$ ,  $\mathbf{q}_0 \in Q_B$ ,  $\mathcal{B}$ -stability is preserved for continuous variation of  $\mathbf{q}_0$  until a boundary  $\partial\mathcal{B}$  is crossed. If the boundary  $\partial\mathcal{B}$  consists of multiple segments  $\partial\mathcal{B}_i$ , then Condition 2. applies to all boundary segments.

Now, consider the FRM of the transfer function  $G(j\omega, \mathbf{q})$ , which shall remain in the  $\mathcal{B}$ -stability region bounded by  $\partial\mathcal{B} = |B(j\omega)|$ . A generalized  $\mathcal{B}$ -specification of this type can be given by the inequality

$$|G(j\omega, \mathbf{q})| < |B(j\omega)|, \quad \forall \omega \in [\omega^-, \omega^+]. \quad (5.4.3)$$

*Remark 5.34*

The generalized  $\mathcal{B}$ -specification given in (5.4.3) can be given in the form of an equivalent  $\infty$ -norm specification, given by

$$\|G(j\omega, \mathbf{q}) B(j\omega)^{-1}\|_\infty < 1. \quad (5.4.4)$$

□

*Remark 5.35*

Instead of an upper bound, a lower bound may also be assumed as suggested in Figure 5.43, i.e.

$$|G(j\omega, \mathbf{q})| > |B(j\omega)|, \quad \forall \omega \in [\omega^-, \omega^+]. \quad (5.4.5)$$

□

*Remark 5.36*

For systems where the dynamics have a significant dependence on the uncertain parameters, it might be useful to adapt the boundary  $\partial\mathcal{B}$  to the plant parameters, i.e.

$$\partial\mathcal{B}(\omega, \mathbf{q}) = |B(j\omega, \mathbf{q})| . \quad (5.4.6)$$

□

For mapping the generalized  $\mathcal{B}$ -specification (5.4.3) into parameter space, the task is to determine the parameter set  $Q_{\mathcal{B}}$  such that  $\mathcal{G}(j\omega, Q_{\mathcal{B}})$  is  $\mathcal{B}$ -stable. To establish the mapping equations for (5.4.3), it suffices to consider two mathematical conditions, the *point condition* and the *tangent condition*:

- The *point condition* is applied when  $|G(j\omega, \mathbf{q})|$  starts or ends on the boundary  $\partial\mathcal{B}$  or runs across a beginning or an end point of  $\partial\mathcal{B}$  or a boundary segment  $\partial\mathcal{B}_i$ .
- The *tangent condition* allows for the mapping of touching points, i.e. the points where  $|G(j\omega, \mathbf{q})|$  becomes tangent to a smooth branch of the boundary  $\partial\mathcal{B}$ .

### The Point Condition

For the point condition w.r.t. an arbitrarily fixed frequency  $\omega = \omega^*$ , the set of parameters  $Q_{\mathcal{B}} \subseteq \mathbb{R}^2$  is determined by finding the boundary  $\partial Q_{\mathcal{B}}$  such that

$$|G(j\omega^*, \mathbf{q})| = |B(j\omega^*)|, \quad \forall \mathbf{q} \in \partial Q_{\mathcal{B}}, \quad (5.4.7)$$

i.e. such that the FRM of  $G$  and  $B$  have a common point at  $\omega^*$ . The boundary  $\partial Q_{\mathcal{B}}$  divides the  $(q_1, q_2)$ -plane into a finite number of regions. All of these regions have to be checked by applying the boundary crossing theorem for FRM specifications, Theorem 5.33. Rearranging and squaring (5.4.7) yields

$$\xi := \operatorname{Re} \left( \frac{G(j\omega, \mathbf{q})}{B(j\omega)} \right)^2 + \operatorname{Im} \left( \frac{G(j\omega, \mathbf{q})}{B(j\omega)} \right)^2 - 1 = 0, \quad (5.4.8)$$

where  $\xi = \xi(\omega, \mathbf{q})$ . Let

$$\xi(\omega, \mathbf{q}) = \frac{p_1(\omega, \mathbf{q})}{d(\omega, \mathbf{q})}. \quad (5.4.9)$$

Further, assuming  $d(\omega, \mathbf{q}) \neq 0$  (this condition must be verified separately), the point condition can be stated as follows: for a fixed  $\omega = \omega^*$  find  $\mathbf{q}$ , i.e.  $q_1$  and  $q_2$ , such that

$$p_1(\omega^*, \mathbf{q}) := 0. \quad (5.4.10)$$

Equation (5.4.10) is a polynomial equation in two variables and may be interpreted as a real curve in implicit form depending on two parameters  $q_1$  and  $q_2$ . The corresponding curve may be plotted by gridding one parameter, e.g.  $q_1 = q_1^*$ ; the parameter value for  $q_2$  then results from computation of the roots of  $p_1(q_1^*, q_2) = 0$ . The number of real solutions may vary since conjugate complex solutions for  $q_2$  may exist. To take this into account, it is useful to determine the values of  $q_1$  for which the number of solutions changes, which can then be used for intelligent gridding. These values of  $q_1$  are determined by computation of the roots of the discriminant

$$\operatorname{discr}_{q_2}(p_1(\omega^*, q_1, q_2)) = \operatorname{res}_{q_2} \left( p_1(\omega^*, q_1, q_2), \frac{\partial p_1(\omega^*, q_1, q_2)}{\partial q_2} \right) = 0. \quad (5.4.11)$$

### The Tangent Condition

For mapping the marginal condition that occurs when  $|G(j\omega, \mathbf{q})|$  touches (i.e. is tangent to) the boundary  $|B(j\omega)|$  for a fixed frequency  $\omega = \omega^*$ , (5.4.10) must hold as well as

$$\frac{\partial |G(j\omega, \mathbf{q})|}{\partial \omega} = \frac{\partial |B(j\omega)|}{\partial \omega}. \quad (5.4.12)$$

It is easy to show that the solution of (5.4.12) is equivalent to the solution of

$$\frac{\partial \xi(\omega, \mathbf{q})}{\partial \omega} = \frac{\partial}{\partial \omega} \left( \frac{p_1(\omega, \mathbf{q})}{d(\omega, \mathbf{q})} \right) = 0. \quad (5.4.13)$$

Further, by applying the quotient rule it holds that

$$\left( \frac{p_1}{d} \right)' = \frac{p_1' d - p_1 d'}{d^2}. \quad (5.4.14)$$

Again, assuming  $d \neq 0$ , then if (5.4.10) is satisfied (i.e.  $p_1 = 0$ ), it can be seen from (5.4.14) that (5.4.13) is satisfied if  $p_1' = 0$ . Letting

$$p_2(\omega, \mathbf{q}) = p_1' = \frac{\partial p_1(\omega, \mathbf{q})}{\partial \omega}, \quad (5.4.15)$$

the condition for a touching point, i.e. the tangent condition can be stated as follows:  
For a fixed  $\omega = \omega^*$ , find  $\mathbf{q}$  such that

$$\begin{aligned} p_1(\omega, \mathbf{q}) &= 0, \\ p_2(\omega, \mathbf{q}) &= 0. \end{aligned} \quad (5.4.16)$$

Note that we do not want to map touching points only at discrete frequencies, but rather the complete branch of the boundary for  $\omega \in [\omega^-; \omega^+]$  is mapped into parameter space. This is done by algebraically eliminating either  $\omega$ ,  $q_1$  or  $q_2$ . The mathematics used to map the point and tangent conditions, i.e. Equations (5.4.10) and (5.4.16) are described in Appendix A.

For the case of multiple  $\mathcal{B}$ -specifications or additional specifications (e.g.  $\Gamma$ -specifications), the intersection of all of the individual regions in the parameter plane that satisfy the individual specifications form the desired parameter region. Thus, multiple specifications can be addressed simultaneously (e.g. sensitivity, loci and eigenvalue specifications) when designing controllers or analyzing uncertain plant parameters for parametric LTI systems.

### Examples

The mapping of frequency response magnitude specifications is demonstrated by means of two examples; an uncertain mass-spring-damper-system and the example introduced in Section 5.1 and Example 5.19.

*Example 5.37 (Uncertain mass-spring-damper-system)*

Consider the transfer function of a mass-spring-damper-system with transfer function

$$G(s, \omega_0, D) = \frac{\omega_0^2}{s^2 + 2D\omega_0 s + \omega_0^2}, \quad (5.4.17)$$

with uncertain parameters  $D \in \mathbb{R}^+$  and  $\omega_0 \in \mathbb{R}^+$ . We are looking for parameter values  $D$  and  $\omega_0$  for which the magnitude plot  $|G(j\omega, \omega_0, D)|$  resides between a lower and upper bound  $|G^-(j\omega)|$  and  $|G^+(j\omega)|$ , respectively, as shown in the left plot of Figure 5.44, i.e.

$$|G^-(j\omega)| < |G(j\omega, \omega_0, D)| < |G^+(j\omega)|.$$

The selected  $\mathcal{B}$ -boundaries are the magnitudes of the two transfer functions

$$\begin{aligned} G^-(s) &= \kappa_1 G(s, \omega_{01}, D_1) = \frac{90}{s^2 + 14s + 100}, \\ G^+(s) &= \kappa_2 G(s, \omega_{02}, D_2) = \frac{1375}{2(s^2 + 5s + 625)}, \end{aligned}$$

i.e.

$$\begin{aligned} \partial\mathcal{B}_1(\omega) &= |G^-(j\omega)|, \\ \partial\mathcal{B}_2(\omega) &= |G^+(j\omega)|, \end{aligned}$$

with parameter values

$$\begin{aligned} \kappa_1 &= 9/10, & D_1 &= 7/10, & \omega_{01} &= 10, \\ \kappa_2 &= 11/10, & D_2 &= 1/10, & \omega_{02} &= 25. \end{aligned}$$

Since it holds that

$$\lim_{\omega \rightarrow 0} G(\omega_0, D, j\omega) = 1, \quad \lim_{\omega \rightarrow 0} G^-(j\omega) = \kappa_1, \quad \lim_{\omega \rightarrow 0} G^+(j\omega) = \kappa_2,$$

it also holds that the locus  $G(j\omega, \omega_0, D)$  and the upper and lower bounds  $\partial\mathcal{B}_1(\omega)$  and  $\partial\mathcal{B}_2(\omega)$ , respectively, do not depend on  $\omega_0$  and  $D$ . The three loci start on the real axis at 1,  $\kappa_2$  and  $\kappa_1$ , respectively. For  $\kappa_2 \neq 1$  and  $\kappa_1 \neq 1$ , no common starting point of locus and upper or lower bound, respectively, exists. Further, the three loci  $G(j\omega, \omega_0, D)$ ,  $G^+(j\omega)$  and  $G^-(j\omega)$  end at the origin, since

$$\lim_{\omega \rightarrow \infty} G(j\omega, \omega_0, D) = \lim_{\omega \rightarrow \infty} G^+(j\omega) = \lim_{\omega \rightarrow \infty} G^-(j\omega) = 0. \quad (5.4.18)$$

Thus, the locus has a common point with its upper and lower bound for  $\omega \rightarrow \infty$ . Applying the point condition (5.4.10), the two results for upper and lower bound are

$$\omega_0 = \omega_{01}\sqrt{\kappa_1} \quad \text{and} \quad \omega_0 = \omega_{02}\sqrt{\kappa_2}.$$

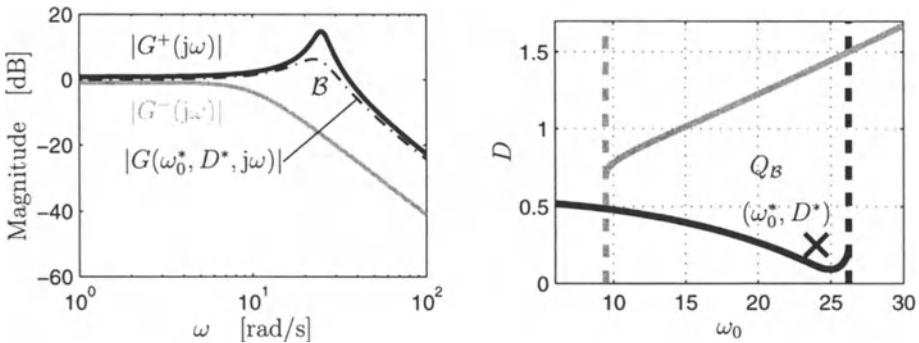


Figure 5.44. Upper and lower bound in parameter space

The two solutions, i.e. the two straight lines are plotted with dashed linestyle in the right plot of Figure 5.44. In the next step, the tangent conditions for upper and lower bounds are formulated. According to (5.4.16), the tangent condition for the lower bound ( $i = 1$ ) and upper bound ( $i = 2$ ) are:

$$\begin{aligned} p_1(\omega, \omega_0, D) &= \omega^4 \omega_0^4 - 2\omega^2 \omega_0^4 \omega_0^2 + 4\omega^2 D_i^2 \omega_0^4 \omega_0^2 - \omega^4 \kappa_i^2 \omega_0^4 \\ &\quad + 2\omega^2 \kappa_i^2 \omega_0^2 \omega_0^4 - 4\omega^2 D^2 \kappa_i^2 \omega_0^2 \omega_0^4 + \omega_0^4 \omega_0^4 - \kappa_i^2 \omega_0^4 \omega_0^4 \\ p_2(\omega, \omega_0, D) &= 2(\omega^2 \omega_0^4 - \omega_0^4 \omega_0^2) + 2D_i^2 \omega_0^4 \omega_0^2 - \omega^2 \kappa_i^2 \omega_0^4 \\ &\quad + \kappa_i^2 \omega_0^2 \omega_0^4 - 2D^2 \kappa_i^2 \omega_0^2 \omega_0^4. \end{aligned}$$

In this case, only even powers of  $\omega$ ,  $\omega_0$  and  $D$  appear in  $p_1$  and  $p_2$ . Therefore, we may substitute  $\bar{\omega} = \omega^2$ ,  $\bar{\omega}_0 = \omega_0^2$  and  $\bar{D} = D^2$ . Note that  $\bar{\omega}$ ,  $\bar{\omega}_0$  and  $\bar{D}$  still enter the coefficients of  $p_1$  and  $p_2$  in a polynomial way. The computation of the parameter space boundaries is done according to Appendix A with the results shown in solid linestyle in the right plot of Figure 5.44.

For the  $\mathcal{B}$ -stable point  $(\omega_0^*, D^*) \in Q_{\mathcal{B}}$  marked with  $\times$  in the right plot of Figure 5.44, the corresponding magnitude plot is drawn in the left plot with dashed-dotted linestyle. As expected, the magnitude plot resides between lower and upper bound.

□

### Example 5.38

The closed-loop system described in Example 5.19 shall be analyzed with respect to the loop-shaping FRM criteria “robust stability” and “nominal performance”. Consider the single-loop unity feedback system in Figure 5.1 with open-loop transfer function  $L(s, q)$  according to (5.1.1), sensitivity function  $S(s, q)$  according to (5.3.3) and complementary sensitivity function  $T(s, q)$  according to (5.3.2). In addition to parametric uncertainty captured in  $q_1$  and  $q_2$ , a multiplicative perturbation model according to (5.3.27) is assumed to account for unmodelled dynamics. The weighting function of the

multiplicative perturbation model is selected as

$$W_\Delta(s) = h_g \frac{s + \omega_T l_g}{s + \omega_T h_g},$$

where  $l_g = 0.2$ ,  $h_g = 5$  and  $\omega_T = 2\pi$  [rad/s], meaning that for low frequencies ( $\omega < 2\pi$  [rad/s]) the model error might be up to 20 % and for high frequencies ( $\omega > 2\pi$  [rad/s]) up to 500 %. Furthermore, to account for good disturbance attenuation properties, we select an upper bound for the magnitude plot of the sensitivity function  $S$ , i.e.

$$\partial\mathcal{B}_S(\omega) = \left| h_g \frac{j\omega + \omega_T l_g}{j\omega + \omega_T h_g} \right|$$

where  $l_g = 0.5$ ,  $h_g = 2$  and  $\omega_T = 0.1\pi$  [rad/s]. This means that for low frequencies, disturbances shall be attenuated to at least 50 % and for frequencies  $\omega > 0.1\pi$  [rad/s] disturbance amplification shall be limited to a maximum of 200 %. The corresponding required Nyquist-stability margin is at least  $1/h_g = 0.5$ .

To satisfy the above-mentioned specifications, three conditions have to be taken into consideration:

- i. Hurwitz-stability of the characteristic polynomial, i.e. the denominator polynomial of (5.3.3) or (5.3.2), respectively, must be proven. Therefore, in the first step the Hurwitz boundaries are mapped into parameter space, i.e. in the plane  $(q_1, q_2)$ . The resulting Hurwitz-stable region is

$$Q_H = \{\mathbf{q} \mid \text{Re}(\text{Roots}(\text{num}(1 + G(s, \mathbf{q})))) < 0\}.$$

- ii. The robust stability condition according to (5.3.34) requires (besides Hurwitz-stability) a magnitude specification on  $T$ . Mapping this condition into parameter space yields the region

$$Q_{\mathcal{B}_T} = \{\mathbf{q} \mid |W_\Delta(j\omega)T(j\omega, \mathbf{q})| < 1, \text{ for } \omega \in [0; \infty)\}.$$

- iii. The nominal performance specification requires (besides Hurwitz-stability) a magnitude specification on  $S$ . The corresponding region in parameter space is defined as

$$Q_{\mathcal{B}_S} = \{\mathbf{q} \mid |S(j\omega, \mathbf{q})| < \partial\mathcal{B}_S(\omega), \text{ for } \omega \in [0; \infty)\}.$$

The resulting Hurwitz-,  $\mathcal{B}_S$ - and  $\mathcal{B}_T$ -stable regions in the parameter plane  $(q_1, q_2)$  are shown in Figure 5.45. The parameter region for which robust stability w.r.t. parametric and unstructured uncertainty can be guaranteed is the intersection of Hurwitz- and  $\mathcal{B}_T$ -stable region, i.e.  $Q_H \cap Q_{\mathcal{B}_T}$ . Good disturbance attenuation properties are guaranteed for all parameter values  $\mathbf{q} \in Q_H \cap Q_{\mathcal{B}_S}$ . Finally, the  $\mathcal{B}$ -stable region might be intersected with the  $\Gamma$ - and  $\Theta$ -stable regions to additionally account for good damping and phase and magnitude margin. The parameter values for which all  $\Gamma$ -,  $\Theta$ - and  $\mathcal{B}$ -specifications are satisfied simultaneously is defined by

$$Q_\Gamma \cap Q_\Theta \cap Q_{\mathcal{B}},$$

where

$$Q_{\mathcal{B}} = Q_{\mathcal{B}_S} \cap Q_{\mathcal{B}_T}.$$

□

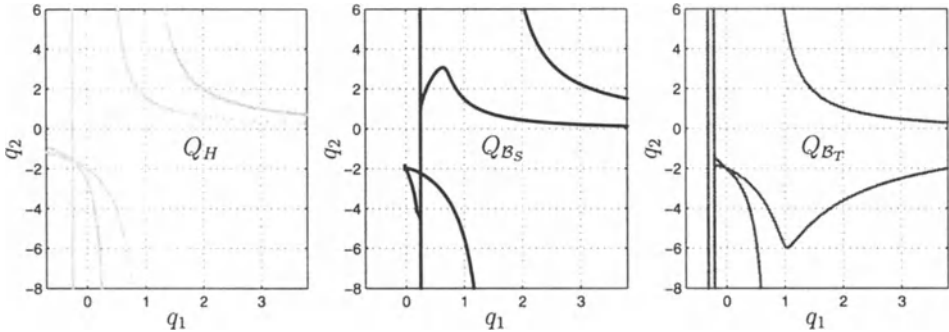


Figure 5.45. Individual parameter regions

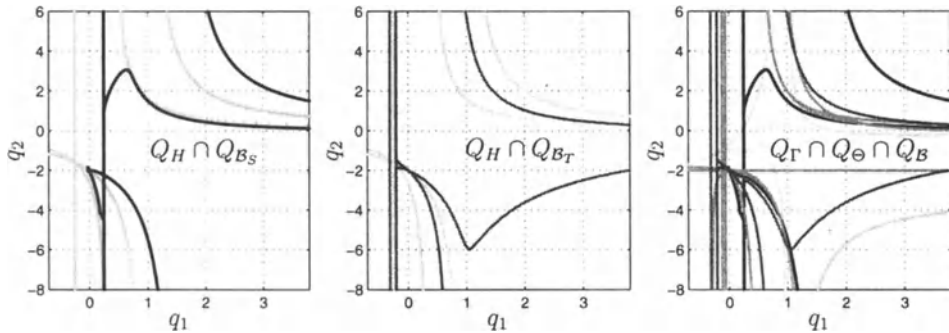


Figure 5.46. Nominal performance (left), robust stability (middle) and simultaneous  $\Gamma$ -,  $\Theta$ - and  $B$ -stability (right) in parameter space

For more details about the mapping of frequency response magnitude specifications into parameter space the reader is referred to [158].

## 5.5 MIMO Systems

In this section, we describe methods to use the parameter space approach to analyze and design control systems for multivariable or multi-input, multi-output (MIMO) systems. While specifications on eigenvalues can be expressed by the characteristic polynomial for both SISO and MIMO systems (see Section 1.5), there are many ways to treat MIMO systems in the frequency domain. Some of the specifications and design techniques for MIMO systems are derived from their SISO counterparts, while the more potential ones take the multivariable nature into account. There has been an enormous interest in the

design of multivariable control systems in the last decades, especially frequency domain approaches [78],[86],[137]. We do not intend to give a comprehensive treatment of all the aspects of multivariable feedback design and refer the reader to the cited literature. Thus, the scope of this section is limited to the presentation of the basic concepts and some examples. As the main result, this section presents the mapping equations for widely used MIMO specifications, which enable the incorporation of these specifications into the parameter space approach.

The model description is given as a transfer matrix representation

$$\mathbf{y} = \mathbf{G}(s, q)\mathbf{u}, \quad (5.5.1)$$

where  $\mathbf{u} \in \mathbb{R}^m$  and  $\mathbf{y} \in \mathbb{R}^p$  are vectors of signals, or as a parametric state space model

$$\begin{bmatrix} \dot{\mathbf{x}} \\ \mathbf{y} \end{bmatrix} = \begin{bmatrix} \mathbf{A}(q) & \mathbf{B}(q) \\ \hline \mathbf{C}(q) & \mathbf{D}(q) \end{bmatrix} \begin{bmatrix} \mathbf{x} \\ \mathbf{u} \end{bmatrix}.$$

For ease of presentation, we consider only systems with the same number of inputs and outputs, i.e.  $m = p$ . Nevertheless, all results are valid for non-square systems with  $m \neq p$ .

### SISO Methods

For SISO control systems, classical gain and phase margins are good measures of robustness. Furthermore, loop-shaping techniques provide a systematic way to attain good robustness margins and desired closed-loop performance. The methods introduced in Sections 5.1–5.4 facilitate such a design. However, the classical gain and phase margins are not reliable measures of robustness for multivariable systems.

The simplest approach to multivariable design is to ignore its multivariable nature and just look at one pair of input and output variables at a time. In that manner, we can apply all SISO methods described in the previous sections of this chapter. A classical design procedure using this idea for multivariable systems is the sequential loop closing method, where a SISO controller is designed for a single loop. After this design has been done successfully, that loop is closed and another SISO controller is designed for a second pair of variables, and so on.

#### *Example 5.39*

Consider the following plant

$$\mathbf{G}(s) = \frac{1}{(s+1)(s+2)} \begin{bmatrix} 2 & -2s \\ s & 3s+2 \end{bmatrix}. \quad (5.5.2)$$

In the first step, we design a constant gain controller  $k_{11}(s) = k_1$ . The transfer function seen by this controller is  $g_{11}(s) = 2/((s+1)(s+2))$ . Setting  $k_1 = 1$  leads to a stable

transfer function. After closing this loop, the transfer function seen by a controller from output 2 to input 2 is

$$\tilde{g}_{22}(s) = g_{22}(s) - \frac{g_{12}(s)k_{11}(s)g_{21}(s)}{1 + k_{11}(s)g_{11}(s)} = \frac{3s + 4}{s^2 + 3s + 4}.$$

A stabilizing controller for this transfer function is  $k_{22}(s) = 1$ . The resulting decentralized controller is thus given by the identity matrix  $\mathbf{K}(s) = \mathbf{I}$ . We will come back to this example with a better solution in Example 5.41 and Example 5.43.  $\square$

This method has a number of weaknesses. During the controller design, the resulting scalar transfer function for the  $i$ -th step might be non-minimal-phase, although all members of  $\mathbf{G}(s)$  are minimal-phase transfer functions. This might pose a severe constraint for the control design, since non-minimal-phase transfer functions limit the maximal usable gain.

## MIMO Specifications

Apart from stability, the most important objective of a control system is to achieve certain performance specifications. One way to describe these performance specifications is to use the size of certain signals of interest. For example, the performance of a regulator could be measured by the size of the error between the reference and measured signals. The size of signals can be defined mathematically using norms. Common norms are the Euclidean vector norms

$$\|\mathbf{x}\|_1 := \sum_{i=1}^n |x_i|, \quad \|\mathbf{x}\|_2 := \sqrt{\sum_{i=1}^n |x_i|^2}, \quad \|\mathbf{x}\|_\infty := \max_{1 \leq i \leq n} |x_i|.$$

The performance of a control system with input and output signals measured by one of the above norms (not necessarily the same) can be evaluated by the induced matrix norms. The most prominent matrix norms used in control theory are the  $H_2$ - and  $H_\infty$ -norms, which will be considered in this section. A detailed treatment of mapping MIMO specifications into parameter space is given in [151].

### $H_2$ -norm

The  $H_2$ -norm is a widely used performance measure that allows to incorporate time-domain specifications into control design. The  $H_2$ -norm arises, for example, in the following physically meaningful situation. Let the system input be zero-mean stationary white noise of unit covariance. Then, at steady state, the variance of the output is given by the square of the  $H_2$ -norm.

The  $H_2$ -norm is defined as

$$\|\mathbf{G}\|_2 := \left( \text{trace} \frac{1}{2\pi} \int_{-\infty}^{\infty} \mathbf{G}(j\omega) \mathbf{G}(j\omega)^* d\omega \right)^{1/2},$$

where  $\mathbf{G}(s)$  is a stable transfer matrix and  $*$  denotes the complex conjugate transpose of a matrix. The above norm definition can be used for generic square integrable functions on the imaginary axis and is then called  $L_2$ -norm. Thus, strictly speaking without the stability condition, we are mapping the  $L_2$  norm instead of the  $H_2$ -norm.

The  $H_2$ -norm defined above is finite if and only if the transfer matrix  $\mathbf{G}(s)$  is strictly proper, i.e. the direct feedthrough matrix  $\mathbf{D} = 0$  for a state space realization of  $\mathbf{G}(s)$ . Hence, we assume  $\mathbf{D} = 0$  in the following presentation.

The  $H_2$ -norm can be expressed as [58]

$$\begin{aligned}\|\mathbf{G}\|_2^2 &= \text{trace} \left( \mathbf{C} \int_0^\infty e^{\mathbf{A}t} \mathbf{B} \mathbf{B}^T e^{\mathbf{A}^T t} dt \mathbf{C}^T \right) \\ &= \text{trace} (\mathbf{C} \mathbf{W}_c \mathbf{C}^T),\end{aligned}\quad (5.5.3)$$

where

$$\mathbf{W}_c = \int_0^\infty e^{\mathbf{A}t} \mathbf{B} \mathbf{B}^T e^{\mathbf{A}^T t} dt$$

is the controllability Gramian of the realization. The controllability Gramian can be obtained from the Lyapunov equation

$$\mathbf{A} \mathbf{W}_c + \mathbf{W}_c \mathbf{A}^T + \mathbf{B} \mathbf{B}^T = 0. \quad (5.5.4)$$

Equation (5.5.4) is affine in the entries of the unknown matrix  $\mathbf{W}_c = \mathbf{W}_c^T$ . This system of  $\frac{1}{2}n(n+1)$  linear equations, where  $n$  is the system order, can be solved for any parametric dependency of  $\mathbf{A}(\mathbf{q})$ ,  $\mathbf{C}(\mathbf{q})$ . Thus, the parametric controllability Gramian  $\mathbf{W}_c(\mathbf{q})$  can be obtained easily.

Substituting this parametric solution  $\mathbf{W}_c(\mathbf{q})$  into (5.5.3), we get the following polynomial mapping equation

$$\|\mathbf{G}\|_2^2 = \text{trace} (\mathbf{C}(\mathbf{q}) \mathbf{W}_c(\mathbf{q}) \mathbf{C}^T(\mathbf{q})) = \gamma^2, \quad (5.5.5)$$

where  $\gamma^2$  specifies the desired performance level. Equation (5.5.5) is an implicit equation in the uncertain parameters  $\mathbf{q}$ . Since the desired performance level is not known a priori, it is recommended to vary  $\gamma$  or determine the set of parameters  $Q_2$  for which  $\|\mathbf{G}\|_2^2 = \gamma^2$  holds for multiple values  $\gamma$ . Also, a gray-tone or color coding of the different sets  $Q_2(\gamma)$  is useful.

Note: unlike other specifications described in this book, the  $H_2$ -norm mapping equation (5.5.5) does not contain an auxiliary parameter or frequency. This is in line with the fact that the  $H_2$ -norm can be expressed as an integral over all frequencies. This fact makes (5.5.5) useful on its own, as opposed to being solely used for mapping  $H_2$  specifications into a parameter plane, especially to analyze and design control systems for more than two parameters.

### *Remark 5.40*

The classical linear-quadratic-regulator (LQR) problem [122], which aims to minimize the objective function

$$J = \frac{1}{2} \int_0^\infty (\mathbf{x}^T \mathbf{Q} \mathbf{x} + \mathbf{u}^T \mathbf{R} \mathbf{u}) dt$$

for a state-feedback controller  $\mathbf{u} = -\mathbf{K}\mathbf{x}$ , can be cast as a  $H_2$ -norm problem [57]. Namely, the LQR problem considers a linear time-invariant system described by the state equations

$$\dot{\mathbf{x}} = \mathbf{Ax} + \mathbf{Bu} + \mathbf{w}, \quad (5.5.6)$$

$$\mathbf{z} = \begin{bmatrix} \mathbf{R}^{\frac{1}{2}} & \mathbf{0} \\ \mathbf{0} & \mathbf{Q}^{\frac{1}{2}} \end{bmatrix} \begin{bmatrix} \mathbf{u} \\ \mathbf{x} \end{bmatrix}, \quad (5.5.7)$$

where  $\mathbf{u}$  is the control input,  $\mathbf{w}$  is unit intensity white noise, and  $\mathbf{z}$  is the output signal of interest. The LQR problem is then to design a state-feedback controller  $\mathbf{u} = -\mathbf{K}\mathbf{x}$ , which minimizes the  $H_2$ -norm between  $\mathbf{w}$  and  $\mathbf{z}$ . The performance index  $J$  is then given as

$$J = \|\mathbf{G}\mathbf{w} \rightarrow \mathbf{z}\|_2^2.$$

The parametric LQR control design described here applies to parametric SISO systems as well. It allows us to explicitly incorporate control effort specifications into a robust controller design, which is not possible with pure eigenvalues specifications.  $\square$

### Example 5.41

Revisit Example 5.39. We will design a decoupled constant-gain output-feedback controller  $\mathbf{u} = -\mathbf{K}\mathbf{y}$  with

$$\mathbf{K} = \begin{bmatrix} k_1 & 0 \\ 0 & k_2 \end{bmatrix}, \quad (5.5.8)$$

which minimizes the following LQR-like performance index

$$J = \frac{1}{2} \int_0^\infty (\mathbf{y}^T \mathbf{y} + \alpha \mathbf{u}^T \mathbf{u}) dt. \quad (5.5.9)$$

This performance index treats both outputs equally, which is reasonable since the open-loop plant has similar gains for these outputs. The parameter  $\alpha$  provides an adjustable design knob, which allows an intuitive trade-off between the integral error of the commanded output and the actuator effort. For this specific example, we assume  $\alpha = 1$ . The open-loop plant has pure real eigenvalues at  $\{-1, -2\}$ . Thus, we additionally require the rather stringent specification that all closed-loop eigenvalues should have a minimal damping of 1.0.

We will solve this problem by mapping the design requirements into the  $k_1, k_2$  controller parameter plane. To this end, we formulate the LQR output problem (5.5.9) in the  $H_2$ -norm framework by employing Remark 5.40.

Using the fact that  $\mathbf{y} = \mathbf{Cx}$ , the LQR weight matrices in (5.5.7) for this problem are given by

$$\mathbf{Q} = \mathbf{C}^T \mathbf{C}, \quad \mathbf{R} = \mathbf{I}.$$

In order to apply the algebraic mapping equations (5.5.5), we need a state space description of the system. A minimal realization of the system (5.5.2) is given by

$$\begin{bmatrix} \dot{\mathbf{x}} \\ \mathbf{y} \end{bmatrix} = \left[ \begin{array}{cc|cc} -2 & 0 & -2 & -4 \\ 0 & -1 & -2 & -2 \\ \hline 1 & -1 & 0 & 0 \\ -1 & 1/2 & 0 & 0 \end{array} \right] \begin{bmatrix} \mathbf{x} \\ \mathbf{u} \end{bmatrix}. \quad (5.5.10)$$

We incorporate the controller  $\mathbf{u} = -\mathbf{K}\mathbf{y}$  in parametric form into (5.5.6) and (5.5.7) to get the state space system  $\mathbf{G}(s)$  defined in the  $H_2$ -norm mapping equation (5.5.5). For the particular problem considered in this example, these equations are given by

$$\dot{\mathbf{x}} = (\mathbf{A} - \mathbf{B}\mathbf{K}\mathbf{C})\mathbf{x} + \mathbf{w}, \quad (5.5.11)$$

$$\mathbf{z} = \begin{bmatrix} -\mathbf{K} \\ \mathbf{I} \end{bmatrix} \mathbf{C}\mathbf{x}. \quad (5.5.12)$$

And the parametric transfer function  $\mathbf{G}(s)_{\mathbf{w} \rightarrow \mathbf{z}}$  becomes

$$\mathbf{G}(s)_{\mathbf{w} \rightarrow \mathbf{z}} = \left[ \begin{array}{cc|cc} 2(k_1 - 2k_2 - 1) & -2(k_1 - k_2) & 1 & 0 \\ 2(k_1 - k_2) & -2k_1 + k_2 - 1 & 0 & 1 \\ \hline -k_1 & k_1 & 0 & 0 \\ k_2 & -\frac{1}{2}k_2 & 0 & 0 \\ 1 & -1 & 0 & 0 \\ -1 & 1/2 & 0 & 0 \end{array} \right].$$

The controllability Gramian for this problem is obtained from (5.5.4) as

$$\mathbf{W}_c(k_1, k_2) = \frac{1}{6(k_1 + 1)(k_2 + 1)^2} \cdot \begin{bmatrix} 4k_1^2 - 5k_1k_2 + 5/2k_2^2 + 3k_1 + 3/2 & (k_1 - k_2)(4k_1 - 5k_2 - 1) \\ (k_1 - k_2)(4k_1 - 5k_2 - 1) & 4k_1^2 - 11k_1k_2 + 10k_2^2 - 3k_1 + 9k_2 + 3 \end{bmatrix}.$$

Finally, the resulting performance index can be computed as

$$J = \frac{(4k_1 + 5k_2 + 9)(2k_1^2k_2 + 2k_1^2 + k_1k_2^2 + k_2^2 + k_1 + 2k_2 + 3)}{24(k_1 + 1)(k_2 + 1)^2}. \quad (5.5.13)$$

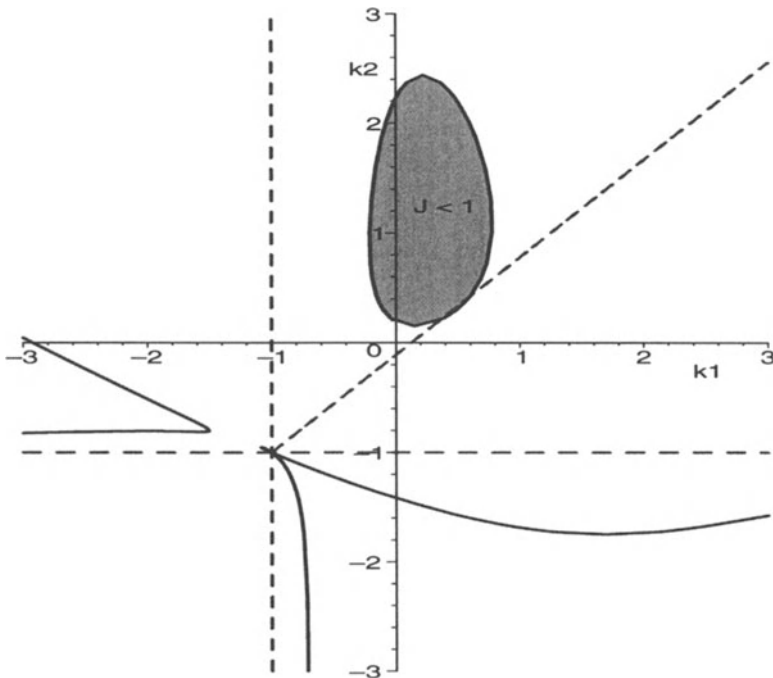


Figure 5.47. LQR boundaries (solid) and  $\Gamma$ -stability (dotted) for MIMO control example

For a given performance level  $J = J^*$ , (5.5.13) provides an implicit mapping equation in the unknowns  $k_1$  and  $k_2$ . The minimal achievable performance level  $J$  for the decentralized output feedback (5.5.8) is bounded from below by the performance level  $J_{full}$  obtainable with a dense static-gain feedback controller. Using classical LQR theory,  $J_{full}$  is easily calculated as  $J_{full} = 0.824$ . In general  $J > J_{full}$ , therefore, we will map  $J = 1$  into the parameter plane. Figure 5.47 shows the resulting parameter set  $Q_2$  for  $J = 1$ . The region satisfying both LQR and  $\Gamma$ -stability requirements is shaded in the figure. The figure actually shows that we can set  $k_1 = 0$ , while still obtaining reasonable controllers. Note that without the damping specification on the closed-loop eigenvalues, we would still need to map the Hurwitz-stability requirement to get the correct LQR set. For this example, stability is assured if

$$k_1 > -1 \quad \wedge \quad k_2 > -1.$$

The actual boundary values  $k_1 = k_2 = -1$  appear in the denominator of (5.5.13).

The minimal obtainable performance level  $J$  for the decentralized controller can be computed using the algebraic equation (5.5.13). For  $k_1 = 0.2074$ ,  $k_2 = 0.9329$ , we get  $J = 0.8421$ , which is only slightly higher than  $J_{full}$ . Compare this to  $J = 1.125$  for the controller designed in Example 5.39.

The numerical values of  $J$  change with the state space representation considered. Thus, the actual values of  $J$  should be only considered to measure the relative per-

formance of a controller compared to a reference controller, e.g. the dense optimal controller or zero-gain controller (open-loop system). This becomes apparent when one is computing  $J$  for the state space representations (5.5.10) and (5.5.23), which both lead to the same input-output behavior but different quantitative values of  $J$ .  $\square$

### $H_\infty$ -norm

The  $H_\infty$ -norm of a transfer matrix  $\mathbf{G}(s)$  is defined as

$$\|\mathbf{G}(s)\|_\infty := \sup_{\omega} \bar{\sigma}(\mathbf{G}(j\omega)), \quad (5.5.14)$$

where  $\bar{\sigma}$  is the largest singular value or maximal principal gain of an asymptotically stable transfer matrix  $\mathbf{G}(s)$ . Note that (5.5.14) defines the  $L_\infty$ -norm if the stability requirement is dropped.

For a scalar transfer function  $G(s)$ , the infinity norm can be interpreted as the maximal distance of the Nyquist plot of  $G(s)$  from the origin or as the peak value of the Bode magnitude plot of  $|G(j\omega)|$ . In that sense, the frequency response magnitude specifications in Section 5.3 could be recast as a scalar  $H_\infty$ -norm problem.

For MIMO systems, the  $H_\infty$ -norm describes the maximum amplitude of the steady state response for all possible unit amplitude sinusoidal input signals. In the context of stochastic input signals, the  $H_\infty$ -norm can be interpreted as the square root of the maximal energy amplification for all input signals with finite energy.

We use robust stabilization as a classical control problem that fits into the  $H_\infty$  framework to motivate the mapping of  $H_\infty$ -norm specifications. Different from the traditional literature about  $H_\infty$  control theory [203],[86] we will treat structured (parametric) and unstructured uncertainties.

### Robust Stability

The well-known small-gain theorem (see, e.g. [203]) states that a simple feedback system is internally stable if the  $H_\infty$ -norm of the resulting open-loop transfer matrix is smaller than 1.

As an example, consider a plant  $\mathbf{G}(s)$  with additive, unknown perturbation  $\Delta(s)$  and a controller with transfer function  $\mathbf{C}(s)$ . The block diagram is shown in Figure 5.48.

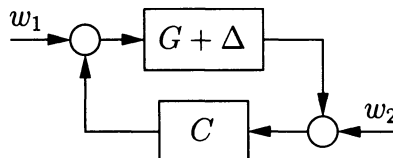


Figure 5.48. Feedback system including plant with additive perturbation

The problem is, how large can  $\|\Delta\|_\infty$  be so that internal stability is preserved? Using simple loop transformations, we can isolate the perturbation  $\Delta$ , which can be seen in Figure 5.49.

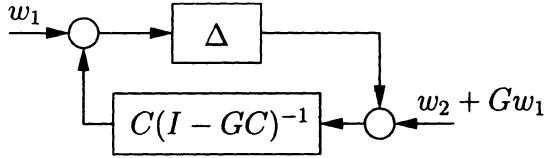


Figure 5.49. Feedback system including plant with additive perturbation

The small-gain theorem now states that the feedback loop is internally stable if

$$\|\Delta \mathbf{C}(\mathbf{I} - \mathbf{G}\mathbf{C})^{-1}\|_\infty < 1. \quad (5.5.15)$$

Since the  $H_\infty$ -norm is an induced norm, the following multiplicative property holds:

$$\|\mathbf{AB}\|_\infty < \|\mathbf{A}\|_\infty \|\mathbf{B}\|_\infty. \quad (5.5.16)$$

And we get the following sufficient condition for internal stability with respect to unstructured uncertainty:

$$\|\Delta\|_\infty \leq \|\mathbf{C}(\mathbf{I} - \mathbf{G}\mathbf{C})^{-1}\|_\infty^{-1}. \quad (5.5.17)$$

### Mapping equations

We now consider the mapping equations for general  $H_\infty$  norm specifications. Here, a condition  $\|\mathbf{G}(s, \mathbf{q})\|_\infty < \gamma$  is mapped into the  $\mathbf{q}$ -space to obtain the set of parameters  $Q_\infty$  for which the condition holds.

In order to get the mapping equations for a parametric system with state space realization  $\mathbf{G}(s, \mathbf{q}) = \mathbf{C}(\mathbf{q})(s\mathbf{I} - \mathbf{A}(\mathbf{q}))^{-1}\mathbf{B}(\mathbf{q}) + \mathbf{D}(\mathbf{q})$ , we define the Hamiltonian matrix

$$\mathbf{H}_\gamma := \begin{bmatrix} \mathbf{A} - \mathbf{B}\mathbf{R}^{-1}\mathbf{D}^T\mathbf{C} & -\gamma\mathbf{B}\mathbf{R}^{-1}\mathbf{B}^T \\ \gamma\mathbf{C}^T\mathbf{S}^{-1}\mathbf{C} & -\mathbf{A}^T + \mathbf{C}^T\mathbf{D}\mathbf{R}^{-1}\mathbf{B}^T \end{bmatrix}, \quad (5.5.18)$$

where  $\mathbf{R} = \mathbf{D}^T\mathbf{D} - \gamma^2\mathbf{I}$  and  $\mathbf{S} = \mathbf{D}\mathbf{D}^T - \gamma^2\mathbf{I}$ .

The following well-known theorem can be used to compute the  $H_\infty$ -norm.

*Theorem 5.42 (Boyd, Balakrishnan, Kabamba [56])*

Let  $\mathbf{A}$  be stable and  $\gamma > \bar{\sigma}(\mathbf{D})$ .

Then  $\|\mathbf{G}\|_\infty \geq \gamma \iff \mathbf{H}_\gamma$  has pure imaginary eigenvalues (i.e. at least one).

□

This theorem has been used to obtain a numerical bisection method to compute the  $H_\infty$  norm of a given transfer matrix [56]. We use the above theorem in its symbolic form to derive mapping equations for the  $H_\infty$ -norm. The boundary of a parameter region with  $\|\mathbf{G}\|_\infty \leq \gamma$  is given by parameters for which  $\mathbf{H}_\gamma$  defined in (5.5.18) has pure imaginary eigenvalues. The eigenvalue equation

$$\det[s\mathbf{I} - \mathbf{H}_\gamma] = 0$$

can be used to check if  $s$  is an eigenvalue of  $\mathbf{H}_\gamma$ . Using Theorem 5.42, we are interested in pure imaginary values, and it follows that

$$e_1(\omega, \gamma, \mathbf{q}) = \det[j\omega\mathbf{I} - \mathbf{H}_\gamma] = 0 \quad (5.5.19)$$

is a necessary condition for parameters  $\mathbf{q}$  for which  $\|\mathbf{G}\|_\infty = \gamma$  holds. Since  $\mathbf{H}_\gamma$  is a Hamiltonian, pure imaginary eigenvalues will exist only as double eigenvalues. Therefore, the following double root condition for polynomial equations applies

$$e_2(\omega, \gamma, \mathbf{q}) = \frac{\partial e_1(s, \gamma, \mathbf{q})}{\partial s} \Big|_{s=j\omega} = 0. \quad (5.5.20)$$

Equations (5.5.19) and (5.5.20) define two polynomial equations that can be used to map a given  $H_\infty$ -norm condition into parameter space. The following simplifications can be made for (5.5.19) and (5.5.20). Equation (5.5.20) contains the factor  $\omega$ , which can be neglected since the equation is only valid for  $\omega > 0$ . After dropping this factor, both equations contain only terms with even powers of  $\omega$ . Thus, it is favorable to substitute  $\omega^2 = \Omega$  in order to reduce the degree of the equations.

Additionally, we have to consider both ends of the imaginary axis. Real eigenvalues can merge at the origin and form a pair of pure imaginary eigenvalues:

$$\det[j\omega\mathbf{I} - \mathbf{H}_\gamma]_{\omega=0} = \det \mathbf{H}_\gamma = 0. \quad (5.5.21)$$

The same applies to eigenvalues becoming imaginary at infinity:

$$\det[j\omega\mathbf{I} - \mathbf{H}_\gamma]_{\omega=\infty} = 0. \quad (5.5.22)$$

Condition (5.5.22) is just the coefficient of the term with the highest degree in  $s$  of the determinant  $\det[s\mathbf{I} - \mathbf{H}_\gamma]$ .

Note that Equations (5.5.21) and (5.5.22) are not sufficient since they determine all parameters for which the Hamiltonian (5.5.18) has a pair of eigenvalues at the origin and infinity, respectively. This includes real pairs of eigenvalues that are just interchanging without becoming imaginary. Thus, in order to get sufficiency, we have to check all parameters satisfying (5.5.21) and (5.5.22) if there are only real eigenvalues.

The mapping equations (5.5.19)–(5.5.22) have a similar structure like the well-known equations for  $\Gamma$ -stability, where (5.5.19) and (5.5.20) can be interpreted as the complex root boundary condition, (5.5.21) as the real root and (5.5.22) as the infinite root boundary condition (see Example 2.6).

Theorem 5.42 has two prerequisites, namely the system should be stable and the maximal singular value of the direct feedthrough matrix  $\mathbf{D}$  should be less than the

desired performance level  $\gamma$ . The stability requirement can be mapped using the mapping equations for Hurwitz-stability described in Chapter 4. Using a frequency domain formulation, it can be shown that the condition  $\sigma_{\max}(\mathbf{D}) < \gamma$  is implicitly mapped by (5.5.21) and (5.5.22).

Note that the mapping equations for the  $H_\infty$ -norm are not just characterizing the parameters for which  $\|\mathbf{G}\|_\infty = \gamma$ . Actually, all parameters for which  $\mathbf{G}(s, q)$  has a singular value such that  $\sigma(\mathbf{G}) = \gamma$  are determined. Thus, we might get boundaries in the parameter space for which the  $i$ -th biggest singular value  $\sigma_i$  has the specified value  $\gamma$ . This is similar to eigenvalue specifications, where we get boundaries for each eigenvalue crossing of the  $\Gamma$ -boundary. Thus, similar to the  $\Gamma$ -case, we have to check the resulting regions in the parameter space if the specifications are fulfilled or violated (possibly multiple times).

### Example 5.43

We analyze the robust stability of the plant given in Example 5.39 for decentralized static-gain controllers

$$\mathbf{C}(s) = \begin{bmatrix} k_1 & 0 \\ 0 & k_2 \end{bmatrix}$$

with respect to unstructured additive uncertainty. Using (5.5.18), the Hamiltonian  $\mathbf{H}_\gamma$  for this problem becomes

$$\mathbf{H}_\gamma = \begin{bmatrix} -2 - k_1 & -2k_2 & 5/\gamma & 3/\gamma \\ -k_1 & -1 - k_2 & 3/\gamma & 2/\gamma \\ -8/\gamma & 6/\gamma & 2 + k_1 & k_1 \\ 6/\gamma & -5/\gamma & 2k_2 & 1 + k_2 \end{bmatrix}.$$

Figure 5.50 shows the gray-tone coded sets of parameters that correspond to different tolerable uncertainty sizes. Dark areas correspond to poor robustness whereas areas with lighter colors indicate good robustness. The initially designed controller  $\mathbf{C}(s) = \mathbf{I}$  yields approximately the same robustness as the open-loop system. It can be seen from Figure 5.50 that decreasing both gains, e.g. to  $\mathbf{C}(s) = 0.5 \mathbf{I}$ , will result in a system that is more robust for the uncertainties considered. □

### Remark 5.44

The mapping equations establish conditions that allow the direct computation of the  $H_\infty$ -norm. Thus, instead of using the numerically attractive bisection algorithm

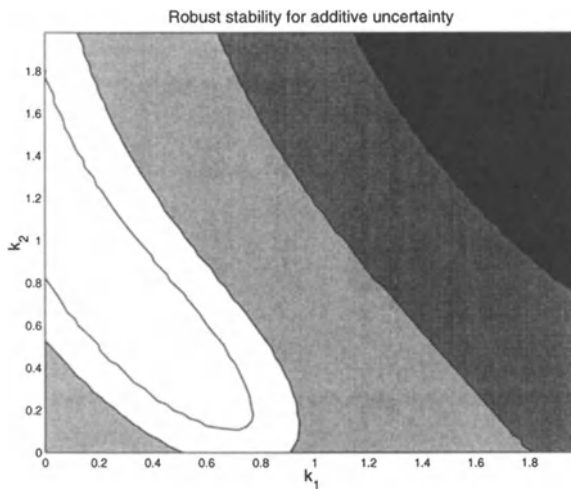


Figure 5.50. Stability with respect to unstructured, additive uncertainty

widely used in control software, the  $H_\infty$ -norm can be computed by solving the two algebraic equations (5.5.19) and (5.5.20) in the two unknowns  $\omega$  and  $\gamma$ . These positive solutions provide candidate values  $\gamma$  for the  $H_\infty$ -norm. Additionally, the solutions of (5.5.21) and (5.5.22) are computed and the  $H_\infty$ -norm of the system is given by the maximal value over all candidate solutions. As a byproduct, we get the frequency  $\omega$ , for which the maximal singular value occurs.  $\square$

### Example 5.45

We use the mapping equations to directly compute the  $H_\infty$ -norm for the open-loop transfer function  $\mathbf{G}(s)$  given in Example 5.39. A state space representation for  $\mathbf{G}(s)$  is given by

$$\mathbf{G}(s) = \left[ \begin{array}{cc|cc} -2 & 0 & 1 & 2 \\ 0 & -1 & 1 & 1 \\ \hline -2 & 2 & 0 & 0 \\ 2 & -1 & 0 & 0 \end{array} \right]. \quad (5.5.23)$$

The mapping equations (5.5.19) and (5.5.20) become

$$\begin{aligned} e_1 &= \gamma^4 \omega^4 + (5\gamma^4 - 14\gamma^2)\omega^2 + 4\gamma^4 - 8\gamma^2 + 4, \\ e_2 &= \omega(4\gamma^4 \omega^2 + 10\gamma^4 - 28\gamma^2). \end{aligned}$$

This polynomial system of equations has only a single relevant solution  $\omega = 1, \gamma = \sqrt{2}$  with  $\omega, \gamma > 0$ .

The DC-gain condition (5.5.21) is

$$\det \mathbf{H}_\gamma = \gamma^4 - 2\gamma^2 + 1,$$

which has the positive solution  $\gamma = 1$ . Note that this can be easily observed by the fact that  $\mathbf{G}(j0) = \mathbf{I}$ , and thus the singular values are given by  $\sigma_1 = \sigma_2 = 1$ .

There is no solution for (5.5.22) and we can conclude that the maximal singular value of  $\mathbf{G}(s)$  is given for  $\omega = 1$  and  $\|\mathbf{G}(s)\|_\infty = \sqrt{2}$ .  $\square$

# 6 Case Studies in Car Steering

Many dangerous situations occur on the roads because a car driver does not react fast enough at the beginning of skidding or rollover. Automatic feedback systems can assist the driver to overcome such dangerous situations. A further step is automatic driving by following a lane reference. In both cases, robustness of the control system with respect to the uncertain road-tire contact is an important requirement. Further uncertain parameters may be, for example, vehicle mass and velocity, or the load-dependent height of the center of gravity (CG) above road level.

In the present chapter, a relatively simple car model is derived. It takes into account only the most essential non-linearities of the lateral tire force characteristic and later the rate limitation of the steering actuator.

## 6.1 Tires, Braking, and Steering

A car driver uses the pedals for commanding the longitudinal motion, and the steering wheel for commanding the lateral motion and heading. What looks like two independent actuators becomes coupled in extreme driving situations, because all commands use the same limited resource, that is, the contact force between tire and road. Its saturation limit is approximately described by the Kamm circle (Coulomb dry friction), see Figure 6.1. In tire coordinates  $xt, yt, zt$ , the resultant of the tire forces  $F_{zt}$  and  $F_{yt}$  cannot exceed the limit given by the normal force  $F_{zt}$  and a maximal adhesion coefficient  $\mu \leq 1$ .

$$\sqrt{F_{zt}^2 + F_{yt}^2} \leq \mu F_{zt}. \quad (6.1.1)$$

Under braking or acceleration of a single tire,  $|F_{zt}|$  is increased. If this happens close to tire saturation, then the available lateral force  $|F_{yt}|$  is decreased. For acceleration and gas release, there is an obvious difference of the vehicle dynamics between front-wheel and rear-wheel drive vehicles. The available maximal force  $\mu F_{zt}$  varies under:

- i. changing road surface (e.g. ice patches on a dry road). This may happen rapidly and unforeseeably.
- ii. braking and acceleration. This changes  $F_{zt}$ , e.g. while braking,  $F_{zt}$  is increased at the front wheels and decreased at the rear wheels.

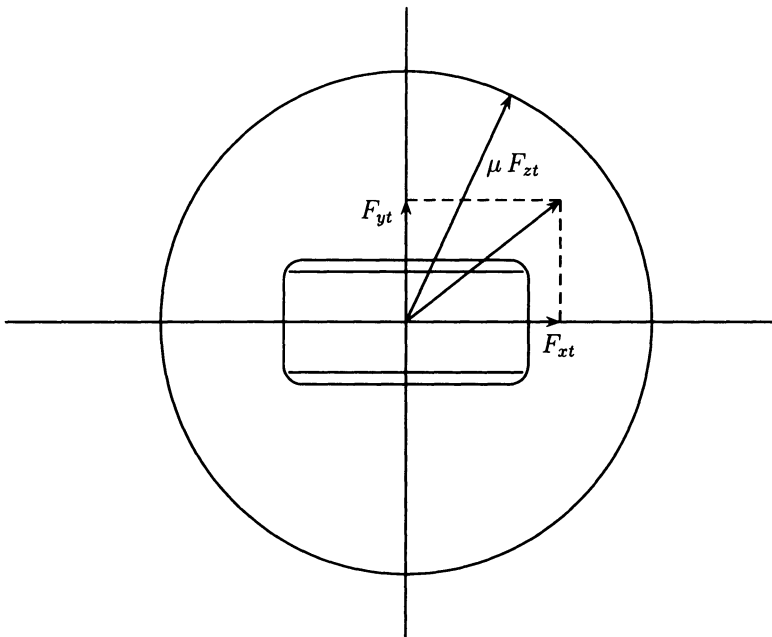


Figure 6.1. Kamm circle.

For the design of vehicle dynamics control systems, the uncertainty i. means that there is no time for identification and adaptation; robust control is needed. The uncertainty ii. means that gain-scheduling, e.g. by the longitudinal acceleration is possible, but in view of i. it is not worthwhile to model the effect very accurately.

For a stepwise change in  $\mu$ , the system inherits an initial condition from the dynamics before the step. The car steering has now to be stable for the new constant value of  $\mu$ . Therefore a constant, but unknown value of  $\mu$  is assumed in this chapter.

### *Remark 6.1*

The reader with a control engineering background should be warned that the notions of *controllability* and *stability* are used in the automotive literature in the following sense: loss of controllability means front-wheel tire saturation, loss of stability means rear-wheel tire saturation. These notions are not identical to the definitions in system theory!

□

The saturation limits are not reached under moderate handling maneuvers on a dry road. Then, the commanded forces in the  $(x, y)$ -plane are below saturation. In this normal driving situation, the foot and hand commands of the driver are independently executed. This is what the driver is used to. Safety-critical situations in handling occur when the response of the car changes suddenly as the car gets onto a slippery road, e.g. on an icy bridge or on wet leaves on the road.

Safety-critical situations also arise under disturbance torques like side wind, asymmetric road surface or tire burst ( $\mu$ -split braking), trailer pulling in gusty wind or bad road surface. Also, an escape maneuver to avoid a collision with a surprisingly appearing human, animal or other car may drive the tires to the limits. In all surprising situations, it takes the driver 0.5 to 1 second to react, and frequently it is an overreaction that makes things worse. Roughly speaking, we may compare the driver in this situation with a feedback system with time delay and high gain, which causes instability. For small continuous disturbances there is also a comfort issue; the driver should still be relaxed after pulling a trailer in gusty wind for some time.

There exist already driver assistant systems (ESP) that use braking (or increased traction) at the individual wheels [195], [153], [72]. These systems are cheap, because they use the hardware of the existing ABS braking system with an additional yaw rate sensor and do not require a new actuator. So, why is it of interest to look at the steering alternative?

The first reason is that we need a torque to compensate yaw disturbance torques. Torque is tire force times lever arm. For braking, the lever arm is half the trackwidth  $t$ , for steering it is approximately half the wheelbase, which is bigger by a factor of approximately two. In other words, only half the tire force is needed to generate a required compensation torque by steering rather than by braking.

The second reason is that different friction coefficients  $\mu$  on the left and right sides ( $\mu$ -split braking) may be the cause of the disturbance torque, which can be reduced only by reduced braking, i.e. longer braking distance. In contrast, a steering torque can compensate the braking torque and achieve a straight short braking path. Figure 6.2 shows the optimal combination of full braking and steering under the assumption, that the CG is in the center of the wheelbase and the wheelbase is twice the trackwidth. (The CG is projected to the road level, where the tire forces occur.) Also, equal vertical forces  $F_{zt}$  for the front and rear wheels are assumed.

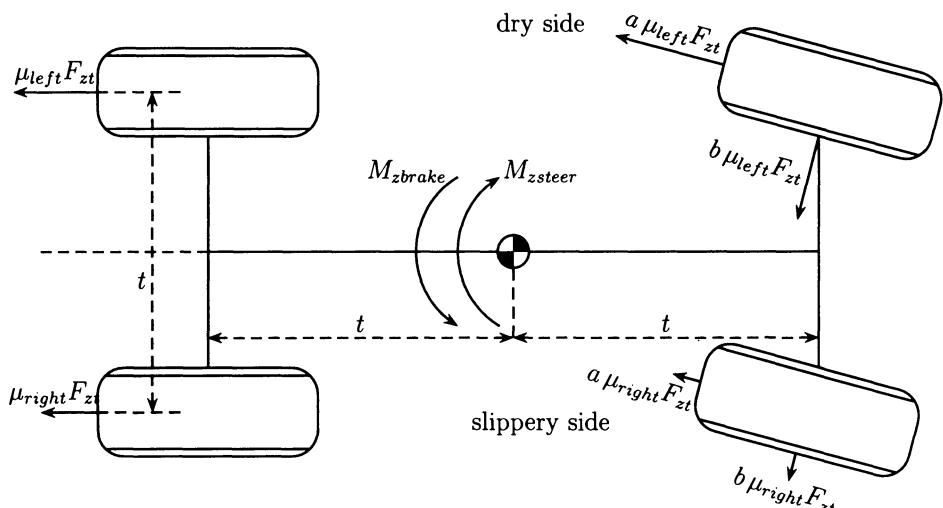


Figure 6.2. Compensation of  $\mu$ -split brake torque by steering torque

The disturbance torque

$$M_{z\text{ brake}} = (\mu_{left} - \mu_{right})F_{zt}(1 + a)t/2 \quad (6.1.2)$$

is compensated by the steering torque

$$M_{z\text{ steer}} = (\mu_{left} + \mu_{right})F_{zt}bt \quad (6.1.3)$$

with the saturation constraint (6.1.1)

$$\sqrt{a^2 + b^2} \leq 1. \quad (6.1.4)$$

The retarding force

$$F_z = (\mu_{left} + \mu_{right})(1 + a)F_{zt} \quad (6.1.5)$$

is maximized under the constraint, that the torques compensate each other.

As a numerical example, let  $\mu_{left} = 1$ ,  $\mu_{right} = 0$ , then  $a = 0.6$ ,  $b = 0.8$  makes the most efficient use of the available tire force  $\mu F_{zt}$ .

For other CG-locations and ratios trackwidth/wheelbase, it is easy to calculate the Pythagoras ratio between braking and steering forces at the front wheels. It may also be scheduled by the rear-front shift of  $F_z$  under braking or acceleration. This braking-steering combination fully exploits the physical limits given by  $\mu_{max}F_z$ .

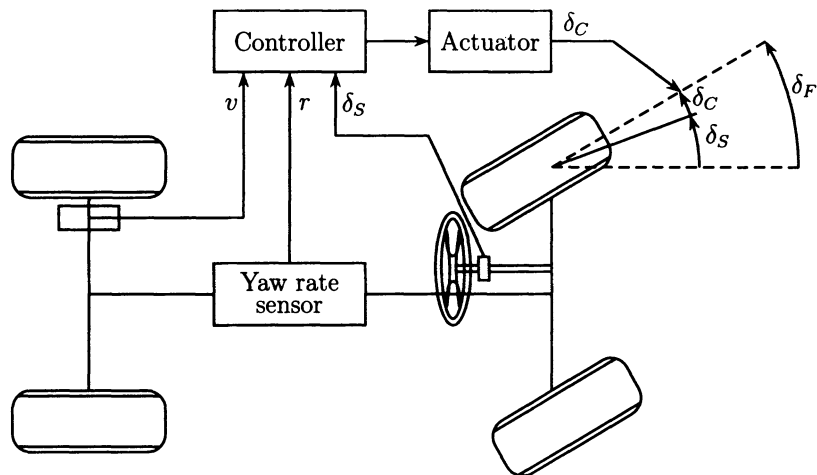
A third reason for driver assistance by steering (rather than by braking) is energy conservation, reduced wear of tires and brakes and smooth operation around zero correction. Practically, braking systems cannot immediately compensate small errors, but they have to intervene relatively late in detected emergency situations when the car is close to skidding and the driver is unpleasantly surprised by the intervention. Only the steering system is feasible for continuous operation, also for better comfort under continuous disturbances.

The implementation of a steering control system is schematically shown in Figure 6.3. The main steering angle  $\delta_S$  is commanded by the driver from the steering wheel. A small corrective steering angle is set by an actuator with input from a feedback controller. The main feedback signal is the yaw rate. (Yaw rate sensors are already used in individual wheel braking systems and are therefore cheap.) The velocity signal from the ABS system may be used for gain-scheduling the controller. The velocity is approximated here by the wheel rotation, neglecting the longitudinal slip. Under normal driving conditions, this slip is smaller than 2 %. From the velocity and the handwheel angle, a reference  $r_{ref}$  for the yaw rate  $r$  is generated in the feedforward path of the controller.

The superposition  $\delta_F = \delta_S + \delta_C$  may be done mechanically, as indicated in Figure 6.4. An alternative is a *steer-by-wire* system with an electrical addition  $\delta_S + \delta_C$  and a common electric actuator. The cost and safety issues related to such an actuator are presently (2001) the bottleneck for the widespread use of active steering.

The tire forces depend on the steering angle  $\delta_F$  and on state variables of the chassis. Figure 6.5 shows the velocity vector  $\vec{v}_F$  under a *sideslip angle*  $\beta_F$  at the front axle with respect to the longitudinal axis ( $x$ -axis) of the chassis. The lateral force  $F_{ytF}$  in tire coordinates is a function of the *tire slip angle*  $\alpha_F = \delta_F - \beta_F$ . Its dominant component in chassis coordinates is

$$F_y = F_{ytF} \cos \delta_F. \quad (6.1.6)$$

Figure 6.3. Feedback controlled additive steering angle  $\delta_C$ 

The small retarding component  $F_{xF} = -F_{ytF} \sin \delta_F$  does not generate a yaw torque, if it occurs symmetrically at the left and right wheel. Its longitudinal effect is compensated by speed control (automatic or by the driver). In a static tire description, the tire side force  $F_{ytF}$  is a function of the tire slip angle  $\alpha_F$ , i.e.

$$\begin{aligned} F_{ytF} &= f(\alpha_F) = f(\delta_F - \beta_F), \\ F_{yF} &= f(\delta_F - \beta_F) \cos \delta_F. \end{aligned} \quad (6.1.7)$$

The index  $F$  indicates the front wheels; it is replaced by  $R$  for the rear wheels.

The non-linear functions are determined experimentally for a specific tire and smoothed by a mathematical approximation, see Figure 6.6. If the velocity vector  $\vec{v}_F$  is aligned with the tire, then the lateral force is zero,  $f(0) = 0$ . For  $\alpha_A > 10^\circ$ , the lateral force is close to saturation. Of course, a control system cannot overcome such

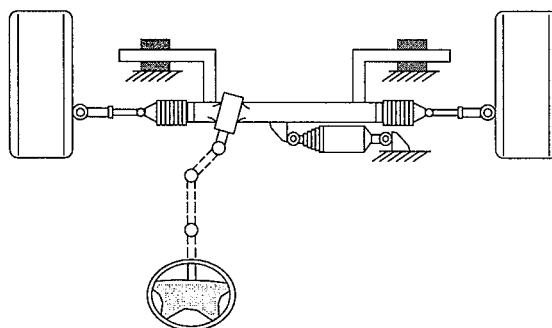


Figure 6.4. Mechanical implementation example for additive steering by linear actuator

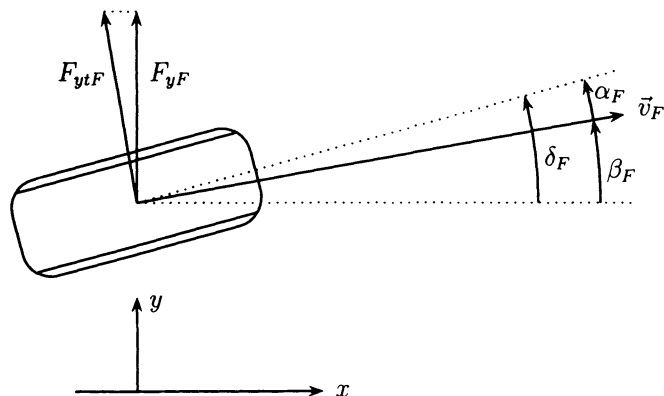


Figure 6.5. Lateral forces  $F_{ytF}$  at the front wheel in tire coordinates and  $F_{yF}$  in chassis coordinates

physical limits. Therefore, it is very important to design steering controllers such that only small tire sideslip angles occur.

In a dynamic description, the lateral tire force does not respond immediately to a step in the steering angle. The steady state deformation of the rubber tire is reached, however, after approximately one half wheel rotation. This phase delay, together with other elasticities in the connection between the steering motor and the steering angle and delays in the steering motor itself, call for sufficient phase margin in the control design.

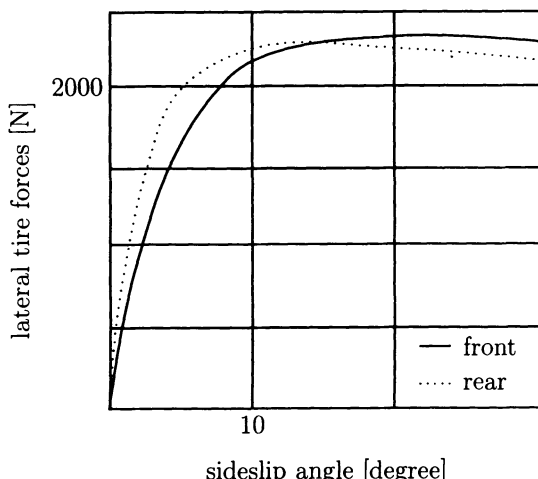


Figure 6.6. Lateral tire forces as a function of the tire sideslip angle

## 6.2 The Two Steering Tasks

An important requirement in all man-machine systems is that the automatic control system should not interfere with the human control task and vice versa. We will distinguish two steering tasks, one to be controlled by the driver, the other one under automatic control. The driver should execute the primary steering task, that is, path tracking. The vehicle is considered here as a point mass  $m_{DP}$  and its velocity vector  $\vec{v}$  must be reoriented by a lateral acceleration  $a_{yDP}$  in order to follow the planned path, see Figure 6.7. The planned path exists only in the mind of the driver (e.g. change lane, enter into a curve), and  $\vec{v}$  is the actual tangent to this path. The path is continuously updated by the driver. The secondary steering task of disturbance compensation is

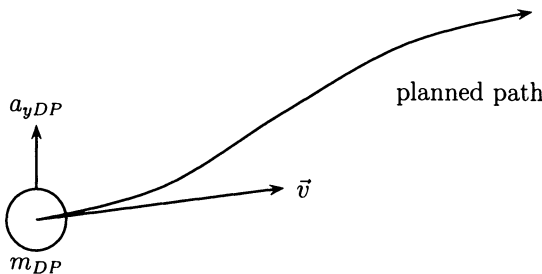


Figure 6.7. Primary steering task: path tracking

assigned to the automatic control system. More realistic than a point mass, the vehicle must be modelled as a rigid body with a moment of inertia  $J$ , represented here by a second mass  $m_R$ , rigidly connected to  $m_{DP}$ , see Figure 6.8. An essential variable to describe the yaw motion around a vertical axis through the CG is the yaw rate  $r$ . Safety-critical situations arise if a *disturbance torque*  $M_{zD}$  acts on the vehicle, for example, by side wind, asymmetric road-tire contact ( $\mu$ -split braking), tire burst. An automatic control system can do this disturbance compensation faster and more precisely than a driver, who is subject to some reaction time and whose late compensation action is frequently an overreaction. The disturbance torques enter directly into the rotational differential equations  $J\dot{r} = \Sigma$  torques. Their indirect influence on the lateral acceleration  $a_{yDP}$  via the vehicle dynamics should be compensated such that the driver controls the undisturbed  $a_{yDP}$ . In system theoretic terms, the task separation requires to make the yaw rate  $r$  non-observable from  $a_{yDP}$ . This unilateral decoupling must be robust for all operating conditions.

Usual vehicle parameters are mass  $m$ , moment of inertia  $J$  and location of the CG.

$$\begin{bmatrix} 1 & 1 \\ \ell_R & -\ell_{DP} \\ \ell_R^2 & \ell_{DP}^2 \end{bmatrix} \begin{bmatrix} m_R \\ m_{DP} \end{bmatrix} = \begin{bmatrix} m \\ 0 \\ J \end{bmatrix} \quad (6.2.1)$$

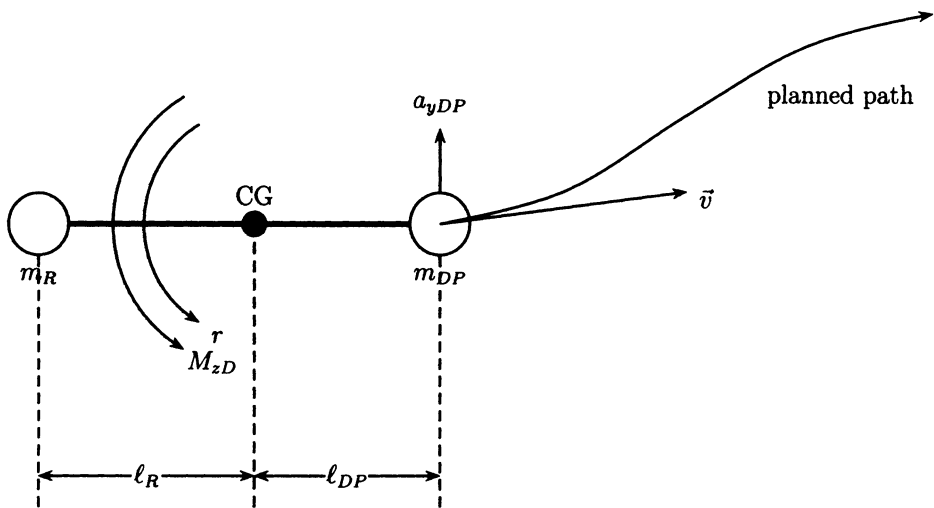


Figure 6.8. Secondary steering task: disturbance compensation

The bar-bell model of Figure 6.8 is now attached to the vehicle geometry of Figure 6.9. The mass  $m_R$  is fixed at the rear axle. The location  $\ell_{DP}$  of the decoupling point is calculated from the requirement, that its lateral acceleration  $a_{yDP}$  does not depend on the rear axle lateral force  $F_{yR}$ . (Note that all axle forces are the sum for the left and right wheel).

The lateral acceleration at the decoupling point is

$$a_{yDP} = a_{yCG} + \ell_{DP}\dot{r} \quad (6.2.2)$$

with

$$\begin{aligned} a_{yCG} &= (F_{yR} + F_{yF} + F_{yD})/m \\ \dot{r} &= (F_{yF}\ell_F - F_{yR}\ell_R + M_{zD})/J \end{aligned}$$

and by substitution

$$\begin{aligned} a_{yDP} &= F_{yF}\left(\frac{1}{m} + \frac{\ell_F\ell_{DP}}{J}\right) + F_{yR}\left(\frac{1}{m} - \frac{\ell_R\ell_{DP}}{J}\right) \\ &\quad + M_{zD}\frac{\ell_{DP}}{J} + F_{yD}\frac{1}{m} \end{aligned} \quad (6.2.3)$$

The factor of  $F_{yR}$  is zero for

$$\ell_{DP} = J/m\ell_R \quad (6.2.4)$$

and with this choice

$$a_{yDP} = [F_{yF}(\beta_F, \delta_F)\ell + M_{zD} + F_{yD}\ell_R]/m\ell_R \quad (6.2.5)$$

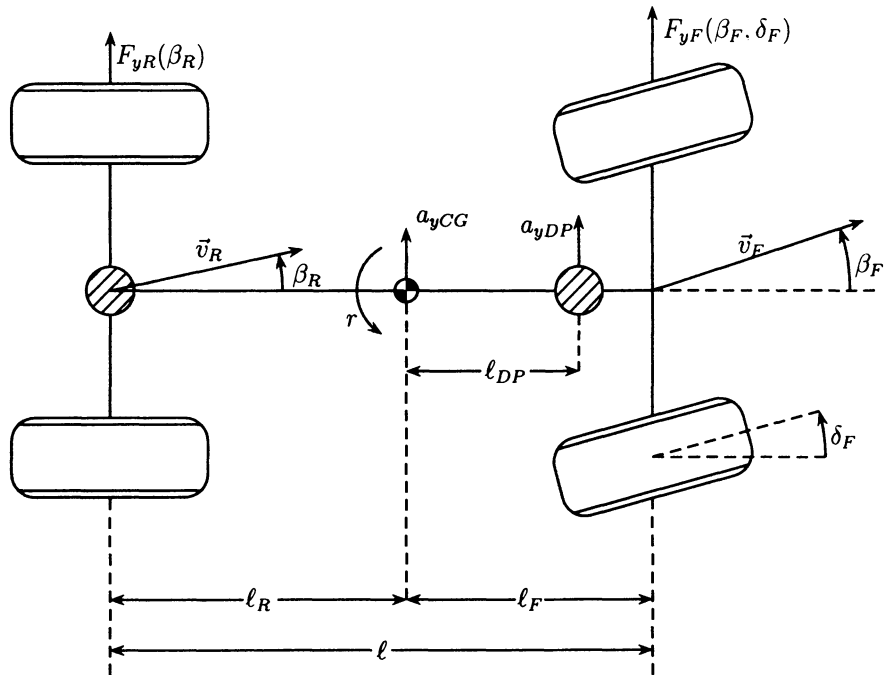


Figure 6.9. Definition of the decoupling point

where  $\ell = \ell_R + \ell_F$  is the wheelbase.

For simplification, the lateral disturbance force  $F_{yD}$  at the CG is set to zero. In a driver support system, the effect of  $F_{yD}$  is compensated by the driver within their normal lane keeping task, while the effect of the disturbance torque  $M_{zD}$  is an undesired yaw rate that should be compensated by an automatic control system.

The desired robust decoupling effect is achieved by cancellation of the effect of  $r$  in the argument of

$$F_{yF}(\beta_F, \delta_F) = f(\delta_F - \beta_F) \cos \delta_F. \quad (6.2.6)$$

For this purpose, we need a dynamic model for the dependency  $\dot{\beta}_F(r)$ .

### Remark 6.2

The reader may wonder why we did not begin with the dynamic model for  $\dot{\beta}_F(r)$ . The reason is that there are many such models. The single-track model will be introduced in the next section. A more detailed model uses 14 degrees of freedom (six for the chassis, four for the wheel rotation, four for suspension hub) plus the tire model and steering actuator dynamics. More detailed multibody models also consider several masses of the suspension and steering system and car body elasticity. Also, aerodynamic forces have an influence on the yaw motion. Such models are useful for simulations if all

the parameters are known. They are, however, not suited to controller design, because a higher complexity of the relation  $\dot{\beta}_F(r)$  makes it less realistic to implement the exact cancellation of  $r$ . If we have to reduce the controller to the essential and measurable effects anyway, then it suffices to model only these effects.

□

We emphasize that the robust decoupling concept is not restricted to certain model simplifications (single-track model, constant velocity, linear tire characteristics, tire dynamics). Therefore, it is the general basis for the separation of the driver task of path tracking via  $a_{yDP}$  from the automatic control of the yaw rate. It is structurally robust with respect to the uncertain road-tire contact and braking and acceleration effects.

### 6.3 The Non-linear Single-track Model and its Robust Unilateral Decoupling

The essential features of car steering dynamics in a horizontal road plane with the CG projected to this plane are described by the *single-track model* by Riekert and Schunk [172]. It is well described in the automotive literature, e.g. [150], [204]. We present it here from a robust control point of view. The possibility of additional rear-wheel steering (4WS = four-wheel steering) is considered, which makes it an interesting MIMO example. Otherwise, a simple version is presented for clarity of the essential effects.

*Remark 6.3*

In the English language the term *bicycle model* is common. This term may be misleading; the dynamics of balancing a bicycle are much more complicated. Therefore, we prefer the term single-track model.

The single-track model is obtained by lumping the two front wheels into one wheel in the center line of the car, the same is done with the two rear wheels. Thereby, the car model of Figure 6.9 is reduced to that of Figure 6.10, and the coupling with roll, pitch, and heave motions is not modelled. The angles  $\delta_F$  and  $\delta_R$  are the front and rear steering angles. The distance between the center of gravity (CG) and the front axle (resp. rear axle) is  $\ell_F$  (resp.  $\ell_R$ ) and the sum  $\ell = \ell_R + \ell_F$  is the wheelbase.

The angle  $\beta$  between the vehicle center line and the velocity vector  $\vec{v}$  at the CG is called the *vehicle sideslip angle*. In the horizontal plane of Figure 6.10, an inertially fixed coordinate system  $(x_0, y_0)$  is shown together with a vehicle fixed coordinate system  $(x, y)$  that is rotated by a *yaw angle*  $\psi$ . In the dynamic equations, the *yaw rate*  $r := \dot{\psi}$

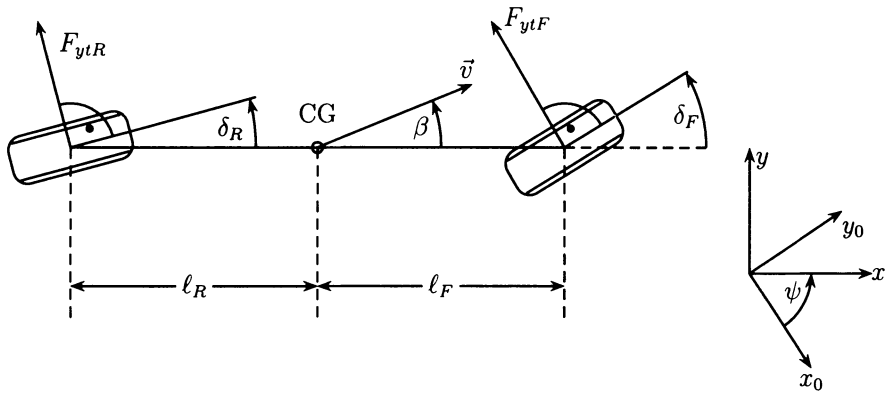


Figure 6.10. Single-track model for car steering

will appear as a state variable. The yaw angle  $\psi$  itself will be included in the model in Section 6.8 in the context of automatic car steering, where the position of the vehicle relative to the lane is considered. For a driver assistant for yaw stabilization, it suffices to model only the velocities as the path tracking task is left to the driver by visual feedback. The velocity vector  $\vec{v}$  has the absolute value  $v = |\vec{v}|$  and the components  $v_x$  and  $v_y$  in chassis coordinates.

The forces transmitted between the road surface and the car chassis via the wheels are represented in Figure 6.10 by the side forces  $F_{ytF}$  and  $F_{ytR}$ . The forces in the longitudinal direction of the tires are assumed to be zero, i.e. the wheels are freely spinning.

Figure 6.11 shows a block diagram of the model. Input to the vehicle dynamics are the lateral forces at the front and rear axles:

$$\begin{aligned} F_{yF} &= F_{ytF} \cos \delta_F, \\ F_{yR} &= F_{ytR} \cos \delta_R, \end{aligned} \quad (6.3.1)$$

and a longitudinal force component

$$F_x = -F_{ytF} \sin \delta_F - F_{ytR} \sin \delta_R. \quad (6.3.2)$$

Note that these axle forces represent the sum of the forces at the left and right tire.

Via the dynamics model, the forces control state variables  $\beta, v, r$ . The equations of motions for three degrees of freedom in the horizontal plane are:

a) Lateral motion

$$mv(\dot{\beta} + \dot{\psi}) \cos \beta + m\dot{v} \sin \beta = F_{yF} + F_{yR}. \quad (6.3.3)$$

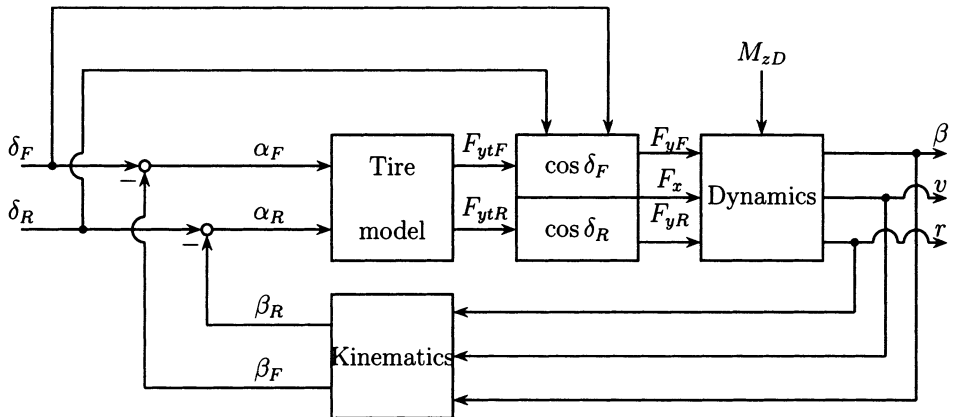


Figure 6.11. Block diagram of car steering

b) Longitudinal motion

$$-mv(\dot{\beta} + \dot{\psi}) \sin \beta + m\dot{v} \cos \beta = F_x. \quad (6.3.4)$$

c) Yaw motion

$$J\ddot{\psi} = F_y \ell_F - F_y R \ell_R + M_{zD}. \quad (6.3.5)$$

With  $r := \dot{\psi}$ , we obtain from (6.3.3) to (6.3.5)

$$\begin{bmatrix} mv(\dot{\beta} + r) \\ m\dot{v} \\ J\dot{r} \end{bmatrix} = \begin{bmatrix} -\sin \beta & \cos \beta & 0 \\ \cos \beta & \sin \beta & 0 \\ 0 & 0 & 1 \end{bmatrix} \begin{bmatrix} F_x \\ F_y \ell_F + F_y R \ell_R \\ F_y \ell_F - F_y R \ell_R + M_{zD} \end{bmatrix}. \quad (6.3.6)$$

In the next step, the sideslip angles  $\alpha_F$  and  $\alpha_R$  at the front and rear tires are obtained by a kinematic model from the steering angles  $\delta_F, \delta_R$ , and from the state variables  $\beta, r$ , and  $v$ . Figure 6.12 illustrates the vehicle motion around a *momentary pole* MP. The local velocity vectors in front ( $\vec{v}_F$ ) and rear ( $\vec{v}_R$ ) and at the CG ( $\vec{v}$ ) are oriented perpendicular to the connecting line to the momentary pole. The front and rear chassis sideslip angles are  $\beta_F$  and  $\beta_R$ . The velocity components in the direction of the longitudinal center line of the vehicle must be equal, i.e.

$$v_R \cos \beta_R = v_F \cos \beta_F = v \cos \beta. \quad (6.3.7)$$

The velocity components perpendicular to the center line depend on the yaw rate  $r$ , as

$$v_F \sin \beta_F = v \sin \beta + \ell_F r, \quad (6.3.8)$$

$$v_R \sin \beta_R = v \sin \beta - \ell_R r.$$

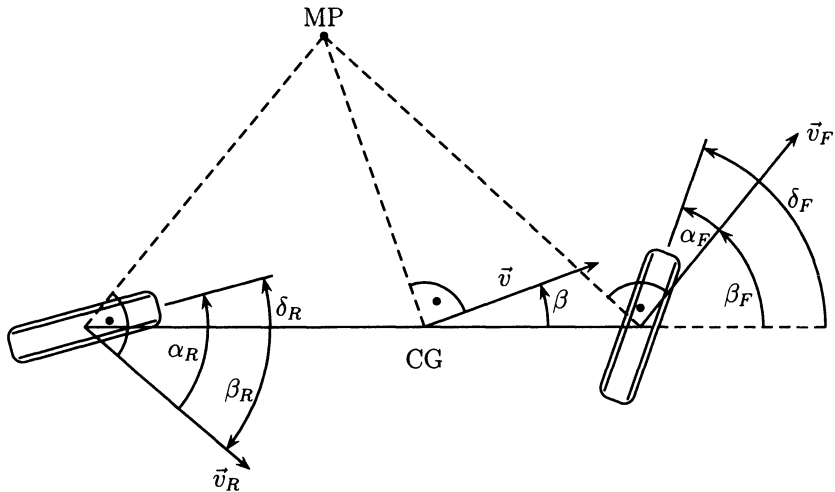


Figure 6.12. Kinematics variables

The velocity terms  $v_F$  and  $v_R$  are eliminated by division by the corresponding terms from (6.3.7). Thus, the kinematic model is

$$\begin{aligned}\tan \beta_F &= \frac{v \sin \beta + \ell_{Fr}}{v \cos \beta} = \tan \beta + \frac{\ell_{Fr}}{v \cos \beta}, \\ \tan \beta_R &= \frac{v \sin \beta - \ell_{Rr}}{v \cos \beta} = \tan \beta - \frac{\ell_{Rr}}{v \cos \beta},\end{aligned}\tag{6.3.9}$$

and the tire sideslip angles (shown in Figure 6.5) are

$$\begin{aligned}\alpha_F &= \delta_F - \beta_F, \\ \alpha_R &= \delta_R - \beta_R.\end{aligned}\tag{6.3.10}$$

The feedback-structured model of Figure 6.11 is now completed by the non-linear tire model:

$$\begin{aligned}F_{ytF} &= f_F(\alpha_F), \\ F_{ytR} &= f_R(\alpha_R).\end{aligned}\tag{6.3.11}$$

### Linearization for Constant Velocity and Small Angles

All four blocks in Figure 6.11 are non-linear. In normal driving situations (except slow parking maneuvers), the most important non-linearity is the uncertain tire model. Therefore, we linearize the three other non-linearities first, and then derive the feedback

control law for robust decoupling without further assumptions on the non-linear tire dynamics. Later, also the static tire characteristics are linearized to allow for a linear analysis of the uncontrolled and of the robustly decoupled cars.

- i. The vehicle dynamics (6.3.6) are non-linear. They may be linearized by the assumption  $v = 0$ . This is justified, because the velocity  $v$  is changing more slowly than the state variables  $r$  and  $\beta$ . The velocity  $v$  is now treated as an uncertain constant parameter. Also, the force component  $F_x \sin \beta$  is neglected. Then, the linearized version of (6.3.6) is

$$\begin{bmatrix} mv(\dot{\beta} + r) \\ J\dot{r} \end{bmatrix} = \begin{bmatrix} (F_{yF} + F_{yR}) \cos \beta \\ F_{yF}\ell_F - F_{yR}\ell_R + M_{zD} \end{bmatrix}. \quad (6.3.12)$$

- ii. The chassis sideslip angles  $\beta$ ,  $\beta_F$  and  $\beta_R$  are small, i.e.  $\cos \beta = 1$  in (6.3.12), and (6.3.9) becomes

$$\begin{aligned} \beta_F &= \beta + \ell_F r / v, \\ \beta_R &= \beta - \ell_R r / v. \end{aligned} \quad (6.3.13)$$

- iii. The steering angles  $\delta_F$  and  $\delta_R$  are small, i.e.  $\cos \delta_F = 1$  in (6.1.7) and  $\cos \delta_R = 1$  for the rear wheels. Then,

$$\begin{aligned} F_{yF} &= F_{yF}(\alpha_F), \\ F_{yR} &= F_{yR}(\alpha_R), \end{aligned} \quad (6.3.14)$$

are the unknown tire characteristics. Equation (6.3.12) now reads

$$\begin{bmatrix} mv(\dot{\beta} + r) \\ J\dot{r} \end{bmatrix} = \begin{bmatrix} F_{yF}(\alpha_F) + F_{yR}(\alpha_R) \\ F_{yF}(\alpha_F)\ell_F - F_{yR}(\alpha_R)\ell_R + M_{zD} \end{bmatrix}, \quad (6.3.15)$$

where  $\alpha_F = \delta_F - \beta_F$ ,  $\alpha_R = \delta_R - \beta_R$ .

Under feedback control according to Figure 6.3, the steering angle  $\delta_F$  is the sum of the driver command  $\delta_S$  and a corrective angle  $\delta_C$ , generated by the feedback system. The relationship between  $\delta_S$ ,  $\delta_C$  and  $\alpha_F$ ,  $\beta_F$ , as shown in Figure 6.5, is illustrated by Figure 6.13.

For feedback control, the angle

$$\gamma := \beta_F - \delta_C \quad (6.3.16)$$

is of particular interest.  $\beta_F$  is a plant state, and the feedback signal  $\delta_C$  is composed of plant and/or controller states, thus  $\gamma$  is continuous and may be used as a state variable

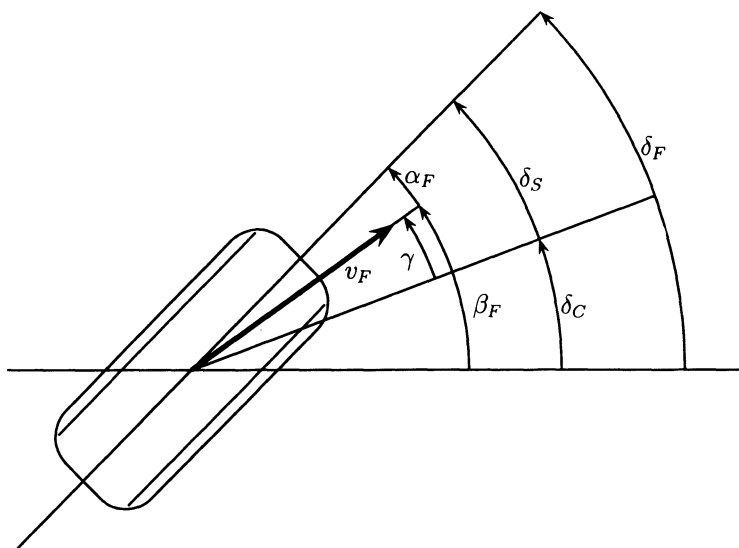


Figure 6.13. Front wheel angles

of the closed-loop system. Without control,  $\delta_C \equiv 0$ ,  $\gamma$  is the (front axle) slip angle  $\beta_F$ . With control,  $\gamma$  is the slip angle correction by control, in short, the *corrective slip angle*.

Similar to the crane example in Chapter 1, we will derive a feedback structure for the car. A first requirement is that it is robust with respect to the uncertain non-linear tire characteristics  $F_{yF}(\alpha_F)$  and  $F_{yR}(\alpha_R)$ . It will be shown that a robust decoupling of the two steering tasks is feasible. As described in Section 6.2, these are the path tracking task of the driver, and the automatically controlled yaw stabilization and disturbance compensation. This generic decoupling controller separates the two tasks, such that they can be improved by independent feedback loop designs.

### Robust Unilateral Decoupling Controller

By (6.2.5), with  $F_{yD} = 0$  and  $F_{yF}(\beta_F, \delta_F) = F_{yF}(\delta_S + \delta_C - \beta_F)$ , the lateral acceleration  $a_{yDP}$  is decoupled from the yaw motion, if

$$a_{yDP} = [F_{yF}(\delta_S + \delta_C - \beta_F)\ell + M_{zD}] / m\ell_R \quad (6.3.17)$$

does not depend on  $r$ , where  $r$  enters through the differential equation as  $\beta_F(r)$ . If we assume that  $\beta_F$  can be measured, then

$$\delta_C = \beta_F \quad (6.3.18)$$

is the ideal decoupling control law, yielding  $\alpha_F = \delta_S$ , and  $\gamma \equiv 0$ . The driver directly commands the tire slip angle  $\alpha_F$  and  $a_{yDP}$  is decoupled from  $r$ .

Since  $\beta_F$  is not available for feedback, we use a *backstepping* approach, i.e. the compensation of  $r$  is done at the input of an integrator with input  $\dot{\delta}_C$ . This additional integrator must be stabilized by closing the loop, such that  $\gamma$  remains small.

*Theorem 6.4 (Robust unilateral decoupling, Ackermann)*

The feedback control law

$$\dot{\delta}_C = r_{ref} - \left[ r + \frac{\ell_{DP} - \ell_F}{v} \dot{r} \right] \quad (6.3.19)$$

makes the yaw rate  $r$  non-observable from the lateral acceleration  $a_{yDP}$  at the decoupling point.

□

*Remark 6.5*

Practically, the control law (6.3.19) is turned on softly for  $v > v_1 > 0$ , such that no division by zero occurs.

Laplace transformation of (6.3.19) yields

$$\delta_C(s) = \frac{r_{ref}(s) - r(s)}{s} - \frac{\ell_{DP} - \ell_F}{v} r(s). \quad (6.3.20)$$

The decoupling feedback controller is illustrated by Figure 6.14.

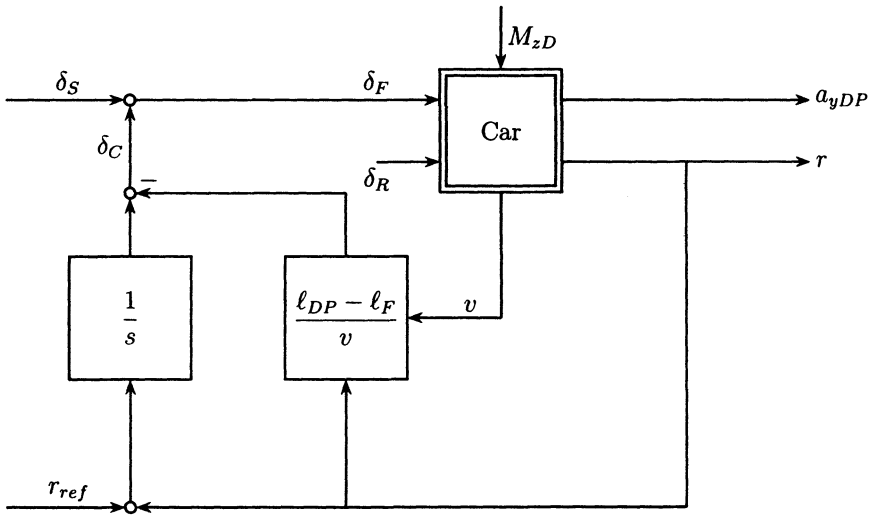


Figure 6.14. Robust unilateral decoupling by feedback of  $r$  to  $\delta_C$

The generation of a reference yaw rate  $r_{ref}$  will be discussed later. The steering command  $\delta_S$  will also enter there. Such a prefilter will be used to shape the response of  $a_{yDP}$  and  $r$  to a steering wheel input. This feedforward path has no influence on the robust decoupling concept in the closed loop. We first prove the robust decoupling property and stability of the two resulting subsystems.

*Proof of Theorem 6.4*

Substitute  $J = m\ell_R \ell_{DP}$  from (6.2.4) in (6.3.15)

$$\begin{bmatrix} mv(\dot{\beta} + r) \\ m\ell_R \ell_{DP} \dot{r} \end{bmatrix} = \begin{bmatrix} F_{yF}(\alpha_F) + F_{yR}(\alpha_R) \\ F_{yF}(\alpha_F)\ell_F - F_{yR}(\alpha_R)\ell_R + M_{zD} \end{bmatrix}, \quad (6.3.21)$$

where  $\alpha_F = \delta_S + \delta_C - \beta - \ell_F r/v$  and  $\alpha_R = \delta_R - \beta + \ell_R r/v$ , and close the loop by the control law (6.3.19).

In a classical approach, we would solve (6.3.19) and (6.3.21) for  $\dot{\beta}$ ,  $\dot{r}$  and  $\dot{\delta}_C$ . A formal proof would then proceed with a transformation to the state vector

$$\begin{bmatrix} \beta_R \\ r \\ \gamma \end{bmatrix} = \begin{bmatrix} 1 & -\ell_R/v & 0 \\ -0 & 1 & 0 \\ 1 & \ell_F/v & -1 \end{bmatrix} \begin{bmatrix} \beta \\ r \\ \delta_C \end{bmatrix}. \quad (6.3.22)$$

It is then, however, not clear, why this state vector was chosen. In order to introduce a general approach that is applicable to other plants as well, we use a different line of proof. As was discussed for the crane example in (1.6.11), it is a basic rule of modelling for robust control to keep the uncertainty in a single place in the model, and not to “smear” it over several model coefficients.

In our case of the car, the dominant uncertainty is in  $F_{yF}(\alpha_F)$  and  $F_{yR}(\alpha_R)$ . Therefore, solve (6.3.21) first for these quantities:

$$m\ell_R[v(\dot{\beta} + r) + \ell_{DP}\dot{r}] = F_{yF}(\alpha_F)\ell + M_{zD}, \quad (6.3.23)$$

$$m[v\ell_F(\dot{\beta} + r) - \ell_R\ell_{DP}\dot{r}] = F_{yR}(\alpha_R)\ell - M_{zD}. \quad (6.3.24)$$

Substitute

$$r = r_{ref} - \dot{\delta}_C - (\ell_{DP} - \ell_F)\dot{r}/v$$

from the control law (6.3.19) into (6.3.23), to obtain

$$m v \ell_R [(\dot{\beta} - \dot{\delta}_C) + \ell_F \dot{r}/v] = F_{yF}(\alpha_F)\ell + M_{zD} - m v \ell_R r_{ref}. \quad (6.3.25)$$

The quantity in square brackets is  $\dot{\gamma}$ , i.e.

$$\gamma = \beta + \ell_F r/v - \delta_C = \beta_F - \delta_C \quad (6.3.26)$$

as defined in (6.3.16). Then, with  $\alpha_F = \delta_S - \gamma$ ,

$$\dot{\gamma} = [F_{yF}(\delta_S - \gamma)\ell + M_{zD}]/m v \ell_R - r_{ref}. \quad (6.3.27)$$

This first order differential equation for  $\gamma$  does not depend on the state variable  $r$ , it is unilaterally decoupled. The decoupling effect is robust with respect to

the uncertain mass  $m$  and velocity  $v$  and, most importantly, with respect to the uncertain lateral forces  $F_{yF}$  and  $F_{yR}$  at the front and rear axles. The only quantity, that must be known for the implementation of the control law (6.3.19) is  $\ell_{DP}$ . It depends on the longitudinal mass distribution, which is constant during a ride of the car.

The lateral acceleration  $a_{yDP}$  at the decoupling point is, by (6.2.5),

$$a_{yDP} = [F_{yF}(\alpha_F)\ell + M_{zD}]/m\ell_R \quad (6.3.28)$$

and, by comparison with (6.3.27),

$$a_{yDP} = v(\dot{\gamma} + r_{ref}). \quad (6.3.29)$$

The decoupled lateral subsystem (6.3.27) is illustrated by Figure 6.15.

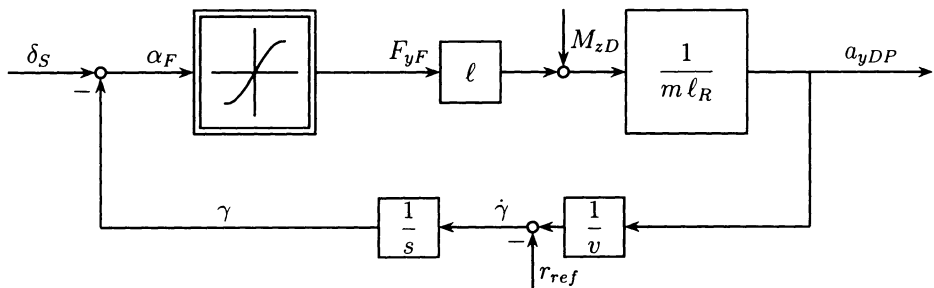


Figure 6.15. Lateral dynamics subsystem with output  $a_{yDP}$

Also,  $a_{yDP}$  is robustly decoupled from the influence of  $r$ . This shows that the yaw rate  $r$  is non-observable from the lateral acceleration  $a_{yDP}$  at the decoupling point.  $\square$

### The Decoupled Yaw Subsystem

For the rear-wheel subsystem also, by analogy with (6.3.16), the state variable

$$\beta_R = \beta - \ell_R r/v = \delta_R - \alpha_R \quad (6.3.30)$$

is chosen, then

$$\dot{\beta}_R = \dot{\beta} - \ell_R \dot{r}/v,$$

and with  $\dot{\beta}$  from (6.3.24),

$$\dot{\beta}_R = \frac{1}{mv\ell_F} [F_{yR}(\delta_R - \beta_R)\ell - M_{zD}] + \frac{\ell_R(\ell_{DP} - \ell_F)}{v\ell_F} \dot{r} - r. \quad (6.3.31)$$

The differential equation for  $r$  follows from the second row of (6.3.21), as

$$\dot{r} = \frac{1}{m\ell_R\ell_{DP}} [F_{yF}\ell_F - F_{yR}\ell_R + M_{zD}]. \quad (6.3.32)$$

$F_{yF}$  is a coupling term from the lateral subsystem of Figure 6.15. From a practical point of view, however, the quantity  $a_{yDP}$  is better suited as a coupling term, because it may be measured by an accelerometer, and also in view of the task separation as illustrated by Figures 6.7 and 6.8. Therefore,

$$F_{yF} = [m\ell_R a_{yDP} - M_{zD}]/\ell$$

from (6.3.28) is substituted in (6.3.32), yielding

$$\dot{r} = \frac{\ell_F}{\ell\ell_{DP}} a_{yDP} - \frac{1}{m\ell_{DP}} F_{yR}(\delta_R - \beta_R) + \frac{1}{m\ell\ell_{DP}} M_{zD}. \quad (6.3.33)$$

This  $\dot{r}$  is now substituted in (6.3.31) and both equations are combined to the state space model of the yaw subsystem

$$\begin{bmatrix} \dot{\beta}_R \\ \dot{r} \end{bmatrix} = \frac{1}{m\ell_{DP}} \begin{bmatrix} (\ell_{DP} + \ell_R)/v & \\ -1 & \end{bmatrix} [F_{yR}(\delta_R - \beta_R) - M_{zD}/\ell] - \begin{bmatrix} 1 \\ 0 \end{bmatrix} r + \frac{1}{\ell\ell_{DP}} \begin{bmatrix} (\ell_R(\ell_{DP} - \ell_F))/v \\ \ell_F \end{bmatrix} a_{yDP}. \quad (6.3.34)$$

Figure 6.16 illustrates the yaw subsystem with the coupling input  $a_{yDP}$  from the lateral subsystem.

The signal flow diagram of Figure 6.17 illustrates the unilaterally decoupled system. The lateral dynamics may be modified by accelerometer feedback of  $a_{yDP}$  to front-wheel steering  $\delta_S$ . If rear-wheel steering  $\delta_R$  is available, then feedback from  $r$  can be used to improve the yaw dynamics. Also, a feedforward path from  $\delta_S$  to  $\delta_R$  can be implemented, for example, to shape the response in the yaw rate  $r$ , or the sideslip angle  $\beta_R$ , to a steering wheel input. The above additional control structures do not destroy the unilateral robust decoupling property. Control system structures will be discussed further after the linearization of the tire characteristics.

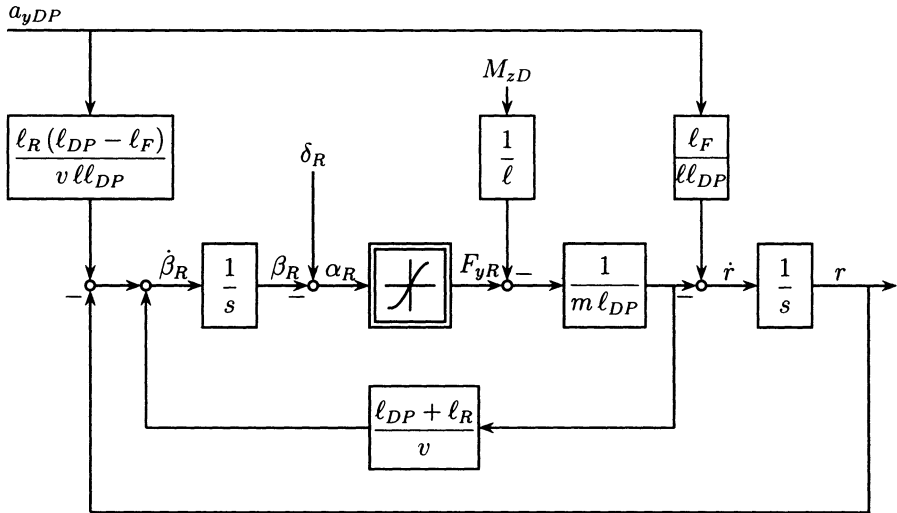
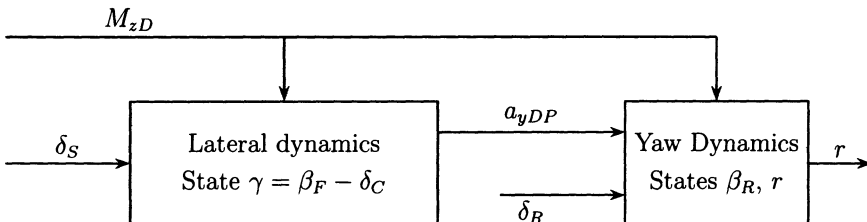


Figure 6.16. Yaw dynamics subsystem

*Remark 6.6*

Note that the control law (6.3.19) was derived structurally and its robustness does not depend on any parameter values (except the decoupling point location  $\ell_{DP} - \ell_F$ , which depends only on the mass distribution and is constant during a ride). Compare this with a classical approach, where the lateral acceleration  $a_{yCG}$  at the CG would be decoupled from  $r$ . Since this is not exactly possible, the influence of  $r$  on  $a_{yCG}$  can be only minimized by numerical optimization for specific vehicle data. The transparency of the structurally robust decoupling controller (6.3.19) would then be completely lost.

□

*Remark 6.7*Figure 6.17. The yaw rate  $r$  is not observable from the lateral acceleration  $a_{yDP}$  at the decoupling point

The assumption of small sideslip angles is not really needed for the derivation of a robustly decoupling control law. In [9], [11] this assumption is dropped. Then

$$\tan \beta_F = v_{yF}/v_x,$$

where  $v_{yF}$  and  $v_x$  are the lateral and longitudinal velocity components of  $\vec{v}$ .

Instead of the control law (6.3.19), there results

$$\dot{\delta}_C = r_{ref} - \left[ r + \frac{(\ell_{DP} - \ell_F) \cos^2 \beta_F \dot{r}}{v_x} \right] + \frac{\ell_F r^2 - a_x}{v_x} \sin \beta_F \cos \beta_F, \quad (6.3.35)$$

where  $a_x$  is the longitudinal acceleration.

The implementation of (6.3.35) requires, however, an accelerometer for  $a_x$  and a reconstruction of  $\beta_F$  in an observer. It is, therefore, eventually simplified to the form (6.3.19), which is used here from the beginning in order to simplify the proof. The last non-linear term in the controller (6.3.35) shows that hard braking produces the maximal value of the term  $\ell_F r^2 - a_x$ . This situation should therefore be considered in simulations. A simulation study for a limousine [178] indicated that the last term in (6.3.35) has only minor influence on the closed-loop behavior.

□

### Stability of the Decoupled Lateral and Yaw Subsystems

The robust decoupling control concept is practically useful, only if the resulting two subsystems are stable, or can be stabilized separately without destroying the decoupling effect.

For no external inputs,  $M_{zD} = 0$ ,  $\delta_S = 0$ ,  $r_{ref} = 0$  and a symmetric tire characteristic, the lateral subsystem is

$$\dot{\gamma} = -F_{yF}(\gamma)\ell/mv\ell_R.$$

The Lyapunov function  $V = \gamma^2$  yields

$$\dot{V} = 2\gamma\dot{\gamma} = -2\gamma F(\gamma)\ell/mv\ell_R. \quad (6.3.36)$$

The condition  $\gamma F(\gamma) > 0$  is satisfied for tire characteristics, see Figure 6.6. Thus,  $\dot{V} < 0$  and the decoupled lateral subsystem is stable in forward driving ( $v > 0$ ).

Alternatively, a Popov test may be applied. The Nyquist and Popov plots of the linear part in Figure 6.15 have  $90^\circ$  phase angle, therefore the upper bound for the sector of absolute stability is infinity.

For the yaw subsystem of Figure 6.16, the phase angle is below  $180^\circ$ , therefore ideally the same conclusion applies. Here, however, we are much closer to the stability boundary. Additional phase delay, e.g. by actuator dynamics or a delayed build-up of the lateral forces  $F_{yF}$  and  $F_{yR}$  may cause instability. If the car is equipped with rear-wheel steering, then a stabilization by feedback from  $r$  to  $\delta_R$  is easy. In Section 6.6, alternatives to rear-wheel steering are discussed.

### Experimental Verification

The effects of the control law (6.3.17) were experimentally tested on a BMW 735i. The data of the linearized model are given in Table 6.1. It turns out that the decoupling point is very close to the front axle, the difference  $\ell_F - \ell_{DP}$  is only 1 % of the wheelbase  $\ell$ . Therefore, the simplified control law

$$\dot{\delta}_C = r_{ref} - r \quad (6.3.37)$$

was used. The test car is equipped with a steer-by-wire system such that the sum  $\delta_S + \delta_C = \delta_F$  (see Figure 6.13) is formed electrically and the steering actuator moves the entire steering angle  $\delta_F$ . The generation of  $r_{ref}$  from  $\delta_S$  and  $v$  will be discussed later; the emphasis of the tests was on the rejection of disturbance torques  $M_{zD}$ . Experimentally,  $M_{zD}$  was generated:

- i. In a side wind test by passing a series of lateral fans.
- ii. In a  $\mu$ -split braking test, with the right tires on a slippery surface (water flooded tiles) and the left tires on a high-grip surface.

The driver just had to keep the handwheel straight and i. pass the side wind machine, or ii. apply full brake on the  $\mu$ -split test track, i.e.  $\delta_S \equiv 0$  and  $r_{ref} \equiv 0$ .

Figures 6.18 and 6.19 show snapshots with 1 second sampling time. The left column is for the conventional vehicle, the right column for our robust decoupling control law. Both experiments show that the control system brings the car back to the original heading within one second.

The robustness of the control system was demonstrated in extensive simulations. For more details, the reader is referred to [18].

Alternative car steering concepts are usually more oriented towards parameter and disturbance identification (e.g. for the road-tire friction coefficient, tire pressure, side wind), i.e. they look at the causes for  $M_{zD}$ . It is, however, difficult to foresee all possible causes of skidding, and to develop specialized sensors for each of them. The robust control concept looks at the effect of disturbances  $M_{zD}$  of unknown origin. This effect is seen in the error signal  $r_{ref} - r$ .

## 6.4 The Linearized Single-track Model

In order to allow for a linear analysis of the car, the lateral tire forces are now linearized about a zero tire sideslip angle as

$$\begin{aligned} F_{yF}(\alpha_F) &= \mu c_F \alpha_F, \\ F_{yR}(\alpha_R) &= \mu c_R \alpha_R. \end{aligned} \quad (6.4.1)$$

The slope  $c_F$  resp.  $c_R$  of the tire characteristic is called *cornering stiffness*. Note that (6.4.1) applies to the front or rear axle, i.e. to the sum of left and right wheel at the respective axle. (Note that some authors use  $2c_F'$  or  $2c_R'$ , where  $c_F'$  or  $c_R'$  refer to the

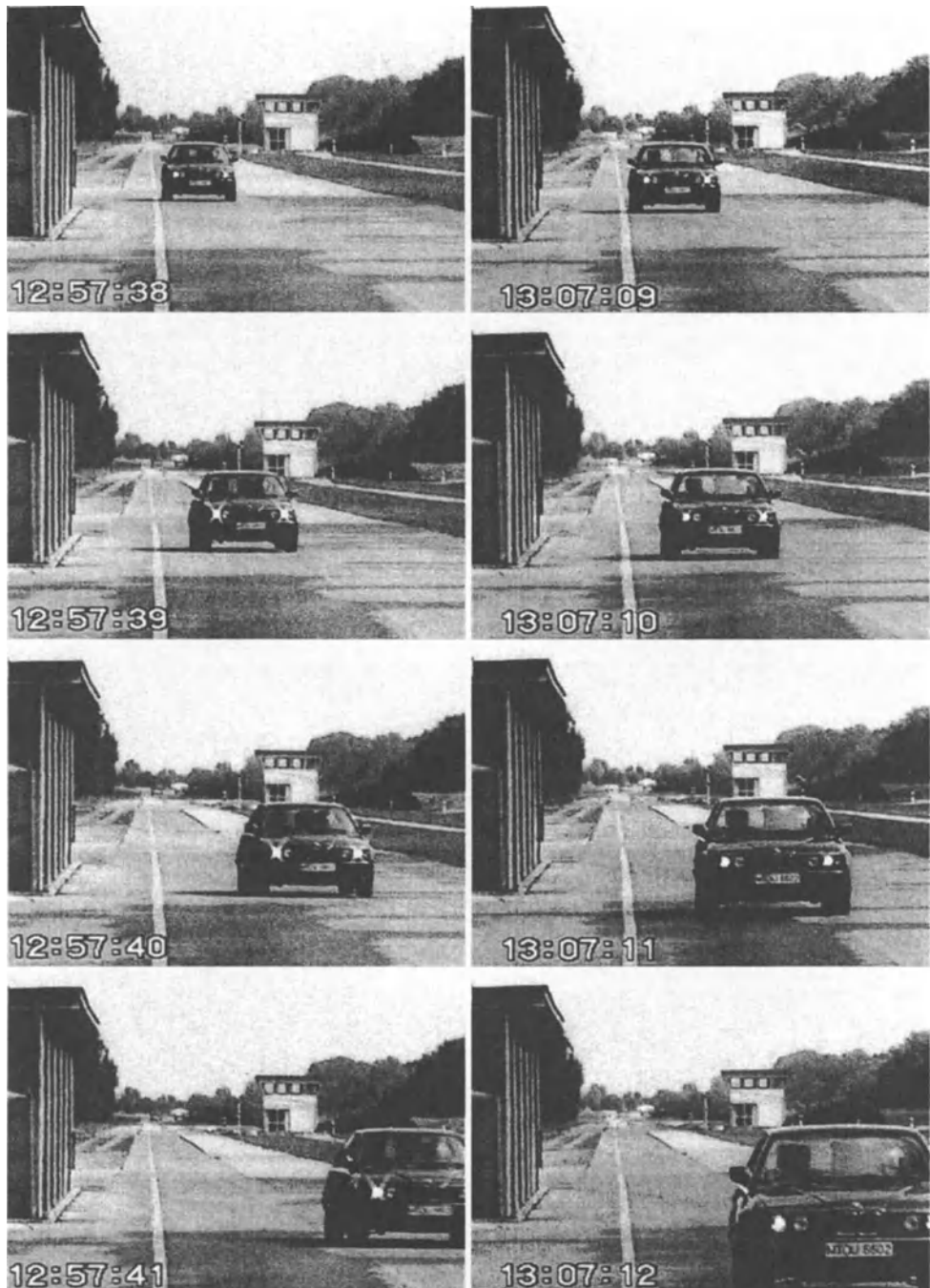


Figure 6.18. Side wind test at  $v = 120$  [km/h] and wind velocity 80 [km/h]; left: conventional, right: decoupled

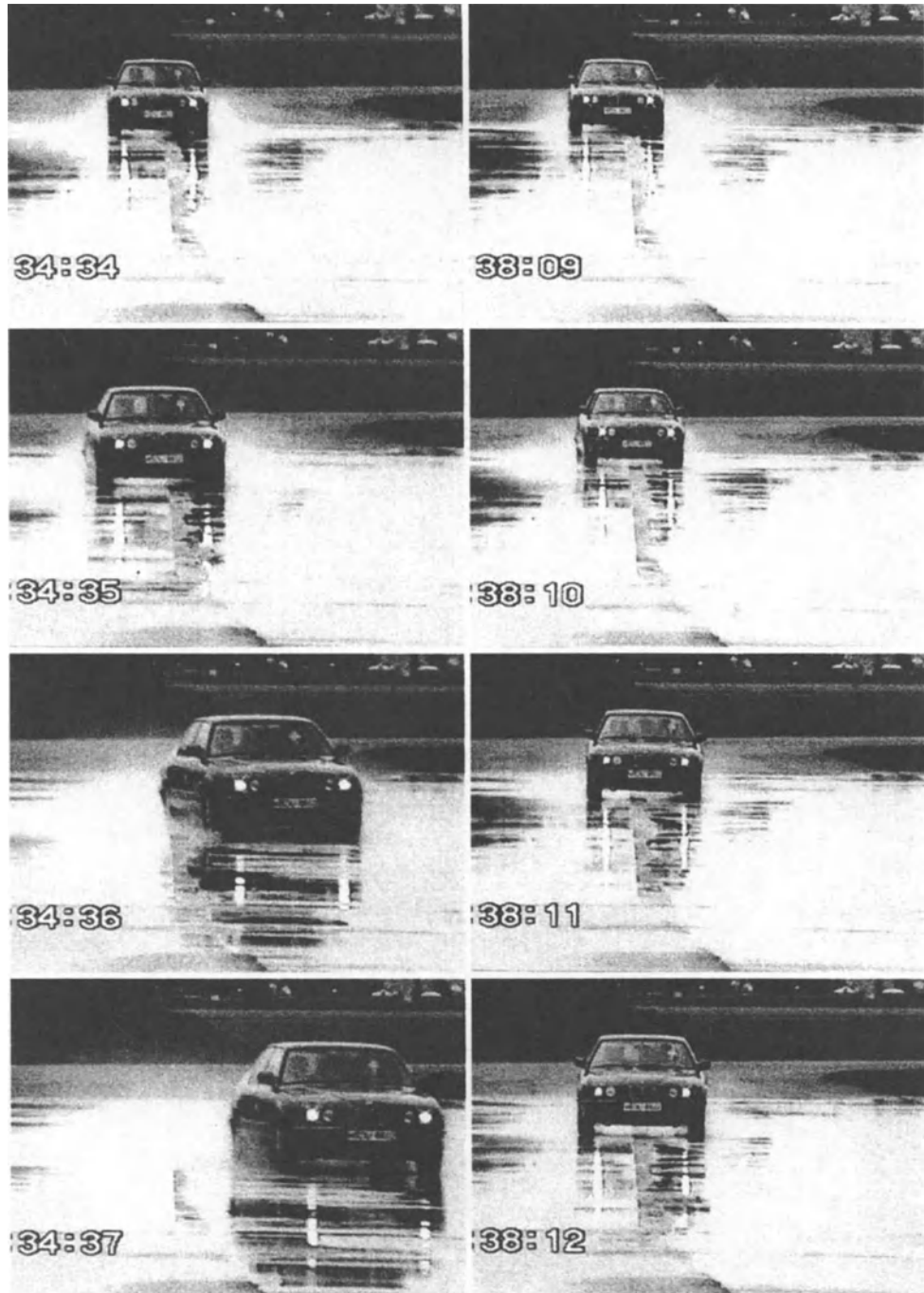


Figure 6.19.  $\mu$ -split-braking at 80 [km/h]; left: conventional, right: decoupled

individual tire.) The friction coefficient  $\mu \leq 1$  is assumed to be the same at the front and rear wheels.

Typical values of the friction coefficient  $\mu$  are

$$\mu = 1 \quad \text{dry road}$$

$$\mu = 0.5 \quad \text{wet road}$$

$$\mu = 0.15 \quad \text{ice}$$

Now, solve (6.3.15) for  $\dot{\beta}$  and  $\dot{r}$ , and substitute the linearized tire characteristics  $F_{yF}$  and  $F_{yR}$ :

$$\begin{bmatrix} \dot{\beta} \\ \dot{r} \end{bmatrix} = \begin{bmatrix} \frac{\mu}{mv}(c_F\alpha_F + c_R\alpha_R) - r \\ \frac{\mu}{J}(c_F\ell_F\alpha_F - c_R\ell_R\alpha_R) + \frac{1}{J}M_{zD} \end{bmatrix}, \quad (6.4.2)$$

and substitute (6.3.10) and (6.3.13)

$$\begin{bmatrix} \dot{\beta} \\ \dot{r} \end{bmatrix} = \begin{bmatrix} \frac{\mu}{mv}[c_F(\delta_F - \beta - \ell_F r/v) + c_R(\delta_R - \beta + \ell_R r/v)] - r \\ \frac{\mu}{J}[c_F\ell_F(\delta_F - \beta - \ell_F r/v) - c_R\ell_R(\delta_R - \beta + \ell_R r/v)] + M_{zD}/J \end{bmatrix}. \quad (6.4.3)$$

This linear state space model is written as

$$\begin{bmatrix} \dot{\beta} \\ \dot{r} \end{bmatrix} = \begin{bmatrix} a_{11} & a_{12} \\ a_{21} & a_{22} \end{bmatrix} \begin{bmatrix} \beta \\ r \end{bmatrix} + \begin{bmatrix} b_{11} & b_{12} \\ b_{21} & b_{22} \end{bmatrix} \begin{bmatrix} \delta_F \\ \delta_R \end{bmatrix} + \begin{bmatrix} 0 \\ b_D \end{bmatrix} M_{zD}, \quad (6.4.4)$$

$$a_{11} = -\mu(c_R + c_F)/mv,$$

$$a_{12} = -1 + \mu(c_R\ell_R - c_F\ell_F)/mv^2,$$

$$a_{21} = \mu(c_R\ell_R - c_F\ell_F)/J,$$

$$a_{22} = -\mu(c_R\ell_R^2 + c_F\ell_F^2)/Jv,$$

$$b_{11} = \mu c_F/mv,$$

$$b_{12} = \mu c_R/mv,$$

$$b_{21} = \mu c_F\ell_F/J,$$

$$b_{22} = -\mu c_R\ell_R/J,$$

$$b_D = 1/J.$$

The lateral acceleration at the decoupling point is by (6.2.5), (6.3.13) and (6.4.1).

$$\begin{aligned} a_{yDP} &= \mu c_F \alpha_F \ell / m \ell_R \\ &= \frac{\mu c_F \ell}{m \ell_R} (\delta_F - \beta - \ell_F r/v) + \frac{M_{zD}}{m \ell_R}. \end{aligned} \quad (6.4.5)$$

This classical form of the single-track model contains the four uncertain parameters  $\mu$ ,  $m$ ,  $J$ , and  $v$ . These parameters may be reduced to two by the introduction of the decoupling point location, see Figure 6.9 and Equation (6.2.4):

$$\ell_{DP} = J/m \ell_R. \quad (6.4.6)$$

It is invariant under changes of  $\mu$  and  $v$ , and depends only on the mass distribution in the vehicle. Vehicles are normally designed such that there are no significant differences in  $\ell_{DP}$  between the empty and the full car (See the data for the City Bus O 305 in Table 6.1). An extreme case is a heavy load in the trunk of a lightweight car, it increases the ratio  $J/m$  and reduces  $\ell_R$ . At least the parameter  $\ell_{DP}$  does not vary much during a ride, and  $\ell_{DP}$  would have to be identified only once after starting the car.

Substitute  $J = m \ell_R \ell_{DP}$  in Equation (6.4.3) or (6.4.4), then the uncertain parameters  $\mu$  and  $m$  appear in their ratio  $\mu/m$ . A reduced  $\mu$  on a slippery road has the same effect as an increased mass  $m$ . Rescale the friction coefficient  $\mu$  and the mass  $m$  by

$$\frac{\tilde{\mu}}{\tilde{m}} = \frac{\mu}{m}, \quad (6.4.7)$$

where  $\tilde{m}$  is fixed as  $\tilde{m} = m^-$ , the mass of the unloaded vehicle (including only a light-weight driver). Then only one parameter

$$\tilde{\mu} = \mu \frac{m^-}{m}, \quad \frac{m^-}{m} \leq 1. \quad (6.4.8)$$

is needed, where  $\tilde{\mu} \in [\mu^- m^- / m, 1]$ .

The four parameters  $\mu, m, J$ , and  $v$  have thus been replaced by two parameters

$$\begin{aligned} v &\in [v^-; v^+], \\ \tilde{\mu} &\in [\tilde{\mu}^-; 1]. \end{aligned} \quad (6.4.9)$$

Then, (6.4.4) becomes

$$\begin{bmatrix} \dot{\beta} \\ \dot{r} \end{bmatrix} = \begin{bmatrix} a_{11} & a_{12} \\ a_{21} & a_{22} \end{bmatrix} \begin{bmatrix} \beta \\ r \end{bmatrix} + \begin{bmatrix} b_{11} & b_{12} \\ b_{21} & b_{22} \end{bmatrix} \begin{bmatrix} \delta_F \\ \delta_R \end{bmatrix} + \begin{bmatrix} 0 \\ b_D \end{bmatrix} M_{zD}. \quad (6.4.10)$$

$$\begin{aligned}
a_{11} &= -\tilde{\mu}(c_R + c_F)/\tilde{m}v, \\
a_{12} &= -1 + \tilde{\mu}(c_R\ell_R - c_F\ell_F)/\tilde{m}v^2, \\
a_{21} &= -\tilde{\mu}(c_R\ell_R - c_F\ell_F)/\tilde{m}\ell_R\ell_{DP}, \\
a_{22} &= -\tilde{\mu}(c_R\ell_R^2 + c_F\ell_F^2)/\tilde{m}v\ell_R\ell_{DP}, \\
b_{11} &= \tilde{\mu}c_F/\tilde{m}v, \\
b_{12} &= \tilde{\mu}c_R/\tilde{m}v, \\
b_{21} &= \tilde{\mu}c_F\ell_F/\tilde{m}\ell_R\ell_{DP}, \\
b_{22} &= -\tilde{\mu}c_R/\tilde{m}\ell_{DP}, \\
b_D &= 1/m\ell_R\ell_{DP}.
\end{aligned}$$

Without loss of generality, the notation may be simplified by omitting the tilde on  $\mu$  and  $m$  and observing that the mass of the empty vehicle is substituted for  $m$ . The actual mass only appears in  $b_D$ .

A typical operating domain for  $v$  and  $\mu$  is shown in Figure 6.20.

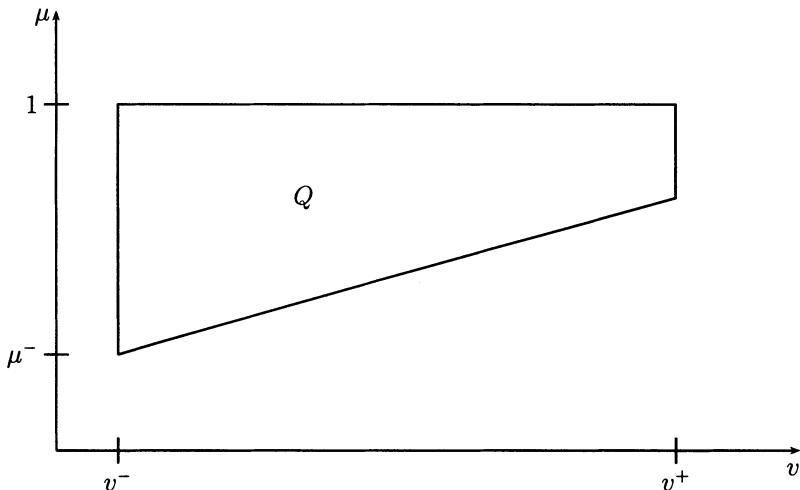


Figure 6.20. Operating domain for car steering control system

At  $v = 0$ , the vehicle is obviously not controllable, therefore specifications for the controlled vehicle can be met only for  $v \geq v^- > 0$ . At the minimum velocity, the controller must guarantee good performance for the whole range from  $\mu^-$  (full load, icy

road) to  $\mu = 1$  (empty vehicle, dry road). The maximum velocity  $v^+$  can be driven only under reasonably good road conditions. The friction coefficient  $\mu$  is a very critical uncertain parameter, because it can vary suddenly when the car drives on an icy bridge or on an icy road in the shade of a forest. There is no time to identify  $\mu$  and a steering control system must be robust with respect to  $\mu$ . Numerical values for the fixed parameters are given in Table 6.1 for a city bus and for a high-speed limousine. Note that the limousine has an almost *ideal mass distribution*, for which the front mass would be at the front axle, i.e.  $\ell_{DP} = \ell_F$ . The difference is only 1% of the wheelbase. The city bus has a relatively short wheelbase for better maneuverability at low speeds. Then, the decoupling point is in front of the front axle. It is remarkable, however, that  $\ell_{DP}$  does not vary between an empty and full vehicle.

Table 6.1. Numerical values for two vehicles

Parameter	Daimler Benz		BMW 735 i
	City Bus O 305 empty	full	
$m$	9950 [kg]	16000 [kg]	1864 [kg]
$J$	105700 [kgm <sup>2</sup> ]	171300 [kgm <sup>2</sup> ]	3654 [kgm <sup>2</sup> ]
$v^+$	20 [m/s]	20 [m/s]	70 [m/s]
$c_R$	470000 [N/rad]	470000 [N/rad]	213800 [N/rad]
$c_F$	198000 [N/rad]	198000 [N/rad]	101600 [N/rad]
$\ell_R$	1.93 [m]	1.93 [m]	1.32 [m]
$\ell_F$	3.67 [m]	3.67 [m]	1.51 [m]
$\ell_{DP} = \frac{J}{m\ell_R}$	5.50 [m]	5.55 [m]	1.48 [m]
$\ell = \ell_R + \ell_F$	5.60 [m]	5.60 [m]	2.83 [m]
$\frac{\ell_F - \ell_{DP}}{\ell}$	-0.33	-0.34	0.01

### Stationary Cornering

Consider the steady state ( $\dot{\beta} = 0, \dot{r} = 0$ ) for the inputs  $\delta_F = \delta_{Fstat}, \delta_R = 0, M_{zD} = 0$ . From (6.4.4), follows

$$\begin{bmatrix} 0 \\ 0 \end{bmatrix} = \begin{bmatrix} a_{11} & a_{12} \\ a_{21} & a_{22} \end{bmatrix} \begin{bmatrix} \beta_{stat} \\ r_{stat} \end{bmatrix} + \begin{bmatrix} b_{11} \\ b_{21} \end{bmatrix} \delta_{Fstat}, \quad (6.4.11)$$

$$\begin{bmatrix} \beta_{stat} \\ r_{stat} \end{bmatrix} = \frac{-1}{a_{11}a_{22} - a_{12}a_{21}} \begin{bmatrix} a_{22} & -a_{12} \\ -a_{21} & a_{11} \end{bmatrix} \begin{bmatrix} b_{11} \\ b_{21} \end{bmatrix} \delta_{Fstat} = \begin{bmatrix} k_{\beta stat} \\ k_{r stat} \end{bmatrix} \delta_{Fstat}. \quad (6.4.12)$$

The evaluation yields

$$k_{\beta stat} = \frac{\mu c_R \ell_R \ell - \ell_F m v^2}{\mu c_R \ell^2 [1 + (v/v_{CH})^2]}, \quad (6.4.13)$$

$$k_{r stat} = \frac{v}{\ell [1 + (v/v_{CH})^2]}, \quad (6.4.14)$$

with the characteristic velocity  $v_{CH}$ .

$$v_{CH}^2 = \frac{\mu c_R c_F \ell^2}{m(c_R \ell_R - c_F \ell_F)}. \quad (6.4.15)$$

For the empty bus, the characteristic velocity at  $\mu = 1$  is  $v_{CH} = 40.3$  [m/sec], for the limousine  $v_{CH} = 26.9$  [m/sec].

The steady state gain  $k_{r stat}$  will be used later for generating a reference yaw rate  $r_{ref}$ .

For the lateral acceleration  $a_{yDP}$ , the steady state gain is, by (6.4.5),

$$\begin{aligned} k_{ayDPstat} &= \frac{\mu c_F \ell}{m \ell_R} \left( 1 - k_{\beta stat} - \frac{\ell_F}{v} k_{r stat} \right) \\ &= \frac{v^2}{\ell [1 + (v/v_{CH})^2]} = v k_{r stat}. \end{aligned} \quad (6.4.16)$$

Note that in stationary cornering the lateral acceleration is the same at all points, otherwise  $\dot{r}$  would not be zero.

Note also that in stationary cornering

$$v = R r, \quad (6.4.17)$$

where  $R$  is the curve radius as illustrated by Figure 6.21. The centripetal acceleration is

$$a_y = v^2/R. \quad (6.4.18)$$

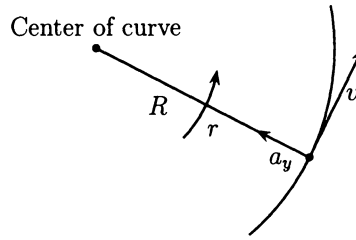


Figure 6.21. Relation between curve radius  $R$ , yaw rate  $r$  and velocity  $v$

It is mathematically inconvenient that the curve radius goes through infinity for a change from left to right turn. Therefore, introduce the *curvature*

$$\varrho = 1/R, \quad (6.4.19)$$

with positive sign in a left curve. Its steady state is

$$\varrho_{stat} = r_{stat}/v = \frac{1}{\ell[1 + (v/v_{CH})^2]} \delta_{stat}. \quad (6.4.20)$$

At low velocities, the driver commands the curvature  $\varrho_{stat} = \delta_{stat}/\ell$ ; at high velocities the lateral acceleration  $k_{ayDPstat} = \delta_{stat}v_{CH}^2/\ell$  is commanded from the steering wheel. At the characteristic velocity  $v = v_{CH}$ , the driver commands essentially the yaw rate  $r_{stat} = v_{CH}/2\ell$ .

The steady state effect in curvature, yaw rate and lateral acceleration as a function of velocity is shown in Figure 6.22. In stationary cornering, the lateral force (or

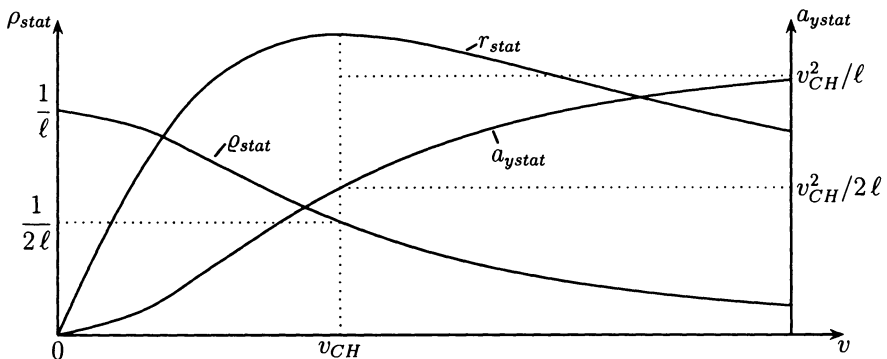


Figure 6.22. Steady state curvature, yaw rate and lateral acceleration as a function of velocity  
acceleration) must balance the centrifugal force (or acceleration).  
Therefore,

$$a_{ystat} = v^2 \varrho_{stat}, \quad (6.4.21)$$

which agrees with (6.4.18).

For a given curve parameter, the required steering angle is

$$\begin{aligned}\delta_{Fstat} &= \ell[1 + (v/v_{CH})^2]\varrho_{stat} \\ &= \ell[1 + (v/v_{CH})^2]r_{stat}/v \\ &= \ell[1 + (v/v_{CH})^2]a_{ystat}/v^2.\end{aligned}\quad (6.4.22)$$

Note that  $v_{CH}$  is proportional to the uncertain friction coefficient  $\mu$ , see (6.4.15).

### Remark 6.8

The first author is frequently asked about his relationship with the *Ackermann angle* and *Ackermann steering*. According to a footnote in [150], the older Ackermann was an English coach-builder, who filed in 1917 an English patent for Lankensperger, the inventor of the knuckle steering. Nothing is known about a kinship.

For slow driving, e.g. in a parking maneuver, the tire slip angles  $\alpha_F$  and  $\alpha_R$  are zero, i.e. in Figure 6.12 the momentary pole is located on a line through the rear axle. The steering angle  $\delta_F$  is then calculated from the triangle of Figure 6.23 as

$$\sin \delta_F = \ell/R.$$

$\delta_F$  is called the *Ackermann angle*.

The *Ackermann steering* is also designed for slow driving with zero sideslip angle. It takes into account that in a curve the inner front wheel is running on a smaller radius than the outer front wheel. Today, steering systems are built with almost parallel deflection of the left and right front wheel [150].  $\square$

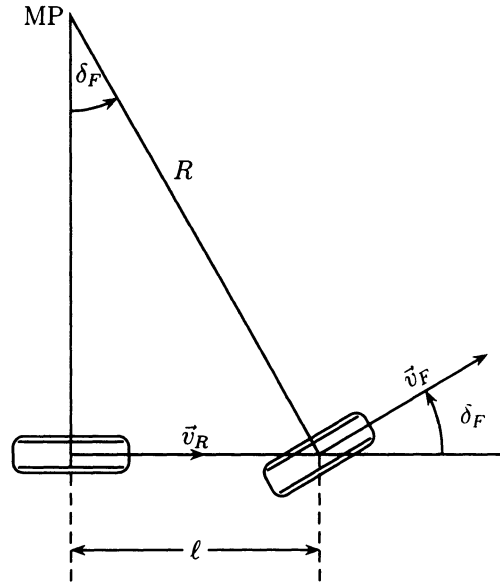
### Poles and Zeros

We first analyze the open-loop system (6.4.4) for eigenvalues and transfer functions from inputs  $\delta_F, \delta_R$  and  $M_{zD}$  to  $r$ , and  $a_{yDP}$ . The characteristic polynomial of the system matrix in (6.4.4) is

$$\begin{aligned}p_A(s) &= (s - a_{11})(s - a_{22}) - a_{12}a_{21} \\ &= a_0 + a_1 s + s^2,\end{aligned}\quad (6.4.23)$$

with the parameter-dependent coefficients

$$\begin{aligned}a_0 &= \frac{\mu}{m\ell_R\ell_{DP}} \left[ \frac{\mu c_F c_R \ell^2}{mv^2} + c_R \ell_R - c_F \ell_F \right], \\ a_1 &= \frac{\mu}{mv} \left[ c_R + c_F + \frac{c_R \ell_R^2 + c_F \ell_F^2}{\ell_R \ell_{DP}} \right].\end{aligned}$$

Figure 6.23. Ackermann angle  $\delta_F$ 

The uncertain parameters  $q_1 = \mu$  and  $q_2 = 1/v$  enter polynomially into the coefficients of the characteristic polynomial

$$p_A(s, q_1, q_2) = a_0(q_1^2 q_2^2, q_1) + a_1(q_1 q_2)s + s^2. \quad (6.4.24)$$

We continue here to use the uncertain physical parameters  $\mu$  and  $v$ , rather than  $q_1$  and  $q_2$ .

The system is stable for  $a_0 > 0$ ,  $a_1 > 0$ . Two cases must be distinguished:

- a) *Understeering*:  $c_R\ell_R - c_F\ell_F \geq 0$ , the system is stable.
- b) *Oversteering*:  $c_R\ell_R - c_F\ell_F < 0$ , the system is stable if the *critical speed*  $v_{crit}$  is not exceeded, where

$$v_{crit}^2 := \frac{\mu c_F c_R \ell^2}{m(c_F \ell_F - c_R \ell_R)}. \quad (6.4.25)$$

Typical road vehicle data correspond to the understeering case, see Table 6.1.

The characteristic polynomial  $p_A(s)$  may be written in terms of damping  $D$  and natural frequency  $\omega_0$  as

$$p_A(s) = \omega_0^2 + 2D\omega_0 s + s^2, \quad (6.4.26)$$

where  $\omega_0$  and  $D$  depend on the physical parameters as follows:

$$\omega_0^2(\mu, v) = \frac{\mu^2 c_F c_R \ell^2 + mv^2 \mu(c_R \ell_R - c_F \ell_F)}{m^2 \ell_R \ell_{DP} v^2}, \quad (6.4.27)$$

$$D(v) = \frac{\ell_R \ell_{DP} (c_R + c_F) + c_R \ell_R^2 + c_F \ell_F^2}{2 \sqrt{\ell_R \ell_{DP} [c_R c_F \ell^2 + mv^2(c_R \ell_R - c_F \ell_F)/\mu]}}. \quad (6.4.28)$$

For large velocities  $v$ , the damping  $D$  goes to zero and the eigenvalues of understeering vehicles approach the imaginary axis at

$$\omega_\infty = \lim_{v \rightarrow \infty} \omega_0 = \sqrt{\frac{\mu(c_R \ell_R - c_F \ell_F)}{m \ell_R \ell_{DP}}}. \quad (6.4.29)$$

With decreasing velocity  $v$ , the damping  $D$  becomes larger than 1, i.e. the pair of complex eigenvalues meets at the real axis and branches into a pair of real eigenvalues. For  $v \rightarrow 0$ , two real eigenvalues go to minus infinity. Figure 6.24 illustrates the velocity dependence of the yaw eigenvalues. Figure 6.24 is not a standard root locus because

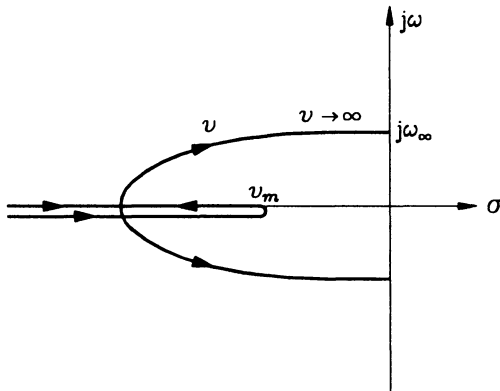


Figure 6.24. Velocity dependence of yaw eigenvalues

the parameter  $v$  enters non-linearly. At some velocity  $v_m$ , one of the real eigenvalues has a maximum.

### Transfer Functions

For the calculation of various transfer functions, first determine

$$(sI - \mathbf{A})^{-1} = \begin{bmatrix} s - a_{11} & -a_{12} \\ -a_{21} & s - a_{22} \end{bmatrix}^{-1} = \frac{1}{p_A(s)} \begin{bmatrix} h_{11}(s) & h_{12} \\ h_{21} & h_{22}(s) \end{bmatrix}, \quad (6.4.30)$$

where

$$\begin{aligned} h_{11}(s) &= s - a_{22} = s + \mu(c_R \ell_R^2 + c_F \ell_F^2)/mv \ell_R \ell_{DP}, \\ h_{12} &= a_{12} = -1 + \mu(c_R \ell_R - c_F \ell_F)/mv^2, \\ h_{21} &= a_{21} = \mu(c_R \ell_R - c_F \ell_F)/m \ell_R \ell_{DP}, \\ h_{22}(s) &= s - a_{11} = s + \mu(c_R + c_F)/mv. \end{aligned}$$

Outputs of particular interest are the yaw rate  $r$  and the lateral acceleration at the decoupling point. By (6.4.5),

$$a_{yDP} = c_1\beta + c_1\ell_F r/v - c_1\delta_F + dM_{zD}, \quad (6.4.31)$$

with  $c_1 = -\mu c_F \ell / m \ell_R$ ,  $d = 1/m \ell_R$ .

The six transfer functions of the system (6.4.4) with inputs  $\delta_F$ ,  $\delta_R$  and  $M_{zD}$  and outputs  $r$  and  $a_{yDP}$  are

$$\begin{aligned} & \begin{bmatrix} r(s) \\ a_{yDP}(s) \end{bmatrix} \\ &= \frac{1}{p_A(s)} \left\{ \begin{bmatrix} 0 & 1 \\ c_1 & c_1\ell_F/v \end{bmatrix} \begin{bmatrix} h_{11}(s) & h_{12} \\ h_{21} & h_{22}(s) \end{bmatrix} \begin{bmatrix} b_{11} & b_{12} & 0 \\ b_{21} & b_{22} & b_D \end{bmatrix} \begin{bmatrix} \delta_F(s) \\ \delta_R(s) \\ M_{zD}(s) \end{bmatrix} \right. \\ & \left. + \begin{bmatrix} 0 \\ -c_1 \end{bmatrix} \delta_F(s) + \begin{bmatrix} 0 \\ d \end{bmatrix} M_{zD}(s) \right\}. \end{aligned} \quad (6.4.32)$$

The transfer functions are written as

$$p_A(s) \begin{bmatrix} r(s) \\ a_{yDP}(s) \end{bmatrix} = \begin{bmatrix} n_{Fr}(s) & n_{Rr}(s) & n_{Dr}(s) \\ n_{Fa}(s) & n_{Ra}(s) & n_{Da}(s) \end{bmatrix} \begin{bmatrix} \delta_F(s) \\ \delta_R(s) \\ M_{zD}(s) \end{bmatrix}, \quad (6.4.33)$$

with the numerator terms

$$\begin{aligned} n_{Fr}(s) &= \left( s + \frac{\mu c_R \ell}{mv \ell_F} \right) \frac{\mu c_F \ell_F}{m \ell_R \ell_{DP}}, \\ n_{Rr}(s) &= -\left( s + \frac{\mu c_F \ell}{mv \ell_R} \right) \frac{\mu c_R}{m \ell_{DP}}, \\ n_{Dr}(s) &= \left( s + \frac{\mu(c_F + c_R)}{mv} \right) \frac{1}{m \ell_R \ell_{DP}}, \\ n_{Fa}(s) &= \left( s^2 + s \frac{\mu c_R(\ell_R + \ell_{DP})}{mv \ell_{DP}} + \frac{\mu c_R}{m \ell_{DP}} \right) \frac{\mu c_F \ell}{m \ell_R}, \\ n_{Ra}(s) &= -\left( s + \frac{v}{\ell_{DP} - \ell_F} \right) \frac{\mu^2 c_F c_R \ell (\ell_{DP} - \ell_F)}{m^2 v \ell_R \ell_{DP}}, \\ n_{Da}(s) &= \left( s^2 + s \frac{\mu c_R(\ell_R + \ell_{DP})}{mv \ell_{DP}} + \frac{\mu c_R}{m \ell_{DP}} \right) \frac{1}{m \ell_R}. \end{aligned}$$

The numerator of the transfer function from front-wheel steering to the sideslip angle  $\beta$  is

$$n_{F\beta}(s) = \left[ s + \frac{v}{\ell_{DP}} \left( \frac{\mu c_R \ell}{mv^2} - \frac{\ell_F}{\ell_R} \right) \right] \frac{\mu c_F}{mv}. \quad (6.4.34)$$

### Controllability

For front-wheel steering of the car (6.4.4), the controllability matrix is

$$[\mathbf{b} \ \mathbf{Ab}] = \begin{bmatrix} b_{11} & a_{11}b_{11} + a_{12}b_{21} \\ b_{21} & a_{21}b_{11} + a_{22}b_{21} \end{bmatrix},$$

and its determinant is

$$\det[\mathbf{b} \ \mathbf{Ab}] = \frac{\mu^2 c_F^2}{m^3 v^2 \ell_R^2 \ell_{DP}^2} [\mu c_R \ell \ell_R (\ell_{DP} - \ell_F) + \ell_F^2 m v^2]. \quad (6.4.35)$$

Controllability is lost for  $\mu = 0$  and at a speed  $v_{nc}$ , where

$$v_{ncF}^2 = \frac{\mu c_R \ell \ell_R (\ell_F - \ell_{DP})}{m \ell_F^2}. \quad (6.4.36)$$

If  $J > m\ell_F \ell_R$ , i.e.  $\ell_F - \ell_{DP} < 0$ , then  $v_{ncF}$  is imaginary and of no practical interest. Otherwise non-controllability occurs at a real velocity. Substituting  $v^2 = v_{ncF}^2$  into  $a_0$  of (6.4.23) and assuming  $\ell_F - \ell_{DP} > 0$ ,  $a_0 > 0$  is obtained. Since also  $a_1 > 0$ , the uncontrollable modes are stable. Thus, the steering dynamics are robustly stable, but not robustly controllable.

For the bus of Table 6.1, we have  $\ell_F - \ell_{DP} = -1.73$  [m], i.e. there is no real  $v_{nc}$ . For the limousine,  $\ell_F - \ell_{DP} = 0.03$  [m]. For  $\mu = 1$ , the controllability is lost at a velocity  $v_{ncF} = 2.38$  [m/sec] (8.6 [km/h]). Typically, the controller is turned on above this velocity. The non-controllable case is relevant for cars with a small moment of inertia (e.g. central engine) or relatively long wheelbase (e.g. Mini type). If  $v_{ncF}$  is in the operating domain of the controller, and a pole placement approach is used, then the non-controllable stable eigenvalue must also be assigned to the closed loop.

For rear-wheel steering of the car (6.4.4), the controllability matrix is

$$[\mathbf{b} \ \mathbf{Ab}] = \begin{bmatrix} b_{12} & a_{11}b_{12} + a_{12}b_{22} \\ b_{22} & a_{21}b_{12} + a_{22}b_{22} \end{bmatrix},$$

$$\det[\mathbf{b} \ \mathbf{Ab}] = \frac{\mu^2 c_R^2}{m^3 v^2 \ell_R \ell_{DP}^2} [\mu c_F \ell (\ell_{DP} - \ell_F) + \ell_R m v^2]. \quad (6.4.37)$$

Controllability is lost at a velocity  $v_{ncR}$ , where

$$v_{ncR}^2 = \frac{\mu c_F \ell (\ell_{DP} - \ell_F)}{m \ell_R}. \quad (6.4.38)$$

It has the opposite sign as  $v_{ncF}$ , thus here the case of large moment of inertia or relatively short wheelbase is critical. For the data of the empty bus on a dry road  $v_{ncR} = 10.28$  [m/sec] (37 [km/h]). Cars with four-wheel steering are controllable, because either  $v_{ncF}$  or  $v_{ncR}$  is imaginary.

## Observability

The determinant of the observability matrix for the output  $\beta$  is

$$\det \begin{bmatrix} \mathbf{c}^T \\ \mathbf{c}^T \mathbf{A} \end{bmatrix} = \det \begin{bmatrix} 1 & 0 \\ a_{11} & a_{12} \end{bmatrix} = a_{12} = -1 + \mu(c_R \ell_R - c_F \ell_F)/mv^2. \quad (6.4.39)$$

In the understeering case ( $c_R \ell_R - c_F \ell_F > 0$ ), the observability is lost for

$$v_{no\beta}^2 = \frac{\mu(c_R \ell_R - c_F \ell_F)}{m}. \quad (6.4.40)$$

The determinant of the observability matrix for the output  $r$  is

$$\det \begin{bmatrix} \mathbf{c}^T \\ \mathbf{c}^T \mathbf{A} \end{bmatrix} = \det \begin{bmatrix} 0 & 1 \\ a_{21} & a_{22} \end{bmatrix} = -a_{21} = -\mu(c_R \ell_R - c_F \ell_F) / m \ell_R \ell_{DP}. \quad (6.4.41)$$

Here, observability is given independent of the velocity. Thus, from a robust observability point of view, the yaw rate  $r$  is more useful for feedback than the sideslip angle  $\beta$ . This fact coincides favorably with the fact that cheap yaw rate sensors are available (see ESP application), whereas there is no cheap sensor for the sideslip angle  $\beta$ . We will assume robust controller structures with feedback of  $r$ . Note that the neutral steer car with  $c_R \ell_R - c_F \ell_F = 0$  is not observable from  $r$ . It is stable, however, because  $a_0 > 0$ ,  $a_1 > 0$  in (6.4.23).

By (6.4.31), the measurement of  $a_{yDP}$  is related to both state variables  $\beta$  and  $r$  via the uncertain friction coefficient  $\mu$ , such that no good reconstruction of  $\beta$  from  $a_{yDP}$  is possible. There are also practical disadvantages in the use of accelerometers. They cannot be mounted on street level as assumed in the single-track model, therefore the measurement includes components of the unmodelled roll acceleration. Also, it is generally not possible to mount the accelerometer above the decoupling point. Interpolation between two accelerometer measurements circumvents this problem, but it increases the cost.

From the above analysis of the choice of sensors, we conclude:

- i. The yaw rate sensor will be used for feedback.
- ii. The velocity is available from the ABS system and may be used for gain-scheduling.
- iii. The steering angle command  $\delta_S$  is measured at the handwheel (considering the gear ratio). It will be used together with the velocity to generate a yaw rate reference  $r_{ref}$ .
- iv. Also, the actual corrective steering angle  $\delta_C$  after the actuator (see Figure 6.3) is a useful feedback signal, or alternatively the actual steering angle  $\delta_F = \delta_S + \delta_C$ . It helps to achieve robustness with respect to unstructured actuator uncertainty.

## 6.5 Linear Analysis of Robust Decoupling

The second order plant (6.4.10) is controlled by the first order controller (6.3.19). In (6.3.27), linearize the front tire characteristic by  $F_{yF}(\delta_S - \gamma) = \mu c_F (\delta_S - \gamma)$  and introduce the angle  $\gamma$  (see Figure 6.13) as the third state variable.

$$\begin{aligned} \dot{\gamma}_{dec} &= e_{33} \gamma_{dec} + f_{31} \delta_S + f_{33} M_{zD} - r_{ref}, \\ e_{33} &= -\mu c_F \ell / m v \ell_R, \\ f_{31} &= \mu c_F \ell / m v \ell_R, \\ f_{33} &= 1 / m v \ell_R. \end{aligned} \quad (6.5.1)$$

Linearize the rear tire characteristic by  $F_{yR}(\delta_R - \beta_R) = \mu c_R(\delta_R - \beta_R)$  and substitute from (6.5.1)

$$a_{yDPdec} = v(\dot{\gamma}_{dec} + r_{ref}) = ve_{33}\gamma_{dec} + vf_{31}\delta_S + vf_{33}M_{zD} + vr_{ref}. \quad (6.5.2)$$

Then, (6.3.34) becomes

$$\begin{bmatrix} \dot{\beta}_{Rdec} \\ \dot{r}_{dec} \\ \dot{\gamma}_{dec} \end{bmatrix} = \begin{bmatrix} e_{11} & -1 \\ e_{21} & 0 \\ 0 & 0 \end{bmatrix} \begin{bmatrix} \beta_{Rdec} \\ r_{dec} \\ \gamma_{dec} \end{bmatrix} + \begin{bmatrix} e_{13} \\ e_{23} \\ e_{33} \end{bmatrix} \gamma_{dec} \\ + \begin{bmatrix} f_{11} & f_{12} & f_{13} & f_{14} \\ f_{21} & f_{22} & f_{23} & f_{24} \\ f_{31} & 0 & f_{33} & -1 \end{bmatrix} \begin{bmatrix} \delta_S \\ \delta_R \\ M_{zD} \\ r_{ref} \end{bmatrix}, \quad (6.5.3)$$

$$e_{11} = -\mu c_R(\ell_{DP} + \ell_R)/mv\ell_{DP},$$

$$e_{21} = \mu c_R/m\ell_{DP},$$

$$e_{13} = -\mu c_F(\ell_{DP} - \ell_F)/mv\ell_{DP},$$

$$e_{23} = -\mu c_F\ell_F/\ell_R\ell_{DP},$$

$$f_{11} = \mu c_F(\ell_{DP} - \ell_F)/mv\ell_{DP},$$

$$f_{21} = \mu c_F\ell_F/m\ell_R\ell_{DP},$$

$$f_{22} = -\mu c_R/m\ell_{DP},$$

$$f_{12} = \mu c_R(\ell_{DP} + \ell_R)/mv\ell_{DP},$$

$$f_{13} = -1/mv\ell_{DP},$$

$$f_{23} = 1/m\ell_R\ell_{DP}.$$

The linearized state space model of the robustly decoupled car is

$$\begin{bmatrix} \dot{\beta}_{Rdec} \\ \dot{r}_{dec} \\ \dot{\gamma}_{dec} \end{bmatrix} = \begin{bmatrix} e_{11} & -1 & e_{13} \\ e_{21} & 0 & e_{23} \\ 0 & 0 & e_{33} \end{bmatrix} \begin{bmatrix} \beta_{Rdec} \\ r_{dec} \\ \gamma_{dec} \end{bmatrix} \\ + \begin{bmatrix} f_{11} & f_{12} & f_{13} & f_{14} \\ f_{21} & f_{22} & f_{23} & f_{24} \\ f_{31} & 0 & f_{33} & -1 \end{bmatrix} \begin{bmatrix} \delta_S \\ \delta_R \\ M_{zD} \\ r_{ref} \end{bmatrix}. \quad (6.5.4)$$

$$\begin{bmatrix} r_{dec} \\ a_{yDPdec} \end{bmatrix} = \begin{bmatrix} 0 & 1 & 0 \\ 0 & 0 & ve_{33} \end{bmatrix} \begin{bmatrix} \beta_{Rdec} \\ r_{dec} \\ \gamma_{dec} \end{bmatrix} + \begin{bmatrix} 0 & 0 & 0 & 0 \\ vf_{31} & 0 & vf_{33} & v \end{bmatrix} \begin{bmatrix} \delta_S \\ \delta_R \\ M_{zD} \\ r_{ref} \end{bmatrix}.$$

The characteristic polynomial of the  $E$  matrix factorizes into

$$p_{dec}(s) = p_{lat}(s)p_{yaw}(s), \quad (6.5.5)$$

$$p_{\ell at} = s - e_{33} = s + \frac{\mu c_F \ell}{m v \ell_R}, \quad (6.5.6)$$

$$p_{yaw} = s^2 - e_{11}s + e_{21} \quad (6.5.7)$$

$$\begin{aligned} &= s^2 + \frac{\mu c_R (\ell_{DP} + \ell_R)}{m v \ell_{DP}} s + \frac{\mu c_R}{m \ell_{DP}} \\ &= s^2 + 2D_{dec} \omega_{0 dec} s + \omega_{0 dec}^2, \end{aligned}$$

with

$$\omega_{0 dec} = \sqrt{\frac{\mu c_R}{m \ell_{DP}}}, \quad (6.5.8)$$

$$D_{dec} = \frac{\ell_R + \ell_{DP}}{2v} \sqrt{\frac{\mu c_R}{m \ell_{DP}}}. \quad (6.5.9)$$

### Remark 6.9

An alternative approach for deriving the closed-loop poles is to use the Laplace domain description (6.3.20) for the controller  $\delta_C(s) = -G_{dec}(s)r(s)$

$$G_{dec}(s) = \frac{1 + s(\ell_{DP} - \ell_F)/v}{s} =: \frac{n_{dec}}{s} :$$

Then the closed-loop characteristic polynomial is

$$p(s) = s p_A(s) + n_{Fr}(s) n_{dec}(s).$$

A symbolic factorization yields

$$p(s) = p_{\ell at}(s) p_{yaw}(s).$$

□

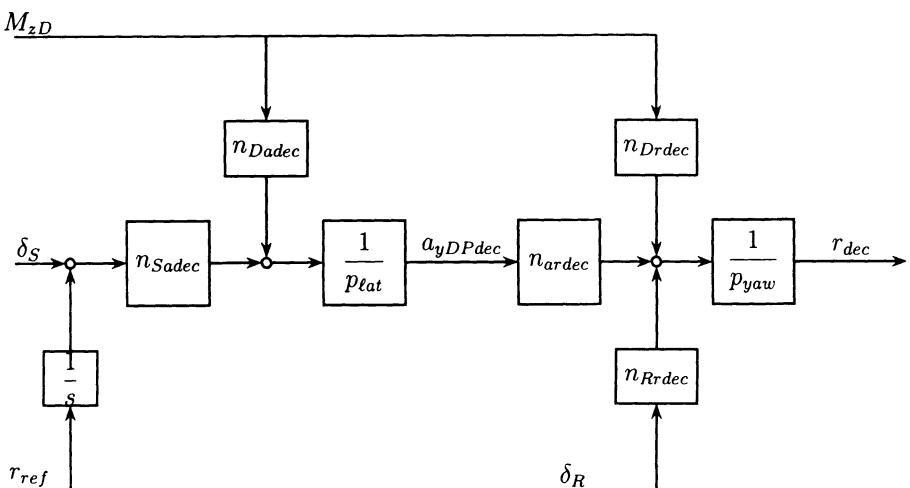


Figure 6.25. Structure of the transfer function model of the decoupled car

In terms of transfer functions, several cancellations of  $p_{\ell at}(s)$  or  $p_{yaw}(s)$  occur. They are best illustrated by a linearized version of Figure 6.17 as shown in Figure 6.25. The figure visualizes the main effects of robust decoupling:

- i. Factorization of the characteristic polynomial into  $p_{\ell at}(s)$  and  $p_{yaw}(s)$ .
- ii. The lateral acceleration  $a_{yDPdec}$  is controlled by the input  $\delta_S$  for the path tracking task of Figure 6.9 via the lateral subsystem  $n_{Sadec}(s)/p_{\ell at}(s)$ . The yaw rate  $r_{dec}$  is not observable from  $a_{yDPdec}$ .
- iii. Rear-wheel steering  $\delta_R$  controls only the yaw subsystem.

The numerators in Figure 6.25 are

$$\begin{aligned} n_{Sadec}(s) &= s\mu c_F \ell / m \ell_R, \\ n_{Dadec}(s) &= s / m \ell_R, \\ n_{ardec}(s) &= \left( s + \frac{\mu c_R \ell}{m v \ell_F} \right) \frac{\ell_F}{\ell \ell_{DP}}, \\ n_{Drdec}(s) &= s / m \ell \ell_{DP}, \\ n_{Rrdec}(s) &= -s \mu c_R / m \ell_{DP}. \end{aligned} \quad (6.5.10)$$

For comparison with the uncontrolled car, i.e. the transfer functions (6.4.33), write

$$\begin{bmatrix} r_{dec}(s) \\ a_{yDPdec}(s) \end{bmatrix} = \begin{bmatrix} G_{Srdec}(s) & G_{Rrdec}(s) & G_{Drdec}(s) \\ G_{Sadec}(s) & G_{Radec}(s) & G_{Dadec}(s) \end{bmatrix} \begin{bmatrix} \delta_S(s) + r_{ref}(s)/s \\ \delta_R(s) \\ M_z D(s) \end{bmatrix} \quad (6.5.11)$$

where

$$\begin{aligned} G_{Srdec}(s) &= \frac{n_{sa}(s)n_{ar}(s)}{p_{\ell at}(s)p_{yaw}(s)}, \\ G_{Rrdec}(s) &= \frac{n_{Rr}(s)}{p_{yaw}(s)}, \\ G_{Drdec}(s) &= \left[ \frac{n_{ar}(s)n_{Da}(s)}{p_{\ell at}(s)} + n_{Mr}(s) \right] \frac{1}{p_{yaw}(s)}, \\ &= \frac{s}{m \ell_{DP} \ell_R p_{\ell at}(s) p_{yaw}(s)} \left( s + \frac{\mu(c_F + c_R)}{mv} \right), \\ G_{Sadec}(s) &= \frac{n_{sa}(s)}{p_{\ell at}(s)}, \\ G_{Radec}(s) &= 0, \\ G_{Dadec}(s) &= \frac{n_{Da}(s)}{p_{\ell at}(s)}. \end{aligned}$$

The  $s$ -factor in the numerators of  $G_{Dadec}(s)$  and  $G_{Drdec}(s)$  indicates the disturbance attenuation at low frequencies and corresponding increased disturbance sensitivity at high frequencies. The effect of the disturbance is quantified by the sensitivity function

$$S(s) = \frac{G_{Drdec}(s)}{G_{Dr}(s)} = \frac{G_{Dadec}(s)}{G_{Da}(s)} = \frac{s p_A(s)}{p_{\ell at}(s) p_{yaw}(s)}. \quad (6.5.12)$$

The acceleration subsystem (that is relevant for the driver task of path tracking) now has only a first order transfer function

$$G_{Sadec}(s) = \frac{vs}{1 + \frac{mvl_R}{\mu c_F \ell} s}. \quad (6.5.13)$$

Its eigenvalue at  $s = -\mu c_F \ell / mvl_R$  may be shifted by accelerometer feedback of  $a_{yDP}$  without affecting the yaw subsystem. This subsystem is, however, well-behaved and there is no need to spend an additional sensor to the car steering system.

The poles of the yaw subsystem (6.5.7) may be expressed in terms of natural frequency  $\omega_o$  and damping  $D$ . Table 6.2 shows these values for the open-loop system and for the decoupled system. The decoupled system is much more transparent in its parameter dependence such that we can continue with symbolic calculations. The natural frequency of the decoupled system is velocity-independent. Solving  $D^2 = D_{dec}^2$  (which is a quadratic equation in  $v^2$ ) for  $v$ , a limit velocity  $v_e$  is calculated, such that the decoupled car has less damping than the conventional car for  $v > v_e$  [10]. Figure 6.26

Table 6.2. Natural frequency and damping of the yaw motion

	open loop	decoupled
$\omega_0^2$	$\frac{\mu^2 c_F c_R \ell^2 + mv^2 \mu(c_R \ell_R - c_F \ell_F)}{m^2 \ell_R \ell_{DP} v^2}$	$\frac{\mu c_R}{m \ell_{DP}}$
$D$	$\frac{\ell_R \ell_{DP} (c_R + c_F) + c_R \ell_R^2 + c_F \ell_F^2}{2\sqrt{\ell_R \ell_{DP} [c_R c_F \ell^2 + mv^2 (c_R \ell_R - c_F \ell_F) / \mu]}}$	$\frac{\ell_R + \ell_{DP}}{2v} \sqrt{\frac{\mu c_R}{m \ell_{DP}}}$

shows the velocity-dependent damping for the uncontrolled and decoupled car using the data of a BMW 735i from Table 6.1.

In summary, the linear analysis of robust decoupling shows that the structurally derived controller (6.3.19) without any tunable parameters (with the possible exception of  $\ell_{DP}$ , which is constant during a ride) yields the cascade structure of Figure 6.25, where the lateral subsystem with output  $a_{yDPdec}$  is relevant for the driver task of path tracking, see Figure 6.7. In contrast to the oscillatory behavior of the uncontrolled car (see  $n_{Fa}(s)$  in (6.4.33)),  $a_{yDPdec}$  is now generated by first order dynamics (see  $G_{sadec}(s)$  in (6.5.11)). The path tracking task of the driver has been simplified.

The structure of Figure 6.25 indicates that the lateral and yaw subsystems may be improved independently.

- i. Accelerometer feedback for  $a_{yDP}$  to  $\delta_S$  changes only the lateral subsystem. Practically, there is no need for such a controller, because decoupling yields well-behaved and sufficiently fast lateral dynamics.
- ii. Yaw rate feedback to rear-wheel steering  $\delta_R$  changes only the yaw dynamics. As Figure 6.26 shows, there is a need for improvement of the damping. It should even in the worst case of  $\mu = \mu^-$  provide a damping better than that of the uncontrolled car. This can be achieved by the following result.

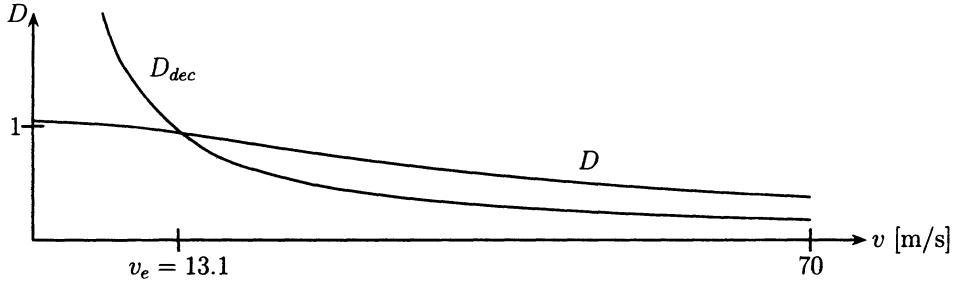


Figure 6.26. Decoupling causes reduced damping for  $v > v_\ell$ . Curves for  $\mu = 1$

*Theorem 6.10 (Ackermann [7], [31])*

The velocity scheduled control law

$$\delta_R(v) = \left( \frac{\ell_{DP} + \ell_R}{v} - 2D_{des}(v) \sqrt{\frac{m\ell_{DP}}{\mu c_R}} \right) (r_{ref} - r) \quad (6.5.14)$$

assigns a desired yaw damping characteristic  $D_{des}(v)$  to the decoupled car steering system. It leaves the natural frequency  $\omega_{0dec} = \sqrt{\mu c_R / m\ell_{DP}}$  unchanged.

□

*Remark 6.11*

Again, the controller is turned on softly for  $v > v_1 > 0$ , such that no division by zero occurs.

□

*Proof of Theorem 6.10*

By the control law (6.5.14), the transfer function from  $\delta_{Rref}$  to  $r$  is

$$\begin{aligned} \frac{r_{damped}(s)}{\delta_{Rref}(s)} &= \frac{\left( \frac{\ell_{DP} + \ell_R}{v} - 2D_{des}(v) \sqrt{\frac{m\ell_{DP}}{\mu c_R}} \right) n_{Rrdec}(s)}{p_{yaw} + \left( \frac{\ell_{DP} + \ell_R}{v} - 2D_{dec}(v) \sqrt{\frac{m\ell_{DP}}{\mu c_R}} \right) n_{Rrdec}(s)} \\ &= \frac{-s\mu c_R \left( \frac{\ell_{DP} + \ell_R}{v} - 2D_{des}(v) \sqrt{\frac{m\ell_{DP}}{\mu c_R}} \right)}{m\ell_{DP} \left( s^2 + 2D_{des}(v) \sqrt{\frac{\mu c_R}{m\ell_{DP}}} s + \frac{\mu c_R}{m\ell_{DP}} \right)}. \end{aligned}$$

The natural frequency is

$$\omega_{0damped} = \omega_{0dec} = \sqrt{\frac{\mu c_R}{m \ell_{DP}}}.$$

It does not depend on the choice of  $D_{des}(v)$  and not on  $v$ . The damping is

$$D_{damped}(v) = D_{des}(v).$$

□

The controller (6.5.14) contains the uncertain parameter  $\mu/m$ . In order to achieve the desired damping also in the worst case of slippery road ( $\mu = \mu^-$ ) and full load ( $m = m^+$ ), these parameter values must be used in the control law. On a dry road and with lower mass, the damping then grows with  $\sqrt{\mu/m}$ .

The modified yaw dynamics have the characteristic polynomial

$$p_{yawdes}(s) = s^2 + \left( 2D_{des}(v) \sqrt{\frac{\mu c_R}{m \ell_{DP}}} \right) s + \frac{\mu c_R}{m \ell_{DP}}, \quad (6.5.15)$$

and the sensitivity function of (6.5.12) is changed to

$$S_{des}(s) = \frac{s p_A(s)}{p_{lat}(s) p_{yawdes}(s)}. \quad (6.5.16)$$

Peaks in  $|S(j\omega)|$  due to insufficient damping in  $p_{yaw}(s)$  are avoided by replacing it with  $p_{yawdes}(s)$  in  $|S_{des}(j\omega)|$ . The choice of  $D_{des}(v)$  should take into account both the damping (see Figure 6.26) and the effect on the sensitivity function (6.5.16).

## Handling

So far, the robust decoupling concept has been analyzed with respect to the robust stabilization and disturbance attenuation aspects. The handling transfer functions from the handwheel angle to the lateral acceleration  $a_{yDP}$  and to the yaw rate  $r$  can be shaped by the second degree of freedom of prefilters providing the inputs  $\delta_S$ ,  $r_{ref}$ , and  $\delta_{Rref}$  to the decoupled system. Here also, subjective performance ratings have to be considered that go beyond the scope of this book. It is, for example, possible to keep the sideslip angle  $\beta$  small during all maneuvers by appropriate choice of the prefilter for  $\delta_{Rref}$  [76].

In the control systems structure of Figure 6.14 we require that the immediate reaction of  $a_{yDP}$  and  $r$  to a steering step input is the same as in the uncontrolled car. This requirement can be met in a robust way by assuring in the feedforward controller structure, that the transfer function from the driver command  $\delta_S = \delta_{Handwheel}/i$  (where  $i$  is the steering gear ratio) to  $\delta_F$  has high-frequency-gain 1, and the transfer function to  $\delta_C$  has relative degree one, such that the step response at  $\delta_C$  begins with zero. For a mechanical addition of angles as in Figure 6.4,  $\delta_F = \delta_S + \delta_C$  is the only choice. The prefilter for generating  $r_{ref}$  from  $\delta_S$  allows more design flexibility.

A simple idea is to use a model following approach, where by (6.4.33) the open-loop transfer function  $n_{F,r}(s)/p_A(s)$  with one zero and two poles and desired parameters is chosen as a prefilter. This would, however, reintroduce the oscillatory behavior of  $a_{yDP}$  that we have eliminated by robust decoupling. Two properties of the above filter should be preserved:

- i. The relative degree one. This assures that the step response in  $r_{ref} - r$  begins at zero with a non-zero slope. Thereby, initial peaks at the steering actuator are avoided.
- ii. The velocity dependence of the gain according to (6.4.14).

A simple candidate that meets both requirements is the following prefilter.

$$\frac{r_{ref}(s)}{\delta_S(s)} = \frac{k_{rstat}(v)}{1 + 0.1s}, \quad (6.5.17)$$

where

$$k_{rstat}(v) = \frac{v}{\ell[1 + (v/v_{CH})^2]}, \quad v_{CH}^2 = \frac{\mu c_R c_F \ell^2}{m(c_R \ell_R - c_F \ell_F)}. \quad (6.5.18)$$

Since  $\mu/m$  is uncertain, only a nominal value for  $v_{CH}$  can be assumed for the prefilter.

The two signal paths from  $\delta_S$  to  $\delta_F$  are combined to

$$\delta_{Fref}(s) = \left[ 1 + s \frac{k_{rstat}(v)}{(1 + 0.1s)} \right] \delta_S(s), \quad (6.5.19)$$

$$a_{yDP}(s) = \frac{n_{Sadec}(s)}{p_{lat}(s)} \delta_{Fref}(s), \quad (6.5.20)$$

$$r_{dec}(s) = \frac{n_{Ardec}(s)}{p_{yawdes}(s)} a_{yDP}(s). \quad (6.5.21)$$

The handling step responses  $a_{yDP}$  and  $r_{dec}$  may be further shaped by an additional (velocity scheduled) prefilter with zero relative degree. Also, the desired yaw damping characteristic  $D_{des}(v)$  enters into the last transfer function from  $a_{yDP}$  to  $r_{dec}$ .

### Fading Effect

The robust decoupling concept is important for the first 0.5 to 1 second after the occurrence of a disturbance torque  $M_{zD}$ , when the driver has not yet reacted. It may be modified such that thereafter the corrective steering angle  $\delta_C$  (see Figure 6.3) returns to zero. This is desirable in order to achieve the same stationary cornering behavior that the driver is used to, and also to unload the actuator for the corrective steering angle when it gets into saturation. Finally, also stability problems in the yaw motion are reduced if the long-term behavior of the car is identical to the conventional car. Since also the immediate reaction to a step in the steering command  $\delta_S$  is unchanged, only the transients are influenced by the driver assistant.

A disadvantage of the three cascaded systems (6.5.19) to (6.5.21) is that they change the steady state response. The latter is determined by the prefilter, because  $r_{ref} - r$  is integrated in the decoupling feedback of Figure 6.14. This long-term effect is not what we want to achieve. The driver support system should give the ideal decoupled behavior immediately after a step of  $\delta_S$  or  $M_{zD}$ . In the long run, however, the driver should take over the control of the steady state, i.e.  $\delta_C$  in Figure 6.14 should return to zero. This effect is also necessary to unload the actuator for  $\delta_C$ , such that it is not

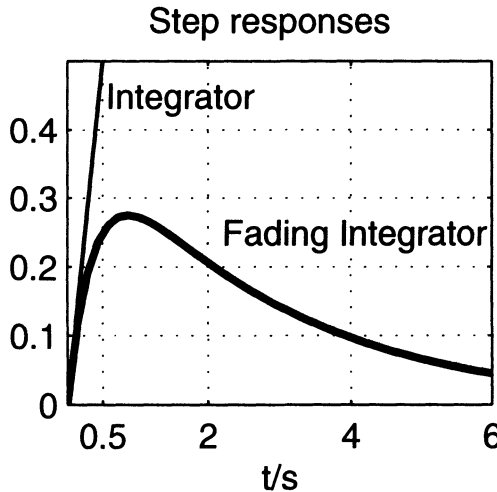


Figure 6.27. The initial response of the fading integrator is the same as that of the integrator locked in saturation. For this purpose, the  $1/s$ -term in the controller transfer function is replaced by a *fading integrator* with transfer function

$$G_{FI}(s) = \frac{s}{s^2 + as + b}. \quad (6.5.22)$$

The immediate reaction corresponding to large  $s$  is  $\lim_{s \rightarrow \infty} G_{FI}(s) = 1/s$ . For  $t \rightarrow \infty$ , the differentiating  $s$  in the numerator brings the response of  $\delta_C$  back to zero. For  $a = 3$  and  $b = 1$  the step responses of the integrator and the fading integrator are shown in Figure 6.27. The fading integrator also eases the yaw damping problem of robust unilateral decoupling, see Figure 6.26, because the system with fading integrator behaves for large  $t$  like the uncontrolled vehicle. Also, the proportional feedback path  $[(\ell_{DP} - \ell_F)/v]r$  may be faded by a filter  $s/(s + c)$ . For a rally driver with extremely short reaction time, the time scale of the fading effect may be changed by smaller values of  $a$  and  $b$ .

## Conclusions

In Section 6.5, an ideal car steering control system has been presented that is based on

- i. Yaw rate feedback to front-wheel steering for robust unilateral decoupling.
- ii. Feedback of the yaw rate to rear-wheel steering for assignment of a desired velocity-dependent yaw damping characteristic  $D_{des}(s)$ .
- iii. Generation of a yaw reference  $r_{ref}$  from the handwheel angle by a velocity-scheduled prefilter.

- iv. The use of a fading integrator, in order to give the full driver-support only for the first 0.5 seconds after a steering wheel or disturbance step, then the controller smoothly fades out such that only the driver commands the steady state.

The control system requires only standard sensors for yaw rate, velocity and handwheel angle. The control laws are derived structurally, thus only parameters of the single-track model must be substituted for a specific vehicle. The decoupling controller under i. requires no tuning at all, for the desired yaw damping controller under ii., the designer only has to specify the yaw damping characteristic  $D_{des}(v)$ . The essential parameters of the prefilter under iii. are structurally fixed, additional velocity-dependent dynamics allow fine tuning of the handling transfer functions. The fading integrator under iv. has two design parameters: parameter  $b$  essentially determines the timescale of the fading effect, it depends on the human reaction time and not on the vehicle. Parameter  $a$  may be tuned in view of closed-loop properties.

Like in the crane example of Chapter 1, the resulting controller structure is:

- |                    |  |
|--------------------|--|
| <i>Lean</i>        | : only a few parameters of a low order controller must be adjusted.  |
| <i>Transparent</i> | : each controller parameter or function has a clear physical meaning.<br>It influences only this property and leaves other input-output relations unchanged. |
| <i>Robust</i>      | : the control system is structurally robust with respect to uncertainty in the road-tire friction, and the vehicle mass and velocity.                        |

It is common practice to define progress in automobiles by comparison of a new model with the predecessor model. If we compare a new model with the ideally controlled vehicle, however, then we now have the possibility to evaluate how close we can come to the best achievable car steering under technical and cost constraints.

## 6.6 Skidding Avoidance Based on Robust Decoupling

The decoupling control concept of Section 6.5 was derived under idealized assumptions. Practically, the following constraints must be considered:

- i. No rear-wheel steering. This means that trade-offs in the front-wheel feedback system must be made in order to achieve sufficient yaw damping at high velocities.
- ii. Inclusion of the actuator dynamics. Its rate limitations may cause limit cycles that must be understood and prevented. Its bandwidth is closely related to the cost, i.e. only the absolutely necessary bandwidth should be specified for the actuator.

### *Yaw Damping by Double Cancellation*

Most cars are not equipped with rear-wheel steering. Then, the yaw damping at high velocities must be improved by yaw-rate feedback to front-wheel steering, rather than

to rear-wheel steering. If the decoupled system of Figure 6.25 is augmented by an additional feedback path from  $r_{dec}$  to  $\delta_S$ , then in general the decoupling effect and also the factorization of the closed-loop characteristic polynomial, in a first order polynomial  $p_{lat}(s)$  and a second order polynomial  $p_{yaw}(s)$ , is destroyed. The latter factorization is, however, very useful to calculate symbolically the yaw damping  $D_{dec}(v)$  as in Table 6.2. This feature may be preserved by a cancellation compensation.

*Theorem 6.12 (Ackermann)*

A second feedback loop

$$\delta_S(s) = \delta_{S\text{ref}}(s) - \left[ 2D_{des}(v) \sqrt{\frac{m\ell_{DP}}{\mu c_R}} - \frac{\ell_R + \ell_{DP}}{v} \right] \frac{1 + T_R s}{1 + T_F s} r_{dec}(s), \quad (6.6.1)$$

with

$$T_R = \frac{mv\ell_R}{\mu c_F \ell}, \quad T_F = \frac{mv\ell_F}{\mu c_R \ell} \quad (6.6.2)$$

around the robustly decoupled system of Figure 6.25 assigns the desired yaw damping characteristic  $D_{des}(v)$  to the system. Both the natural frequency  $\omega_{0dec} = \sqrt{\mu c_R / m\ell_{DP}}$  and the lateral dynamics pole  $p_{lat}(s) = s + \mu c_F \ell / mv\ell_R$  are invariant under the feedback (6.6.1).

□

*Proof of Theorem 6.12*

The proof proceeds in two steps:

1. It is shown that the control law

$$\delta_S(s) = \delta_{S\text{ref}}(s) - (D_{des}(v) - D_{dec}(v)) \omega_{0dec} \frac{2m\ell_R}{\mu c_F \ell} \frac{p_{lat}(s)}{n_{ardec}(s)} r_{dec}(s) \quad (6.6.3)$$

assigns the desired  $D_{des}(v)$ .

2. It is shown by substitution of  $\omega_{0dec}$  and  $d_{dec}$  that (6.6.3) is equal to (6.6.1),(6.6.2).

In the first step, the loop is closed with the plant

$$r_{dec}(s) = \frac{n_{Sadec}(s) n_{ardec}(s)}{p_{lat}(s) p_{yaw}(s)} \delta_S(s). \quad (6.6.4)$$

A double cancellation of the two stable first order polynomials  $p_{lat}(s)$  and  $n_{ardec}(s)$  occurs, and the closed-loop characteristic polynomial is

$$p(s) = p_{lat}(s) n_{ardec}(s) \left[ p_{yaw}(s) + (D_{des}(v) - D_{dec}(v)) \frac{2m\ell_R}{\mu c_F \ell} \omega_{0dec} n_{Sadec}(s) \right].$$

With  $p_{yaw}(s)$  from (6.5.7) and  $n_{Sadec}$  from (6.5.10), the term in square brackets becomes

$$\begin{aligned} s^2 + 2D_{dec}(v)\omega_{0dec}s + \omega_{0dec}^2 + (D_{des}(v) - D_{dec}(v)) \frac{2m\ell_R}{\mu c_F \ell} \omega_{0dec} \frac{\mu c_F \ell}{m\ell_R} s \\ = s^2 + 2D_{des}(v)\omega_{0dec}s + \omega_{0dec}^2. \end{aligned}$$

It has the desired damping characteristic  $D_{des}(v)$  and the unchanged natural frequency  $\omega_{0dec}$ . Also, the factor  $p_{lat}(s)$  of  $p(s)$  is unchanged.

In the second step,  $\omega_{0dec}$  from (6.5.8) and  $D_{dec}(v)$  from (6.5.9) is substituted in the control law (6.6.3) to obtain

$$\delta_S(s) = \delta_{Sref}(s) - \left( D_{des}(v) + \frac{\ell_R + \ell_{DP}}{2v} \sqrt{\frac{\mu c_R}{m\ell_{DP}}} \right) 2\sqrt{\frac{m\ell_{DP}}{\mu c_R}} \frac{1 + T_R s}{1 + T_F s},$$

which agrees with (6.6.1).  $\square$

The dynamic part of the controller (6.6.1) is

$$\frac{1 + T_R s}{1 + T_F s}$$

For the typical understeering car  $c_R\ell_R - c_F\ell_F > 0$ , i.e.  $T_R > T_F$ , the additional controller has high-pass behavior (lead-lag filter).

Practically,  $D_{des}(v) = D_{dec}(v)$  may be chosen for small  $v$ , such that the full decoupling effect is preserved. For  $v > v_2$ , then the additional yaw damping is softly turned on. This destroys the non-observability of  $r$  from  $a_{yDP}$ , but it yields good yaw damping at high velocities, and the design remains transparent because the symbolic factorization of the closed-loop characteristic polynomial is preserved. Note that the controller (6.6.1) depends on the uncertain parameters  $\mu/m$  and  $v$ . The velocity dependence may be scheduled, for  $\mu/m$  the worst case  $\mu^-/m^+$  is substituted.  $D_{des}(v)$  should be chosen such that in this worst case the damping gets never lower than for the conventional uncontrolled car.

### Analysis and Prevention of Active Steering Limit Cycles

In practical driving experiments, the effect of robust decoupling was demonstrated, see Figs. 6.18 and 6.19. At that time, also the benefit of additional feedback of the lateral acceleration  $a_{yDP}$  at the decoupling point was experimentally investigated. At low speed, stability problems in terms of oscillatory steering occurred and called for further investigation. It turned out, that the oscillations were limit cycles, and due to rate limitation of the steering actuator. The risk of unexpected occurrence of steering oscillations obviously threatens driving safety severely. It constituted the need to have a means to prove robust avoidance of limit cycles for any steering control at all operating points of interest. Hence, the combination of the dual locus method with the parameter space method was developed [16]. (Later this approach was generalized to other frequency loci specifications as described in Sections 5.1 and 5.2.)

The scope of this paragraph is to

- explain the limit cycles which were experienced in driving tests,
- propose a remedy against limit cycles, for the robustly decoupled steering dynamics,
- demonstrate the application of  $\Theta$ -stability mapping into parameter space for the proof of robust limit cycle avoidance.

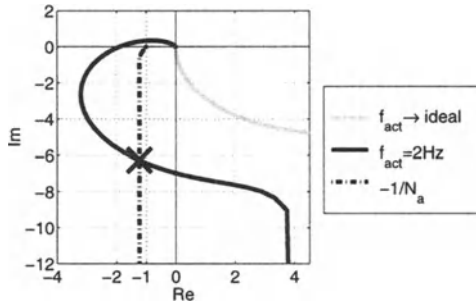


Figure 6.28. Reconstruction of steering limit cycles at  $v = 5 \text{ m/s}$ ,  $\mu = 1$  with additional feedback of lateral acceleration.

Figure 6.28 shows a reconstruction of the limit cycles at a specific operating point. If (using additional feedback of the lateral acceleration  $a_{yDP}$  at the decoupling point) the gain exceeded a certain value, then limit cycles occurred in driving tests at that operating point. The system used to generate Figure 6.28 consists of the linearized single track model ((6.4.10) with BMW 735i data from Table 6.1) with robust decoupling control (6.3.37) plus negative feedback of  $a_{yDP}$  to the input  $\delta_S$  with a gain of 1.8. The front steering angle  $\delta_F$  is set by a steering actuator  $\delta_F(s) = G_a(s)(\delta_S(s) + \delta_C(s))$ . For investigation, the control loop is cut open at the input of the steering actuator, and zero steering command  $\delta_S = 0$  is assumed. The gray line in Figure 6.28 is the locus of the transfer function of the open loop assuming an ideal steering actuator ( $G_a(s) = 1$ ). Since the steering actuator of the testing car was rate limited for hardware protection, Figure 6.28 also shows the locus of the rate limiter negative-inverse describing function as derived for Figure 5.13. No intersections between the two loci are present, hence no limit cycles may occur. Now, a more realistic steering actuator model

$$G_a(s) = \frac{\omega_a^2}{s^2 + 2D_a\omega_a s + \omega_a^2} \quad (6.6.5)$$

with damping  $D_a = 0.7$  and bandwidth  $\omega_a = 12.6[\text{rad/s}] \hat{=} 2 \text{ [Hz]}$  is applied. The black solid line in Figure 6.28 represents the corresponding Nyquist plot of the open loop linear part. Here, an intersection point between this locus and the locus of the rate limiter negative-inverse describing function appears. This indicates, that a limit cycle may occur. Moreover, the Nyquist criterion indicates that the system is unstable in the linear framework, i.e. even if no rate saturation is considered. This explains, why limit cycles occurred in the driving experiments right after the controller had been

switched on. The reason for linear instability is the phase delay caused by the real steering actuator in connection with the applied total loop gain. The effect of the rate limiter caused the oscillatory instability to close in a steady limit cycle. The frequency and amplitude of this limit cycle can be determined from the parameterization of the two loci at the intersection point  $z = -1.23 - 6.27i$ . The frequency of the linear part transfer function locus is  $\omega_{gz} = 7.9$  [rad/s]  $\hat{=} 1.26$  [Hz] at the intersection point. If this value is substituted in (5.1.9), iterative solution yields

$$R/A = 0.97 [1/s]. \quad (6.6.6)$$

The rate limitation of the real steering actuator was determined experimentally. It depends on the actuator load but can be restricted to be in the interval  $R = 400\ldots 800^\circ/\text{s}$  (referring to the steering column angle). Using (6.6.6), the theoretic amplitude  $A$  of the limit cycles corresponds to one or two revolutions of the steering wheel. Both the frequency and the amplitude comply approximately with the experimental limit cycles. Hence, the real limit cycles can be well explained by applying the presented system modeling and analysis.

Further theoretic investigations resulted in the awareness, that even with the employment of a significantly higher bandwidth steering actuator ( $\omega_a = 63$  [rad/s]) and even with no lateral acceleration feedback the risk of limit cycles is present. Consider the operating point with 70 m/s vehicle speed on dry road. The respective loci are

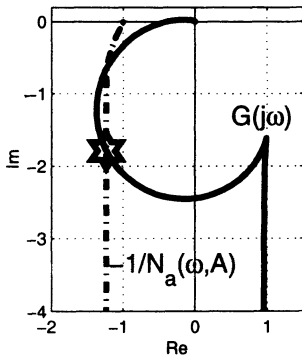


Figure 6.29. Decoupled steering dynamics loci at  $v = 70$  m/s,  $\mu = 1$  for rate limited steering actuator with  $\omega_a = 2\pi \cdot 10$  [Hz] bandwidth.

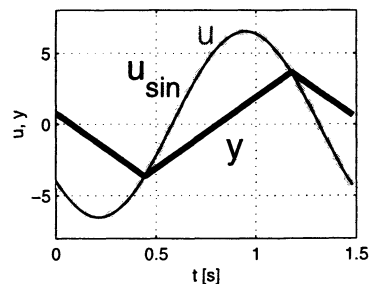


Figure 6.30. Rate limiter input  $u$  and output  $y$  plots of steady limit cycle simulations. The dashed line shows a sinusoidal approximation of  $u$ .

displayed in Figure 6.29. There are two intersection points indicating possible limit cycles. However, only the intersection point marked by a star represents a stable limit cycle. A numeric simulation of the closed loop system was performed starting with an initial state, which lies outside the region of attraction of the equilibrium state. In fact, a steady limit cycle can be observed, which is depicted in Figure 6.30 in terms of the actuator rate limiter input and output signals. The oscillation frequency ( $\omega_{gz} \approx 4.15$  [rad/s] and amplitude are well in accordance with the parameterization of the loci in

Figure 6.29 at the intersection point indicated by the star marker. The input to the rate limiter input signal can be well approximated by a sinusoidal. This indicates that the harmonic linearization of the rate limiter to its describing function is legitimate, which is due to distinct low-pass properties of the open control loop. A rule of thumb

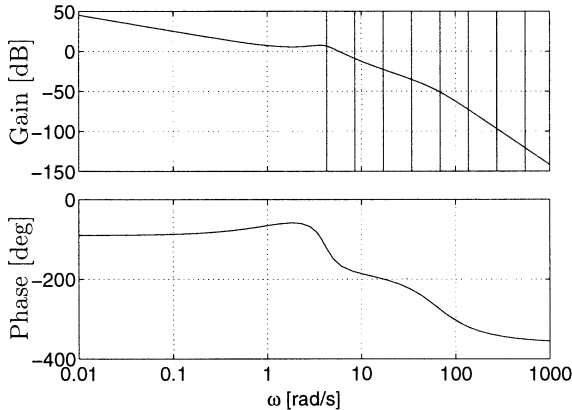


Figure 6.31. Bode plot of the open loop linear part at  $v = 70$  m/s,  $\mu = 1$ .

requires an open loop relative degree of at least two. Moreover, it is important that the associated gain reduction is already effective at the frequency of the limit cycle oscillation. Figure 6.6 shows the Bode plot. The vertical lines indicate the frequency region above the limit cycle. At all frequencies greater than the limit cycle frequency there is a decline of at least [-40 dB/decade]. Hence the basic assumptions for applying the dual locus method are met, see Section 5.1.

### *Nonlinear Control Enhancement for Limit Cycle Avoidance with Robustly Decoupled Steering Dynamics*

One fact, which essentially contributed to the occurrence of limit cycles, is the rate limitation of the steering actuator. This physical limit has to be considered for control design. The goal followed here is, in the first place, to reduce the controlled system's susceptibility to limit cycles. Secondly, for the sake of safety, robust avoidance of limit cycles must be proven for the whole operating domain of the actively steered car.

It turns out, that reducing the susceptibility to limit cycles is fairly simple in the context of robust decoupling control [16] as will be demonstrated in the sequel. Therefore, note that right before the control signal enters the actuator as its set point, there is an integration of the signal  $r_{ref} - r$ , see (6.3.37). The environment of this part of the control loop is illustrated in Figure 6.32. The output  $\delta_{Cref}$  of the decoupling controller (integrator)  $\dot{\delta}_{Cref} = r_{ref} - r$  enters the rate limiter, which is a part of the actuator. At the input of the integrator there is the derivative w.r.t. time of the input to the rate

limiter, i.e. the demanded rate. This quantity is limited by the rate limiter for the sake of hardware protection. Now a saturation of  $\dot{\delta}_{Cref}$  is introduced as a part of the control with

$$r_s \leq R \quad (6.6.7)$$

as illustrated in Figure 6.32. Hence, by the effect of this modification the rate limiter will never be activated. The demanded rate (i.e. the absolute value of the derivative of  $\dot{\delta}_{Cref}$ ) is a priori limited to  $r_s$ . As a consequence, for any consideration and analysis, the rate limiter can be neglected. However, the saturation needs to be taken into account instead. There is a great benefit from this nonlinear control enhancement in terms of stability. This is due to the fact, that in contrast to a rate limiter, the saturation does not introduce any phase delay into the control loop, when the demanded rate exceeds the allowed one. In fact, it turns out that the region in the  $((v, \mu))$  plane of operating parameters, where limit cycles may occur with the present system, shrinks considerably, since the saturation does not cause phase delay in the control loop [16]. Figure 6.33 illustrates this for the operating condition, which has already been considered in Figure 6.29. By means of the respective negative-inverse describing function loci the effect on limit cycle existence can be directly compared for both nonlinearities. The real locus  $-1/N_s(A)$ , which belongs to the saturation, is positioned much more advantageous (i.e. farer away from the Nyquist plot) than the locus  $-1/N_a(\omega, A)$  of the rate limiter. With the saturation, there are no more loci intersections, hence no limit cycles exist. Moreover, there is significant space between the loci, indicating a convenient safety distance in terms of phase and gain margins. The introduction of the saturation to the controller thus drastically reduces the risk of limit cycles. Nevertheless, the saturation now takes over the task of rate limiting the actuator input. The risk reduction can only be stated for the considered operating point. However, it is important for stability robustness, that limit cycles may not occur at any operating point in the operating domain (Figure 6.20).

The presented nonlinear control enhancement can be combined also with the fading integrator, as illustrated in Figure 6.34. A controller-internal feedback is applied from the integrator output  $\delta_{Cref}$  to the saturation input via the filter

$$G_f(s) = \frac{as + b}{s} \quad (6.6.8)$$

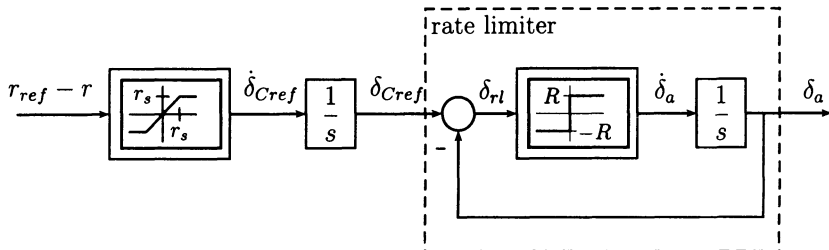


Figure 6.32. By limitation of the control signal the rate limiter becomes disarmed.

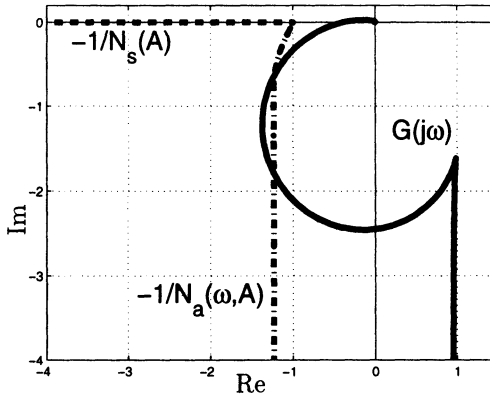


Figure 6.33. Nyquist plot (solid line) for  $v = 70$  m/s,  $\mu = 1$  and loci of negative-inverse describing functions of rate limiter (dash-dotted) and saturation (dashed).

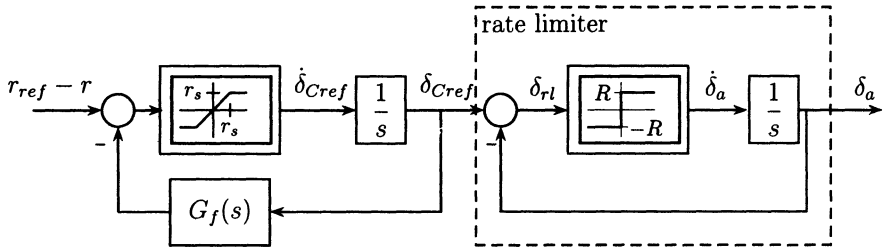


Figure 6.34. Nonlinear controller enhancement of the fading integrator.

such that the linearized transfer function from  $r_{ref} - r$  to  $\delta_{Cref}$  is just the one of the fading integrator (6.5.22)

$$G_{fi}(s) = \frac{1/s}{1 + G_f(s)/s} = \frac{s}{s^2 + a s + b}. \quad (6.6.9)$$

Still the absolute value of the derivative w.r.t. time of the input to the rate limiter can not exceed  $r_s$ , and therefore the rate limiter never gets activated. For the application of the dual locus method for analysis of limit cycle existence, the control loop is cut open between the saturation and the integrator. The transfer function  $G_f(s)$  becomes part of the open loop linear part, and thereby affects the course of the Nyquist plot. It contributes to reducing the risk of limit cycles, since the loop gain at low frequencies is significantly lower. This reduces the input to the actuator at low frequencies, which reduces the probability of the saturation in the controller to be activated. Figure 6.35 shows the result of  $\Theta$ -stability margin mapping into the  $(v, \mu)$ -plane for active car steering with fading integrator, where  $\Theta$  the locus of the negative-inverse

saturation describing function. For any operating point to the left hand side of the boundaries, the open loop transfer function locus does not intersect  $-1/N_s(A)$ , i.e. this is the  $\Theta$ -stable region. The boundaries were produced assuming two different actuator bandwidths. With the gray line, the actuator bandwidth is 1 [Hz], and the boundary is quite close to the operating domain. To ensure some safety margin, the actuator bandwidth should therefore be greater. Assuming 2 [Hz] actuator bandwidth, the  $\Theta$ -stability boundary recedes from the operating domain which enlarges the security distance. This trend continues for further increase of the bandwidth. By this approach, an actuator bandwidth can be specified such that limit cycles can be excluded.

*Remark 6.13*

If the results shown in Figure 6.35 are investigated in more detail, then it turns out that no tangent condition, but only the point condition for the closing point  $-1$  (where  $-1/N_s(A)$  starts), contributes to the boundaries being present in the depicted part of the  $(v, \mu)$ -plane. These boundaries can be considered as Hurwitz-stability boundaries of the corresponding linear systems if the saturation in the controller is neglected, since the closing point of  $-1/N_s(A)$  is the critical point  $-1$  w.r.t. the Nyquist criterion.  $\square$

## 6.7 Skidding Avoidance Based on the Disturbance Observer

In this section, another robust steering controller is introduced for improving the yaw dynamics of a passenger car. It is independent of the idea of robustly decoupling the

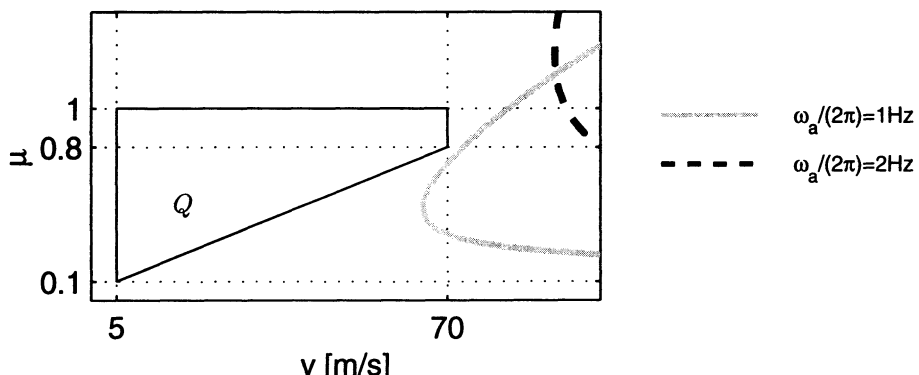


Figure 6.35. Limit cycle  $\Theta$ -stability boundaries in the  $(v, \mu)$ -plane.

lateral motion from the yaw dynamics of the car. Here, rather the disturbance rejection control architecture shown in Figure 1.11 is adapted to the vehicle yaw dynamics control problem and shown to robustly improve performance in terms of driving safety and handling qualities. The relevant design specifications are formulated in terms of eigenvalues ( $\Gamma$ -stability) and in the frequency domain as bounds on weighted sensitivity and complementary sensitivity functions ( $\mathcal{B}$ -stability). The parameter space method is used to consider the specifications for controller design. A Popov criterion - based non-linear stability analysis is also carried out to prove robust absolute stability ( $\Theta$ -stability) in the presence of actuator rate limitation. Simulations demonstrate the effectiveness of the design.

The steering control system should be robust w.r.t. large variations in longitudinal speed, payload and road adhesion and w.r.t. unstructured uncertainty (unmodelled dynamics) as well. Moreover, its actions should not be uncomfortable for the driver and passengers. A steering controller structure that effectively satisfies the requirements outlined above is presented along with its associated design and analysis procedures.

### *Vehicle Model and Steering Actuator Model*

For modelling the vehicle yaw dynamics, the linearized single track model from Section 6.4 is employed as a parametric linear time-invariant plant (parametric LTI). The transfer function from the front wheel steering angle  $\delta_F$  to the yaw rate  $r$  can be computed from (6.4.4):

$$G(s) = \frac{r(s)}{\delta_F(s)} = \frac{b_0 + b_1 s}{a_0 + a_1 s + a_2 s^2}, \quad (6.7.1)$$

with

$$\begin{aligned} b_0 &= \mu^2 c_F c_R (l_F + l_R) v, \\ b_1 &= \mu c_F l_F m v^2, \\ a_0 &= \mu^2 c_F c_R (l_F + l_R)^2 + \mu(c_R l_R - c_F l_F) m v^2, \\ a_1 &= \mu(c_F(J + l_F^2 m) + c_R(J + l_R^2 m))v, \\ a_2 &= J m v^2. \end{aligned}$$

The steady state gain of the nominal vehicle steering transfer function is

$$K_n(v) = \lim_{s \rightarrow 0} G(s) \Big|_{\mu=\mu_n} \quad (6.7.2)$$

at a nominal friction coefficient  $\mu = \mu_n$ .

In this section, both the conventional car and the controlled car are equipped with a steer-by-wire actuator, which sets the total front steering angle. Therefore, the steering transfer function of the conventional car is

$$G_{conv}(s) = \frac{r(s)}{\delta_S(s)} = G(s) G_a(s), \quad (6.7.3)$$

where  $\delta_S$  denotes the steering wheel angle and  $G_a$  represents the actuator dynamics (see (6.7.5) below).

### Vehicle Model Data and Operating Domain

The nominal parameter values for the linearized single track model assumed in this section are  $l_F = 1.25 \text{ [m]}$ ,  $l_R = 1.32 \text{ [m]}$ ,  $m = 1296 \text{ [kg]}$ ,  $J = 1750 \text{ [kg m}^2]$ ,  $c_F = 84243 \text{ [N/rad]}$  and  $c_R = 95707 \text{ [N/rad]}$ . The nominal friction coefficient is  $\mu_n = 1$ , which corresponds to a dry road.

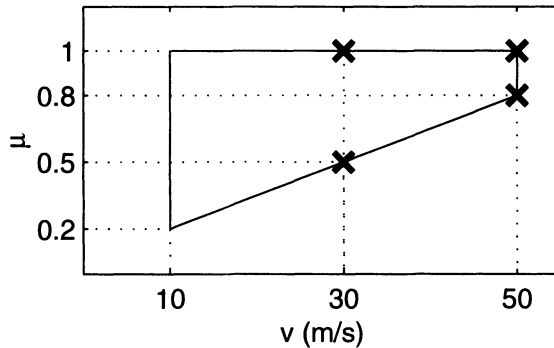


Figure 6.36. Operating domain and considered operating points

The tire cornering stiffnesses  $\mu c_F$  and  $\mu c_R$  can exhibit large variations due to variations in the friction coefficient  $\mu$  between the road and the tires. The longitudinal speed  $v$  is assumed to vary only slowly during operation in the range between zero and 50 [m/s]. Gain-scheduling will be necessary firstly to switch on the controller starting from zero speed. Secondly, gain scheduling is required to meet all specifications also at low speed. Therefore, in this section only high-speed operation is investigated at two exemplary speeds:  $v = 30 \text{ [m/s]}$  and  $v = 50 \text{ [m/s]}$ . The assumed operating domain of the vehicle in terms of the speed  $v$  and the road adhesion coefficient  $\mu$  is displayed in Figure 6.36. The maximum value of  $\mu$  is 1 (dry road) at all speeds while it is assumed that the minimum value increases linearly from 0.2 (icy road) at low speeds up to 0.8 (wet road) at high speeds. (Additional uncertainties will be considered on p. 230.) Cross markers in Figure 6.36 indicate specific operating points, which will be particularly looked at later.

### Steering Actuator Model

An electric motor under position control is assumed here to be a steer-by-wire actuator, which is used to set the total front wheel steering angle. The actuator model used in this section is shown in Figure 6.37. Notations and assumed numerical values of the model variables are compiled in Table 6.3. The third order transfer function of the linearized actuator model according to Figure 6.37 while neglecting the voltage limitation, is given

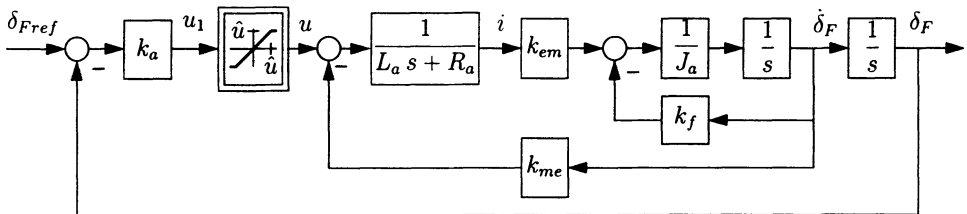


Figure 6.37. Actuator model

by

$$G_a(s) = \frac{\delta_F(s)}{\delta_{Fref}(s)} = \frac{k_{em}k_a}{J_a L_a s^3 + (k_f L_a + J_a R_a)s^2 + (k_{me}k_{em} + k_f R_a)s + k_{em}k_a}. \quad (6.7.4)$$

With the data from Table 6.3, the linearized steering actuator model transfer function is

$$G_a(s) = \frac{\delta_F(s)}{\delta_{Fref}(s)} = \frac{\omega_a^2}{\omega_a^2 + 2D_a\omega_a s + s^2}. \quad (6.7.5)$$

with  $D_a = 0.7$  and  $\omega_a = 2\pi \cdot 5$  [rad/s]. Under the assumption of a 12 V power supply, the voltage is limited to  $|u| \leq \hat{u} = 12$  V.

### Problem Specifications

The aim in yaw dynamics controller design is to make sure that stable and improved yaw dynamics is achieved for all operating conditions and all possible values of the uncertain parameters despite the presence of additional unstructured uncertainty representing unmodelled dynamics, e.g. sensor dynamics, neglected flexible body modes, etc. Here, improved yaw dynamics means good disturbance rejection properties where

Table 6.3. Notations and numerical values of actuator variables.

$J_a$	0.004053 [kg m <sup>2</sup> ]	motor inertia
$k_f$	0.01625 [Nm s/rad]	motor damping coefficient
$L_a$	0 [H]	inductivity (electric time constant neglected here)
$R_a$	5 [ $\Omega$ ]	electrical resistance
$k_{me} = k_{em}$	0.9 [Nm/A]	electromagnetic constant
$k_a$	22.22 [V/rad]	control gain of actuator position control
$\hat{u}$	12 [V]	voltage limitation

the possible disturbances include the effect of wind forces and  $\mu$ -split braking. Good steering tracking performance is required as well. A disturbance observer-based steering controller is designed and shown to effectively achieve the desired aim in the following sections.

### The Disturbance Observer

The disturbance observer is a specific method of designing a disturbance rejection architecture (see Figure 1.11) to achieve insensitivity to both modelling errors and disturbances [163], [193]. It has been used successfully in a variety of motion control applications, including high-speed direct drive positioning [124] and friction compensation [102]. The disturbance observer can also be used to achieve dynamics similar to those obtained by the use of inner feedback loops through control [100]. The application of the disturbance observer control scheme to vehicle yaw dynamics control is introduced in the following.

The vehicle model can also be expressed as

$$r = G \delta_F + d = (G_n(1 + \Delta_m)) \delta_F + d, \quad (6.7.6)$$

where  $G$  is the actual vehicle dynamics input-output relation between steering wheel angle  $\delta_F$  and yaw rate  $r$ . The term  $\Delta_m$  is a multiplicative uncertainty w.r.t. to an adopted nominal model  $G_n$ , which may as well represent the desired dynamics. So  $\Delta_m$  comprises any dynamic divergence (also structured and unstructured uncertainty) between  $G_n$  and the actual  $G$  but the effect of external disturbance  $d$ . The aim in disturbance observer design is to approximately obtain

$$\frac{r}{\delta_S} = G_n G_a \quad (6.7.7)$$

(rather than (6.7.3)) as the input-output relation (steering transfer function) despite the presence of  $\Delta_m$  and external disturbance  $d$ . This aim is achieved by treating the effect of  $\Delta_m$  and  $d$  as an extended disturbance  $e$  in disturbance observer design and solving for it as

$$r = G_n \delta_F + (G_n \Delta_m \delta_F + d) = G_n \delta_F + e, \quad (6.7.8)$$

$$e = r - G_n \delta_F, \quad (6.7.9)$$

and using the new control signal  $\delta_S$  given by

$$\delta_F = G_a \left( \delta_S - \frac{e}{G_n} \right) = G_a \left( \delta_S - \frac{1}{G_n} r + \delta_F \right) \quad (6.7.10)$$

to approximately cancel its effect in (6.7.8). Substituting (6.7.10) into (6.7.8) shows that the desired steering transfer function (6.7.7) is achieved if a good actuator ( $G_a \rightarrow 1$ ) is used. The front wheel steering angle  $\delta_F$  is assumed to be the output of the steering actuator  $G_a$ . With the aim of trying to limit the compensation to a preselected low frequency range (in an effort not to overcompensate at high frequencies), the feedback

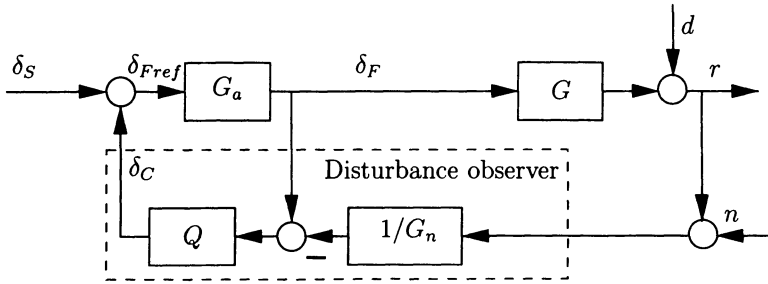


Figure 6.38. Closed-loop structure with disturbance observer

signals in (6.7.10) are multiplied by the low-pass filter  $Q$  to obtain the implementation equation

$$\delta_F = G_a (\delta_S + Q (\delta_F - 1/G_n r)) , \quad (6.7.11)$$

which can also be seen in the block diagram of Figure 6.38. Including  $G_a$  in the inner feedback loop helps in reducing the effect of actuator saturation on disturbance observer performance [34]. The relative degree of the unity d.c. gain low-pass filter  $Q$  is chosen to be at least equal to the relative degree of  $G_n$  for causality of  $Q/G_n$ . In the sequel, the structure of  $Q$  is assumed to be

$$Q(s) = \frac{1}{\tau_Q s + 1} . \quad (6.7.12)$$

The nominal steering transfer function is chosen as a first order system, here given by

$$G_n(s) = \frac{K_n(v)}{\tau_n s + 1} , \quad (6.7.13)$$

and  $K_n(v)$  is the steady state gain of the nominal single-track model (i.e. on a dry road,  $\mu_n = 1$ ) at the actual longitudinal speed  $v$  from (6.7.2).

The open-loop transfer function at signal  $r$  of the disturbance observer compensated yaw dynamics model is (for the sake of brevity, the Laplace operator  $s$  is partly omitted in the sequel)

$$L := \frac{G_a Q}{1 - G_a Q} \frac{G}{G_n} . \quad (6.7.14)$$

The steering transfer function, disturbance rejection (i.e. sensitivity function  $S$ ) and sensor noise rejection (i.e. complementary sensitivity function  $T$ ) transfer functions given are then

$$\frac{r}{\delta_S} = \frac{G_n G_a G}{G_n(1 - G_a Q) + G_a G Q} , \quad (6.7.15)$$

$$S := \frac{r}{d} = \frac{1}{1 + L} = \frac{G_n(1 - G_a Q)}{G_n(1 - G_a Q) + G_a G Q} , \quad (6.7.16)$$

$$T := -\frac{r}{n} = \frac{L}{1 + L} = \frac{G_a G Q}{G_n(1 - G_a Q) + G_a G Q} , \quad (6.7.17)$$

from which it is obvious that for good performance,  $Q$  must be a unity gain low-pass filter ( $G_a$  is a unity gain low-pass filter as well). This choice will result in  $r/\delta_S \rightarrow G_n$ ,  $r/d \rightarrow 0$  at low frequencies where  $Q \rightarrow 1$  and  $r/n \rightarrow 0$  at high frequencies where  $Q \rightarrow 0$  as is desired. Disturbance observer design is thus mainly shaping the filter  $Q$  to satisfy the design objectives. The first limitation on the bandwidth of  $Q$  comes from the sensor noise rejection at sensor noise frequencies. The second limitation is that the bandwidth of  $Q$  should not be larger than the bandwidth of the actuator used as it makes no sense to command what cannot be achieved. The other entity that significantly affects the properties of the controlled system is the choice of the desired dynamics  $G_n$ . With the assumed structures (6.7.12) and (6.7.13), tuning the implemented disturbance observer controller (6.7.11) means tuning the parameters  $\tau_Q$  and  $\tau_n$ . This is the scope of the following section in order to achieve robust matching of the design objectives.

## Parameter Space Design

The parameter space approach is applied for robust controller design and analysis. Besides eigenvalue specifications ( $\Gamma$ -stability), Bode magnitude type specifications ( $\mathcal{B}$ -stability) on sensitivity functions are also incorporated into the controller design to enhance vehicle stability as well as performance and handling qualities robustly w.r.t. structured ( $v, \mu$ ) and unstructured uncertainty (unmodelled dynamics).

First, the problem set-up is stated. Then, the stability and performance specifications in eigenvalue and frequency domain for controller design are described. The parameter space approach is used to map these specifications into the plane of the two controller parameters  $\tau_Q$  and  $\tau_n$ . Finally, the resulting controller is analyzed in terms of sensitivity.

## Problem Set-up

Consider Figure 6.38 and (6.7.12).  $Q$  is chosen as a unity d.c. gain first order low-pass filter with time constant  $\tau_Q$ . The open-loop single-input-single-output transfer function  $L$ , sensitivity function  $S$  and complementary sensitivity function  $T$  are given by (6.7.14), (6.7.16) and (6.7.17), respectively. Furthermore, the characteristic polynomial of the closed-loop system is defined as

$$p = \text{num}(1 + L) . \quad (6.7.18)$$

In the following demonstration of the design procedure applying  $\Gamma$ - and  $\mathcal{B}$ -stability, the time constants  $\tau_n$  of the nominal model  $G_n$  in (6.7.13) and  $\tau_Q$  of the filter  $Q$  in (6.7.12), respectively, are considered as controller parameters. These time constants shall be tuned such that the feedback provides  $\Gamma$ - and  $\mathcal{B}$ -stability for the whole operating domain given in Figure 6.36. In the first design step being described in this section, only the four operating conditions marked by crosses in Figure 6.36 are considered. For each of them, the  $\Gamma$ - and  $\mathcal{B}$ -stability specifications given below are mapped into the controller parameter plane  $(\tau_n, \tau_Q)$ .

### Control Design Specifications: $\Gamma$ -stability

Figure 6.39 shows the  $\Gamma$ -region representing the eigenvalue specifications that are one part of multiple specifications for the design of  $\tau_n$  and  $\tau_q$  for all  $(\mu, v)$  in the operating domain. The boundary  $\partial\Gamma$  of  $\Gamma$  is composed of three geometric elements. The first

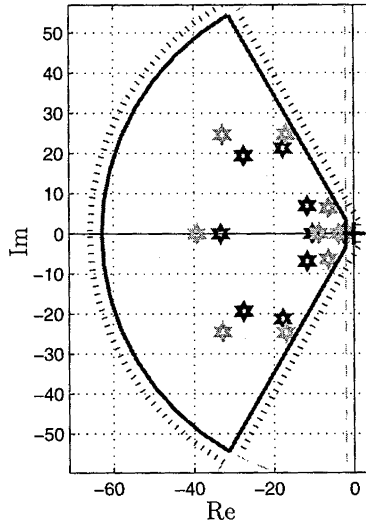


Figure 6.39.  $\Gamma$ -specifications in eigenvalue domain

boundary is a shifted imaginary axis  $s = -2$ , which ensures that the system's settling time is limited. Two lines of constant damping guarantee a minimum damping of 0.5 of all poles, and a circle centered at the origin guarantees that the natural frequency of any pole does not exceed  $2\pi \cdot 10$ [rad/s]. The poles of the closed-loop system shall be located in the admissible eigenvalue region  $\Gamma$  as shown in Figure 6.39, i.e.

$$\text{roots}\{p(s, \tau_n, \tau_Q, v, \mu)\} \subset \Gamma . \quad (6.7.19)$$

### Control Design Specifications: $\mathcal{B}$ -stability

#### *Disturbance rejection*

- a) To ensure disturbance attenuation at low frequencies,  $|S(j\omega)| \ll 1$  must hold.
- b) However, since  $L$  is a robustly stable transfer function with a relative degree of three, Bode's integral theorem [55] applies, which means that attenuating disturbances at low frequencies unavoidably results in amplifying them at high frequencies. Therefore, the amplification must also be restricted to an acceptable level, i.e.  $\|S(j\omega)\|_\infty < 1/\rho_S$ , where  $\rho_S$  is equivalent to the required Nyquist-stability margin.

These two specifications a) and b) are combined into one specification by selecting an upper bound on the FRM of  $S$  (see Figure 6.44), i.e.

$$|S(j\omega\omega, \tau_n, \tau_Q, v, \mu)| < |W_S(j\omega)|^{-1}, \quad \forall \omega, \quad (6.7.20)$$

where

$$W_S(s)^{-1} = 1.8 \frac{s + 0.7}{s + 12.6}.$$

*Robustness w.r.t. unstructured uncertainty* Two magnitude bounds on  $T$ , i.e. the magnitudes of  $W_{T,1}(s)^{-1}$  and  $W_{T,2}(s)^{-1}$  are selected to capture robustness w.r.t. unstructured uncertainty, i.e. using a multiplicative uncertainty model.

- a) The disturbance observer shall guarantee robustness to 10 % magnitude uncertainty at low frequencies, i.e. where the model of the vehicle and the actuator is reasonably accurate, and 500 % uncertainty at high frequencies, i.e. where unmodelled dynamics come into play. Thereby, a transition frequency of  $2\pi \cdot 6$  [rad/s] between low gain and high gain of the weighting function  $W_T(s)$  is selected based on the knowledge of the vehicle model's accuracy and the performance specification of the steering actuator.
- b) A second bound on  $T$ , i.e.  $W_{T,2}(s)^{-1}$  is used to cover the disturbance observer stability specifications subject to model uncertainty in  $m$  and  $J$  [65].

Hence, the following  $\mathcal{B}$ -specifications will be used as constraints for  $T$ :

$$|T(j\omega, \tau_n, \tau_Q, v, \mu)| < |W_{T,i}(j\omega)|^{-1}, \quad \forall \omega, i = 1, 2, \quad (6.7.21)$$

where

$$\begin{aligned} W_{T,1}(s) &= 5 \frac{s + 3.77}{s + 188.5}, \\ W_{T,2}(s) &= \frac{0.12804(s + 43.98)(s + 0.4833)}{(s + 6.124)(s + 2.882)} \end{aligned}$$

(see Figure 6.45). Note that (6.7.21) represents the “robust stability” criterion for two different multiplicative uncertainty models. At low frequencies, unstructured uncertainty subject to uncertainty in  $m$  and  $J$  is relevant and for high frequencies uncertainty subject to unmodelled dynamics is relevant.

### Mapping of $\Gamma$ - and $\mathcal{B}$ -stability Boundaries into Parameter Space

The mapping of the  $\Gamma$ -stability boundaries defined on p. 230 is based on the limit condition that the characteristic polynomial  $p(s, \tau_n, \tau_Q, v, \mu)$  has a root exactly on the  $\Gamma$ -region boundary  $\partial\Gamma$ . Therefore, the condition  $\partial\Gamma = s(\alpha) = \sigma(\alpha) + j\omega(\alpha)$ , where  $\alpha$  is the parameterization of  $\partial\Gamma$ , is substituted into the characteristic polynomial given by (6.7.18), which is separated into two equations for its real and imaginary parts, respectively:

$$\begin{aligned} \operatorname{Re}(p(\alpha, \tau_n, \tau_Q, v, \mu)) &= 0, \\ \operatorname{Im}(p(\alpha, \tau_n, \tau_Q, v, \mu)) &= 0. \end{aligned} \quad (6.7.22)$$

The mapping of the  $\Gamma$ -stability boundaries into the parameter plane  $(\tau_n, \tau_Q)$  requires algebraic solution of these two equations, see Appendix A. Figure 6.40 shows the result for the mapping of the  $\Gamma$ -stability boundaries (as defined in Figure 6.39) for the two operating conditions with  $v = 50$  [m/s] and  $\mu \in \{0.8; 1\}$  (see Figure 6.36). The  $(\tau_n, \tau_Q)$ -region, which simultaneously  $\Gamma$ -stabilizes the two operating points, is denoted  $K_\Gamma$ . In this plot and also in Figure 6.41 and Figure 6.42 the grey lines correspond to the operating condition with  $\mu = 0.8$ , and the black lines to that with  $\mu = 1$ . For a better distinction between  $\Gamma$ - and  $\mathcal{B}$ -stability boundaries, dashed linestyle is used for  $\Gamma$ -stability in this plot and in the subsequent plots. For the sake of conciseness, the  $\Gamma$ -stability boundaries for  $v = 30$  [m/s] and  $\mu \in \{0.5; 1\}$  are not displayed in Figure 6.40, Figure 6.41 and Figure 6.42. To establish the mapping equations of the  $\mathcal{B}$ -stability boundaries defined by Equations (6.7.20) and (6.7.21), it suffices to consider two mathematical conditions, the point and the tangent condition [159]. The point condition applies when  $|S(j\omega, \tau_n, \tau_Q, v, \mu)|$  or  $|T(j\omega, \tau_n, \tau_Q, v, \mu)|$ , respectively, starts ( $\omega = 0$ ) or ends ( $\omega \rightarrow \infty$ ) on the boundary  $\partial\mathcal{B}_S = |W_S(j\omega)^{-1}|$  or  $\partial\mathcal{B}_{T,i} = |W_{T,i}(j\omega)^{-1}|$ , respectively. The tangent condition allows for the mapping of touching points, i.e. the points where  $|S(j\omega, \tau_n, \tau_Q, v, \mu)|$  or  $|T(j\omega, \tau_n, \tau_Q, v, \mu)|$ , respectively, becomes tangent to  $\partial\mathcal{B}_S$  or  $\partial\mathcal{B}_{T,i}$ , respectively. Details about the mapping of  $\mathcal{B}$ -specifications are described in Section 5.3.

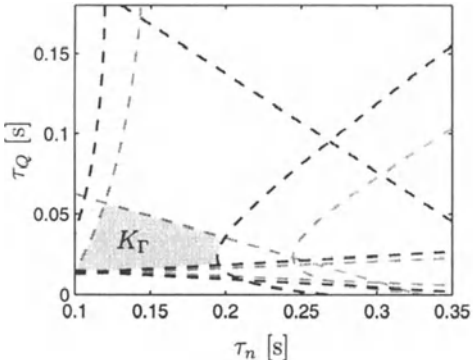


Figure 6.40.  $\Gamma$ -stable region for  $v = 50$  [m/s] and  $\mu \in \{0.8; 1\}$

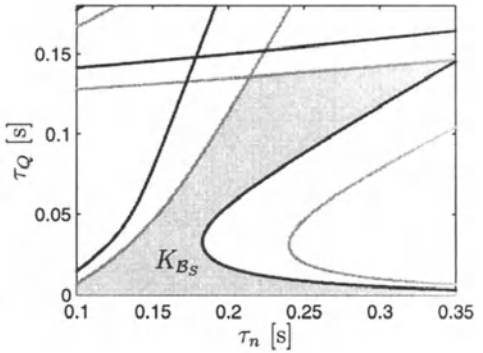


Figure 6.41. Nominal performance in parameter space for  $v = 50$  [m/s.] and  $\mu \in \{0.8; 1\}$

To ensure that the magnitude of the sensitivity function  $|S(j\omega, \tau_n, \tau_Q, v, \mu)|$  remains below its upper bound, Condition (6.7.20) is mapped into the  $(\tau_n, \tau_k)$  controller parameter plane. Figure 6.41 shows the resulting region  $K_{B_S}$  for the two operating points at  $v = 50$  [m/s] with  $\mu \in \{0.8; 1\}$ . For any parameter combination  $(\tau_n, \tau_Q)$  taken from this region, Condition (6.7.20) is satisfied for both operating points simultaneously.

For consideration of robust stability, Condition (6.7.21) is mapped into the  $(\tau_n, \tau_Q)$  controller parameter plane (see Figure 6.42). The dotted lines correspond to the Hurwitz-stability condition, i.e. the nominal stability condition, for the two operating points considered. This non-conservative mapping shows which set of  $(\tau_n, \tau_Q)$  controller parameters (i.e. the region  $K_{B_T}$  in Figure 6.42) will guarantee robust stability in the

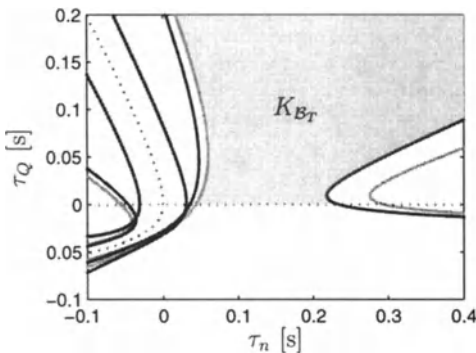


Figure 6.42. Robust stability in parameter space for  $v = 50$  [m/s] and  $\mu \in \{0.8; 1\}$

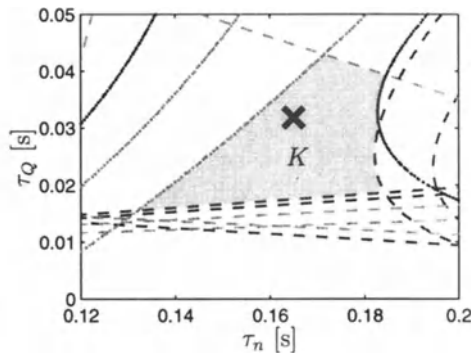


Figure 6.43. Parameter region which meets all  $\mathcal{B}$ - and  $\Gamma$ -specifications for  $v = 50$  [m/s],  $\mu \in \{0.8; 1\}$  and  $v = 30$  [m/s],  $\mu \in \{0.5; 1\}$

presence of actuator uncertainty, unmodelled dynamics and/or structured uncertainty due to the disturbance observer specifications simultaneously for the two operating points at  $v = 50$  [m/s] with  $\mu \in \{0.8; 1\}$ . Similar results are achieved for the other two operating points  $v = 30$  [m/s] and  $\mu \in \{0.5; 1\}$ .

The final step in controller design is superimposing the previously determined stability regions in parameter space. The intersection of all of the individual regions in the  $(\tau_n, \tau_Q)$  plane that satisfy the formulated  $\Gamma$ - and  $\mathcal{B}$ -specifications for all four operating points form the desired parameter region  $K$  shown in Figure 6.43. For any choice of  $(\tau_n, \tau_Q) \in K$ , all previously described requirements in terms of  $\Gamma$ - and  $\mathcal{B}$ -stability are met simultaneously for the four operating conditions.

### Controller Selection

Note that satisfying all specifications postulated also for low speed (e.g.  $v = 10$  [m/s]) requires gain-scheduling of  $\tau_n$  and  $\tau_Q$  with speed since the vehicle yaw dynamics is much faster at low speeds. This is not considered here for the sake of brevity. Instead, from the region  $K$  in Figure 6.43 the parameters  $\tau_n = 0.165$  [s] and  $\tau_Q = 0.0318$  [s] are chosen as fixed controller parameters (marked with a cross). Figure 6.39 shows all eigenvalues of the closed-loop system for the four operating conditions. They are all included in the desired  $\Gamma$ -region.

### Sensitivity Analysis

Figures 6.44 and 6.45 show  $|S(j\omega)|$  and  $|T(j\omega)|$  for the four operating points. They all remain below  $|W_S(j\omega)^{-1}|$ ,  $|W_{T,1}(j\omega)^{-1}|$  and  $|W_{T,2}(j\omega)^{-1}|$ , respectively, i.e. they are entirely included in the  $\mathcal{B}$ -stable regions.

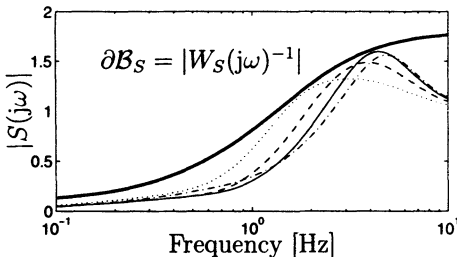


Figure 6.44. FRM-plot of the sensitivity function

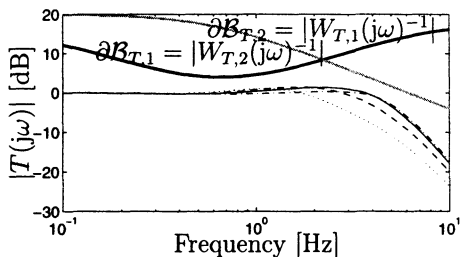
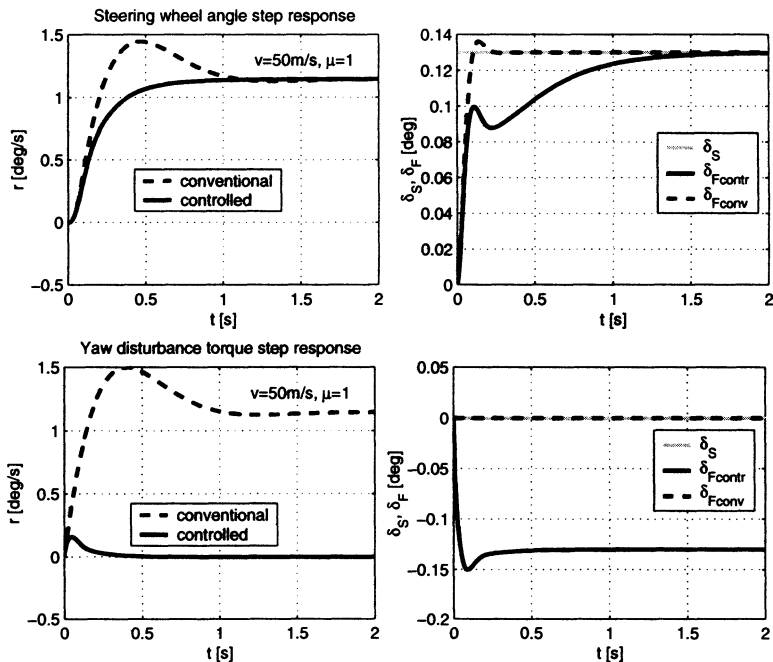
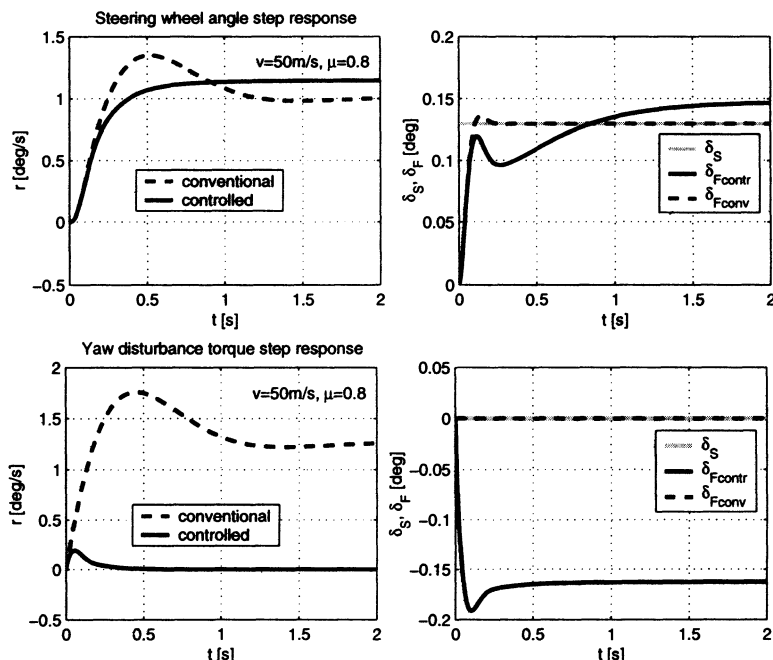


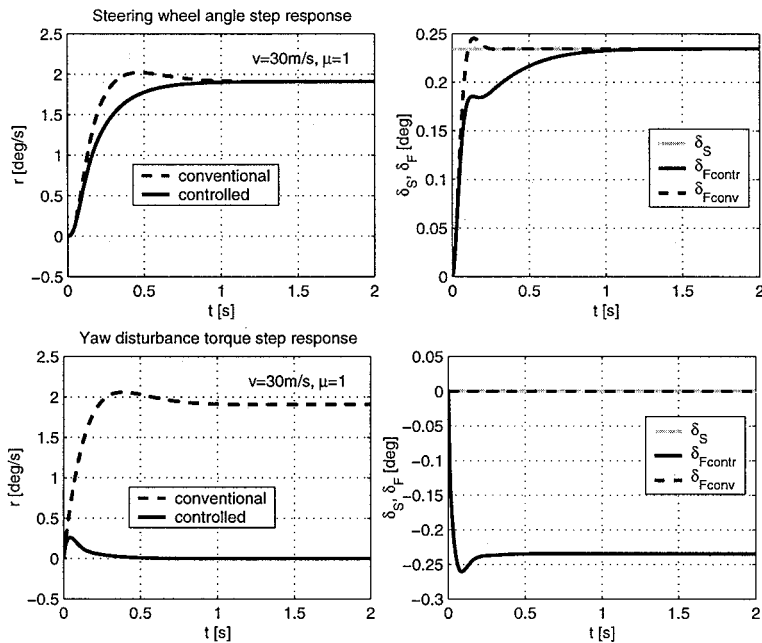
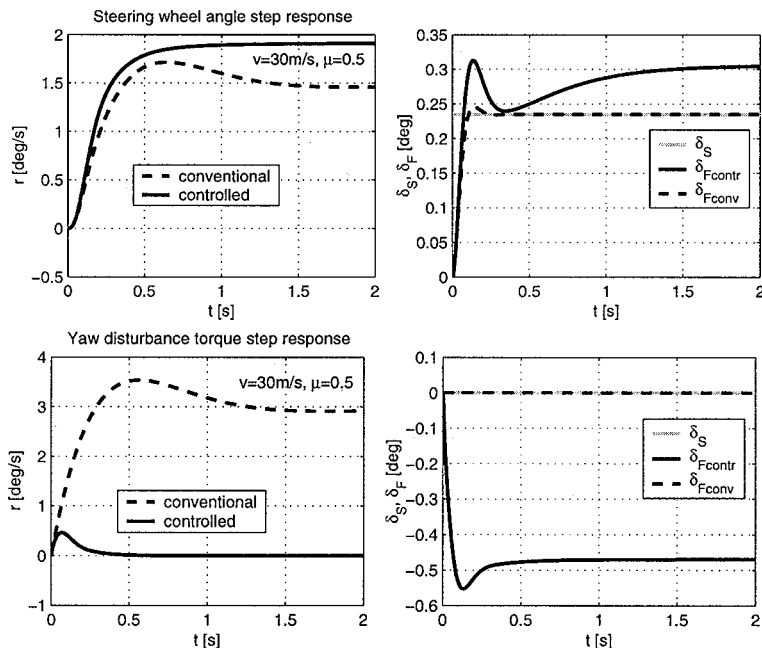
Figure 6.45. FRM-plot of the complementary sensitivity function

### Simulation Results

Two versions of the vehicle are compared in this section by means of linear simulation: the conventional car and the controlled car. For the sake of comparability, the conventional car is assumed to be a steer-by-wire vehicle equipped with the same steering actuator as the controlled car (see (6.7.3)). The steering transfer function of the controlled car is given by (6.7.15). The controller parameters are set according to the design results:  $\tau_n = 0.165$  [s] and  $\tau_Q = 0.0318$  [s]. Two maneuvers are investigated: A steering wheel step input and a yaw disturbance torque step input. The maneuvers are performed at the four operating points marked in Figure 6.36. The results are shown in Figures 6.46–6.49 in terms of the yaw rate  $r$ , the steering wheel angle  $\delta_S$  and the front wheel steering angle  $\delta_F$ . The simulations show that the controller provides excellent disturbance rejection and a good steering tracking at all investigated operating points. The yaw disturbances are robustly attenuated within 0.5 s. The control action is finished before the driver is even capable of starting his countersteering due to his reaction time of about 1 s. The yaw rate responses to a steering wheel input are well in accordance with the desired steering transfer function (6.7.7) not exhibiting any overshoot. Zero steady state error is inherent to the control structure as already discussed by means of (6.7.15)–(6.7.17). The steady state gain of the controlled vehicle steering transfer function is  $K_n(v)$ . This gain has been calculated to be identical to the conventional vehicle steady state gain for  $\mu_n = 1$ . Therefore, the steady state yaw rate of the conventional vehicle and the controlled vehicle after a steering wheel input are identical for  $\mu = 1$  (Figure 6.46 and Figure 6.48) but differ otherwise.

Note that other choices for  $Q$  and  $G_n$  than given by (6.7.12) and (6.7.13) are feasible and may be reasonable depending on the specifications. For example, a second order filter for  $G_n$  to represent a certain desired single-track steering transfer function can be used. If this model is well in accordance with the actual vehicle, then the steering transfer function is not significantly changed by control. However, good disturbance rejection is retained. On the other hand, a band-pass filter can be applied for  $Q$  instead of a low-pass filter. This removes control action at low frequencies (“fading controller”) and transfers the task of compensating steady state errors back to the driver [33].

Figure 6.46. Linear simulation results at  $v = 50$  [m/s],  $\mu = 1$ .Figure 6.47. Linear simulation results at  $v = 50$  [m/s],  $\mu = 0.8$ .

Figure 6.48. Linear simulation results at  $v = 30$  [m/s],  $\mu = 1$ .Figure 6.49. Linear simulation results at  $v = 50$  [m/s],  $\mu = 0.5$ .

### Non-linear Stability Analysis

Previous experimental experience shows that limit cycles with actively steered cars can occur due to actuator non-linearities [16]. In this section, the rate limitation of the steering actuator is considered in terms of the limitation of the electric voltage of the motor. The Popov criterion [168] is employed to prove absolute stability for the controlled car such that the existence of limit cycles can be excluded in the whole operating domain of the car. The foundations of mapping the Popov criterion to parameter space are described in Section 5.1. With the Popov absolute stability criterion, the Popov plot of the system's linear part is considered, whereas for the static time-invariant non-linear part only a sector needs to be known, which includes the non-linearity characteristics. The transfer function of the system's linear part is the transfer function from signal  $u$  to signal  $-u_1$  in Figure 6.37. Therefore, the actuator is considered to be connected to the control loop as shown in Figure 6.38 with  $\delta_{Fref} = \delta_S + \delta_C$ . The Popov plot is derived from the locus of the linear part transfer function, whereupon its imaginary part is multiplied with the respective frequency. The saturation in Figure 6.37 is a characteristic that is included in a sector formed by the two straight lines  $u = 0$  and  $u = k \cdot u_1$  with  $k = 1$ . According to the Popov criterion, absolute stability is proven if

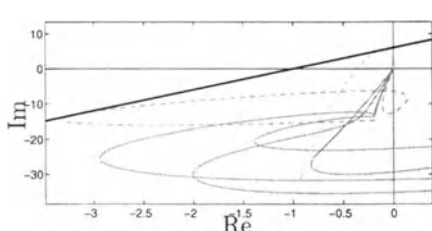


Figure 6.50. Popov-line (black) and Popov plots (grey) for six operating conditions marked in Figure 6.51

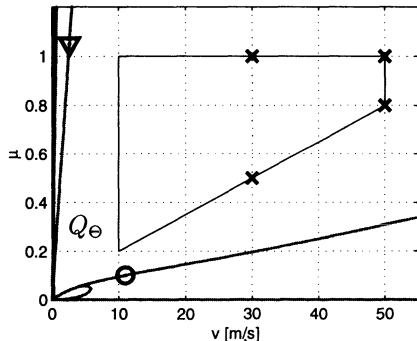


Figure 6.51. Region  $Q_\Theta$  of absolute stability using a Popov-line with slope  $M = 6.0$

the linear part is Hurwitz and the Popov plot lies to the right hand side of the so-called Popov-line. (This definition is adopted for  $\Theta$ -stability here.) The Popov-line intersects the real axis at  $-1/k = -1$ . The slope  $M$  of the Popov-line may be chosen arbitrarily. We chose  $M = 6.0$  (see Figure 6.50), which turns out to be favorable in terms of the resulting  $\Theta$ -stable parameter region  $Q_\Theta$ . Thus, the whole operating domain of the vehicle is included in  $Q_\Theta$ , i.e.  $Q_\Theta \subset Q$  as illustrated in Figure 6.51. Figure 6.50 also shows six Popov plots corresponding to six operating points marked in Figure 6.51. Solid lines are used for the Popov plots of the operating points indicated by cross markers. The Popov plot belonging to the circular mark is plotted dashed, the one belonging to the triangular marker is plotted with dotted linestyle. The latter two cases are exemplary  $\Theta$ -limit-stable operating points since the points are located on a  $\Theta$ -stability boundary in the  $(v, \mu)$ -plane. This illustrates the limit case of a Popov plot touching the Popov-line,

which was used for mapping stability boundaries into parameter space. By this approach, the robust non-existence of limit cycles in the operating domain is proven while accounting for the presence of the saturation non-linearity. A similar proof, however, applying the dual locus method has been shown in [16] for a different control structure.

### **Conclusions**

A two degree of freedom steering controller based on the disturbance observer for vehicle yaw dynamics improvement was introduced here. For robust controller design, frequency magnitude specifications ( $\mathcal{B}$ -stability) and eigenvalue specifications ( $\Gamma$ -stability) were mapped into the parameter plane of two controller parameters. Simulation results based on the linear single-track model were used to demonstrate the achievement of excellent disturbance rejection and steering command responses that match well the desired dynamics. In addition, considering the possibility of steering actuator rate limitation due to electric voltage limitation, a Popov criterion - based non-linear analysis was performed for proving robust absolute stability. Therefore, respective  $\Theta$ -stability boundaries were mapped into a plane of operating parameters.

## **6.8 Rollover Avoidance**

Rollover accidents very often cause severe injuries or even death of the involved road users and are therefore in the focus of public interest. By continuously improving active and passive safety systems, the number of accidents with severe personal damage has been reduced significantly during the last decade. However, these systems have not been developed in the context of rollover avoidance, with the result that the percentage of rollover accidents has not decreased.

Common accident causes for passenger cars are skidding induced by braking or accelerating on a unilateral icy road, sudden loss of tire pressure, or side-wind. For vehicles with an elevated center of gravity, the same critical driving situations may yield rollover even though all tires of the vehicle are far away from their saturation limits.

Driving situations can directly induce vehicle rollover that are excessive speed when entering a curve, severe lane change or obstacle avoidance maneuvers, or disturbance impacts like side-wind gusts. Vehicles with an elevated CG are especially prone to rollover. Moreover, many driver mistakes result from an overestimation of the vehicle's roll stability, which varies due to large changes of the payload-dependent CG height. Also, very often heavy truck drivers do not keep in mind the load, mass of the load and mass distribution. From common sense, it is clear that the ratio of the track width and the height of the CG (the so-called track width ratio) is the most important vehicle parameter affecting the rollover risk, and accident analysis results [35] confirm this fact.

In this section, a vehicle dynamics control concept for rollover avoidance of vehicles with an elevated center of gravity is introduced. The two main goals of the control

concept are first to avoid rollover in emergency situations by combined steering and braking control, and second to improve the roll damping of the vehicle and thus the roll stability, which reduces the roll overshoot in transient driving maneuvers. It is shown that these design goals can be achieved for a wide range of varying or uncertain operating conditions. Here, together with parametric (structured) uncertainty (vehicle speed and height of CG), unstructured uncertainty is considered to account for the influence of unmodelled dynamics, e.g. due to neglected flexible modes of the chassis or steering and tire elasticities. The desired stability and performance specifications, i.e. good handling qualities and stability requirements, are formulated in terms of eigenvalues ( $\Gamma$ -stability), frequency loci ( $\Theta$ -stability) and frequency magnitudes ( $\mathcal{B}$ -stability). For controller design, an augmented single-track model, denoted single-track model with roll augmentation, is introduced to describe the interrelation of lateral and yaw dynamics on the one hand and the roll dynamics on the other hand. In contrast to passenger vehicles, this interrelation is particularly relevant for vehicles with an unfavorable relation of CG height and track width in context of rollover. The active steering concept is based on the assumption of an additive front-wheel steering actuator, i.e. the front-wheel steering angle is composed of the steering angle commanded by the driver and an additional steering angle set by the steering actuator. The effectiveness and robustness of the vehicle dynamics control structure, which is based on combined active steering and braking, is shown by means of sensitivity analysis and simulation results.

### Rollover Coefficient

Consider Figure 6.52. As a good indicator for the quantification of rollover risk, the distribution of the vertical tire loads is used here, resulting in the following definition of a rollover coefficient:

$$R = \frac{F_{zR} - F_{zL}}{F_{zR} + F_{zL}}. \quad (6.8.1)$$

The tire loads left  $F_{zL}$  (right  $F_{zR}$ ) front and rear are added. For straight driving on a horizontal road, assuming symmetric load distribution, it holds that  $F_{zR} = F_{zL}$ , which means that  $R = 0$ . When  $F_{zR} = 0$  ( $F_{zL} = 0$ ), the right (left) wheels lift off the road and the rollover coefficient takes on the value  $R = -1$  ( $R = 1$ ). For  $|R| < 1$ , the vehicle is termed rollover-stable. From that, it can be seen that  $R$  is an intuitive measure for the risk of rollover.

If one wants to use the rollover coefficient as a control signal and/or as a visual, an acoustic, or haptic warning signal for the driver, it must be determined permanently during the ride. For the determination of  $R$ , different sensor signals and measurement principles may be applied.

First of all,  $R$  can be determined directly by measuring or observing the vertical tire loads. The spreading of air suspensions, especially in heavy trucks, has increased significantly during the last decade. This technology facilitates determination of the spring and damping forces based on the measurement of air spring pressure while also spring and damper characteristics are well known. Furthermore, vertical acceleration sensors mounted on the front and rear axles can be used for measuring a correction term describing the influence of the unsprung mass, i.e. of tires and axles. Thus, spring

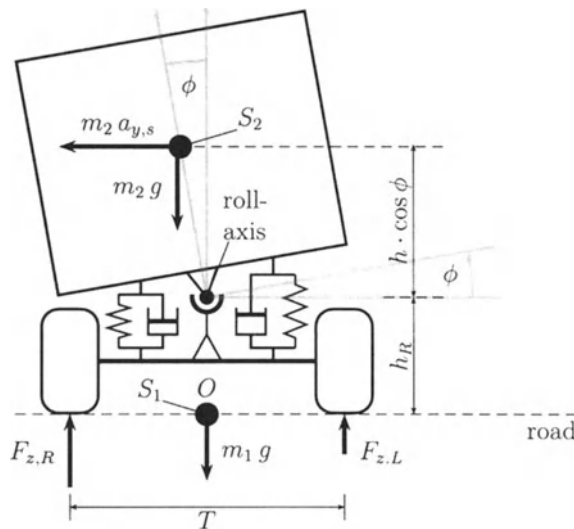


Figure 6.52. Variables for determination of a rollover coefficient

and damping forces plus correction term approximately equals the tire vertical load.

However, for vehicles with conventional suspensions additional, effort (sensors) is required to determine spring and damping forces. For these types of vehicles, an approximation of the rollover coefficient may be used. Therefore, Figure 6.52 shall be interpreted as a front view of a vehicle in steady state cornering. The following assumptions are made:

- Pitch and plunge mode are neglected.
- CG of chassis (unsprung mass) is in the road plane.
- The location of the roll axis is assumed constant in a height  $h_R$  parallel to the ground.
- CG of roll body (sprung mass plus payload) is in a height  $h$  above the roll axis.
- The payload is assumed symmetric (no eccentricity of the roll body CG).
- The spring deflection of the tires is neglected.

The forces acting on the vehicle (which are relevant for determination of the rollover condition) are the gravitational forces  $m_1 g$  and  $m_2 g$ , the vertical tire loads  $F_{zL}$  and  $F_{zR}$ , and the centrifugal force of the roll body  $m_2 a_{y,2}$ . The equilibrium condition for the vertical forces is

$$\sum F_z = F_{zR} + F_{zL} - (m_1 + m_2)g \equiv 0 . \quad (6.8.2)$$

The equilibrium condition of torques w.r.t. point O in Figure 6.52 is

$$\sum M_x = \frac{T}{2}(F_{zL} - F_{zR}) + m_2 g h \sin \phi + (h_R + h \cos \phi)m_2 a_{y,2} \equiv 0 . \quad (6.8.3)$$

Substituting (6.8.2) and (6.8.3) into (6.8.1) yields an approximation of the rollover coefficient:

$$R = \frac{m_2}{m T/2} \left( (h_R + h \cos \phi) \frac{a_{y,2}}{g} + h \sin \phi \right), \quad (6.8.4)$$

where  $m = m_1 + m_2$  is the total mass of the vehicle. To determine  $R$  corresponding to (6.8.4), the mass of the payload or mass of the roll body  $m_2$ , respectively, and the height  $h$  have to be estimated at the beginning of each ride and the roll angle has to be measured. The latter might be done by measuring the spring deflection. Linearization ( $\phi$  small) yields

$$R = \frac{m_2}{m T/2} \left( (h_R + h) \frac{a_{y,2}}{g} + h\phi \right) = a_R a_{y,2} + b_R \phi, \quad (6.8.5)$$

where

$$a_R = \frac{m_2(h_R + h)}{m g T/2}, \quad b_R = \frac{m_2 h}{m T/2}.$$

Further, assuming  $m_1 \ll m_2$  and the second term of (6.8.5) to be negligible compared to the first one, yields

$$R \approx \frac{h_R + h}{T/2} \frac{a_{y,2}}{g}. \quad (6.8.6)$$

This approximation reflects the accident analysis results in [35], where it was stated that the track width ratio  $(h_R + h)/(T/2)$  is the most important vehicle parameter affecting rollover risk.

Determination of  $R$  corresponding to (6.8.4), (6.8.5) or (6.8.6) requires the knowledge of the height  $h$ , which for a truck may vary largely from ride to ride due to varying payloads. Online-estimation methods may be applied to estimate  $h$  at the beginning of each ride as suggested in [96], [103], [115]. After a reliable estimate of  $h$  is available,  $R$  can be calculated subject to the lateral acceleration of the roll body at the CG  $a_{y,2}$  (and, if available, the measurement of the roll angle). The lateral acceleration of the roll body may be determined by interpolation between different acceleration signals (and using  $h$ ), measured, e.g. by lateral and vertical acceleration sensors.

## General Considerations for Rollover Avoidance

In the sequel, we will distinguish between direct and indirect rollover avoidance meaning that the strategy for rollover risk reduction explicitly depends on  $R$  (*direct rollover avoidance*) or it does not (*indirect rollover avoidance*).

### Direct Rollover Avoidance

The vehicle becomes hard to control if front and rear wheels on one side lift off the road. Therefore, the goal of the pursued direct rollover avoidance strategy, [158], [161], [160], is to avoid any wheel lift-off meaning to keep the vehicle in a rollover-stable mode, i.e.

$$|R| < 1. \quad (6.8.7)$$

Based on steady state considerations, the objective is to satisfy this requirement by keeping the absolute value of the roll body's lateral acceleration below:

$$|a_{y,2}| < a_{y,RL} = \frac{T/2}{h + h_R} g . \quad (6.8.8)$$

The steady state lateral acceleration limit due to rollover  $a_{y,RL}$  may vary from ride to ride, subject to largely varying payloads. Its value decreases with an increasing height of CG.

*Remark 6.14*

Vehicles with moving or swashing load may roll over in transient driving situations far before the steady state threshold  $a_{y,RL}$  has been reached. For other vehicles, the dynamical rollover limit, e.g. in transient lane change or obstacle avoidance maneuvers, may exceed the steady state threshold.  $\square$

The lateral acceleration limit due to skidding (compare to (6.1.1)) is approximately defined by

$$a_{y,SL} = \sqrt{(\mu g)^2 - a_x^2} . \quad (6.8.9)$$

Hence, to avoid skidding and rollover at the same time, the lateral acceleration has approximately to be limited by

$$|a_y| < \min(a_{y,SL}, a_{y,RL}) . \quad (6.8.10)$$

Also, from this formula it might be derived that for most of the passenger cars the skidding limit is relevant. For these vehicles, rollover may only occur posterior to skidding. In steady state cornering, the lateral acceleration mainly depends on curvature  $\rho$  and speed  $v$ , i.e.

$$a_{y,st} = v^2 \rho . \quad (6.8.11)$$

From this simple formula, it can be directly seen what has to be done in critical driving situations (skidding or rollover). To reduce  $a_{y,st}$ , either curvature or speed has to be reduced. This can be done by braking to reduce speed and/or by active steering to decrease curvature by means of driving into a wider curve (increasing radius of driven curve). The active steering impact can be performed very fast because of the small masses (steering wheel, column, steering rod, tires) that have to be moved. Braking requires deceleration of the total vehicle mass and is therefore much slower.

The strategy for direct rollover avoidance applied here is to combine active steering and braking. Thereby, rollover avoidance is given priority over ideal lane keeping. The active steering impact on the vehicle dynamics is prior to the effect of braking. By active steering, curvature can be decreased to avoid rollover. However, at the same time it has to be guaranteed that the vehicle remains on the road. Therefore, active braking is applied to reduce speed, and which allows the return of steering command to the driver after a little while.

### Indirect Rollover Avoidance

Indirect rollover avoidance here means to decrease the rollover risk by improving driving safety. Vehicle dynamics control systems using individual wheel braking (e.g. Electronic Stability Program, ESP [195]) or active steering for stabilization of the yaw movement as described in the previous sections have been firstly established for passenger cars with a low CG. Some effort has been done to adapt individual wheel braking concepts to vehicles with an elevated CG [106], [166]. These concepts can, in general, help to avoid critical situations and thus indirectly help to reduce rollover risk. An effective way to reduce the rollover risk in transient driving maneuvers such as lane change or obstacle avoidance is to apply active and semi-active chassis control systems such as e.g. ABC (active body control, [91]) or dynamic drive (ARC  $\equiv$  active roll control) [126]. Besides these chassis control systems, active steering can also be used to shape the vehicle dynamics such that the roll dynamics is damped and thus the transient roll overshoot of the vehicle's body is reduced [158], [25], [26].

### Rollover Avoidance Control Concept

The vehicle dynamics control approach for rollover avoidance described here aims at two goals. One is to improve the damping of the roll dynamics by active steering. This reduces the risk of rollover in dynamic steering maneuvers. The other task is to improve safety in emergency situations when the vehicle is already very close to rollover. Here, in addition to active steering, adapted braking is applied. The key idea of the rollover avoidance control concept is that in critical situations, rollover avoidance is temporarily given priority over ideal lane keeping.

The structure of the entire rollover avoidance control system is shown in Figure 6.53. The system consists of the plant, which is the vehicle, sensors for measuring the vehicle dynamics states, steering and braking actuators, and the vehicle dynamics control system. The vehicle dynamics control system itself combines three feedback loops: continuous operation steering control, emergency steering control and emergency braking control.

Subsequently, the design models for the vehicle dynamics and the steering actuator are described and the design of the three feedback loops is shown.

### Single-track Model with Roll Augmentation

The single-track model [172] has been proven to be an adequate model for investigation of the vehicle dynamics of passenger cars with a low center of gravity. In this model, the roll, pitch, and plunge mode of the vehicle are neglected. However, for vehicle dynamics investigations of vehicles with an elevated center of gravity, it is necessary to at least additionally consider the roll dynamics of the roll body relative to the chassis. For this reason, a single-track model with roll augmentation is considered, which will serve as a design model for the rollover avoidance control system in this section.

The vehicle is modelled as a multibody system consisting of two rigid bodies: 1) The chassis with mass  $m_1$  is composed of the front and rear axles, the four wheels and the frame, and 2) the roll body (payload included) is the sprung mass  $m_2$ . The

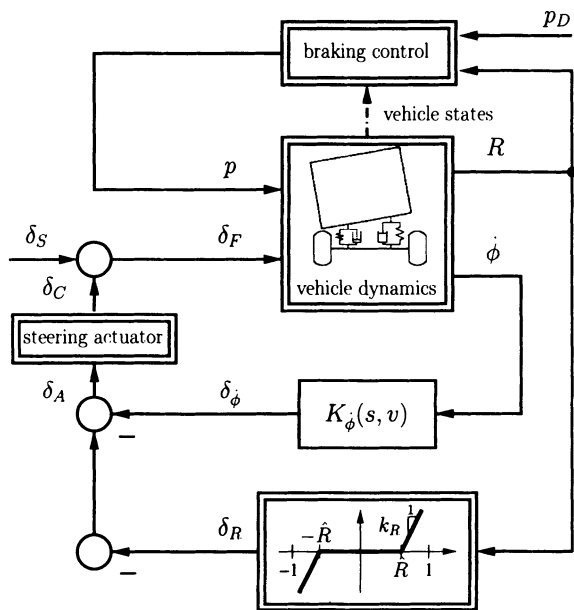


Figure 6.53. Structure of rollover avoidance control concept

position of the vehicle's roll axis, i.e. the front and rear roll center, depends on the suspension kinematics. The model assumes a fixed roll axis parallel to the road plane in the longitudinal direction of the vehicle at a height  $h_R$  above the street. Hence, body 2 is linked to body 1 with a one degree of freedom joint. The roll movement of the roll body is damped and sprung by suspensions and stabilizers with an effective roll damping coefficient  $d_\phi$  and roll stiffness  $c_\phi$ . The CG of the chassis, i.e. CG<sub>1</sub> is assumed to be in the road plane below CG<sub>2</sub> since its contribution to the roll movement is considered to be negligible. For the chassis, the same assumptions as for the single-track model [172] are used in order to represent the main features of vehicle steering dynamics in the horizontal plane. Linear spring, damping and tire characteristics are assumed. The latter assumption is permissible for vehicles and operating conditions where  $a_{y,RL} \ll a_{y,SL}$ .

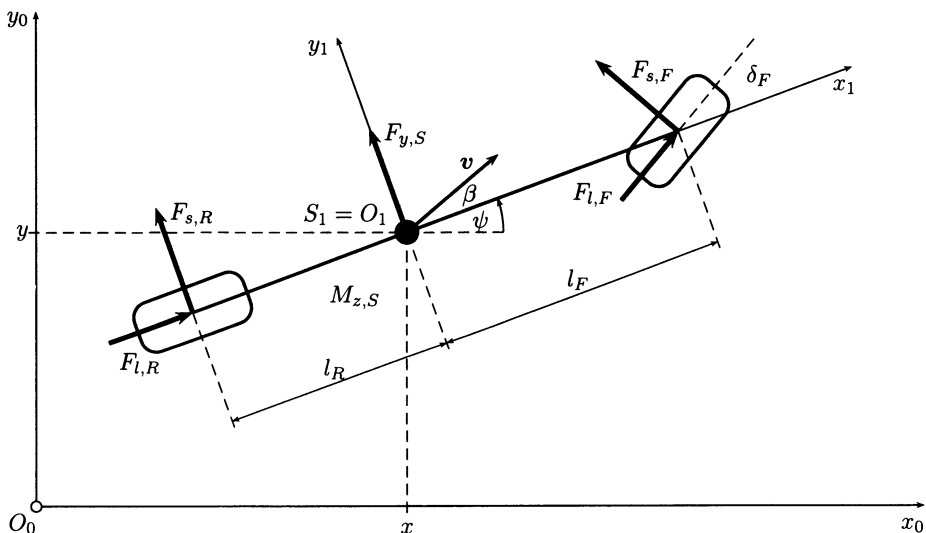


Figure 6.54. Model assumptions for the chassis

The model parameters used here are compiled in Table 6.4. The data are taken from [133].

The multibody system describes the vehicle's longitudinal, lateral, yaw, and roll dynamics. A similar description of a vehicle model can, e.g. be found in [179]. Applying Jourdain's principle of virtual power, the non-linear equations of motion are obtained according to a proper choice of minimal velocities and minimal coordinates, respectively, e.g.

$$\begin{aligned}\dot{\mathbf{z}} &= [v_x \ v_y \ r \ \dot{\phi}]^T, \\ \mathbf{z} &= [\int_0^t v_x dt \ \int_0^t v_y dt \ \psi \ \phi]^T,\end{aligned}$$

where  $v_x$  and  $v_y$  are the velocity components of body 1 in longitudinal and lateral direction,  $\psi$  is the yaw angle,  $r = \dot{\psi}$  is the yaw rate of body 1,  $\phi$  is the roll angle and  $\dot{\phi}$

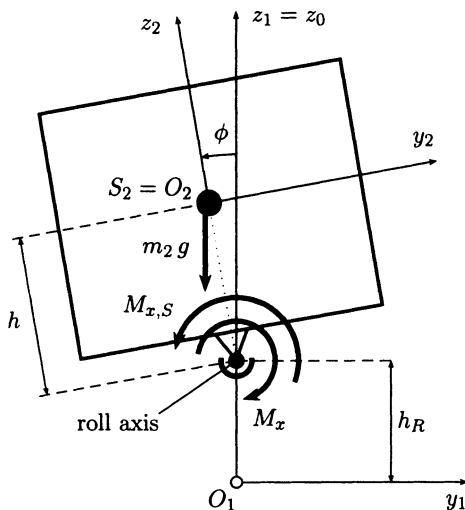


Figure 6.55. Model assumptions for the roll body

Table 6.4. Numerical vehicle data

$c_F = 582 \text{ [kN/rad]}$	front cornering stiffness
$c_R = 783 \text{ [kN/rad]}$	rear cornering stiffness
$c_\phi = 457 \text{ [kN m/rad]}$	roll stiffness of passive suspension
$d_\phi = 100 \text{ [kN/rad]}$	roll damping of passive suspension
$g = 9.81 \text{ [m/s}^2\text{]}$	acceleration due to gravity
$h_R = 0.68 \text{ [m]}$	height of roll axis over ground
$h = 1.15 \text{ [m]}$	nominal height of CG <sub>2</sub> over roll axis
$J_{2,x} = 24201 \text{ [kg m}^2\text{]}$	roll moment of inertia, sprung mass
$J_z = 34917 \text{ [kg m}^2\text{]}$	overall yaw moment of inertia
$l_F = 1.95 \text{ [m]}$	distance front axle to CG <sub>1</sub>
$l_R = 1.54 \text{ [m]}$	distance rear axle to CG <sub>1</sub>
$m = 14300 \text{ [kg]}$	overall vehicle mass
$m_2 = 12487 \text{ [kg]}$	sprung mass
$\mu = 1$	nominal road adhesion coefficient
$T = 1.86 \text{ [m]}$	track width

is the roll rate of body 2 relative to body 1. Note that the triple  $\{\int_0^t v_x dt, \int_0^t v_y dt, \psi\}$  describes the vehicle location and orientation. It does not affect the vehicle dynamics. The model inputs are the front wheel steering angle  $\delta_F$ , the disturbance side force  $F_{yD}$ , the disturbance yaw torque  $M_{zD}$  and the disturbance roll torque  $M_{xD}$ , summarized to the input vector

$$\mathbf{u} = [\delta_F \ F_{yD} \ M_{zD} \ M_{xD}] . \quad (6.8.12)$$

Note that any external disturbance like side-wind gusts or sudden unilateral loss of tire pressure may be composed of these three disturbance inputs. The non-linear equations of motion are given by

$$\mathbf{M}(\mathbf{z}) \ddot{\mathbf{z}} + \mathbf{k}(\dot{\mathbf{z}}, \mathbf{z}) = \mathbf{Q}(\dot{\mathbf{z}}, \mathbf{z}, \mathbf{u}) , \quad (6.8.13)$$

where

$$\mathbf{M}(\mathbf{z}) = \begin{bmatrix} m & 0 & h m_2 \sin(\phi) & 0 \\ 0 & m & 0 & -h m_2 \cos(\phi) \\ h m_2 \sin(\phi) & 0 & M_{(3,3)} & 0 \\ 0 & -h m_2 \cos(\phi) & 0 & J_{x,2} + h^2 m_2 \end{bmatrix} , \quad (6.8.14)$$

$$M_{(3,3)} = J_{z,1} + J_{z,2} \cos^2 \phi + (J_{y,2} + h^2 m_2) \sin^2 \phi ,$$

$$\mathbf{k}(\mathbf{z}, \dot{\mathbf{z}}) = \begin{bmatrix} -m r v_y + 2 h m_2 \dot{\phi} r \cos(\phi) \\ m r v_x + h m_2 (\dot{\phi}^2 + r^2) \sin(\phi) \\ r \sin(\phi) (-h m_2 v_y + 2 (J_{y,2} - J_{z,2} + h^2 m_2) \dot{\phi} \cos(\phi)) \\ -r \cos(\phi) (h m_2 v_x + (J_{y,2} - J_{z,2} + h^2 m_2) r \sin(\phi)) \end{bmatrix} \quad (6.8.15)$$

$$\mathbf{Q}(\dot{\mathbf{z}}, \mathbf{z}, \mathbf{u}) = \begin{bmatrix} F_{l,H} + F_{l,V} \cos(\delta_F) - F_{s,V} \sin(\delta_F) \\ F_{s,V} \cos(\delta_F) + F_{l,V} \sin(\delta_F) + F_{s,H} + F_{yD} \\ l_F (F_{s,V} \cos(\delta_F) + F_{l,V} \sin(\delta_F)) - l_R F_{s,H} + M_{zD} \\ h m_2 g \sin(\phi) - F_\phi - F_{\dot{\phi}} + M_{xD} \end{bmatrix} . \quad (6.8.16)$$

Further, the change in vehicle speed is assumed to be small compared to the lateral, yaw and roll motion. Therefore, the speed is considered an uncertain or varying plant parameter. Linearization w.r.t. straight driving at constant speed ( $v_x = v = const$ ) yields the linear second order equations of motion:

$$\mathbf{M} \ddot{\mathbf{z}} + (\mathbf{D} + \mathbf{G}) \dot{\mathbf{z}} + (\mathbf{K} + \mathbf{N}) \mathbf{z} = \mathbf{S} \mathbf{u} , \quad (6.8.17)$$

where

$$\mathbf{M} = \left. \frac{\partial \xi}{\partial \ddot{\mathbf{z}}} \right|_{st} , \quad (6.8.18)$$

$$\mathbf{D} + \mathbf{G} =: \mathbf{DG} = \left. \frac{\partial \xi}{\partial \dot{\mathbf{z}}} \right|_{st} , \quad (6.8.19)$$

$$\mathbf{K} + \mathbf{N} =: \mathbf{KN} = \left. \frac{\partial \xi}{\partial \mathbf{z}} \right|_{st} , \quad (6.8.20)$$

$$\mathbf{S} = - \left. \frac{\partial \xi}{\partial \mathbf{u}} \right|_{st} . \quad (6.8.21)$$

From a mechanical point of view, (6.8.17) is a gyroscopic dissipative system, where  
 $\mathbf{M}$  is the mass matrix (symmetric, positive definite),  
 $\mathbf{D}$  the damping matrix (symmetric),  
 $\mathbf{G}$  the gyroscopic matrix (skew-symmetric),  
 $\mathbf{K}$  the conservative location matrix (symmetric),  
 $\mathbf{N}$  the circulatory matrix (skew-symmetric), and  
 $\mathbf{S}$  the operating matrix.

The matrices of the single-track model with roll augmentation become:

$$\begin{aligned}\mathbf{M} &= \begin{bmatrix} m & 0 & -h m_2 \\ 0 & J_z & 0 \\ -h m_2 & 0 & J_{x,2} + h^2 m_2 \end{bmatrix}, \\ \mathbf{D} &= \begin{bmatrix} (c_F + c_R) \frac{\mu}{v} & (c_F l_F - c_R l_R) \frac{\mu}{v} + \frac{1}{2} m v & 0 \\ (c_F l_F - c_R l_R) \frac{\mu}{v} + \frac{1}{2} m v & (c_F l_F^2 + c_R l_R^2) \frac{\mu}{v} & -\frac{1}{2} h m_2 v \\ 0 & -\frac{1}{2} h m_2 v & d_{\dot{\phi}} \end{bmatrix}, \\ \mathbf{G} &= \begin{bmatrix} 0 & \frac{1}{2} m v & 0 \\ -\frac{1}{2} m v & 0 & \frac{1}{2} h m_2 v \\ 0 & -\frac{1}{2} h m_2 v & 0 \end{bmatrix}, \\ \mathbf{K} &= \begin{bmatrix} 0 & 0 & 0 \\ 0 & 0 & 0 \\ 0 & 0 & c_{\dot{\phi}} - m_2 g h \end{bmatrix}, \\ \mathbf{N} &= \mathbf{0}, \\ \mathbf{S} &= \begin{bmatrix} c_F \mu & 0 & 1 & 0 \\ c_F l_F \mu & 1 & 0 & 0 \\ 0 & 0 & 0 & 1 \end{bmatrix}.\end{aligned}$$

### *Equations of Motion in State Space Form*

Now, let the state vector be defined as

$$\mathbf{x} = [\phi \ v_y \ r \ \dot{\phi}]^T. \quad (6.8.22)$$

Then, the state space equations resulting from (6.8.17) are

$$\dot{\mathbf{x}} = \mathbf{Ax} + \mathbf{Bu}, \quad (6.8.23)$$

where

$$\mathbf{A} = \begin{bmatrix} \mathbf{0} & \mathbf{t} \\ -\mathbf{M}^{-1}(\mathbf{K} + \mathbf{N}) & -\mathbf{M}^{-1}(\mathbf{D} + \mathbf{G}) \end{bmatrix}, \quad (6.8.24)$$

$$\mathbf{B} = \begin{bmatrix} \mathbf{0} \\ \mathbf{b}_2 \end{bmatrix} = \begin{bmatrix} \mathbf{0} \\ \mathbf{M}^{-1}\mathbf{S} \end{bmatrix}, \quad (6.8.25)$$

$$\mathbf{t} = [0 \ 0 \ 1], \quad (6.8.26)$$

and  $\mathbf{b}_2 = \mathbf{M}^{-1}\mathbf{S}$ . This fourth order state space system describes the vehicles lateral, yaw and roll modes.

### Equations of Motion in Transfer Form

From (6.8.17), the equations of motion in transfer form are derived:

$$\underbrace{\begin{bmatrix} c_F + c_R + m v s & \frac{c_F l_F - c_R l_R}{v} + m v & -h m_2 s^2 \\ c_F l_F - c_R l_R & J_z s + \frac{c_F l_F^2 + c_R l_R^2}{v} & 0 \\ -h m_2 v s & -h m_2 v & G_{N(3,3)} \end{bmatrix}}_{=: \mathbf{G}_N} \begin{bmatrix} \beta \\ r \\ \phi \end{bmatrix} = \underbrace{\begin{bmatrix} c_F & 1 & 0 & 0 \\ c_F l_F & 0 & 1 & 0 \\ 0 & 0 & 0 & 1 \end{bmatrix}}_{=: \mathbf{G}_Z} \begin{bmatrix} \delta_F \\ F_{yD} \\ M_{zD} \\ M_{xD} \end{bmatrix} \quad (6.8.27)$$

where  $\beta = v_y/v$  is the sideslip angle and

$$G_{N(3,3)} = c_\phi - m_2 g h + d_\phi s + (J_{x,2} + h^2 m_2) s^2.$$

The transfer function matrix from  $[\delta_F \ F_{yD} \ M_{zD} \ M_{xD}]^T$  to  $[\beta \ r \ \phi]^T$  becomes

$$\mathbf{G} = \mathbf{G}_N^{-1} \mathbf{G}_Z. \quad (6.8.28)$$

The inverse of  $\mathbf{G}_N$  can be determined symbolically by computing the adjunct matrix. Following Cramer's formula, the element  $[\mathbf{G}_N^{-1}]_{ik}$  of the inverse of  $\mathbf{G}_N^{-1}$  is given by

$$[\mathbf{G}_N^{-1}]_{ik} = \frac{\text{adj}_{ik}(\mathbf{G}_N)}{\det(\mathbf{G}_N)}, \quad (6.8.29)$$

where the polynomial  $\text{adj}_{ik}(\mathbf{G}_N)$  is the adjunct of the element  $G_{N_{ki}}$ , which results from  $\mathbf{G}_N$  by crossing out the  $k$ -th row and the  $i$ -th column multiplied by  $(-1)^{i+k}$ .

The two transfer functions required for controller design are the transfer functions from front-wheel steering angle  $\delta_F$  to either roll rate  $\dot{\phi}$ , i.e.  $G_{\delta_F}^\phi$ , and rollover coefficient  $R$  corresponding to (6.8.5), i.e.  $G_{\delta_F}^R$ . Here, the lateral acceleration of the roll body is given by

$$a_{y,2} = v(\dot{\beta} + r) - h \ddot{\phi}. \quad (6.8.30)$$

### Operating Domain

The most essential uncertain or varying parameters entering into the rollover coefficient  $R$  are the vehicle speed  $v$  and the height of CG  $h$ , which is uncertain due to varying payloads. For controller design,  $v$  and  $h$  are assumed uncertain in an operating domain  $Q$  corresponding to Figure 6.56. Operating domain  $Q$  and set of vertices  $Q_V$  are defined as:

$$Q = \left\{ \mathbf{q} = [v \ h]^T \mid v \in [v^-, v^+], h \in [h^-, h^+] \right\}, \quad (6.8.31)$$

$$Q_V = \left\{ \mathbf{q} = [v \ h]^T \mid v \in \{v^-, v^+\}, h \in \{h^-, h^+\} \right\}, \quad (6.8.32)$$

$$V_1 : \quad \mathbf{q}_{V_1} = [v^- \ h^-]^T, \quad V_2 : \quad \mathbf{q}_{V_2} = [v^+ \ h^-]^T, \\ V_3 : \quad \mathbf{q}_{V_3} = [v^+ \ h^+]^T, \quad V_4 : \quad \mathbf{q}_{V_4} = [v^- \ h^+]^T,$$

where

$$\begin{aligned} v^- &= 20 \text{ [km/h]} & h^- &= 0.67 \text{ [m]} \\ v^+ &= 100 \text{ [km/h]} & h^+ &= 1.55 \text{ [m]} \end{aligned}$$

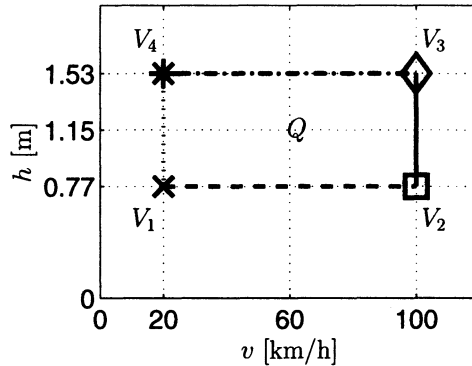


Figure 6.56. Operating domain  $Q$

The robustness of the resulting controlled system w.r.t. the uncertain friction coefficient  $\mu$  is not considered here, since a dry road is the most critical driving condition subject to rollover. However,  $\mu$  may be considered for robustness analysis.

Further vehicle parameters may depend significantly on the payload that are the mass of the roll body  $m_2$ , the inertias  $J_{x,2}$ ,  $J_{z,2}$ , the roll stiffness  $c_\phi$  and damping coefficient  $d_\phi$ , the nominal cornering stiffnesses  $c_F$  and  $c_R$  or their ratio, and the locus of the CG in longitudinal direction, i.e.  $l_F$  and  $l_R$ . To account for these uncertainties, a multiplicative perturbation model is introduced, assuming that for these parameters only small deviations from their nominal values occur. The multiplicative perturbation model may also be used to account for unmodelled sensor and/or actuator dynamics. In this context, the multiplicative perturbation is applied to the open-loop transfer function, i.e.

$$\tilde{L}(s, \mathbf{q}) = L(s, \mathbf{q})(1 + W_\Delta(s)\Delta(s)). \quad (6.8.33)$$

The weighting function  $W_\Delta(s)$  can be determined by experiments or in simulations with varying payloads.

In the sequel,  $L$  is assumed to be well known for low frequencies, i.e. the model error does not exceed 10 %. For high frequencies, the effect of unmodelled dynamics is assumed to be evident. The model error might be up to 200 % for frequencies  $\omega > 10\pi$  [rad/s]. The weighting function  $W_\Delta$  is selected to

$$W_\Delta(s) = 2 \frac{s + 0.1 \cdot 2 \cdot \pi \cdot 5}{s + 2 \cdot 2 \cdot \pi \cdot 5}. \quad (6.8.34)$$

### Stability

The characteristic polynomial of the uncontrolled vehicle is

$$p = \det(s\mathbf{I} - \mathbf{A}) = a_0 + a_1 s + a_2 s^2 + a_3 s^3 + a_4 s^4, \quad (6.8.35)$$

where

$$\begin{aligned}
 a_0 &= (c_\phi - m_2 g h) \mu (c_F c_R l^2 \mu + (c_R l_R - c_F l_F) m v^2), \\
 a_1 &= \mu \left( (c_F c_R d_\phi l^2 \mu) + (c_F (J_z + l_F^2 m) + c_R (J_z + l_R^2 m)) (c_\phi - m_2 g h) v + \right. \\
 &\quad \left. d_\phi (c_R l_R - c_F l_F) m v^2 \right), \\
 a_2 &= (c_F c_R l^2 (J_{x,2} + h^2 m_2) \mu^2) - d_\phi (c_F (J_z + l_F^2 m) + c_R (J_z + l_R^2 m)) \mu v - \\
 &\quad (J_z m (c_\phi - m_2 g h) - (c_F l_F - c_R l_R) (J_{x,2} m + h^2 m_1 m_2) \mu) v^2, \\
 a_3 &= v (c_F (J_z (J_{x,2} + h^2 m_2) + l_F^2 (J_{x,2} m + h^2 m_1 m_2)) \mu + \\
 &\quad c_R (J_z (J_{x,2} + h^2 m_2) + l_R^2 (J_{x,2} m + h^2 m_1 m_2)) \mu + J_z d_\phi m v), \\
 a_4 &= J_z (J_{x,2} m + h^2 m_1 m_2) v^2.
 \end{aligned}$$

Note that the parameters  $v$  and  $h$  enter in a polynomial way into the characteristic polynomial. Masses and inertia enter multilinearly. The location of the eigenvalues of the uncontrolled system for the edges of the operating domain  $Q$  are shown in Figure 6.57, i.e. the root locus of  $p(s)$  for variation of vehicle speed  $v$  and height of CG  $h$  along the edges of  $Q$ . For  $q \in Q$ , all eigenvalues robustly lie in the left half plane. The eigenvalues that correspond to the roll dynamics are shown in the magnified right plot of Figure 6.57. The roll damping increases with increasing speed but is nearly independent of the CG height. The natural roll frequency is nearly independent of speed but decreases with increasing  $h$ . The eigenvalues that correspond to the lateral and yaw mode are well damped for  $q \in Q$ .

Table 6.5 shows damping coefficients  $D_{\dot{\phi},0}$ , natural frequencies  $\omega_0$  in rad/s and maximum real parts  $\sigma_0$  of the corresponding roll dynamics eigenvalues of the four vertices of the operating domain of the uncontrolled system.

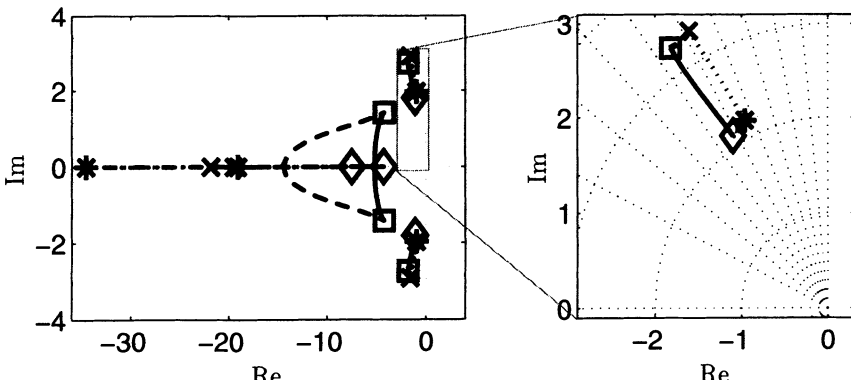


Figure 6.57. Eigenvalues of the uncontrolled vehicle for the edges of the operating domain (the right plot is a magnification of the left one)

Table 6.5. Roll dynamics of the conventional vehicle

	$v = 20 \text{ [km/h]}$	$v = 100 \text{ [km/h]}$
$h = 1.53 \text{ [m]}$	$D_{\dot{\phi},0} = 0.44$ $V_3 : \omega_0 = 2.19$ $\sigma_0 = -0.96$	$D_{\dot{\phi},0} = 0.52$ $V_4 : \omega_0 = 2.11$ $\sigma_0 = -1.10$
$h = 0.77 \text{ [m]}$	$D_{\dot{\phi},0} = 0.48$ $V_1 : \omega_0 = 3.43$ $\sigma_0 = -1.61$	$D_{\dot{\phi},0} = 0.55$ $V_2 : \omega_0 = 3.29$ $\sigma_0 = -1.82$

### Controllability

For front-wheel steering of the single-track model with roll augmentation, controllability is lost if

$$\det [ \mathbf{b} \quad \mathbf{Ab} \quad \mathbf{A}^2\mathbf{b} \quad \mathbf{A}^3\mathbf{b} ] = 0, \quad (6.8.36)$$

where

$$\begin{aligned} \mathbf{b} &= \begin{bmatrix} \mathbf{0} \\ \mathbf{b}_2 \end{bmatrix}, \\ \mathbf{Ab} &= \begin{bmatrix} \mathbf{t}^T \mathbf{b}_2 \\ -\mathbf{M}^{-1}(\mathbf{D} + \mathbf{G}) \mathbf{b}_2 \end{bmatrix}, \\ \mathbf{A}^2\mathbf{b} &= \begin{bmatrix} -\mathbf{t}^T \mathbf{M}^{-1}(\mathbf{D} + \mathbf{G}) \mathbf{b}_2 \\ -\mathbf{M}^{-1}(\mathbf{K} + \mathbf{N}) \mathbf{t} \mathbf{t}^T \mathbf{b}_2 + (\mathbf{M}^{-1}(\mathbf{D} + \mathbf{G}))^2 \mathbf{b}_2 \end{bmatrix} \\ &= \begin{bmatrix} -\mathbf{t}^T \mathbf{M}^{-1}(\mathbf{D} + \mathbf{G}) \mathbf{b}_2 \\ (\mathbf{M}^{-1}(\mathbf{D} + \mathbf{G}))^2 \mathbf{b}_2 \end{bmatrix}, \\ \mathbf{A}^3\mathbf{b} &= \begin{bmatrix} \mathbf{t}^T (\mathbf{M}^{-1}(\mathbf{D} + \mathbf{G}))^2 \mathbf{b}_2 \\ \mathbf{M}^{-1}(\mathbf{K} + \mathbf{N}) \mathbf{t} \mathbf{t}^T \mathbf{M}^{-1}(\mathbf{D} + \mathbf{G}) \mathbf{b}_2 - (\mathbf{M}^{-1}(\mathbf{D} + \mathbf{G}))^3 \mathbf{b}_2 \end{bmatrix}. \end{aligned}$$

Symbolic evaluation of (6.8.36) yields that the system is controllable for:  $c_F \neq 0$ ,  $h \neq 0$ ,  $m_2 \neq 0$ ,  $\mu \neq 0$ ,  $J_z \neq 0$ , and  $J_{x,2} m + h^2 m_1 m_2 \neq 0$ . The latter condition results from the requirement of positive definiteness of the mass matrix, namely

$$\det \mathbf{M} = J_z (J_{x,2} m + h^2 m_1 m_2) > 0. \quad (6.8.37)$$

### Observability

Observability is lost if

$$\det \begin{bmatrix} \mathbf{c}^T \\ \mathbf{c}^T \mathbf{A} \\ \mathbf{c}^T \mathbf{A}^2 \\ \mathbf{c}^T \mathbf{A}^3 \end{bmatrix} = 0. \quad (6.8.38)$$

Subsequently, the four states are checked for controllability. Note that only the non-trivial solutions ( $h \neq 0$ ,  $\mu \neq 0$ ,  $m_2 \neq 0$ ,  $c_F \neq 0$ ) are investigated:

- $y = \beta$ , i.e.  $\mathbf{c}^T = [1 \ 0 \ 0 \ 0]$ :  $\beta$  is observable if:  
 $\bullet c_F c_R l^2 (c_R l_R - c_F l_F) \mu - (c_F + c_R)^2 J_z v^2 \neq 0$ .

In the understeering case ( $c_R l_R - c_F l_F > 0$ ), observability is lost at a velocity

$$v_{no\beta}^2 = \frac{c_F c_R l^2 (c_R l_R - c_F l_F) \mu}{(c_F + c_R)^2 J_z v^2} \neq 0. \quad (6.8.39)$$

- $y = r$ ,  $\mathbf{c}^T = [0 \ 1 \ 0 \ 0]$ :  $r$  is observable if:
  - $\bullet (c_R l_R - c_F l_F) \neq 0$ .
  - $\bullet m_2 g h - c_\phi \neq 0$ .

Note that for neutral steering ( $c_R l_R = c_F l_F$ ), the vehicle is not observable from  $r$  and thus the vehicle cannot be stabilized by yaw rate feedback. Controllability is also lost for  $m_2 g h - c_\phi = 0$ . The roll body might be considered an inverted pendulum mounted on the single-track model. For  $m_2 g h = c_\phi$ , the equilibrium becomes metastable. Note that in this case, the conservative location matrix  $\mathbf{K}$  in (6.8.17) becomes zero.

- $y = \phi$ , i.e.  $\mathbf{c}^T = [0 \ 0 \ 1 \ 0]$ :  $\phi$  is observable if:
  - $\bullet c_F c_R l^2 (-(c_F l_F) + c_R l_R) \mu - (c_F + c_R)^2 J_z v^2 \neq 0$ .

In the understeering case ( $c_R l_R - c_F l_F > 0$ ), observability is lost at a velocity

$$v_{no\phi}^2 = \frac{c_F c_R l^2 (c_R l_R - c_F l_F) \mu}{(c_F + c_R)^2 J_z v^2} \neq 0. \quad (6.8.40)$$

- $y = \dot{\phi}$ , i.e.  $\mathbf{c}^T = [0 \ 0 \ 0 \ 1]$ :  $\dot{\phi}$  is observable if:
  - $\bullet m_2 g h - c_\phi \neq 0$ .
  - $\bullet c_F c_R l^2 \mu^2 + (c_R l_R - c_F l_F) \mu m v^2 \neq 0$ .

Observability is lost at the characteristic velocity

$$v_{no\dot{\phi}}^2 = v_{CH}^2 = \frac{\mu c_R c_F l^2}{m(c_F l_F - c_R l_R)}. \quad (6.8.41)$$

## Actuator Model

The actuator model used here has the same structure as the actuator used in the previous section, which is given by Figure 6.37. However, in this section the actuator is considered to be an additional steering actuator. The data of the model used here are compiled in Table 6.6. For the actuator transfer function  $G_a(s)$ , it is assumed that all poles have the same natural frequency  $\omega_a$ , i.e.

$$G_a(s) = \frac{\omega_a^3}{(s^2 + 2d_a \omega_a s + \omega_a^2)(s + \omega_a)}. \quad (6.8.42)$$

Superposition of (6.7.4) and (6.8.42) yields

$$\omega_a = \sqrt[3]{\frac{k_{em} k_a}{J_a L_a}} \quad \text{and} \quad d_a = \frac{1}{2} \left( \frac{k_f L_a + J_a R_a}{J_a L \omega_a} - 1 \right).$$

Table 6.6. Notations and numerical values of actuator variables

$J_a$	0.00619 [kg m <sup>2</sup> ]	motor inertia
$k_f$	0.0619	motor damping coefficient
$L_a$	0.0759 [H]	inductivity
$R_a$	5 [Ω]	resistance
$k_{me} = k_{em}$	0.9	electromechanical constant
$k_a$	16.186	control gain of actuator position control

Substituting numerical parameter values from Table 6.6 into (6.7.4) results in a 3rd order actuator transfer function with an actuator damping coefficient  $d_a = 1/\sqrt{2}$  and a natural frequency of 5 [Hz], i.e.  $\omega_a = 10\pi$  [rad/s]. This correlates to an actuator bandwidth of 3.7 [Hz], i.e.  $\omega_B = 7.4\pi$  [rad/s], because of  $|G_a(j\omega_B)| = |G_a(0)|/\sqrt{2}$ .

### Roll Damping by Continuous Steering Control

In transient driving maneuvers such as lane change or obstacle avoidance (elk test) vehicles with an elevated center of gravity tend to distinctive roll movements that may lead to rollover. Especially steering or disturbance excitations in the range of the natural roll frequency may yield to a swinging up of the roll body in such situations. Then, the driver even may feel urged to destabilizing steering commands (in flight dynamics a comparable effect is called pilot induced oscillations [80]). In the sequel, it is shown that besides active and semi-active chassis control systems, an active front-wheel steering system can be used to improve roll damping, and it thus decreases the risk of rollover in transient maneuvers.

#### Controller Structure

For controller design of the roll damping, a single-loop feedback structure corresponding to Figure 6.58 is assumed. Proportional feedback of the roll rate  $\dot{\phi}$  and the roll

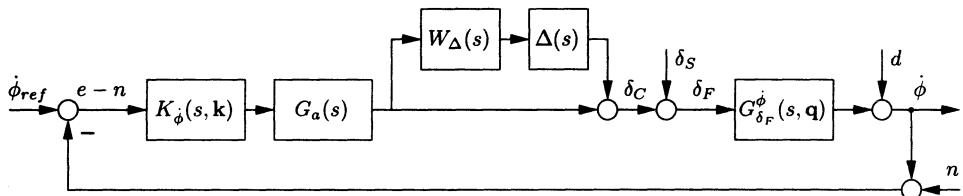


Figure 6.58. Controller structure for roll damping by active steering

acceleration  $\ddot{\phi}$  is used, i.e.

$$K_{\dot{\phi}}(s, \mathbf{k}) = k_p + k_d s, \quad (6.8.43)$$

where  $\mathbf{k} = [k_p \ k_d]^T$  is the controller parameter vector for which the gains will be determined subsequently. The exogenous inputs of the closed system are the roll rate reference input  $\dot{\phi}_{ref}$ , the steering angle commanded by the driver  $\delta_S$ , output disturbance  $d$  and sensor noise  $n$ . The roll rate reference is assumed to be  $\dot{\phi}_{ref} = 0$ . Formally,  $\delta_S$  may be interpreted as external plant input signal (compare to  $d_1$  in Figure 5.32). The output disturbance  $d$  is considered representatively for the three disturbances  $F_{yD}$ ,  $M_{zD}$ , and  $M_{xD}$ . If good disturbance attenuation properties for  $d$  are achieved, then this result can be directly transmitted to the three output disturbances and thus to any impact on the vehicle like side-wind.

In Figure 6.58,  $G_{\dot{\phi}_F}^{\dot{\phi}} = G_{\dot{\phi}_F}^{\dot{\phi}}(s, \mathbf{q})$  denotes the transfer function

$$G_{\dot{\phi}_F}^{\dot{\phi}} := \frac{\dot{\phi}}{\delta_F}, \quad (6.8.44)$$

which depends on the plant parameters  $\mathbf{q} = [v \ h]^T$ .

The closed-loop performance of Figure 6.58 is rated by the transfer matrix of the external inputs  $\dot{\phi}_{ref}$ ,  $n$ ,  $\delta_S$ , and  $d$  to the internal closed-loop signals tracking error  $e$ , additional steering angle  $\delta_C$ , front wheel steering angle  $\delta_F$ , and controlled input  $\phi$ , i.e. by

$$\begin{bmatrix} e \\ \delta_C \\ \delta_F \\ \dot{\phi} \end{bmatrix} = \begin{bmatrix} S & T & S_G & -S \\ S_K & -S_K & -T & -S_K \\ S_K & -S_K & S & -S_K \\ T & -T & S_G & S \end{bmatrix} \begin{bmatrix} \dot{\phi}_{ref} \\ n \\ \delta_S \\ d \end{bmatrix}. \quad (6.8.45)$$

Open-loop transfer function  $L$  and closed-loop characteristic polynomial  $p$  are given by

$$L(s, \mathbf{q}, \mathbf{k}) = K_{\dot{\phi}}(s, \mathbf{k}) G_a(s) G_{\dot{\phi}_F}^{\dot{\phi}}(s, \mathbf{q}), \quad (6.8.46)$$

$$p(s, \mathbf{q}, \mathbf{k}) = \text{num} \left( 1 + K_{\dot{\phi}}(s, \mathbf{k}) G_a(s) G_{\dot{\phi}_F}^{\dot{\phi}}(s, \mathbf{q}) \right). \quad (6.8.47)$$

Sensitivity function  $S$ , complementary sensitivity  $T$ , input and output sensitivity function  $S_K$  and  $S_G$  of the closed-loop system are given corresponding to (5.3.8), (5.3.9), (5.3.10), and (5.3.11), i.e. by

$$S(s, \mathbf{q}, \mathbf{k}) = \frac{1}{1 + K_{\dot{\phi}}(s, \mathbf{k}) G_a(s) G_{\dot{\phi}_F}^{\dot{\phi}}(s, \mathbf{q})}, \quad (6.8.48)$$

$$T(s, \mathbf{q}, \mathbf{k}) = \frac{K_{\dot{\phi}}(s, \mathbf{k}) G_a(s) G_{\dot{\phi}_F}^{\dot{\phi}}(s, \mathbf{q})}{1 + K_{\dot{\phi}}(s, \mathbf{k}) G_a(s) G_{\dot{\phi}_F}^{\dot{\phi}}(s, \mathbf{q})}, \quad (6.8.49)$$

$$S_K(s, \mathbf{q}, \mathbf{k}) = \frac{K_{\dot{\phi}}(s, \mathbf{k}) G_a(s)}{1 + K_{\dot{\phi}}(s, \mathbf{k}) G_a(s) G_{\dot{\phi}_F}^{\dot{\phi}}(s, \mathbf{q})}, \quad (6.8.50)$$

$$S_G(s, \mathbf{q}, \mathbf{k}) = \frac{G_{\dot{\phi}_F}^{\dot{\phi}}(s, \mathbf{q})}{1 + K_{\dot{\phi}}(s, \mathbf{k}) G_a(s) G_{\dot{\phi}_F}^{\dot{\phi}}(s, \mathbf{q})}. \quad (6.8.51)$$

Note that the output sensitivity function  $S_G$  corresponds to the closed-loop steering transfer function from  $\delta_S$  to the roll rate  $\dot{\phi}$ .

For controller design, a third order linear transfer function for  $G_a(s)$  corresponding to (6.8.42) is assumed.

### Design Specifications

The primary goal of the continuous operation steering control in this section is the improvement of the roll dynamics. At the same time, it is useful to take some other design requirements into account. The design goals considered are:

- i. The roll damping of the controlled vehicle shall be better than that of the uncontrolled one.
- ii. The steering performance must not get worse (yaw damping, responsiveness).
- iii. Following a basic principle of robust control, the dynamics of the modes (modes corresponding to roll, yaw and lateral dynamics, actuator modes) shall not change fundamentally, i.e. a slow mode should stay slow, a fast mode should stay fast.
- iv. Disturbances, e.g. induced by side-wind or  $\mu$ -split braking shall be attenuated in the lower frequency range that is relevant for vehicle dynamics, i.e. in between 0 and 3 [Hz].
- v. It follows from Bode's integral theorem (5.3.45) that if disturbances are attenuated at low frequencies they will be amplified at high frequencies. In the frequency range from 4–8 [Hz] oscillations of the vertical and roll dynamics feel uncomfortable to the driver. Therefore, it has to be ensured that disturbance amplification is limited up to a tolerable value.
- vi. Unmodelled dynamics should not have an effect on the system stability.
- vii. Sensor noise should not affect stability and performance.
- viii. From the outset, limit cycles induced by the actuator rate limitation should be avoided.
- ix. All above-mentioned specifications shall be met robustly w.r.t. varying or uncertain operating conditions, i.e. speed  $v$  and uncertain height of CG  $h$ .

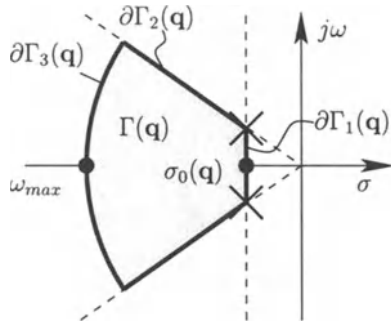
Specifications i and iii are realized by the definition of  $\Gamma$ -stability regions as shown in Figure 6.59. The  $\partial\Gamma$ -parameters  $\sigma_0$  and  $D_{\dot{\phi},0}$  are chosen separately for each operating condition (the vertices in Figure 6.56 as given in Table 6.5). This guarantees that damping and real parts in the closed loop cannot be worse than the respective open-loop values for the vertex operating conditions. The eigenvalue locations of the yaw and lateral mode, i.e. specification ii, are not considered separately. However, they have to be taken into account for analysis.

In steady state, roll rate  $\dot{\phi}$  and roll acceleration  $\ddot{\phi}$  are zero and therefore it holds that  $S(0, \mathbf{q}, \mathbf{k}) = 0$ . Disturbances shall be attenuated in the frequency range  $[0, 3]$  [Hz]. Therefore, as in specification iv, an upper bound for the sensitivity function  $S$  is used, i.e.

$$|S(j\omega, \mathbf{q}, \mathbf{k})| \leq 1, \quad \forall \omega \in [0, 6\pi]. \quad (6.8.52)$$

On the other hand, disturbances shall not be amplified more than 10% for high frequencies (for frequencies above the transition frequency), i.e.

$$|S(j\omega, \mathbf{q}, \mathbf{k})| < 1.1, \quad \forall \omega \in (6\pi, \infty), \quad (6.8.53)$$

Figure 6.59. Definition of  $\mathbf{q}$ -dependent  $\Gamma$ -stability regions

which corresponds to a Nyquist-stability margin of  $\varrho_S(\mathbf{q}) > 1/1.1$ .

The sensors are assumed to work well in the frequency range  $[0, 20]$  [Hz]. Thus, noise rejection for frequencies  $\omega > 40\pi$  [rad/s] is guaranteed if

$$|T(j\omega, \mathbf{q}, \mathbf{k})| \ll 1 \quad \text{for } \omega > 40\pi \text{ [rad/s].} \quad (6.8.54)$$

To ensure robustness w.r.t. unmodelled dynamics, a multiplicative perturbation corresponding to (6.8.33) with weighting function (6.8.34) is taken into account. Robust stability then requires

$$|W_\Delta(j\omega)T(j\omega, \mathbf{q}, \mathbf{k})| < 1, \quad \omega \in [0, \infty), \quad (6.8.55)$$

where  $W_\Delta$  is given by (6.8.34).

The specifications as shown in Figure 6.59, (6.8.52) and (6.8.55) will be used for controller design. The corresponding  $\Gamma$ - and  $\mathcal{B}$ -stability regions  $\Gamma$ ,  $\mathcal{B}_S$  and  $\mathcal{B}_T$  are bounded by

$$\begin{aligned} \partial\Gamma_1(\mathbf{q}) : s(\mathbf{q}) &= \sigma_0(\mathbf{q}) + j\omega(\mathbf{q}), \\ &\text{for } \omega(\mathbf{q}) \in \left[0, -\frac{\sqrt{1-d_{\phi,0}(\mathbf{q})^2}}{d_{\phi,0}(\mathbf{q})}\sigma_0(\mathbf{q})\right], \end{aligned}$$

$$\begin{aligned} \partial\Gamma_2(\mathbf{q}) : s(\mathbf{q}) &= \frac{d_{\phi,0}(\mathbf{q})}{\sqrt{1-d_{\phi,0}(\mathbf{q})^2}}\omega(\mathbf{q}) + j\omega(\mathbf{q}), \\ &\text{for } \omega(\mathbf{q}) \in \left[-\frac{\sqrt{1-d_{\phi,0}(\mathbf{q})^2}}{d_{\phi,0}(\mathbf{q})}\sigma_0(\mathbf{q}), \omega_{max}\sqrt{1-d_{\phi,0}(\mathbf{q})^2}\right], \end{aligned}$$

$$\begin{aligned} \partial\Gamma_3(\mathbf{q}) : s(\mathbf{q}) &= -\sqrt{\omega_{max}^2 - \omega(\mathbf{q})^2} + j\omega(\mathbf{q}), \\ &\text{for } \omega(\mathbf{q}) \in \left[0, \omega_{max}\sqrt{1-d_{\phi,0}(\mathbf{q})^2}\right], \end{aligned}$$

$$\partial\mathcal{B}_S(\omega) = 1, \quad \forall \omega \in [0, 6\pi)$$

$$\partial\mathcal{B}_T(\omega) = |W_\Delta^{-1}(j\omega)|, \quad \forall \omega \in [0, \infty).$$

### Controller Design

For robust control design, the parameter space in combination with a multi-model approach is applied. The design task is to determine the set of controller parameters  $k_p$  and  $k_d$  for which all design specifications are robustly met. Thereby, the operating domain is represented by its four vertices  $V_i$ ,  $i = 1, \dots, 4$ , i.e. by the parameter values  $v_i$  and  $h_i$ .

The  $\Gamma$ - and  $\mathcal{B}$ -stability regions will now be mapped into parameter space, i.e. into the plane of controller parameters  $k_p$  and  $k_d$ . The desired regions in parameter space are defined as

$$K_{\Gamma,i} = \{\mathbf{k} \mid \text{Roots}[p(s, k_p, k_d, v_i, h_i)] \subset \Gamma(v_i, h_i)\}, \quad (6.8.56)$$

$$K_{\mathcal{B}_{S,i}} = \{\mathbf{k} \mid |S(j\omega, k_p, k_d, v_i, h_i)| \subset \mathcal{B}_S\}, \quad (6.8.57)$$

$$K_{\mathcal{B}_{T,i}} = \{\mathbf{k} \mid |T(j\omega, k_p, k_d, v_i, h_i)| \subset \mathcal{B}_T\}. \quad (6.8.58)$$

Figure 6.60 shows the resulting  $\Gamma$ -stable controller parameter regions for the four vertices

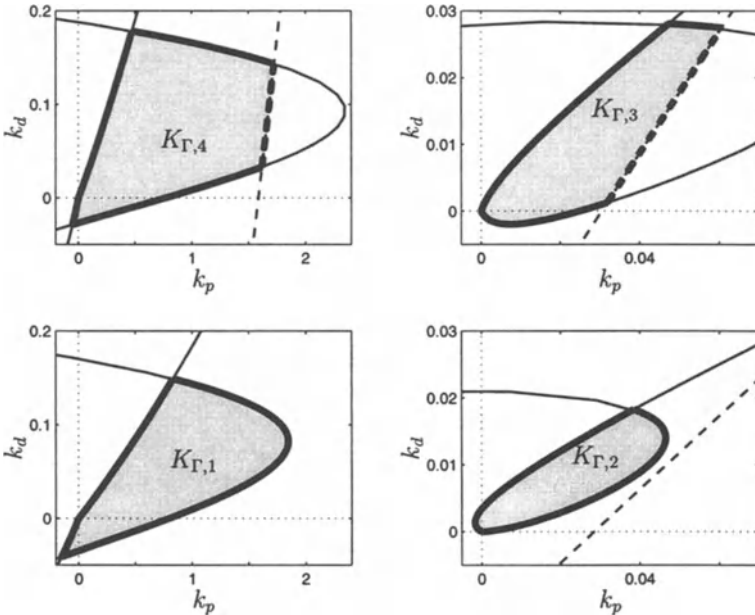


Figure 6.60.  $\Gamma$ -stable controller parameter regions for  $V_1 - V_4$

of the operating domain as given in Figure 6.56. For any controller parameters  $[k_p, k_d]^T \in K_{\Gamma,i}$ , the eigenvalue design specifications for vertex  $V_i$  are met. By intersection of all four regions, the controller parameter values are found for which the eigenvalue specifications are satisfied robustly for all vertices, i.e.

$$K_\Gamma = \bigcap_{i=1}^4 K_{\Gamma,i},$$

as shown in Figure 6.61. Note that in Figure 6.60 different scalings for the plots were

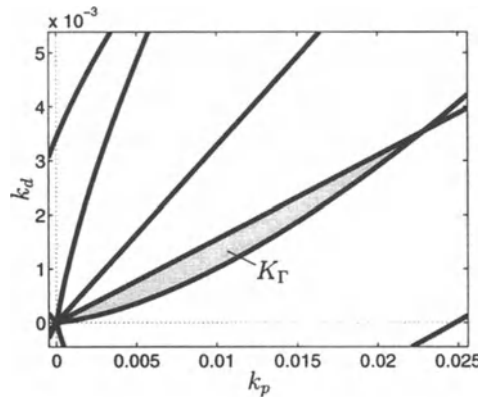


Figure 6.61. Region of robustly  $\Gamma$ -stabilizing controllers

used.

Figure 6.62 and Figure 6.63 depict the controller parameter regions for which the  $\mathcal{B}$ -stability specifications are met. Finally, in Figure 6.64 the controller regions are shown that meet all  $\Gamma$ - and  $\mathcal{B}$ -specifications simultaneously, i.e.

$$K_i = K_{\mathcal{B},i} \cap K_{\Gamma,i} \quad \text{for } i = 1, \dots, 4, \quad (6.8.59)$$

where  $K_{\mathcal{B},i} = K_{\mathcal{B}_{T,i}} \cap K_{\mathcal{B}_{S,i}}$ . Note that there are no controller parameters for which all specifications are met robustly, i.e.

$$\bigcap_{i=1}^4 K_i = \{\}.$$

Therefore, gain-scheduling of the controller parameters with speed  $v$  is required. The procedure for controller selection is as follows. First, a controller in each region  $K_i$  is selected subject, e.g. to additional design specifications. Alternatively, the specifications already used may be tightened as illustrated in Figure 6.65. Here, the design specification corresponding to damping is tightened exemplarily for one operating condition. In the left plot, the grey-scale coded  $\Gamma$ -regions for improvement of roll damping of 0 %, 10 %, 20 % is shown, while in the right plot the shrinking  $\Gamma$ -stable region is illustrated. The resulting control law is represented by a look-up-table as shown in Figure 6.66. Here, gain-scheduling with both speed and height of CG is assumed. Note that if the height is uncertain, i.e. cannot be estimated at the start of each ride, gain scheduling only with speed is sufficient (all specifications are still met).

#### Eigenvalue Analysis

In Figure 6.67 damping coefficients and maximum real parts of the roll dynamics eigen-

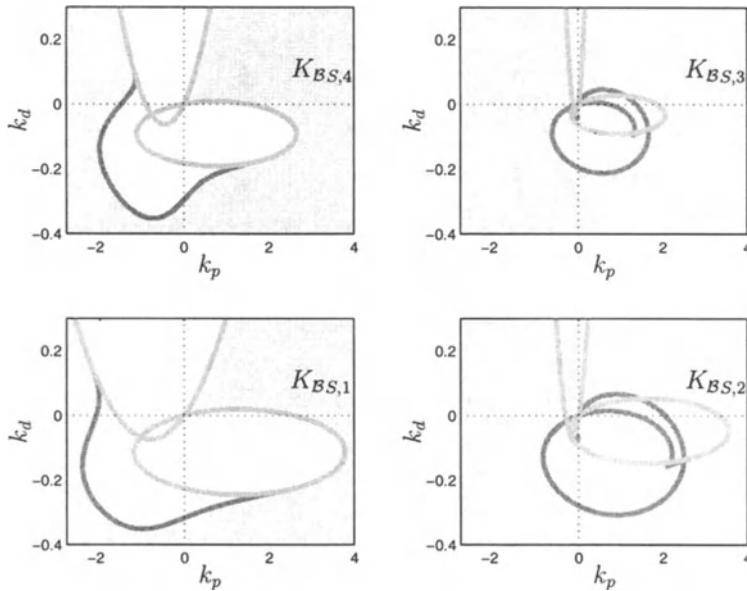


Figure 6.62. Controller parameter regions satisfying the specifications on  $S$  for  $V_1 - V_4$

values are compared to those of the conventional vehicle by means of plotting the damping coefficients and the maximum real parts, respectively, versus velocity and height of the CG<sub>2</sub>. The black surface plot belongs to the controlled system while the grey one belongs to the conventional system. From this it can be seen that the controller is not only robustly  $\Gamma$ -stable with respect to the representatives considered but also to the entire operating domain. Significant improvement is achieved w.r.t. both damping of the roll mode and settling time of the roll mode.

### Sensitivity Analysis

Figure 6.68 depicts the Bode magnitudes of the sensitivity function for  $V_1 - V_4$  (left) and for a fine grid of the operating domain (right). The transmission frequency is bigger than 3 [Hz] for all operating points considered. Since the set of suitable driver steering excitations and disturbance impacts is assumed to lie in between 0 [Hz] and about 2.5 [Hz], this means that transient steering reduction can be assured for the entire operating domain. Furthermore, transient steering reduction is particularly distinctive for the input range close to the natural frequency of the roll dynamics of the conventional system (marked as crosses in the left plot of Figure 6.68). The amplification becomes at a maximum 108 %, meaning that driving comfort is only slightly affected in the frequency range 4–8 [Hz]. The stability margin  $\varrho_S = 1/1.08$  is still sufficient.

In Figure 6.69 the magnitude of the output sensitivity function  $S_G$  is compared to the magnitude of the plant  $G$ , which illustrates the bandpass characteristic of the roll damping control law. Only in an intermediate frequency range of approximately

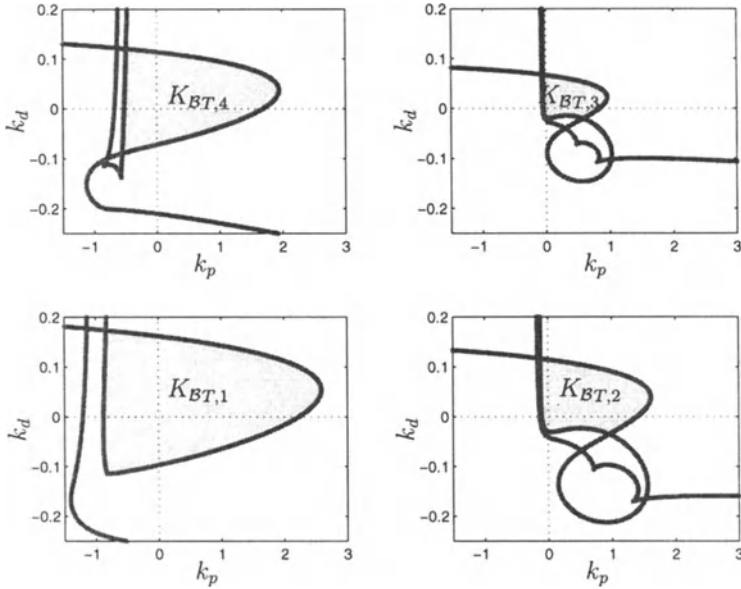


Figure 6.63. Controller parameter regions satisfying the specifications on  $T$  for  $V_1 - V_4$

$0.2 - 2$  [Hz] is the roll damping active. In steady state maneuvers ( $\dot{\phi} \approx 0$ ) as well as for high-frequency disturbances, the behavior of the controlled and uncontrolled vehicle are nearly identical.

#### Absolute Stability in the Presence of Steering Actuator Rate Limitation

As in Section 6.7, limit cycles might be induced by the rate limitation of the front wheel steering actuator, i.e. by the voltage limitation as shown in Figure 6.37. The Popov-criterion is applied to prove for absolute stability. The transfer function from  $u$  to  $u_1$  of the closed-loop system is given by

$$G(s, \mathbf{q}) = -\frac{u_1}{u} = \frac{k_{em}k_a(1 + K_\phi(\mathbf{k}(\mathbf{q}))G_{\delta_V}^\phi(s, \mathbf{q}))}{k_{em}k_{me} + (J_a s + k_f)(L_a s + R_a)} . \quad (6.8.60)$$

In Figure 6.70 the Popov-line and the Popov-loci for the four vertices of the operating domain  $V_1-V_4$  are plotted. Since all loci reside to the right of the Popov-line, robust absolute stability of the roll damping can be guaranteed.

#### Rollover Avoidance by Coordinated Steering and Braking Control

With the feedback of  $\dot{\phi}$  and  $\ddot{\phi}$  to the front-wheel steering angle, the roll damping of the vehicle is improved considerably. In fact, the steering transfer function has been shaped such that the roll mode is excited less in the frequency range of the roll resonance

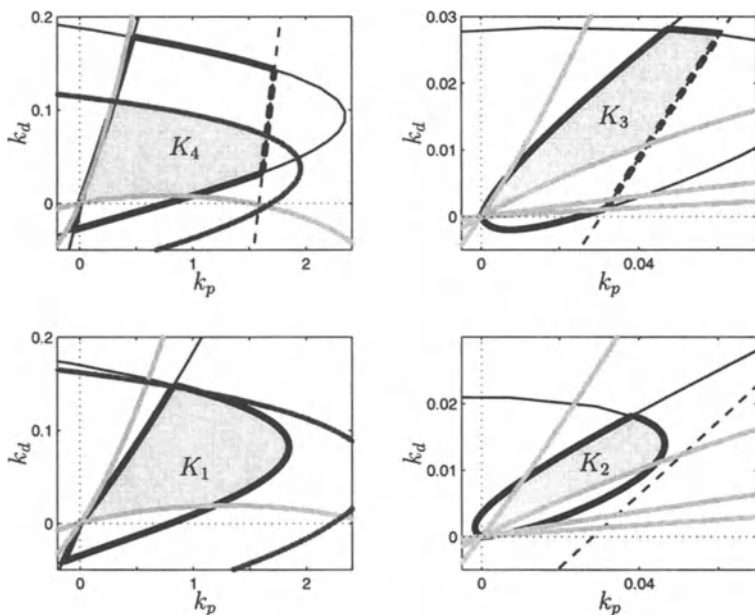


Figure 6.64. Simultaneous  $\Gamma$ - and  $\mathcal{B}$ -stabilizing controller parameter regions for  $V_1 - V_4$

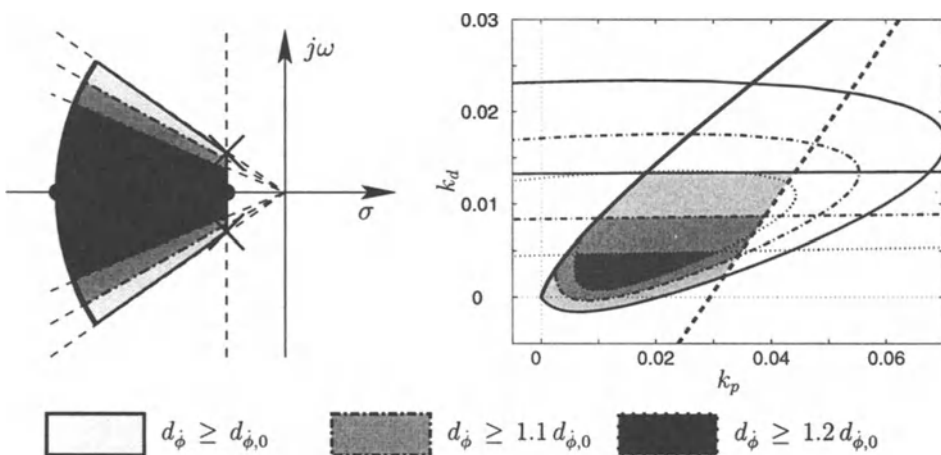


Figure 6.65. Contraction of  $\Gamma$ -stable region

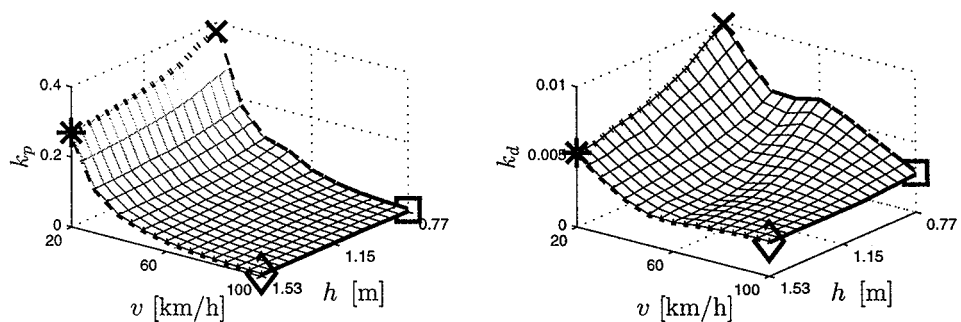


Figure 6.66. “Look-up-table” for gain-scheduling with speed and height of CG

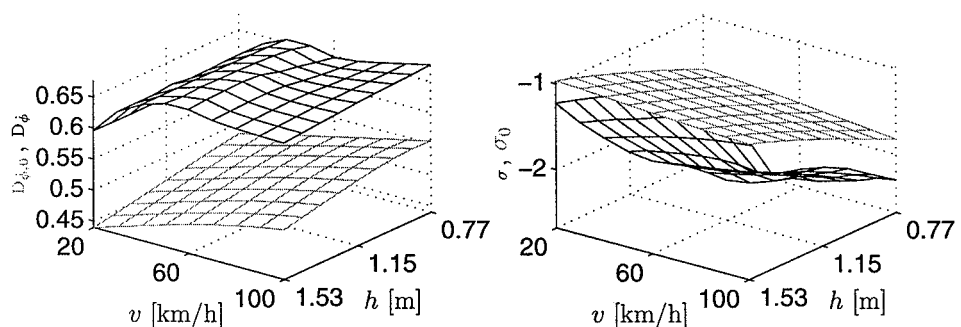


Figure 6.67. Characteristic roll dynamic values

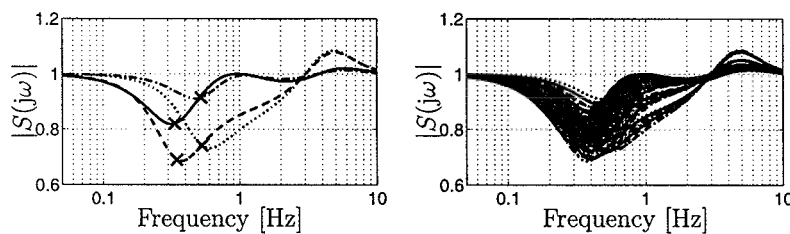


Figure 6.68. Bode magnitude plots of the sensitivity function  $S$

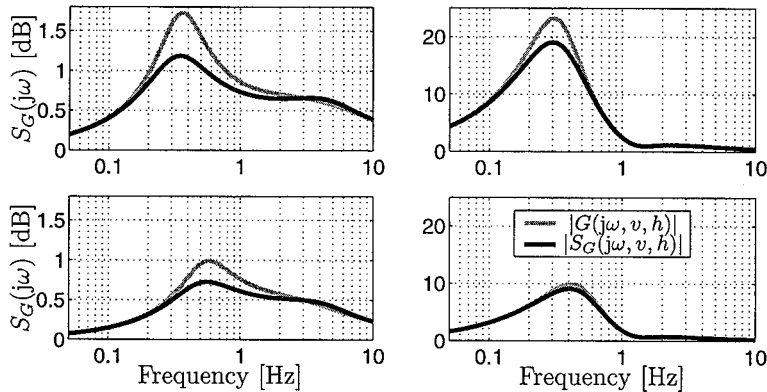


Figure 6.69. Bode magnitude plots of the output sensitivity function  $S_G$  and the plant  $G$  for  $V_1 - V_4$

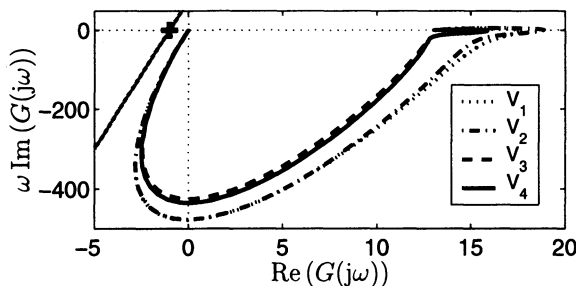


Figure 6.70. Popov-line and Popov-loci for  $V_1 - V_4$  considering voltage limitation of the steering actuator

frequency. Thus, the risk of causing a rollover by steering excitation has been reduced. However, even the controlled vehicle can roll over if the steering input is large enough. Also, in quasi-steady state driving maneuvers the roll dynamics are not excited and thus the automatic steering system is deactivated.

Therefore, the rollover coefficient  $R$  is used for feedback. The non-linear control introduced subsequently can be interpreted as an “intelligent” steering angle limitation such that rollover on a plane road can be completely avoided. The key idea is that rollover avoidance is given priority over lane keeping because a tipped vehicle is no longer steerable. To drive the narrowest curve that is physically possible, maximum lateral acceleration must be applied. The lateral acceleration is limited, however, by the boundary where rollover occurs. This boundary is reached if the vehicle is steered such that the inner wheels are just about to lift off the road, corresponding to  $|R| = 1$ . The optimal strategy to keep the narrowest curve possible while avoiding rollover would be to keep  $|R| = 1$ . With some safety margin, this idea is implemented in a non-linear steering control law. Therefore, if the magnitude of  $R$  exceeds  $\hat{R}$ , then the oversteering difference  $\delta_R = k_R \cdot \text{sign}(R) \cdot (|R| - \hat{R})$  is fed back to the front-wheel steering angle  $\delta_F$  such that the curvature of the course is slightly reduced and rollover is avoided, i.e. the emergency steering control feedback is described by the relation

$$\delta_R = \begin{cases} k_R \cdot \text{sign}(R) \cdot (|R| - \hat{R}) & \forall |R| > \hat{R} \\ 0 & \forall |R| \leq \hat{R} . \end{cases} \quad (6.8.61)$$

In order to implement the prescribed effect, a dead zone element is introduced into the emergency steering feedback loop. The black line in Figure 6.72 shows the char-

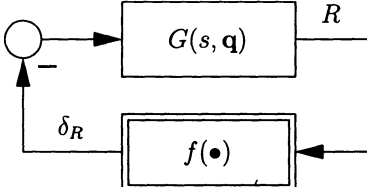


Figure 6.71. Closed loop with linear and non-linear part

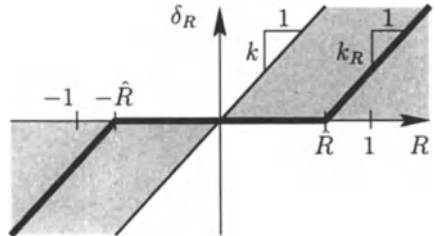


Figure 6.72. Popov-sector and the non-linear emergency steering control characteristics

acteristics of the dead zone with an absolute value threshold of  $\hat{R}$  and a slope of  $k_R$ . This corresponds to the dead zone element in the emergency steering feedback loop in Figure 6.53. However, this non-linear element in the loop induces the risk of limit cycles. Therefore, a stability analysis is performed using Popov’s sufficient criterion on absolute stability as described in Section 5.1. Subsequently, mere feedback of  $R$  to the front-wheel steering angle is considered. The control loop is subdivided into the non-linear characteristics and the transfer function

$$G(s, q) := -\frac{R}{\delta_R} = G_a(s) G_{\delta_F}^R(s, q) , \quad (6.8.62)$$

as shown in Figure 6.71. The critical Popov-line or Popov-sector, respectively, can be computed symbolically by evaluation of a tangent or double tangent condition, respectively, or numerically by solving the optimization problem

$$\frac{1}{k^+} = \inf_{\theta \in \mathbb{R}} \sup_{\omega \in \mathbb{R}_\nu^+} -\operatorname{Re}((1 + j\omega\theta)G(j\omega)), \quad (6.8.63)$$

which directly results from the Popov condition (5.1.13). In Figure 6.73 a comparison

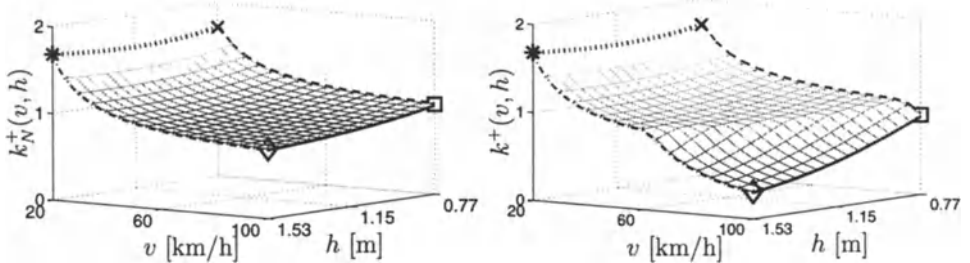


Figure 6.73. Upper bound of Nyquist- (left) and Popov-sector.(right) for an equidistant grid of the operating domain

of the upper bounds for Nyquist- (left) and Popov-sector (right) is shown. The edge in the Popov-surface characterizes the operating conditions for which necessary and sufficient condition for absolute stability start to differ. The upper bound  $k_{\max}$  of the maximum Popov-sector  $[0, k_{\max}]$  is computed by

$$k_{\max} = \inf_{\mathbf{q} \in Q_V} k^+(\mathbf{q}). \quad (6.8.64)$$

The result is  $k_{\max} = k^+(\mathbf{q}_{V_3}) = 0.3091$  (for comparison, the numerical value of the upper bound of the Nyquist-sector is  $\inf_{\mathbf{q} \in Q_{V_3}} k_N^+(\mathbf{q}_{V_3}) = 0.8031$ ).  $k^+(\mathbf{q}_{V_3})$  is the value for the critical operating point  $V_3$  with  $v = 100$  [km/h] and  $h = 1.53$  [m]. The slope of the corresponding Popov-line becomes  $1/\theta^+(\mathbf{q}_{V_3}) = 5.984$ . For the four vertices of the operating domain, i.e.  $\mathbf{q} \in Q_V$ , the control loop is absolutely stable if  $k_R \in [0, k(\mathbf{q}_{V_3})]$  as shown in Figure 6.74. To ensure robust absolute stability for the continuum of the entire operating domain, i.e.  $\mathbf{q} \in Q$ , the robust absolute stability condition is mapped into parameter space as suggested in Section 5.1. The region

$$Q_{\Theta_{P,\theta}} = \left\{ \mathbf{q} \mid \frac{1}{k} + \operatorname{Re}((1 + j\omega\theta)G(j\omega, \mathbf{q})) > 0, \forall \omega \in \mathbb{R}_0^+, \theta \in \mathbb{R}_0 \right\} \quad (6.8.65)$$

shown in Figure 6.75 signifies the region in the plane of plant parameters  $\mathbf{q}$ , for which the Popov-locus for all  $\mathbf{q} \in Q_{\Theta_{P,\theta}}$  resides to the right of the Popov-line with slope  $1/\theta$ . The control loop in Figure 6.71 is robustly absolute stable since the operating domain is entirely included in this region, i.e.  $Q \in Q_{\Theta_{P,\theta}}$ .

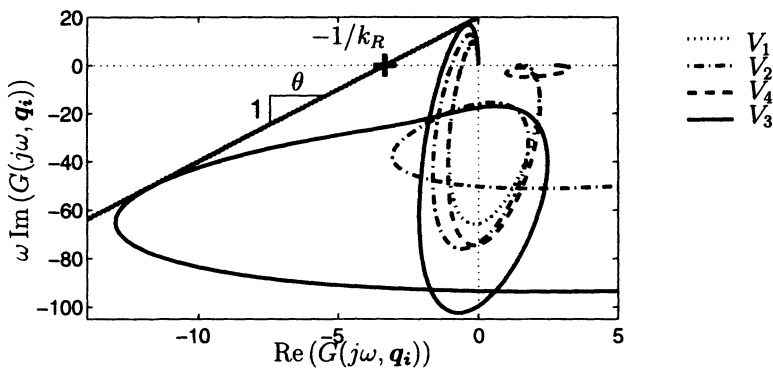


Figure 6.74. Popov-line and Popov-locus for the four vertices

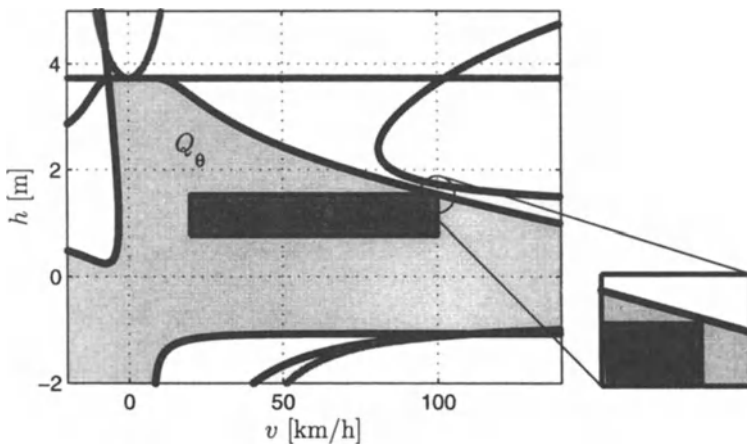


Figure 6.75. Popov region in parameter space

### Combined Continuous Operation and Emergency Steering Control

For absolute stability of the closed loop with combined continuous operation and emergency steering control, the linear part of the system becomes

$$G(s, \mathbf{q}) := -\frac{R}{\delta_R} = \frac{G_a(s)G_{\delta_F}^R(s, \mathbf{q})}{1 + G_a(s)K_\phi(\mathbf{k}(\mathbf{q}))G_{\delta_F}^\phi(s, \mathbf{q})}, \quad (6.8.66)$$

where controller parameters for  $K_\phi(\mathbf{k}(\mathbf{q}))$  are selected corresponding to the look-up-table in Figure 6.66. Figure 6.76 depicts the course of the upper bound of the corresponding Popov-sector for a fine grid of the operating domain  $Q$ . Thereby, the left plot in Figure 6.76 corresponds to  $\mu = 1$ , the right one to  $\mu = 0.2$ . For all  $k_R \in [0, k_{max}]$  with

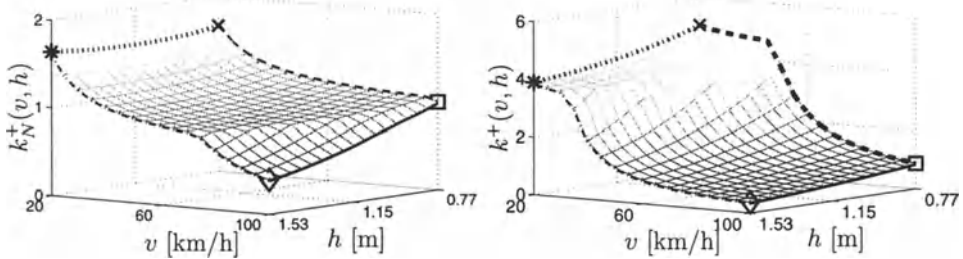


Figure 6.76. Upper bound of Popov sector for  $\mu = 1$  (left) and  $\mu = 0.2$  (right) for combined emergency steering and continuous operation steering control

$k_{max} = \inf_{v, h} k^+(v, h) = 0.394$  ( $\mu = 1$ ) or  $k^+(v, h) = 0.372$  ( $\mu = 0.2$ ), the controlled system corresponding to Figure 6.53 (neglecting braking control) is robustly absolutely stable.

### Emergency Braking Control

Applying braking control requires the application of a non-linear dynamic model of the vehicle with longitudinal velocity  $v$  as an additional state variable and the braking pressure  $p$  or a corresponding longitudinal force  $f_x = m a_x$  as an additional input (see Figure 6.53). The force  $f_x$  is assumed to act on CG<sub>1</sub> in the vehicle's longitudinal direction. The time delay effect of the brakes is modelled by a first order lag with a time constant of 0.1 s. The intention of emergency braking is to make the deviation from the desired course being induced by emergency steering control as small as possible. This task is realized by decelerating the vehicle as soon as the rollover coefficient becomes critical. Reducing speed means also to reduce lateral acceleration. Energy is taken out of the system. Therefore, braking contributes essentially to rollover risk reduction. Two non-linear effects must be taken into consideration for minimization of the deviation from the desired path:

- By the inertia of the vehicle mass, the loads on the front tires are increased while the loads on the rear tires are decreased by the same amount. The front and rear sideslip angles increase, the rear more than the front one. By magnification of the rear sideslip angle, a yaw movement to the inside to the curve is induced [150].

- b) Assuming understeering behaviour steady state decelerating in cornering means that the front wheel steering angle has to be taken back to remain on the desired path, which also induces a yaw movement to the inside of the curve.

Figure 6.77 depicts the structure of the emergency braking control system. Note that  $p_D$

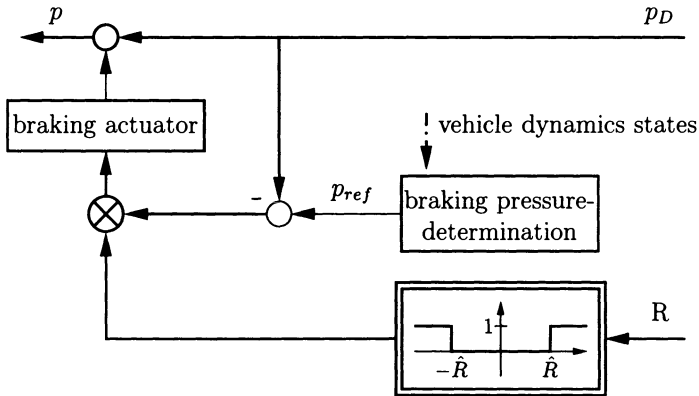


Figure 6.77. Structure of the emergency braking control system

Figure 6.53 describes the braking pressure set by the driver corresponding to the brake pedal force. Consider the left plot of Figure 6.78. Assuming an ideal braking actuator

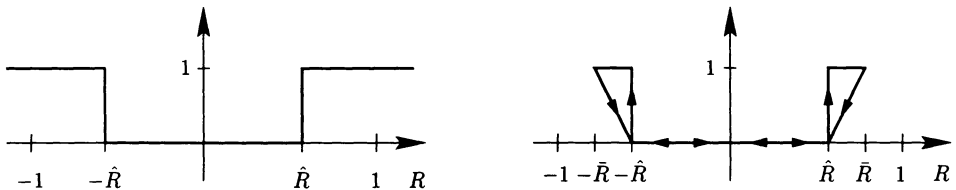


Figure 6.78. Static and dynamic braking control characteristics

and no braking of the driver ( $p_D = 0$ ), the automatic braking action is described by the following relation:

$$p = \begin{cases} 0, & \forall |R| \leq \hat{R} \\ p_{ref}, & \forall |R| > \hat{R}. \end{cases} \quad (6.8.67)$$

Alternatively, in a refined realization shown in the right plot of Figure 6.78 a dynamic characteristic is applied to distinguish between decreasing ( $\dot{R} \text{ sign}(R) > 0$ ) and increasing ( $\dot{R} \text{ sign}(R) < 0$ ) rollover stability. Assuming decreasing rollover stability,

braking shall be implemented as fast as possible, while in increasing rollover stability the breaking force shall be withdrawn. Such a dynamical relation is, e.g. given by

$$p = \begin{cases} 0 & \forall |R| \leq \hat{R} \\ p_{ref} & \forall |R| > \hat{R} \wedge \dot{R} \text{ sign}(R) > 0 \\ \frac{|R| - \hat{R}}{\hat{R} - R} p_{ref} & \forall |R| > \hat{R} \wedge \dot{R} \text{ sign}(R) < 0 \end{cases}, \quad (6.8.68)$$

where  $\bar{R}$  denotes the (dynamic) maximum absolute rollover coefficient that is stored in a memory while in increasing rollover stability state.

Here, the braking pressure reference value  $p_{ref}$  is assumed fixed, i.e. its value corresponds to a predetermined deceleration.

### *Remark 6.15*

However,  $p_{ref}$  also might be computed subject to other vehicle dynamics states. For example, if the run of the road and also the road conditions are measured and available to the driver assistance system (e.g. assuming a telematic system with electronic map or an automated highway system), then automatic steering and braking impact can be adapted such that rollover avoidance and lane keeping can be achieved simultaneously without any driver impact.

□

### *Simulation Results*

The functioning of the emergency control system are now explained by means of simulation results. The simulations were performed using the non-linear dynamic vehicle model, assuming a dry road ( $\mu = 1$ ) and an unfavourably large height,  $h = 1.53$  m. Figure 6.79 shows the responses of the conventional (dashed-dotted line) and two controlled vehicles (solid lines) when a ramp-like input signal is applied to the steering wheel angle  $\delta_S$ . Both braking control approaches are investigated. The black solid line corresponds to braking action due to (6.8.67), the grey line is according to (6.8.68). This maneuver is similar to driving through a highway exit with increasing curvature (clotoidal transition). After about 2 s, the rollover coefficient of conventional vehicle approaches 1 and the wheels on one side lift off the road. For the sake of comparability, the simulation is continued until the end of the maneuver. Note that the simulation model is no longer valid if  $|R| > 1$ .

Emergency steering and braking control is switched on after about 1.8 s when the rollover coefficient  $R$  implies that the vehicle is close to rollover, i.e.  $|R| > 0.9$ . Due to the fast and precise steering intervention, the rollover is avoided. Speed is reduced by braking control and therefore also the lateral acceleration is reduced such that after about 1 s the steering command can be returned to the driver. However, only little track error occurs in the vehicle's position plot ( $x, y$ ) in Figure 6.79 because the vehicle is simultaneously decelerated by the emergency braking system.

Comparably advantageous results were obtained when other maneuvers, e.g. lane change maneuvers, and variations of  $v$  and  $h$  were investigated in further simulations.

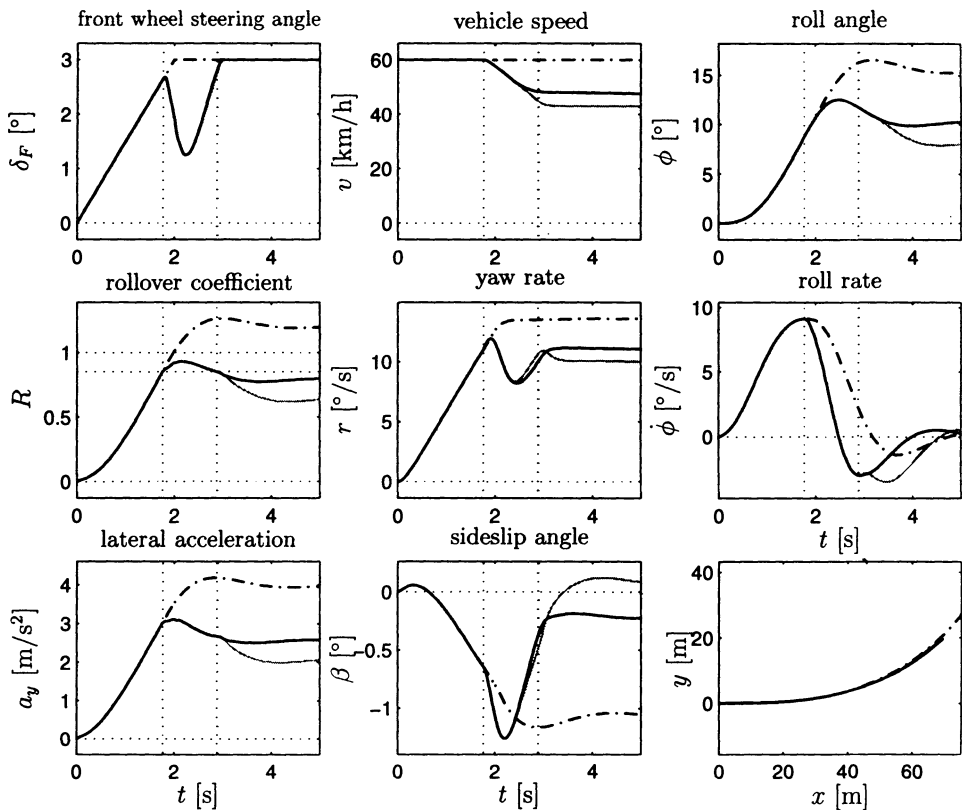


Figure 6.79. Simulation results for a driver steering input ramp

### Concluding Remarks

The rollover control concept introduced in this section basically depends on robust steering control. It is especially suitable for vehicles with an unfavorable relation of height of CG and track width. By continuous steering control and using feedback of the roll rate, the roll damping is improved significantly. Thus, especially in transient driving maneuvers such as double lane change or obstacle avoidance the risk of rollover can be reduced significantly. If the vehicle is already close to rollover, rollover is avoided by additional feedback of a rollover coefficient, i.e. by suited driving state limitation. Especially in quasi-steady state driving maneuvers, e.g. when entering a curve with excessive speed, rollover can be prevented. By means of principal considerations it was shown that the deviation from the desired course can be minimized by the automatic braking impact. By combination of the roll damping and emergency actions clear synergistic effects can be exploited.

By systematic use of the parameter space method for design and analysis of the rollover avoidance control system, a multitude of design specifications, covering eigen-

value ( $\Gamma$ -stability), frequency loci ( $\Theta$ -stability), and frequency magnitude ( $\mathcal{B}$ -stability) specifications were incorporated. While all design specifications could be treated exactly for parametric uncertainty (height  $h$  and speed  $v$ ), the effect of unstructured uncertainty (unmodelled dynamics) was also considered. On the basis of the simple controller structure, the transparency of the design procedure, and the results as well as the multitude of performance and stability criteria used, the rollover avoidance control design procedure may be adapted easily to different types of vehicles.

For more details the reader is referred to [158].

## 6.9 Patents

The authors hold several patents on car steering methods and their implementation.

- i. The basic idea of robust unilateral decoupling for a car with linearized tire and ideal mass distribution is patented by [5]. It involves the feedback of the yaw rate  $r$  to the front steering angle  $\delta_F$ .
- ii. For cars with rear-wheel steering  $\delta_R$ , the yaw damping can be improved by feedback of  $r$  do  $\delta_R$ , [7].
- iii. A lateral acceleration  $a_{yp}$  can be generated more quickly by feedback of  $a_{yp}$  to  $\delta_F$ , [8].
- iv. Modelling restrictions of i – iii have been relaxed in [9]. The method is generalized for a non-linear uncertain tire model with delayed generation of lateral force, non-ideal mass distribution , acceleration and braking effects, feedback of longitudinal velocity and longitudinal and lateral accelerations. A desired function of the yaw damping on the velocity is implemented and the fading integrator replaces the ideal integrator.
- v. As an alternative to robust unilateral decoupling, a disturbance observer feedback structure is assumed in [101].
- vi. The concept of assigning a desired dependence of yaw damping on the velocity by a double cancellation is developed in [12] for a car with front-wheel steering only.
- vii. While items i to vi deal with skidding avoidance, [160] uses feedback steering for rollover avoidance.
- viii. A hardware implementation of mechanical addition of steering angles is described in [17].
- ix. The electrical addition of steering angles requires a steer-by-wire system. This should give the same feeling for the driver as a conventional steering system [162].

## 6.10 Automatic Car Steering

In the previous sections, the path tracking task was left with the driver. Consider now automatic following of a lane reference. Such a reference may be provided by

the electromagnetic field of a guiding wire in the center of the lane [69], [190], or equivalently by passive magnets on this lane center [196] or by processing the images from a car-mounted video camera [74], [143],[77]. In this section, we assume that the lateral deviation of the vehicle from the lane reference is available as a controller input.

In order to study automation of car steering, the steering model must be extended. The model must include not only velocities, but also the vehicle heading and the lateral position of the sensor with respect to the reference path. For simplicity, this extended model will only be derived using a linear model that is valid for small deviations from a stationary circular path. It is assumed that the reference path consists of circular arcs. Figure 6.80 shows the transition from an arc with radius  $R_1$  and center  $M_1$  to an arc with radius  $R_2$  and center  $M_2$ . At the transition point, the tangent to the path is continuous. There is, however, a step change in the reference input from  $R_{ref} = R_1$  to  $R_{ref} = R_2$ . For straight path segments, the radius is  $R_{ref} = \infty$ . It is more convenient to introduce the curvature  $\varrho_{ref} := 1/R_{ref}$  as the input that generates the reference path. The curvature is defined positive for left cornering, and negative for right cornering.

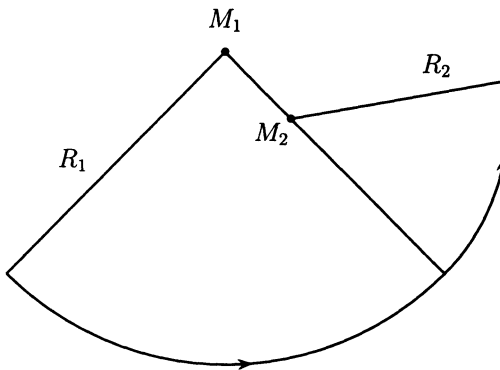


Figure 6.80. The reference path is comprised of circular arcs

The vehicle motion in circular cornering will now be modelled for small deviations from a stationary circular path, see Figure 6.81. The radial line from the center  $M$  passing through the center of gravity CG of the vehicle intersects a point  $z_{ref}$  on the desired path. The distance from the reference point  $z_{ref}$  to the CG is the deviation  $y_{CG}$ . Figure 6.81 shows an inertially fixed coordinate system  $x_0, y_0$  and a car body fixed coordinate system  $x, y$ , which is rotated by the yaw angle  $\psi$ . The tangent to the path at  $z_{ref}$  – denoted by  $\vec{v}_t$  – is rotated by a reference yaw angle  $\psi_t$  with respect to  $x_0$ .

A model for the rate of change of  $y_{CG}$  will now be developed. The component of the car velocity  $\vec{v}$  that is perpendicular to  $\vec{v}_t$  is equal to the rate of change of  $y_{CG}$ . This perpendicular component is given by  $v \sin(\beta + \Delta\psi)$ , where  $\beta$  is the car sideslip angle and  $\Delta\psi := \psi - \psi_t$  is the angle between the tangent to the path at  $z_{ref}$  and the centerline of the car, see Figure 6.81.

With the linearization  $\sin(\beta + \Delta\psi) \approx \beta + \Delta\psi$ , the deviation  $y_{CG}$  changes according to

$$\dot{y}_{CG} = v(\beta + \Delta\psi). \quad (6.10.1)$$

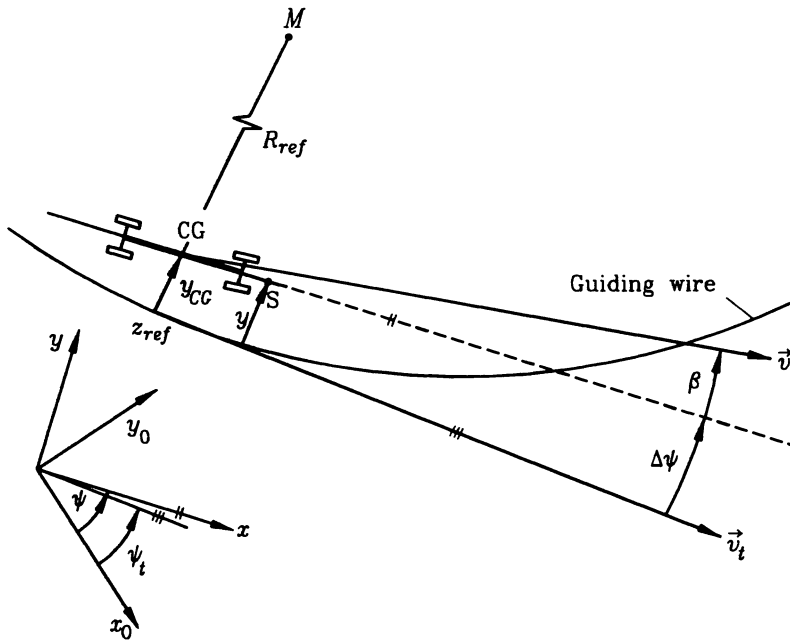


Figure 6.81. Vehicle heading and measured displacement  $y$  from the guiding wire in stationary circular cornering

Actually, the sensor S is not mounted in the CG but in a distance  $\ell_S$  in front of the CG with  $\ell_S \ll R_{ref}$ . The measured displacement  $y$  from the guiding wire now changes both with  $\dot{y}_{CG}$  and under the influence of the yaw rate  $r = \dot{\psi}$ . Taking this into account, the rate of change of the measured displacement is

$$\dot{y} = v(\beta + \Delta\psi) + \ell_S r. \quad (6.10.2)$$

Determination of  $\dot{y}$  requires knowledge of three variables  $\beta$ ,  $r$ , and  $\Delta\psi$ . The variables  $\beta$ , and  $r$  are given by the basic car model (6.4.4). (Assume only front-wheel steering, i.e.  $\delta_R \equiv 0$ .) The angle  $\Delta\psi$  will be obtained by integrating its derivative

$$\begin{aligned}\Delta\dot{\psi} &= \dot{\psi} - \dot{\psi}_t \\ &= r - r_{st}.\end{aligned}$$

The term  $r_{st}$  is the yaw rate of the path tangent, i.e.  $r_{st} = v/R_{ref} = v\varrho_{ref}$  in stationary circular cornering. Hence,

$$\Delta\dot{\psi} = r - v\varrho_{ref}. \quad (6.10.3)$$

Combining (6.4.4), (6.10.2), and (6.10.3), the extended state space model is obtained as

$$\begin{bmatrix} \dot{\beta} \\ \dot{r} \\ \Delta\dot{\psi} \\ \dot{y} \end{bmatrix} = \begin{bmatrix} a_{11} & a_{12} & 0 & 0 \\ a_{21} & a_{22} & 0 & 0 \\ 0 & 1 & 0 & 0 \\ v & \ell_s & v & 0 \end{bmatrix} \begin{bmatrix} \beta \\ r \\ \Delta\psi \\ y \end{bmatrix} - \begin{bmatrix} 0 \\ 0 \\ v \\ 0 \end{bmatrix} \varrho_{ref} + \begin{bmatrix} b_{11} \\ b_{21} \\ 0 \\ 0 \end{bmatrix} \delta_F$$

$$+ \begin{bmatrix} 1/mv & 0 \\ 0 & 1/m\ell_R\ell_{DP} \\ 0 & 0 \\ 0 & 0 \end{bmatrix} \begin{bmatrix} F_{yD} \\ M_{zD} \end{bmatrix}. \quad (6.10.4)$$

In addition to the eigenvalues of (6.4.4), there is a double eigenvalue at  $s^2 = 0$ . The reference curvature  $\varrho_{ref}$  appears as an additional input to the system. The transition to a new curvature corresponds to a step input in  $\varrho_{ref}$ . Fig. 6.82 illustrates (6.10.4) in the form of a block diagram.

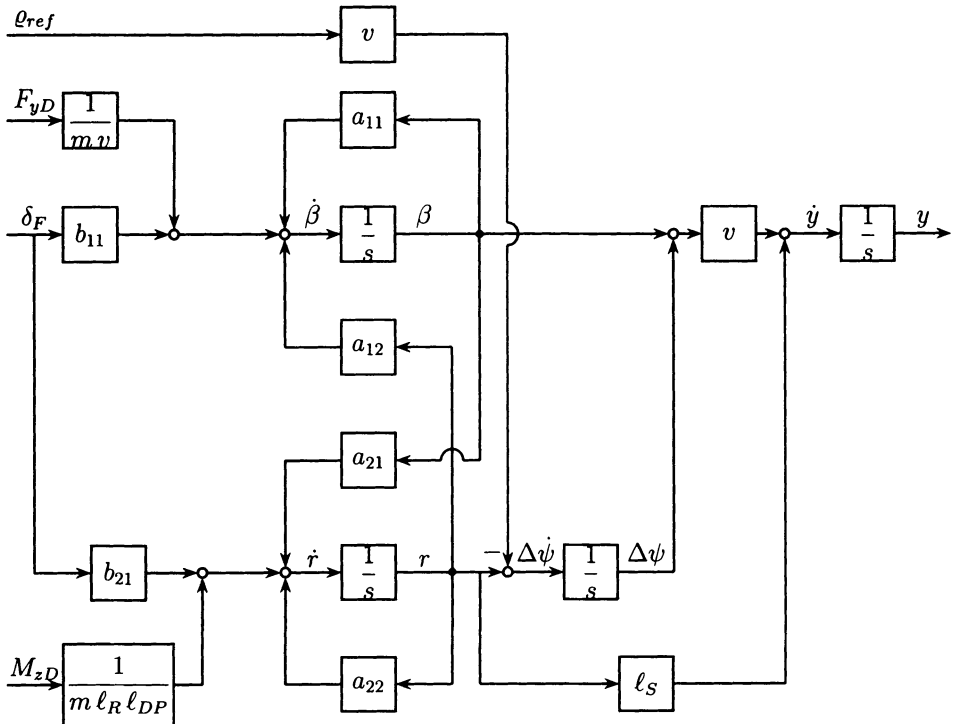


Figure 6.82. Block diagram of automatic steering with reference curvature  $\varrho_{ref}$

By aggregating the single-track model, the block diagram Figure 6.83 is obtained.

The transfer function from the steering angle  $\delta_F$  to the measured displacement from the guiding wire  $y$  satisfies

$$y(s) = \frac{n(s)}{(a_0 + a_1 s + s^2)s^2} \delta_F(s), \quad (6.10.5)$$

with  $a_0$  and  $a_1$  given in (6.4.23). The numerator  $n(s)$  can be reduced to  $n_{F\beta}$  and  $n_{Fr}$  according to Fig. 6.82.

$$p_A(s)y(s) = \frac{1}{s} \left\{ v \left[ n_{F\beta}(s) + \frac{1}{s} n_{Fr}(s) \right] + \ell_S n_{Fr}(s) \right\} \delta_F(s), \quad (6.10.6)$$

$$n(s) = s^2 \left\{ \left( \frac{v}{s^2} + \frac{\ell_S}{s} \right) n_{Fr}(s) + \frac{v}{s} n_{F\beta}(s) \right\},$$

and with  $n_{Fr}(s)$  from (6.4.33) and  $n_{F\beta}$  from: (6.4.34)

$$\begin{aligned} n(s) &= b_2 s^2 + b_1 s + b_0, \\ b_2 &= \frac{\mu c_F \ell \ell_S}{m \ell_R \ell_{DP}} + v, \\ b_1 &= \frac{\mu c_F}{m \ell_{DP}} \left[ v + \frac{\mu c_R \ell}{m v \ell_R \ell_F} \left( \frac{\ell \ell_S}{\ell_R \ell_F} + 1 \right) \right], \\ b_0 &= \frac{\mu^2 c_R c_F \ell^2}{m^2 \ell_F \ell_R \ell_{DP}}. \end{aligned} \quad (6.10.7)$$

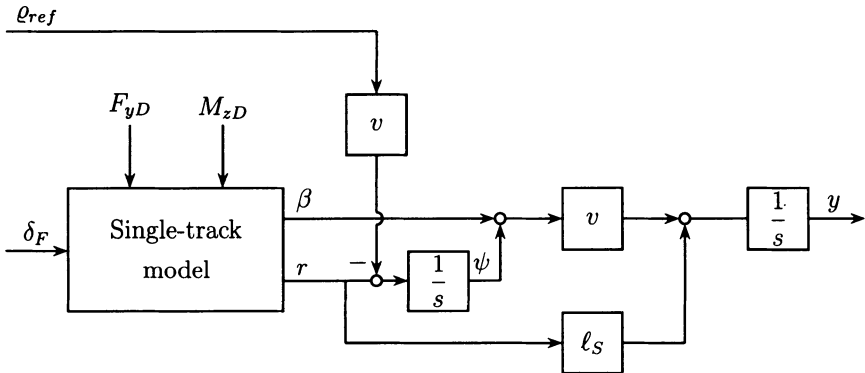


Figure 6.83. Aggregated block diagram with external reference input

### Controllability

The pair  $(A, b)$  in (6.10.4) is written in  $2 \times 2$  block form as

$$A = \begin{bmatrix} A_{11} & 0 \\ A_{21} & A_{22} \end{bmatrix}, b = \begin{bmatrix} b_1 \\ 0 \end{bmatrix}, \quad (6.10.8)$$

where

$$\begin{aligned} A_{11} &= \begin{bmatrix} a_{11} & a_{12} \\ a_{21} & a_{22} \end{bmatrix}, \quad A_{21} = \begin{bmatrix} 0 & 1 \\ v & \ell_S \end{bmatrix}, \\ A_{22} &= \begin{bmatrix} 0 & 0 \\ v & 0 \end{bmatrix}, \quad A_{22}^2 = 0. \end{aligned}$$

Then

$$\begin{aligned}\mathbf{A}\mathbf{b} &= \begin{bmatrix} \mathbf{A}_{11} \\ \mathbf{0} \end{bmatrix} \mathbf{b}_1, \\ \mathbf{A}^2\mathbf{b} &= \begin{bmatrix} \mathbf{A}_{11}^2 \\ \mathbf{A}_{21}\mathbf{A}_{11} + \mathbf{A}_{22}\mathbf{A}_{21} \end{bmatrix} \mathbf{b}_1, \\ \mathbf{A}^3\mathbf{b} &= \begin{bmatrix} \mathbf{A}_{11}^3 \\ \mathbf{A}_{21}\mathbf{A}_{11}^2 + \mathbf{A}_{22}\mathbf{A}_{21}\mathbf{A}_{11} \end{bmatrix} \mathbf{b}_1.\end{aligned}$$

The first two columns of the controllability matrix become linearly dependent, i.e.

$$\det[\mathbf{b}_1 \mathbf{A}_{11} \mathbf{b}_1] = 0 \quad (6.10.9)$$

under the conditions already analyzed in (6.4.35) for the single-track model. Then, also  $\mathbf{A}_{11}^2\mathbf{b}_1$  and  $\mathbf{A}_{11}^3\mathbf{b}_1$  are linearly dependent on  $\mathbf{b}_1$ . Further conditions of non-controllability can only arise if

$$\begin{aligned}d &= \det[(\mathbf{A}_{21}\mathbf{A}_{11} + \mathbf{A}_{22}\mathbf{A}_{21})\mathbf{b}_1 (\mathbf{A}_{21}\mathbf{A}_{11}^2 + \mathbf{A}_{22}\mathbf{A}_{21}\mathbf{A}_{11})\mathbf{b}_1] = 0 \\ &= \det(\mathbf{A}_{21}\mathbf{A}_{11} + \mathbf{A}_{22}\mathbf{A}_{21})(\mathbf{b}_1, \mathbf{A}_{11}\mathbf{b}_1)\end{aligned},$$

i.e. for the same condition as above and for

$$\det(\mathbf{A}_{21}\mathbf{A}_{11} + \mathbf{A}_{22}\mathbf{A}_{21}) = \frac{-\mu^2\ell^2c_Rc_R}{m^2v\ell_R\ell_{DP}} = 0, \quad (6.10.10)$$

which is not satisfied for  $\mu \neq 0$ .

### Observability

For the output  $y$ , the rows of the observability matrix are

$$\begin{aligned}\mathbf{c}^T &= [\mathbf{0} \quad \mathbf{c}_2^T], \quad \mathbf{c}_2^T = [0 \quad 1], \\ \mathbf{c}^T \mathbf{A} &= \mathbf{c}_2^T [\mathbf{A}_{21} \quad \mathbf{A}_{22}] = [v \quad \ell_s \quad v \quad 0], \\ \mathbf{c}^T \mathbf{A}^2 &= \mathbf{c}_2^T [\mathbf{A}_{21}\mathbf{A}_{11} + \mathbf{A}_{22}\mathbf{A}_{21} \quad 0], \\ \mathbf{c}^T \mathbf{A}^3 &= \mathbf{c}_2^T [\mathbf{A}_{21}\mathbf{A}_{11}^2 + \mathbf{A}_{22}\mathbf{A}_{21}\mathbf{A}_{11} \quad 0].\end{aligned}$$

The structure of the observability matrix is

$$\begin{bmatrix} \mathbf{c}^T \\ \mathbf{c}^T \mathbf{A} \\ \mathbf{c}^T \mathbf{A}^2 \\ \mathbf{c}^T \mathbf{A}^3 \end{bmatrix} = \begin{bmatrix} 0 & 0 & 0 & 1 \\ v & \ell_s & v & 0 \\ m_{31} & m_{32} & 0 & 0 \\ m_{41} & m_{42} & 0 & 0 \end{bmatrix}.$$

The last two columns related to the position state variables  $\Delta\Psi$  and  $y$  are linearly independent for  $v \neq 0$ . The first two columns complement the rank of the observability matrix to 4 if

$$\det \begin{bmatrix} m_{31} & m_{32} \\ m_{41} & m_{42} \end{bmatrix} = -\frac{-\mu^2\ell^2}{m^2v\ell_R\ell_{DP}} \neq 0 ,$$

which is true for  $\mu \neq 0$ .

The observability of  $\beta$  and  $r$  can be improved considerably by yaw rate feedback. It yields velocity-independent observability as shown in (6.4.41). The resulting feedback structure is illustrated by Figure 6.84.

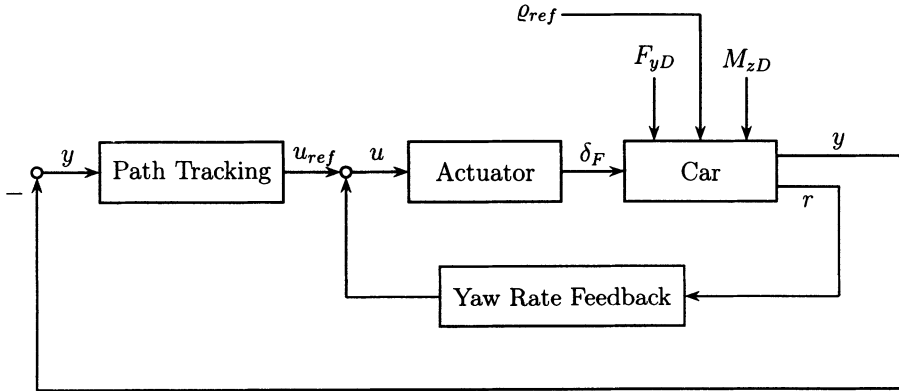


Figure 6.84. Feedback structure for automatic car steering

The measured output  $y$  is the deviation between the reference position  $y_{ref}$  and the absolute position  $y_{abs}$ . Therefore,

only a single degree of freedom controller is feasible for feedback of  $y$ . A further feedback path is obtained by a second displacement sensor in a distance  $\ell_{SR}$  behind the CG (if the second sensor is mounted in front of the CG then  $\ell_{SR}$  is negative). The block diagram Figure 6.83 is augmented and modified to Figure 6.85. The front sensor quantities are now characterized by the index  $F$ .

Finally,  $\delta_F$  may also be measured and fed back to the actuator input. This is helpful for actuator uncertainties or if the actuator poles have been shifted to an unfavorable location by the yaw damper and the path tracking controllers.

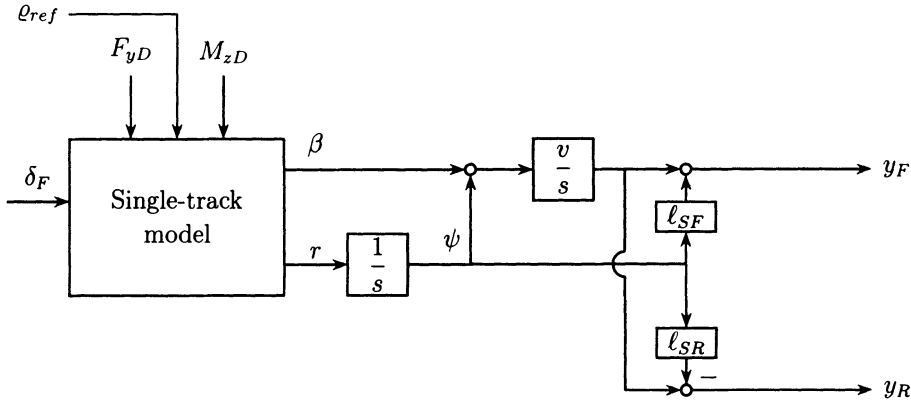


Figure 6.85. Two lateral displacement sensors for  $y_F$  and  $y_R$

### Remark 6.16

In the early days of automatic steering around 1980, rate sensors were still expensive and gyros had not yet been considered. The front displacement sensor for  $y_F$  is always used. Typical sensor concepts for additional sensors are:

1. MAN [190] used  $y_R$  for estimation of the road curvature, a sensor for  $\delta_F$  and gain scheduling by  $v$ .
2. Daimler-Benz started with front and tail displacement sensors and a sensor for  $\delta_F$ . Later, the system was reduced to just the front displacement sensor [69].
3. The sensor concept of Figure 6.84 with front displacement and yaw rate feedback was proposed in [28].
4. In the PATH project [99], front and tail displacement sensors were used and curvature preview is encoded in the road using binary polarity coding of the magnetic lane reference markers.

□

### Path Tracking Controller Design for the Bus

The aim of path tracking is to keep  $y$  small at all times under the influence of changing reference curvature  $\varrho_{ref}$ , disturbance torques  $M_{zD}$ , and lateral disturbance forces  $F_{yD}$ . The control system must be robust with respect to uncertain road-tire contact, mass and velocity.

Like in Fig. 1.5 for the crane, the controller in Figure 6.84 may still be non-linear, adaptive, etc. In the following discussion, however, we design linear controllers. The next question is then, what dynamic order of the controllers is required? The actuator is modelled simply as a first order low-pass  $1/(1 + Ts)$  for actuation at the steering column or  $1/s$  for force addition at the wheels by an hydraulic actuator without position feedback [69]. For the latter case, the plant plus actuator transfer function is

$$G(s) = \frac{b(s^2 + b_1 s + b_0)}{(s^2 + a_1 s + a_0)s^3}. \quad (6.10.11)$$

Figure 6.86 shows the root locus for proportional feedback of  $y_F$  for the data of the bus in Table 6.1 at  $v = v^+$  and  $\mu = \mu^-$ . The sensor position is  $\ell_S = 6.12$  [m].

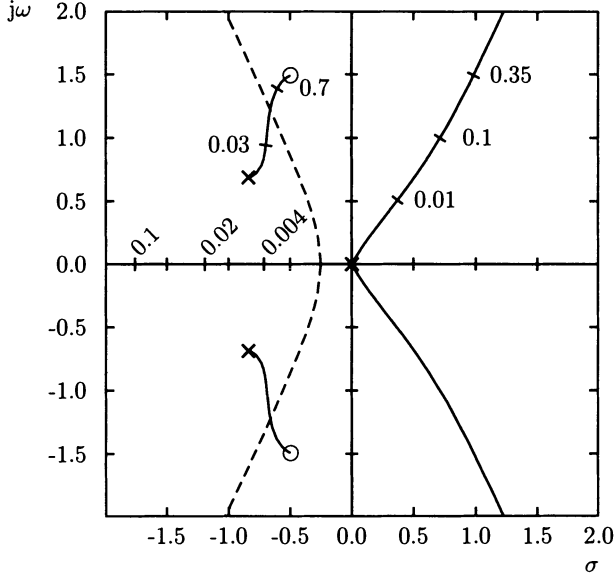


Figure 6.86. Root locus of an automatic car steering system with proportional feedback of the front displacement from the guideline

The transfer function (6.10.11) has a triple pole at  $s = 0$ . Thus, there are three root locus branches at zero with breakaway angles  $\pm 60^\circ$  and  $180^\circ$  and the closed loop is unstable for small loop gains, see Figure 6.86. The loop is also unstable for large loop gains, because the asymptotes of the root locus have angles  $\pm 60^\circ$  and  $180^\circ$ . In order to stabilize the system at intermediate gains, it is necessary to place two fine-tuned zeros in the left half plane that attract the two right half plane branches of the root locus or allow the two plant zeros to attract these branches. The first alternative is favorable in view of  $\Gamma$ -stabilization where  $\partial\Gamma$  is the dotted hyperbola in Figure 6.86. Thus, the controller order must be at least two. In the road tests, it turned out that high-frequency noise enters with  $y_F$  originating from inaccuracies in the guiding wire reference. Therefore a path tracking controller with relative degree one and a Butterworth pole configuration was assumed, i.e.

$$\delta_F(s) = \frac{k_1 + k_2 s + k_3 s^2}{(1 + s/\omega_0 + s^2/\omega_0^2)(1 + s/\omega_0)} y(s). \quad (6.10.12)$$

For frequencies  $\omega < \omega_0$ , the gain  $k_1$  may be viewed as proportional gain,  $k_2$  as derivative gain, and  $k_3$  as second derivative gain. During the design, primarily  $k_1$ ,  $k_2$ , and  $k_3$  were varied, i.e. a pair of zeros and the loop gain.

This controller structure is:

- i. Lean: only four essential parameters  $k_1, k_2, k_3$  and  $\omega_0$  must be tuned.
- ii. Transparent: the parameters have a well-defined influence on the car steering system. The controller is of the minimal required order.

Robustness with respect to uncertain operating conditions will be achieved by parameter space design.

The specification for the closed loop are given in the time-domain:

- i. Less than 2 [cm] track deviation on a straight lane without wind, less than 15 [cm] under sidewind of 20 [m/sec].
- ii. Less than 15 [cm] peak deviation after entering a curve.
- iii. Observing the  $|\dot{\delta}| \leq 23$  [degree/s] steering rate constraint also in the worst case of entering a narrow parking bay.
- iv. Smooth transition from manual to automatic control.
- v. Keep the lateral acceleration below 2 [m/sec<sup>2</sup>] for passenger comfort.

A first design iteration showed that these specifications can be met with all poles in a  $\Gamma$ -stable region to the left of the hyperbola

$$\left(\frac{\sigma}{0.35}\right)^2 - \left(\frac{\omega}{1.75}\right)^2 = 1, \quad \sigma < -0.35.$$

#### *Remark 6.17*

A design based on three sensors for  $y_F$ ,  $y_R$  and  $\delta_f$  and an actuator transfer function  $4.7/(s + 4.7)$  was performed in [32]. The approach was to intersect  $\Gamma$ -stable regions for the four vertex operating conditions. This was done in an invariance plane that permitted only the shifting of the double eigenvalue at zero. This invariance plane was chosen for an average velocity  $v = 10$  [m/s] and the worst case  $\tilde{\mu} = \mu^- m^- / m^+ = 0.5 \cdot 9.95/16 = 0.31$ . The unmeasured state variables  $\dot{y}_F$  and  $\dot{y}_R$  were approximated by low-pass filtered differentiation of  $y_F$  and  $y_R$ . For details of this design the reader is referred to [www.op.dlr/FF-DR-RR/paradise](http://www.op.dlr/FF-DR-RR/paradise).

□

#### *Design with Front Displacement Feedback*

The design with only one sensor for  $y_F$ , an actuator transfer function  $1/s$ , and the controller (6.10.12) was performed in [154]. The approach was to begin with a high controller bandwidth  $\omega_0 = 100$  and reduce it stepwise. This requires an adjustment of  $k_1$  in order to obtain a reasonably large simultaneously  $\Gamma$ -stabilizing region in the  $(k_2, k_3)$ -plane. This process led to the values  $\omega_0 = 25$ ,  $k_1 = 0.6$ . The four  $\Gamma$ -stable regions in the  $(k_2, k_3)$ -plane for the vertices of the Q-box are shown in Figures 6.87–6.90. The set of simultaneous  $\Gamma$ -stabilizers in the intersection of the four operating points is shown in Figure 6.91.

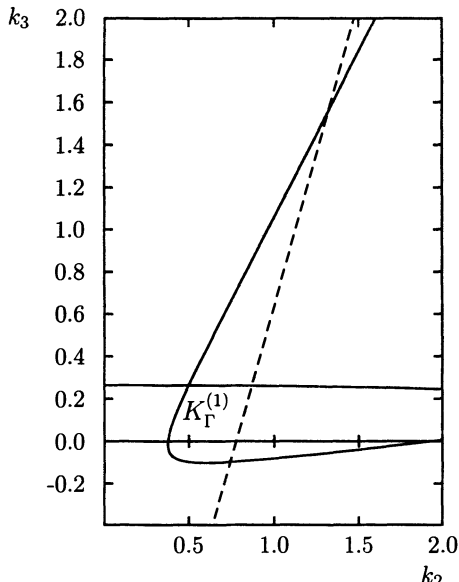


Figure 6.87. Set of  $\Gamma$ -stabilizing controllers for  $\tilde{m} = 9950 \text{ [kg]}$ ,  $v = 3 \text{ [m} \cdot \text{s}^{-1}]$ ,  $\omega_0 = 25$ ,  $k_1 = 0.6$

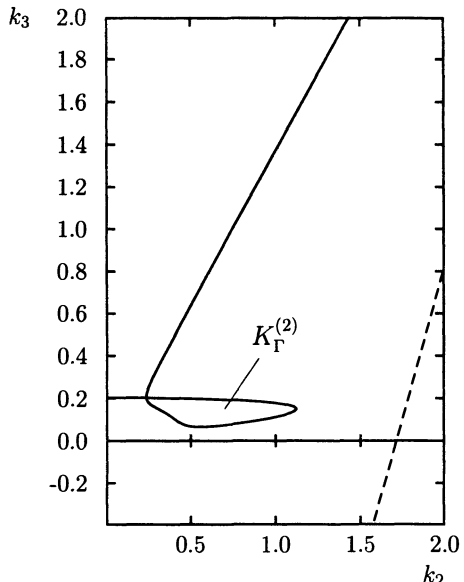


Figure 6.88. Set of  $\Gamma$ -stabilizing controllers for  $\tilde{m} = 9950 \text{ [kg]}$ ,  $v = 20 \text{ [m} \cdot \text{s}^{-1}]$ ,  $\omega_0 = 25$ ,  $k_1 = 0.6$

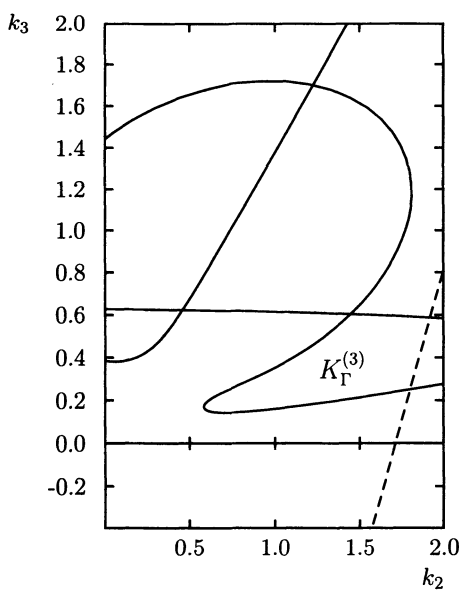


Figure 6.89. Set of  $\Gamma$ -stabilizing controllers for  $\tilde{m} = 32000 \text{ [kg]}$ ,  $v = 20 \text{ [m} \cdot \text{s}^{-1}]$ ,  $\omega_0 = 25$ ,  $k_1 = 0.6$

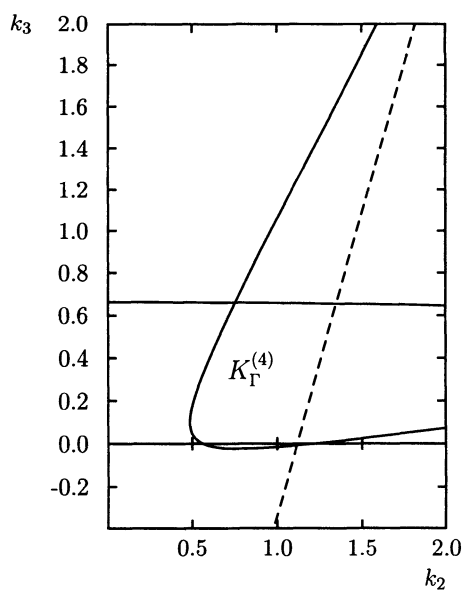


Figure 6.90. Set of  $\Gamma$ -stabilizing controllers for  $\tilde{m} = 32000 \text{ [kg]}$ ,  $v = 3 \text{ [m} \cdot \text{s}^{-1}]$ ,  $\omega_0 = 25$ ,  $k_1 = 0.6$

From the set., we pick the point  $k_2 = 0.7$  and  $k_3 = 0.15$ . The resulting controller is then

$$G_C(s) = 25^3 \frac{0.6 + 0.7s + 0.15s^2}{(s + 25)(s^2 + 25s + 625)}. \quad (6.10.13)$$

This controller  $\Gamma$ -stabilizes the plant at least for the extremal operating conditions. In a stability analysis, the  $\Gamma$ -stability of this controller is verified for the whole range of operating conditions [23]. The stability boundaries in the  $(v, \tilde{m} = m/\mu)$ -plane for this controller were already shown in Fig. 4.5. The vertices are stable and none of the boundaries intersects the  $Q$ -box. A real root boundary passes by very close to the  $Q$ -box. This happens, however, for low velocities and is therefore not critical because a sluggish time response resulting from a real pole close to the origin means only a short driving distance at low speeds.

#### *Remark 6.18*

The result of Fig. 4.6 is amazing, because  $\Gamma$ -stability of the four vertices guarantees  $\Gamma$ -stability for the entire  $Q$ -box. In Section 9.1, an example is constructed with one coefficient containing a bilinear term  $q_1 q_2$ . This non-linearity destroys the nice properties of linear parameter dependence (see Chapter 8) it does not suffice to check vertices or edges of the  $Q$ -box. The track-guided bus example with  $q_1 = v$ ,  $q_2 = m/\mu$  has the terms  $q_1, q_1^2, q_1 q_2, q_1^2 q_2, q_1^2 q_2^2$  in the coefficients of the characteristic polynomial. It looks much more nasty than the above bilinear example, but Fig. 4.6 shows that it is well behaved.

□

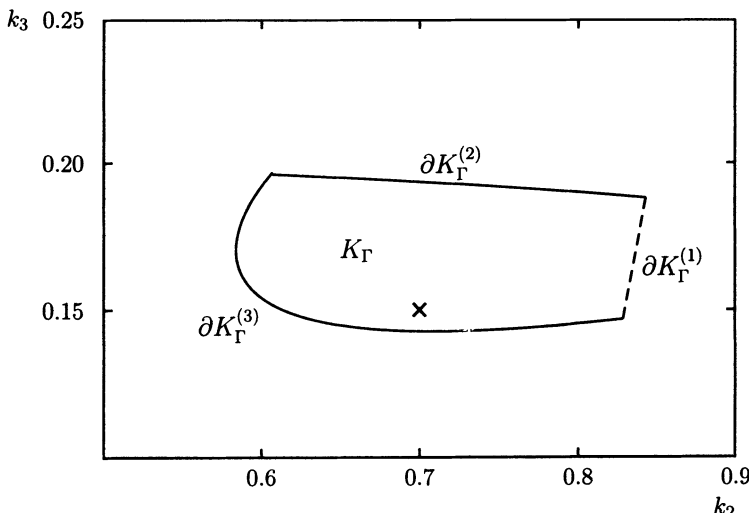


Figure 6.91. Simultaneously stabilizing set for the extremal plants for  $\omega_0 = 25$ ,  $k_1 = 0.6$

The controller has now to be tested in simulations where the design specifications are checked. A simulation of the transition from manual to automatic steering is shown

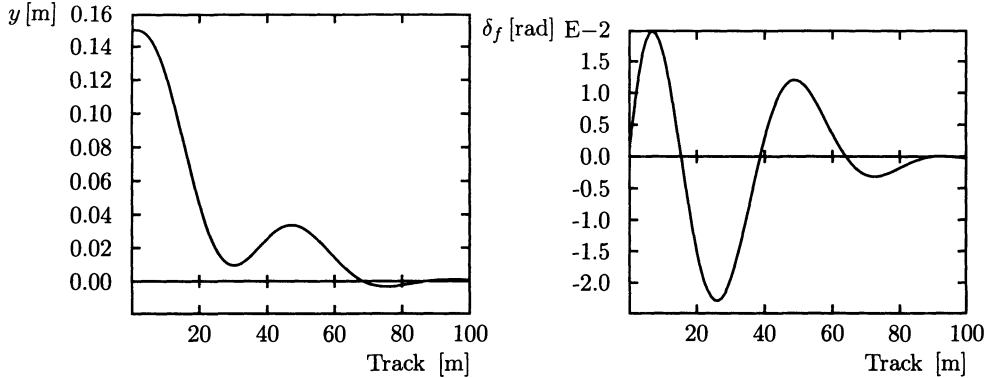


Figure 6.92. Simulation of a transition from manual to automatic steering for  $v = 20 [\text{m} \cdot \text{s}^{-1}]$  and  $\tilde{m} = 32000 [\text{kg}]$ .

in Figure 6.92. This case is especially critical because here the largest deviations from the guideline may occur. Additionally, this is the only operating case where a step input appears. The controller is not started from a zero initial condition, instead, the controller is connected to the plant before switching. Then, only the controller output is switched to the actuator. Thus, no differentiation of a step input occurs. The simulation was made for an initial deviation of 15 [cm]. At  $t = 0$ , the driver switches to automatic steering. Also, in other cases like crosswind, entering a curve, etc. the controller shows satisfactory behavior.

### *Design with Feedback of Front Displacement and Yaw Rate*

In a later design study [28], it was shown that the performance of the automatic steering system of the previous section can be considerably improved by additional yaw rate feedback. The feedback structure is shown in Figure 6.84. The design idea is to exploit the simplicity of the robust decoupling concept as illustrated by Figure 6.8. Specify accurate and robust path tracking not for the sensor at the front bumper ( $\ell_S = 6.12$  [m] for the bus) but for the decoupling point ( $\ell_{DP} = 5.5$  [m]), for example, by placing the magnetometer in this position ( $\ell_S = 5.5$  [m]).

The lateral acceleration  $a_{yDP}$  is integrated twice to the lateral position  $y(s) = a_{yDP}(s)/s^2$ , such that the transfer function from  $\delta_F(\Delta\delta_S)$  to  $y$  is, by (6.5.13):

$$G_{sydec}(s) = \frac{v}{s(1 + T_{dec}s)}, \quad T_{dec} = \frac{mv\ell_R}{\mu c_F \ell} \quad (6.10.14)$$

and for the input  $u_{ref}(s)$ ,

$$G_{uydec}(s) = \frac{v}{s^2(1 + T_{dec}s)}. \quad (6.10.15)$$

This “robustified” system is much easier to control by the path tracking controller than the bus without yaw rate feedback, i.e. with the transfer function (6.10.11).

For alternative parameter space designs of automatic steering systems the reader is referred to [19], [99].

## 7 Case Studies in Flight Control

Models of aircraft dynamics and their linearization can be found in standard books on aircraft dynamics and control, e.g. [81], [142], [189], [60]. When treated as a rigid body, an aircraft has six degrees of freedom of motion: three coordinates of the center of gravity position and three rotation coordinates for roll, yaw, and pitch. In stationary flight, two subsystems may be considered as decoupled:

- i. The longitudinal motion in pitch, altitude, and longitudinal position.
- ii. The lateral motion in roll, yaw, and sideward position.

The first case study deals with a severe perturbation in the yaw motion by an engine fault (called EO=*engine out*). The normal flight control system cannot compensate this effect, thus the pilot has to take over. That may take two seconds and significant effects in the roll and sideward position occur during this reaction time. The strong pilot input for reduction of the yaw rate then induces high peak loads (shear forces) at the root of the vertical tail. These shear forces constitute design loads and essentially determine the static design of the vertical tail and thereby its structural weight. An automatic control system can alleviate this load by the same robust yaw-lateral decoupling concept that was used in Chapter 6 for car steering. By a fast reaction, the disturbance compensation occurs essentially in the yaw degree of freedom as a full simulation with a flight test-validated high-precision simulation program proves.

The other two case studies deal with the longitudinal dynamics. They are characterized by a slow oscillation of the CG around its trajectory (phugoid) and a much faster pitch motion of the fuselage around its CG. The latter is called the *short period longitudinal mode*. Both modes are weakly coupled. We consider here only the second mode. It can be measured by a gyro and an accelerometer and it can be controlled by elevator and horizontal canard rudders. The use of canards is efficient from a flight mechanics point of view. However, they cause instability of the uncontrolled aircraft in some flight conditions. Thereby, the robust pitch stabilization is a demanding problem.

The second section on robust and fault-tolerant Gamma-stabilization of the short period longitudinal mode gives a practical motivation for the simultaneous Gamma-stabilization of four representative flight conditions (three of them unstable) by a fixed-gain robust controller. Paralleled sensors are used in order to maintain robust stabilization immediately after a sensor fault.

The third case study investigates the task of designing a large envelope pitch-rate (i.e. short period longitudinal) controller for a high-performance aircraft, and

demonstrates the use of  $\Gamma$ - and  $\mathcal{B}$ -stability specifications to design a controller that is robust to both parametric and unstructured uncertainty. This is a challenging problem, as the controlled pitch-rate response must satisfy strict performance requirements despite the fact that the aircraft dynamics vary significantly throughout the flight envelope. The design uses an analytical model of the short period equations of motion that describes the dependence of the aircraft's pitch dynamics on altitude and Mach number over a large flight envelope. In addition to the parametric "uncertainty" introduced by this model, the design also incorporates unstructured uncertainty to account for unmodelled dynamics (e.g. flexible modes of the aircraft).  $\Gamma$ - and  $\mathcal{B}$ -stability specifications are mapped into parameter space to obtain a robust controller that guarantees the required performance throughout the design envelope despite the model uncertainty.

## 7.1 Aircraft Load Alleviation in case of an Engine Out by Robust Yaw-lateral Decoupling

Engine out, abbreviated EO, is a design-critical operating condition for large transport aircraft from the viewpoint of flight safety, handling qualities, robust design of the electronic flight control system, comfort, structural dynamics (structural loads), and static aircraft structure design. As the EO constitutes a yaw disturbance torque, see Figure 7.1 for the stable lateral aircraft motion, the EO by itself is not harmful to the aircraft. Nevertheless, large magnitudes of the yaw rate, the sideslip angle and the roll rate occur. Several authors [85], [110], [141], [46], [129], [127] have revealed the poten-

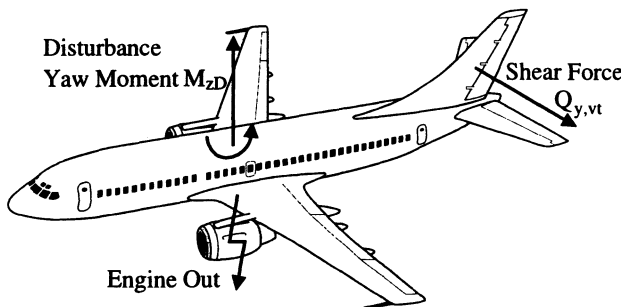


Figure 7.1. Disturbance torque from an engine out results in a shear force at the vertical tail

tial of modern control systems and electrohydraulic actuation technology to increase the already high safety standards and to fulfill stronger requirements than those which the above-mentioned disciplines impose today. Favre [85] discusses the integration of the EO problem into the design of the standard lateral command and stability augmentation system (CSAS). The CSAS is based on the measurement or the observation of the yaw and the roll rate, the bank angle [140] and, optionally, the sideslip angle.

The aircraft is safely stabilized after the EO. The corresponding equilibrium condition is characterized by significant magnitudes of the yaw rate, the sideslip, and the bank angle, which clearly indicate the EO condition and cause the pilot to interact early, but without overreaction in order to stabilize the aircraft with zero yaw rate and low bank angle and to recover the original flight path. Hopkins [110] and McLean [141] use standard controller design methodologies to design a command and stability augmentation system, which is only activated after the detection of the EO. The system is therefore termed the EO controller. In contrast to Favre [85], no significant magnitudes of the yaw rate, the sideslip, or the bank angle occur. McLean [141] focuses on a general aviation aircraft. As Hopkins [110] describes a new system of the *Boeing B777*, only a few details with regard to the design and the architecture of the system are given. Benani, Magni and Terlouw [46] and Lambregts [129] integrate the EO control problem into the autopilot design. As the autopilot is based on more measured or estimated quantities than the CSAS (e.g. quantities characterizing the flight path), good performance can be achieved more easily than in the case of the command and stability augmentation system. The above authors already cover the requirements of the initially mentioned disciplines handling qualities, safety and comfort. Benani, Magni and Terlouw [46] and Lambregts [129], moreover, tackle the robustness requirements.

Here, we investigate whether the aspects of structural dynamics (load alleviation at the vertical tailplane) and thereby of the static aircraft structure design can be integrated into the design of an EO controller. During an EO and the corresponding corrective pilot action, large loads, i.e. shear forces, bending and torsion moments occur at the vertical tailplane. In fact, the EO case is a sizing case for the structural dynamic and the static design of the vertical tailplane. One third of the structural dynamic simulation time is spent on this case because the changing mass and mass distribution and the uncertain aerodynamic properties, in particular due to variations of the velocity, the altitude, and the flap-/slat-setting, have to be covered. A considerable saving in structural weight of the vertical tailplane is possible if the maximal loads are reduced. The main contribution to the loads at the vertical tailplane are the aerodynamic forces due to the sideslip angle, the rudder deflection and the inertia term [135].

Consequently, for the structural loads computation and the resulting design of the vertical tailplane, a worst case rudder deflection commanded by the pilot and a worst case sideslip angle have to be considered. According to the Joint-Aviation-Requirements JAR 25.367 [114], [135] the pilot begins to react at the first maximum of the yaw rate, but not earlier than 2 seconds after the EO. In consequence of the 2 seconds delay, a large sideslip angle has built up. The pilot reaction is then to reduce the yaw rate by the maximal rudder deflection rate until the derivative  $\dot{\beta}$  of the sideslip angle passes zero, i.e. they pushes the pedal into the stops as quickly as they can. Consequently, the rudder can even reach the rudder travel limitation. Afterwards, the pilot reduces the rudder deflection angle to a value that is approximately required to maintain  $\dot{\beta} = 0$ . Thereby, the essential characteristics of a human controller in a disturbance rejection problem are covered:

1. The human controller is possibly too slow due to their reaction time.
2. In a delayed corrective action, they may even overreact and make a critical situation worse.

The same aspects can be observed in a yaw moment disturbance rejection in the case of a car. An example is the skidding of a car on an icy road. The driver reacts when already a considerable yaw rate has been built up and an overreaction may drive the tire force into saturation. Such a safety-critical situation can be avoided by an automatic yaw control system, with feedback of the yaw rate to a corrective steering angle that is added to the driver-commanded steering angle. This control system will compensate the disturbance torque faster and more accurately than the human driver, see Chapter 6.

This control concept is transferred to the EO problem of the aircraft, constituting of a feedback of the yaw rate to the rudder: due to the early feedback of the yaw rate measurement after the EO, such a system can react faster and more accurately to the disturbance torque than the pilot. The yaw rate after the EO is kept small, there is no reason for a corrective reaction of the pilot, and there is very little energy transfer to the roll motion. Moreover, the shear force reduction at the vertical tailplane is explicitly considered in the controller design.

The essential aspect of the control concept is that the effect of a yaw disturbance torque is compensated so fast in the planar lateral motion that in the closed-loop system the coupling into other degrees of freedom is small, in particular, the yaw rate (which is an unavoidable initial consequence of the EO yaw disturbance torque) should not influence the lateral acceleration. The planar lateral motion consists of the lateral translational motion and the rotational (yaw) motion, which are bidirectionally coupled. Within this planar lateral motion, the controller achieves a separation into the following two subsystems:

- A first order system for generating the lateral acceleration at a decoupling point which is close to the vertical tailplane.
- A second order subsystem involving the yaw rate.

In the controlled system, there is only a coupling from the lateral acceleration to the yaw rate, but not vice versa. The system is unilaterally decoupled in the sense that the yaw rate is made non-observable from the lateral acceleration at the decoupling point, see Section 6.3. Hence, the yaw rate in consequence of the EO will not influence the lateral acceleration. Exploiting the design freedoms in the controller allows us to achieve a yaw rate that has approximately no influence on the shear force.

An important requirement for both the car and the airplane application is the robustness of the unilateral decoupling controller. For the car, the control concept allows us to achieve robustness with respect to the uncertain tire side force characteristics, the mass and the velocity. For the aircraft, robustness has to be achieved with respect to the uncertain aerodynamics, in particular due to the variation of the velocity, the altitude and the flap-/slat-settings, and with respect to the changing mass.

In contrast to the car, the aircraft is already equipped with a lateral control system. As this system is designed to use only moderate control surface deflection angles [85], the drastic EO controller is switched on with full authority after the detection of the EO. Simultaneously, the standard controller is immediately switched off. For simple detection mechanisms, detection times up to 500 [ms] have to be assumed. More sophisticated detection mechanisms yield a detection time of 20 [ms].

## Robust Unilateral Decoupling

For cars, it is usual to describe the steering motion in a plane on road surface level. In the case of an aircraft, the planar motion is strongly coupled with the roll motion due to the vertical tail (fin) and the different lift of the left and right wing due to different velocities under a yaw motion. This coupling is important for stability and manoeuvrability [82], [140]. The disturbance torque of an EO fault and the compensating torque from the rudder deflection occur essentially in the body-fixed  $(x, y)$ -plane [135]. A design goal is to prevent the energy resulting from the unbalanced engine after the EO from being transferred from the yaw motion into the roll motion. This should not affect the yaw motion, which has been commanded by the pilot.

Only the disturbance-induced yaw motion and the corresponding disturbance-induced energy flow should be kept low. To achieve this, the coupled yaw and lateral translational motion resulting from EO has to be kept small. In order to distinguish between a yaw rate that has been commanded by the pilot, and a yaw rate in consequence of an engine out, the EO controller has to be combined with a prefilter generating the reference yaw rate  $r_{ref}$  from the pilot command. The disturbance is already compensated within the planar lateral motion after having induced only small deviations from the reference yaw rate. If this goal is to be achieved, then this is an a posteriori justification for using a planar model to derive the controller structure.

If the disturbance only induces small amplitudes in the closed-loop system, then even non-linear effects [82], [140] can be neglected in the controller design. Such a linear planar model allows us to design a simple controller for the aircraft in detailed analogy to the car. Due to the superposition principle of linear system theory, the prefilter design can be straightforwardly done after the controller design, so that only the case  $r_{ref} \equiv 0$  is considered here for brevity. The prefilter is analyzed in non-linear simulations in [127]. The planar model is illustrated by Figure 7.2. In the case of the car, the starting point of the controller design are the lateral forces between the tires and the road, see Chapter 6. They are concentrated at the front and the rear axes,  $F_{Y,F}$  and  $F_{Y,R}$  in Figure 7.2. The corresponding lever arms are  $l_F$  and  $l_R$ .

In the case of the aircraft, such a pair of forces in the  $(x, y)$ -plane can be introduced by discretizing the distributed aerodynamic forces and summing them up for wing, fuselage and pods:  $F_{Y,wfp}$  and for the tail:  $F_{Y,tail}$ , see Figure 7.2.  $F_{Y,wfp}$  depends on the state  $\mathbf{x}$  of the aircraft and has a lever arm  $l_{wfp}$  with respect to the center of gravity (CG). The state  $\mathbf{x} = [\beta \ r]^T$  consists of the yaw rate  $r$  and the sideslip angle  $\beta$ . Within linear aerodynamic theory,  $F_{Y,wfp}(\mathbf{x})$  can be expressed by aerodynamic derivatives

$$F_{Y,wfp}(\mathbf{x}) = Y_{\beta,wfp}\beta + (b/V_{TAS})Y_{r,wfp}r, \quad (7.1.1)$$

where  $b$  is a reference length like the half span length and  $V_{TAS}$  is true airspeed [82]. The force derivatives  $Y_{\beta,wfp}$ ,  $Y_{r,wfp}$  result from windtunnel tests, which are validated by flight tests. They depend on varying parameters: velocity, altitude and wing configuration, i.e. flap-/slat-setting [140], [82]. In that sense,  $F_{Y,wfp}$  is an uncertain function. The force  $F_{Y,tail}(\mathbf{x}, \delta_R)$  depends on both the state  $\mathbf{x}$  and the input of the system, i.e. the rudder deflection angle  $\delta_R$ , see Figure 7.2. In analogy to (7.1.1),  $F_{Y,tail}$  is given by

$$F_{Y,tail}(\mathbf{x}, \delta_R) = Y_{\beta,tail}\beta + (b/V_{TAS})Y_{r,tail}r + Y_{\delta_R}\delta_R. \quad (7.1.2)$$

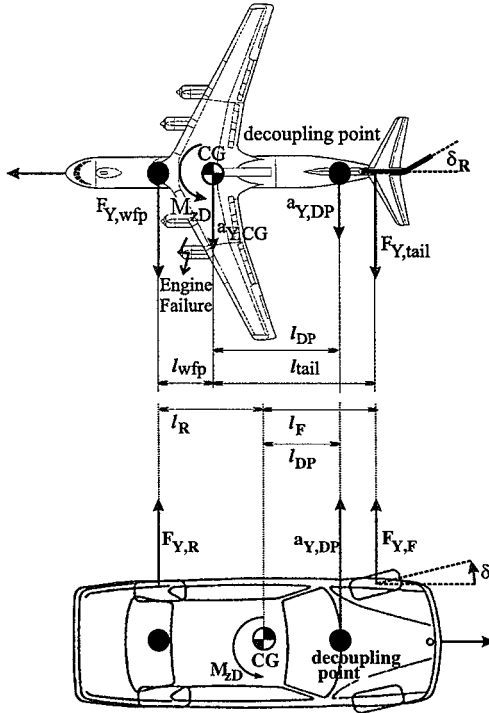


Figure 7.2. Planar model for the compensation of a yaw disturbance torque  $M_{zD}$  (engine out torque/ $\mu$ -split braking torque) by a rudder deflection angle  $\delta_R$  / front tire angle  $\delta$

The lever arm of  $F_{Y,tail}$  is  $l_{tail}$ . The derivatives  $Y_{\beta,tail}$ ,  $Y_{r,tail}$  and  $Y_{\delta_R}$  depend on the same varying parameters as  $Y_{\beta,wfp}$ ,  $Y_{r,wfp}$ . In that sense,  $F_{Y,tail}$  is an uncertain function. Ideally, the desired balance of torques would be achieved by choosing the rudder deflection angle  $\delta_R$  such that

$$F_{Y,wfp}(\mathbf{x}) l_{wfp} - F_{Y,tail}(\mathbf{x}, \delta_R) l_{tail} + M_{zD} = 0. \quad (7.1.3)$$

The forces and the disturbance torques are unknown, however, such that a robust implementation of the control laws resulting from (7.1.3) is impossible.

An alternate approach was very successful in the automotive application and is applied to the aircraft here. The idea is to split the vehicle dynamics robustly into two subsystems. A first order subsystem with output lateral acceleration should not be influenced by the yaw rate. A simple choice would be the decoupling of the lateral acceleration at the CG. Then, however, the yaw rate  $r$  as part of the state  $\mathbf{x}$  enters into  $a_{Y,CG}$  via both unknown forces  $F_{Y,wfp}(\mathbf{x})$  and  $F_{Y,tail}(\mathbf{x}, \delta_R)$ , and again the ideal robustness cannot be achieved. Therefore, we first define a *decoupling point* DP in a distance  $l_{DP}$  from the CG so that  $F_{Y,wfp}(\mathbf{x})$  does not enter into the lateral acceleration  $a_{Y,DP}$  at the

decoupling point. The latter is

$$a_{Y,DP} = a_{Y,CG} - l_{DP}\dot{r}. \quad (7.1.4)$$

Here,  $a_{Y,CG}$  and  $\dot{r}$  are expressed in terms of the pair of forces:

$$a_{Y,CG} = \frac{F_{Y,wfp} + F_{Y,tail}}{m}, \quad (7.1.5)$$

$$\dot{r} = \frac{F_{Y,wfp} l_{wfp} - F_{Y,tail} l_{tail} + M_{zD}}{I_z}, \quad (7.1.6)$$

where  $m$  is the mass and  $I_z$  is the moment of inertia of the aircraft. This yields

$$\begin{aligned} a_{Y,DP} &= \frac{F_{Y,wfp} + F_{Y,tail}}{m} \\ &\quad - l_{DP} \frac{F_{Y,wfp} l_{wfp} - F_{Y,tail} l_{tail} + M_{zD}}{I_z} \\ &= F_{Y,wfp} \left( \frac{1}{m} - \frac{l_{DP} l_{wfp}}{I_z} \right) \\ &\quad + F_{Y,tail} \left( \frac{1}{m} + \frac{l_{DP} l_{tail}}{I_z} \right) - \frac{l_{DP}}{I_z} M_{zD}. \end{aligned} \quad (7.1.7)$$

The location  $l_{DP}$  of the decoupling point is calculated from the condition that the factor of  $F_{Y,wfp}$  is zero, i.e.

$$l_{DP} = \frac{I_z}{m l_{wfp}} \quad (7.1.8)$$

and for this choice of  $l_{DP}$ , we have

$$a_{Y,DP} = F_{Y,tail}(\mathbf{x}, \delta_R) \frac{l_{wfp} + l_{tail}}{m l_{wfp}} - \frac{1}{m l_{wfp}} M_{zD}. \quad (7.1.9)$$

Note that this derivation of the decoupling point is done in complete physical analogy to the derivation of the decoupling point in the case of the car in (6.2.4). Equation (7.1.8) corresponds to a representation of the mass and the moment of inertia by two masses in the positions  $l_{wfp}$  and  $l_{DP}$  from the CG. The position  $l_{DP}$  of the decoupling point is close to the vertical tail and varies only slightly with the distribution of the mass, i.e. with the payload and with the fuel consumption. For controller design, it is therefore assumed to be constant. The induced error has to be analyzed in a detailed assessment of the closed-loop system by a non-linear high precision simulation.

According to (7.1.9) and (7.1.2), the lateral acceleration  $a_{Y,DP}$  at the decoupling point depends on the yaw rate  $r$  only via the uncertain function  $F_{Y,tail}(\beta, r, \delta_R) = Y_{\beta,tail}\beta + (b/V_{TAS})Y_{r,tail}r + Y_{\delta_R}\delta_R$ . The crucial step for robustly eliminating the influence of  $r$  on  $a_{Y,DP}$  by a robust unilateral decoupling controller is to choose the rudder deflection angle  $\delta_R$  such that it cancels  $r$  in the argument of the function  $F_{Y,tail}(\beta, r, \delta_R)$ , see Figure 7.3 and 7.4. More precisely,  $a_{Y,DP}$  shall be robustly decoupled from the yaw rate by a controller, i.e. the yaw rate should be not observable from  $a_{Y,DP}$  for all variations in mass and aerodynamics due to variations in velocity, altitude and flap-/slat-setting.

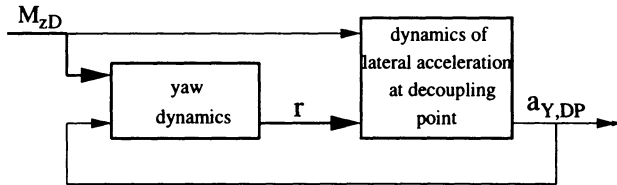


Figure 7.3. Bidirectional coupling between the lateral acceleration  $a_{Y,DP}$  at the decoupling point DP and the yaw rate  $r$  in the planar lateral aircraft motion in the case of an engine out disturbance torque  $M_{zD}$

These variations are equivalent to variations in  $l_{wfp}$ ,  $l_{tail}$ ,  $m$ ,  $F_{Y,tail}$ , and  $F_{Y,wfp}$ , [82] and [140]. Physically speaking, the yaw rate  $r$  grows rapidly after the EO and induces a large acceleration  $a_{Y,DP}$  and large shear forces at the vertical tail. It is this dominating effect which the robust unilateral decoupling EO controller (in the following abbreviated by r. u. d. EO controller) directly compensates. Detailed numerical simulations in the next section reveal that the remaining immediate effect of the EO on  $a_{Y,DP}$  in terms of  $(1/m l_{wfp}) N_{zD}$  has an acceptable level from the viewpoint of structural dynamics and handling qualities.

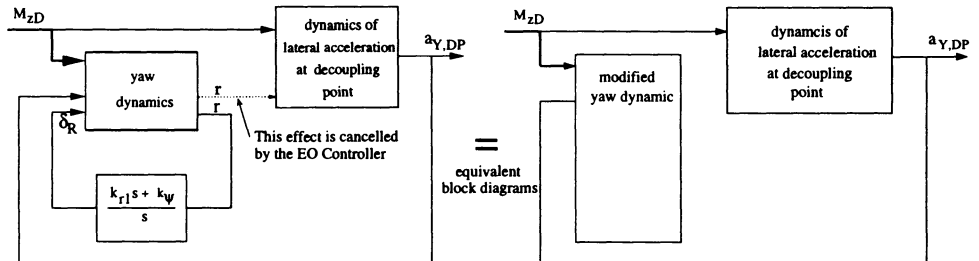


Figure 7.4. Robust unilateral decoupling of the lateral acceleration  $a_{Y,DP}$  from the yaw rate  $r$  by a dynamic feedback of the yaw rate to the rudder in case of an engine out. Thereby, the shear force is reduced

So far, only the requirement of safe flight path stabilization is directly covered by this physical controller design approach. Next, the requirement for low shear forces  $Q_{y,vt}$  at the vertical tail (load alleviation) has to be incorporated into the controller design approach.  $Q_{y,vt}$  is approximately given by Lomax [135] as

$$Q_{y,vt} \approx -m_{tail} a_{Y,tail} + F_{Y,tail}, \quad (7.1.10)$$

where  $m_{tail}$  is the mass of the vertical tail. As the decoupling point is close to the vertical tail for all operating conditions of the aircraft, the lateral acceleration at the decoupling point  $a_{Y,DP}$  approximates the lateral acceleration  $a_{Y,tail}$  at the vertical tail. The yaw rate

is made robustly non-observable from  $F_{Y,tail}$  and by (7.1.10) also from  $Q_{y,vt}$ . Hence, the controller design approach covers the requirement to alleviate the loads at the vertical tail.

Next, the r. u. d. EO controller is symbolically derived. The rudder angle is composed of a reference part  $\delta_{R,pilot}$  and a feedback part:  $\delta_{R,control}$  resulting from the r. u. d. EO controller:

$$\delta_R = \delta_{R,pilot} + \delta_{R,control}. \quad (7.1.11)$$

In the closed-loop system, the differential equation of  $F_{Y,tail}$  should not depend on the yaw rate  $r$ , i.e. it should have the general form

$$\dot{F}_{Y,tail} = f(F_{Y,tail}, \delta_{R,pilot}, \dot{\delta}_{R,pilot}, M_{zD}). \quad (7.1.12)$$

Next, it is shown that already a first order controller structure is sufficient for fulfilling the condition (7.1.12):

$$\begin{aligned} \dot{\delta}_{R,control} &= k_\psi r + k_r \dot{r} + K_{prefilter} \delta_{R,pilot}, \\ \delta_R &= \delta_{R,control} + \delta_{R,pilot}, \end{aligned} \quad (7.1.13)$$

with free controller parameters  $k_\psi$  and  $k_r$ . To show this, the differential equations for  $\beta$  and  $r$  are expressed in terms of  $F_{Y,wfp}$  and  $F_{Y,tail}$ :

$$\begin{aligned} \dot{\beta} &= ((F_{Y,wfp} + F_{Y,tail})/mV_{TAS}) - r, \\ \dot{r} &= (l_{wfp}F_{Y,wfp} - l_{tail}F_{Y,tail} + N_{zD})/I_z. \end{aligned} \quad (7.1.14)$$

Now, differentiating (7.1.2) and then substituting  $\dot{\beta}$ ,  $\dot{r}$  and  $\dot{\delta}_R$  by the expressions in Equations (7.1.11), (7.1.13) and (7.1.14) yields:

$$\begin{aligned} \dot{F}_{Y,tail} &= (Y_{\delta_R} k_\psi - Y_{\beta,tail})r \\ &+ (Y_{\delta_R} k_r + \frac{b}{V_{TAS}} Y_{r,tail}) \frac{l_{wfp}F_{Y,wfp} - l_{tail}F_{Y,tail} + M_{zD}}{I_z} \\ &+ Y_{\beta,tail} \frac{F_{Y,wfp} + F_{Y,tail}}{mV_{TAS}} \\ &+ Y_{\delta_R} (K_{prefilter} \delta_{R,pilot} + \dot{\delta}_{R,pilot}). \end{aligned} \quad (7.1.15)$$

Then, requiring the explicit terms in  $r$ , i.e.  $(Y_{\delta_R} k_\psi - Y_{\beta,tail})r$ , to be cancelled, allows us to derive the controller parameter  $k_\psi$  symbolically:

$$k_\psi = Y_{\beta,tail}/Y_{\delta_R}. \quad (7.1.16)$$

However,  $r$ -dependent terms also implicitly enter in (7.1.15) via the terms in  $F_{Y,wfp}$ . By choosing

$$k_r = \frac{-1}{Y_{\delta_R} V_{TAS}} (l_{DP} Y_{\beta,tail} + b Y_{r,tail}), \quad (7.1.17)$$

all terms in  $F_{Y,wfp}$  cancel. Herein, (7.1.8) has been used. With this choice of controller parameters, the differential equation for  $F_{y,tail}$  is

$$\begin{aligned}\dot{F}_{y,tail} &= \left( \frac{b}{V_{TAS}} Y_{r,tail} + Y_{\delta_R} k_r \right) \frac{-l_{tail} F_{y,tail} + M_{zD}}{I_z} \\ &+ Y_{\beta,tail} \frac{F_{y,tail}}{m V_{TAS}} \\ &+ Y_{\delta_R} (K_{prefilter} \delta_{R,pilot} + \dot{\delta}_{R,pilot}).\end{aligned}\quad (7.1.18)$$

This equation shows that the yaw rate  $r$  of the controlled system has no influence on  $F_{Y,tail}$  and by Equation (7.1.9) also no influence on  $a_{Y,DP}$ . Hence, the choice of the controller structure is adequate to derive a robust gain-scheduling controller, which makes  $F_{Y,tail}$  independent of the yaw rate for all variations of the mass and the aerodynamics. Since the variations of the aerodynamic derivatives of the tail  $Y_{\beta,tail}$ ,  $Y_{r,tail}$  and  $Y_{\delta_R}$  can be expressed in terms of the variations of the velocity, the altitude and the flap-/slat-setting [82], [140], and as  $l_{DP}$  is assumed to be constant, a gain-scheduling is only required in the velocity, the altitude and the flap-/slat-setting, which can be easily measured.

It is an essential robustness advantage of the controller that it does not depend on the aerodynamic derivatives  $Y_{\beta,wfp}$  and  $Y_{r,wfp}$  of Equation (7.1.1), because these derivatives cannot be exactly expressed in terms of the velocity, the altitude and the flap-/slat-setting, [82], [140]. Hence, these derivatives would have induced an uncertainty in the gain-scheduling. As the rudder deflection angle  $\delta_R$  is the input, the controller consists of a proportional and an integral feedback of the yaw rate. It has to be emphasized that the controller is not a standard PI controller, which primarily ensures steady state accuracy.

The controller, (7.1.13), (7.1.16), (7.1.17), essentially achieves the robust decoupling of  $F_{Y,tail}$  from the yaw rate. By doing a state transformation in Equation (7.1.14) from  $[\beta \quad r]^T$  to  $[a_{Y,DP} \quad r]^T$  and then computing the closed-loop system makes the unilateral decoupling more evident. The yaw and the controller dynamics

$$\begin{aligned}\begin{bmatrix} \dot{r} \\ \dot{\delta}_{R,control} \end{bmatrix} &= \begin{bmatrix} a_{22} & a_{23} \\ a_{32} & a_{33} \end{bmatrix} \begin{bmatrix} r \\ \delta_{R,control} \end{bmatrix} \\ &+ \begin{bmatrix} a_{21} \\ a_{31} \end{bmatrix} [ a_{Y,DP} ] \\ &+ \begin{bmatrix} b_{21} \\ b_{31} \end{bmatrix} [ \delta_{R,pilot} ] \\ &+ \begin{bmatrix} e_{21} \\ e_{31} \end{bmatrix} [ M_{zD} ]\end{aligned}\quad (7.1.19)$$

still depend on  $a_{Y,DP}$ , but the dynamics of the lateral acceleration at the DP

$$\begin{aligned}[\dot{a}_{Y,DP}] &= [a_{11}] [a_{Y,DP}] \\ &+ [b_{11} \quad b_{12}] \begin{bmatrix} \delta_{R,pilot} \\ \dot{\delta}_{R,pilot} \end{bmatrix} \\ &+ [e_{11} \quad e_{12}] \begin{bmatrix} M_{zD} \\ \dot{M}_{zD} \end{bmatrix}\end{aligned}\quad (7.1.20)$$

are robustly decoupled from the yaw and the controller dynamics, Figure 7.4. The decoupled first order dynamics have additional advantage that any maneuver that the pilot performs in an EO will not excite any complex dynamics but only moderate first order transients in  $a_{Y,DP}$  will occur.

To provide the coefficients of the robust unilateral decoupled state space model, Equation (7.1.19), (7.1.20), it is useful to express the sum of the planar linear lateral aerodynamic forces and corresponding moments by the standard aerodynamic force and moment derivatives  $Y_\beta$ ,  $Y_r$ ,  $Y_{\delta_R}$ ,  $N_\beta$ ,  $N_r$ ,  $N_{\delta_R}$  [140], [82]:

$$\begin{aligned} F_{Y,wfp} + F_{Y,tail} &= \underbrace{(Y_{\beta wfp} + Y_{\beta,tail})\beta}_{=: Y_\beta} \\ &\quad + b/V_{TAS} \underbrace{(Y_{r,wfp} + Y_{r,tail}))r}_{=: Y_r} + Y_{\delta_R}\delta_R \end{aligned} \quad (7.1.21)$$

and, equivalently,

$$\begin{aligned} l_{wfp}F_{Y,wfp} - l_{tail}F_{Y,tail} &= N_\beta\beta + (b/V_{TAS})N_rr \\ &\quad + N_{\delta_R}. \end{aligned} \quad (7.1.22)$$

The differential equations of the planar lateral motion, (7.1.14), can then be rewritten as

$$\dot{r} = \frac{1}{I_z}(\bar{N}_rr + N_\beta\beta + N_{\delta_R}\delta_R), \quad (7.1.23)$$

$$\dot{\beta} = \frac{1}{mV_{TAS}}(\bar{Y}_r + Y_\beta\beta + Y_{\delta_R}\delta_R) - r, \quad (7.1.24)$$

$$\text{where } \bar{N}_r = (b/V_{TAS})N_r, \quad \bar{Y}_r = (b/V_{TAS})Y_r.$$

The coefficients of the state space model, (7.1.19), can be directly derived from (7.1.4), (7.1.5), (7.1.21), (7.1.14), (7.1.23), and (7.1.13). They read:

$$\begin{aligned} a_{22} &= \frac{K_1}{mV_{TAS}I_z}(Y_\beta\bar{N}_r - \bar{Y}_rN_\beta), \quad \text{where:} \\ K_1 &= V_{TAS}/(Y_\beta/m - N_\beta l_{DP}/I_z), \\ a_{23} &= b_{21} = \frac{K_1}{mV_{TAS}I_z}(Y_\beta N_{\delta_R} - Y_{\delta_R}N_\beta), \\ a_{21} &= K_1 N_\beta / (m V_{TAS} I_z), \\ e_{21} &= K_1 Y_\beta / (m V_{TAS} I_z), \\ a_{32} &= k_\psi + k_r a_{22}, \\ a_{33} &= k_r a_{23}, \\ b_{31} &= K_{prefilter} + k_r b_{21}, \\ e_{31} &= k_r e_{21}. \end{aligned}$$

The coefficients of the state space model, (7.1.20), can be directly derived from (7.1.9) and (7.1.18). They read:

$$\begin{aligned} a_{11} &= -K_2 l_{tail}/I_z + Y_{\beta,tail}/(mV_{TAS}), \quad \text{where:} \\ K_2 &= Y_{\delta_R} k_r + (b/V_{TAS}) Y_{r,tail}, \\ b_{11} &= Y_{\delta_R} K_{Prefilter}(l_{wfp} + l_{tail})/(ml_{wfp}), \\ b_{12} &= Y_{\delta_R}(l_{wfp} + l_{tail})/(ml_{wfp}), \\ e_{11} &= K_2/(mI_z) + Y_{\beta,tail}/(m^2 V_{TAS} l_{wfp}), \\ e_{12} &= -1/(ml_{wfp}). \end{aligned}$$

### *Application to Aircraft Load Reduction*

To analyze the application of the robust unilateral decoupling EO controller (r. u. d. EO controller) to an aircraft encountering an EO, it has to be compared with a standard lateral controller of an electronic flight control system (EFCS) in the following abbreviated by the normal law. This normal law consists of a feedback of the yaw rate  $r$ , the sideslip angle  $\beta$ , the roll rate  $p$ , and the bank angle  $\phi$  to the rudder and the aileron deflection angles  $\delta_R$  and  $\delta_A$ . It has to ensure a sufficient stability margin and to fulfill standard handling quality and performance criteria [82], [140]. For an adequate comparison, the r. u. d. EO controller has to be consistently integrated into such a normal law [127].

The EO is simulated as a worst case, i.e. the thrust is reduced in the form of a step from maximum thrust to zero. This corresponds to a burst or the initial dynamics in the case of a flame out or a mechanical fault and yields a quicker loss in thrust than in the case of a very simple first order modelling of the engines [46]. The r. u. d. EO controller is switched on after a detection time of 20 [ms] [60]. Detection times of 0.5 [s], resulting from less sophisticated detection mechanisms, are considered later. For structural dynamic analysis, a second comparison is necessary, i.e. a corrective rudder deflection of the pilot according to JAR 25.367 [114], [135] has to be superimposed over the rudder deflection from the normal law. This corrective pilot action was defined in the introduction and is illustrated by the corresponding rudder deflection angle in Figure 7.5 and the yaw rate  $r$  in Figure 7.6. The large yaw rate  $r$ , which has been built up within the first two seconds after the EO, explains the large corrective rudder deflection of the pilot. This case is abbreviated by the normal law + pilot. Simulations are performed on a non-linear high-precision model with the following characteristics [82], [140]: i) complete non-linear differential equation for the rigid body motion, ii) detailed non-linear aerodynamic model, iii) structural flexibility, approximated by flexible factors (residual stiffness method [140]), iv) non-linear actuator and electronic flight control system (normal law) modelling.

Flight conditions characterized by a low altitude and a low velocity are the most critical operating conditions in the case of an EO. These are take-off conditions, with maximum thrust and therefore maximal disturbing yaw moment, requiring the largest rudder deflection angles for stabilization, which in turn cause large loads at the vertical tail. To show robustness, eleven critical operating conditions (i.e. different mass

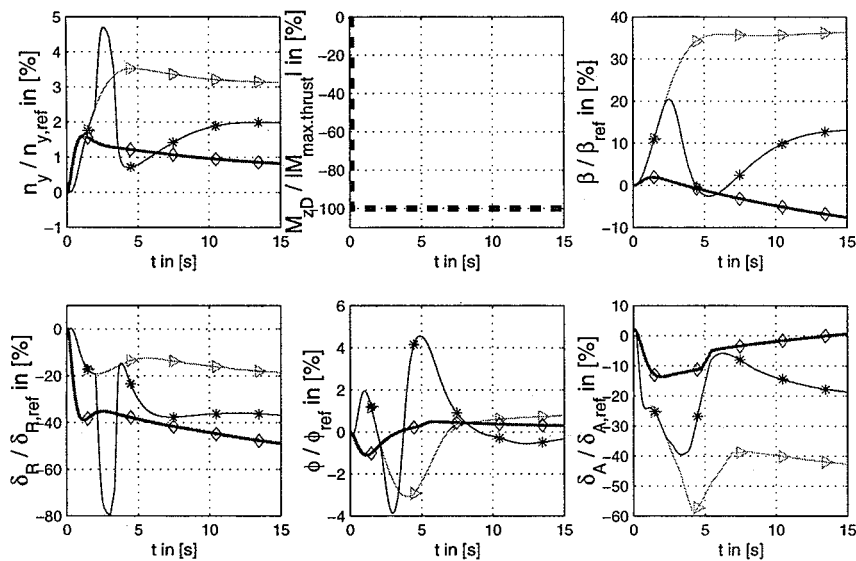


Figure 7.5. Time histories of lateral load factor  $n_y$  at CG, engine out moment  $M_{zD}$ , sideslip angle  $\beta$ , rudder deflection  $\delta_R$ , bank angle  $\phi$  and aileron deflection  $\delta_A$  for a critical flight condition in the case of EO on left side ( $>$ : normal law,  $*$ : normal law + pilot,  $\diamond$ : r. u. d. EO controller). The yaw rate is given in Figure 7.6

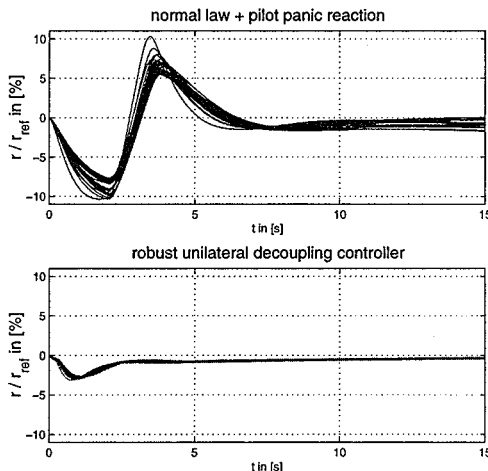


Figure 7.6. Time histories of the yaw rate  $r$  for the comparison of the r. u. d. EO controller switched on after a detection time of 20 [ms] and the normal law + pilot for eleven flight conditions at  $M = 0.2$  and 0.35 at “zero” altitude

and mass distribution) at  $M = 0.2$  and  $0.35$  and zero altitude are considered. These operating conditions yield the highest loads at the vertical tail in both cases with and without the r. u. d. EO controller.

### *Structural Dynamic and Robustness Analysis*

A first indicator for an adequate dynamic performance is the lateral acceleration  $n_y$  at the CG in units of the constant of gravity  $g$ , usually referred to as the lateral load factor. The first transient peak is reduced to one third compared to the normal law + pilot and to one half compared to the normal law, Figure 7.5, which shows that an automatic control system can fully prevent critical scenarios within man's reaction time (in Figure 7.5, 7.6 and 7.7 the reference or scaling values,  $n_{y,ref}$ , etc. are maximal values that are derived or roughly estimated from maneuvers of civil and military aircraft covering the whole flight envelopes. As here only a maneuver of a civil aircraft is considered, a ratio of 100 % does not occur).

In other words, what has been missed in the first two seconds, i.e. the two-third extra amplitude in  $n_y$  can be compensated for later on at only the cost of substantially higher loads and unwanted coupling into the roll motion. In stationary values, there is a reduction of more than one third (normal law) and of one half (normal law + pilot), which again shows the advantages of an early drastic compensation.

In structural dynamics and in statics, the shear force at the vertical tail  $Q_{y,vt}$  and the corresponding bending  $M_{x,vt}$  and torsion moments  $M_{z,vt}$  at the vertical tail are analyzed in phase diagrams, so-called *phase loads diagrams*, see Figure 7.7. Critical operating conditions are represented by regions in phase loads diagrams. Here, a local structural dynamic coordinate system has been chosen: the  $x$ - and  $z$ -axis are inverted and rotated around the  $y$ -axis (by the swept-back angle of the vertical tail) so that the  $z$ -axis is parallel to the elastic axis of the vertical tail. Figure 7.7 compares the r. u. d. EO controller (center, right) with the normal law + pilot (left). Two detection times for the EO are considered: a time of 20 [ms] (Figure 7.7, center) and a time of 0.5 [s] (right). Figure 7.7 indicates that the regions of simultaneously large shear force and torsion moment are avoided in a nearly ideal way in consequence of the r. u. d. EO controller. The extreme values in shear force and torsion moment are nearly reduced to one half by the r. u. d. EO controller. In more detail, the r. u. d. EO controller reduces peaks in the transients of the shear force by more than one half (normal law + pilot), whereas the stationary values are reduced by 50 % compared to the normal law + pilot. Concerning the torsion moment  $M_{z,vt}$ , the r. u. d. EO controller reduces the transient peak (normal law + pilot) by 55 % and brings about a much better performance in transients than the normal law + pilot. This is a result of the achieved reduction in sideslip angle, Figure 7.5, showing the interplay between flight mechanics and structural dynamics. The achieved robustness is remarkable, i.e. the area covered by all the various phase curves corresponding to different flight conditions is nearly condensed to one curve. For static analysis, this means significantly reduced work in assessment. Even more important is that in consequence of the achieved load reduction for future large aircraft, the vertical tail can become lighter in combination with the r. u. d. EO controller than for today's aircraft.

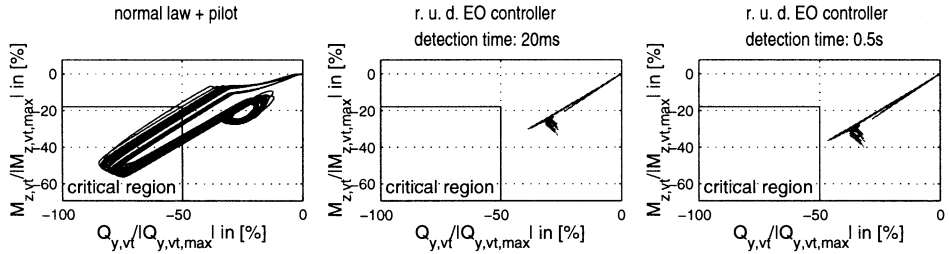


Figure 7.7. Phase loads diagram: shear force  $Q_{y,vt}$  against torsion moment  $M_{z,vt}$  at the vertical tail, comparison of the normal law + pilot and r. u. d. EO controller for eleven flight conditions at  $M = 0.2$  and  $0.35$  at “zero” altitude. In the case of the r. u. d. EO controller, a detection time of  $20$  [ms] (center) and of  $0.5$  [s] (right) are considered

### Flight Mechanical and Robustness Analysis

In contrast to the normal law and the normal law + pilot, the r. u. d. EO controller avoids large magnitudes in transient and final states, in particular in the yaw rate  $r$ , see Figure 7.5 and 7.6. Thereby, large aircraft motions in consequence of the EO are avoided so that any pilot interference becomes unnecessary. The reference or scaling values  $n_{y,ref}$ ,  $\beta_{ref}$ ,  $\delta_{R,ref}$ ,  $\delta_{A,ref}$ ,  $\phi_{ref}$ , and  $r_{ref}$  are maximal values that are derived from maneuvers of civil and military aircraft covering the whole flight envelopes. The r. u. d. EO controller achieves such a performance by an immediate and sufficiently strong rudder command, nearly reaching the final rudder deflection angle for yaw moment compensation already after one second. Therefore, the EO is fully compensated, i.e. the aircraft is in a nearly steady state after a second, which is half the pilot’s reaction time according to JAR 25.367, see in particular the yaw rate  $r$  in Figure 7.6. Additionally, the commanded rudder rate is lower than that in the case of the corrective pilot action. The later the yaw moment compensation is achieved, the more energy is transferred into the roll motion and the more aileron activity is necessary to compensate and to reduce this effect. Therefore, the reduced rudder deflection angle in the case of the normal law has to be compensated by large aileron and spoiler angles, Figure 7.5. Moreover, this means being far away from an optimal flight condition in terms of an optimal lift, flight safety, passenger comfort, heading, and drag. Concerning the flight mechanical quantities in more detail, the following improvements can be observed:

#### i. yaw rate and bank angle

The yaw rate  $r$ , which directly indicates the achieved yaw moment compensation, is reduced to less than one third in transient peaking compared to the normal law and the normal law + pilot, Figure 7.6. After one second, the yaw acceleration already changes its sign, so that there will be no reason for any overreaction. The yaw rate goes to zero sufficiently fast. Therefore, only little deviations will occur in heading in contrast to the normal law and the normal law + pilot. The transient peak in bank angle  $\phi$ , Figure 7.5, is reduced to one third (normal law + pilot) and to one eighth (normal law), which means significantly improved passenger comfort.

ii. *aileron angle*

The peak in aileron angle  $\delta_A$  is reduced by 60 % compared to the normal law + pilot and by 80 % compared to the normal law, Figure 7.5.

iii. *sideslip angle*

The sideslip angle  $\beta$ , see Figure 7.5, is reduced in transient peaking by more than 80 % and in its final value by 40 % (normal law + pilot) and 80 % (normal law), which guarantees, combined with the achieved yawing performance, a significantly lower lateral deviation from the flight path. Taking low roll controls into account, the drag will be significantly reduced.

As two inputs (rudder and aileron deflection angle) are available to stabilize the aircraft with zero roll and yaw rate, there are arbitrarily many combinations of steady states and stationary inputs to achieve the stabilization. However, a sufficiently large rudder deflection angle  $\delta_R$  and a finite sideslip angle  $\beta$  ensure that the magnitudes of all states and inputs remain in acceptable boundaries for the stabilization. Due to the different stabilization strategies in the case of the r. u. d. EO controller, in the case of the normal law and in the case of the normal law + pilot, different stationary values of the states occur. The moderate use of the rudder in the case of the normal law requires large stationary sideslip and aileron deflection angles. To avoid this, the pilot has to bring down the sideslip by a large rudder deflection angle. The r. u. d. EO controller avoids this large rudder deflection angle, the large sideslip and the aileron deflection angle by an early rudder deflection.

These benefits of the r. u. d. EO controller and the resulting reduction of the loads at the vertical tail become apparent in Figure 7.8. For an outer left EO at  $t = 0$  [s], Figure 7.8 compares the r. u. d. EO controller (upper aircraft with the light grey vertical tail, the corresponding shear force  $Q_{y,\text{vt}}$  is illustrated by the right, light grey column at the right bottom of each subplot in the six subplots) with the normal law (lower aircraft and left column in each subplot). Six time steps are considered. At 0.5 [s], the early rudder deflection angle of the r. u. d. EO controller is illustrated and the following subplots show the resulting early stabilization of the flight path and the loads in contrast to the conventional aircraft. At 2.5 [s] the corrective pilot action (JAR 25.367) becomes evident. It is clearly justified by the yaw rate and the sideslip angle, and the resulting heading angle and the flight path deviation that have been built up. The benefits of the r. u. d. EO controller with regard to the shear force, the energy transfer into the roll motion, the bank angle and the heading angle become obvious at 2.5 [s], 3 [s] and 3.5 [s].

Figure 7.6 and 7.7 show that the r. u. d. EO controller has better robustness properties than the normal law. The robustness of the normal law has been achieved by applying an iterative optimization over the whole flight envelope [46]. It therefore serves as a reference to evaluate the robustness of the r. u. d. EO controller. The amplitude variations of the yaw rate time histories in the first peak, which are caused by parameter variations, are reduced by more than one half by the r. u. d. EO controller compared to the normal law. It should be emphasized that this performance was achieved with a very simple controller structure.

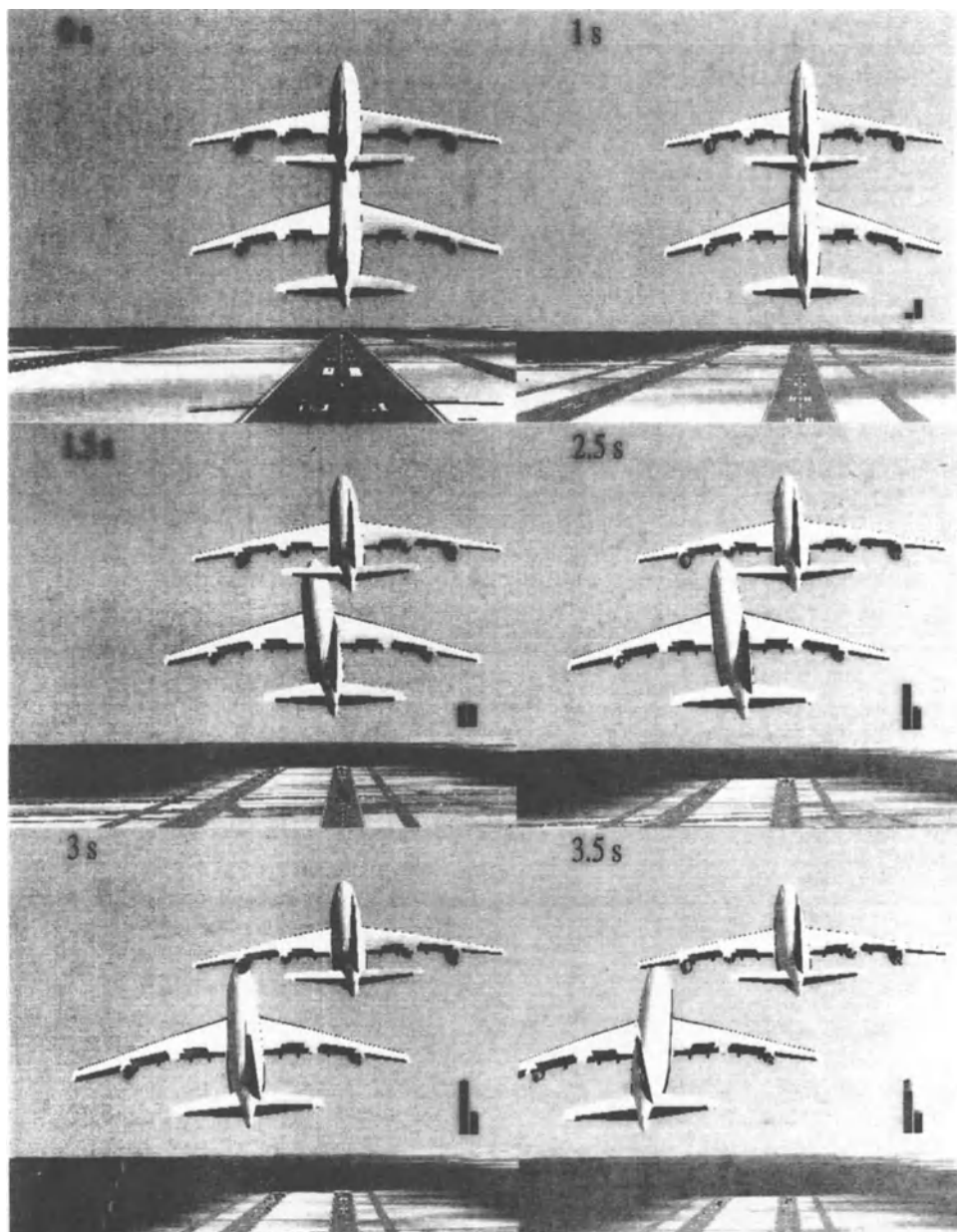


Figure 7.8. Aircraft and shear force dynamics at the vertical tail in an outer left EO for six time steps: r. u. d. EO controller (upper aircraft with the light grey vertical tail, corresponding shear force: right, light grey column at the right bottom of each subplot) compared to the normal law + pilot (lower aircraft and left column)

The assumption of a linear planar model for controller design is justified by the small amplitudes of all relevant lateral quantities (Figure 7.5 and 7.6), which occur in the EO simulation based on the high-precision closed-loop system.

## Conclusion

A new type of pilot assistance control system for the yaw disturbance moment compensation has been transferred from cars ( $\mu$ -split braking) to aircraft (engine out situation). This transfer includes the analytical controller derivation. The new pilot assistance system is characterized by a very early interference within man's reaction time: obviously, an automatic system can master critical situations in a much better way by avoiding any time wasting in consequence of the pilot reaction time and by avoiding any overreaction. Instead of first letting the aircraft drift into an extreme flight situation, which then is hard to master, the early yaw moment compensation keeps the aircraft in a moderate flight condition. Consequently, the pilot has time for other safety tasks like the engine management (e.g. in case of a flame out) and is not subject to a panic or an overreaction. Thereby, a task separation is achieved, which enables the pilot to concentrate on planning and performing long-term tasks. Here, man is superior to any automatic system. The short-term task, in particular within the reaction time where an automatic system is superior to man, is performed by the automatic system. In simulations on a non-linear high-precision model, the control system has turned out to be very robust to any parameter variations (mass, mass distribution, aerodynamics) and to non-linearities. The above features have been achieved with a simple controller of dynamic order 1 for all flight conditions. The design procedure is simple and physically transparent and yields symbolic expressions for the controller parameters.

## 7.2 Robust and Fault-tolerant Gamma-stabilization of an F4-E

Consider the short period longitudinal mode of the fighter aircraft F4-E in Figure 7.9. The F4-E is a modified military aircraft. In particular, the maneuverability was increased by additional horizontal canards. This results in a loss of longitudinal aerodynamic stability, however. The short period mode is unstable in subsonic flight and only weakly damped in supersonic flight. The equations of motion are linearized for small deviations from a stationary controlled flight (i.e. constant altitude and velocity, small angle of attack  $\alpha$ ). In flight mechanics, it is usual to take  $\alpha$  and the pitch rate  $q$  as state variables. Here, we transform the equations to sensor coordinates, i.e. the normal acceleration  $x_1 = n_z$  and the pitch rate  $x_2 = q$  are introduced as states. This simplifies the design for robustness with respect to accelerometer fault [3], [88]. The actuator for the elevator is modelled as a low-pass filter with the transfer function  $14/(s + 14)$ . Its state variable is  $\delta_e$ . For the state vector, we take

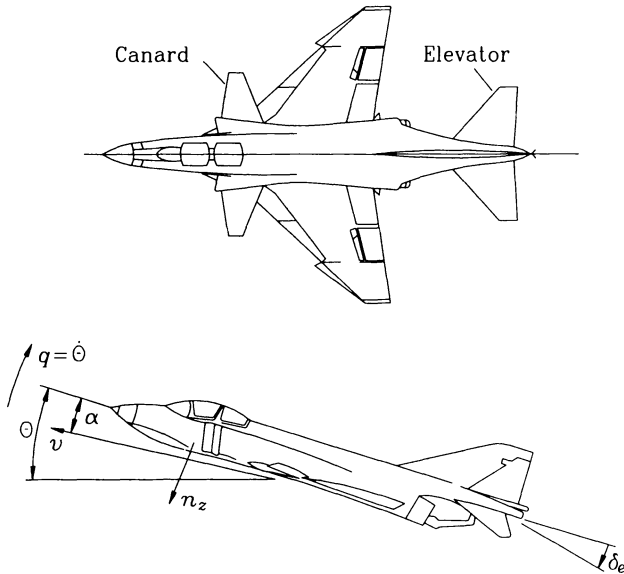


Figure 7.9. Fighter aircraft F4-E

$$\mathbf{x} = [n_z \ q \ \delta_e]^T \quad (7.2.1)$$

and the linearized state equations

$$\dot{\mathbf{x}} = \mathbf{A}\mathbf{x} + \mathbf{b}u$$

have the following structure:

$$\mathbf{A} = \begin{bmatrix} a_{11} & a_{12} & a_{13} \\ a_{21} & a_{22} & a_{23} \\ 0 & 0 & -14 \end{bmatrix}, \quad \mathbf{b} = \begin{bmatrix} b_1 \\ 0 \\ 14 \end{bmatrix}. \quad (7.2.2)$$

### Remark 7.1

The model (7.2.2) is based on some simplifying assumptions:

- a) Elevator ( $\delta_e$ ) and the canard rudder ( $\delta_c$ ) are not used independently of each other for small deviations from stationary flight. The two commanded input variables are coupled by

$$\begin{aligned} \delta_{ecom} &= u, \\ \delta_{ccom} &= -0.7u. \end{aligned} \quad (7.2.3)$$

The factor  $-0.7$  was chosen for minimum drag. Therefore, the system (7.2.2) has only one input  $u$ .

- b) Structural vibrations are not modelled. The bandwidth for the rigid body control is limited to be below the first structural mode frequency of 85 [rad/s] to avoid excitation of structural modes.

□

The possible flight conditions of this aircraft are represented in the Mach-number altitude diagram, Figure 7.10.

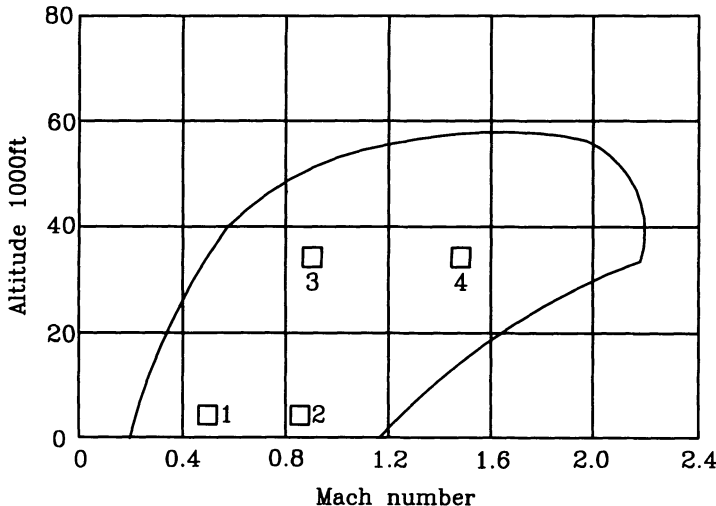


Figure 7.10. Envelope of the possible flight conditions and four representative cases

Numerical values for four representative flight conditions (FC) as indicated in Figure 7.10 have been taken from [47] and were transformed to the state equation (7.2.2). They are listed together with the respective eigenvalues  $s_1, s_2$  in Table 7.1. The third eigenvalue of (7.2.2) is fixed at  $s_3 = -14$ .

#### *Robustness with Respect to Flight Conditions*

Based on pilot ratings, admissible intervals for damping and frequency of the short period mode have been determined and must be verified in the qualification tests for the certification of a new aircraft [146]. For the characteristic polynomial  $p(s) = a_0 + a_1 s + s^2 = \omega_0^2 + 2D\omega_0 s + s^2$ , the following bounds are prescribed for damping  $D$  and natural frequency  $\omega_0$ :

$$0.35 \leq D \leq 1.3; \quad \omega_a \leq \omega_0 \leq \omega_b. \quad (7.2.4)$$

The bounds  $\omega_a$  and  $\omega_b$  depend on the flight condition and are given in Table 7.2.

Comparing the eigenvalue distances from the origin for the open-loop poles in Table 7.1 and the closed-loop pole specifications in Table 7.2, it is obvious that a basic rule of robust control is observed: *keep a fast system fast and keep a slow system slow*.

The admissible region is defined in the plane of coefficients  $a_0, a_1$  by (7.2.4). It is bounded by the lines  $a_0 = \omega_a^2$  and  $a_0 = \omega_b^2$  as well as the two parabolas  $a_0 = \omega_0^2$ ,

Table 7.1. Model data for an F4-E aircraft for four typical flight conditions. The eigenvalues  $s_1$  and  $s_2$  result from  $(s - a_{11})(s - a_{22}) - a_{12}a_{21} = 0$

Mach Altitude [ft]	FC 1 5000	FC 2 5000	FC 3 35 000	FC 4 35 000
$a_{11}$	-0.9896	-1.702	-0.667	-0.5162
$a_{12}$	17.41	50.72	18.11	26.96
$a_{13}$	96.15	263.5	84.34	178.9
$a_{21}$	0.2648	0.2201	0.08201	-0.6896
$a_{22}$	-0.8512	-1.418	-0.6587	-1.225
$a_{23}$	-11.39	-31.99	-10.81	-30.38
$b_1$	-97.78	-272.2	-85.09	-175.6
$s_1$	-3.07	-4.90	-1.87	$-0.87 \pm j4.3$
$s_2$	1.23	1.78	0.56	

Table 7.2. Military specifications for the admissible natural frequency  $\omega_0$  of the short period mode of an aircraft

Flight Condition	Velocity [Mach]	Altitude [Feet]	$\omega_a$ [Radian / Second]	$\omega_b$ [Radian / Second]
1	0.50	5000	2.02	7.23
2	0.85	5000	3.50	12.60
3	0.90	35 000	2.19	7.86
4	1.50	35 000	3.29	11.80

$a_1 = 2D_{min}\omega_0 = 0.7\omega_0$  and  $a_0 = \omega_0^2$ ,  $a_1 = 2D_{max}\omega_0 = 2.6\omega_0$ . The region for flight condition 2 is represented in Figure 7.11. If  $D$  is increased beyond 1, then the complex pole pair in the  $s$ -plane unites at a branching point for  $D = 1$  and then separates into two real poles of which one moves to the left and the other to the right as  $D$  increases. The pole moving to the right often leads to an undesired decrease in the bandwidth of the closed loop; this corresponds in the time-domain to a sluggish response. These less desirable domains lie above the parabola for  $D = 1$  in Figure 7.11. Therefore, the admissible region in coefficient space will be contracted by replacing the upper bound for  $a_1$  by the straight lines  $a$  and  $b$  (the tangents of the curve  $D = 1$  at  $\omega_a^2 = 3.5^2$  and  $\omega_b^2 = 12.6^2$ ). The coefficient region between  $a$ ,  $b$  and the curve  $D = 1$  describes exactly the polynomials with a pair of real roots in the interval  $s \in [-\omega_a; -\omega_b]$ . The reduced coefficient region corresponds to the “pineapple segment”, which is displayed in Figure 7.12 with solid lines. The expanded region shown in dashed lines is chosen for further eigenvalues that do not belong to the short period mode. The values  $\omega_a$ ,  $\omega_b$ , and the open-loop eigenvalues 1, 2, and 3 are displayed in Figure 7.12 for flight condition 2.

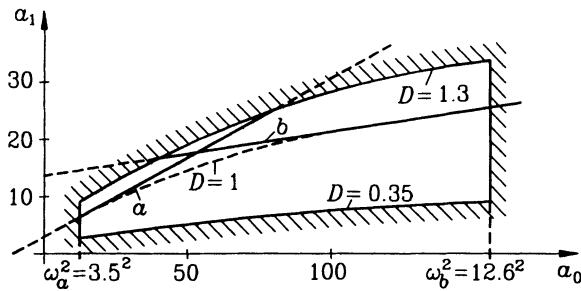


Figure 7.11. Required stability region for flight condition 2 in coefficient plane and replacement of the boundary  $D = 1.3$  by the two boundaries  $a$  and  $b$

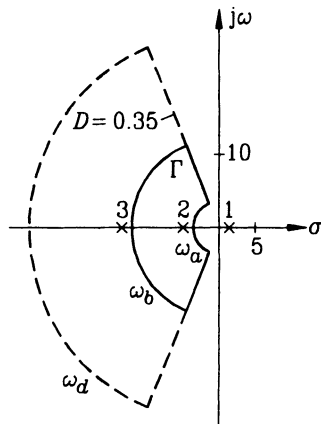


Figure 7.12.  $\Gamma$ -stability region in the  $s$ -plane

The controller structure that is easiest to implement is

$$u = - [ \begin{matrix} k_{n_x} & k_q & 0 \end{matrix} ] x = -k^T x, \quad (7.2.5)$$

where  $x_1$  is measured by an accelerometer and  $x_2$  with a gyro. The third state  $\delta_e$  is the deviation of the elevator from its trim position. The latter is not known with sufficient accuracy, therefore  $\delta_e$  is not used for feedback. The viewpoint of each of the two sensors would suffice. But it is not clear at this point which sensor is better suited for robust control. During the design, both alternatives will be considered and it will be shown why the gyro is the better choice. This example illustrates that the controller structure may not always be fixed before the controller design, it may also be a result of the design process.

The resulting two-dimensional cutting plane through the three-dimensional region of  $\Gamma$ -stability is shown in Figure 7.13 for  $\omega_d = 70$  [rad/s] and flight condition 2.

For  $k = 0$ , the eigenvalues are those of the open-loop, see 1, 2, and 3, in the  $s$ -plane figure. If the boundary  $\sigma_a$  is crossed by a variation of  $k$  starting with  $k = 0$ , then eigenvalue 2 moves across the point  $\sigma_a$  to the right.

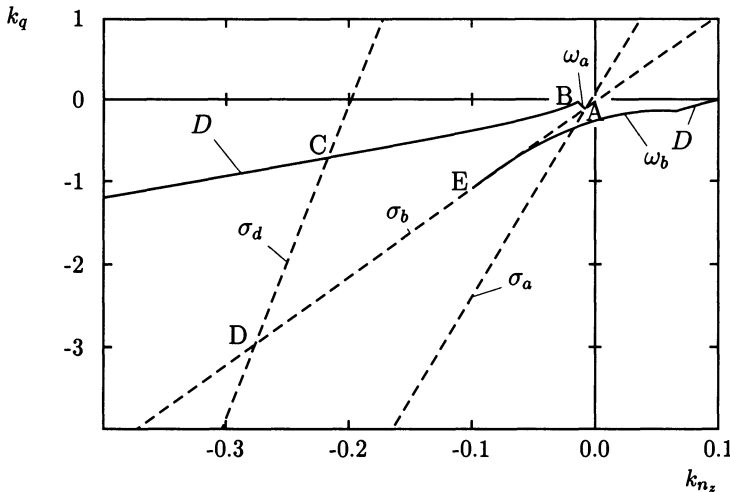


Figure 7.13. Two-dimensional cross-section of the  $\Gamma$ -stability region in  $\mathbf{k}$ -space

The eigenvalue pair  $(1, 2)$ , which describes the short period longitudinal mode, now moves as a complex conjugate pole pair into the desired region if the boundaries  $\omega_a$  or  $D$  are crossed. The desired region is thus ABCDEA. On AB, the eigenvalues 1 and 2 lie on the circle  $\omega_a$ , on BC they lie on  $D$ , and on CD eigenvalue 3 lies at  $\sigma_d$ . On DE, one of the eigenvalues  $(1, 2)$  lies at  $\sigma_b$ , on EA eigenvalue 3 lies at  $\sigma_b$ .

#### *Remark 7.2*

A one-to-one correspondence of the eigenvalues of the closed-loop to those of the open-loop is preserved on the described path in the  $(k_q, k_{n_z})$ -plane. Such a relation can be lost, for example, if eigenvalues 2 and 3 combine to form a complex pair, then a branching point is crossed. This would be the case, for example, if after leaving  $\mathbf{k} = 0$ , first  $\sigma_b$  and subsequently  $\omega_b$  were crossed. Pole 3 then moves to the right first and the pair  $(2, 3)$  moves over the boundary  $\omega_b$  in the  $s$ -plane.  $\square$

Correspondingly, the  $\Gamma$ -stability regions are determined for the other three flight conditions. All four regions intersect in the region represented in Figure 7.14. Thus, the assumed controller structure leads to an admissible solution set.

Figure 7.14 provides the design engineer with essential information as to which demands are critical in which flight cases. The flight condition numbers are used as indices at the boundary line names. The stimulation of structural oscillations is especially critical near the boundary  $\sigma_2 = -70$ , i.e. for flight condition 2 (high velocity, low-level). Insufficient damping is critical near the boundary  $D_4$  for flight condition 4 (fast flight at high altitude). The other two boundaries originate from flight condition 1 (landing approach). Near the boundary  $\sigma_1 = -2.02$ , a real pole moves toward the origin. A real pole would cross over to the left at the boundary  $\sigma_1 = -7.23$ . Flight condition 3 is not critical in this controller structure.

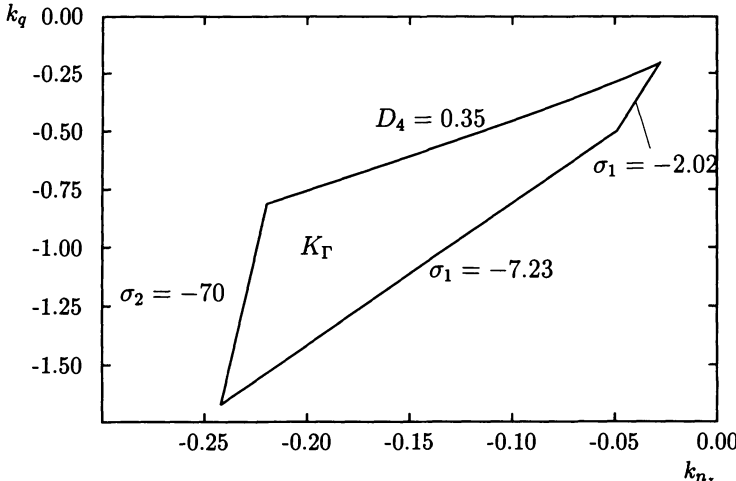


Figure 7.14. Intersection of the regions of  $\Gamma$ -stability for all four flight conditions

Information on the possible demands that can be met by a control system and the possibilities for compromise is usually more helpful for the control engineer than an optimization process, which requires that the trade-offs for all conceivable conflicts are decided beforehand by the choice of weightings in a performance criterion.

Figure 7.14 suggests different possibilities for coming closer to the selection of a point from the solution set. One possibility is to reduce the eigenvalue region  $\Gamma$  of Figure 7.12. Figure 7.15 shows the tightened region obtained by a reduction of  $\omega_d$  from 70 to 50 [rad/s], an increase of the minimum damping from 0.35 to 0.5 and an increase of all minimum natural frequencies  $\omega_a$  by 50 %. The boundary  $\sigma_1 = -7.23$  serves only to keep the eigenvalues in separate regions; it remains unchanged. There still exists an intersection for the four flight conditions and the designer may decide which of these specifications they want to tighten even more and thereby narrow the admissible region further.

However, other requirements can also be incorporated into the solution choice which have not been taken into consideration so far. As an example, suppose the limitation of the elevator deflection  $x_3$  and its derivative  $\dot{x}_3 = -14x_3 + 14k^T x$  is essential. Then, a solution with a smaller loop-gain is preferred. In order to illustrate this effect, the  $c^*$ -response to a unit step input given by the pilot has been calculated, as well as the required elevator deflection  $x_3$  for the points  $g_1$ ,  $g_2$ , and  $g_3$  in Figure 7.15, see Figure 7.17. The quantity

$$c^* = (n_z + 12.43q)/c_\infty$$

is a common variable in flight mechanics for the evaluation of the step response. The stationary value  $c_\infty$  is used for normalization. The  $c^*$ -step response should lie in the envelope shown in Figure 7.16. If the eigenvalues are suitably located in the eigenvalue region  $\Gamma$ , then the step responses are slightly faster than required. By a small delay in a prefilter they can be modified such that they fit into the envelope in Figure 7.16. For this design study, the prefilter  $6/(s + 6)$  was given.

The elevator deflection is decreased significantly for a small loop-gain  $g_1$  and the

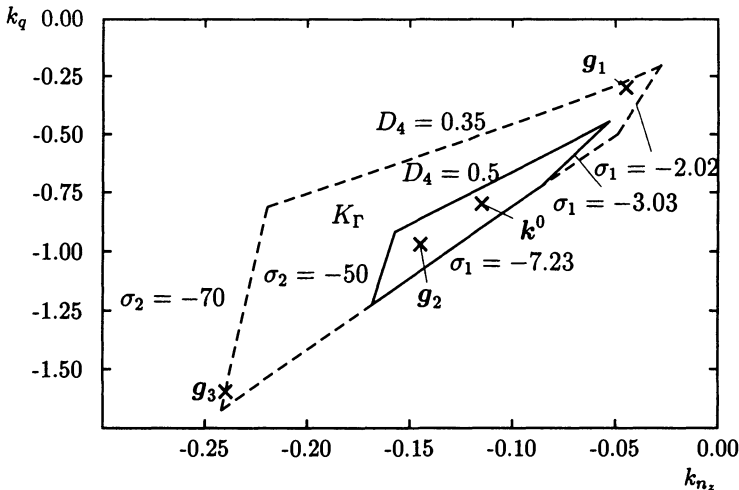


Figure 7.15. Tightened specifications reduce the admissible solution set

step response is correspondingly slow. A high loop-gain  $g_3$  is unsatisfactory due to too much overshoot of the step response, greater amplitude, and extension of the bandwidth to the vicinity of the structural-oscillation frequency. The medium loop-gain  $g_2$  is the best in this comparison, it produces a solution that is closer to  $g_3$  than to  $g_1$  and a point  $k^0$  slightly closer to  $g_1$  is finally selected. The chosen controller is

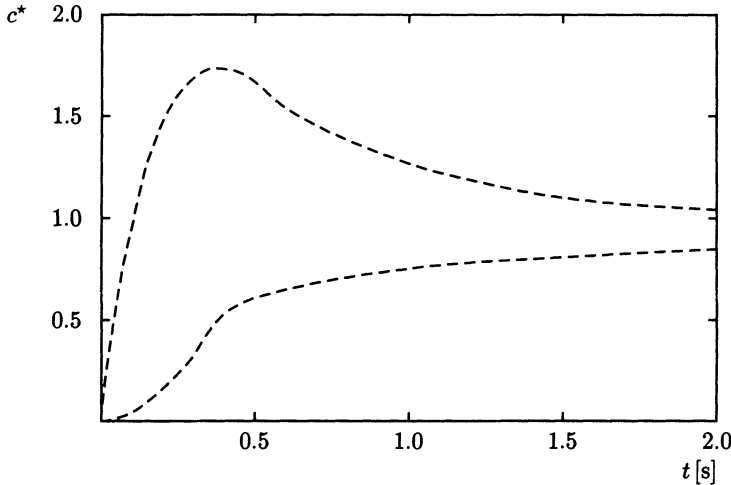
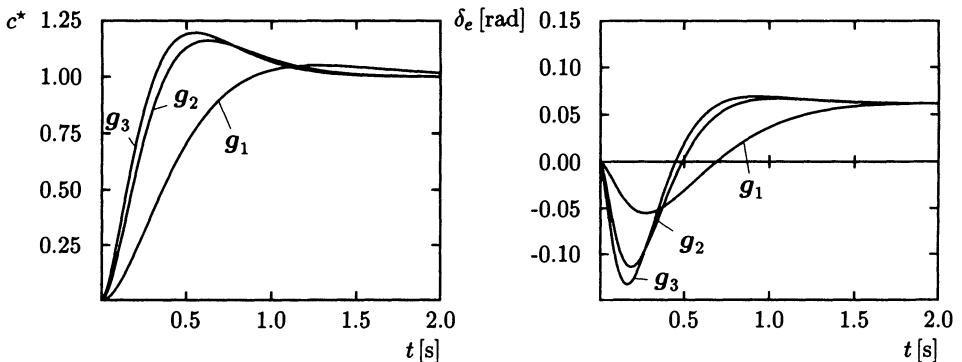
$$u = -k^{0T} \mathbf{x} = [ -0.115 \quad -0.8 \quad 0 ] \mathbf{x}. \quad (7.2.6)$$

The point  $k^0$  is indicated in Figure 7.15. Calculating and testing the eigenvalues shows that they lie in their respective prescribed regions for all flight conditions.

### Fault Tolerance

Usually, control systems are designed under the assumption that sensors do not fail. Redundancy management has then to provide the required measurements with only very short interruptions due to faults of individual sensors. If the plant is an unstable aircraft, this means that fault detection is vital for stabilization. Detection must operate quickly and this is in conflict with the requirement of low probability of false alarms.

An alternative is the use of a hierarchical concept. Its basic level is a fixed-gain control system, which is designed such that pole region requirements are robust with respect to component faults and uncertain parameters [3]. All the more sophisticated tasks, like fault detection and redundancy management, plant parameter identification and controller parameter adaptation, or gain-scheduling, are assigned to higher levels if they are required for best performance. The higher levels process more information and are operating in a slower timescale than the basic level. Since the higher levels are not vital for stabilization, they can make their decisions without panic.

Figure 7.16. Admissible envelope for the  $c^*$ -responseFigure 7.17.  $c^*$  response and elevator deflection  $\delta_e$  for low ( $g_1$ ), medium ( $g_2$ ) and high ( $g_3$ ) loop-gain. The elevator deflection is normalized to the stationary value of  $-\delta_e(t, g_1)$ 

Assume that a sensor fault has two effects as illustrated by Figure 7.18.

- i. The multiplicative effect reduces the gain  $V$  from its nominal value 1 to zero or some value in between.
- ii. The additive effect introduces a bias or noise  $d$  at the output.

As far as the eigenvalue location is concerned, only the multiplicative effect is important. The additive effect may require that the failed sensor signal is switched off. This decision of a fault detecting system may be slow, e.g. if the plant operates in a steady state and one of the sensors sticks at one value.

If the measured variables are used as state variables ("sensor coordinates"), then the sensor fault is equivalent to reducing the corresponding feedback gain. For  $V = 0$ , a solution for which  $\Gamma$ -stability is robust against fault of the sensor for the state variable  $x_i$  is characterized in gain space by the fact that the projection of  $k$  on the subspace  $k_i = 0$  is contained in  $K_\Gamma$ . A two-dimensional cross-section through gain space

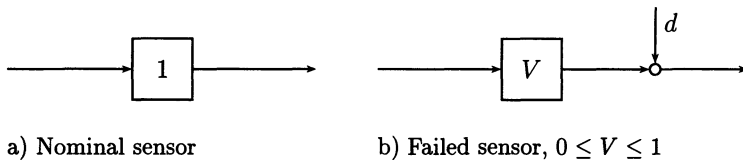


**Figure 7.18.** Model of sensor faults

is shown in Figure 7.19. Assume that the admissible region  $K_F$  is the triangle ABC. Robustness against fault of sensor  $i$  is achieved if the projection of the appropriate gain is on GE. This property holds for DEFG. Similarly, HCJKL is robust against fault of sensor  $j$  and KLMN is robust against fault of either  $i$  or  $j$ .

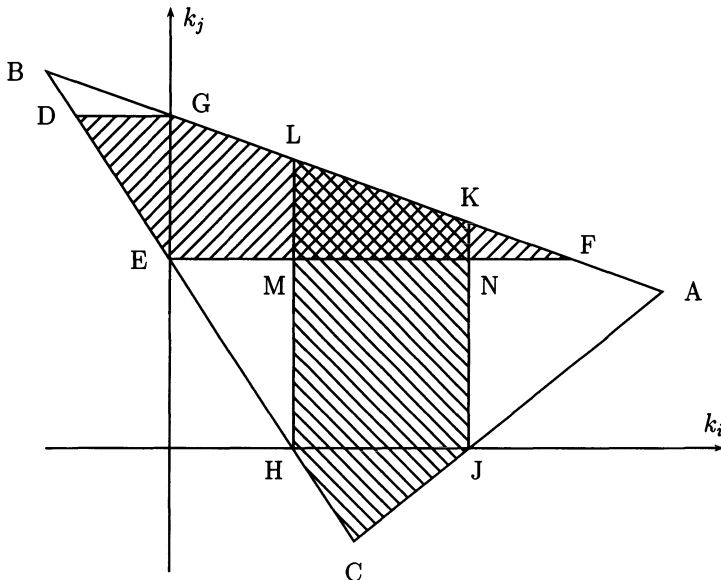


Figure 7.19. In KLMN,  $\Gamma$ -stability is robust against faults of the type  $k_i = 0$  or  $k_j = 0$

If no such intersection of the  $\Gamma$ -stability region with the axes exists, then the designer may use redundant sensors in parallel. The simplest possibility is to use two parallel sensors. Their outputs are multiplied by a factor  $1/2$  and added to produce  $x_i$  in the unfailed case. If one of the two sensors fails, then  $k_i$  is reduced by 50 %. In order to achieve robustness,  $k_i$  has to be selected such that it has a 50 % gain reduction margin in  $k_i$  for  $\Gamma$ -stability. If  $K_\Gamma$  is the triangle ABC in Figure 7.20, then DEF is the region for which  $\Gamma$ -stability is achieved after a 50 % reduction of  $k_i$ . Thus, the triangle EGH contains the admissible points which are  $\Gamma$ -stable and also remain  $\Gamma$ -stable after 50 % gain reduction.

If an intersection still does not exist for two parallel sensors, then three sensors in parallel may be considered. An advantage of this choice is that it can be combined with a fault detection procedure on the next higher hierarchical level. Its structure is

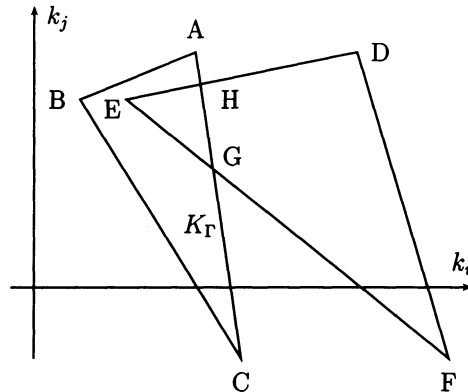


Figure 7.20. In EGH,  $\Gamma$ -stability is preserved under 50 % gain reduction in  $k_i$

shown in Figure 7.21.

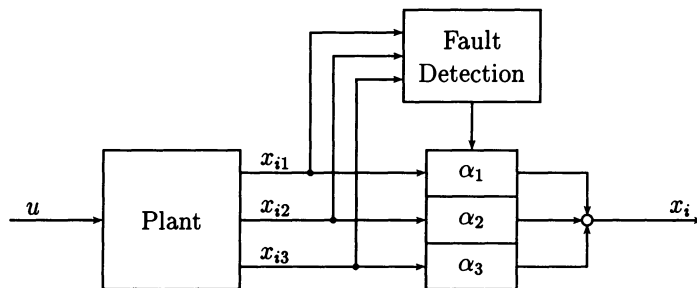


Figure 7.21. A triplex system

The fault detection system forms the three decision functions:

$$\begin{aligned} d_1(t) &= [x_{i1}(t) - x_{i2}(t)][x_{i1}(t) - x_{i3}(t)], \\ d_2(t) &= [x_{i2}(t) - x_{i3}(t)][x_{i2}(t) - x_{i1}(t)], \\ d_3(t) &= [x_{i3}(t) - x_{i1}(t)][x_{i3}(t) - x_{i2}(t)]. \end{aligned} \quad (7.2.7)$$

The  $d_k$ 's are nominally zero;  $|d_k| \geq \varepsilon$  indicates a fault of sensor  $k$ . In order to avoid false alarms from short impulses,  $d_k(t)$  is low-pass filtered first and then compared to a threshold value.

$$\begin{aligned} \dot{f}_1(t) &= af_1(t) + d_1(t), \\ \dot{f}_2(t) &= af_2(t) + d_2(t), \\ \dot{f}_3(t) &= af_3(t) + d_3(t). \end{aligned} \quad (7.2.8)$$

The decision logic is then

Nominal state:

$$\begin{aligned} |f_1(t)| < \varepsilon, \quad |f_2(t)| < \varepsilon, \quad |f_3(t)| < \varepsilon, \\ \alpha_1 = \alpha_2 = \alpha_3 = 1/3. \end{aligned} \quad (7.2.9)$$

Fault of sensor  $k$ :

$$\begin{aligned} |f_k(t)| &> \varepsilon, \quad |f_j(t)| < \varepsilon \text{ for } j \neq k, \\ \alpha_k &= 0, \quad \alpha_j = 1/2 \text{ for } j \neq k. \end{aligned} \quad (7.2.10)$$

No changes are made in the  $\alpha$ 's after a second fault. The parameters  $a$  and  $\varepsilon$  are chosen in view of safety against false alarms, i.e. both are not too small. This means that the decision may take some time. Between fault and decision times, the gain is reduced to  $2/3$ . If a second fault occurs after the first decision, then the gain is reduced to  $1/2$ . In the unlikely case that a second fault occurs before the first one is detected, the gain is only  $1/3$ . Thus, the basic robust control system should be designed for this gain reduction margin of 50 % or 67 % for  $\Gamma$ -stability.

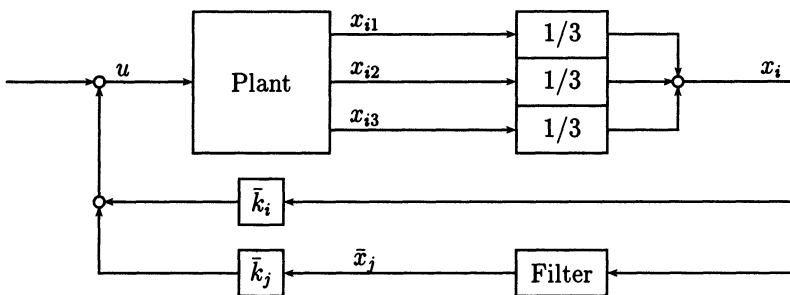


Figure 7.22. Substituting the measurement of  $x_j$  by a filter producing  $\bar{x}_j$

Here, a filter produces a substitute feedback variable  $\bar{x}_j$  for the true state-variable  $x_j$ . The filter transfer function is chosen such that the transfer function from  $u$  to  $\bar{x}_j$  at least crudely approximates the transfer function from  $u$  to  $x_j$  within the desired closed-loop bandwidth and over the range of plant parameter variations. The controller structure of Figure 7.22 is especially useful if the transfer function from  $u$  to  $x_i$  is minimum-phase, because then cancellations or near-cancellations by filter poles can be made. Instability of the transfer function is no disadvantage if the same instability also occurs, as is usual, in the transfer function from  $u$  to  $x_j$ .

In the filter structure, a fault effects both feedback channels simultaneously, i.e. both gains  $\bar{k}_i$  and  $\bar{k}_j$  are reduced. For example, let a fault of one sensor occur such that the sensor and feedback gain is reduced by a factor  $2/3$ . If ABC in Figure 7.23 is the  $\Gamma$ -stability region, then DEF is the region for which  $\Gamma$ -stability is maintained after one-third gain reduction in  $\bar{k}_i$  and  $\bar{k}_j$ . Thus, AGH is the region in which  $\Gamma$ -stability is achieved both nominally and after the sensor fault.

The configuration of Figure 7.22 with one measured state variable immediately gives the same gain reduction margin in both channels in the case of fault of one of several parallel sensors.

The above ideas on fault tolerance are now applied to the F4-E example and robustness with respect to gyro or accelerometer faults. Figure 7.14 shows that the  $\Gamma$ -stability region does not intersect the axes  $k_{n_z}$  and  $k_q$ . Therefore, one of the two feedbacks alone is not sufficient.

A first attempt would be to use two parallel gyros and two parallel accelerometers. From Figure 7.14, it is seen that there are no points in the  $\Gamma$ -stability region that

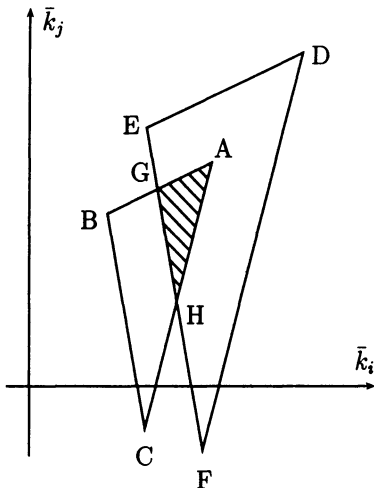


Figure 7.23. In AGH,  $\Gamma$ -stability is preserved under 1/3 gain reduction in both channels

admit 50 % gain reduction of both  $k_n$ , or  $k_q$ . Interestingly, the shape of  $K_\Gamma$  in Figure 7.14 with its lengthy extension away from the origin is such that the flying qualities are improved if a second fault in the other channel occurs, i.e. for a simultaneous 50 % reduction of gyro and accelerometer gain. This indicates that a controller structure as in Figure 7.22 with only gyros or with only accelerometers is advantageous. Here, any gain reduction occurs in both feedback gains simultaneously.

Of course, the unmeasured variable cannot be really reconstructed for all four flight conditions simultaneously by a constant filter. Also, the system order is increased by the filter such that additional eigenvalues occur. Therefore, the new stability region in the plane of the two feedback gains must be established. A similar form of the stability region can be expected, at least if the filter is chosen such that it yields an approximation for the unmeasured variable.

In deciding whether to use only gyros or only accelerometers, we consider the zeros of the two transfer functions. In the four flight conditions, the zeros in the accelerometer transfer function vary between  $-0.4 \pm j5.7$  and  $-0.9 \pm j9.1$ . They are minimum-phase but outside the  $\Gamma$ -stability region. Also, they may vary widely such that an approximate cancellation by the polynomial of averaged zeros  $s^2 + 1.172s + 49.9$  is not advisable. This would generate closed-loop poles that are not  $\Gamma$ -stable, possibly not even stable.

The gyro transfer function has one real zero varying between  $-0.64$  and  $-1.57$ . Here, an approximate cancellation by the polynomial of averaged zeros of the four operating conditions ( $s + 0.98$ ) is no problem. By this near-cancellation, this filter pole will be only weakly controllable from  $u$  and will not be shifted much by closing the loop. Also, it is weakly observable from the pitch rate and can be exempted from the pole region requirement.

Both transfer functions from  $u$  to  $n_z = x_1$  and  $q = x_2$  have the same poles; one pole is unstable in subsonic flight. The filter must replace the numerator of the gyro transfer function by the numerator of the accelerometer transfer function. Taking the averaged

zeros of the two transfer functions, the filter is

$$f(s) = a \cdot \frac{s^2 + 1.172s + 49.9}{s + 0.98} \cdot \frac{10}{s + 10}. \quad (7.2.11)$$

The term  $10/(s + 10)$  is introduced to make the filter realizable. The gain ratio  $a$  varies between 0.527 and 0.577 in the four flight conditions and is chosen at the average value  $a = 0.543$ .

By introducing the filter, the system order is raised to  $n = 5$ . The chosen controller structure of Figure 7.22 defines a plane of the free controller parameters  $\bar{k}_{n_z}$  and  $\bar{k}_q$ . In this plane, the intersection of  $\Gamma$ -stability regions for the four flight conditions must be analyzed. It is represented in Figure 7.24. The allowable region is clearly different

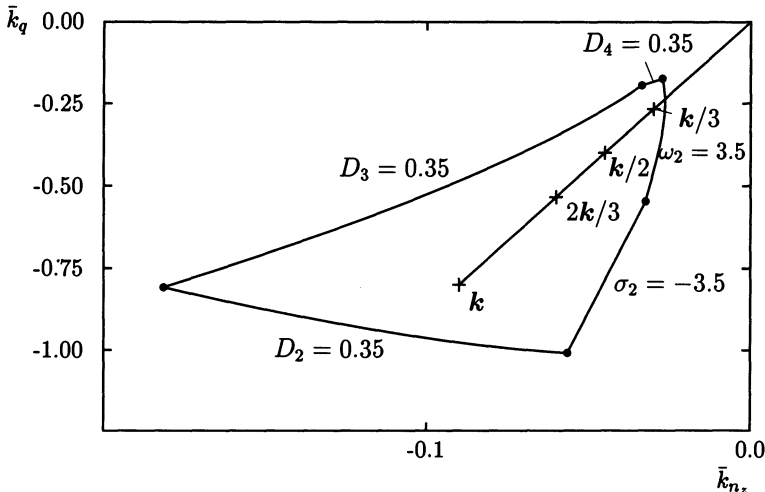


Figure 7.24. Intersection of the  $\Gamma$ -stability regions for the four flight conditions for the controller structure using only gyros and a feedback filter

from the region in Figure 7.14. Also, flight condition 3 instead of flight condition 1 now contributes to the boundary. Nevertheless, it confirms our expectation that a large simultaneous gain-reduction margin is now achievable, in the extreme case 80 %. If one chooses the indicated point  $k = [-0.09 \quad -0.8 \quad 0]^T$ , then the points  $2k/3$ ,  $k/2$ , and  $k/3$  lie well in the admissible region. Therefore, the system can handle the fault of two of the three gyros, even if the second fault occurs before the first one is detected. For the  $c^*$ -step responses in Figure 7.25, it is also worth remarking how little the step response is changed in all four flight conditions if  $k$  (steeply climbing curve) is reduced to  $k/2$ . If the two feedback paths via  $\bar{k}_q$  and  $\bar{k}_{n_z}$  are combined, then the controller

$$\begin{aligned} \frac{-u_S(s)}{x_{2S}(s)} &= -0.8 - 0.09 \cdot 0.543 \cdot \frac{s^2 + 1.172s + 49.9}{s + 0.98} \cdot \frac{10}{s + 10} \\ &= -\frac{1.29s^2 + 9.36s + 32.23}{s^2 + 10.98s + 9.8} \end{aligned} \quad (7.2.12)$$

is obtained. The minus sign is explained by the common flight mechanics definitions of the sign of the elevator deflection  $\delta_e$  and the pitch angle  $q$ , which causes a minus sign of the plant transfer function.

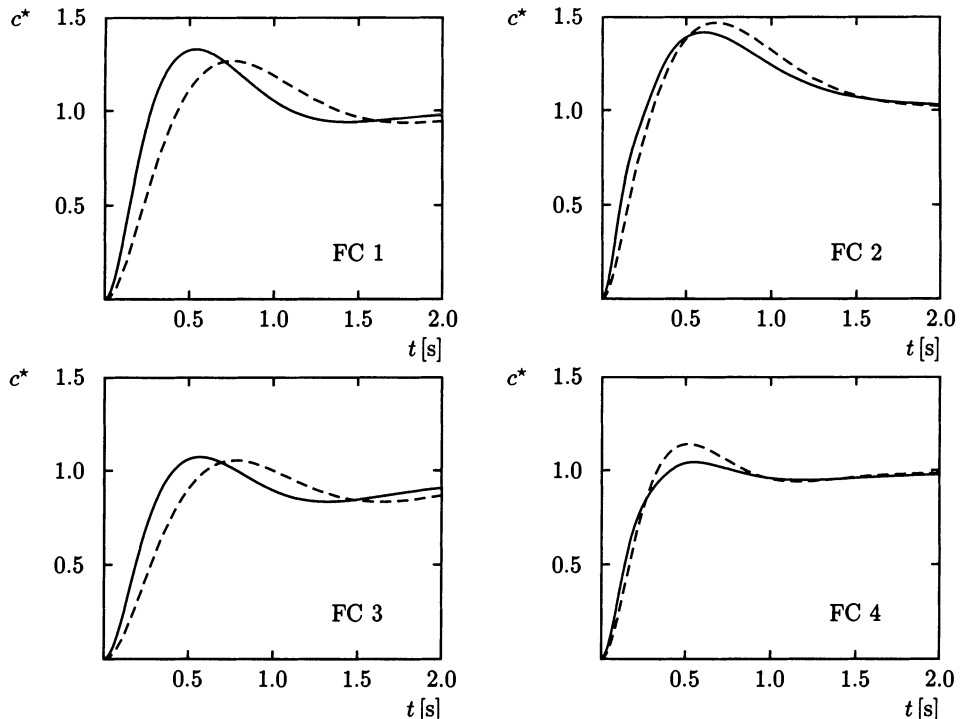


Figure 7.25.  $c^*$ -step response in four flight conditions. Each case shows nominal and 50% reduced loop-gains. The nominal gain results in the steeper initial rise

The procedure for the design of robust stabilization for the F4-E is certainly not a general design recipe, but similar results can be expected for other aircrafts. In the robust design of a back-up controller for the Swedish fighter JAS 39, it was assumed from the beginning that only the gyro is used for feedback. The controller in this case was assumed as a proportional channel plus two channels with first order delay. A robust level 1 controller for 10 flight conditions was designed using both the parameter space technique and a vector optimization method [98].

This extensive F4-E example shows how the design tool of two-dimensional cross-sections through regions of  $\Gamma$ -stability is applied and combined with other design considerations. The controller structure was developed in steps. The design would be less transparent if the second order controller of (7.2.12) with five free controller parameters had been assumed from the beginning.

## 7.3 Large Envelope Flight Control of a High Performance Aircraft

The design of flight control systems for fighter aircraft is an extremely demanding task. These aircraft must meet stringent performance specifications [147] throughout a large envelope of operating conditions despite large variations in system dynamics (including variations in open-loop stability), which result from varying operating conditions and the presence of significant nonlinearities. These large variations in the dynamics of the aircraft often make it impossible to achieve the required level of performance throughout the flight envelope with a fixed controller. Practically, this results in the design of several controllers at trim points throughout the flight envelope, which are then scheduled with the operating condition. While this gain-scheduling procedure has been successfully implemented on a number of fighter aircraft, it is extremely tedious and time consuming to design. The complex task of traditional gain-scheduling has resulted in a significant amount of research in recent years to develop methods of designing controllers that are “automatically” gain-scheduled. While significant progress has been made in this effort, e.g. [52], these methods are still quite involved and result in complex controllers that are often very conservative.

In this section, the parameter space methods presented in the previous chapters are used to provide a much simpler approach for designing large envelope flight controllers that provide the desired performance throughout the design envelope without gain-scheduling. The design procedure presented here [53] uses a variation of the control architecture shown in Figure 1.12 along with  $\Gamma$ - and  $\mathcal{B}$ -stability specifications to form a unified approach for designing robust flight controllers for high performance aircraft. The procedure enables the designer to explicitly define the desired closed-loop dynamics and ensures that the closed-loop satisfies  $\Gamma$ - and  $\mathcal{B}$ -stability (i.e.  $H_\infty$ ) specifications. The result is a straightforward procedure that allows the design of a robust flight controller that “forces” the closed-loop dynamics to behave like the specified “desired dynamics” despite disturbances, modeling uncertainties, and variations in aircraft dynamics due to changing flight conditions.

The procedure is presented here by designing a pitch-rate controller for the F-16 Variable Stability In-Flight Simulator Test Aircraft (VISTA), and clearly demonstrates the “simplistic” power of the parameter space design method. The resulting controller provides the desired performance throughout the large design flight envelope, which is demonstrated using both linear simulations and a high fidelity, non-linear simulation.

### Pitch-Rate Control of the F-16 VISTA

VISTA is a modified F-16 with the capability of simulating advanced aircraft configurations and testing advanced flight control concepts. A detailed description of the VISTA aircraft is given in [148]. In this section, a linear parameter-varying (LPV) model of the F-16 VISTA’s short-period dynamics and design specifications for an F-16 pitch-rate controller are reviewed.

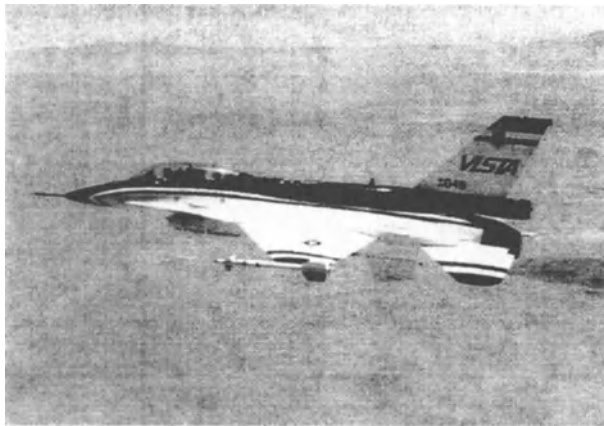


Figure 7.26. F-16 Variable Stability In-Flight Simulator Test Aircraft (VISTA).

*Remark 7.3*

Linear parameter-varying (LPV) models and controllers are linear systems whose coefficients have a parametric dependence. Note that the assumptions made about the parameters appearing in an LPV system are problem specific; the parameters may be constant or time-varying, they may be unknown or measured, or any combination of these. For example, an LPV controller is a linear controller whose coefficients depend on some measured parameters.  $\square$

### *LPV Model of the F-16 VISTA Longitudinal Dynamics*

The actual longitudinal dynamics of the VISTA aircraft, which vary significantly with flight condition (i.e. altitude  $h$  and Mach number  $M$ ), are denoted by  $\mathcal{G}(h, M)$ . For the pitch-rate control design,  $\mathcal{G}(h, M)$  is modeled using the standard short period equations of motion (7.3.1) and a first order approximation of the actuator dynamics (7.3.2).

$$\frac{d}{dt} \begin{bmatrix} \alpha \\ q \end{bmatrix} = \begin{bmatrix} Z_\alpha & 1 \\ M_\alpha & M_q \end{bmatrix} \begin{bmatrix} \alpha \\ q \end{bmatrix} + \begin{bmatrix} Z_{\delta_e} \\ M_{\delta_e} \end{bmatrix} \delta_{ed} \quad (7.3.1)$$

where,  $\alpha$  is the angle-of-attack,  $q$  is the pitch-rate, and  $\delta_{ed}$  is the elevator deflection.

$$\begin{aligned} \delta_{ed} &= G_a \delta_{ec} \\ G_a &= \frac{-20.2}{s + 20.2} \end{aligned} \quad (7.3.2)$$

where,  $\delta_{ec}$  is the elevator command.

*Remark 7.4*

Note that the negative sign in (7.3.2) is simply a result of the “command” sign convention used. In standard aircraft modeling (e.g. (7.3.1)), a positive elevator deflection produces a negative change in pitch-rate. The command sign convention used here (7.3.2) was chosen so that a positive elevator command produces a positive change in pitch-rate, which requires a negative elevator deflection.  $\square$

At trimmed level flight, the dimensional coefficients  $Z_\alpha$ ,  $M_\alpha$ ,  $M_q$ ,  $Z_{\delta_e}$  and  $M_{\delta_e}$  depend mainly on the altitude  $h$  and Mach number  $M$ . An LPV version of (7.3.1) for VISTA was developed by trimming and linearizing the United States Air Force Research Laboratory’s high fidelity nonlinear simulation model of the F-16 VISTA at the operating conditions

$$\begin{aligned} M &= [0.35 \ 0.45 \ 0.55 \ 0.65 \ 0.75 \ 0.85] \\ h &= [1000 \ 5000 \ 15000 \ 25000][\text{ft}] \end{aligned}$$

and fitting the corresponding data for the dimensional coefficients with polynomial functions of  $h$  and  $M$ . The resulting expressions for the coefficients are given by (7.3.3). The dependence of these parameterized coefficients on flight condition is shown in Figure 7.27.

$$\begin{aligned} Z_\alpha(h, M) &= 0.22 - 4.1 \cdot 10^{-7}h - 2.6M + 5.15 \cdot 10^{-5}Mh \\ M_\alpha(h, M) &= 17.1 - 8.07 \cdot 10^{-4}h - 68.4M \\ &\quad + 3.31 \cdot 10^{-3}Mh + 56.2M^2 - 2.92 \cdot 10^{-3}M^2h \\ M_q(h, M) &= -0.228 + 7.06 \cdot 10^{-6}h - 2.12M + 4.86 \cdot 10^{-5}Mh \\ Z_{\delta_e}(h, M) &= -1.38 \cdot 10^{-3} + 8.75 \cdot 10^{-8}h - 0.34M + 7.98 \cdot 10^{-6}Mh \\ M_{\delta_e}(h, M) &= -8.16 + 1.73 \cdot 10^{-4}h + 40.6M \\ &\quad - 8.96 \cdot 10^{-4}Mh - 99.3M^2 + 2.42 \cdot 10^{-3}M^2h \end{aligned} \tag{7.3.3}$$

The LPV model of the short period equations of motion (7.3.4) obtained when these polynomial expressions (7.3.3) are used with (7.3.1) is given by

$$\frac{d}{dt} \begin{bmatrix} \alpha \\ q \end{bmatrix} = \begin{bmatrix} Z_\alpha(h, M) & 1 \\ M_\alpha(h, M) & M_q(h, M) \end{bmatrix} \begin{bmatrix} \alpha \\ q \end{bmatrix} + \begin{bmatrix} Z_{\delta_e}(h, M) \\ M_{\delta_e}(h, M) \end{bmatrix} \delta_{ed} \tag{7.3.4}$$

and denoted by  $G_{LPV}(h, M)$ . Then, the model used to represent  $\mathcal{G}(h, M)$  for the pitch-rate control design is given by

$$G(h, M) = G_{LPV}(h, M) \cdot G_a \tag{7.3.5}$$

and accurately represents the F-16 VISTA’s short period dynamics throughout the flight envelope  $h \in [5000; 25000][\text{ft}]$  and  $M \in [0.4; 0.8]$ . Of course, even though  $G(h, M)$  accurately represents  $\mathcal{G}(h, M)$ , there are obviously modeling errors, which results in

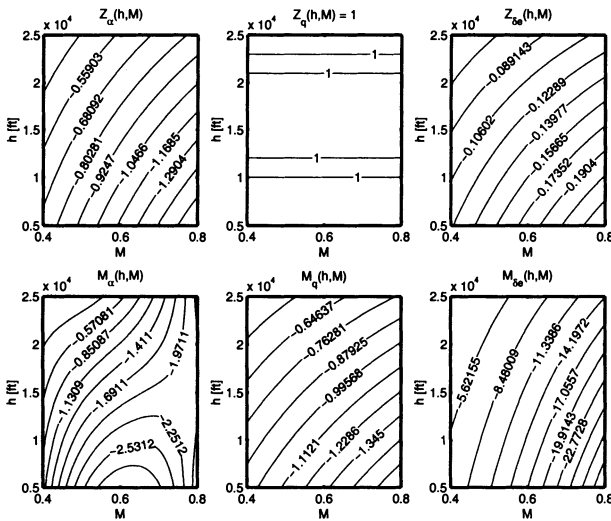


Figure 7.27. Dependence of the parameterized dimensional coefficients (7.3.3) on flight condition.

model uncertainty denoted by  $\Delta_m$ , where  $\Delta_m$  represents the difference (in a multiplicative sense) between the actual aircraft dynamics and the model (7.3.5). That is, we assume

$$\mathcal{G}(h, M) = G(h, M)(1 + \Delta_m) \quad (7.3.6)$$

The unstructured (i.e. non-parametric) uncertainty  $\Delta_m$  is often represented (as described in Section 5.3) by

$$\Delta_m = W_\Delta \cdot \Delta \quad (7.3.7)$$

where  $\|\Delta\|_\infty < 1$  and  $W_\Delta$  defines the frequency content of the uncertainty. As shown in Figure 5.36,  $W_\Delta$  is typically small at low frequencies where the model represents the actual system fairly well, and larger at high frequencies where unmodeled dynamics are prevalent. Then, substituting (7.3.7) in (7.3.6) gives,

$$\mathcal{G}(h, M) = G(h, M)(1 + W_\Delta \cdot \Delta) \quad (7.3.8)$$

as depicted in Figure 7.28.

### F-16 Pitch-Rate Control Design Specifications

The objective is to design a controller for the F-16 VISTA that provides robust 'Level 1' pitch-rate command tracking throughout the design envelope  $h \in [5000; 25000]$  [ft] and  $M \in [0.4; 0.8]$  (i.e. the flight envelope for which (7.3.5) is valid). This design

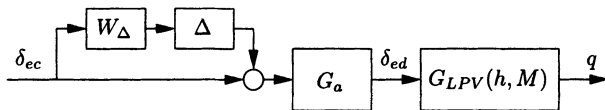


Figure 7.28. Block diagram representation of (7.3.8).

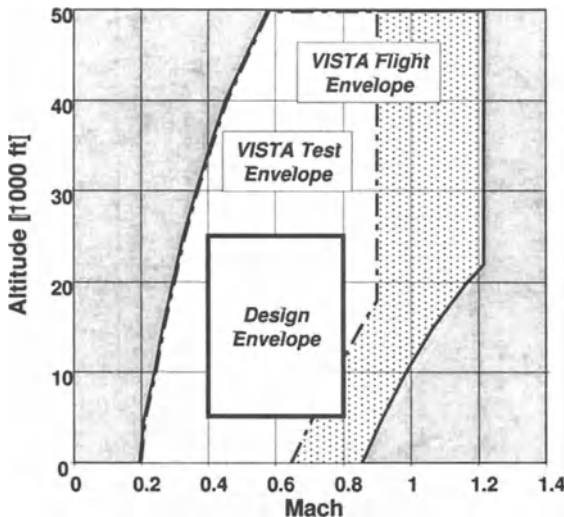


Figure 7.29. VISTA flight envelope.

envelope includes a large part of the VISTA aircraft's test flight envelope [148], as shown in Figure 7.29. 'Level 1' (i.e. acceptable) time domain handling quality specifications for the pitch-rate response [147] are shown in Figure 7.30 and Table 7.3.

A reference model that satisfies the 'Level 1' pitch-rate 'Handling Quality Specifications' over the entire design envelope is given by

$$G_d = \frac{4^2}{s^2 + 2 \cdot 0.5 \cdot 4 \cdot s + 4^2} . \quad (7.3.9)$$

In the sequel, the reference model  $G_d$  will be referred to as the "desired dynamics". Then, the design objective can be satisfied by designing a controller that "forces" the closed-loop system to behave like the desired dynamics  $G_d$  (7.3.9) throughout the design envelope.

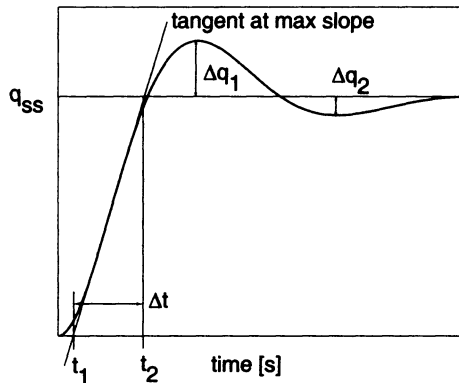


Figure 7.30. Pitch-rate handling qualities specifications.

Table 7.3. Pitch-Rate Handling Quality Specifications.

Parameter	Level I	Level II
$t_1 \text{ max}$	0.12 [s]	0.17 [s]
$\Delta q_2 / \Delta q_1 \text{ max}$	0.30	0.60
$\Delta_t \text{ max}$	$500 / V_T$ [s]	$1600 / V_T$ [s]
$\Delta_t \text{ min}$	$9 / V_T$ [s]	$3.2 / V_T$ [s]
$V_T$ represents the true velocity [ft/s]		

## Large Envelope Flight Control Design

### Control Architecture and Design Objectives

The control architecture used in this example was first applied to large envelope flight control in [53] and is based on the control structure shown in Figure 1.12, which provides insensitivity to disturbances and model uncertainty. Furthermore, as implemented here, this architecture enables the desired dynamics of the closed-loop to be explicitly defined. The control architecture used here for the VISTA pitch-rate controller is shown in Figure 7.31, where  $\mathcal{G}(h, M)$  denotes the open-loop aircraft dynamics from elevator command to pitch-rate response and  $G_d$  denotes the desired pitch dynamics of the aircraft. The two filters  $G_d$  and  $Q$  form the pitch-rate controller when utilized as shown in Figure 7.31. In general, designing the two degree of freedom controller shown in Figure 7.31 would involve the design of both the filter  $Q$  and the desired dynamics  $G_d$ . However, as in this example,  $G_d$  is usually selected based on some knowledge of the desired closed-loop performance and independent of  $Q$ . Then, the objective is to design the filter  $Q$  so that a given pitch-rate command  $\delta_C$  provides the desired response despite changing flight condition  $(h, M)$ , disturbances  $d$ , sensor noise  $n$ , and model uncertainty.

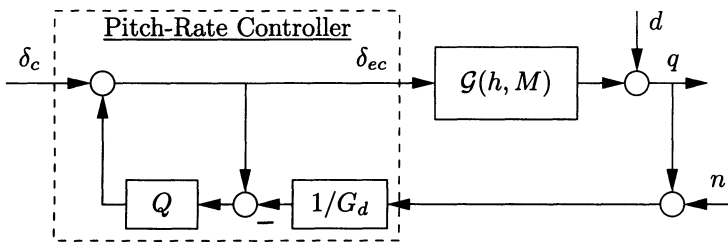


Figure 7.31. Pitch-rate controller architecture.

That is, design a  $Q$  so that the closed-loop represented by Figure 7.31 has

$$q = G_d \delta_C \quad (7.3.10)$$

as its input - output relation (within the frequency range of interest) throughout the design envelope.

#### *Remark 7.5*

In contrast to the control architecture shown in Figure 1.12, the controller shown in Figure 7.31 does not contain a nominal plant model, but rather the desired closed-loop dynamics represented by  $G_d$ .  $\square$

#### *Remark 7.6*

The relative degree of the filter  $Q$  is chosen to be at least equal to the relative degree of  $G_d$  for causality of  $Q/G_d$ .  $\square$

#### *Remark 7.7*

It may not be immediately obvious that there is a  $Q$  such that the controlled aircraft provides the desired response (7.3.10). However, the following discussion will provide some insight regarding the form of  $Q$  required to do just that and the design to follow will in fact find such a  $Q$ .  $\square$

Investigating the input-output transfer functions associated with the proposed architecture provides insight regarding the required form of  $Q$  and the expected characteristics of the resulting closed-loop. The loop-gain for the closed-loop aircraft represented by Figure 7.31 is

$$L(h, M) = \frac{Q}{1 - Q} \cdot \frac{\mathcal{G}(h, M)}{G_d} \quad (7.3.11)$$

As described in Section 5.3, the model regulation  $H$ , disturbance rejection (sensitivity)  $S$ , sensor noise rejection (complementary sensitivity)  $T$ , and performance (error)  $E$ , transfer functions of the controlled system are given by

$$H(h, M) := \frac{q}{\delta_C} = \frac{G_d \cdot \mathcal{G}(h, M)}{G_d \cdot (1 - Q) + \mathcal{G}(h, M) \cdot Q} \quad (7.3.12)$$

$$S(h, M) := \frac{q}{d} = \frac{1}{1 + L(h, M)} = \frac{G_d \cdot (1 - Q)}{G_d \cdot (1 - Q) + \mathcal{G}(h, M) \cdot Q} \quad (7.3.13)$$

$$T(h, M) := \frac{-q}{n} = \frac{L(h, M)}{1 + L(h, M)} = \frac{\mathcal{G}(h, M) \cdot Q}{G_d \cdot (1 - Q) + \mathcal{G}(h, M) \cdot Q} \quad (7.3.14)$$

$$E(h, M) := G_d - H(h, M). \quad (7.3.15)$$

It is obvious from (7.3.12) - (7.3.14) that the design objective can be satisfied by the selection of an appropriate low pass  $Q$  filter with unity gain, which results in  $q/\delta_C \rightarrow G_d$  and  $q/d \rightarrow 0$  at low frequencies where  $Q \rightarrow 1$  and  $q/n \rightarrow 0$  at high frequencies where  $Q \rightarrow 0$ . In order to explicitly show the characteristics of this control architecture,  $Q$  is set to 1 in (7.3.12) and (7.3.13) and  $Q$  is set to 0 in (7.3.14) to obtain

$$H_{Q=1}(h, M) = \frac{q}{\delta_C} = \frac{G_d \cdot \mathcal{G}(h, M)}{\mathcal{G}(h, M)} = G_d \quad (7.3.16)$$

$$S_{Q=1}(h, M) = \frac{q}{d} = \frac{0}{\mathcal{G}(h, M)} = 0 \quad (7.3.17)$$

$$T_{Q=0}(h, M) = \frac{-q}{n} = \frac{0}{G_d} = 0 \quad (7.3.18)$$

which clearly shows that good model regulation and disturbance rejection are achieved within the bandwidth of  $Q$  (despite variations in  $\mathcal{G}(h, M)$ ). Of course, it is not possible to achieve model regulation or disturbance rejection at frequencies above the actuator's bandwidth, so nothing is gained by having the bandwidth of the  $Q$  filter significantly larger than that of the actuator. Furthermore, as shown by (7.3.18), limiting the bandwidth of  $Q$  is required to reject high frequency sensor noise.

### Parameter Space Control Design

In this section, the parameter space techniques of previous chapters are used to design the filter  $Q$  to obtain a pitch-rate controller that robustly satisfies the design objective (i.e. provides a pitch-rate response as defined by (7.3.10) as closely as possible despite varying dynamics and uncertainty). This is accomplished by mapping  $\Gamma$ - and  $\mathcal{B}$ -stability specifications into the free parameter space of  $Q$ . The desired dynamics given by (7.3.9) mandates a  $Q$  filter with a relative degree of at least two for implementation purposes (i.e. causality of  $Q/G_d$ ). Opting for a simple controller, the  $Q$  filter structure is chosen as

$$Q = \frac{\omega_Q^2}{s^2 + 2D_Q\omega_Q s + \omega_Q^2} \quad (7.3.19)$$

giving free parameters  $\omega_Q$  and  $D_Q$ . Then, parameter space methods are used to map the  $\Gamma$ -stability specification (7.3.20) and the  $\mathcal{B}$ -stability specifications (7.3.21) and (7.3.22)

into the  $(\omega_Q, D_Q)$  parameter plane resulting in the feasible region of the  $(\omega_Q, D_Q)$  space (i.e. the set of  $(\omega_Q, D_Q)$  that satisfy the mapping equations).

$$\text{Roots}(p_{ce}(h, M, \omega_Q, D_Q)) \subset \mathbb{C}^- \quad (\text{Hurwitz Stability}) \quad (7.3.20)$$

$$\|W_\Delta \cdot \hat{T}(h, M, \omega_Q, D_Q)\|_\infty \leq 1 \quad (\text{Robust Stability}) \quad (7.3.21)$$

$$\|W_P \cdot \hat{E}(h, M, \omega_Q, D_Q)\|_\infty \leq 1 \quad (\text{Nominal Performance}) \quad (7.3.22)$$

Equation (7.3.20) ensures that all of the roots of the closed-loop characteristic equation given by

$$p_{ce}(h, M, \omega_Q, D_Q) := \text{num}\left(1 + \hat{L}(h, M, \omega_Q, D_Q)\right) \quad (7.3.23)$$

are in the negative complex plane (i.e. ensures stability of the nominal closed-loop throughout the design envelope).

### Remark 7.8

$\hat{T}$ ,  $\hat{E}$  and  $\hat{L}$  in (7.3.21), (7.3.22), and (7.3.23) are the same as  $T$ ,  $E$  and  $L$  defined in the previous section, except that the actual VISTA longitudinal dynamics represented by  $G(h, M)$  are replaced by the model of these dynamics  $G(h, M)$  as defined in (7.3.5).  $\square$

The weights  $W_\Delta$  and  $W_P$  in (7.3.21) and (7.3.22) are given by [53]

$$W_\Delta = 2 \frac{s + 1256 \cdot 0.2}{s + 1256 \cdot 2} \quad (7.3.24)$$

$$W_P = 0.4 \frac{s + 10 \cdot 10}{s + 10 \cdot 0.4} \quad (7.3.25)$$

and shown in Figure 7.32.

As discussed previously, the uncertainty weight  $W_\Delta$  is used to account for model uncertainties  $\Delta_m$  (7.3.6) in  $G(h, M)$  (7.3.5). Examining Figure 7.32 shows that  $W_\Delta$  represents 20 percent model uncertainty at low frequencies and that the uncertainty grows rapidly at higher frequencies, where unmodeled dynamics are significant. Then, satisfying equations (7.3.20) and (7.3.21) ensures robust stability throughout the design envelope despite the uncertainties represented by  $W_\Delta$ .

The performance weight  $W_P$  penalizes the error between the desired and actual pitch-rate response and is large in the frequency range where good model matching is desired. Figure 7.32 shows that the error in the controlled aircraft's pitch-rate response must be less than 10 percent within the frequency range of interest in order for the performance specification to be satisfied. Thus, satisfying (7.3.22) ensures nominal performance throughout the design envelope; that is, it ensures that the actual response is within 10 percent of the desired response for the nominal model  $G(h, M)$  (7.3.5) (i.e. (7.3.6) with  $\Delta_m = 0$ ).

Further insight regarding the interpretation of the weights (7.3.24) and (7.3.25) can be obtained by reviewing the descriptions of (5.3.23) and (5.3.28) and in [109], where

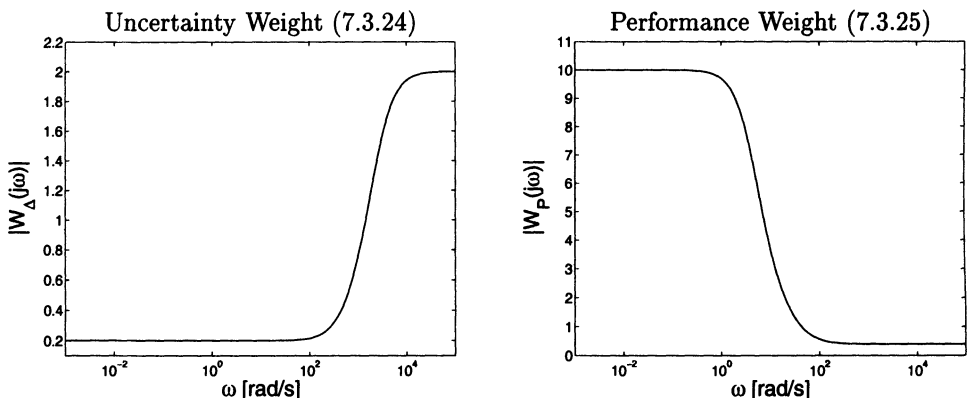


Figure 7.32. Design weights.

a detailed explanation of weights appropriate for flight control is given. Additionally, further interpretation of (7.3.21) and (7.3.22) can be seen by examining the weighted design model in Figure 7.33, where

$$\frac{e_u}{d_u} = -W_\Delta \cdot \hat{T}(h, M, \omega_Q, D_Q) \quad (7.3.26)$$

$$\frac{e_P}{\delta_C} = W_P \cdot \hat{E}(h, M, \omega_Q, D_Q) \quad (7.3.27)$$

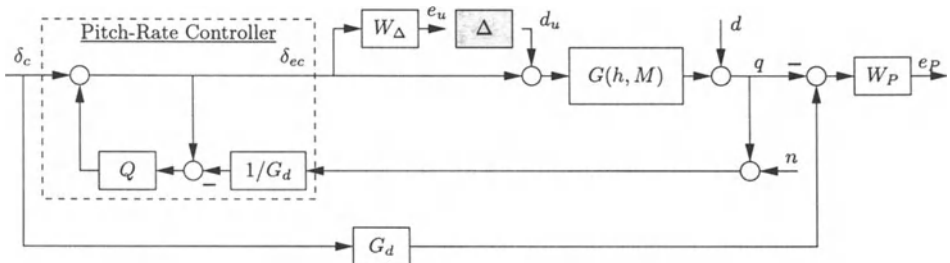


Figure 7.33. Weighted design model.

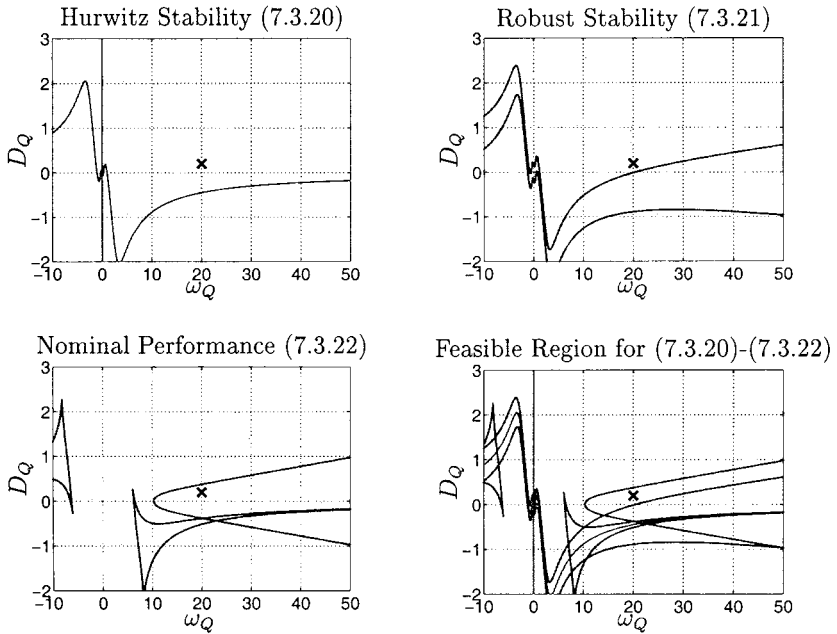


Figure 7.34. Feasible  $(\omega_Q, D_Q)$  region for  $h = 5000$  [ft],  $M = 0.8$ .

### Remark 7.9

The weighted design model in Figure 7.33 along with the specifications given by (7.3.20) - (7.3.22) are in a form typically used for “classical”  $H_\infty$  control design. In fact, a very similar problem formulation was used in [188] and [52] to design an LPV controller for VISTA using  $\mu$ -synthesis (i.e.  $H_\infty$  design method). Thus, this example clearly demonstrates that the parameter space techniques presented in Chapter 5 can be used to design controllers that satisfy  $H_\infty$  design specifications.  $\square$

After (7.3.20) - (7.3.22) are mapped to  $(\omega_Q, D_Q)$ , the feasible region that simultaneously satisfies all three requirements is formed by the intersection of the feasible region obtained from each individual requirement. Note that since (7.3.20) - (7.3.22) depend on flight condition  $(h, M)$ , the set of feasible  $(\omega_Q, D_Q)$  satisfying these equations also depends on  $(h, M)$ . Figure 7.34 shows the results of mapping (7.3.20) - (7.3.22) into  $(\omega_Q, D_Q)$  for  $h=5000$  [ft] and  $M=0.8$ , where the  $\times$  indicates the feasible region.

Since the objective is to design a controller that satisfies these specifications over the entire design envelope, (7.3.20) - (7.3.22) are mapped for as many additional operating conditions deemed necessary to ensure that the specifications are met throughout the design envelope. The region in the  $(\omega_Q, D_Q)$  plane that satisfies (7.3.20) - (7.3.22) at the four “corners” of the design envelope is shown in Figure 7.35. Note that for this design, the feasible region obtained by mapping the corners of the design envelope

lope is not reduced by mapping additional flight conditions. The design is completed by picking one point from this feasible region. This can be done arbitrarily; however, if after mapping all design requirements, the feasible region is still large, additional demands can be placed on the controlled system. For example, the feasible solution that minimizes the structured singular value could be selected, or the original design specifications could be “tightened”, which was done here. In this design, after mapping (7.3.20) - (7.3.22) using the “initial” weights, the feasible region was rather large, so the uncertainty weight  $W_\Delta$  (7.3.24) was adjusted to account for more uncertainty, which increases the guaranteed robustness of the resulting closed-loop system. After changing the uncertainty weight to that given in (7.3.24), the final design, which is marked with an  $\times$  in Figures 7.34 and 7.35 was chosen (rather arbitrarily) as  $D_Q=0.7$  and  $\omega_Q=40$  [rad/s].

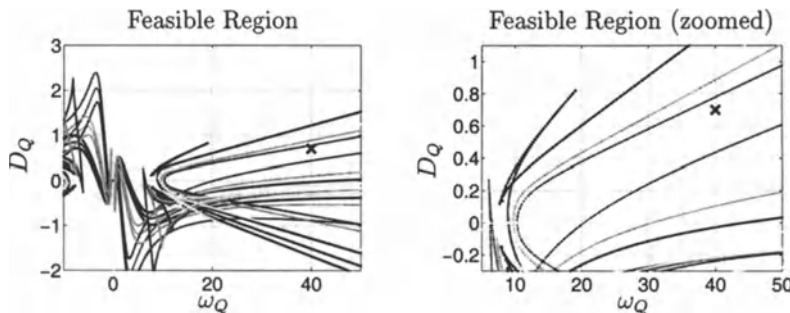


Figure 7.35. Feasible region obtained by mapping (7.3.20) - (7.3.22) into  $(\omega_Q, D_Q)$  at the four corners of the design envelope.

## Controller Evaluation

### Verifying Mapping Equations

Selecting  $D_Q$  and  $\omega_Q$  from the feasible region, as shown in Figure 7.35, ensures that the mapping equations (7.3.20) - (7.3.22) are satisfied, which can be easily verified. Verifying that the  $\Gamma$ -stability specification (7.3.20) is satisfied simply involves checking that the eigenvalues of the closed-loop system are negative at all flight conditions, which they are. Verifying that the  $\mathcal{B}$ -stability (i.e.  $H_\infty$ ) specifications (7.3.21) and (7.3.22) are satisfied can be easily checked by examining the frequency response magnitude (i.e. Bode magnitude) plots of  $W_\Delta \cdot \hat{T}(h, M, \omega_Q, D_Q)$  and  $W_P \cdot \hat{E}(h, M, \omega_Q, D_Q)$  to ensure that they are less than one at all flight conditions and frequencies. Figure 7.36 shows these frequency response magnitude plots at the four corners of the design envelope.

### Linear Simulations

Linear simulations were performed throughout the design envelope using the controller designed in the previous section. The results corresponding to the four corners of the

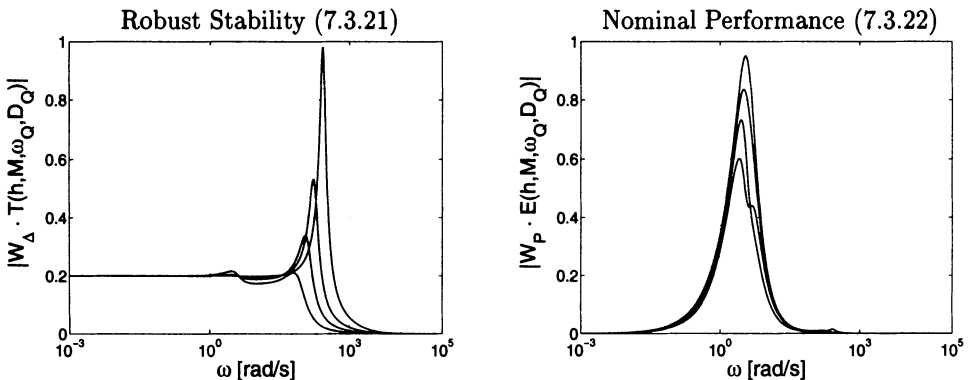


Figure 7.36. Mapping equations (7.3.21) and (7.3.22) verified at the four corners of the design envelope.

design envelope are shown in Figure 7.37, which also shows the pitch-rate command (the step) and the response of the desired dynamics  $G_d$  (7.3.9). It is clear from this

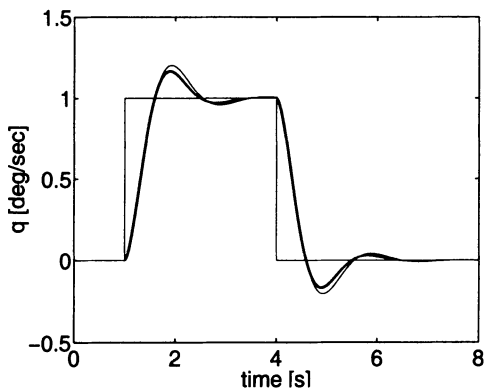


Figure 7.37. Linear simulation results.

figure that the pitch-rate response demonstrates predicted 'Level 1' handling qualities at all four corners of the design envelope. At three of these flight conditions, the pitch-rate response is essentially the same as the desired response. While the response at  $h = 25000[\text{ft}]$  and  $M = 0.4$  does have a little more overshoot than the desired response, it is certainly within the 'Level 1' specifications.

### Non-linear Simulations

High-fidelity, nonlinear simulations were also performed, since achieving the desired performance in linear simulations is not sufficient when assessing the controlled dynamic behavior of the highly nonlinear F-16 VISTA aircraft. The nonlinear simulations also demonstrated a predicted ‘Level 1’ pitch-rate response throughout the design envelope. Figure 7.38 shows the simulation results when the maneuver starts at the center of the design envelope (i.e.  $h=15000$  [ft],  $M=0.6$ ). Again, the pitch-rate plot includes the step command and the response of the desired dynamics.

#### *Remark 7.10*

In order to better assess the merits of the design procedure presented, the VISTA pitch-rate controller designed here (i.e. parameter space controller) was compared with previous VISTA pitch-rate control designs [52] and [188], which also provided ‘Level 1’ responses throughout the same design envelope. The pitch-rate controllers presented in [52] and [188] were designed using  $H_\infty$  and  $\mu$ -synthesis methods and are both LPV controllers (i.e. gain-scheduled). This comparison highlighted a number of noteworthy points.

First, comparing the weighted design models Figure 7.33 used for the different designs showed that the same VISTA model  $G(h, M)$ , desired dynamics  $G_d$ , and performance weight  $W_P$  were used for all three designs. However, the parameter space design used a considerably more demanding uncertainty weight  $W_\Delta$  (i.e. accounted for more uncertainty) than the LPV designs.

Second, a detailed robustness analysis (i.e.  $\mu$ -analysis) revealed that the parameter space controller guarantees a much higher level of robust performance (i.e. guaranteed level of performance despite uncertainty) than the LPV controllers. This difference in guaranteed robust performance is actually quite remarkable, since the LPV controllers were designed using methods ( $\mu/H_\infty$ ) intended to “maximize” this robustness, while robust performance was not even an explicit design specification for the parameter space controller. Recall, the design specifications for the parameter space controller were robust stability (7.3.21) (i.e. stability despite uncertainty) and nominal performance (7.3.22) (i.e. performance without uncertainty).

Third, comparing the design methods revealed that the parameter space procedure presented provides a significantly more straightforward and transparent design approach. With the parameter space approach, the design specifications are mapped into the plane of two design parameters (e.g.  $D_Q$  and  $\omega_Q$ ) and a feasible controller is selected. If no feasible controller exists, the conflicting specifications are immediately obvious, as the feasible regions of the individual specifications do not have an intersection. Additionally, if many feasible controllers exist (i.e. the intersection of feasible regions is large), then it is immediately obvious which specifications can be strengthened. On the other hand, the LPV procedures involve several design iterations, and it is not obvious whether or not the specifications are feasible until they are satisfied. Furthermore, if after several iterations the design specifications are not satisfied, it is not clear whether it is because they are infeasible, because additional iterations are necessary, or because poor design choices were made in previous iterations.

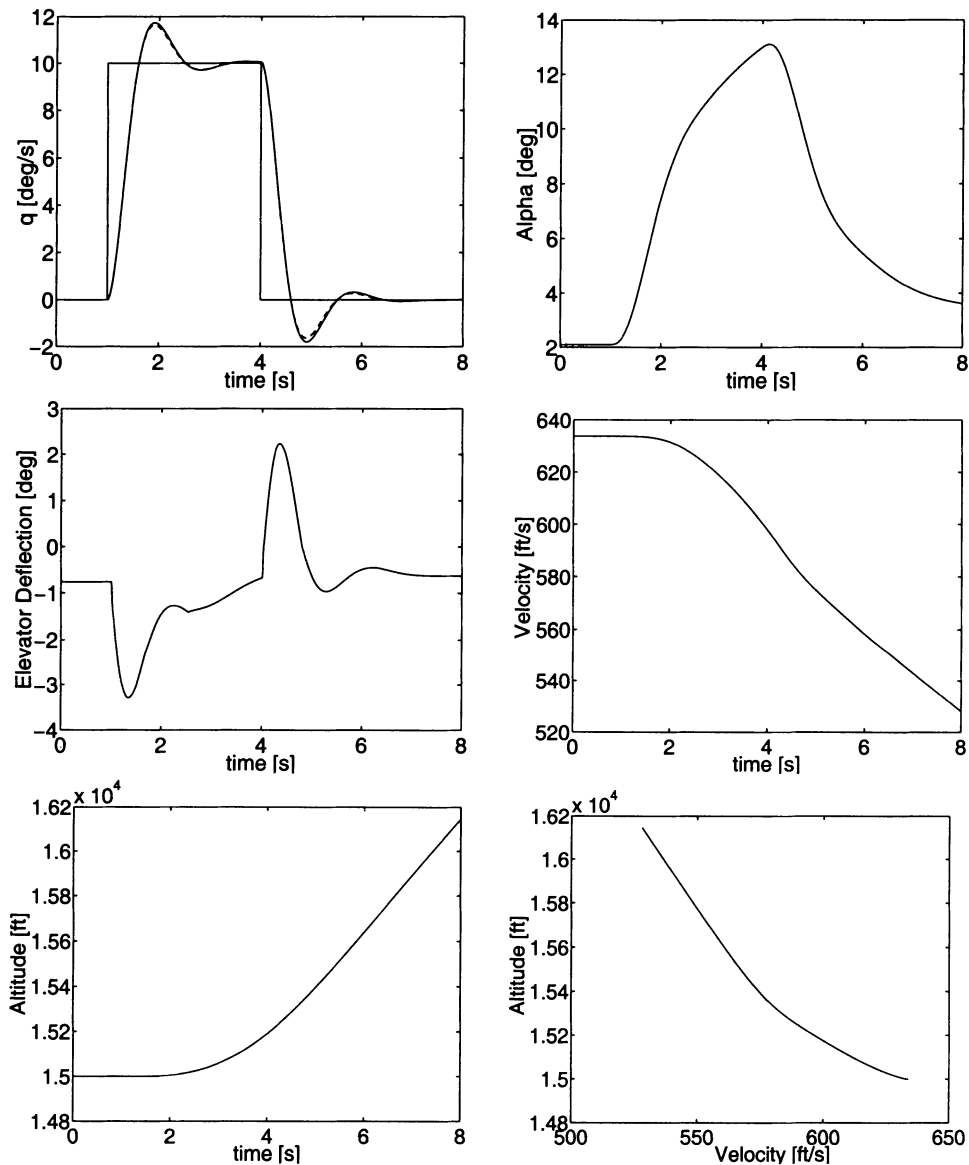


Figure 7.38. Nonlinear simulation results.

Finally, comparing the controller architectures showed that the parameter space controller is easier to implement and maintain. It only requires the feedback of the pitch-rate (i.e. the controlled variable), while both LPV controllers depend on the flight condition (i.e. gain-scheduled) and require the feedback of both the pitch-rate and the angle-of-attack. Furthermore, the parameter space controller consists of just two 2nd order filters, while the LPV controllers were 7th and 10th order systems.  $\square$

### Concluding Remarks

This case study demonstrated the “simplistic power” and transparency of the parameter space design method by using  $\Gamma$ - and  $\mathcal{B}$ -stability specifications to design a robust controller for the extremely challenging “real-world” problem of large envelope flight control of high-performance aircraft. The pitch-rate controller designed here for the VISTA F-16 aircraft satisfies ( $H_\infty$ ) robustness and performance specifications throughout the large design envelope without gain-scheduling, and high fidelity nonlinear simulations showed that it provides a robust ‘Level 1’ pitch-rate response throughout the design envelope. Furthermore, this controller is far simpler and provides better robust performance than previous LPV controllers designed for VISTA to meet the same objective (i.e. robust ‘Level 1’ pitch-rate response throughout the design envelope) using  $H_\infty$  and  $\mu$ -synthesis methods. This rather remarkable achievement is the result of both the parameter space method’s explicit, non-conservative treatment of physical parameters (e.g. flight condition parameters  $h$  and  $M$ ) and the properties of the two-degree of freedom control architecture used. This control architecture is extremely attractive for a number of reasons, most notably, its insensitivity to disturbances and model uncertainty and its unambiguous structure, which enables the explicit definition of the desired closed-loop dynamics. Together, this control architecture and parameter space techniques were shown to give a straightforward and transparent procedure for designing robust, large envelope controllers for high-performance aircraft that provide explicitly defined desired closed-loop dynamics without gain-scheduling.

# 8 Robustness Analysis by Value Sets

In this chapter, we return to Hurwitz-stability analysis of a polynomial family

$$p(s, \mathbf{q}) = [1 s \dots s^n] \mathbf{a}(\mathbf{q}), \mathbf{q} \in Q, \quad (8.0.1)$$

where  $Q$  is a hyperrectangle (“box”).

The obvious limitation of the parameter space approach is that it can practically handle only a small number of uncertain parameters in  $\mathbf{q}$ . This limitation is avoided by the value set approach in this chapter. On the other hand, this approach has other restrictions. It is primarily suited for robustness analysis, not for design; the operating domain  $\mathbf{q} \in Q$  must be fixed; and the uncertain parameters can enter  $\mathbf{a}(\mathbf{q})$  only in restricted structures.

The basic idea of the value set approach may be explained by the imaginary axis crossing conditions (2.2.1):

$$\begin{aligned} \operatorname{Re} p(j\omega, \mathbf{q}) &= a_0(\mathbf{q}) - a_2(\mathbf{q})\omega^2 + a_4(\mathbf{q})\omega^4 - \dots = 0, \\ \operatorname{Im} p(j\omega, \mathbf{q}) &= a_1(\mathbf{q})\omega - a_3(\mathbf{q})\omega^3 + a_5(\mathbf{q})\omega^5 - \dots = 0. \end{aligned} \quad (8.0.2)$$

This condition may be tested graphically for a fixed  $\mathbf{q} = \mathbf{q}^*$  from a plot of  $p(j\omega, \mathbf{q}^*) = \operatorname{Re} p(j\omega, \mathbf{q}^*) + j \operatorname{Im} p(j\omega, \mathbf{q}^*)$ ,  $\omega \geq 0$ . Equation (8.0.2) is satisfied for those special values  $\mathbf{q}^*$ , for which this plot passes through the origin. For uncertain  $\mathbf{q}$ , the plot blows up to a family of plots (for example, generated by gridding the  $Q$ -box). The polynomial family is stable if and only if i) it contains a stable polynomial and ii) for no  $\mathbf{q} \in Q$  the plot passes through the origin, i.e. the origin is excluded from the family of plots. This test is known as the *zero exclusion condition*.

## 8.1 Mikhailov Plot

Consider first a fixed  $\mathbf{q}$ . The plot  $p(j\omega)$ ,  $\omega \geq 0$  in the complex  $p$ -plane is referred to as a Mikhailov plot. Stability or instability of the polynomial can be determined by inspection of this plot.

Stability conditions stated in terms of frequency plots have a long history. In their most general form, these conditions were given by Cauchy’s principle of the argument around 1829. For the specific case of polynomials, conditions of this form also follow from the Hermite-Biehler theorem [107], [50], see also [94]. The graphical use of

the argument principle was introduced to the engineering community by Nyquist [157] in 1932. In 1938, Mikhailov [145] gave simpler graphical conditions for analyzing stability of known polynomials. In 1944 and 1947, Leonhard [131] and Cremer [68], respectively, gave similar conditions. For this reason, the Mikhailov plot is sometimes called the Cremer-Leonhard plot. Extensions of this method from known polynomials to families of polynomials are also available. In the 1950s, a frequency plot method for families of polynomials was originated by Curtis. This method was made known to the control community by Zadeh and Desoer [202]. This approach has been labelled by Barmish [40] as the *value set* approach using the zero exclusion theorem (Theorem 8.6). It is not fully clear which author should get the credit for this theorem. An assertion close to Theorem 8.6 is given in a book by Zadeh and Desoer [202]. Also, Frazer and Duncan [89] were not far from this result. A historical review of the zero exclusion theorem was given in a survey by Barmish [39].

This section will review both the Mikhailov stability conditions and the principles of the value set approach.

*Theorem 8.1 (Mikhailov, Leonhard and Cremer)*

The polynomial

$$p(s) = a_0 + a_1 s + \cdots + a_n s^n, \quad a_n > 0, \quad (8.1.1)$$

is stable if and only if the frequency plot  $p(j\omega)$ ,  $0 \leq \omega < \infty$  satisfies the following two conditions:

- i.  $p(j0) = a_0 > 0$ , i.e. the plot starts on the positive real axis.
- ii. As  $\omega$  increases, the plot of  $p(j\omega)$  encircles the origin in a counterclockwise direction and its phase goes to  $n\frac{\pi}{2}$  for  $\omega \rightarrow \infty$ .

□

*Proof*

To prove necessity, we first assume that the polynomial is stable and show that the Mikhailov conditions must be satisfied. The first condition,  $a_0 > 0$ , is satisfied for a stable polynomial. The second condition follows from the argument principle. The stable polynomial  $p(s)$  can be factorized:

$$\begin{aligned} p(j\omega) = a_n \prod_{i=1}^n (j\omega - s_i) &= a_n \prod_{i=1}^n |j\omega - s_i| e^{j \arg(j\omega - s_i)} \\ &= \left( a_n \prod_{i=1}^n |j\omega - s_i| \right) e^{j \sum_{i=1}^n \arg(j\omega - s_i)}, \end{aligned}$$

where all  $s_i$  have a negative real part. If a root is real, say  $s_1$ , then  $\alpha := \arg(j\omega - s_1)$  increases from zero to  $\frac{\pi}{2}$  as  $\omega$  goes from zero to  $\infty$  (see Figure 8.1). If a root is complex, say  $s_2$ , then  $s_3 = \bar{s}_2$  is also a root of  $p(s)$ . The argument of  $(j\omega - s_2)$  changes from  $-\beta$  to  $\frac{\pi}{2}$ , the argument of  $(j\omega - s_3)$  from  $\beta$  to  $\frac{\pi}{2}$  as  $\omega$  goes from zero to  $\infty$ . So the total argument variation of a conjugate complex root

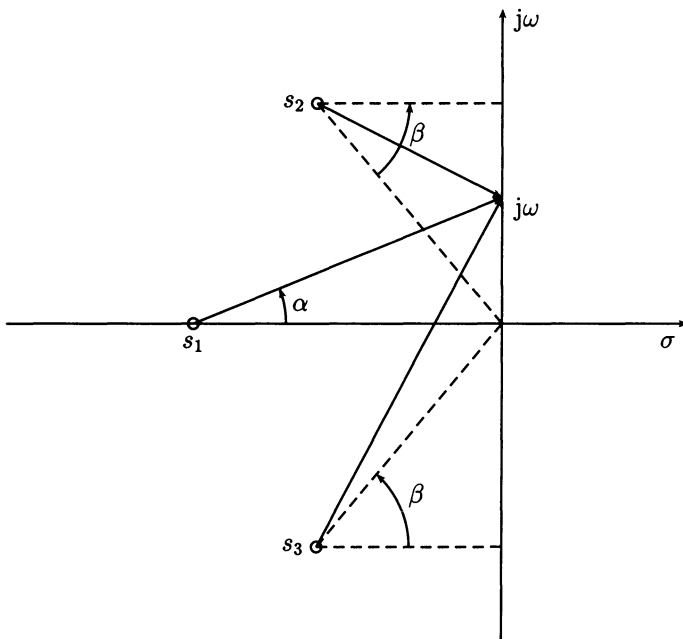


Figure 8.1. The variation of  $\arg(j\omega - s_i)$

pair is  $2\frac{\pi}{2}$ . Adding the contribution of each root, the total argument variation of all roots is  $n\frac{\pi}{2}$ . Thus,  $p(j\omega)$  must encircle the origin corresponding to the second condition.

To prove sufficiency, assume that the Mikhailov conditions are satisfied. It must be shown that the polynomial is stable. We will show the equivalent statement: whenever a polynomial is unstable, it will violate the Mikhailov conditions. Assume that the polynomial has  $m$  roots in the right half plane and  $n - m$  roots in the left half plane. By the argument principle, each root in the right half plane contributes a change of the argument of  $-\pi/2$  as  $\omega$  goes from zero to infinity. Thus, the total phase change is  $(n - 2m)\pi/2$  and the second Mikhailov condition is violated. In the special case of a root on the positive imaginary axis, it has to be circumvented by a small semicircle into the left half plane in order to count the root correctly as unstable. Thus, the phase jumps by  $-\pi$  as  $\omega$  crosses the imaginary root (Figure 8.2).

□

Note that the above proof also shows that the phase of the Mikhailov plot for a stable polynomial is monotonically increasing, i.e.

$$\frac{\partial \arg\{p(j\omega)\}}{\partial \omega} > 0 \text{ for all } \omega \geq 0. \quad (8.1.2)$$

For every polynomial, the total variation of the phase of  $p(j\omega)$  of  $(n - 2m)\pi/2$  determines the number  $n - m$  of left half plane roots and the number  $m$  of right half plane roots.

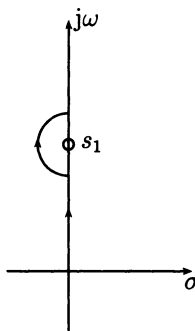


Figure 8.2. The variation of  $\arg(j\omega - s_i)$  for imaginary roots

Note also that for one or more unstable roots, the phase of the Mikhailov plot cannot exceed  $(n - 1)\frac{\pi}{2}$ , i.e. once the Mikhailov plot has reached the  $n$ -th quadrant as  $\omega$  increases, stability is guaranteed. This condition gives an upper bound  $\omega^+$  for the frequencies  $\omega$  that must be tested, where

$$\arg p(j\omega^+) = (n - 1)\frac{\pi}{2}. \quad (8.1.3)$$

The minimal distance between the Mikhailov plot of a stable polynomial and the origin is not an absolute measure for the stability margin because  $p(s)$  may be multiplied with an arbitrary factor without changing its roots. This distance is, however, a relative measure that indicates frequencies that are critical for stability. If the Mikhailov plot passes through the origin, then the polynomial has a root on the imaginary axis at the corresponding frequency. Given the frequency plot of a polynomial, the Mikhailov conditions indicate at a glance whether or not the polynomial is stable.

The Mikhailov condition is often interpreted in another form. The phase condition is equivalent to requiring the frequency plot to intersect the axes in the following order: positive real (for  $\omega = 0$ ), positive imaginary, negative real, negative imaginary, positive real, ..., until  $n$  such intersections have been made. This formulation is equivalent to the Hermite-Biehler theorem [107], [50] that requires an “interlacing property” of the roots of  $\operatorname{Re} p(j\omega) = 0$  and  $\operatorname{Im} p(j\omega) = 0$ .

### Example 8.2

Recall the characteristic polynomial of the crane from (1.5.18) with  $m_C = 1000$ ,  $\ell = 12$ ,  $m_L = 1500$ ,  $k_1 = 500$ ,  $k_2 = 2850$  and  $k_4 = 0$ .

$$p(s, k_3) = 12\,000s^4 + 34\,200s^3 + (31\,000 - k_3)s^2 + 28\,500s + 5000.$$

For  $k_3 = 0$ , the plot satisfies the Mikhailov stability condition, for  $k_3 = 16\,000$  it does not, see Figure 8.3. Between these two values there must be a stability boundary, for which the Mikhailov plot passes through the origin.  $\square$

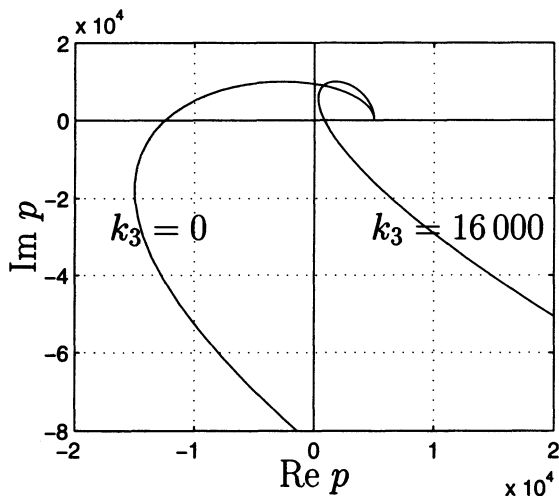


Figure 8.3. Frequency plot of two polynomials

## 8.2 Value Sets and Zero Exclusion

An obvious way to use the Mikhailov conditions for a family of polynomials is to compute the frequency plot of each polynomial in the family and to check the Mikhailov conditions one polynomial at a time. As was discussed in the root set section, the family normally has an infinite number of members, so this approach is not really possible. In practical terms, however, computing the frequency plots for a sufficiently dense grid of the parameter set is adequate. The frequency plots are placed together on a single graph. This procedure is illustrated by two examples.

### *Example 8.3*

Again, recall the characteristic polynomial of the crane from (1.5.18) with  $m_C = 1000$ ,  $\ell = 12$ ,  $m_L = 1500$ ,  $k_1 = 500$  and  $k_4 = 0$ .

$$p(s, k_2, k_3) = 12000s^4 + 12k_2s^3 + (31000 - k_3)s^2 + 10k_2s + 5000.$$

For the range of gains

$$1000 \leq k_2 \leq 11000, \quad (8.2.1)$$

$$12000 \leq k_3 \leq 17000, \quad (8.2.2)$$

a  $6 \times 6$  grid point grid was used to compute the frequency plots; they are displayed in Figure 8.4. The set contains plots that pass through zero. The family of control systems is not robustly stable.

This example was repeated using another range for  $k_3$ :

$$0 \leq k_3 \leq 5000. \quad (8.2.3)$$

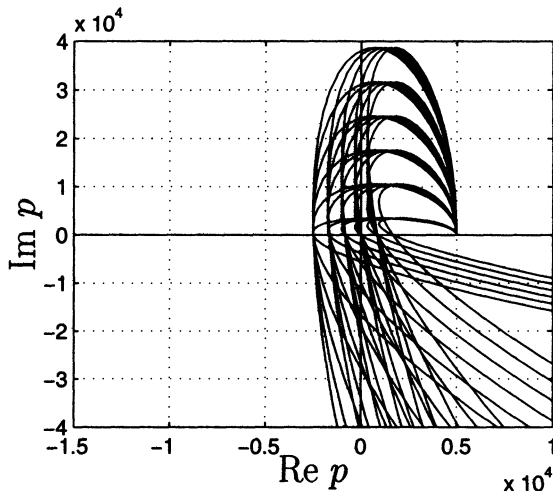


Figure 8.4. Frequency plots of an unstable family of polynomials

The corresponding collection of frequency plots were computed and displayed in Figure 8.5. The family defined by this range of gains is known to contain at least one stable polynomial for  $k_3 = 0$ , see Figure 8.3. Figure 8.5 shows that the frequency plots do not intersect the origin and hence none of the complex numbers  $p(j\omega, k_2, k_3)$  equal zero. This implies there are no possible roots on the  $j\omega$ -axis, and hence by the boundary crossing theorem, the polynomial is robustly stable for the given range of gains. The line of reasoning used in these two examples is true in general and will be stated in theorem form.  $\square$

#### *Theorem 8.4*

The polynomial family  $P(s, Q)$  is robustly stable, if and only if:

- i. There exists a stable polynomial  $p(s, q) \in P(s, Q)$ .
- ii. There does not exist a  $q \in Q$  such that the frequency plot  $p(j\omega, q)$ ,  $\omega \geq 0$ , intersects the origin.

$\square$

The gridding approach suggested in this section has one of the same drawbacks as computing the multiparameter root set. It is quite easy to select a grid that would cause the computations to take an excessively long time. For this reason, it is generally better to use a slightly different approach in computing the set of frequency plots.

Rather than computing the frequency plot  $p(j\omega, q)$ ,  $\omega \geq 0$ , for each  $q$  on a grid of  $Q$ , it is advisable to compute the *value set*

$$\mathcal{P}(j\omega, Q) = \{ p(j\omega, q) \mid q \in Q \}$$

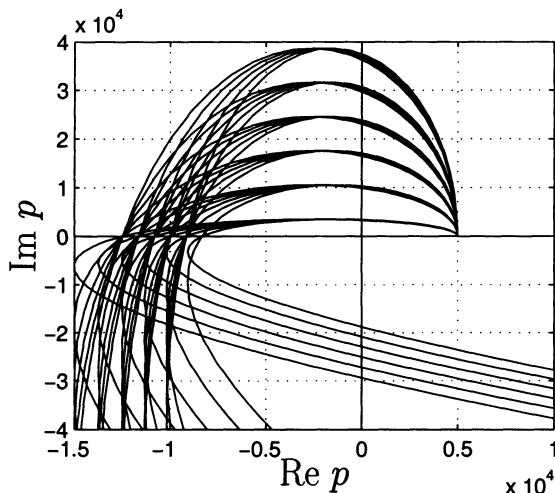


Figure 8.5. Frequency plots of a stable family of polynomials

for each  $\omega$  on a grid of frequencies from 0 to  $+\infty$ . This slight modification makes it possible to reap significant computational savings by exploiting the structure of the uncertain polynomial in terms of the uncertain parameters  $q_i$  in  $q$ .

#### *Example 8.5*

Consider the uncertain polynomial of Example 8.3 with  $k_2 \in [1000 ; 11\,000]$  and  $k_3 \in [0 ; 5000]$ . Since the gains enter the coefficients in an affine manner, value sets of this polynomial are four-sided convex polygons. In addition, the vertices of these polygons are determined by the extreme values of the gains. These are the four complex numbers  $p(j\omega, k_2^-, k_3^-)$ ,  $p(j\omega, k_2^-, k_3^+)$ ,  $p(j\omega, k_2^+, k_3^-)$ , and  $p(j\omega, k_2^+, k_3^+)$ . From just these four gain combinations rather than from a large grid of gains, it is possible to completely determine the value set at each frequency. For a grid on  $\omega$  in the interval  $[0.5 ; 1.5]$ , the value set is the family of rectangles in Figure 8.6. Obviously, it is much simpler to construct the Mikhailov set by a one-dimensional grid on  $\omega$  rather than by a multi-dimensional grid of  $q$ .  $\square$

The result of the above discussion is summarized in the following zero exclusion theorem.

#### *Theorem 8.6 (zero exclusion)*

Given a polynomial family  $P(s, Q)$  as in (8.0.1), the set  $P(s, Q)$  is robustly stable, if and only if:

- i. There exists a stable polynomial  $p(s, q) \in P(s, Q)$ .
- ii.  $0 \notin \mathcal{P}(j\omega, Q)$  for all  $\omega \geq 0$ .

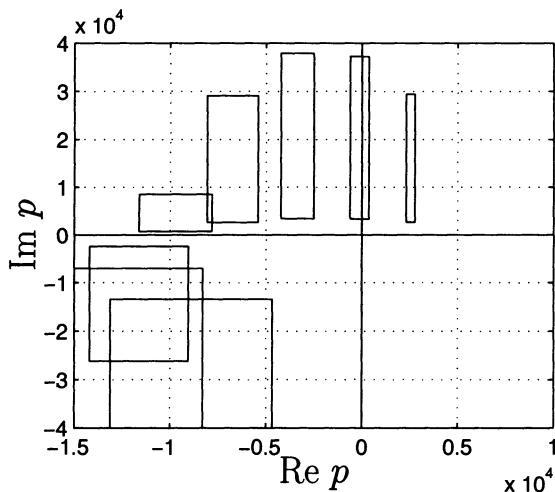


Figure 8.6. Value set for some discrete frequencies

□

### 8.3 Interval Polynomials, Kharitonov Theorem

In some simple structures of  $\mathbf{a}(q)$ , it is not necessary to plot value sets. Simple stability tests can be derived, however, using the concept of zero exclusion from the value set. The simplest structure is the *interval polynomial*.

*Definition 8.7*

A polynomial

$$p(s, \mathbf{a}) = a_0 + a_1 s + \dots + a_n s^n \quad (8.3.1)$$

with the uncertain coefficient vector

$$\mathbf{a} := [a_0 \ a_1 \ \dots \ a_n]^T \quad (8.3.2)$$

is called an *interval polynomial*, if  $\mathbf{a}$  ranges over the box

$$\mathcal{A} := \{\mathbf{a} \mid a_i \in [a_i^-; a_i^+], \ i = 0, 1, \dots, n\}. \quad (8.3.3)$$

□

For an interval polynomial, the uncertain parameters are identified with the polynomial coefficients  $a_i$ , that means  $a_i$  is not considered as a function of other parameters. Then each uncertain coefficient in (8.3.1) is independent of all other coefficients. An interval polynomial generates the polynomial family

$$P(s, \mathcal{A}) = \{ p(s, \mathbf{a}) \mid \mathbf{a} \in \mathcal{A} \}. \quad (8.3.4)$$

In 1953, Faedo [83] formulated the problem of a necessary and sufficient condition for robust stability of an interval polynomial. Faedo obtained only a sufficient condition. In 1979, Kharitonov published a surprisingly simple necessary and sufficient stability condition for interval polynomials [125]. Kharitonov's result is: only *four* polynomials of the continuum  $\mathcal{A}$  have to be checked for robust stability.

### Theorem 8.8 (Kharitonov)

The polynomial family

$$P(s, \mathcal{A}) = \{ p(s, \mathbf{a}) = a_0 + a_1 s + \dots + a_n s^n \mid \mathbf{a} \in \mathcal{A} \}, \quad a_n > 0, \quad (8.3.5)$$

is stable if and only if the following four polynomials are stable:

$$\begin{aligned} p^{+-}(s) &= a_0^+ + a_1^- s + a_2^- s^2 + a_3^+ s^3 + a_4^+ s^4 + \dots, \\ p^{++}(s) &= a_0^+ + a_1^+ s + a_2^- s^2 + a_3^- s^3 + a_4^+ s^4 + \dots, \\ p^{-+}(s) &= a_0^- + a_1^+ s + a_2^+ s^2 + a_3^- s^3 + a_4^- s^4 + \dots, \\ p^{--}(s) &= a_0^- + a_1^- s + a_2^+ s^2 + a_3^+ s^3 + a_4^- s^4 + \dots. \end{aligned} \quad (8.3.6)$$

□

The polynomials (8.3.6) are called Kharitonov polynomials. The superscripts indicate the upper and lower bounds of the coefficients  $a_0$  and  $a_1$ .

### Remark 8.9

A simple rule for constructing the Kharitonov polynomials is the “Kharitonov melody” ...two high, two low, two high,... with four possibilities for the two initial values. The upper and lower bounds occur in the four polynomials as

$$\begin{array}{ccccccccc} + & - & - & + & + & - & - & + \\ + & + & - & - & + & + & - & - \\ - & + & + & - & - & + & + & - \\ - & - & + & + & - & - & + & + \end{array}$$

□

The original proof of Theorem 8.8 by Kharitonov is complicated. Meanwhile, a much simpler proof was found [36], which is based on the zero exclusion from the value set of  $p(j\omega, \mathbf{a})$ . First, we prove the following lemma, [70]:

*Lemma.*

For each fixed  $\omega = \omega^* \geq 0$ , the value set  $P(j\omega^*, \mathcal{A}) = \{p(j\omega^*, \mathbf{a}) | \mathbf{a} \in \mathcal{A}\}$  is a rectangle with edges parallel to the coordinate axes and with vertices determined by the values of the four Kharitonov polynomials  $p^{+-}(j\omega^*)$ ,  $p^{++}(j\omega^*)$ ,  $p^{-+}(j\omega^*)$ ,  $p^{--}(j\omega^*)$ , see Figure 8.7.

□

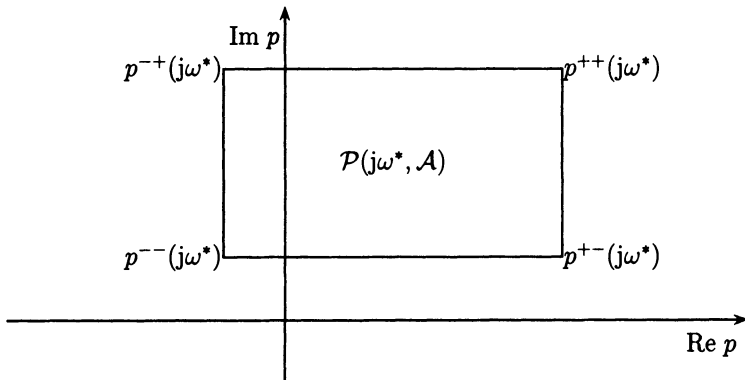


Figure 8.7. Value set of an interval polynomial for fixed  $\omega = \omega^*$

*Proof*

For all  $\omega \geq 0$  and all  $\mathbf{a} \in \mathbb{R}^{n+1}$ , the real and imaginary parts of  $p(j\omega, \mathbf{a}) = \operatorname{Re} p(j\omega, \mathbf{a}) + j \operatorname{Im} p(j\omega, \mathbf{a})$  have the lower and upper bounds

$$a_0^- - a_2^+ \omega^2 + a_4^- \omega^4 - \dots \leq \operatorname{Re} p(j\omega, \mathbf{a}) \leq a_0^+ - a_2^- \omega^2 + a_4^+ \omega^4 - \dots, \quad (8.3.7)$$

$$\omega(a_1^- - a_3^+ \omega^2 + a_5^- \omega^4 - \dots) \leq \operatorname{Im} p(j\omega, \mathbf{a}) \leq \omega(a_1^+ - a_3^- \omega^2 + a_5^+ \omega^4 - \dots). \quad (8.3.8)$$

Since  $\operatorname{Re} p(j\omega, \mathbf{a})$  is a function of the even indexed parameters  $a_i$  and  $\operatorname{Im} p(j\omega, \mathbf{a})$  is a function of the odd indexed parameters  $a_i$ , all bounds are mutually independent. Since the two functions are continuous, the set  $P(j\omega^*, \mathcal{A})$  must be a rectangle. Its edges are parallel to the coordinate axes.

The four Kharitonov polynomials defined in Theorem 8.8, can be represented as follows:

$$\begin{aligned} p^{+-}(j\omega) &= a_0^+ - a_2^- \omega^2 + a_4^+ \omega^4 - \dots + j\omega(a_1^- - a_3^+ \omega^2 + a_5^- \omega^4 - \dots), \\ p^{++}(j\omega) &= a_0^+ - a_2^- \omega^2 + a_4^+ \omega^4 - \dots + j\omega(a_1^+ - a_3^- \omega^2 + a_5^+ \omega^4 - \dots), \\ p^{-+}(j\omega) &= a_0^- - a_2^+ \omega^2 + a_4^- \omega^4 - \dots + j\omega(a_1^+ - a_3^- \omega^2 + a_5^+ \omega^4 - \dots), \\ p^{--}(j\omega) &= a_0^- - a_2^+ \omega^2 + a_4^- \omega^4 - \dots + j\omega(a_1^- - a_3^+ \omega^2 + a_5^- \omega^4 - \dots). \end{aligned} \quad (8.3.9)$$

Obviously, for each  $\omega \geq 0$  the vertices of the rectangle  $P(j\omega, \mathcal{A})$  are the values of the four Kharitonov polynomials.

□

Using the lemma, we now prove Kharitonov's theorem.

*Proof*

The necessary part of the theorem is trivial. To prove sufficiency, assume that the four Kharitonov polynomials are stable. Then, the Mikhailov plot (see Section 8.1) of each Kharitonov polynomial starts on the positive real axis and circles the origin in counterclockwise direction until its phase is  $n\pi/2$ . Since the edges of the value set are parallel to the coordinate axes and their end points satisfy the Mikhailov stability condition, the origin cannot enter into the value set through an edge of the value set. Hence, all Mikhailov curves for  $p(j\omega, \mathbf{a})$  with  $\mathbf{a} \in \mathcal{A}$  are stable and  $P(s, \mathcal{A})$  is stable.

□

For low order polynomials, even less than the four Kharitonov polynomials suffice for a stability test.

*Theorem 8.10 (Anderson, Jury, Mansour)*

An interval polynomial family

$$p(s, \mathbf{a}) = a_0 + a_1 s + \dots + a_n s^n, \quad a_0^- > 0 \quad (8.3.10)$$

is robustly Hurwitz-stable, if and only if the following polynomials are stable:

$$\begin{aligned} n = 3 : \quad & p^{+-}(s), \\ n = 4 : \quad & p^{+-}(s), p^{++}(s), \\ n = 5 : \quad & p^{+-}(s), p^{++}(s), p^{-+}(s), \\ n \geq 6 : \quad & p^{+-}(s), p^{++}(s), p^{-+}(s), p^{--}(s). \end{aligned}$$

□

For  $n = 2$  and  $n = 1$ , the conditions  $a_i^- > 0$  are necessary and sufficient.

*Proof*

Let  $n = 3$  and assume that  $p^{+-}(j\omega)$  is stable. Then, its Mikhailov plot traverses through the quadrants I, II, and III, as illustrated by Figure 8.8, and with  $a_0^- > 0$ , the same is true for all  $p(j\omega, \mathbf{a}) \in P(j\omega, \mathcal{A})$ . Let  $n = 4$  and assume that both  $p^{+-}(j\omega)$  and  $p^{++}(j\omega)$  are stable as illustrated by the Mikhailov plots in Figure 8.9. Then, with  $a_0^- > 0$ , the same is true for the entire rectangle  $\mathcal{P}$ . Finally, for  $n = 5$ ,  $p^{-+}(j\omega)$  must also be stable to guarantee that all  $p \in \mathcal{P}$  are stable, see Figure 8.10. For  $n > 4$ , the condition  $a_0^- > 0$  needs not be tested separately, it is implied by stability for  $p^{-+}(s)$ .

□

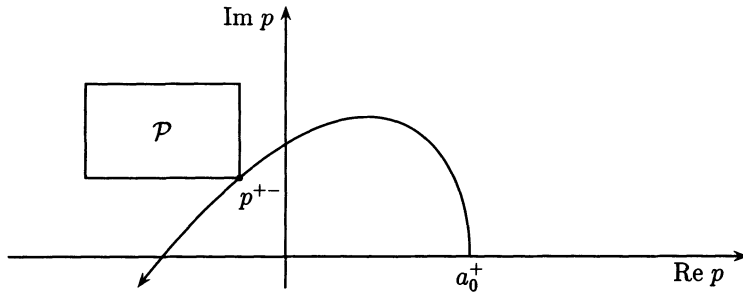


Figure 8.8. For polynomials of degree three, only  $p^{+-}(s)$  has to be tested

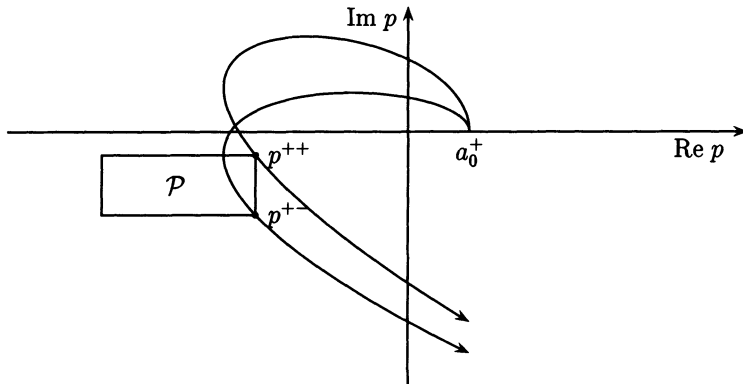


Figure 8.9. For polynomials of degree four, only  $p^{+-}(s)$  and  $p^{++}(s)$  have to be tested

For testing the stability of a polynomial, plotting its Mikhailov curve is not necessary. Using the Hurwitz test or factorizing the polynomials are other possibilities.

#### Example 8.11

Recall the characteristic polynomial of the crane with state feedback, Equation (1.5.18), with the fixed physical parameters  $g = 10$ ,  $m_C = 1000$ ,  $\ell = 10$ ,  $m_L = 1000$ , with fixed feedback gains  $k_1 = 600$ ,  $k_2 = 2000$ , and nominal values  $k_3 = -10\ 000$  and  $k_4 = 0$ . The controller parameters may vary in the intervals  $k_3 \in [-20\ 000 ; 0]$  and  $k_4 \in [-10\ 000 ; 10\ 000]$ . We check the stability of the polynomial family. With the given parameter values, the characteristic polynomial is

$$p(s, k_3, k_4) = 6000 + 20\ 000s + (26\ 000 - k_3)s^2 + (20\ 000 - k_4)s^3 + 10\ 000s^4. \quad (8.3.11)$$

This, obviously, is an interval polynomial. Because of the degree four, only  $p^{+-}(s)$  and  $p^{++}(s)$  have to be tested.

$$p^{+-}(s) = 2000(3 + 10s + 13s^2 + 15s^3 + 5s^4), \quad (8.3.12)$$

$$p^{++}(s) = 2000(3 + 10s + 13s^2 + 5s^3 + 5s^4). \quad (8.3.13)$$

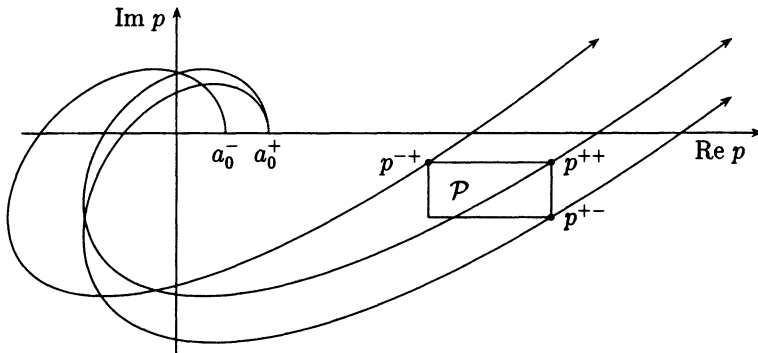


Figure 8.10. For polynomials of degree five,  $p^{+-}(s)$ ,  $p^{++}(s)$  and  $p^{-+}(s)$  have to be tested

Both polynomials are stable as can, for instance, be shown by a Hurwitz test. Therefore, the entire polynomial family is stable.  $\square$

### Example 8.12

The characteristic polynomial of the crane with the state feedback is, by (1.5.18),

$$p(s) = k_1 g + k_2 g s + [(m_L + m_C)g + k_1 \ell - k_3]s^2 + (k_2 \ell - k_4)s^3 + \ell m_c s^4.$$

Suppose all parameters except the load mass  $m_L$  are fixed, then this is an interval polynomial with  $a_2^\pm = (m_L^\pm + m_C)g + k_1 \ell - k_3$ . Only  $a_2^-$ , i.e. only  $m_L^-$  enters into  $p^{+-}(s)$  and  $p^{++}(s)$ . In other words:

for the stabilization of cranes by state feedback, it suffices to stabilize the minimum load  $m_L^-$ .  $\square$

Note that the Kharitonov theorem applies only to Hurwitz-stability, for  $\Gamma$ -stability the value set is no longer a rectangle parallel to the axes. Figure 3.16 illustrates that it does not suffice to  $\Gamma$ -stabilize the crane only for the minimum load  $m_L^-$ .

Also note that the Kharitonov theorem is necessary and sufficient only if the coefficients are truly independent. If they are dependent and overbounded by the maximal and minimal individual coefficient bounds, then the criterion is only sufficient and may give very conservative results as in the following examples.

### Example 8.13

Analyze robust stability of the polynomial

$$p(s, q_1, q_2) = (1 + 2q_1 + q_2) + (1 + q_1 + 2q_2)s + 2s^2 + s^3,$$

with  $q_1 \in [0; 1]$ ,  $q_2 \in [0; 1]$ .

Overbounding yields  $a_0^- = 1$ ,  $a_0^+ = 4$ ,  $a_1^- = 1$ ,  $a_1^+ = 4$ .

The Kharitonov polynomial

$$\begin{aligned} p^{+-} &= a_0^+ + a_1^- s + a_2^- s + a_3^+ s^3 \\ &= 4 + s + 2s^2 + s^3 \end{aligned}$$

is unstable, thus the overbounding polynomial family is not robustly stable. However, the coefficients  $a_0$  and  $a_1$  do not vary independently. Their domain is a rhombus with the following four vertices:

1.  $a_0(q_1^-, q_2^-) = 1$ ,  $a_1(q_1^-, q_2^-) = 1$ ,
2.  $a_0(q_1^-, q_2^+) = 2$ ,  $a_1(q_1^-, q_2^+) = 3$ ,
3.  $a_0(q_1^+, q_2^+) = 4$ ,  $a_1(q_1^+, q_2^+) = 4$ ,
4.  $a_0(q_1^+, q_2^-) = 3$ ,  $a_1(q_1^+, q_2^-) = 2$ .

It is shown in Figure 8.11 together with the stability boundary of  $a_0 + a_1 s + 2s^2 + s^3$ , i.e.  $2a_1 > a_0$ . It is seen that the given polynomial family is robustly stable.

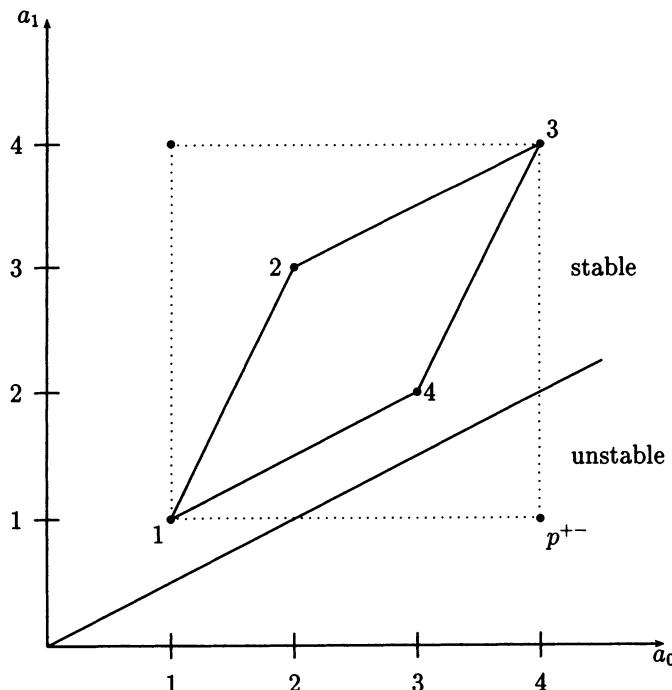


Figure 8.11. The rhombus (image of  $Q$ ) is stable, the overbounding rectangle with the vertex  $p^{+-}$  is not robustly stable

□

*Example 8.14*

Continue Example 8.12 with the fixed parameters  $m_L = 1, m_C = 1000, k_1 > 0, k_2 > 0, k_3 = 0, k_4 = 0$ . Then, we know by (1.6.9) that the system is stable for all  $\ell > 0$ . We now try to show stability for  $\ell \in [9.99; 10.01]$ , by overbounding. Consider the Kharitonov polynomial

$$\begin{aligned} p_3^{++}(s) &= a_0^+ + a_1^+ s + a_2^- s^2 + a_3^- s^3 + a_4^+ s^4 \\ &= k_1 g + k_2 g s + (1001g + 9.99k_1)s^2 + 9.99k_2s^3 + 10.010s^4. \end{aligned}$$

Its coefficients are positive and the critical stability test is  $\Delta_3^{++} > 0$ .

$$\begin{aligned} \Delta_3^{++} &= a_1^+ a_2^- a_3^- - a_0^+ (a_3^-)^2 - (a_1^+)^2 a_4^+ \\ &= k_2^2 g^2 [9.99 m_L - 0.02 m_C] \\ &= -10.01 k_2^2 g^2. \end{aligned}$$

$\Delta_3^{++}$  is negative,  $p_3^{++}(s)$  is unstable, the sufficient criterion does not even give a useful answer for a 0.1 % rope length variation around  $\ell = 10$ . The reason is that the polynomial  $p_3^{++}(s)$  does not describe a controlled crane, because  $a_2^-$  and  $a_3^-$  contain  $\ell^- = 9.99$ , whereas  $a_4^+$  contains  $\ell^+ = 10.01$ .

This example may serve as a warning that overbounding without a measure of conservativeness may lead to a useless result. At least the correct solution should be estimated in a small gap between overbounding (=sufficient stability criterion) and underbounding (=necessary stability criterion). In this book, we do not deal with such estimates, but only with exact stability boundaries. Therefore, we recommend the use of the Kharitonov theorem only for interval polynomials like in Example 8.11 and 8.12.

□

*Remark 8.15*

In the first edition of this book, some results on *interval plants* have been described. An interval plant has independent coefficient intervals for the numerator and denominator of its transfer function. These results are not repeated in this second edition for three reasons:

- i. Interval plants have little practical importance. Even in the very simple crane example (1.3.3) the rope length enters both into numerator and denominator.
- ii. It is easy to rewrite the problem in the characteristic polynomial format.
- iii. If the open-loop transfer function includes a dynamic compensator, then an interval property of the plant is, in general, destroyed. As an example, consider the denominator of (1.6.10). The parameter  $m_L$  now occurs in the coefficients of  $s^2$  and  $s^3$  by the low-pass filter term  $(1 + Ts)$ . A result worth mentioning is that a first order controller stabilizes an interval system, if and only if it stabilizes 16 extreme points resulting from the Kharitonov conditions applied to the numerator and denominator polynomials of the interval plant transfer function [41].

□

*Remark 8.16*

The proof of Kharitonov's theorem is easy after the observation that the value set  $p(j\omega, \mathcal{A})$  of an interval polynomial for fixed  $\omega$  is a rectangle with edges parallel to the real and imaginary axes. A natural question is: are there other classes of polynomials which have such a rectangular value set? Indeed, it is easy to show that polynomials with *even-odd decoupling*

$$p(s, \mathbf{q}, \mathbf{r}) = p_{\text{even}}(s^2, a_0(\mathbf{q}), a_2(\mathbf{q}), \dots) + s p_{\text{odd}}(s^2, a_1(\mathbf{r}), a_3(\mathbf{r}), \dots)$$

have the above property.

The uncertain parameters  $\mathbf{q}$  enter only in the even order coefficients, the uncertain parameters  $\mathbf{r}$  enter only in the odd ordered coefficients. Then, as in (8.3.7) and (8.3.8), the bounds of the real and imaginary parts are mutually independent and the value set is a rectangle with edges parallel to the real and imaginary axis.

$$\begin{aligned} p_{\text{even}}^-(\omega^2, a_0(\mathbf{q}), a_2(\mathbf{q}), \dots) &\leq \operatorname{Re} p(j\omega, \mathbf{q}) \leq p_{\text{even}}^+(\omega^2, a_0(\mathbf{q}), a_2(\mathbf{q}), \dots), \\ \omega p_{\text{odd}}^-(\omega^2, a_1(\mathbf{r}), a_3(\mathbf{r}), \dots) &\leq \operatorname{Im} p(j\omega, \mathbf{q}) \leq \omega p_{\text{odd}}^+(\omega^2, a_1(\mathbf{r}), a_3(\mathbf{r}), \dots). \end{aligned}$$

The determination of  $p_{\text{even}}^\pm$  and  $p_{\text{odd}}^\pm$  is easy if the uncertain parameters  $\mathbf{q}$  and  $\mathbf{r}$  enter affinely into the coefficients  $a_i$ . Then, a feasible testing set consists of all combinations of extremal values of  $\mathbf{q}$  and  $\mathbf{r}$ , see Panier et al. [167].  $\square$

## 8.4 Affine Coefficients: Edge Theorem

When Kharitonov discovered his amazingly simple result, it took some time before it got published and then known in the international literature. The author remembers that he first heard about it from A. Olbrot in 1981 at a meeting in Bielefeld, and could not believe it. It became much better understood by the value set interpretation given in the preceeding section. The Kharitonov theorem and the value set approach triggered a research direction in the 1980s, see [41] for a historical account. Practially the most important result of this period is the *edge theorem* by Bartlett, Hollot and Huang [43]. Simply speaking, it states that for the stability of a polynomial with linear parameter dependency, it suffices to check the edges of the  $Q$ -box.

Consider the polynomial family

$$P(s, Q) = \{ p(s, q_1, q_2, \dots, q_\ell) = p_0(s) + \sum_{i=1}^{\ell} q_i p_i(s) \mid q_i \in [q_i^-; q_i^+], \quad i = 1, 2, \dots, \ell \}. \quad (8.4.1)$$

The coefficients depend linearly on the uncertain parameter vector  $\mathbf{q} = [q_1 \ q_2 \ \dots \ q_\ell]^T$ . More precisely, it is an affine dependency because of the additional constant terms in  $p_0(s)$ , i.e. each coefficient  $a_i$  has the form

$$a_i = a_i^0 + f_{1i} q_1 + f_{2i} q_2 + \dots + f_{\ell i} q_\ell, \quad i = 0, 1, \dots, n. \quad (8.4.2)$$

The parameters  $q_i$  vary in an  $\ell$ -dimensional box  $Q$ :

$$q_i \in [q_i^-; q_i^+], \quad i = 1, 2, \dots, \ell. \quad (8.4.3)$$

The polynomial family  $P(s, Q) = \{ p(s, \mathbf{q}) \mid \mathbf{q} \in Q \}$  represents a parallelepiped (the generalization of the parallelogram to higher dimensional spaces) in the coefficient space because of the affine mapping (8.4.2). Its vertices and edges are generated by vertices and edges of the  $Q$ -box. If all parameter values  $q_i$  take their minimum or maximum value, then the corresponding polynomial is called a *vertex polynomial*. If exactly one of these parameters varies between its minimum and maximum value while the remaining  $\ell - 1$  parameters stick either to their minimal or maximal values, then this polynomial family is called an *edge polynomial family*.

For notational convenience, the original box is scaled to the unit box with center zero and sidelength 2 by the transformation

$$\tilde{q}_i = \frac{2q_i - q_i^+ - q_i^-}{q_i^+ - q_i^-}, \quad i = 1, 2, \dots, \ell. \quad (8.4.4)$$

It maps  $q_i = q_i^-$  to  $\tilde{q}_i = -1$  and  $q_i = q_i^+$  to  $\tilde{q}_i = +1$ . The tilde is now omitted and we have without loss of generality  $q_i \in [-1; +1]$ .

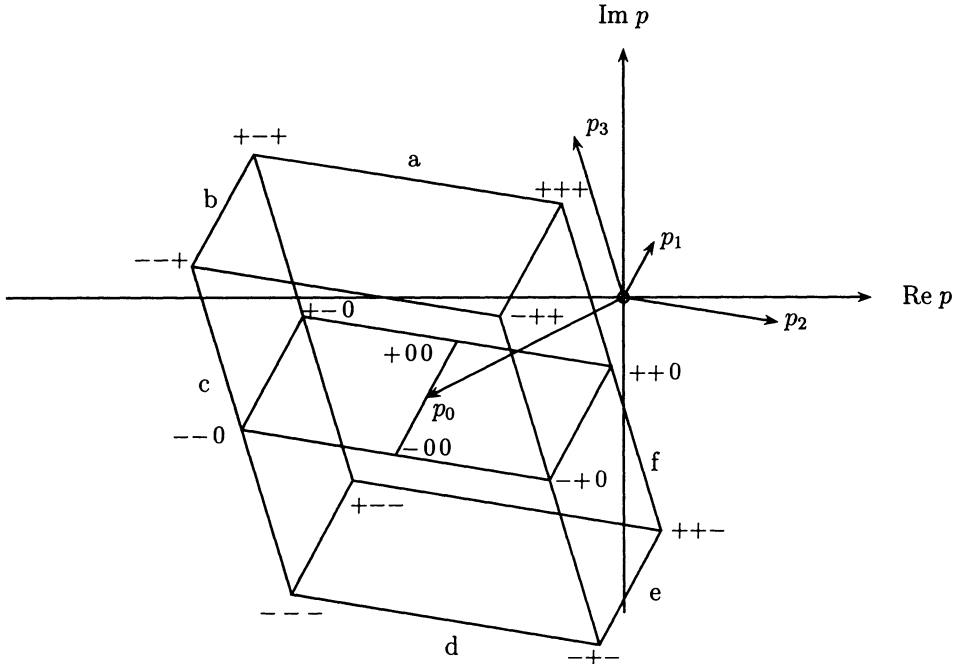


Figure 8.12. The construction of the value set with three parameters and fixed  $\omega$

First, the value set  $\mathcal{P}(j\omega, Q)$  with affine coefficient functions will be constructed. In the case of two parameters, the value set  $\mathcal{P}(j\omega, Q)$  for fixed  $\omega$  is a parallelogram in the complex plane.

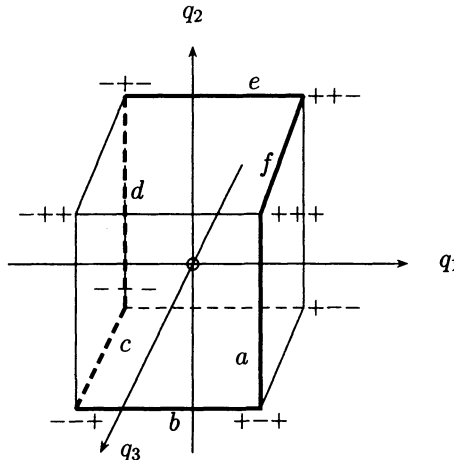


Figure 8.13. The edges  $a - f$  generate the boundary of the value set of Figure 5.7

Consider now a third parameter, i.e. we have the affine polynomial family

$$\{ p(s, q_1, q_2, q_3) = p_0(s) + q_1 p_1(s) + q_2 p_2(s) + q_3 p_3(s) \mid q_i \in [-1; +1], \quad i = 1, 2, 3 \}. \quad (8.4.5)$$

For fixed frequency  $s = j\omega^*$ , we calculate the four complex numbers  $p_0(j\omega^*)$ ,  $p_1(j\omega^*)$ ,  $p_2(j\omega^*)$ ,  $p_3(j\omega^*)$  and draw four vectors at the origin that represent these numbers (see Figure 8.12).

Starting from  $p_0$ , add the vectors  $q_1^+ p_1$  and  $q_1^- p_1$  and obtain the points  $+00$  and  $-00$  respectively. The segment  $[+00; -00]$  is the value set for the polynomial family  $p(s, q_1, 0, 0)$ . In  $+00$ , we add  $q_2^+ p_2$  (arriving at  $++0$ ) resp.  $q_2^- p_2$  (arriving at  $+-0$ ) and repeat this procedure at  $-00$ . We obtain the parallelogram  $++0, +-0, --0, -+0$ , which corresponds to the polynomial family  $p(s, q_1, q_2, 0)$ . The last step is adding  $q_3^+ p_3$  resp.  $q_3^- p_3$  at all four vertices to get a hexagon  $+++, ++-, --+, ---, -+-, +-+$ , which is the value set of the polynomial family (8.4.5) for the fixed frequency  $\omega^*$ .

Denote the six edges of the value set  $a$  to  $f$ , see Figure 8.12. They are the image of six pairwise adjacent edges of the  $Q$ -box as indicated in Figure 8.13. The other six edges and also two vertices are mapped into the interior of the hexagon. Observe that vertices and edges that contribute to the boundary of the hexagon are not the same with varying frequency. Changing the frequency leads to different values of  $p_i(j\omega)$ ,  $i = 0, 1, 2, 3$ , where  $p_0(j\omega)$  determines the midpoint of the hexagon and the vectors  $p_1(j\omega)$ ,  $p_2(j\omega)$  and  $p_3(j\omega)$  determine the size and orientation. The *transition frequencies*, where the image of an edge of the  $Q$ -box changes from the boundary into the interior and vice versa, may be calculated by comparing the phases of  $p_1(j\omega)$ ,  $p_2(j\omega)$  and  $p_3(j\omega)$ . If two of them are equal, then a transition occurs. At the transition frequency, the value set  $P(j\omega, Q)$  degenerates from a hexagon to a parallelogram.

Adding a further term  $q_4 p_4(s)$  to (8.4.5) requires adding  $q_4^+ p_4$  resp.  $q_4^- p_4$ , which yields an octagon. Obviously, the value set of an affine family of polynomials for fixed frequency is always a convex polygon with, at most,  $2\ell$  vertices (this number may

decrease for special frequencies). Two opposite vertices are parallel. This special kind of polygon is called a *parpolygon*.

With these preparations, we are now ready to formulate and prove the edge theorem.

*Theorem 8.17 (edge theorem of Bartlett, Hollot and Huang)*

The polynomial family  $P(s, Q) = \{ p(s, \mathbf{q}) = \sum_{i=0}^n a_i(\mathbf{q}) s^i \mid \mathbf{q} \in Q \}$  with affine coefficient functions  $a_i(\mathbf{q})$  and  $Q = \{ \mathbf{q} \mid q_i \in [q_i^-; q_i^+], i = 1, 2, \dots, \ell \}$  is stable if and only if the edges of  $Q$  are stable.

□

*Proof*

The necessity is obvious. We use the zero exclusion principle for the proof of sufficiency. With varying frequency, the shape of the parpolygon is changing and is moving around the origin. If the polynomial family is unstable, then there is a frequency where the boundary of the parpolygon, i.e. an edge goes through the origin of the  $p$ -plane. Because this edge is the image of an edge of the  $Q$ -box, the instability can be recognized by testing all edges of the  $Q$ -box.

□

*Remark 8.18*

It is not necessary to test all edges as illustrated by Figure 8.13, however, the amount of calculation to determine the critical edges for each frequency interval between the transition frequencies is about the same as to test all edges. A procedure that avoids the mapping of superfluous edges was given by Fu [92]. It reduces the problem of the computation of all  $2^\ell$  extremal points to the computation of  $\ell$  points followed by a sorting problem.

□

*Remark 8.19*

The edge theorem is valid for a more general class of polynomial families than those bounded by a  $Q$ -box. It was shown in [43] that a “polytope” of polynomials is robustly stable if and only if all its edges are stable. A polytope of polynomials is the higher dimensional generalization of a convex polygon in two dimensions. It is the convex hull of a finite number of points. A polytope of polynomials can be written in the form

$$\begin{aligned} P_\ell &= \text{conv} \{ p_1(s), p_2(s), \dots, p_\ell(s) \} \\ &= \{ p(s) = \sum_{i=1}^{\ell} \lambda_i p_i(s) \mid \sum_{i=1}^{\ell} \lambda_i = 1, \quad \lambda_i \geq 0, \quad i = 1, 2, \dots, \ell \}. \end{aligned}$$

Each edge corresponds to polynomials  $p(s, \mathbf{q})$  where exactly one parameter  $q_i$  varies between its given limits, while the remaining  $\ell - 1$  parameters take their minimum or maximum value. The  $\lambda_i$  are called *barycentric coordinates*. The name barycenter (= center of gravity) stems from the fact that every point inside the polytope can be made the center of gravity by distributing a unit mass over the vertices of the polytope. A barycenter is outside the polytope if and only if at least one of the vertex masses is negative.  $\square$

The edge theorem reduces the robustness analysis of an affine polynomial family to a finite number of one-dimensional tests. This is a drastic reduction of the testing set compared with the complete set. An  $\ell$ -dimensional box has  $2^\ell$  vertices. From each vertex there start  $\ell$  edges. The number  $\ell 2^\ell$  would count each edge two times, thus, the total number of edges is  $\ell 2^{\ell-1}$ . For some values of  $\ell$ , the number of vertices and edges is given in Table 8.1. Obviously, for a large number of parameters the number of edges to be tested becomes prohibitively large.

Table 8.1: Number of vertices and edges of an  $\ell$ -dimensional box

$\ell$	$2^\ell$ vertices	$\ell 2^{\ell-1}$ edges
1	2	1
2	4	4
3	8	12
4	16	32
5	32	80
10	1024	5120
20	1 048 576	10 485 760

Consider an edge with end points  $p_b$  and  $p_c$ , i.e. the polynomial family

$$P(s, Q) = \{ (1 - q_1)p_b(s) + q_1 p_c(s) \mid q_1 \in [0; 1] \}. \quad (8.4.6)$$

A stability test for families of polynomials generated by a linear dependence on a single uncertain parameter was given by Bialas [49].

### Theorem 8.20 (Bialas)

Let  $\mathbf{H}_n^b$  and  $\mathbf{H}_n^c$  be the Hurwitz matrices of

$$p_b(s) = b_0 + b_1 s + b_2 s^2 + \cdots + b_n s^n, \quad b_n > 0,$$

$$p_c(s) = c_0 + c_1 s + c_2 s^2 + \cdots + c_n s^n, \quad c_n > 0,$$

respectively. The polynomial family

$$P(s, Q) = \{ (1 - q)p_b(s) + qp_c(s) \mid q \in [0; 1] \}$$

is stable, if and only if:

1.  $p_b(s)$  is stable.
2. The matrix  $(\mathbf{H}_n^b)^{-1} \mathbf{H}_n^c$  has no non-positive *real* eigenvalues.

$\square$

*Proof*

Polynomial  $p_b(s)$  is in  $P(s, Q)$ , so obviously, Condition 1 of the present theorem is necessary. Furthermore, its satisfaction implies the existence of a stable starting point  $q = 0$ . Now, assuming that Condition 1 is indeed satisfied, the second condition is investigated. For an arbitrary polynomial

$$p(s, q) = (1 - q)p_b(s) + qp_c(s),$$

in  $P(s, Q)$  it can be shown by straightforward algebraic manipulations that the polynomial's Hurwitz matrix satisfies the following relationship:

$$\mathbf{H}_n(q) = (1 - q)\mathbf{H}_n^b + q\mathbf{H}_n^c.$$

Condition 1 and Theorem 2.1 imply that for  $q = 0$

$$\det \mathbf{H}_n(0) = \det \mathbf{H}_n^b \neq 0.$$

This implies that  $\mathbf{H}_n^b$  is invertible, so for arbitrary  $q \in (0, 1]$ , it can be written that

$$\begin{aligned} \det \mathbf{H}_n(q) &= \det \left( -q\mathbf{H}_n^b \left[ \left( \frac{1-q}{-q} \right) \mathbf{I} - (\mathbf{H}_n^b)^{-1} \mathbf{H}_n^c \right] \right) \\ &= (-q)^n \det \mathbf{H}_n^b \det \left( \left( \frac{1-q}{-q} \right) \mathbf{I} - (\mathbf{H}_n^b)^{-1} \mathbf{H}_n^c \right). \end{aligned}$$

This implies that, for any  $q \in (0, 1]$ ,  $\det \mathbf{H}_n(q) = 0$  if and only if

$$\det \left( \left( \frac{1-q}{-q} \right) \mathbf{I} - (\mathbf{H}_n^b)^{-1} \mathbf{H}_n^c \right) = 0. \quad (8.4.7)$$

Recall that by definition,  $s \in \mathbb{C}$  is an eigenvalue of a matrix  $\mathbf{A}$  if and only if  $\det(s\mathbf{I} - \mathbf{A}) = 0$ . This makes it clear that (8.4.7) is satisfied if and only if there is a  $q \in (0; 1]$  such that  $-(1-q)/q$  is an eigenvalue of  $(\mathbf{H}_n^b)^{-1} \mathbf{H}_n^c$ . Since  $-(1-q)/q$  is real and ranges from  $-\infty$  up to 0 as  $q$  ranges from 0 to 1, it follows that (8.4.7) is satisfied if and only if  $(\mathbf{H}_n^b)^{-1} \mathbf{H}_n^c$  has a non-positive real eigenvalue. This argument has shown the equivalence of Condition 2 of this theorem with Condition 2 of Theorem 2.1 (when Condition 1 is assumed to be satisfied). This equivalence completes the proof.  $\square$

The test of the second condition in Theorem 8.20 can be simplified. By 1.6.4, we have

$$\det \mathbf{H}_n(q) = a_0(q) \det \mathbf{H}_{n-1}(q),$$

where

$$\begin{aligned} a_0(q) &= (1 - q)b_0 + qc_0, \\ \mathbf{H}_{n-1} &= (1 - q)\mathbf{H}_{n-1}^b + q\mathbf{H}_{n-1}^c. \end{aligned}$$

By Condition 1  $p_b(s)$  is stable, thus  $b_0 > 0$  and  $c_0 = p_c(0) > 0$  must be required for  $a_0(q) > 0$ . For the second factor, the proof of Theorem 8.20 may be written with  $\mathbf{H}_n$  replaced by  $\mathbf{H}_{n-1}$  [14]. Thus, we have

*Theorem 8.21*

$P(s, Q) = \{(1 - q)p_b(s) + qp_c(s) \mid q \in [0; 1]\}$  is stable, if and only if:

1.  $p_b(s)$  is stable.
2.  $p_c(0) > 0$ .
3. The matrix  $(\mathbf{H}_{n-1}^b)^{-1} \mathbf{H}_{n-1}^c$  has no non-positive real eigenvalues.

□

The Bialas test can be executed by a standard eigenvalue program for the calculation of all eigenvalues of the Bialas matrices  $(\mathbf{H}_{n-1}^b)^{-1} \mathbf{H}_{n-1}^c$ .

*Remark 8.22*

If the two vertices  $p_b$  and  $p_c$  are exchanged, then the eigenvalues are reciprocal. This fact follows from the relation

$$(\mathbf{A}^{-1} \mathbf{B})^{-1} = \mathbf{B}^{-1} \mathbf{A} \quad (8.4.8)$$

for square, non-singular matrices  $\mathbf{A}$  and  $\mathbf{B}$ . This means that the eigenvalues of  $(\mathbf{H}_{n-1}^b)^{-1} \mathbf{H}_{n-1}^c$  and  $(\mathbf{H}_{n-1}^c)^{-1} \mathbf{H}_{n-1}^b$  have the same angle with respect to the axes and reciprocal absolute values. This has no influence on the existence of negative real eigenvalues. □

*Example 8.23*

Return to the crane of Example 8.14 with a larger rope length variation  $\ell \in [5; 15]$  and  $k_1 = k_2 = 1, k_3 = k_4 = 0$ . Note that the 0.1 % variation around 10 is embedded in this interval. The vertex polynomials are

$$\begin{aligned} p_a(s) &= p(s, \ell^-) = 10 + 10s + 10015s^2 + 5s^3 + 5000s^4, \\ p_b(s) &= p(s, \ell^+) = 10 + 10s + 10025s^2 + 15s^3 + 15000s^4. \end{aligned}$$

The real root and infinite root conditions are satisfied, the complex root condition follows from the Hurwitz matrices

$$\mathbf{H}_3^b = \begin{bmatrix} 5 & 10 & 0 \\ 5000 & 10015 & 10 \\ 0 & 5 & 10 \end{bmatrix}, \quad \mathbf{H}_3^c = \begin{bmatrix} 5 & 10 & 0 \\ 15000 & 10025 & 10 \\ 0 & 5 & 10 \end{bmatrix}.$$

The MATLAB command `eig(inv(Hb) * Hc)` yields the eigenvalues  $\lambda_{1,2} = 1, \lambda_3 = 3$ , `eig(inv(Hc) * Hb)` yields  $\lambda_{1,2} = 1, \lambda_3 = 1/3$ . The interval  $[5; 15]$  of the rope length is stable. (As we know already, all  $\ell > 0$  are stable with any  $k_1 > 0, k_2 > 0$ ). □

## 8.5 Edge Theorem for Gamma-stability

The generalization of the zero exclusion theorem to  $\Gamma$ -stability is obvious:

*Theorem 8.24*

The polynomial family  $P(s, Q)$  is robustly  $\Gamma$ -stable, if and only if:

1. There exists a  $\Gamma$ -stable polynomial  $p(s, \mathbf{q}) \in P(s, Q)$ .
2.  $0 \notin \mathcal{P}(\sigma(\alpha) + j\omega(\alpha), Q)$  for all  $\alpha \in [\alpha^-; \alpha^+]$ .

If  $\partial\Gamma$  is composed of several boundary segments then all of them must be included in checking the second condition.

□

The proof of the edge theorem in Section 8.4 was based on the fact that the value set is a parpolygon whose edges originate from edges of the  $Q$ -box, and the origin can enter the value set only through one of the edges of the parpolygon. In (8.4.5),  $s = j\omega^*$  was substituted. All arguments remain valid if  $s = \sigma(\alpha^*) + j\omega(\alpha^*)$  is substituted. Thus, the following theorem holds:

*Theorem 8.25 (Bartlett, Hollot, Huang)*

The polynomial family

$$P(s, Q) = \{ p(s, \mathbf{q}) = \sum_{i=0}^n a_i(\mathbf{q}) s^i \mid \mathbf{q} \in Q \}$$

with affine coefficient functions  $a_i(\mathbf{q})$  and  $Q = \{ \mathbf{q} \mid q_i \in [q_i^-; q_i^+], i = 1, 2, \dots, \ell \}$  is  $\Gamma$ -stable if and only if the edges of  $Q$  are  $\Gamma$ -stable.

□

It remains to provide a  $\Gamma$ -stability test for an edge with endpoints  $\mathbf{q}_b$  and  $\mathbf{q}_c$  corresponding to the polynomials  $p_b(s) = p(s, \mathbf{q}_b)$  and  $p_c(s) = p(s, \mathbf{q}_c)$ . Since  $a(\mathbf{q})$  is affine, the set of polynomials corresponding to the edge of the  $Q$ -box is

$$P(s, Q) = \{ (1-q)p_b(s) + qp_c(s) \mid q \in [0; 1] \}.$$

A generalization of the Bialas test (Theorem 8.20 or 8.21) requires an algebraic formulation of the stability conditions. Such a generalization will be given for the unit circle, i.e. Schur stability, in Chapter 11. For other  $\Gamma$ -stability regions, the algebraic formulation of stability criteria is more complicated, see (4.4.18). But in principle, a finite test may be derived.

A practical approach is a root locus plot for

$$(1-q)p_b(s) + qp_c(s) = 0,$$

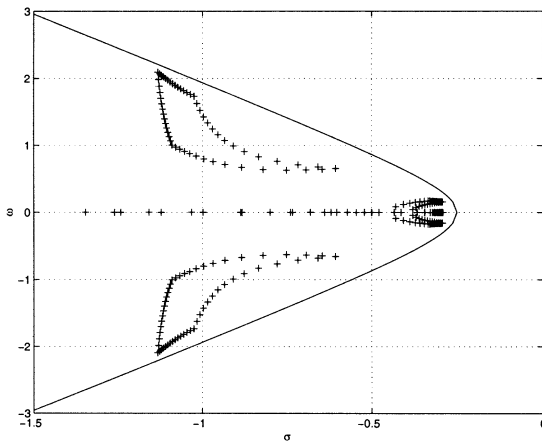


Figure 8.14. The four edges of  $Q$  are  $\Gamma$ -stable

which may be written as

$$1 + q \frac{p_c(s) - p_b(s)}{p_b(s)} = 0.$$

The root locus for  $q \in [0; 1]$  must have  $\Gamma$ -stable end points and must not intersect any branch of  $\partial\Gamma$ . This is a necessary and sufficient condition for  $\Gamma$ -stability of the edge connecting the vertices  $\mathbf{q}_b$  and  $\mathbf{q}_c$ .

#### Example 8.26

Consider the crane with parameters  $m_C = 1000, m_L \in [1000; 2000], \ell \in [8; 16]$  and output feedback  $u = -[500 \ 2850 \ -22800 \ 0]\mathbf{x}$ . It has been designed in Chapter 3 for  $\Gamma$ -stability for the four vertices of  $Q$ , where  $\partial\Gamma$  is the hyperbola  $\omega^2 = 4\sigma^2 - 0.25$ ,  $\sigma \leq -0.25$ . From the parameter space analysis in Figure 3.16 we know that the entire  $Q$ -box is  $\Gamma$ -stable. This result shall now be verified by checking the four edges of  $Q$ . Figure 8.14 shows the four root loci for the four edges. They stay on the stable side of  $\partial\Gamma$ . Then, by the edge theorem the entire  $Q$  is  $\Gamma$ -stable.  $\square$

The comparison of the parameter-plane in Figure 3.16 and the gridded edge mapping of Figure 8.14 allows some statements about the relative merits of the two approaches:

1. The parameter plane figure immediately shows the margins in terms of the uncertain parameters  $q_1 = m_L$  and  $q_2 = \ell$ . Since the entire  $\Gamma$ -stable region is shown, it is easy to test other operating domains  $Q$  for  $\Gamma$ -stability or to find the “largest” one.
2. The gridded edge mapping figure immediately shows the margins in terms of the definition of  $\Gamma$ -stability. Since all eigenvalues for  $\mathbf{q} \in Q$  are enclosed by the string of eigenvalues along the four edges, it is easy to test other  $\Gamma$ -stability definitions or to find the “tightest” one.

3. A third parameter  $q_3$  entering linearly may be gridded in both approaches. In the parameter space the discrete family of boundaries for the grid on  $q_3$  is projected on the  $(q_1, q_2)$ -plane, where the projection of the  $Q$ -box is a rectangle. This idea may be extended to more uncertain parameters. In the gridded edge mapping approach, a third parameter requires root loci for the 12 edges of the  $Q$ -box. Also, this idea may be extended to more uncertain parameters with the obvious practical limit given by the exponentially increasing number of edges, see Table 8.1.
4. For a third parameter  $q_3 = m_C$  (the crab mass) entering bilinearly, the parameter space projection approach was applied in Figure 3.21. The edge result does not apply to bilinear parameters, see Figure 4.6. Here also the interior of the  $Q$ -box must be tested for  $\Gamma$ -stability.
5. Two parameters entering polynomially into the coefficients of the characteristic polynomial, have been analyzed in Figure 4.9 and the projection method for further gridded parameters may be applied also.

The advantages of the edge result for robustness analysis are obvious for Hurwitz-stability by the Bialas edge test and a larger number  $\ell$  of uncertain plant parameters entering linearly. The test requires one eigenvalue calculation per edge. In other situations, the parameter space approach is advantageous for robustness analysis. Also, the parameter space approach is superior for systematic design steps by the intersection of admissible sets of controller parameters.

### *Remark 8.27*

The derivation of the zero exclusion result from Mikhailov's theorem suggests the construction of value sets in a complex plane

$$\operatorname{Re} p[\sigma(\alpha) + j\omega(\alpha)] + j \operatorname{Im} p[\sigma(\alpha) + j\omega(\alpha)].$$

If the  $\Gamma$ -stability boundary is represented by the recursion formula (4.2.6), then its relationship with the real and imaginary parts of (4.2.21) may be used:

$$\begin{bmatrix} \operatorname{Re} p[\sigma(\alpha) + j\omega(\alpha)] \\ \operatorname{Im} p[\sigma(\alpha) + j\omega(\alpha)] \end{bmatrix} = \begin{bmatrix} 1 & -\sigma(\alpha) \\ 0 & \omega(\alpha) \end{bmatrix} \begin{bmatrix} d_0(\alpha) & d_1(\alpha) & \dots & d_n(\alpha) \\ 0 & d_0(\alpha) & \dots & d_{n-1}(\alpha) \end{bmatrix} \mathbf{a}.$$

The RRB,  $\omega(\alpha) = 0$ , is treated separately, then for the CRB,  $\omega(\alpha) \neq 0$ , the following two equations must be analyzed:

$$\begin{bmatrix} f_1(\alpha) \\ f_2(\alpha) \end{bmatrix} = \begin{bmatrix} d_0(\alpha) & d_1(\alpha) & \dots & d_n(\alpha) \\ 0 & d_0(\alpha) & \dots & d_{n-1}(\alpha) \end{bmatrix} \mathbf{a} = \begin{bmatrix} 1 & \frac{\sigma(\alpha)}{\omega(\alpha)} \\ 0 & \frac{1}{\omega(\alpha)} \end{bmatrix} \begin{bmatrix} \operatorname{Re} p[\sigma(\alpha) + j\omega(\alpha)] \\ \operatorname{Im} p[\sigma(\alpha) + j\omega(\alpha)] \end{bmatrix}.$$

The zero exclusion condition for  $p[\sigma(\alpha) + j\omega(\alpha)]$  directly translates to zero exclusion conditions in the  $(f_1, f_2)$ -plane.

□

The difficulty of a robustness test increases enormously from the interval or affine case to multilinear or polynomial coefficient functions. Therefore, it is important to bring a given polynomial first to its simplest form. We have done this already by converting the rational coefficient function in  $p(s)$  of (1.5.17) to the coefficient function in  $\bar{p}(s) = \ell m_c p(s)$  of (1.5.18).

Sometimes, simple polynomials look complicated but can be factorized into

$$p(s, \mathbf{q}) = f(\mathbf{q})\bar{p}(s, \mathbf{q}), \quad f(\mathbf{q}) \neq 0 \text{ for all } \mathbf{q} \in Q. \quad (8.5.1)$$

Then,  $p(s, \mathbf{q})$  and  $\bar{p}(s, \mathbf{q})$  have the same roots but  $\bar{p}(s, \mathbf{q})$  may be simpler.

### Example 8.28

$p(s, \mathbf{q}) = q_1 + q_1^2 s + q_1 q_2 s^2 + q_1 s^3$  can be converted into an interval polynomial because

$$\bar{p}(s, \mathbf{q}) = \frac{p(s, \mathbf{q})}{q_1} = (1 + q_1 s + q_2 s^2 + s^3).$$

□

### Example 8.29

$$p(s, \mathbf{q}) = \left(1 + \frac{q_1}{q_2}\right) + \frac{1 + q_1}{q_2} s + \left(5 + \frac{2 + q_1}{q_2}\right) s^2 + s^3$$

can be converted into an affine polynomial

$$\bar{p}(s, \mathbf{q}) = q_2 p(s, \mathbf{q}) = (q_1 + q_2) + (1 + q_1)s + (2 + q_1 + 5q_2)s^2 + q_2 s^3.$$

□

### Example 8.30

Consider the polynomial

$$p(s, \mathbf{q}) = (1 + q_1^2) + (q_2 e^{q_3^2} + q_3^2)s + s^2, \quad q_i \in [1; 2], \quad i = 1, 2, 3 \quad (8.5.2)$$

with three uncertain parameters

$$\mathbf{q} = [q_1 \ q_2 \ q_3]^T. \quad (8.5.3)$$

At first glance, this polynomial looks complicated for a robustness analysis. But note that each independent variable  $q_i$  appears only in a single coefficient function:

$$\begin{aligned} a_0(\mathbf{q}) &= a_0(q_1) &= 1 + q_1^2, \\ a_1(\mathbf{q}) &= a_1(q_2, q_3) &= q_2 e^{q_3^2} + q_3^2, \\ a_2(\mathbf{q}) &= a_2 &= 1. \end{aligned} \quad (8.5.4)$$

The coefficient functions are independent of each other and generate a rectangle in the  $(q_1, q_2)$ -plane. Therefore, the Kharitonov theorem may be applied.

□

## 8.6 Singularity of Value Sets

In Section 2.7, we have investigated Hurwitz-stability of a polynomial family

$$P(s, q) = A(s)Q(s) + B(s), \quad (8.6.1)$$

with given  $A(s), B(s)$  and the uncertain polynomial

$$Q(s) = q_0 + q_1 s + \dots + q_m s^m. \quad (8.6.2)$$

The occurrence of singular frequencies for fixed  $K_P$  will now be explained in terms of value sets.

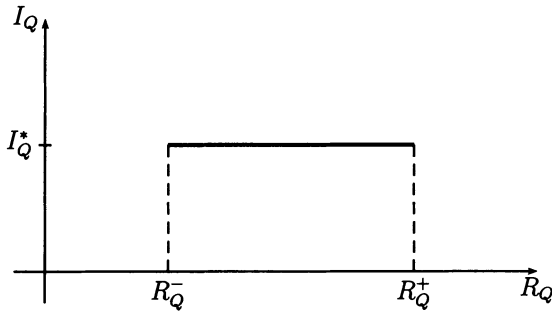


Figure 8.15. Value set of  $Q(j\omega)$

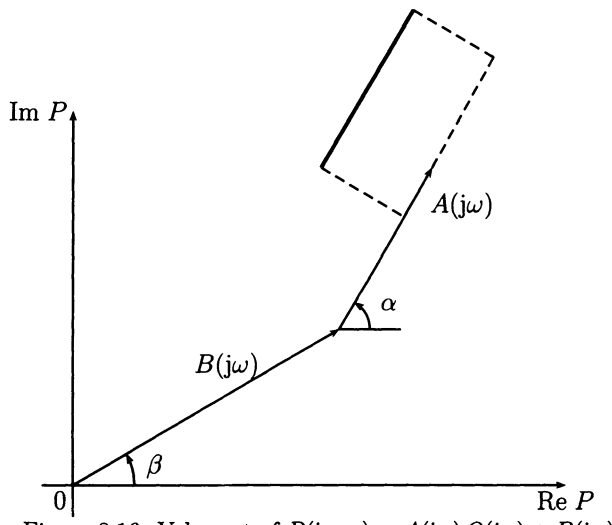
For  $s = j\omega$ ,  $Q(j\omega)$  is split into its real and imaginary parts

$$\begin{aligned} Q(j\omega) &= R_Q + jI_Q, \\ R_Q &= q_0 - q_2\omega^2 + q_4\omega^4 - + \dots, \\ I_Q &= \omega(q_1 - q_3\omega^2 + q_5\omega^4 - + \dots), \end{aligned} \quad (8.6.3)$$

with the extremal values

$$\begin{aligned} R_Q^- &= q_0^- - q_2^+\omega^2 + q_4^-\omega^4 - + \dots, \\ R_Q^+ &= q_0^+ - q_2^-\omega^2 + q_4^+\omega^4 - + \dots. \end{aligned} \quad (8.6.4)$$

Suppose  $I_Q = I_Q^*$  is fixed, in the PID case this corresponds to  $K_P$  fixed. The corresponding value set is constructed now for fixed  $\omega$ . Figure 8.15 shows the value set of  $Q(j\omega)$ , it is a straight line segment parallel to the real axis. Multiplication with the complex number  $A(j\omega) = |A|e^{j\alpha}$  rotates the line segment by an angle  $\alpha$  and stretches or shrinks it by a factor  $|A|$ . Finally, it is added to  $B(j\omega) = |B|e^{j\beta}$ . For the frequency  $\omega$  illustrated in Figure 8.16, the line segment may be extended arbitrarily far without ever hitting the origin. A stability boundary occurs only at the singular frequencies, when the straight line through the segment passes through the origin. Then,  $\text{Im } P(j\omega) = c \text{Re } P(j\omega)$ . This is the singular case of the two equations  $\text{Re } P(j\omega) = 0$  and  $\text{Im } P(j\omega) = 0$  that was analyzed in Sections 2.6 and 2.7.

Figure 8.16. Value set of  $P(j\omega, q) = A(j\omega)Q(j\omega) + B(j\omega)$

# 9 Value Sets for Non-linear Coefficient Functions

Results for robustness analysis of polynomials with interval or affine coefficient functions have been shown in Chapter 8. Simple testing sets (vertices, edges) have been found whose stability guarantees stability of the entire  $Q$ -box. It is tempting to look for further results (faces?, diagonals?) for multilinear coefficient functions (terms like  $q_1 q_2, q_2 q_3, q_1 q_2 q_3$ ) and polynomial coefficient functions (terms like  $q_1^2 q_2$  and no possibility to introduce  $q_3 = q_1^2$  as an independent parameter). Such hopes for general classes like multilinear or polynomial coefficient functions have been buried by the following example. It shows that testing sets in general cannot be derived from the  $Q$ -box alone, they also depend on the specific polynomial and its Jacobian. Special uncertainty structures are exploited for robust stability analysis, e.g. tree-structures in the polynomial, e.g.  $p(s, q_1, q_2, q_3) = p_1(s, q_1)p_2(s, q_2) + p_3(s, q_3)$ .

## 9.1 A Warning Example

*Example 9.1 (see [21])*

Let

$$p(s, q_1, q_2) = (2 + r^2 + 6q_1 + 6q_2 + 2q_1 q_2) + (2 + q_1 + q_2)s + (2 + q_1 + q_2)s^2 + s^3. \quad (9.1.1)$$

Note that this is a generalization of Example 4.17, there  $r = 0.2$  was chosen. Let  $q_1 > 0$ ,  $q_2 > 0$ , then  $a_0 > 0$ ,  $a_1 > 0$ , and  $a_2 > 0$ , and the stability condition is

$$a_1 a_2 - a_0 = (q_1 - 1)^2 + (q_2 - 1)^2 - r^2 > 0.$$

The system is stable outside a circle with center  $q_1 = 1$ ,  $q_2 = 1$  and radius  $r$ , see Figure 4.5. Now, let  $r$  go to zero. There remains an isolated unstable point (IUP) at  $q_1 = 1$ ,  $q_2 = 1$ . We can choose an arbitrary  $Q$ -box that contains the IUP and obviously stability is not related to other points in  $Q$  than just the IUP. In this special case,  $r = 0$  instead of  $r = 0.2$  of Figure 4.6, the root set just touches the imaginary axis

in a single point  $\omega = 2$ . The radius  $r$  does not enter into the Jacobian of Example 4.19, thus it is unchanged ( $q_1 = q_2$ ) as shown in the right part of Figure 4.7. For the construction of the value set, the segment inside  $Q$  of the Jacobi line ( $\det J = 0$ ) line must be considered. The line obviously only depends on the polynomial; only the endpoints of the line segment depend on the box  $Q$ . Figure 9.1 shows the value set at the frequency  $\omega = 2$  for this example. At this frequency, the image of the Jacobi line passes through the origin. At all other frequencies, zero is excluded from the value set.

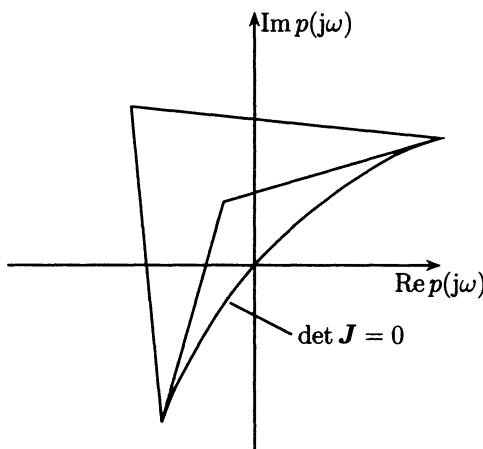


Figure 9.1. Value set of the warning example at  $\omega = 2$  (not to scale)

□

### Remark 9.2

In order to rule out further conjectures, e. g. about faces of  $Q$ , the example was generalized to a parameter space of arbitrary dimension  $\ell$  [6]. Let

$$p(s, \mathbf{q}) = a_0(\mathbf{q}) + a_1(\mathbf{q})s + a_2(\mathbf{q})s^2 + s^3, \quad (9.1.2)$$

with the bilinear coefficient functions

$$a_0(\mathbf{q}) = \ell(\ell - 1) + r^2 + 2(\ell + 1) \sum_{i=1}^{\ell} q_i + 2 \sum_{i=1}^{\ell-1} \sum_{j=i+1}^{\ell} q_i q_j,$$

$$a_1(\mathbf{q}) = \ell + \sum_{i=1}^{\ell} q_i,$$

$$a_2(\mathbf{q}) = a_1(\mathbf{q}).$$

Let  $\mathbf{q} \in Q^+ = \{ \mathbf{q} \mid q_i > 0, i = 1, 2, \dots, \ell \}$ , then all coefficients  $a_i(\mathbf{q})$  are positive and the only remaining Hurwitz-stability conditions is  $a_1(\mathbf{q})a_2(\mathbf{q}) - a_0(\mathbf{q}) > 0$ . It is easily verified that

$$a_1(\mathbf{q})a_2(\mathbf{q}) - a_0(\mathbf{q}) = \sum_{i=1}^{\ell} (q_i - 1)^2 - r^2.$$

The resulting stability condition

$$\sum_{i=1}^{\ell} (q_i - 1)^2 > r^2 \quad (9.1.3)$$

is satisfied outside a ball of radius  $r$  and center  $\mathbf{q}^0 = [1 \ 1 \ \dots \ 1]^T$ .

Next, we let  $r$  go to zero. Thus, the unstable ball shrinks to an isolated unstable point  $\mathbf{q}^0$ . With the exception of this point, the polynomial is stable for all  $\mathbf{q} \in Q^+$ . This example has been used as a benchmark test in many publications. It also illustrates the risk in gridding methods without graphical warning on closeness to instability.  $\square$

The values set of Figure 9.1 may be generated by a chord approximation. For  $r = 0$  and  $s = j2$ , the value of the polynomial is

$$p(j2, q_1, q_2) = (2 + 6q_1 + 6q_2 + 2q_1q_2) - (8 + 4q_1 + 4q_2) + j(-4 + 2q_1 + 2q_2).$$

For fixed  $q_2$ , the expression is linear in  $q_1$ , therefore the dotted lines in the  $Q$ -box of Figure 9.2 map into straight line segments in the value set. For example, the center

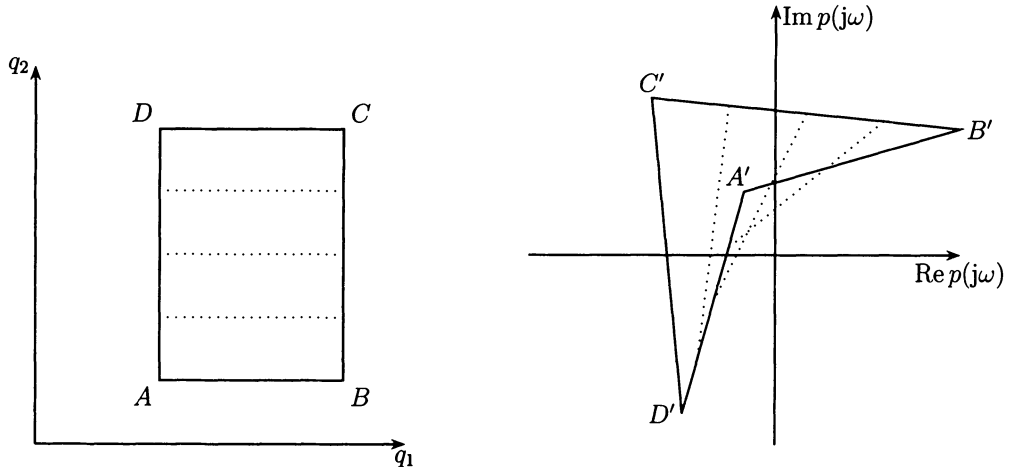


Figure 9.2. Chord approximation of  $\det \mathbf{J} = 0$  (not to scale).

point of  $A'D'$  is connected by a line segment with the center point of  $B'C'$ . The chord approximation may be refined by a further bisection

In general, we can draw the following conclusions for bilinear coefficient functions:

- a) If the image  $A'B'C'D'$  of the rectangle  $ABCD$  is a convex quadrangle, then this is the value set.
- b) If  $A'B'C'D'$  is not convex, then the value set is contained in the convex hull, in Figure 9.2 this is the triangle  $B'C'D'$ . This result will be generalized in Section 9.2.

In the previous example with only two uncertain parameters, there is no advantage of the value set approach over the parameter space approach. For more parameters, however, the value set and its union for all frequencies can be easily inspected for stability. The complexity of the problem enters into the boundary of the value set in the complex  $p(j\omega)$ -plane, as the following example illustrates.

*Example 9.3*

Construct the value set of the polynomial

$$p(s, \mathbf{q}) = \prod_{i=1}^3 (s + q_i) \quad (9.1.4)$$

for  $s = 0.5j$  and  $q_i \in [-\sqrt{3}; \sqrt{3}]$ . The value sets of the three subpolynomials  $s + q_i$  are straight lines parallel to the real axis in the complex plane, see Figure 9.3. Thus, for

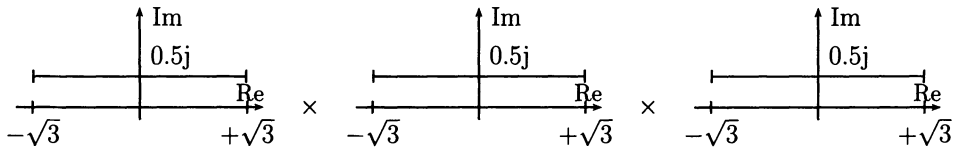


Figure 9.3. Value sets of the subpolynomials

generating the set  $\mathcal{P}$ , three line segments have to be multiplied with each other.

First, the four extremal points are determined:

$$\begin{aligned} A &= (\sqrt{3} + 0.5j)^3 &= \frac{9}{4}\sqrt{3} + \frac{35}{8}j &\approx 3.9 + 4.4j, \\ B &= (\sqrt{3} + 0.5j)^2(-\sqrt{3} + 0.5j) &= -\frac{13}{4}\sqrt{3} - \frac{13}{8}j &\approx -5.6 - 1.6j, \\ C &= (\sqrt{3} + 0.5j)(-\sqrt{3} + 0.5j)^2 &= \frac{13}{4}\sqrt{3} - \frac{13}{8}j &\approx 5.6 - 1.6j, \\ D &= (-\sqrt{3} + 0.5j)^3 &= -\frac{9}{4}\sqrt{3} + \frac{35}{8}j &\approx -3.9 + 4.4j. \end{aligned}$$

They have all the same absolute value  $|A| = \frac{13}{8}\sqrt{3} \approx 5.9$  and the phase angles are

$$\begin{aligned} \varphi_A &= 3 \cdot \tan^{-1} 0.5/\sqrt{3} &= 3 \cdot 16.1^\circ &= 48.3^\circ, \\ \varphi_B &= 2 \cdot 16.1^\circ + 163.9^\circ &= 196.1^\circ, \\ \varphi_C &= 16.1^\circ + 2 \cdot 163.9^\circ &= 343.9^\circ, \\ \varphi_D &= 3 \cdot 163.9^\circ &= 491.7^\circ. \end{aligned}$$

On the edge  $AB$ , two factors are fixed at  $\sqrt{3} + 0.5j$ , the remaining one moves from  $\sqrt{3} + 0.5j$  to  $-\sqrt{3} + 0.5j$ . On the edge  $BC$ , one factor is fixed at  $\sqrt{3} + 0.5j$  and another one at  $-\sqrt{3} + 0.5j$ . By continued bisection of  $AB$  and  $BC$  and connecting the corresponding points for fixed  $\sigma_1$ , the image of the polynomial  $(\sqrt{3} + 0.5j)(\sigma_1 + 0.5j)(\sigma_2 + 0.5j)$  for  $\sigma_2 \in [-\sqrt{3}; \sqrt{3}]$  is generated. These images are straight lines because the polynomial is linear in  $\sigma_2$ . By continuing this construction for the edges  $BC$  and  $DC$ , Figure 9.4 is generated. Alternatively, the Jacobian condition

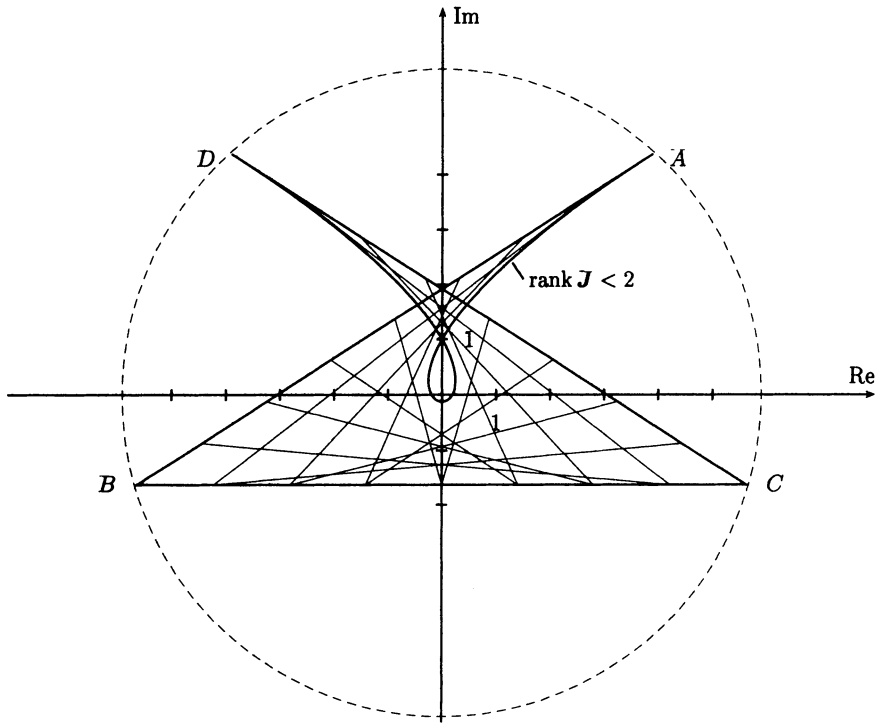


Figure 9.4. Value set of the polynomial  $\prod_{i=1}^3 (s + q_i)$  for  $s = 0.5j$  and  $q_i \in [-\sqrt{3}; \sqrt{3}]$

$$\text{rank } \mathbf{J} = \text{rank} \begin{bmatrix} q_2 q_3 - \omega^2 & q_1 q_3 - \omega^2 & q_3 q_1 - \omega^2 \\ q_2 + q_3 & q_1 + q_3 & q_2 + q_1 \end{bmatrix}$$

can be used. We have  $\text{rank } \mathbf{J} < 2$  for  $q_1 = q_2 = q_3$ , i.e. a part of the boundary is generated by  $(\sigma + 0.5j)^3$ ,  $\sigma \in [-\sqrt{3}; \sqrt{3}]$ . Also, this Jacobian is plotted in Figure 9.4. In Figure 9.5, the value set is plotted without its internal structure. The value set is contained in the convex hull, i.e. the rectangle  $ADBC$ . Zero is not contained in the value set.  $\square$

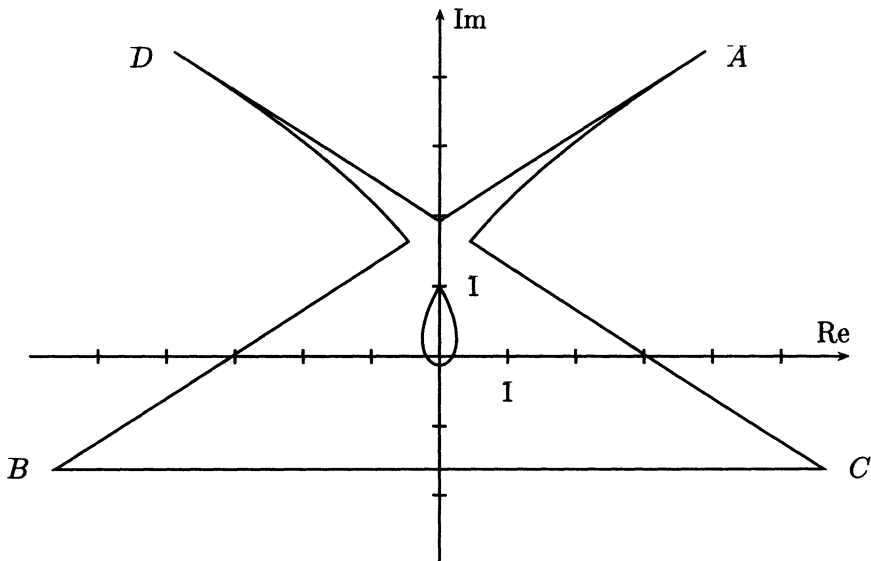


Figure 9.5. Product of three straight line segments

## 9.2 Desoer Mapping Theorem

For multilinear polynomial families, the *mapping theorem* of Desoer [202] yields a useful sufficient stability condition that can restrict frequency gridding to a subset of the non-negative frequencies. The robust stability test is by zero exclusion from the value set, see Theorem 8.6. The mapping theorem gives a simple description of the convex hull of the value set.

*Theorem 9.4 (mapping theorem of Desoer)*

The convex hull of the value set  $\mathcal{P}(j\omega^*, Q)$  of a polynomial with multilinear coefficient functions is the convex hull of the images of the vertices of  $Q$ .

□

*Proof*

Without loss of generality, let  $q_i \in [0 ; 1]$ ,  $i = 1, 2, \dots, \ell$ . We will demonstrate the proof of the mapping theorem for three parameters  $q_1, q_2, q_3$ . The generalization to  $\ell$  parameters is obvious (induction over  $\ell$ ). In four steps, we show that the image of an interior point  $p$  of the  $Q$ -box is contained in the convex hull of the images of the eight vertices. Let  $\text{conv}\{p_1, p_2, \dots, p_m\}$  denote the convex hull of  $m$  points that is the set

$$\text{conv}\{p_1, p_2, \dots, p_m\} :=$$

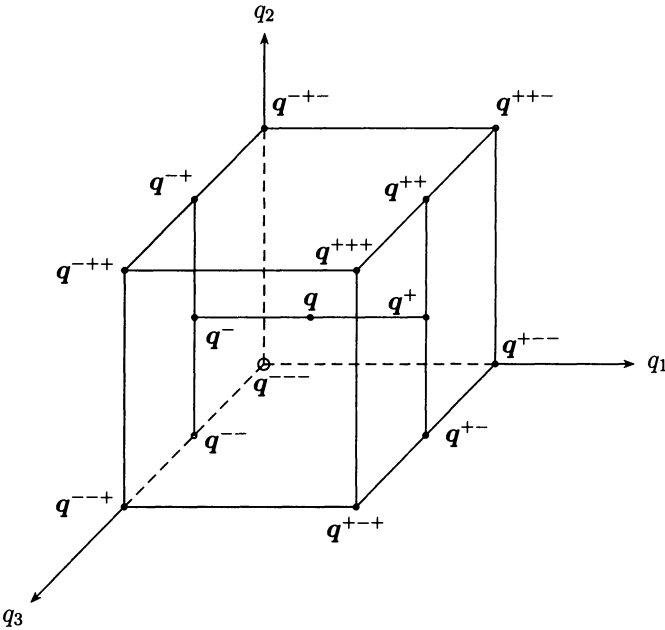


Figure 9.6. Notations used in the proof of Theorem 9.4

$$\{ p \mid p = \sum_{i=1}^m \lambda_i p^{(i)}, \quad \sum_{i=1}^m \lambda_i = 1, \quad \lambda_i \geq 0, \quad i = 1, 2, \dots, m \}. \quad (9.2.1)$$

The polynomials  $p^{(i)} = p(\mathbf{q}^{(i)})$  are generated by the corresponding vectors  $\mathbf{q}^{(i)}$  as indicated in Figure 9.6. For fixed  $q_2 = q_2^*$  and  $q_3 = q_3^*$ , and  $q_1 \in [0 ; 1]$ , we have

$$p(j\omega^*, q_1, q_2^*, q_3^*) = (1 - q_1)p^- + q_1 p^+, \quad (9.2.2)$$

where  $p^- = p(j\omega^*, 0, q_2^*, q_3^*)$ ,  $p^+ = p(j\omega^*, 1, q_2^*, q_3^*)$ . Using the notation of (9.2.1), (9.2.2) may be written as

$$p \subset \text{conv} \{p^-, p^+\}. \quad (9.2.3)$$

Analogously, we have

$$p^- \subset \text{conv} \{p^{--}, p^{-+}\}, \quad p^+ \subset \text{conv} \{p^{+-}, p^{++}\}. \quad (9.2.4)$$

The third step is combining (9.2.3) and (9.2.4):

$$p \subset \text{conv} \{p^{--}, p^{-+}, p^{+-}, p^{++}\} \quad (9.2.5)$$

and the last step gives

$$p \subset \text{conv} \{p^{---}, p^{---+}, p^{-+-}, p^{-++}, p^{---}, p^{--+}, p^{++-}, p^{+++}\}. \quad (9.2.6)$$

□

*Example 9.5*

The crane as given in (1.5.15) with  $\ell \in [8; 16]$  [m],  $m_C \in [100; 2000]$  [kg],  $m_L = 2000$  [kg] and  $g = 10$  [ $\text{ms}^{-2}$ ] with the control law

$$u = -[500 \ 100 \ -100 \ 0] \mathbf{x}$$

has to be checked for Hurwitz-stability. Its characteristic polynomial is

$$p(s, m_C, \ell) = 5000 + 1000s + (20100 + 500\ell + 10m_C)s^2 + 100\ell s^3 + \ell m_C s^4.$$

We can verify stability easily for a nominal point in the given domain of interest, for instance  $\ell = 8$  [m] and  $m_C = 1000$  [kg]. Then, the frequency is gridded and for each grid point  $s = j\omega^*$ , the convex hull of the value set is constructed. The result is shown in Figure 9.7. For higher frequencies (which are not shown for reasons of scale of the figure), the quadrangles move away from the origin and into the fourth quadrant. The frequency grid for this fourth degree polynomial can be terminated as soon as the entire convex hull lies in the fourth quadrant. Obviously, the origin is excluded from

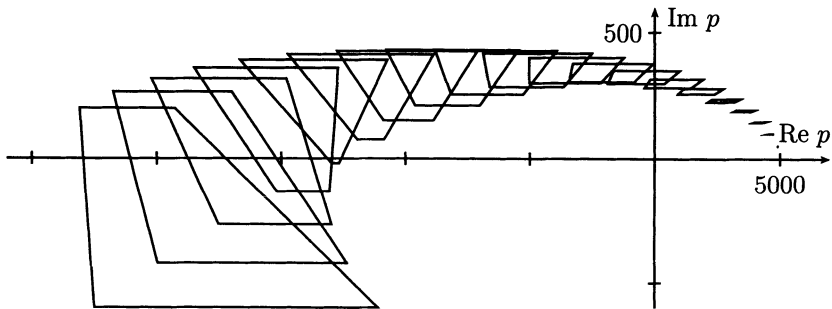


Figure 9.7. Convex hulls for the given example with  $\omega^* = k \cdot 0.05$ ,  $k = 0, 1, \dots, 20$

the convex hull of the value sets at all frequencies. Thus, the origin is also excluded from the value sets at all frequencies and the system is stable.  $\square$

If the origin is included in the convex hull of the value sets for a frequency band  $\omega \in \Omega$ , then the mapping theorem does not give a conclusive answer about the stability of the polynomial family. A necessary and sufficient stability condition is then obtained by the actual construction of the value set for a grid on  $\omega \in \Omega$  and checking for zero exclusion from the value set. For frequencies  $\omega \notin \Omega$ , the value set need not be constructed in view of the sufficient condition obtained from the convex hull of the value set.

*Remark 9.6*

An interesting use of the mapping theorem is in domain splitting algorithms [73],[180],[181]. The  $Q$ -box is split into two parts. The value set is contained in the

union of the convex hulls of the two parts. Further bisection improves this outer approximation of the value set. In addition to the outer bound of the value set (sufficient condition) the algorithms also generate an inner bound (necessary condition) from the fact that images of the additional edges must belong to the value set. The algorithm stops when either a sufficient condition for zero exclusion is satisfied or a necessary condition for zero exclusion is violated.  $\square$

For the case of multilinear coefficient functions, the sufficient condition of the convex hull and construction of the actual value set by families of straight lines inside this hull have been shown in this section. Note that the convex hull condition does not hold for polynomial coefficient functions.

### *Example 9.7*

Consider the polynomial family

$$p(s, q_1) = s + q_1^2 - 6q_1 + 8, \quad q_1 \in [1; 5].$$

Both  $p(s, 1) = s + 3$  and  $p(s, 5) = s + 3$  are stable, but  $p(s, 3) = s - 1$  is unstable. The value set  $p(j\omega, q_1) \in [j\omega - 1 ; j\omega + 3]$  can be calculated from the extremal eigenvalue locations. For  $\omega = 0$ , the value set contains the origin. The convex hull of the value set is the set itself, it is not generated by the extremal values of the parameter  $q_1$ .

This example suggests that further results may be obtained if the monotonous parts of the non-linearity are considered separately, i. e. the intervals  $q_1 \in [1 ; 3]$  and  $q_1 \in [3 ; 5]$ .  $\square$

For polynomial coefficient functions there remains the brute force gridding of  $Q$  for generating the value set. This is computationally prohibitive even for a medium number of parameters. For two parameters the parameter space method is clearly superior, see Example 4.17.

## 9.3 Tree-structured Value Set Construction

In the previous chapter, the stability test by zero exclusion from the value set at all frequencies was used as a concept for proofs of Kharitonov's theorem and the edge theorem. For non-linear parameter dependence, there are no such simple results; it may be possible, however, to construct the value set and to use it for the stability test by zero exclusion. We will see that the construction of value sets can be performed extremely fast if the system has a so-called *tree-structure*.

In Theorem 8.6, it was shown that an uncertain system with characteristic polynomial  $p(s, \mathbf{q})$  is robustly stable if and only if:

- There exists a  $\mathbf{q}_0 \in Q$  for which  $p(s, \mathbf{q}_0)$  is stable.
- The value sets  $\mathcal{P}(j\omega, Q)$  do not contain the origin for all frequencies  $\omega \in [0 ; \infty)$ .

One advantage of this approach is that even a high dimensional operating domain  $Q$  is always mapped into the two-dimensional complex plane  $\mathbb{C}$ . Therefore, the construction of value sets is well suited to a graphical display. The sets can be visualized for various frequencies on a computer display and the user can investigate the stability of the uncertain polynomial by visual inspection of the sets. If the construction of the value sets is fast enough, then it is even possible to create a computer animation where the value sets are displayed on the screen with increasing frequency.

If we are interested in generating the exact value set for non-linear parameter dependency, dense gridding of the uncertainty domain will often be the only possibility. In certain cases, however, the construction of the value sets can be simplified drastically if the characteristic equation has special structural properties.

Models of mechanical and electrical systems frequently have a *tree-structure*, for example a chain of mass-spring-damper (MSD) elements or a corresponding electric RLC network or a robot in free motion(i.e. without hand contact with the environment). Such physical tree-structures are preserved under state and output feedback. It is therefore worthwhile, to exploit tree-structures in the construction of value sets.

### Example 9.8

Consider the crane with outputs crab position  $x_1$  and rope angle  $x_3$ . The respective transfer function are, by (1.3.5) and (1.3.6),

$$\begin{aligned}\frac{x_1(s)}{u(s)} &= \frac{s^2\ell + g}{s^2[m_C\ell s^2 + (m_L + m_C)g]}, \\ \frac{x_3(s)}{u(s)} &= \frac{-1}{m_C\ell s^2 + (m_L + m_C)g}.\end{aligned}$$

These transfer functions, and with feedback the resulting closed-loop characteristic polynomials, are not treated as functions of  $s$  as in numerical analysis for given parameter values. In the construction of value sets for fixed  $\omega$  (or  $\alpha$  on  $\partial\Gamma$ ),  $s$  is just a fixed complex number and we are only interested in how the value sets depend on the uncertain parameters. Assume that  $\ell, m_L$  and  $m_C$  are uncertain. Now, consider the feedback system of Figure 1.8 with  $w = 0$ , i.e.  $u = -\left(k_1 + \frac{k_2 s}{1+Ts}\right)x_1 - k_3 x_3$ ,  $T$  fixed.

Its characteristic polynomial is (see also (1.6.10))

$$p(s, \ell, m_L, m_C, k_1, k_2, k_3) = (s^2\ell + g)[(s^2m_C + k_1)(1+Ts) + k_2s] + s^2(m_Lg - k_3)(1+Ts). \quad (9.3.1)$$

All six parameters appear only once in (9.3.1). For construction of the value set  $p(j\omega, \ell, m_L, m_C, k_1, k_2, k_3)$  with given lower and upper bounds for the parameters, the value sets of  $(s^2\ell + g)$ ,  $(s^2m_C + k_1)$ ,  $(m_Lg - k_3)$  and  $k_2$  are constructed independently and combined to the value set  $p(s, \ell, m_L, m_C, k_1, k_2, k_3)$ , where  $s$  is a fixed complex number on the boundary  $\partial\Gamma$ . Figure 9.8 illustrates the sequential operations on value sets of the subpolynomials until  $p(s, q)$  is reached. The construction is started with the term  $k_1 + m_C s^2$ . Its value set for fixed  $s = j\omega$  is  $k_1 - m_C \omega^2$ , i.e. it is the real interval  $[k_1^- - m_C^+ \omega^2 ; k_1^+ - m_C^- \omega^2]$ . The next step is to generate the set for  $(1 + j\omega T)(k_1 - m_C \omega^2) + k_2 j\omega$ . The multiplication by the complex number  $(1 + j\omega T)$

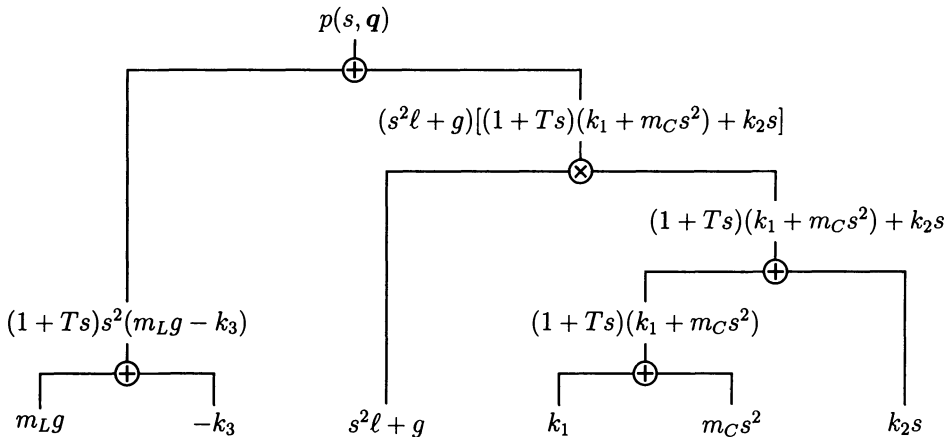
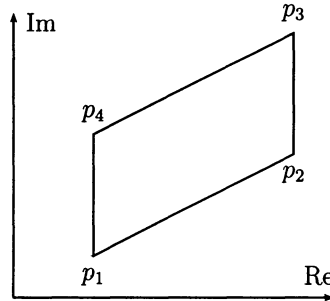


Figure 9.8. Tree-structure of the characteristic polynomial (9.3.1)

means a rotation and scaling corresponding to the phase and magnitude of  $(1 + j\omega T)$ . The line segment  $p_1 p_2$  in Figure 9.9 is the result. The set of  $k_2 j\omega$  has to be added. The result is the parallelogram  $p_1 p_2 p_3 p_4$  in Figure 9.9. Its vertices are

$$\begin{aligned} p_1 &= (1 + j\omega T)(k_1^- - m_C^+ \omega^2) + k_2^- j\omega, & p_2 &= (1 + j\omega T)(k_1^+ - m_C^- \omega^2) + k_2^- j\omega, \\ p_3 &= (1 + j\omega T)(k_1^+ - m_C^- \omega^2) + k_2^+ j\omega, & p_4 &= (1 + j\omega T)(k_1^- - m_C^+ \omega^2) + k_2^+ j\omega. \end{aligned}$$

Similarly, the set of  $s^2\ell + g$  and  $(1 + j\omega T)s^2(m_{LG} - k_3)$  can be constructed easily. The

Figure 9.9. Value set of  $(1 + j\omega T)(k_1 + m_C s^2) + k_2 s$  for a fixed frequency  $s = j\omega$ 

last construction step is then the multiplication of the sets  $s^2\ell + g$  and  $(1 + j\omega T)(k_1 + m_C s^2) + k_2 s$ . The tools for the execution of this set multiplication will be introduced in the following sections. The main point is that the value set can be constructed sequentially. Much more effort would have been spent if the uncertain parameters in a six-dimensional  $Q$ -box had been gridded.  $\square$

Tree-structures can be found in several control system configurations. The question is how to recognize these structures. The conventional way of modelling hides tree-structures by smearing uncertain parameters over the coefficients of the characteristic

polynomial. A first advice is not to unnecessarily manipulate the system equations. For example, in mechanical systems the differential equations are represented in the form

$$\mathbf{M}(\mathbf{q})\ddot{\mathbf{x}} + \mathbf{D}(\mathbf{q})\dot{\mathbf{x}} + \mathbf{K}(\mathbf{q})\mathbf{x} = \mathbf{u}. \quad (9.3.2)$$

In the usual way to arrive at a state space representation, this system of equations is premultiplied by the inverse of the mass matrix  $\mathbf{M}(\mathbf{q})$ . This distributes the elements in this matrix all over the system of equations. A better approach is to directly determine the Laplace transform of (9.3.2). The characteristic polynomial is then

$$p(s, \mathbf{q}) = \det [\mathbf{M}(\mathbf{q})s^2 + \mathbf{D}(\mathbf{q})s + \mathbf{K}(\mathbf{q})] \quad (9.3.3)$$

and the value set for  $s = j\omega$  is

$$p(j\omega, \mathbf{q}) = \det [\mathbf{K}(\mathbf{q}) - \omega^2 \mathbf{M}(\mathbf{q}) + j\omega \mathbf{D}(\mathbf{q})]. \quad (9.3.4)$$

This determinant can be evaluated step by step, and possible tree-structures can be recognized more easily.

Even if the system does have a mechanical loop, i.e. no tree structure, it is possible to gain large computational advantages if only one of the connections is gridded rather than all parameters.

### Example 9.9

In Figure 9.10, a schematic representation of a mechanical system taken from [29] is given. All elements are assumed to be uncertain. Its differential equations are

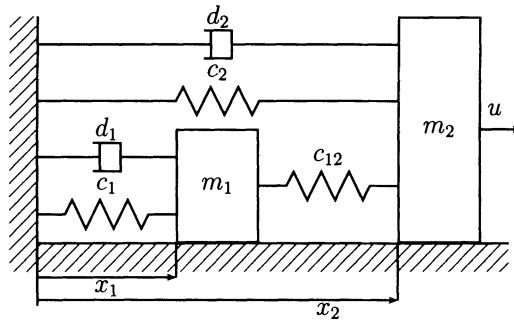


Figure 9.10. Schematic representation of a mechanical system

$$\begin{aligned} m_1\ddot{x}_1 + d_1\dot{x}_1 + c_1x_1 + c_{12}(x_1 - x_2) &= 0, \\ m_2\ddot{x}_2 + d_2\dot{x}_2 + c_2x_2 + c_{12}(x_2 - x_1) &= u, \end{aligned}$$

and their Laplace transform is

$$\begin{bmatrix} m_1s^2 + d_1s + c_1 + c_{12} & -c_{12} \\ -c_{12} & m_2s^2 + d_2s + c_2 + c_{12} \end{bmatrix} \begin{bmatrix} x_1(s) \\ x_2(s) \end{bmatrix} = \begin{bmatrix} 0 \\ u(s) \end{bmatrix}.$$

The characteristic polynomial is

$$p(s, \mathbf{q}) = p_1(s, m_1, d_1, c_1, c_{12}) \cdot p_2(s, m_2, d_2, c_2, c_{12}) - c_{12}^2, \quad (9.3.5)$$

with

$$p_i(s, m_i, d_i, c_i, c_{12}) = m_i s^2 + d_i s + c_i + c_{12}, \quad i = 1, 2. \quad (9.3.6)$$

The system does not have a tree-structure because the uncertain parameter  $c_{12}$  appears both in  $p_1(s, \mathbf{q})$  and  $p_2(s, \mathbf{q})$ . If, however, this single parameter is assumed to be constant, then the system has a tree-structure in the remaining six parameters. The parameter  $c_{12}$  has to be gridded and for each grid point the stability analysis can be done very fast by exploiting the tree-structure. This is much better than gridding all seven uncertain parameters. For a given grid point  $c_{12} = c_{12}^*$  and  $s = j\omega^*$ , the sets of  $p_i(s, m_i, d_i, c_i, c_{12})$ ,  $i = 1, 2$  are rectangles, see Figure 9.11. These two rectangles have

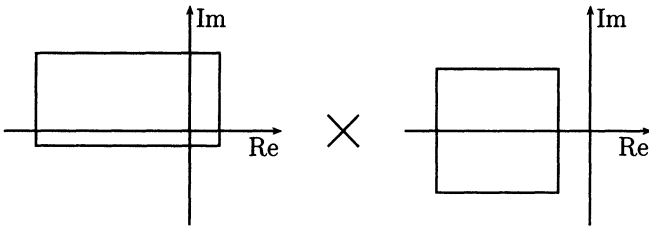


Figure 9.11. Computation of the value set by multiplication of two rectangles in the complex plane

to be multiplied and  $c_{12}^2$  is subtracted. The value set of the characteristic polynomial (9.3.4) for  $m_1 \in [1 ; 3]$ ,  $d_1 \in [0.5 ; 2]$ ,  $c_1 \in [1 ; 2]$ ,  $m_2 \in [2 ; 5]$ ,  $d_2 \in [0.5 ; 2]$ ,  $c_2 \in [2 ; 4]$ ,  $c_{12}^* = 1$ , and  $\omega^* = 1$  is to be constructed.

For the multiplication of two rectangles in a complex plane, note that the product of a test point on the boundary of the first rectangle (i.e. a complex number) with the second rectangle is a rotated and scaled rectangle. As the testpoint wanders around the first rectangle, many such rectangles are generated and the product set is the union of rectangles as shown in Figure 9.12. The actual value set is bounded by the contour of Figure 9.12, it is shown in Figure 9.13. This contour may be generated by a standard contour algorithm [169]. This reduction step is particularly important if further value sets of other subpolynomials are added or multiplied. Practically, between any two additions or multiplications, a reduction to the contour is performed.

For a stability analysis, the value sets for all frequencies  $0 \leq \omega < \omega_{max}$  must be constructed and checked for zero exclusion. For the example,  $\omega_{max}$  is the frequency where the set is for the first time entirely contained in the fourth quadrant. Figure 9.14 shows the union of value sets  $\mathcal{P}(j\Omega, Q)$ . Zero is not included in the union, thus the system is robustly stable.  $\square$

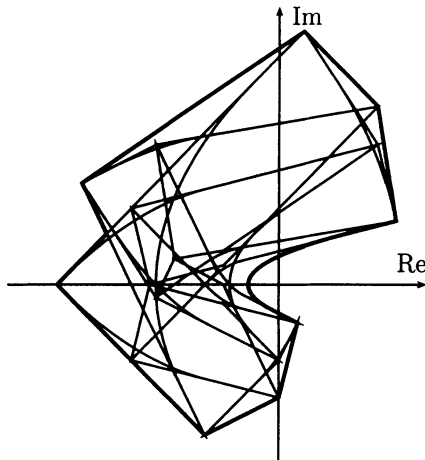


Figure 9.12. Value set for the mechanical system of Figure 9.10 at  $\omega^* = 1$

*Remark 9.10*

A stability test of the above mechanical system is trivial. It is a passive system and therefore stable, independent of the values for masses, springs, and dampers. If, however, one would like to check if the system guarantees a certain stability margin, for example, a negative real part  $\sigma < \sigma_0$  for all  $q \in Q$ , then the stability test is no longer simple, but the same tree-structure can be exploited.

Note also that the origin is not contained in the value set of Figure 9.13, but it is contained in its convex hull. Therefore the sufficient condition of Theorem 9.4 does not give a conclusive answer.  $\square$

*Example 9.11 (Example 9.9 continued)*

An alternative method is the graphical visualization of sets for increasing frequency. The engineer can watch a “movie” of the animated set on the computer display and thereby perform the zero exclusion test by visual inspection of the set. Some scenes of the animated sequence of the value set of the mechanical system given in Example 9.9 are shown in Figure 9.15. The animated value set not only gives a yes/no answer about robust stability, but it also shows critical frequency ranges, for which the value set comes close to the origin, and where better compensation is required. In Figure 9.15, we recognize that for this example the frequency range  $\omega \in [0.75 ; 1.5]$  seems to be especially critical. In case of a controlled system, controller parameters can be modified during the animation with appropriate input devices (e.g. dial box, joystick, steering ball) and the engineer can immediately recognize the consequences of this modification. With this interactive search in the space of controller parameters, a robustly  $\Gamma$ -stabilizing controller can be quickly found [24].  $\square$

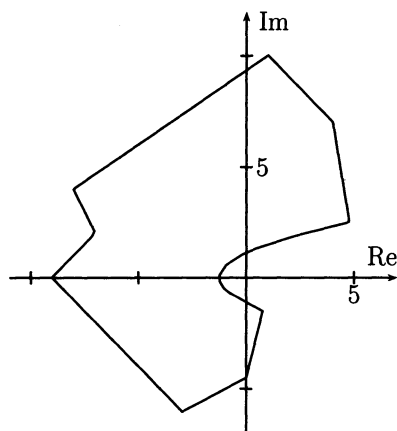


Figure 9.13. Contour of the value set of Figure 9.12

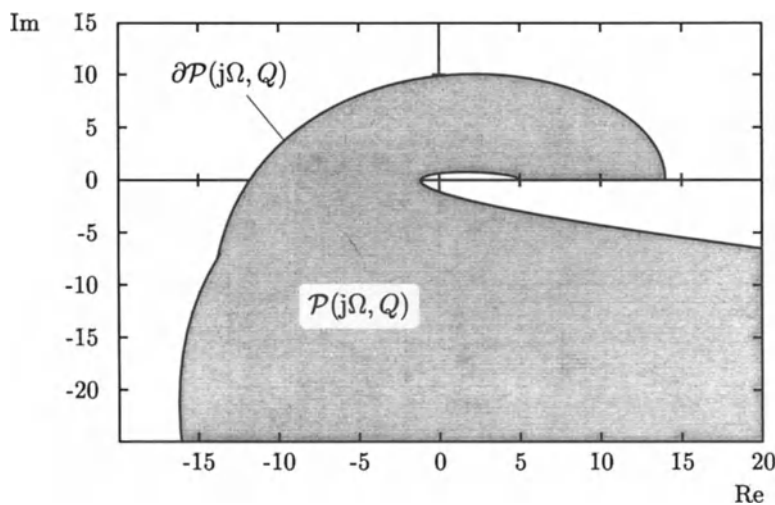


Figure 9.14. Union of the value sets of the mechanical system

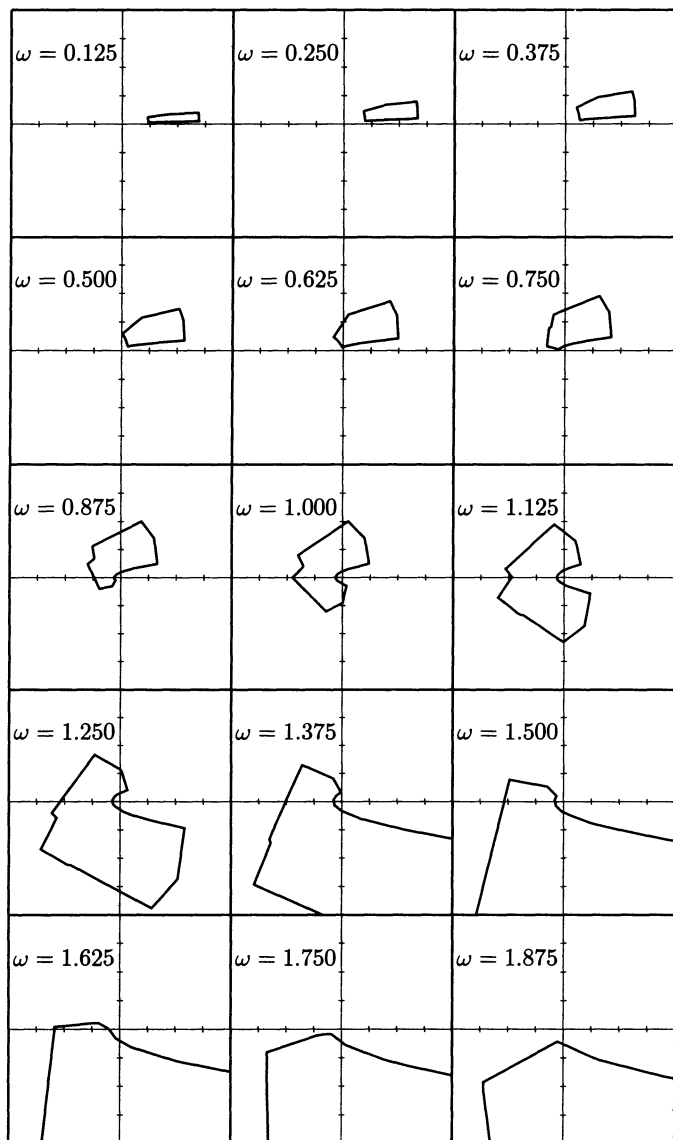


Figure 9.15. Scenes from a value set animation

## 9.4 Computer-aided Execution of Value Set Operations

For the set operations, we assume all value sets to be closed and bounded. The complex set operations we are interested in are addition and multiplication. They are defined as

$$\mathcal{C} = \mathcal{A} + \mathcal{B} = \{a + b \mid a \in \mathcal{A}, b \in \mathcal{B}\}, \quad (9.4.1)$$

$$\mathcal{C} = \mathcal{A} \cdot \mathcal{B} = \{a \cdot b \mid a \in \mathcal{A}, b \in \mathcal{B}\}. \quad (9.4.2)$$

Every point of set  $\mathcal{A}$  is added to (or multiplied by) each point of set  $\mathcal{B}$ .

For an interior point point  $a \in \mathcal{A}$ , there exists an open neighborhood  $\mathcal{N}(a)$  in the set  $\mathcal{A}$ . If this open set  $\mathcal{N}(a)$  is multiplied by any point  $b \in \mathcal{B}$ , this will again result in an open set. Therefore, boundary points in the set  $\mathcal{C} = \mathcal{A} \cdot \mathcal{B}$ , for which no open neighborhood in the set  $\mathcal{C}$  exists, can only stem from points  $a \in \mathcal{A}$  and  $b \in \mathcal{B}$ , which also do not have an open neighborhood in the sets  $\mathcal{A}$  and  $\mathcal{B}$ . These are boundary points,  $a \in \partial\mathcal{A}$  and  $b \in \partial\mathcal{B}$ , thus,

$$\partial\mathcal{C} \subset \partial\mathcal{A} \cdot \partial\mathcal{B}. \quad (9.4.3)$$

Similarly, if  $\mathcal{C} = \mathcal{A} + \mathcal{B}$ , then

$$\partial\mathcal{C} \subset \partial\mathcal{A} + \partial\mathcal{B}. \quad (9.4.4)$$

The main use for constructing value sets is to check the resulting set  $\mathcal{C}$  for exclusion of the origin. For this purpose, it suffices to construct the boundary of the set, for which (9.4.3) and (9.4.4) are exploited.

A first problem is a suitable way of representing the set boundaries in the computer. Here, we could think of an analytic computation of the boundaries. Then, the boundary is represented by piecewise continuous and differentiable curves. If two sets are multiplied, not only will the order of these curves be increased but also the number of curve segments forming the boundary. For further operations, it will become more and more complicated to determine the correct representation of the resulting boundaries. The complexity of the problem enters into the fine detail of the contour of the sets.

For our purpose, it is more practical to approximate the boundaries by chords. Before an operation  $\mathcal{A} + \mathcal{B}$  or  $\mathcal{A} \cdot \mathcal{B}$ , both boundaries of  $\mathcal{A}$  and  $\mathcal{B}$  have to be approximated by polygons. Both these polygons consist of line segments like the ones shown in Figure 9.16. For addition and multiplication, each line segment representing a part of the boundary of  $\mathcal{A}$  is added to (or multiplied by) each line segment representing the boundary of  $\mathcal{B}$ . The result is the union of the sets obtained by these elementary operations, which are shown next.

### Addition

The result of the addition of two line segments is a parallelogram, like that shown in Figure 9.17. The vertices are  $c_{ij} = a_i + b_j$ ,  $i, j = 1, 2$ .

### Multiplication

Two line segments have to be multiplied with each other. The line segments are described by  $a_1 + \alpha(a_2 - a_1)$ ,  $\alpha \in [0; 1]$  and  $b_1 + \beta(b_2 - b_1)$ ,  $\beta \in [0; 1]$ . The product is

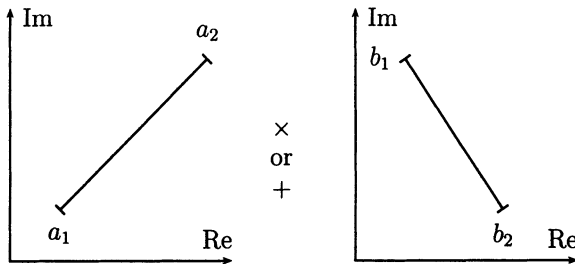


Figure 9.16. Elementary set operations

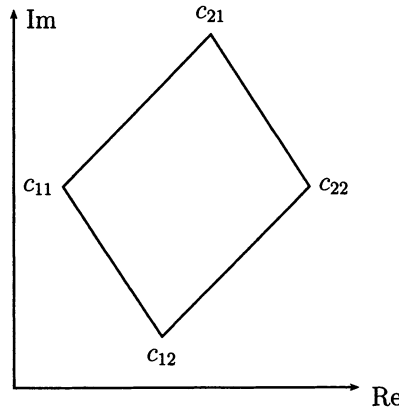


Figure 9.17. Sum of two line segments

then

$$\mathcal{C} = \{c(\alpha, \beta) \mid \alpha \in [0; 1], \beta \in [0; 1]\}, \quad (9.4.5)$$

with

$$c(\alpha, \beta) = [a_1 + \alpha(a_2 - a_1)] \cdot [b_1 + \beta(b_2 - b_1)]. \quad (9.4.6)$$

We can consider this as an uncertain multilinear term in  $\alpha$  and  $\beta$ . Thus, its value set can be constructed easily using the Jacobian (see Chapter 4). Besides the edges of the uncertainty domain, points at which the Jacobian determinant

$$J(\alpha, \beta) = \begin{vmatrix} \frac{\partial \operatorname{Re} c(\alpha, \beta)}{\partial \alpha} & \frac{\partial \operatorname{Re} c(\alpha, \beta)}{\partial \beta} \\ \frac{\partial \operatorname{Im} c(\alpha, \beta)}{\partial \alpha} & \frac{\partial \operatorname{Im} c(\alpha, \beta)}{\partial \beta} \end{vmatrix} \quad (9.4.7)$$

vanishes, also contribute to the boundary of the resulting set. The resulting curve is a parabola, which again is approximated by a polygon. If the Jacobian does not vanish for  $\alpha \in [0; 1]$  and  $\beta \in [0; 1]$ , then the resulting value set is a convex quadrangle. The vertices of this convex set are determined by the four points  $c_{ij} = a_i \cdot b_j$ ,  $i, j = 1, 2$ . Two possible forms of the result are shown in Figure 9.18. It is also possible to determine the product of two line segments without computing the Jacobian determinant. First,

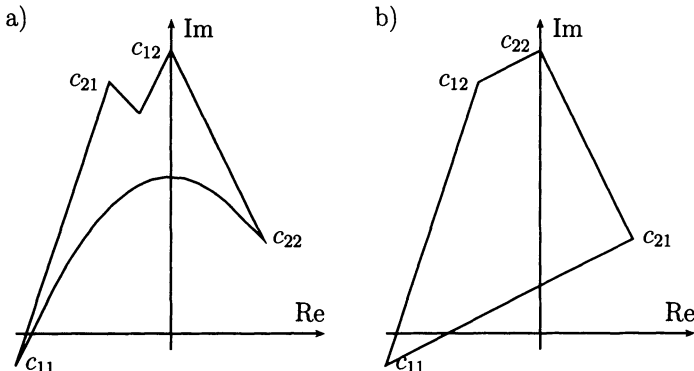


Figure 9.18. Products of two line segments: a) the Jacobian determinant vanishes for  $\alpha \in [0; 1]$  and  $\beta \in [0; 1]$ , b) the Jacobian determinant does not vanish, i.e. the set is convex

the four points  $c_{ij}$  are computed and connected in the sequence  $c_{11}-c_{12}-c_{22}-c_{21}-c_{11}$ . If the resulting set is convex, then the final result is already obtained. If the resulting set is non-convex, then one of the line segments has to be gridded and the other line segment is multiplied with these grid points. The result is shown in Figure 9.19. The parabola generated by the Jacobian is approximated by a chain of chords, which are well suited to next-set operation in the tree-structure. We have seen that tree-structures of the

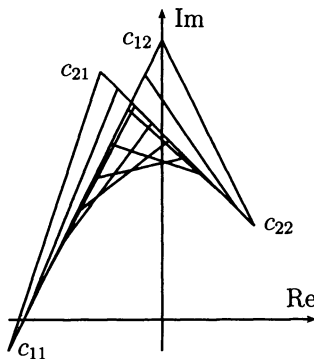


Figure 9.19. Construction of the product of two line segments by approximation

characteristic polynomial arise naturally from modelling of physical systems, which have a tree-structure with respect to the uncertain parameters. If necessary, in a mechanical or electrical system a loop may be cut by gridding the parameters of a connection that does not satisfy the structural assumption. In the example of Figure 9.10 this was the coupling parameter  $c_{12}$ .

On the other hand, a parametric polynomial may be given for which the existence of a tree-structure is not obvious. In this case we try to decompose it, i.e. to find its *tree-structured decomposition* (TSD).

First, a partition of the uncertainties  $q_1, q_2, \dots, q_\ell$  in  $\mathbf{q}$  is defined.  $\mathbf{q}$  is decomposed into *subvectors*  $\mathbf{q}^{(1)}$  and  $\mathbf{q}^{(2)}$  with no common elements, i.e. each uncertainty  $q_i$  belongs

either to  $\mathbf{q}^{(1)}$  or to  $\mathbf{q}^{(2)}$ .

We call a polynomial  $p(s, \mathbf{q})$  *sum decomposable*, if there exists a partition  $\mathbf{q}^{(1)}, \mathbf{q}^{(2)}$  such that

$$p(s, \mathbf{q}) = p_1(s, \mathbf{q}^{(1)}) + p_2(s, \mathbf{q}^{(2)}). \quad (9.4.8)$$

A polynomial  $p(s, \mathbf{q})$  is *product decomposable*, if there exists a partition  $\mathbf{q}^{(1)}, \mathbf{q}^{(2)}$  such that

$$p(s, \mathbf{q}) = p_1(s, \mathbf{q}^{(1)}) \cdot p_2(s, \mathbf{q}^{(2)}) + p_0(s). \quad (9.4.9)$$

The polynomials  $p_1(s, \mathbf{q}^{(1)})$  and  $p_2(s, \mathbf{q}^{(2)})$  are called *subpolynomials* of  $p(s, \mathbf{q})$ . Further subpolynomials may arise if  $p_1(s, \mathbf{q}^{(1)})$  or  $p_2(s, \mathbf{q}^{(2)})$  are sum or product decomposable. A subpolynomial is called *undecomposable* if neither a sum nor a product decomposition is possible.

### Example 9.12

$$p(s, \mathbf{q}) = (q_1 q_2 + q_3 + q_3^2) + (q_1 - 4q_2 + q_3 + 3)s \quad (9.4.10)$$

In the first step, a sum decomposition can be performed, that separates the parameters  $q_1$  and  $q_2$  from  $q_3$ . It is

$$p(s, \mathbf{q}) = p_1(s, q_1, q_2) + p_2(s, q_3),$$

with

$$\begin{aligned} p_1(s, q_1, q_2) &= q_1 q_2 + (q_1 - 4q_2)s, \\ p_2(s, q_3) &= q_3 + q_3^2 + q_3 s + 3s. \end{aligned}$$

Note that the sum decomposition is not unique with respect to the constant term  $3s$ . Any polynomial  $\tilde{p}(s)$  could be added to  $p_1(s, q_1, q_2)$  and subtracted from  $p_2(s, q_3)$ . The polynomial  $p_1(s, q_1, q_2)$  is further product decomposable by adding the term  $(-4s^2)$  and including  $(+4s^2)$  to  $p_0(s)$ , such that

$$p_1(s, q_1, q_2) = p_{11}(s, q_1) \cdot p_{12}(s, q_2) + p_0(s),$$

with

$$\begin{aligned} p_{11}(s, q_1) &= q_1 - 4s, \\ p_{12}(s, q_2) &= q_2 + s, \\ p_0(s) &= 4s^2. \end{aligned}$$

This example demonstrates that the degree of the subpolynomials in  $s$  may be higher than the degree of the polynomial itself. For the construction of value sets, larger powers of  $s$  are not difficult to handle, since they are merely complex numbers for a fixed frequency  $s = j\omega^*$ . Also, a non-linear dependency on a single parameter  $q_3$  in the subpolynomial  $p_2(s, q_3)$  is no difficulty, see Example 9.7.  $\square$

*Remark 9.13*

In more difficult cases, the tree-structure is not obvious, e.g. if we deal with an expanded characteristic polynomial with a high number of uncertain parameters, or the system is too complicated to recognize a tree-structure while already modelling. These cases require a suitable tool that brings to light the structures. Algorithms for the tree-structured decompositions of a parametric polynomial are given in the first edition of this book of 1993, see also [182]. The basic idea for the decomposition (9.4.9) is to factorize symbolically the derivative of  $p(s, \mathbf{q})$  with respect to  $\mathbf{q}$ -elements, thereby  $p_0(s)$  does not enter into the factorization.  $\square$

## 9.5 Tree-structured Transfer Functions

In the preceding sections, we have analyzed control systems by their characteristic polynomials. We now extend the analysis to frequency domain specifications. Also, in rational transfer functions, we can exploit specific structures in order to construct, for example, Nyquist and Popov value sets. The only additional operation on complex sets is their inversion.

Consider a transfer function

$$G(s, \mathbf{n}, \mathbf{d}) = \frac{n(s, \mathbf{n})}{d(s, \mathbf{d})} \quad (9.5.1)$$

with uncertain parameters  $\mathbf{n} \in Q_n$  in the numerator and  $\mathbf{d} \in Q_d$  in the denominator and assume that  $\mathbf{n}$  and  $\mathbf{d}$  do not contain common uncertain elements. The two polynomial value sets  $\mathcal{N}(j\omega, Q_n)$  and  $\mathcal{D}(j\omega, Q_d)$  can be constructed independently. Then the set  $\mathcal{D}(j\omega, Q_d)$  must be inverted and multiplied by  $\mathcal{N}(j\omega, Q_n)$ . An example is the continued fraction form (1.6.11) of the crane transfer function.

Value set multiplication was already defined in Section 9.4. Thus, we have to show the inversion of a complex set. The inversion of a complex set  $\mathcal{A} \subset \mathbb{C}, 0 \notin \mathcal{A}$  is defined as

$$\mathcal{A}^{-1} = \{1/a \mid a \in \mathcal{A}\}. \quad (9.5.2)$$

Each point of the set  $\mathcal{A}$  has to be inverted. If zero is excluded from  $\mathcal{A}$ , then the inversion  $w = 1/z$  is a bijective and continuous function. An interior point of  $\mathcal{A}$  is mapped into an interior point of  $\mathcal{A}^{-1}$ . A boundary point of  $\mathcal{A}$  is mapped into a boundary point of  $\mathcal{A}^{-1}$ . Thus, only the boundary of  $\mathcal{A}$  has to be inverted to get the boundary of  $\mathcal{A}^{-1}$ :

$$\partial(\mathcal{A}^{-1}) = (\partial\mathcal{A})^{-1}, \quad (0 \notin \mathcal{A}). \quad (9.5.3)$$

In a polar coordinate representation of the inversion map applied to a complex point  $z = |z|e^{j\varphi}$ , we obtain the inverse

$$w = \frac{1}{|z|}e^{-j\varphi}. \quad (9.5.4)$$

It can easily be seen that the interior (exterior) of the unit circle in the  $z$ -plane is mapped onto the exterior (interior) of the unit circle in the  $w$ -plane. The unit circle itself is mapped onto the unit circle in the  $w$ -plane. Written in real and imaginary parts of  $z = x + jy$  and  $w = u + jv$ , the mapping equation is

$$w = u + jv = \frac{1}{x + jy} = \frac{x}{x^2 + y^2} + j \frac{-y}{x^2 + y^2}, \quad (9.5.5)$$

and thus

$$u = \frac{x}{x^2 + y^2}, \quad v = \frac{-y}{x^2 + y^2}, \quad (9.5.6)$$

and conversely

$$x = \frac{u}{u^2 + v^2}, \quad y = \frac{-v}{u^2 + v^2}. \quad (9.5.7)$$

For a computer-aided value set construction, set boundaries are approximated by a chain of chords. Therefore, we are mainly interested in how a line segment is transformed by the inversion map.

We consider all points  $z = x + jy$  on the straight line determined by the equation

$$2ax + 2by = 1. \quad (9.5.8)$$

Substituting  $x$  and  $y$  from (9.5.7) yields

$$2a \frac{u}{u^2 + v^2} + 2b \frac{-v}{u^2 + v^2} = 1,$$

and after some elementary transformations,

$$(u - a)^2 + (v + b)^2 = a^2 + b^2. \quad (9.5.9)$$

This is the equation of a circle with center  $(a, -b)$  and radius  $\sqrt{a^2 + b^2}$ . The circle always passes through the origin  $(0, 0)$  of the coordinate system. The point  $w = 0$  is the image of the point at  $z = \infty$  on the line. The resulting circle may also be determined easily with two additional points on the line to be mapped. Since we want to map a line segment with endpoints  $z_1$  and  $z_2$ , these points are the natural choice. The three points determine the circle, see Figure 9.20. The image of the line segment  $\overline{z_1 z_2}$  is the arc not containing the origin.

### Example 9.14

Consider the mechanical system given in Figure 9.10. In Example 9.9, the value set of the characteristic polynomial of the system was constructed. In the example, it was mentioned that the system is passive, which implies Hurwitz-stability for arbitrary positive parameter values. However, if for instance the damping of the system is not sufficiently high, feedback control has to be introduced. For this example we consider the transfer function from input  $u$  to the position  $x_1$  of the mass  $m_1$

$$\frac{x_1(s)}{u(s)} = \frac{c_{12}}{p_1(s, \mathbf{q}^{(1)}, c_{12}) \cdot p_2(s, \mathbf{q}^{(2)}, c_{12}) - c_{12}^2} =: \frac{c_{12}}{p_p(s, \mathbf{q}^{(1)}, \mathbf{q}^{(2)}, c_{12})},$$

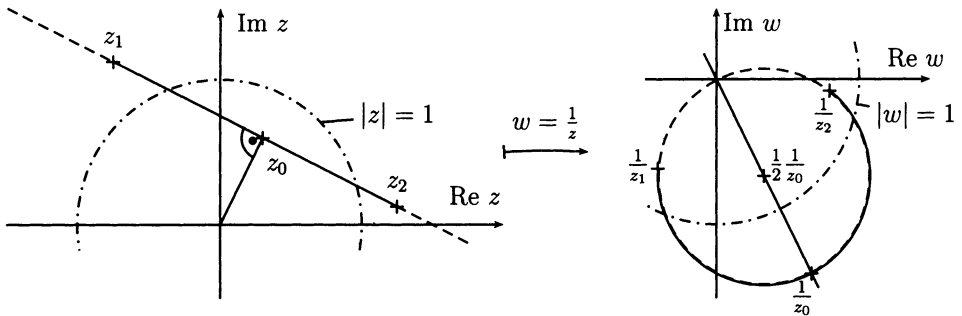


Figure 9.20. Inversion of a line segment

with  $p_1(s, \mathbf{q}^{(1)}, c_{12})$  and  $p_2(s, \mathbf{q}^{(2)}, c_{12})$  given in (9.3.5). The parameter intervals were given as follows:  $m_1 \in [1 ; 3]$ ,  $d_1 \in [0.5 ; 2]$ ,  $c_1 \in [1 ; 2]$ ,  $m_2 \in [2 ; 5]$ ,  $d_2 \in [0.5 ; 2]$ ,  $c_2 \in [2 ; 4]$ . In [29], the controller

$$\frac{n_c(s)}{d_c(s)} = 471250 \frac{0.5 + 1.9s + 1.7s^2 + s^3}{19000 + 1450s + 62s^2 + s^3}$$

was proposed for position control of the mass  $m_1$ . The open-loop transfer function has a tree-structure if the parameter  $c_{12}$  is fixed,  $c_{12} = c_{12}^*$ . (If  $c_{12}$  is uncertain then this one parameter must be gridded.) The characteristic equation is

$$1 + G_0(s, \mathbf{q}^{(1)}, \mathbf{q}^{(2)}) = 1 + \frac{n_c(s)}{d_c(s)} \frac{c_{12}^*}{p_p(s, \mathbf{q}^{(1)}, \mathbf{q}^{(2)}, c_{12}^*)} = 0. \quad (9.5.10)$$

In the following, the value set of the open-loop frequency response  $G_0(j\omega, \mathbf{q}^{(1)}, \mathbf{q}^{(2)})$  is constructed and checked for exclusion of the critical point  $-1$ . (Note that the existence of a stable Nyquist plot in the Nyquist set is guaranteed by stable pole assignment for the center of the  $Q$ -box.)

For a fixed frequency  $\omega = \omega^*$ , the value set of the denominator polynomial  $p_p(j\omega^*, \mathbf{q}^{(1)}, \mathbf{q}^{(2)}, c_{12}^*)$  is constructed as demonstrated in Example 9.9. The resulting set is inverted and multiplied by  $c_{12}^*$ . The value set for  $\omega^* = 1$  and  $c_{12}^* = 1$  is displayed in Figure 9.21. To obtain the value set of the open-loop transfer function, this set has to be multiplied by the transfer function of the controller. For a fixed frequency, this is a complex number. In Figure 9.22, the union of the Nyquist sets of the open-loop transfer function for fixed  $c_{12}$  and a grid on  $\omega$  is displayed. Figure 9.23 shows a detailed view of the neighborhood of the critical point  $-1$ . The critical point  $-1$  is excluded from the union of the sets. Hence, the closed-loop system is robustly stable. The minimal distance of the Nyquist sets from the critical point is a measure for the stability margin of the closed-loop system, see Chapter 5. In the example, the radius of this circle is approximately 0.24.

□

With the use of transfer functions for value set operations, tree-structures can be exploited in complex control system structures. For more complicated networks, Mason's formula [202] can be used to compute the characteristic equation. Similar as in the polynomial context, a basic rule for modelling of structured systems is:

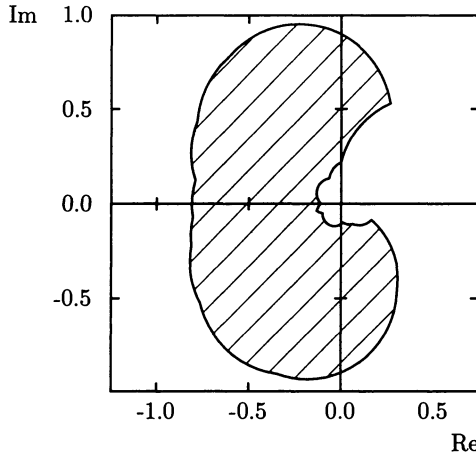


Figure 9.21. Plant transfer function set for  $\omega = 1$ ,  $c_{12} = 1$

*never execute additions or multiplications of transfer functions with disjoint uncertainties.*

The tree-structured decomposition of polynomials and transfer functions is a powerful tool for robustness analysis. It can handle an extremely large number of uncertain parameters. In [30], for example, a chain of 17 mass-spring-damper systems with 51 uncertain parameters is analyzed. In [183], a control system for a finite-element model of a plate with 60 uncertain parameters is analyzed. The concept of tree-structures is also useful for feedback connected subsystems with independent uncertainties as illustrated by the following examples.

#### Example 9.15

In this example, we assume that the transfer functions have disjoint parameter sets in the numerator and denominator polynomials and that different transfer functions have no uncertain parameters in common.

In the feedback loop of Figure 9.24 the closed-loop characteristic polynomial

$$\begin{aligned} p(s, \mathbf{n}, \mathbf{d}) &= n_1(s, \mathbf{n}_1)n_2(s, \mathbf{n}_2)n_c(s, \mathbf{n}_c) \\ &\quad + d_1(s, \mathbf{d}_1)d_2(s, \mathbf{d}_2)d_c(s, \mathbf{d}_c) \end{aligned} \quad (9.5.11)$$

with  $\mathbf{n} := [\mathbf{n}_1^T \mathbf{n}_2^T \mathbf{n}_c^T]^T$ ,  $\mathbf{d} := [\mathbf{d}_1^T \mathbf{d}_2^T \mathbf{d}_c^T]^T$  has a tree-structure. However, the characteristic polynomial of the feedback loop in Figure 9.25 does not have a tree-structure:

$$\begin{aligned} p(s, \mathbf{n}, \mathbf{d}) &= [n_1(s, \mathbf{n}_1)d_2(s, \mathbf{d}_2) + n_2(s, \mathbf{n}_2)d_1(s, \mathbf{d}_1)]n_c(s, \mathbf{n}_c) \\ &\quad + d_1(s, \mathbf{d}_1)d_2(s, \mathbf{d}_2)d_c(s, \mathbf{d}_c). \end{aligned} \quad (9.5.12)$$

The parameters  $\mathbf{d}_1$  and  $\mathbf{d}_2$  appear in two terms of  $p$ . However, in the characteristic

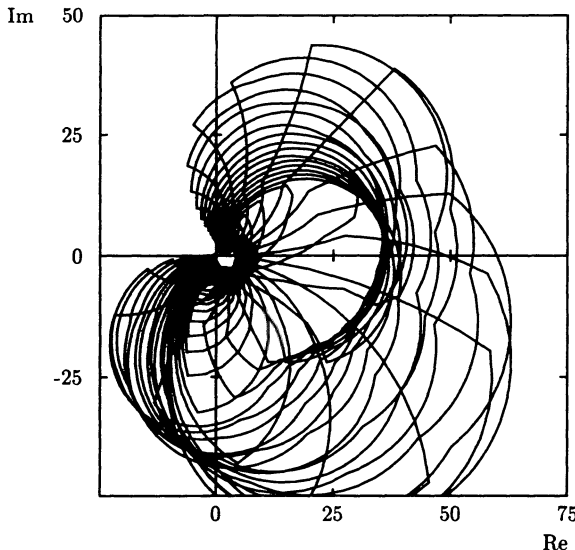


Figure 9.22. Union of Nyquist sets for a grid on  $\omega$

equation of this feedback loop

$$\begin{aligned} r(s, \mathbf{n}, \mathbf{d}) &= 1 + g(s, \mathbf{n}, \mathbf{d}) \\ &= 1 + \left[ \frac{n_1(s, \mathbf{n}_1)}{d_1(s, \mathbf{d}_1)} + \frac{n_2(s, \mathbf{n}_2)}{d_2(s, \mathbf{d}_2)} \right] \frac{n_c(s, \mathbf{n}_c)}{d_c(s, \mathbf{d}_c)}, \end{aligned} \quad (9.5.13)$$

where  $g(s, \mathbf{n}, \mathbf{d})$  is the open-loop transfer function, each uncertainty vector appears just once, either in a numerator or in a denominator polynomial. Thus, the value set of the open-loop transfer function  $g(s, \mathbf{n}, \mathbf{d})$  can be constructed sequentially. Also, the closed-loop transfer function

$$g_c(s, \mathbf{n}, \mathbf{d}) := \frac{1}{\frac{n_c(s, \mathbf{n}_c)}{d_c(s, \mathbf{d}_c)} + \frac{1}{\frac{n_1(s, \mathbf{n}_1)}{d_1(s, \mathbf{d}_1)} + \frac{n_2(s, \mathbf{n}_2)}{d_2(s, \mathbf{d}_2)}}} \quad (9.5.14)$$

can be constructed sequentially from the value sets of the three subsystems.  $\square$

### Example 9.16

The transfer function of the crane with full state feedback from input  $u$  to the position  $x_1$  is

$$\frac{x_1(s)}{u(s)} = \frac{g + \ell s^2}{gk_1 + gk_2s + (k_1\ell - k_3 + g(m_C + m_L))s^2 + (k_2\ell - k_4)s^3 + \ell m_C s^4}.$$

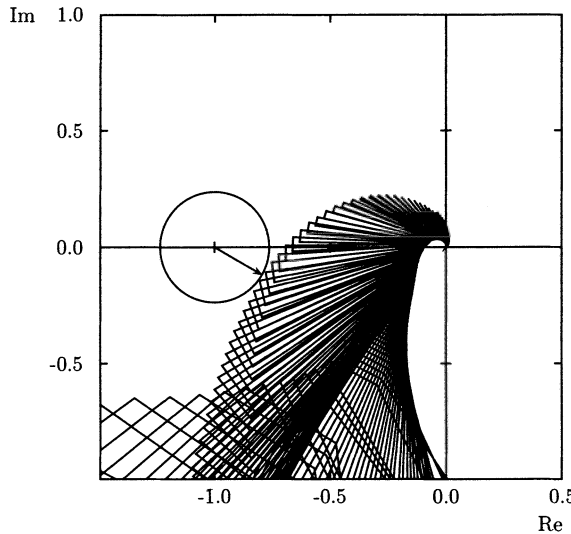


Figure 9.23. Detailed view of the union of Nyquist sets

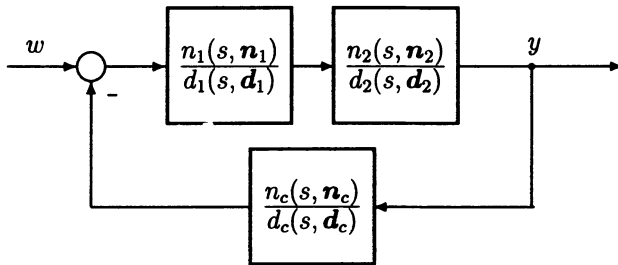


Figure 9.24. Serial connection with feedback

The numerator is unchanged from the open-loop transfer function (1.3.3). The denominator has been changed by state feedback to the form (1.5.18). The numerator and denominator have the uncertain parameter rope length  $\ell$  in common. Dividing both the numerator and the denominator polynomial by the numerator, we get a continued fraction with each uncertain parameter appearing just once:

$$\frac{x_1(s)}{u(s)} = \frac{1}{k_1 + k_2 s + m_C s^2 + \frac{g m_L s^2 - (k_3 + k_4 s)s^2}{g + \ell s^2}}.$$

Thus, the value set of the closed-loop transfer function can be constructed sequentially.  $\square$

A standard form of the characteristic equation is  $1 + G_0(s, q) = 0$ , where  $G_0(s, q)$  is the open-loop transfer function. Remember that  $G_0(s, q)$  is not necessarily given in

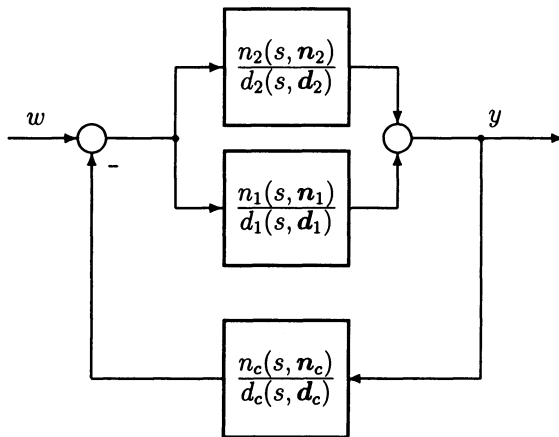


Figure 9.25. Parallel connected transfer functions with feedback

form of a ratio of two polynomials. The two examples have led to a continued fraction form. Any other nested rational form would be feasible too. The important point for the construction of the value set of  $G(s, \mathbf{q})$  is only that it is in a form such that each uncertain parameter appears only once.

If the transfer function of a plant has a tree-structure, then it is also easy to construct the family of Popov plots

$$P(j\omega, Q) = \{p(j\omega, \mathbf{q}) = \operatorname{Re} G_0(j\omega, \mathbf{q}) + j\omega \operatorname{Im} G_0(j\omega, \mathbf{q}) \mid \mathbf{q} \in Q\}.$$

For each frequency grid  $\omega = \omega^*$ , the imaginary part of the set  $G_0(j\omega, \mathbf{q})$  must be multiplied by  $\omega^*$ . Thus, also robust stability of a system with a sector non-linearity and a large number of uncertain parameters in the linear part can be analyzed, provided that it has a tree-structure.

### Example 9.17

Consider the crane (1.1.6), uncertain in the rope length  $\ell \in [8 ; 16] [\text{m}]$ , the load mass  $m_L \in [50 ; 2000] [\text{kg}]$ , and the crab mass  $m_C \in [800 ; 1200] [\text{kg}]$ . Using full state feedback  $\mathbf{u} = \mathbf{k}^T \mathbf{x} = k_1 x_1 + k_2 x_2 + k_3 x_3 + k_4 x_4$ , it can be shown that the closed-loop system is robustly stable for a controller coefficient vector  $\mathbf{k}$  with values arbitrarily chosen in the intervals  $k_1 \in [500 ; 700]$ ,  $k_2 \in [3000 ; 4000]$ ,  $k_3 \in [-30\,000 ; -25\,000]$ ,  $k_4 \in [-2800 ; -2400]$ . Now, we assume that the unmodelled actuator has a sector non-linearity. We want to determine the greatest sector for that non-linear function, for which the closed-loop system is absolutely stable. The linear part of the system is described by the transfer function

$$G_0(s, \mathbf{q}) = \frac{(k_1 + k_2 s)(\ell s^2 + g) - (k_3 + k_4 s)s^2}{s^2[m_C(s^2\ell + g) + m_L g]}, \quad (9.5.15)$$

where  $\mathbf{q} = [\ell \ m_L \ m_C \ k_1 \ k_2 \ k_3 \ k_4]^T$ . Since  $G_0$  is unstable, the Popov theorem cannot directly be applied. Thus, the system first has to be transformed to the standard form in Figure 5.16.

From the above, we know that the closed-loop linear part of the system is robustly stable for  $\rho = 1$ . That value is used for constructing the Popov value set of  $\tilde{G}_0 = G_0/(1+G_0) = 1/(1+1/G_0)$ . In the transfer function (9.5.15), all uncertain parameters but the rope length appear just once, i.e. the transfer function has a tree-structure if the rope length  $\ell$  is gridded. For the following,  $\ell$  is assumed fixed with  $\ell = 12$  [m]. The Popov value set can be constructed sequentially, the union of the sets is shown in Figure 9.26. From that plot, we get the Popov-sector  $[0 ; \infty)$  for the non-linear function

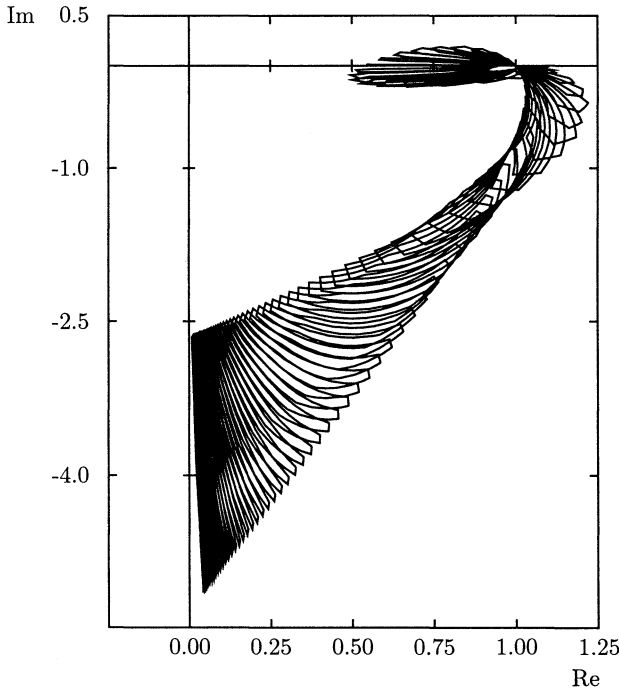


Figure 9.26. Union of Popov value sets

$\tilde{f}(.) = (f - \rho)(.).$  Thus, for the transfer function  $G_0$ , that means for the crane with the above state feedback, absolute stability is guaranteed in a  $k$ -sector  $[1 ; \infty)$ .  $\square$

## 9.6 The Stability Profile

In Section 3.2, we have discussed root sets in the  $s$ -plane, see, for example, Figure 3.7. For a large number of uncertain parameters, the computation times for root sets are

prohibitive. If the parameters appear in a tree-structure, however, then it becomes feasible to compute the right hand boundary of the root set. This boundary is called the *stability profile*. The stability profile contains important information, e.g. on worst case damping or the real part of all eigenvalues for all operating conditions.

First, the Hurwitz-stability analysis is generalized to  $\Gamma$ -stability with respect to the boundary

$$\partial\Gamma = \{\sigma_0 + j\omega \mid \omega \geq 0\}. \quad (9.6.1)$$

All eigenvalues should have a real part smaller than  $\sigma_0$  ( $\sigma_0$ -stability). The polynomial family

$$P(s, Q) = \{p(s, q) \mid, q \in Q\}$$

is  $\sigma_0$ -stable, if and only if:

1. There is a  $\sigma_0$ -stable polynomial in the family.
2. The value set  $P(\sigma_0 + j\omega, Q)$  excludes the origin at all frequencies  $\omega \geq 0$ .

In order to construct the values, we only have to substitute  $s = \sigma_0 + j\omega$  instead of  $s = j\omega$ . A tree-structure of the system is not destroyed by this substitution.

#### Example 9.18

Consider the value set of Figure 9.13 for the mass-spring-damper system of Figure 9.10. For the fixed frequency  $\omega^* = 1$ , the real part  $\sigma_0$  is shifted to the left in small steps until at  $\sigma_0 = -0.062$  the contour passes through the origin, see Figure 9.27. The

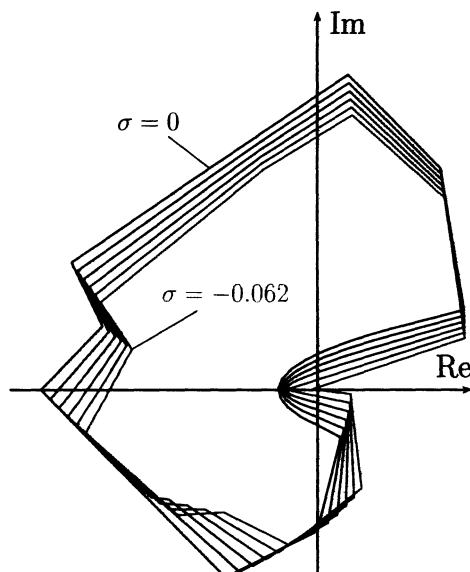


Figure 9.27. The real part is shifted to the left until zero is no longer excluded for  $\sigma_0 = -0.062$

same procedure is repeated for a grid on  $\omega$ . The resulting stability profile is shown in Figure 9.28. The two squares indicate the eigenvalues for the center of the  $Q$ -box.  $\square$

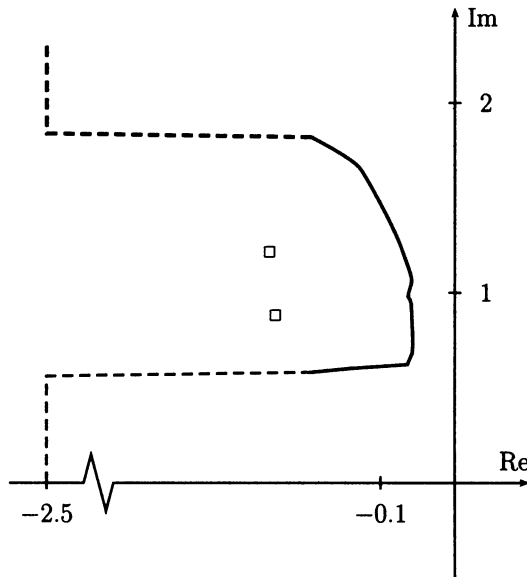


Figure 9.28. Stability profile for the mass-spring-damper system of Figure 9.10

Rather than shifting  $\sigma$  in small steps, it is more efficient to use a bisection as schematically illustrated by Figure 9.29. For the DLR plate experiment with 60 uncertain parameters in the finite-element model, the stability profile is shown in Figure 9.30 and Figure 9.31. For the details the reader is referred to [184].

## 9.7 Synopsis of Parametric Robustness Analysis

The different approaches for parametric robustness analysis presented in this book are summarized in the following synopsis.

Consider the polynomial family

$$P(s, Q) = \{p(s, \mathbf{q}) | \mathbf{q} \in Q\}, \quad (9.7.1)$$

where  $\mathbf{q} = [q_1 \ q_2 \dots q_\ell]$  can take on any value in the operating domain

$$Q = \{\mathbf{q} | q_i \in [q_i^- ; q_i^+], i = 1, 2, \dots, \ell\}. \quad (9.7.2)$$

Is the polynomial family robustly  $\Gamma$ -stable (defined by a given eigenvalue region  $\Gamma$  with boundary  $\partial\Gamma = \sigma(\alpha) + j\omega(\alpha), \alpha \in [\alpha^- ; \alpha^+]$ ) ?

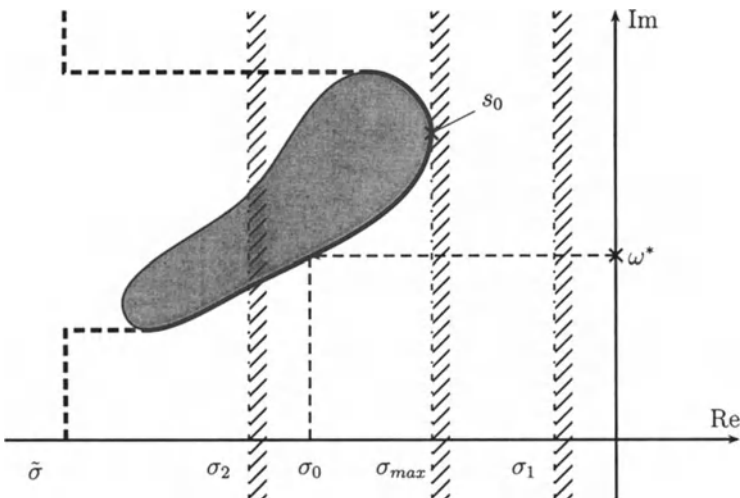


Figure 9.29. The real value  $\sigma_0$  is founded by repeated bisection between a  $\Gamma$ -stable value  $\sigma_1$  and a  $\Gamma$ -unstable value  $\sigma_2$ . Then  $\sigma_{\max} = \max_{\omega} \sigma_0(\omega)$

1. Grid  $Q$ , factorize  $p(s, q)$  for grid points, and plot the root set in  $s$ -plane. For  $\Gamma$ -stability it must be contained in  $\Gamma$ . For calculation of the right hand boundary of the root set (stability profile) see 2.2.2.4.
2. Check an arbitrary  $q \in Q$  for  $\Gamma$ -stability. Its stable neighborhood  $Q_\Gamma$  is bounded by

$$\begin{aligned} \operatorname{Re} p[\sigma(\alpha) + j\omega(\alpha), q] &= 0, \text{ and} \\ \operatorname{Im} p[\sigma(\alpha) + j\omega(\alpha), q] &= 0. \end{aligned} \quad (9.7.3)$$

- 2.1 Eliminate  $\alpha$  from (9.7.3). For  $\Gamma =$  left half plane this leads to the last Hurwitz determinant

$$\det H_n(q) = 0. \quad (9.7.4)$$

- 2.2 Grid  $\alpha \in [\alpha^-; \alpha^+]$ .  
Check for singular frequencies; in their vicinity use fine grid, otherwise coarse grid.
- 2.2.1 For two parameters  $q_1, q_2$  entering polynomially, multilinearly or linearly into characteristic polynomial coefficients, solve for  $q_1(\alpha), q_2(\alpha)$  or  $f_1(\alpha, q_1, q_2) = 0$  and plot the  $\Gamma$ -stability boundary in the  $(q_1, q_2)$ -plane.  $Q$  is robustly stable if  $Q \subset Q_\Gamma$ . Grid further parameters  $q_3, q_4 \dots$  and project boundaries.

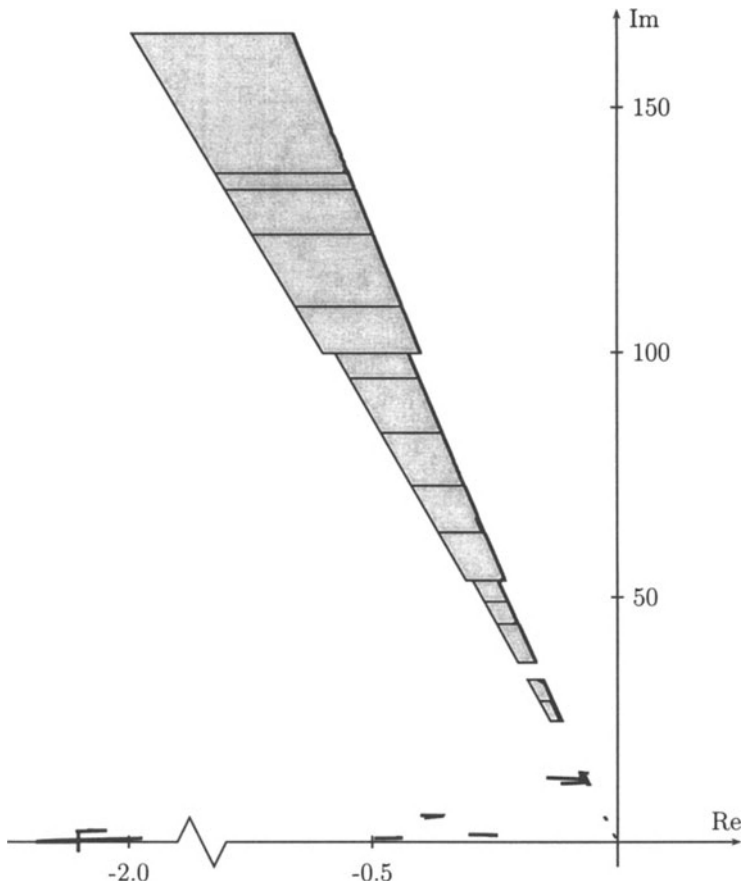


Figure 9.30. Stability profile for a finite-element model with 60 uncertain parameters

- 2.2.2 Use zero exclusion from the value set with the following cases:
  - 2.2.2.1 For interval polynomials and  $\Gamma =$  left half plane, check four Kharitonov polynomials (8.3.6).
  - 2.2.2.2 For affine coefficient functions, check all edges of the  $Q$ -box for  $\Gamma$ -stability.
  - 2.2.2.3 For multilinear coefficient functions, the Desoer mapping theorem is a useful sufficient condition.
  - 2.2.2.4 For non-linear coefficient functions, check for a tree-structure that simplifies the construction of value sets and stability profile.

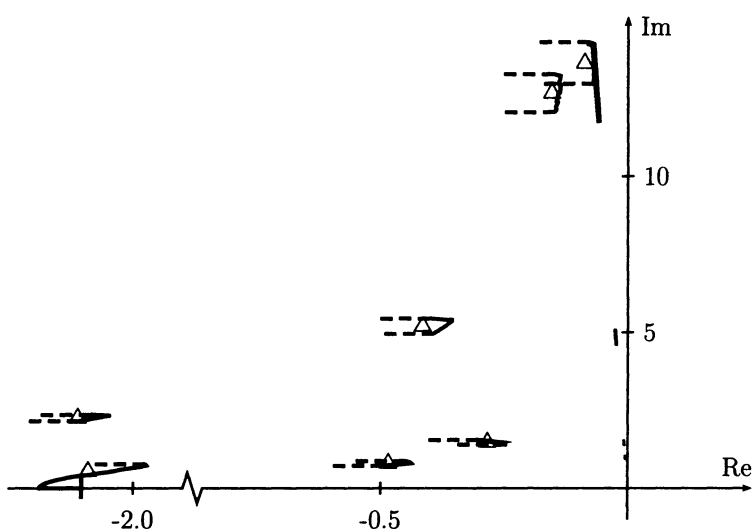


Figure 9.31. Clipping of Figure 9.30

# 10 The Stability Radius

In Chapters 8 and 9, the stability of polynomial families

$$P(s, Q) = \{ p(s, \mathbf{q}) \mid \mathbf{q} \in Q \}, \quad (10.0.1)$$

with  $p(s, \mathbf{q}) = a_0(\mathbf{q}) + a_1(\mathbf{q})s + \dots + a_n(\mathbf{q})s^n$  and  $q_i \in [q_i^-; q_i^+]$ ,  $i = 1, 2, \dots, \ell$  was investigated. The primary interest was necessary and sufficient conditions for stability. These conditions give primarily a yes or no answer to the robust stability problem. If the answer is yes, then there is some kind of stability margin of the uncertain parameters, the domain  $Q$  of the parameters can be enlarged without loosing stability. The next question is: what is the smallest perturbation in the parameters  $\mathbf{q}$  that destabilizes the system?

Assume that  $p(s, \mathbf{q})$  is stable for the center point  $\mathbf{q}^0$  of the  $Q$ -box. Then, the polynomial family is stable in a sufficiently small neighborhood of  $\mathbf{q}^0$  because of the continuity of the roots. By shifting the origin of the parameter space, it is always possible to have  $\mathbf{q}^0 = \mathbf{0}$ . The box centered at  $\mathbf{q}^0 = \mathbf{0}$  may now be blown up by a dilation factor  $\gamma$ , i.e. the polynomial family

$$P(s, \gamma Q) = \{ p(s, \mathbf{q}) \mid \mathbf{q} \in \gamma Q \} \quad (10.0.2)$$

is considered. By increasing  $\gamma$ , a value  $\rho$  must be reached where a member of the polynomial family becomes unstable, i.e. the box  $\gamma Q$  hits a stability boundary; this value  $\rho$  is called the *stability radius* of the polynomial family, it is a measure for the smallest destabilizing perturbation. For all  $\mathbf{q}$  with  $\|\mathbf{q}\|_\infty = \max_{i=1,2,\dots,\ell} |q_i| < \rho$ , the polynomial family is stable. Note that the value  $\rho$  may be  $\infty$ , for example, consider  $p(s, q) = s + 1 + q^2$ .

The sidelength of the  $Q$ -box provides a scaling for the individual uncertain parameters  $q_i$ . After that scaling, a unit box  $Q_\infty = \{ \mathbf{q} \mid q_i \in [-1; 1] \}$  is enlarged by the dilation factor  $\gamma$ . For computational simplicity, a unit ball  $Q_2 = \{ \mathbf{q} \mid \sum_{i=1}^\ell q_i^2 = 1 \}$  may be dilated. The stability radius  $\rho_2$  is then defined as the smallest  $\gamma$  for which  $\gamma Q_2$  touches a stability boundary. The difficulty of finding the stability radius  $\rho$  depends again on the type of coefficients functions  $a_i(\mathbf{q})$ ,  $i = 0, 1, \dots, n$ . For affine dependency, two methods are demonstrated. The case of polynomial dependence (which includes multilinear dependency) will be treated in the third section. There, the problem is solved in theory but in applications only a small number of parameters can be handled.

## 10.1 Tsypkin-Polyak Loci

In Chapter 8 in the interval and affine cases, algebraic tests have been used to check the stability of testing sets. An alternative approach is the use of graphical frequency domain stability criteria. This approach is particularly useful if the largest stable  $Q$ -box around its stable center with coordinates

$$q_i^0 = \frac{q_i^+ + q_i^-}{2}, \quad i = 1, 2, \dots, \ell \quad (10.1.1)$$

has to be determined. A given  $Q$ -box with  $q_i \in [q_i^-; q_i^+]$  may then be described by

$$|q_i - q_i^0| \leq \alpha_i = \frac{q_i^+ - q_i^-}{2}, \quad i = 1, 2, \dots, \ell. \quad (10.1.2)$$

A variable size of the uncertainty box can now be introduced by a common real dilation factor  $\gamma \geq 0$  for all uncertainties, i.e.

$$|q_i - q_i^0| \leq \gamma \alpha_i, \quad i = 1, 2, \dots, \ell. \quad (10.1.3)$$

The case  $\gamma = 1$  coincides with the given box in (10.1.2). For  $\gamma < 1$ , the box size is reduced and by increasing  $\gamma$  beyond 1 the uncertainty box is blown up. The  $\gamma$ -value, for which the box around a stable center point (10.1.1) first hits the stability boundary, is called the *stability radius*.

### Case 1: Interval Coefficients

Consider the polynomial family

$$P(s) = a_0 + a_1 s + \dots + a_n s^n, \quad (10.1.4)$$

with the coefficients subject to the following constraints:

$$|a_i - a_i^0| \leq \gamma \alpha_i, \quad i = 0, 1, \dots, n, \quad a_0^0 > 0. \quad (10.1.5)$$

This means that for each coefficient  $a_i$ , there is a nominal value  $a_i^0$  and a scaling factor  $\alpha_i \geq 0$  for the coefficient perturbation.

If  $p^0(s) = a_0^0 + a_1^0 s + \dots + a_n^0 s^n$ ,  $a_0^0 > 0$ , is the nominal polynomial, then

$$p^0(j\omega) = \operatorname{Re} p^0(j\omega) + j \operatorname{Im} p^0(j\omega) =: U(\omega) + j\omega V(\omega), \quad 0 \leq \omega < \infty \quad (10.1.6)$$

represents the usual Mikhailov curve. For testing the polynomial family, introduce the two scaling polynomials

$$S(\omega) = \alpha_0 + \alpha_2 \omega^2 + \alpha_4 \omega^4 + \dots, \quad (10.1.7)$$

$$T(\omega) = \alpha_1 + \alpha_3 \omega^2 + \alpha_5 \omega^4 + \dots, \quad (10.1.8)$$

and construct the frequency plot

$$z(\omega) = x(\omega) + jy(\omega), \quad (10.1.9)$$

with

$$x(\omega) := \frac{U(\omega)}{S(\omega)}, \quad (10.1.10)$$

$$y(\omega) := \frac{V(\omega)}{T(\omega)}. \quad (10.1.11)$$

Observe that the coefficients of the numerator polynomials only depend on the coefficients of the nominal polynomial, whereas the denominator coefficients depend on the scaling factors  $\alpha_i$ . If the  $\alpha_i$  are positive, then the denominator polynomials are positive so that  $z(\omega)$  is finite for all finite  $\omega > 0$ . The boundary points  $z(0)$  and  $z(\infty)$  are

$$x(0) = \frac{a_0^0}{\alpha_0}, \quad (10.1.12)$$

$$y(0) = \frac{a_1^0}{\alpha_1}, \quad (10.1.13)$$

and

$$x(\infty) = \begin{cases} \frac{a_n^0}{\alpha_n}, & n \text{ even} \\ \frac{a_{n-1}^0}{\alpha_{n-1}}, & n \text{ odd} \end{cases}, \quad (10.1.14)$$

$$(\infty) = \begin{cases} \frac{a_n^0}{\alpha_n}, & n \text{ odd} \\ \frac{a_{n-1}^0}{\alpha_{n-1}}, & n \text{ even} \end{cases}. \quad (10.1.15)$$

*Theorem 10.1 (Tsypkin and Polyak theorem for interval polynomials)*

For the stability of the polynomial family (10.1.4) and (10.1.5), it is necessary and sufficient that the following conditions hold for the plot  $z(\omega)$ :

1. It goes through  $n$  quadrants in counterclockwise direction for  $\omega \in [0; \infty)$ .
2. It does not intersect the square centered at the origin with sidelength  $2\gamma$ .
3. Its boundary points  $z(0), z(\infty)$  have coordinates with absolute values larger than  $\gamma$ .

□

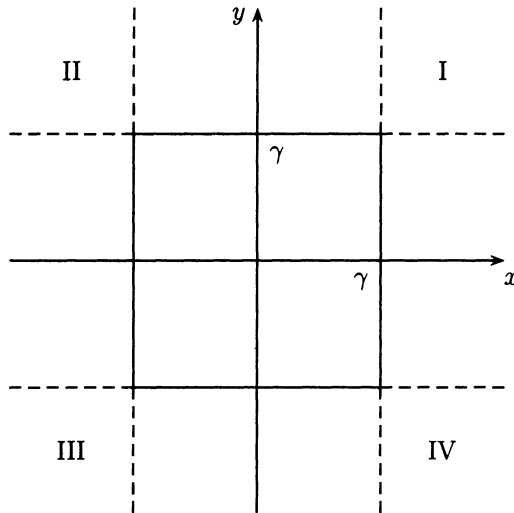


Figure 10.1. The feasible domain for the Tsyplkin-Polyak locus

Condition 2 requires that  $z(\omega)$  is outside the square. Condition 3 means that  $|x(0)| > \gamma$ ,  $|y(0)| > \gamma$ ,  $|x(\infty)| > \gamma$ ,  $|y(\infty)| > \gamma$ . Thus,  $z(0)$  and  $z(\infty)$  must lie in the regions I, II, III or IV of Figure 10.1.

This theorem is a frequency domain version of Kharitonov's Theorem. The advantage compared to plotting four Mikhailov curves is that only one plot (even bounded if  $\alpha_0 \neq 0, \alpha_1 \neq 0, \alpha_{n-1} \neq 0, \alpha_n \neq 0$ ) is needed and the stability radius can be determined easily. When  $\gamma$  is enlarged until one of the conditions of the theorem is violated, then the critical frequency is also known, i.e. the frequency where the root set crosses the imaginary axis.

#### *Remark 10.2*

Theorem 10.1 is a simplified version of the original theorem in [191]. Tsyplkin and Polyak additionally allow other types of perturbations. For the long proof the reader is referred to the original paper. A simpler proof was given by Mansour [138].  $\square$

#### *Example 10.3*

Recall the characteristic polynomial (1.5.18) of the crane with  $k_1 = 600$ ,  $k_2 = 2000$ ,  $k_3 = -10000$ ,  $k_4 = 0$ ,  $m_C = 1000$  [kg],  $\ell = 10$  [m]. We want to check the stability of the polynomial family for  $m_L \in [50; 2395]$  [kg]. This family

$$p(s, m_L) = 0.6 + 2s + (2.6 + 0.001m_L)s^2 + 2s^3 + s^4$$

has first to be scaled. With  $k_3^0 = -10000$ ,  $k_4^0 = 0$ ,  $\gamma = 1$  and

$$k_3 = -10000 + 10000q_1, \quad (10.1.16)$$

$$k_4 = 10000q_2, \quad (10.1.17)$$

the Tsypkin-Polyak locus  $z(\omega)$  of the transformed polynomial family

$$p(s, q_1, q_2) = 3 + 10s + (18 + 5q_1)s^2 + (10 + 5q_2)s^3 + 5s^4 \quad (10.1.18)$$

must avoid the unit square. The polynomials (10.1.6) (10.1.8) are  $U(\omega) = 3 - 18\omega^2 + 5\omega^4$ ,  $V(\omega) = 10 - 10\omega^2$  and  $S(\omega) = T(\omega) = 5\omega^2$ . The frequency plot

$$z(\omega) = \frac{3 - 18\omega^2 + 5\omega^4}{5\omega^2} + j \frac{10 - 10\omega^2}{5\omega^2} \quad (10.1.19)$$

must go through four quadrants and avoid the unit square. The boundary conditions are satisfied because  $z(0) = \infty + j\infty$  and  $z(\infty) = \infty - 2j$ . The plot starts in the first quadrant and goes through four quadrants. Thus, the nominal polynomial for  $q_1 = q_2 = 0$  is stable, see Figure 10.2.

To determine the stability radius, the box is enlarged until it hits the Tsypkin-Polyak locus. From Figure 10.2, it follows that the box touches the Tsypkin-Polyak plot for  $x(\omega) = y(\omega)$ , i.e.  $5\omega^4 - 18\omega^2 + 3 = -10\omega^2 + 10$  or  $5\omega^4 - 8\omega^2 - 7 = 0$ . The only real positive root  $\omega_m = 1.49$  leads to  $z_m = -1.1 - 1.1j$  and to the stability radius  $\rho = \gamma_{max} = 1.1$ .

□

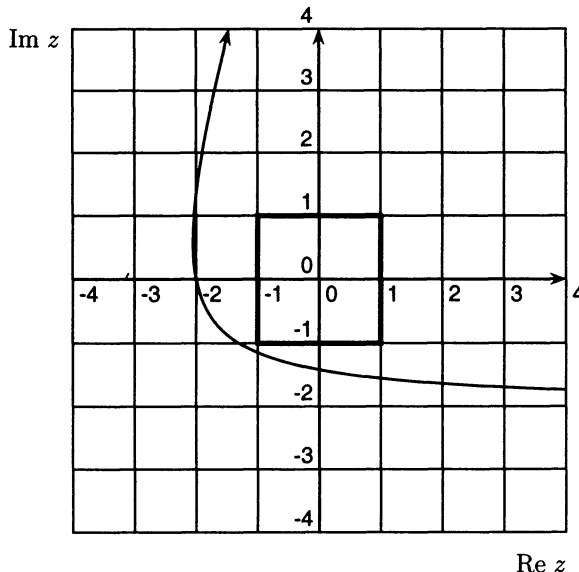


Figure 10.2. The Tsypkin-Polyak locus

### Case 2: Affine Coefficients

The next step is now the extension of the frequency domain approach to affine dependency of the polynomial coefficients. The polynomial family  $P(s, Q)$  can be rewritten in the form

$$\begin{aligned} p(s, \mathbf{q}) &= p_0(s) + \sum_{i=1}^{\ell} q_i p_i(s), \\ p_0(s) &= a_0^0 + a_1^0 s + \dots + a_n^0 s^n, \quad a_n^0 > 0, \\ p_i(s) &= a_0^i + a_1^i s + \dots + a_n^i s^n, \quad i = 1, 2, \dots, \ell. \end{aligned} \quad (10.1.20)$$

$\mathbf{q}$  may vary in an  $\ell$ -dimensional box, i.e.  $q_i \in [q_i^-; q_i^+]$ ,  $i = 1, 2, \dots, \ell$ . Shifting the origin and scaling the  $q_i$ -axes in the parameter space, the box  $Q$  is transformed to an  $\ell$ -dimensional cube with sidelength 2 and center at  $\mathbf{q} = [0 \dots 0]^T$ , see (8.4.4). Let  $\omega_s$  be a common real zero of the rational functions

$$\operatorname{Im}(p_k(j\omega)/p_0(j\omega)) = 0$$

for  $k = 1, 2, \dots, \ell$ .

Now, a real-valued function  $\tau(\omega)$  is defined by

$$\tau(\omega) = \max_{1 \leq k \leq \ell} \frac{\left| \operatorname{Im}(p_0(j\omega)/p_k(j\omega)) \right|}{\sum_{i=1}^{\ell} \left| \operatorname{Im}(p_i(j\omega)/p_k(j\omega)) \right|}, \quad 0 < \omega < \infty, \quad \omega \neq \omega_s, \quad (10.1.21)$$

$$\tau(\omega) = \frac{|p_0(j\omega)|}{\sum_{i=1}^{\ell} |p_i(j\omega)|}, \quad \omega = \omega_s, \quad (10.1.22)$$

$$\tau(0) = \frac{|a_0^0|}{\sum_{i=1}^{\ell} |a_0^i|}, \quad \tau(\infty) = \frac{|a_n^0|}{\sum_{i=1}^{\ell} |a_n^i|}. \quad (10.1.23)$$

For  $\omega = 0$ ,  $\omega = \infty$ , and  $\omega = \omega_s$ , the function is, in general, discontinuous. The first two cases correspond again to roots at  $s = 0$  and  $s = \infty$ . The separate definition of  $\tau(\omega)$  for  $\omega_s$  is necessary because  $\tau(\omega)$  is discontinuous at the singular frequencies  $\omega_s$ , a formal evaluation of  $\tau(\omega_s)$  with (10.1.21) would lead to 0/0.

*Theorem 10.4 (Tsypkin and Polyak theorem for affine coefficients)*

The polynomial family  $P(s, Q)$  is stable, if and only if:

1.  $p_0(s)$  is stable.
2.  $\tau(\omega) > 1$ ,  $0 \leq \omega \leq \infty$ .

□

A slightly different form of this theorem, which resembles the Mikhailov plot, is

*Theorem 10.5 (Tsypkin and Polyak theorem for affine coefficients)*

The polynomial family  $P(s, Q)$  is stable, if and only if,

1.  $p_0(j\omega) \neq 0$ .
2.  $z(\omega) = \frac{p_0(j\omega)}{|p_0(j\omega)|} \tau(\omega)$  goes for  $0 \leq \omega < \infty$  through  $n$  quadrants and does not intersect the unit circle.

□

The difference between Theorem 10.4 and Theorem 10.5 is only the graphical representation. For a stability test by Theorem 10.4, the function  $\tau(\omega)$  is plotted. Its plot must be entirely above the line  $\tau = 1$ . In Theorem 10.5, a polar plot is generated, where  $\tau(\omega)$  is the distance from the origin and the phase angle is that of the nominal polynomial i.e.  $\frac{p_0(j\omega)}{|p_0(j\omega)|}$ .

*Remark 10.6*

The function  $\tau(\omega)$  can also be defined using trigonometric functions. However, for computational purposes, it is more convenient to have a non-trigonometric version. For the proof, the reader again is referred to the original paper [192]. Using Theorem 10.4 or Theorem 10.5 beyond a yes or no answer, critical frequencies are recognized. □

What is the amount of calculation for this test? First, the frequency  $\omega$  has to be gridded and the polynomials  $p_0(s), p_i(s), i = 1, 2, \dots, \ell$  have to be evaluated at  $s = j\omega$ . Then,  $\ell$  functions have to be calculated and their maximum has to be determined. The singular frequencies  $\omega_s$  can be found by transforming  $\text{Im}(p_k(j\omega)/p_0(j\omega))$ . With  $p_k = R_k + jI_k$  and  $p_0 = R_0 + jI_0$ , it is

$$\text{Im}(p_k(j\omega)/p_0(j\omega)) = \text{Im} \frac{R_k + jI_k}{R_0 + jI_0} = \frac{R_0 I_k - R_k I_0}{R_0^2 + I_0^2} = 0. \quad (10.1.24)$$

So  $\omega_s$  must be a common (real) root of the polynomials

$$\begin{aligned} R_0 I_1 - R_1 I_0 &= 0, \\ R_0 I_2 - R_2 I_0 &= 0, \\ &\vdots \\ R_0 I_\ell - R_\ell I_0 &= 0. \end{aligned} \quad (10.1.25)$$

*Example 10.7*

Recall the characteristic polynomial family (1.5.18) of the crane with  $k_1 = 300$ ,  $k_4 = 0$ ,  $m_C = 100$  [kg],  $m_L = 1000$  [kg],  $\ell = 10/3$  [m]. The transformation

$$k_2 = 535 + 5q_1, \quad k_3 = 7662.5 + 87.5q_2$$

allows  $q_1$  and  $q_2$  to vary in the square of sidelength 2. The polynomial family is

$$p(s, q_1, q_2) = p_0(s) + q_1 p_1(s) + q_2 p_2(s), \quad (10.1.26)$$

with

$$\begin{aligned} p_0(s) &= 129 + 166s + 237s^2 + 108s^3 + 80s^4, \\ p_1(s) &= -16 + 24s - 12s^2 + 4s^3, \\ p_2(s) &= -21 + 42s - 21s^2. \end{aligned}$$

At first, a check is made for the existence of isolated frequencies. The polynomials (10.1.25) are

$$\begin{aligned} R_0 &= 129 - 237\omega^2 + 80\omega^4, \\ I_0 &= 166\omega - 108\omega^3, \\ R_1 &= -16 + 12\omega^2, \\ I_1 &= 24\omega - 4\omega^3, \\ R_2 &= -21 + 21\omega^2, \\ I_2 &= 42\omega, \end{aligned}$$

and

$$\begin{aligned} R_0 I_1 - R_1 I_0 &= -4\omega(\omega^2 - 2)(80\omega^4 - 881\omega^2 + 719), \\ R_0 I_2 - R_2 I_0 &= 84\omega(\omega^2 - 2)(67\omega^2 - 53). \end{aligned}$$

Common real roots are  $\omega_s = 0$  (which is always the case) and  $\omega_s = \sqrt{2}$ .

$$\tau(\sqrt{2}) = \frac{|p_0(j\sqrt{2})|}{\sum_{i=1}^2 |p_i(j\sqrt{2})|} = \frac{R_0(\sqrt{2})}{R_1(\sqrt{2}) + R_2(\sqrt{2})} = \frac{I_0(\sqrt{2})}{I_1(\sqrt{2}) + I_2(\sqrt{2})} = 25/29.$$

The test could be finished because this value is smaller than 1 and the polynomial family must be unstable. For completeness, the other values of  $\tau(\omega)$  are calculated. They are

$$\begin{aligned} \tau(0) &= \frac{R_0(0)}{R_1(0) + R_2(0)} = 129/37, \\ \tau(\infty) &= \infty, \end{aligned}$$

and otherwise

$$\begin{aligned}\tau_1(\omega) &= \frac{|\text{Im}(p_0(j\omega)/p_1(j\omega))|}{|\text{Im}(p_2(j\omega)/p_1(j\omega))|}, \\ \tau_2(\omega) &= \frac{|\text{Im}(p_0(j\omega)/p_2(j\omega))|}{|\text{Im}(p_1(j\omega)/p_2(j\omega))|}, \\ \tau(\omega) &= \max\{\tau_1(\omega), \tau_2(\omega)\}.\end{aligned}$$

From Figure 10.3 (the ordinate is logarithmically scaled), it can be seen that  $\tau(\omega) > 1$  for all  $\omega \neq \sqrt{2}$ . The minimum of the function  $\tau(\omega)$  is  $25/29$  for the frequency  $\omega = \sqrt{2}$ . The modulus of the components  $q_1$  and  $q_2$  must be smaller than  $25/29$ . The corresponding intervals for the original feedback gains are then  $k_1 \in [530.7; 539.3]$  and  $k_2 \in [7587; 7738]$ . The parameter combination  $q_1 = q_2 = 25/29$  produces a polynomial with a root pair at  $s = j\sqrt{2}$ .

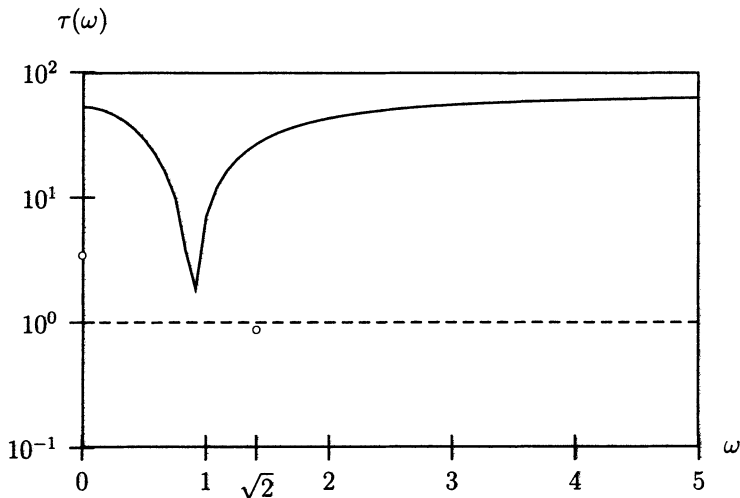


Figure 10.3. The distance function  $\tau(\omega)$  for testing the stability.  $\tau(\omega) > 1$  at the continuous part, but  $< 1$  at the isolated frequency  $\omega_s = \sqrt{2}$ , so the polynomial family is unstable

An alternative method is using Theorem 10.5. The magnitude of the complex-valued function  $z(\omega) = \frac{p_0(j\omega)}{|p_0(j\omega)|} \tau(\omega)$  is evaluated for all  $\omega$  and the infimum of this function determines the stability radius. This is equivalent to enlarging the unit circle in the complex plane until there is an intersection with the frequency plot  $z(\omega)$ . In Figure 10.4, the alternative Tsypkin-Polyak locus is plotted for determining the stability radius. The function  $z(\omega)$  is discontinuous at the singular frequencies  $\omega_{s1} = 0$  and  $\omega_{s2} = \sqrt{2}$  (marked with  $\circ$ ). The continuous part avoids the unit circle but  $z(\sqrt{2})$  is inside the unit circle. Thus, the polynomial family is unstable and to get stability the operating domain of  $q_1$  and  $q_2$  must be reduced by a factor  $< z(\sqrt{2}) = 25/29$ .  $\square$

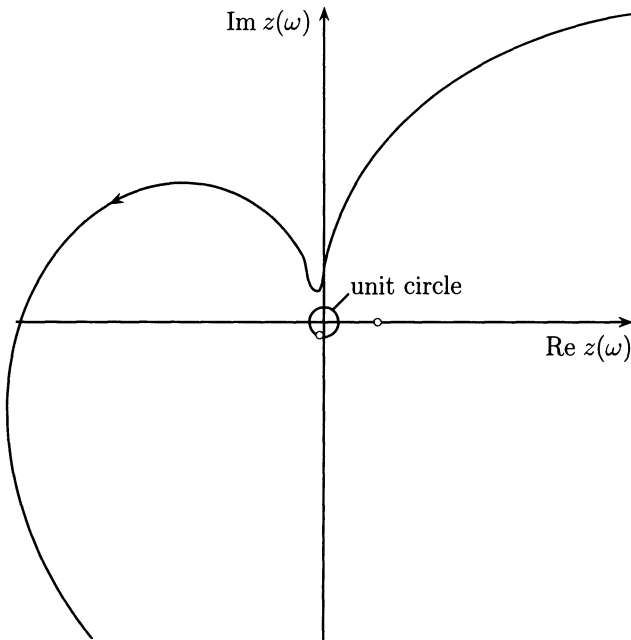


Figure 10.4. The alternative Tsyplkin-Polyak locus for testing the stability radius, it is discontinuous and does not avoid the unit circle at the isolated frequency  $\omega_{s2} = \sqrt{2}$ , so the polynomial family is unstable

## 10.2 Affine Dependence: The Largest Hypersphere in Parameter Space

The evaluation of  $\tau(\omega)$  and the determination of the largest stable box is a rather expensive task. A more effective method is now presented for a closely related problem, namely calculating the largest stable hypersphere in the space of parameters  $\mathbf{q}$ . This problem was first solved by Soh et al. [186]. A simpler solution was given by the authors [119], it is presented here.

Consider an uncertain polynomial  $p(s, \mathbf{q}) = [1 s \dots s^n] \mathbf{a}(\mathbf{q})$  with affine dependency of the coefficient vector  $\mathbf{a}$  on  $\mathbf{q}$ , i.e.

$$\mathbf{a} = \mathbf{a}^0 + \mathbf{F}\mathbf{q}, \quad (10.2.1)$$

with  $\mathbf{a}^0 \in \mathbb{R}^{n+1}$  and  $\mathbf{F} \in \mathbb{R}^{(n+1) \times \ell}$ . Each element  $q_i$  of  $\mathbf{q}$  is scaled by a “high value”  $q_i^+$ , and this scaling factor is included in the  $i$ -th column of  $\mathbf{F}$ . Then, a hypersphere  $\sum_{i=1}^{\ell} q_i^2 = \text{const.}$  in  $\mathbf{q}$ -space is a reasonable measure for the neighborhood of  $\mathbf{q} = \mathbf{0}$ . The parameter vector  $\mathbf{q} = \mathbf{0}$  is the nominal point, i.e. the coefficient vector of the unperturbed polynomial is  $\mathbf{a}^0$ . Assume that  $p(s, \mathbf{0})$  is stable. For  $\ell = n + 1$  and  $\mathbf{F} = \mathbf{I}$ , the polynomials are interval polynomials. The monic case ( $a_n = 1$ ) is also included if the last element of  $\mathbf{a}^0$  is 1 and the elements of the last row of  $\mathbf{F}$  are zero.

A geometric approach is used to determine the largest hypersphere. The knowledge of some fundamental definitions and formulas of higher dimensional geometry is needed. In  $\mathbb{R}^3$ , a plane is defined by

$$E = e_1 q_1 + e_2 q_2 + e_3 q_3 + e_0 = 0. \quad (10.2.2)$$

The generalization to  $\mathbb{R}^\ell$  is the  $(\ell - 1)$ -dimensional hyperplane

$$E = e_1 q_1 + e_2 q_2 + \dots + e_\ell q_\ell + e_0 = 0. \quad (10.2.3)$$

The normal vector  $\mathbf{e} (\neq \mathbf{0})$  of a hyperplane is given by

$$\mathbf{e} = \begin{bmatrix} e_1 \\ e_2 \\ \vdots \\ e_\ell \end{bmatrix}. \quad (10.2.4)$$

Two hyperplanes are orthogonal if their normal vectors  $\mathbf{e}_1, \mathbf{e}_2$  are orthogonal, that is,  $\mathbf{e}_1^T \mathbf{e}_2 = 0$ . The squared distance  $d^2$  of the origin from the hyperplane is

$$d^2 = \frac{e_0^2}{e_1^2 + e_2^2 + \dots + e_\ell^2} = \frac{e_0^2}{\mathbf{e}^T \mathbf{e}}. \quad (10.2.5)$$

Starting from the stable nominal point and varying  $\mathbf{q}$ , the boundary crossing theorem states that there are three possibilities for the polynomial to become unstable:

- i. A real zero goes through the origin ( $s = 0$ ).
- ii. A real zero goes through infinity ( $s = \infty$ ).
- iii. A pair of conjugate zeros crosses the imaginary axis ( $s = \pm j\omega$ ).

In the parameter space, each of the three cases corresponds to a hypersurface. Parts of these hypersurfaces are the stability boundaries. The minimal distance of the origin from these hypersurfaces determines the largest hypersphere.

The first hypersurface is given by  $p(0, \mathbf{q}) = [1 \ 0 \ \dots \ 0] \mathbf{a} = [1 \ 0 \ \dots \ 0] [\mathbf{a}^0 + \mathbf{F}\mathbf{q}] = 0$ . Only the first row of (10.2.1) is important. Because of the affine dependency, the hypersurface is a hyperplane with the equation

$$E_0 = a_0^0 + f_{11} q_1 + f_{12} q_2 + \dots + f_{1\ell} q_\ell = 0, \quad (10.2.6)$$

and the squared distance to the origin is with (10.2.5)

$$r_0^2 = \frac{(a_0^0)^2}{f_{11}^2 + f_{12}^2 + \dots + f_{1\ell}^2}. \quad (10.2.7)$$

If  $a_0^0 \neq 0$  and  $f_{11} = f_{12} = \dots = f_{1\ell} = 0$ , then case a) is not possible and the hyperplane does not exist. No combination of the parameters  $q_1, q_2, \dots, q_\ell$  will produce a zero at  $s = 0$ . A reasonable choice for the distance is  $r_0 = \infty$ .

The same conclusion leads to the hyperplane for case b). It is  $p(\infty, \mathbf{q}) = 0$  (the leading coefficient must vanish) and

$$E_\infty = a_n^0 + f_{n+1,1} q_1 + f_{n+1,2} q_2 + \dots + f_{n+1,\ell} q_\ell = 0, \quad (10.2.8)$$

with the squared distance

$$r_\infty^2 = \frac{(a_n^0)^2}{f_{n+1,1}^2 + f_{n+1,2}^2 + \dots + f_{n+1,\ell}^2}. \quad (10.2.9)$$

For a constant leading coefficient  $a_n$ , again  $r_\infty = \infty$ .

For the more complicated case c), the polynomial  $p(s, \mathbf{q}) = [1 \ s \ \dots \ s^n] \ \mathbf{a} = [1 \ s \ \dots \ s^n] [\mathbf{a}^0 + \mathbf{F}\mathbf{q}]$  must have a root on the imaginary axis. For  $s = j\omega$  with  $\omega \neq 0$ , the complex equation is equivalent to the following two real equations:

$$E_1 = \operatorname{Re} p(j\omega, \mathbf{q}) = [1 \ 0 \ -\omega^2 \ 0 \ \omega^4 \ \dots] [\mathbf{a}^0 + \mathbf{F}\mathbf{q}] = 0 \quad (10.2.10)$$

and

$$E_2 = \frac{1}{\omega} \operatorname{Im} p(j\omega, \mathbf{q}) = [0 \ 1 \ 0 \ -\omega^2 \ 0 \ \omega^4 \ \dots] [\mathbf{a}^0 + \mathbf{F}\mathbf{q}] = 0. \quad (10.2.11)$$

The complex root boundary is generated by the intersection of the two hyperplanes  $E_1 = 0$  and  $E_2 = 0$  that vary with  $\omega$ . The set of intersection points for fixed  $\omega$  is an  $(\ell - 2)$ -dimensional hyperplane. The distance of the origin to this  $(\ell - 2)$ -dimensional hyperplane is a function of  $\omega$ , call it  $r_C(\omega)$ , and the distance from the complex root boundary is the minimum of this function  $r_C(\omega)$ .

The calculation of  $r_C(\omega)$  would be easy if the two hyperplanes (10.2.10) and (10.2.11) were orthogonal. This is, in general, not true, however it is possible to replace  $E_2 = 0$  by a third hyperplane  $E_3 = 0$ , which is orthogonal to  $E_1 = 0$  such that  $E_1 \cap E_2 = E_1 \cap E_3$ . The important point to note is that the equation

$$E_3 = (1 - \lambda)E_1 + \lambda E_2 = 0 \quad (10.2.12)$$

is satisfied for all points lying on both  $E_1 = 0$  and  $E_2 = 0$ . (10.2.12) represents another  $(\ell - 2)$ -dimensional hyperplane, which contains the intersection points of  $E_1 = 0$  and  $E_2 = 0$ , whatever the value of  $\lambda$ . As  $\lambda$  is varied, a set of  $(\ell - 2)$ -dimensional hyperplanes is formed, two of which are  $E_1 = 0$  (when  $\lambda = 0$ ) and  $E_2 = 0$  (when  $\lambda = 1$ ).  $E_1 \cap E_3$  will produce the same set as  $E_1 \cap E_2$  if  $\lambda \neq 0$  (see Figure 10.5). The value of  $\lambda$  can now be chosen in such a way that  $E_1 = 0$  and  $E_3 = 0$  are orthogonal. The normal vector  $\mathbf{e}_3$  of  $E_3 = 0$  is

$$\mathbf{e}_3 = (1 - \lambda)\mathbf{e}_1 + \lambda\mathbf{e}_2, \quad (10.2.13)$$

and  $\mathbf{e}_1$  and  $\mathbf{e}_3$  are orthogonal if

$$\mathbf{e}_1^T \mathbf{e}_3 = (1 - \lambda)\mathbf{e}_1^T \mathbf{e}_1 + \lambda\mathbf{e}_1^T \mathbf{e}_2 = 0 \quad (10.2.14)$$

or

$$\lambda = \frac{\mathbf{e}_1^T \mathbf{e}_1}{\mathbf{e}_1^T \mathbf{e}_1 - \mathbf{e}_1^T \mathbf{e}_2}. \quad (10.2.15)$$

Note that  $\lambda$  is a function of  $\omega$ . This orthogonalization procedure is not possible if (for singular frequencies  $\omega = \omega_s$ ) the hyperplanes  $E_1 = 0$  and  $E_2 = 0$  are parallel. This means a) that for these values, both hyperplanes have no common points and  $r_C(\omega_s) = \infty$ , or b)  $E_1 \equiv E_2$  and it is obvious how to determine the distance to the origin.

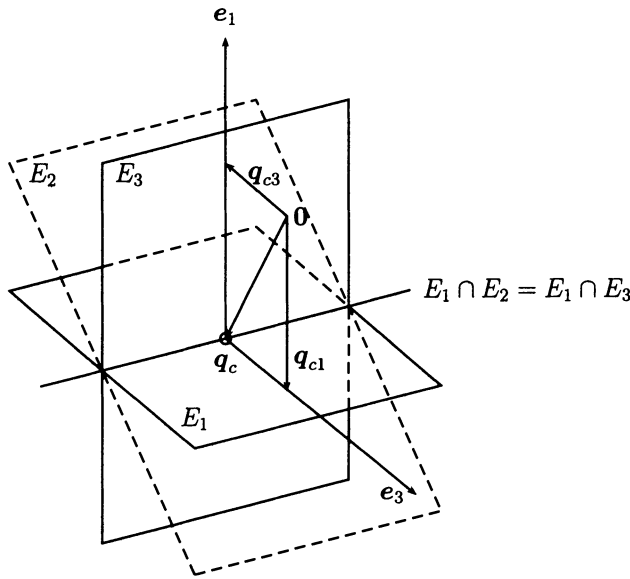


Figure 10.5. For each frequency  $\omega$  the complex root boundary is generated by the intersection of the two hyperplanes  $E_1$  and  $E_2$ , which is equal to the intersection of  $E_1$  and  $E_3$

Case b) produces a discontinuity in the distance function. It is another appearance of the isolated frequencies that were discussed in Section 4.4.

If the polynomial coefficients vary in the coefficient space between given bounds (interval polynomial) rather than in the parameter space, then the hyperplanes  $E_1 = 0$  and  $E_2 = 0$  are orthogonal and there cannot be any singular frequencies ( $\mathbf{F} = \mathbf{I}$  and the normal vectors are orthogonal, i.e.  $\mathbf{d}_1^T \mathbf{d}_2 = 0$ ).

The reason for orthogonalizing is that afterwards the distance function  $r_C(\omega)$  can be determined. (10.2.10) and (10.2.11) can be written as

$$\mathbf{D}(\mathbf{a}^0 + \mathbf{F}\mathbf{q}) = \mathbf{D}\mathbf{a}^0 + \mathbf{G}\mathbf{q} = \begin{bmatrix} 0 \\ 0 \end{bmatrix}, \quad (10.2.16)$$

where

$$\mathbf{D} = \begin{bmatrix} 1 & 0 & -\omega^2 & 0 & \omega^4 & \dots \\ 0 & 1 & 0 & -\omega^2 & 0 & \dots \end{bmatrix} = \begin{bmatrix} \mathbf{d}_1^T \\ \mathbf{d}_2^T \end{bmatrix}, \quad (10.2.17)$$

$$\mathbf{G} := \mathbf{DF} = \begin{bmatrix} \mathbf{e}_1^T \\ \mathbf{e}_2^T \end{bmatrix}. \quad (10.2.18)$$

Thus, in the parameter space the equations of the two hyperplanes are

$$E_1 = \mathbf{d}_1^T \mathbf{a}^0 + \mathbf{e}_1^T \mathbf{q} = 0, \quad (10.2.19)$$

$$E_2 = \mathbf{d}_2^T \mathbf{a}^0 + \mathbf{e}_2^T \mathbf{q} = 0, \quad (10.2.20)$$

where  $\mathbf{e}_1$  and  $\mathbf{e}_2$  are the normal vectors of  $E_1 = 0$  and  $E_2 = 0$ . For each non-singular frequency  $\omega$ , it is possible to construct the hyperplane  $E_3 = 0$  of (10.2.12) with  $\lambda$  of (10.2.15) such that the two hyperplanes  $E_1 = 0$  and  $E_3 = 0$  are orthogonal:  $\mathbf{e}_1^T \mathbf{e}_3 = 0$ . This situation is illustrated by Figure 10.5. The nominal point is  $\mathbf{q} = \mathbf{0}$ . Seen from there, the closest point on the complex root boundary is  $\mathbf{q}_c = \mathbf{q}_{c1} + \mathbf{q}_{c3}$ . The unit vector parallel to  $\mathbf{e}_1$  is  $\mathbf{e}_1 / \sqrt{\mathbf{e}_1^T \mathbf{e}_1}$  and by (10.2.5)  $\mathbf{d}_1^T \mathbf{a}^0 / \sqrt{\mathbf{e}_1^T \mathbf{e}_1}$  is the distance between the origin and  $E_1 = 0$ , thus,

$$\mathbf{q}_{c1} = -\frac{\mathbf{d}_1^T \mathbf{a}^0}{\mathbf{e}_1^T \mathbf{e}_1} \mathbf{e}_1.$$

Analog reasoning for  $\mathbf{q}_{c3}$  leads to

$$\mathbf{q}_c = -\frac{\mathbf{d}_1^T \mathbf{a}^0}{\mathbf{e}_1^T \mathbf{e}_1} \mathbf{e}_1 - \frac{\mathbf{d}_3^T \mathbf{a}^0}{\mathbf{e}_3^T \mathbf{e}_3} \mathbf{e}_3. \quad (10.2.21)$$

The distance  $r_C(\omega)$  is

$$r_C(\omega) = \|\mathbf{q}_c\|_2 = \sqrt{\frac{(\mathbf{d}_1^T \mathbf{a}^0)^2}{\mathbf{e}_1^T \mathbf{e}_1} + \frac{(\mathbf{d}_3^T \mathbf{a}^0)^2}{\mathbf{e}_3^T \mathbf{e}_3}}. \quad (10.2.22)$$

The squared distance  $r_C^2(\omega)$  is a rational function of  $\omega$  and the necessary condition for the minimum at  $\omega^*$  is that the derivative vanishes. However, keep in mind that (10.2.22) is only valid for non-singular frequencies. At a singular frequency  $\omega_s$ , the normal vectors are parallel. It follows that either the hyperplanes  $E_1 = 0$  and  $E_2 = 0$  are parallel and not identical then no  $(\ell - 2)$ -dimensional hyperplane is generated and  $r_C(\omega_s) = \infty$  can be set, or the hyperplanes are identical, i.e.  $E_1 = E_2 = 0$  and the formula used for  $E_0 = 0$  can be applied.

After the distances  $r_0, r_\infty, r_C(\omega^*)$  of the origin of the three boundaries are determined, the stability radius  $\rho$  is found as

$$\rho = \min\{r_0, r_\infty, r_C(\omega^*)\}. \quad (10.2.23)$$

In comparison to the method described in Section 10.1 for the affine case where  $\ell$  functions have to be evaluated, here only one function has to be evaluated.

### Example 10.8

Recall Example 10.7 The matrices  $\mathbf{a}^0$  and  $\mathbf{F}$  are

$$\mathbf{a}^0 = \begin{bmatrix} 129 \\ 166 \\ 237 \\ 108 \\ 80 \end{bmatrix}, \quad \mathbf{F} = \begin{bmatrix} -16 & -21 \\ 24 & 42 \\ -12 & -21 \\ 4 & 0 \\ 0 & 0 \end{bmatrix}. \quad (10.2.24)$$

The real root boundary for  $s = 0$  is the straight line

$$E_0 = -16q_1 - 21q_2 + 129 = 0, \quad (10.2.25)$$

which gives  $r_0 = 129/\sqrt{16^2 + 21^2} \approx 4.89$ . The real root boundary for  $s = \infty$  does not exist, so  $r_\infty = \infty$ . The orthogonalization procedure leads for  $\omega \neq \sqrt{2}$  to

$$r_C^2(\omega) = \frac{10(640\omega^8 - 14096\omega^6 + 287085\omega^4 - 439886\omega^2 + 175573)}{441(\omega^2 + 1)^2} \quad (10.2.26)$$

and

$$\mathbf{q}_c = \begin{bmatrix} -\frac{67\omega^2 - 53}{\omega^2 + 1} \\ -\frac{80\omega^4 - 881\omega^2 + 719}{21(\omega^2 + 1)} \end{bmatrix}. \quad (10.2.27)$$

There is a singular frequency at  $\omega = \sqrt{2}$  and  $E_1(\sqrt{2}) = E_2(\sqrt{2}) = 8q_1 + 21q_2 - 25 = 0$ . Thus,

$$r_C(\sqrt{2}) = \frac{25}{\sqrt{8^2 + 21^2}} \approx 1.11. \quad (10.2.28)$$

A plot of  $r_C(\omega)$  in Figure 10.6 (with logarithmic scaling on the ordinate) shows that this is the minimum. Thus, the stability radius is  $\rho_2 = r_C(\sqrt{2})$ . Note that in Example 10.7,

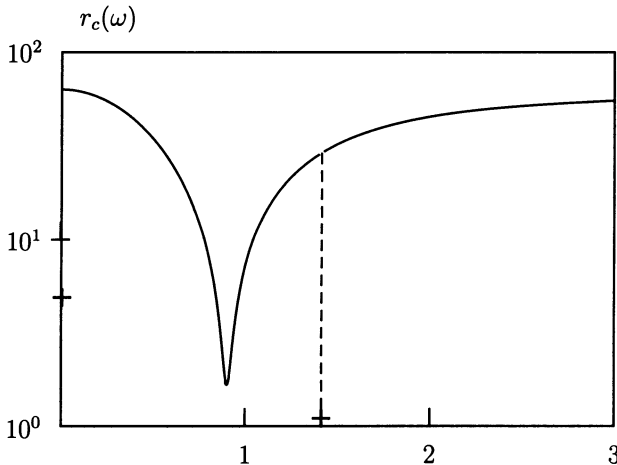


Figure 10.6. The distance function  $r_C(\omega)$  with two discontinuities at  $\omega = 0$  and  $\omega = \sqrt{2}$

a smaller stability radius of  $\rho = 25/29$  was obtained for the maximum size of the box uncertainty. The hypersphere, i.e. circle for  $\ell = 2$  of Example 10.9 is contained in the box and can be dilated further before it hits the stability boundary.  $\square$

## 10.3 Polynomial Dependence

In this section, polynomials are considered whose coefficients depend polynomially on the elements of an uncertain parameter vector. The size of perturbation is characterized

by the weighted norm of the parameter vector. The smallest destabilizing perturbation defines the stability radius of the set of uncertain polynomials.

It will be shown that determining this radius is equivalent to solving a finite set of systems of algebraic equations and then selecting the real solution with the smallest norm. The number of systems of equations depends crucially on the dimension  $\ell$  of the parameter vector, whereas the complexity of systems of equations increases mainly with the kind of polynomial dependence  $a(\mathbf{q})$  and the degree  $n$  of the polynomial. This method also yields the smallest destabilizing parameter combination and the corresponding critical frequency.

Vicino et al. [197] transform the problem into an optimization problem and present a numerical algorithm to find the solution. It will be shown that the problem can also be solved in an analytical-numerical way, that is, systems of algebraic equations [118] have to be solved. The derivation and solution of these systems of equations will be demonstrated in this section.

Given an uncertain polynomial  $p(s, \mathbf{q})$  with  $\mathbf{q} \in \mathbb{R}^\ell$  and real polynomials  $a_i(\mathbf{q})$ . The nominal polynomial  $p(s, \mathbf{0})$  is stable. Find the maximal  $\rho$  such that  $p(s, \mathbf{q})$  is stable for all  $\|\mathbf{q}\|_p < \rho$ .  $\rho$  is called the stability radius and the index  $p$  characterizes the type of norm.

Concerning the choice of the norm, i.e.  $p$ , there are three important possibilities. For  $p = \infty$  the set of admissible  $\mathbf{q}$  describes an  $\ell$ -dimensional hypercube. Dual to this norm is  $p = 1$ , which corresponds to a diamond.  $p = 2$  yields an  $\ell$ -dimensional hypersphere in  $Q$ -space. From the practical point of view, the case  $p = \infty$  is the most important one, because there the bounds for the uncertain parameters are independent. The case  $p = \infty$  will be handled in detail. For the other cases, it is not difficult to derive the corresponding results.

It was shown in Section 10.2 that the stable set of  $\mathbf{q}$  is bounded by three hypersurfaces, namely  $a_0(\mathbf{q}) = 0$ ,  $a_n(\mathbf{q}) = 0$  and  $\Delta_{n-1}(\mathbf{q}) = 0$ , see Figure 10.7. The last equation is the last but one Hurwitz determinant, which is the critical one. It results from the elimination of  $\omega$  from the two equations  $\text{Re } p(j\omega) = 0$  and  $\text{Im } p(j\omega) = 0$  as was shown in the proof of Theorem 2.1. Here, linear or non-linear dependence make a big difference. For fixed  $\omega$  and linear dependence  $\text{Re } p = 0$ ,  $\text{Im } p = 0$  represent a linear manifold; this means, for example, that for  $\ell = 3$ ,  $\Delta_2(\mathbf{q}) = 0$  is generated by the continuous movement of a straight line. In the case of non-linear dependency, a set of curves in  $\mathbb{R}^3$  generate  $\Delta_2 = 0$ . Computing  $\Delta_{n-1}(\mathbf{q})$  must, in general, be done by a computer algebra program.

All three equations of the hypersurfaces will be treated in the same way. The only difference is that the third one will be the complicated one with respect to the number of terms and degree of the terms. In the sequel, the notation  $F(\mathbf{q}) = 0$  is used for each of these equations.

Consider first the case of two parameters for which the basic idea is demonstrated. The polynomial family with  $\|\mathbf{q}\|_\infty \leq \gamma$  ( $\gamma$  sufficiently small) is stable and can be described by a square of sidelength  $2\gamma$ . Enlarge this square continuously until there is an intersection point with the curve  $F(q_1, q_2) = 0$ , as demonstrated in Figure 10.7. This point of first contact with a stability boundary may lie on a vertex or on an edge of the square (see Figure 10.8). The first situation is characterized by the fact that  $q_1 = q_2$

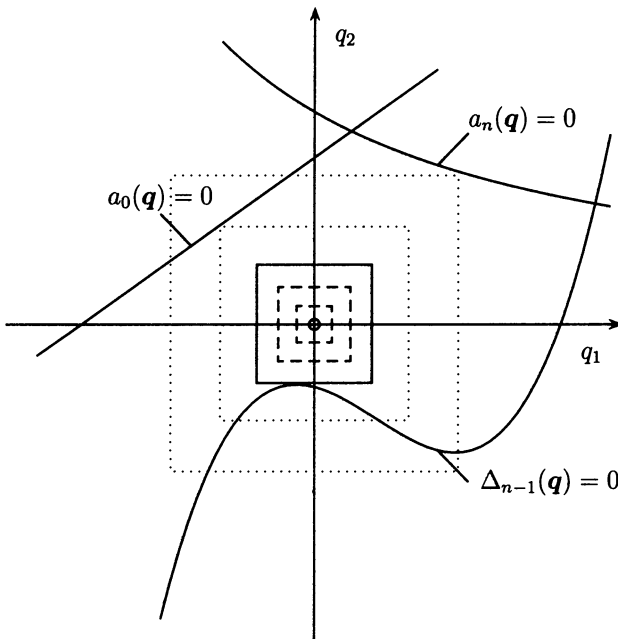


Figure 10.7. The stable region is bounded by at most three hypersurfaces

(marked *a*) or  $q_1 = -q_2$  (marked *b*), which results in the two polynomial equations

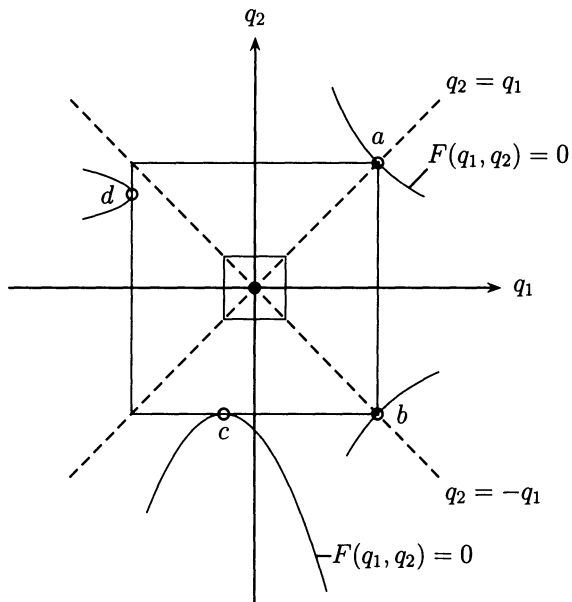
$$\begin{aligned} F(q_1, q_1) &= 0, \\ F(q_1, -q_1) &= 0. \end{aligned} \quad (10.3.1)$$

The second case is an intersection point on an edge. This means that  $F(q_1, q_2) = 0$  has a horizontal (marked *c*) or a vertical tangent (marked *d*). This necessary condition leads to the two systems of equations in two unknowns

$$\begin{aligned} F(q_1, q_2) &= 0, \quad \frac{\partial F(q_1, q_2)}{\partial q_1} = 0, \\ F(q_1, q_2) &= 0, \quad \frac{\partial F(q_1, q_2)}{\partial q_2} = 0. \end{aligned} \quad (10.3.2)$$

It may be possible that in the intersection point, the curve  $F(q_1, q_2) = 0$  cannot be differentiated, i.e. the curve has, for example, a cusp or a singular frequency. For these points, both partial derivatives vanish and these solutions are already obtained by (10.3.2).

Finding the real roots of the two polynomials and the real solution vectors of the two systems of equations gives a set of points  $(q_1, q_2)$  that are candidates for the first contact. For the first case (vertex contact)  $\|(\pm q, \pm q)\|_\infty = \|q\|_\infty = |q|$  and for the second case (edge contact)  $\|(q_1, q_2)\|_\infty = \max\{|q_1|, |q_2|\}$ . The solution vector with the smallest norm  $q^* = [q_1^*; q_2^*]^T$  yields the stability radius. This critical parameter combination  $q^*$  also determines the critical frequency. The polynomial  $p(s, q_1^*, q_2^*) = 0$  has a root at  $s = 0$

Figure 10.8. The case  $p = \infty$ 

or at  $s = \infty$ , or a root pair at  $s = \pm j\omega$ . All other roots are not in the open right half plane.

Consider the case of three parameters. A surface  $F(q_1, q_2, q_3) = 0$  replaces the curve  $F(q_1, q_2) = 0$ . This surface bounds the stable polynomials and now a cube instead of a square is enlarged. The intersection points lie either on a vertex, on an edge, or on a face of the cube. These subsets of the cube are called *subpolytopes*. Corresponding to the eight vertices of the cube, the four polynomials

$$\begin{aligned} F(q, +q, +q) &= 0 , \\ F(q, +q, -q) &= 0 , \\ F(q, -q, +q) &= 0 , \\ F(q, -q, -q) &= 0 \end{aligned}$$

describe this situation. In case of the twelve edges, two intersection points must coincide, i.e. the partial derivatives must vanish and the six systems of equations

$$F(q_1, +q, +q) = 0, \quad \left. \frac{\partial F}{\partial q_1} \right|_{q_2=+q, q_3=+q} = 0,$$

$$F(q_1, +q, -q) = 0, \quad \left. \frac{\partial F}{\partial q_1} \right|_{q_2=+q, q_3=-q} = 0,$$

$$F(+q, q_2, +q) = 0, \quad \left. \frac{\partial F}{\partial q_2} \right|_{q_1=+q, q_3=+q} = 0,$$

$$F(-q, q_2, +q) = 0, \quad \left. \frac{\partial F}{\partial q_2} \right|_{q_1=-q, q_3=+q} = 0,$$

$$F(+q, +q, q_3) = 0, \quad \left. \frac{\partial F}{\partial q_3} \right|_{q_1=+q, q_2=+q} = 0,$$

$$F(+q, -q, q_3) = 0, \quad \left. \frac{\partial F}{\partial q_3} \right|_{q_1=+q, q_2=-q} = 0$$

in two unknowns have to be solved.

If the intersection is on one of the six surfaces, then the normal vector of the surface  $F(q_1, q_2, q_3) = 0$  is parallel to one of the coordinate axes, which means that two of the three partial derivatives vanish simultaneously and the three systems

$$F(q_1, q_2, q_3) = 0, \quad \frac{\partial F}{\partial q_1} = 0, \quad \frac{\partial F}{\partial q_2} = 0,$$

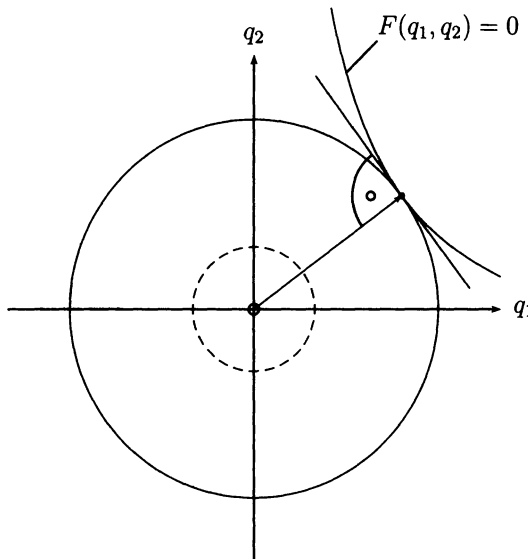
$$F(q_1, q_2, q_3) = 0, \quad \frac{\partial F}{\partial q_1} = 0, \quad \frac{\partial F}{\partial q_3} = 0,$$

$$F(q_1, q_2, q_3) = 0, \quad \frac{\partial F}{\partial q_2} = 0, \quad \frac{\partial F}{\partial q_3} = 0,$$

in three unknowns characterize this situation.

For  $\ell > 3$  parameters, the number of polynomials and systems of equations obviously grows with the number of subpolytopes of an  $\ell$ -dimensional cube. The derivation of the polynomials and systems of equations for arbitrary  $\ell$  is straightforward. But, now again occurs what is called the combinatorial explosion. The number of equations grows exponentially with the number of parameters.

Using other norms ( $p = 2$  or  $p = 1$ ) gives similar equations. In any case, equations that are linear combinations of  $F$  and their partial derivatives have to be solved. For  $p = 2$ , the number of systems is smaller, but the equations are more complicated. In that case at the intersection point, the vector  $q$  must be parallel to the gradient of  $F$  as indicated in Figure 10.9.

Figure 10.9. The case  $p = 2$ 

Only one system of equations,

$$F(\mathbf{q}) = 0, \quad \frac{\partial F}{\partial \mathbf{q}} = \lambda \mathbf{q},$$

is necessary for describing this situation.

A restriction for practical applications is the problem to find all solutions of the system of equations. The theorem of Bezout (see Appendix A) says that, for example, a system of three equations with the degrees  $m_i$ ,  $i = 1, 2, 3$  has up to  $m_1 \cdot m_2 \cdot m_3$  solution vectors. So the resulting polynomial in one variable after eliminating the other two variables may have the degree  $m_1 \cdot m_2 \cdot m_3$ . Therefore, this method is recommended for up to only three uncertain parameters. The restriction to few parameters seems to be severe, but a quotation of Lazard [130] in 1991 on software for the solution of algebraic equations gives hope for the future. “Five years ago, problems with four or five unknowns were outside of the capabilities of most available softwares. Recent progresses made or will make accessible problems with six or seven unknowns.”

### *Example 10.9*

Consider the track-guided bus of Section 6.8. The transfer function of the uncontrolled bus depends on the virtual mass  $\tilde{m}$  and on the velocity  $v$ . For the data given in Table 6.1, it is

$$g(s, \tilde{m}, v) = \frac{6.079 \cdot 10^5 \tilde{m}v^2 s^2 + 3.886 \cdot 10^{11} vs + 4.803 \cdot 10^{10} v^2}{s^3(\tilde{m}^2 v^2 s^2 + 9.818 \cdot 10^5 \tilde{m}vs + 1.663 \cdot 10^4 \tilde{m}v^2 + 2.690 \cdot 10^{11})}.$$

In [154], a controller was designed that led to the closed-loop polynomial

$$p(s, \tilde{m}, v) = \sum_{i=0}^8 a_i s^i,$$

with

$$\begin{aligned} a_0 &= 453 \cdot 10^6 v^2, \\ a_1 &= 528 \cdot 10^6 v^2 + 3640 \cdot 10^6 v, \\ a_2 &= 5.72 \cdot 10^6 \tilde{m}v^2 + 113 \cdot 10^6 v^2 + 4250 \cdot 10^6 v, \\ a_3 &= 6.93 \cdot 10^6 \tilde{m}v^2 + 911 \cdot 10^6 v + 4220 \cdot 10^6, \\ a_4 &= 1.45 \cdot 10^6 \tilde{m}v^2 + 16.8 \cdot 10^6 \tilde{m}v + 338 \cdot 10^6, \\ a_5 &= 15.6 \cdot 10^3 \tilde{m}^2 v^2 + 840 \tilde{m}v^2 + 1.35 \cdot 10^6 \tilde{m}v + 13.5 \cdot 10^6, \\ a_6 &= 1.25 \cdot 10^3 \tilde{m}^2 v^2 + 16.8 \tilde{m}^2 v^2 + 53.9 \cdot 10^3 \tilde{m}v + 270 \cdot 10^3, \\ a_7 &= 50 \tilde{m}^2 v^2 + 1080 \tilde{m}v, \\ a_8 &= \tilde{m}^2 v^2. \end{aligned}$$

Let the nominal point be  $v = 20$  [ $\text{ms}^{-1}$ ] and  $\tilde{m} = 20$  [ $10^3 \text{ kg}$ ]. For determining the

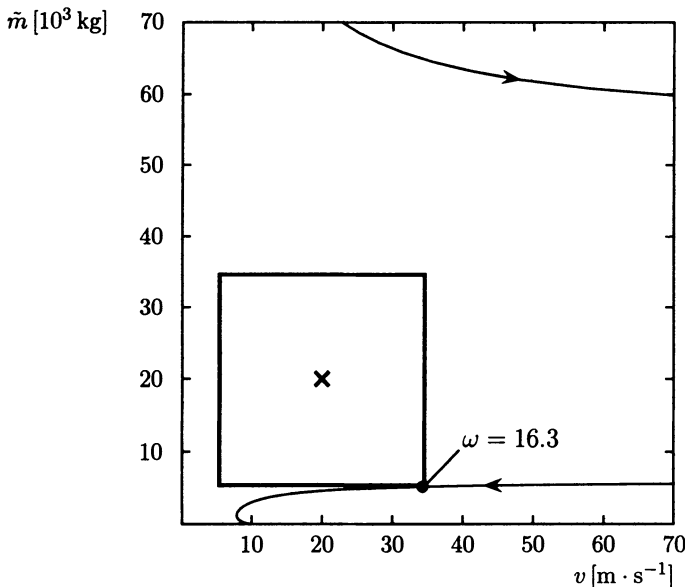


Figure 10.10. The maximal square around the nominal point (20,20)

stability radius, the parameter space method can be applied, i.e. plotting the stability boundaries in the  $(v, \tilde{m})$ -plane, see Figure 10.10. But, the analytical method of this section is also applicable. The distances to the real root boundaries  $\tilde{m} = 0$  and  $v = 0$  are trivial, but for the distance to the complex root boundary the Hurwitz determinant, which is of order seven, has to be calculated. This must be done by a computer algebra

program. Solving (10.3.1) and (10.3.2) with  $q_1 = v - 20$  and  $q_2 = \tilde{m} - 20$  yields an intersection point of the growing box with the complex root boundary at  $q_1 = 14.8$ ,  $q_2 = -q_1$  for  $\omega = 16.3$ , see Figure 10.10.

□

# 11 Robustness of Sampled-data Control Systems

Controllers are usually implemented in a digital computer. Figure 11.1 shows a single-loop sampled-data control system with  $c_z(z)$  representing the  $z$ -transfer function of the digital controller, and  $(1 - e^{-Ts})/s$  as the transfer function of the hold element,  $T$  is the sampling interval. The problems and solution approaches treated in Chapters 1

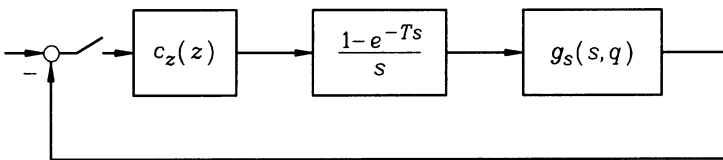


Figure 11.1. Sampled-data control system with uncertain physical parameters  $q$  in the continuous-time plant

through 10 have their counterparts for sampled-data control systems and Sections 11.1 to 11.9 are organized accordingly. Before we go into details, we should however discuss an obvious question:

Assume that a robust continuous controller was designed for the plant  $g_s(s, q)$ . Is it possible to find an approximately equivalent discrete-time controller  $c_z(z)$  that preserves robust stability?

Discretization of a continuous-time controller is a topic of research interest. For a nominal plant  $g_s(s)$ , a controller discretization procedure was shown in [139] that preserves the closed-loop stability. The controller, however, depends on the nominal plant model and therefore does not meet our requirement of a fixed-gain robust controller for an uncertain plant.

Since robust stability is not guaranteed after controller discretization, there remain two alternatives:

- Try a controller discretization procedure that does not involve the plant transfer function, e.g. the Tustin approximation with

$$s \approx \frac{2(z - 1)}{T(z + 1)}, \quad (11.0.1)$$

and do a robust stability analysis for the resulting discrete-time system. For “sufficiently small” sampling intervals  $T$ , the approximation is good. Essentially, it replaces each continuous integrator  $1/s$  in the controller by a discrete approximation using the trapezoidal rule for integration with  $z$ -transfer function  $T(z+1)/2(z-1)$ .

- b) Discretize the plant model and try any design tool to simultaneously stabilize the plant for some representative operating conditions. Then, do a robust stability analysis for the continuum of parameter values. If we adopt this *multi-model approach*, then design of the discrete-time controller is not more complicated than the continuous-time design, because numerator and denominator coefficients of  $c_z(z)$  in Figure 11.1 enter linearly into the closed-loop characteristic polynomial like in the continuous-time case.

For both approaches, a robust stability analysis of the resulting closed-loop discrete-time system is required, in case a) because stability cannot be guaranteed after approximate controller discretization, and in case b) because only representative operating conditions were considered in the design.

## 11.1 Plant and Controller Discretization

In Chapters 6 and 7, we have seen examples of parametric state-space and transfer-function models of continuous-time plants. Now, the plant inputs  $\mathbf{u}(t)$  are generated by a sampler and hold, i.e.

$$\mathbf{u}(t) = \mathbf{u}(iT), \quad t \in [iT; iT + T], \quad i = 0, 1, 2, \dots \quad (11.1.1)$$

and the plant model may be discretized to obtain a description of states and signals at the sampling instants  $t = iT$ . The discretization process is derived in many textbooks on sampled-data control systems, e.g. [37] [87] [4] and the results are only summarized here.

A state space model

$$\begin{aligned} \dot{\mathbf{x}} &= \mathbf{A}(\mathbf{q})\mathbf{x} + \mathbf{B}(\mathbf{q})\mathbf{u}, \\ \mathbf{y} &= \mathbf{C}(\mathbf{q})\mathbf{x}, \end{aligned} \quad (11.1.2)$$

with input (11.1.1), yields the discretized system

$$\begin{aligned} \mathbf{x}(iT + T) &= \mathbf{A}_d(\mathbf{q})\mathbf{x}(iT) + \mathbf{B}_d(\mathbf{q})\mathbf{u}(iT), \\ \mathbf{y}(iT) &= \mathbf{C}(\mathbf{q})\mathbf{x}(iT). \end{aligned} \quad (11.1.3)$$

Let

$$\mathbf{R}(\mathbf{q}) := \int_0^T e^{\mathbf{A}(\mathbf{q})v} dv, \quad (11.1.4)$$

then

$$\begin{aligned} \mathbf{A}_d(\mathbf{q}) &= e^{\mathbf{A}(\mathbf{q})T} = \mathbf{I} + \mathbf{R}(\mathbf{q})\mathbf{A}(\mathbf{q}), \\ \mathbf{B}_d(\mathbf{q}) &= \mathbf{R}(\mathbf{q})\mathbf{B}(\mathbf{q}). \end{aligned} \quad (11.1.5)$$

Each eigenvalue of  $\mathbf{A}$  at  $s_i$  is mapped to an eigenvalue of  $\mathbf{A}_d$  at  $z_i = e^{s_i T}$  with the same multiplicity.

The  $z$ -transfer function matrix of the system (11.1.3) with  $z = e^{sT}$  is

$$H_z(z, \mathbf{q}) = \mathbf{C}(\mathbf{q})[z\mathbf{I} - \mathbf{A}_d(\mathbf{q})]^{-1}\mathbf{B}_d(\mathbf{q}) \quad (11.1.6)$$

and, in the single-input, single-output case,

$$h_z(z, \mathbf{q}) = \mathbf{c}^T(\mathbf{q})[z\mathbf{I} - \mathbf{A}_d(\mathbf{q})]^{-1}\mathbf{b}_d(\mathbf{q}). \quad (11.1.7)$$

An alternative approach to plant discretization starts from the plant transfer function  $g_s(s, \mathbf{q})$ . ( $g_s(s, \mathbf{q})$  may also be an element of a transfer function matrix.) First, the  $z$ -transfer function for sampler, hold, and plant is determined as

$$h_z(z, \mathbf{q}) = \frac{z-1}{z} \mathcal{Z} \left\{ \frac{g_s(s, \mathbf{q})}{s} \right\}, \quad (11.1.8)$$

or, equivalently, by the Poisson sum [136] [134]

$$h_z(e^{sT}, \mathbf{q}) = (1 - e^{-sT}) \sum_{m=-\infty}^{\infty} \frac{g_s(s + jm2\pi/T, \mathbf{q})}{sT + jm2\pi}. \quad (11.1.9)$$

### Example 11.1

$$g_s(s, q) = \frac{1}{s(1+s/q)}, \quad (11.1.10)$$

$$h_z(z, q) = \frac{(1 - qTe^{-qT} - e^{-qT}) - (1 - qT - e^{-qT})z}{q(z-1)(z - e^{-qT})}. \quad (11.1.11)$$

The poles of  $g_s(s, \mathbf{q})$  at  $s_1 = 0$  and  $s_2 = -q$  are transformed to poles of  $h_z(z, \mathbf{q})$  at  $z_1 = e^{s_1 T} = 1$  and  $z_2 = e^{s_2 T} = e^{-qT}$ . The zero of  $h_z(z, \mathbf{q})$ , however, does not even have a continuous-time counterpart. In the numerator, it is not possible to introduce only one new uncertain variable  $e^{-qT}$  instead of  $q$ , because  $qT$  also enters in form of a sum and a product. Therefore, we have to deal with an exponential parameter dependence that also enters into the closed-loop characteristic polynomial.

The Poisson form of the  $z$ -transfer function is

$$h_z(e^{sT}, q) = \frac{1 - e^{-sT}}{T} \sum_{m=-\infty}^{\infty} \frac{1}{(s + jm2\pi/T)^2[1 + (s + jm2\pi/T)/q]}. \quad (11.1.12)$$

For numerically given  $q$ , the form (11.1.11) of the  $z$ -transfer function is more convenient. For uncertain  $q$ , however, (11.1.12) is a useful form because  $h_z(e^{sT}, q)$  may be approximated by truncation of the series, see Section 11.8. This approximation is rational in  $q$ .  $\square$

## 11.2 Discrete-time Controllers

Controllability and observability of a controllable single-input single-output plant get lost in the discretization process, whenever two distinct eigenvalues  $s_1 \neq s_2$  of the continuous-time plant map into identical eigenvalues  $e^{s_1 T} = e^{s_2 T}$  of the discrete-time plant [122].

*Example 11.2 (Crane)*

By (1.1.7), the crane has eigenvalues on the imaginary axis at  $s_{3,4} = \pm j\sqrt{g(m_L + m_C)/\ell m_C}$ . Controllability gets lost for  $e^{s_3 T} = e^{s_4 T}$ , i.e.  $T_k = k\pi\sqrt{\ell m_C/g(m_L + m_C)}$ ,  $k = 1, 2, \dots$ . For  $T = T_1$ , two distinct eigenvalues of the continuous system coincide after transformation at  $z = -1$  in the discrete-time model. A good choice for  $T$  is  $T \leq T_1/4$ .

In the parameter-dependent case, the sampling interval must be chosen for the worst case  $T_1 = T_1^-$ , i.e.

$$T \leq \frac{\pi}{4} \sqrt{\frac{\ell^-}{g(1 + m_L^+ / m_C^-)}}. \quad (11.2.1)$$

If we let the minimum rope length  $\ell^-$  go to zero then also  $T$  goes to zero. Therefore, it is necessary to specify positive values for  $\ell^-$  and  $m_C^-$  in order to obtain a non-zero  $T$ .  $\square$

*Remark 11.3*

From a practical point of view, one may want to fix the sampling interval  $T$  at an early stage of analysis and design. In the case of uncertain parameters, the usual rules for choosing  $T$  apply to the operating condition  $\mathbf{q}^*$  with the fastest plant dynamics or largest bandwidth. Alternatively,  $T$  may be treated as an additional undetermined parameter in robustness analysis.  $T$  is not an additional parameter if the system is *scalable* [20]. Roughly speaking, a system with uncertain parameters  $\mathbf{q}$  is scalable if there is a rescaling of  $\mathbf{q}$  that changes only the timescale of all solutions to the differential equations describing the plant. It is then possible to introduce new parameters in a vector  $\mathbf{r} = \mathbf{r}(\mathbf{q}, T)$ , where  $\mathbf{r}$  has the same dimension as  $\mathbf{q}$ . The number of uncertain parameters is not increased by allowing an uncertain  $T$ . Conceptually, scalability is important if we want to compare continuous and sampled systems by their respective stability regions in the same scaled parameter space, where for  $T \rightarrow 0$  identical bounds are obtained.  $\square$

The general discussion on controller structures remains valid for discrete-time controllers. There are, however, some additional considerations: discrete-time compensators for single-loop systems are assumed with the same numerator and denominator degree. A non-zero relative degree would introduce undesirable time delays into the

loop. In continuous-time systems, frequently a strictly proper controller transfer function is assumed in order to reduce high-frequency disturbances (e.g. measurement noise, high-frequency model uncertainty). In a sampled-data system, the same effect can be achieved by an analog anti-aliasing filter before the sampler. This is a low-pass filter with a bandwidth  $\omega_B$  of, at most, half the sampling frequency, i.e.  $\omega_B \leq 2\pi/T$ .

The problem classes of parametric polynomials (interval, affine, multilinear, polynomial) must be augmented by polynomials with an even more complicated *exponential* parameter dependence. Such polynomials must be tested for Schur-stability, i.e. all their roots must be located inside the unit circle in the  $z$ -plane.

#### *Example 11.4*

Consider the sampled-data feedback loop of Figure 11.1 with  $g_s(s, q)$  as in (11.1.10) and a proportional controller  $c_z(z) = k$ . The closed-loop characteristic polynomial is

$$\begin{aligned} p(z, q, k) &= a_0 + a_1 z + a_2 z^2, \\ a_0 &= q e^{-qT} + k(1 - q T e^{-qT} - e^{-qT}), \\ a_1 &= -q(1 + e^{-qT}) - k(1 - q T - e^{-qT}), \\ a_2 &= q. \end{aligned} \tag{11.2.2}$$

The coefficient functions are exponential for the uncertain plant parameter  $q$ , they are affine for the controller parameter  $k$ .  $\square$

## 11.3 Eigenvalue Specifications

The open-loop eigenvalue locations of sampled-data systems depend on the sampling interval. An extreme case is obtained with  $T \rightarrow 0$  and all eigenvalues  $z_i = e^{s_i T}$  approaching  $z = 1$ . Practically,  $T$  is chosen such that the eigenvalues are in some neighborhood of  $z = 1$ . In [4], a rule of thumb is given:  $T$  should be chosen such that all open-loop eigenvalues are located in a unit circle centered at  $z = \sqrt{2}$ .

For closed-loop stability, these eigenvalues must be shifted inside the unit circle. The eigenvalue locations  $s_i$  recommended in Chapter 3 may be directly mapped into the  $z$ -plane via  $z_i = e^{s_i T}$ . The type of discrete-time solutions is quite similar to the corresponding continuous-time solutions as long as  $\operatorname{Re} z_i > 0$ . The mapping of lines of constant damping and constant natural frequency from the  $s$ -plane to the  $z$ -plane is illustrated by Figure 11.2.

A special feature of sampled-data systems is the existence of deadbeat solutions. They are achieved with all eigenvalues located at  $z = 0$ . Practically, this requires relatively long sampling intervals  $T$  in order to avoid excessive magnitudes of the plant inputs  $u$ . Deadbeat control is an ideal case achievable with finite controller gains. We can come close, the ideal case by shifting the eigenvalues close to the origin.

Another special case in sampled-data systems occurs for an eigenvalue at  $z = -1$ . The corresponding solution term at the plant input is shown in Figure 11.3. Consider

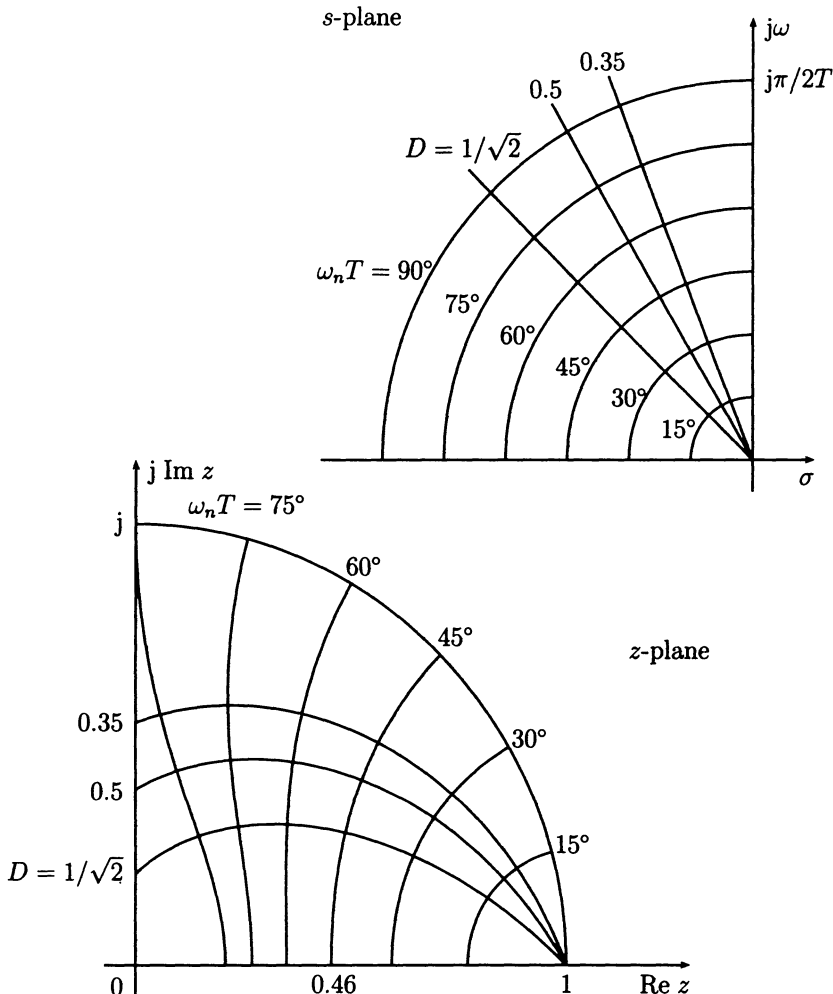


Figure 11.2. Mapping of constant damping ( $D$ ) lines and constant natural frequency ( $\omega_n$ ) lines from the *s*-plane to the plane  $z = e^{sT}$

the situation for a sampling interval  $T$  that is long compared to the settling time of the plant step response. Then, the response has approximately reached its stationary value before the next sampling occurs, and the plant response to the input signal shown in Figure 11.3 consists of consecutive full length step responses. This type of solution and its neighborhood is obviously very undesirable. It is an indication either of a too-long sampling interval compared to the plant dynamics, or of a bad design that has placed closed-loop eigenvalues too close to  $z = -1$ . Closed-loop poles on the negative real axis at  $z_i \in (-1; 0)$  give rise to decaying solution terms with alternating sign of  $u(iT)$ . Such excessive actuator activity is inefficient and should be avoided.

In later sections, we will formally treat the real root stability boundaries at  $z = 1$

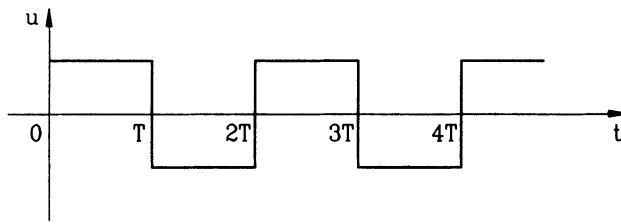


Figure 11.3. Solution term corresponding to an eigenvalue at  $z = -1$

and  $z = -1$ . We should keep in mind that a good practical solution cannot be close to the  $z = -1$  boundary. Closeness to the  $z = 1$  boundary may be tolerable if the sampling interval  $T$  is short. For example, an eigenvalue at  $z = 0.98$  yields a solution term 0.98<sup>t</sup> that decays only by 2% from sampling instant to sampling instant. For small  $T$ , this may be a rapid exponential decay in real time  $t$ .

We will now move towards a definition of a useful  $\Gamma$ -stability region in the  $z$ -plane that takes into account the above discussion and is also computationally tractable. Consider the  $\Gamma$ -stability regions shown in Figure 11.4.

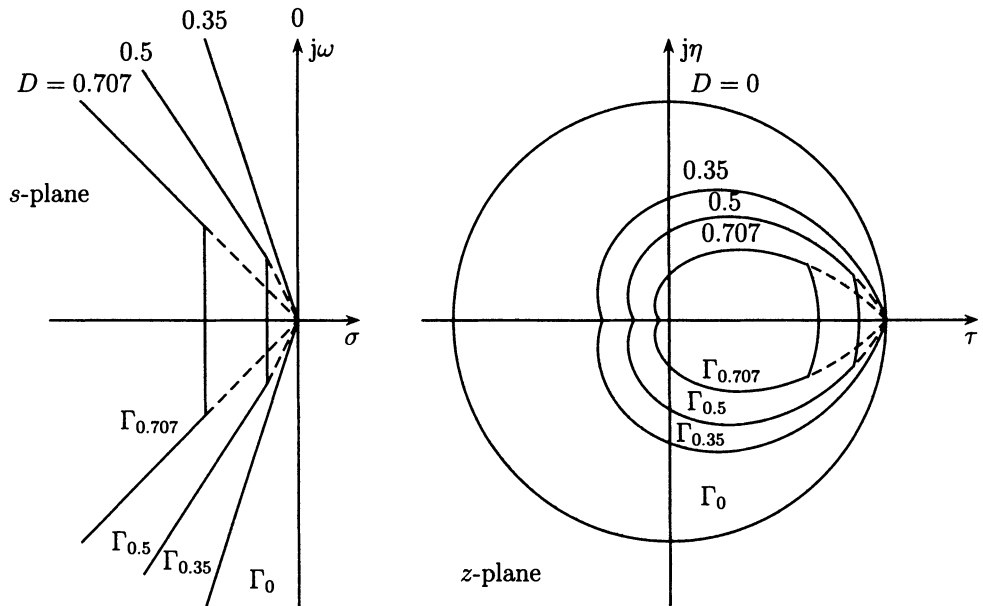


Figure 11.4. Mapping of  $\Gamma$ -stability regions from  $s$ -plane to  $z$ -plane

Constant damping lines in the  $s$ -plane map into logarithmic spirals in the  $z$ -plane, constant real part lines in the  $s$ -plane map into circles centered at  $z = 0$ . Three

examples with increasing damping (0.35, 0.5, 0.707) and decreasing real part boundary are mapped via  $z = e^{sT}$  into the corresponding boundaries in the  $z$ -plane.

In the  $s$ -plane, we have smoothed the piecewise defined boundary by a hyperbola, see Figure 3.8, because a hyperbola is reasonably well tractable as a  $\Gamma$ -stability boundary. In the  $z$ -plane, we may smooth the image by an even simpler boundary that is a circle. Let  $z = \tau + j\eta$  and consider a circle

$$(\tau - \tau_0)^2 + \eta^2 = r^2 \quad (11.3.1)$$

The circle has center  $\tau_0$  and radius  $r$ . Now let

$$\tau_0 = \begin{cases} r & \text{for } 0 \leq r \leq 0.5, \\ 1 - r & \text{for } 0.5 \leq r \leq 1, \\ 0 & \text{for } 1 \leq r. \end{cases} \quad (11.3.2)$$

Figure 11.5 shows some circles for  $r = 1, 0.8, 0.6, 0.5, 0.44, 0.33$ . Given that we are

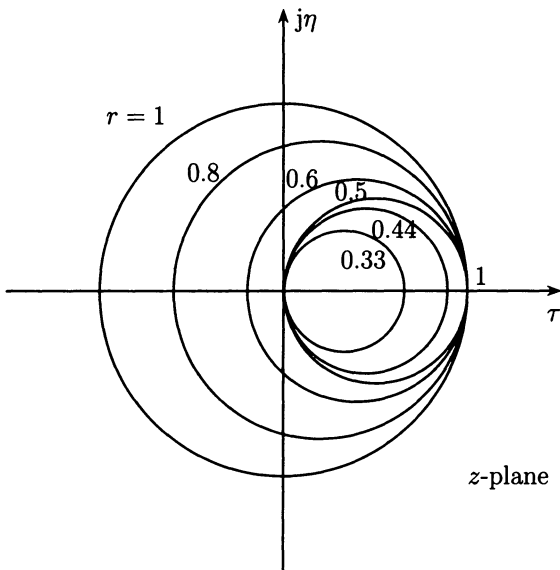


Figure 11.5. Approximation of  $\Gamma$ -stability regions of Figure 10.4 by circles

talking about a rule of thumb, the  $\Gamma$ -stability regions are reasonably well approximated with the following correspondence:

$D$	$r$	$\tau_0$
0	1	0
0.35	0.5	0.5
0.5	0.44	0.44
0.707	0.33	0.33

Conceptually, a design process may be viewed as follows. By choice of the sampling interval  $T$ , the open-loop eigenvalues are located in a unit circle centered at  $\sqrt{2}$ . Thus, a circle with radius  $r = 1 + \sqrt{2} \approx 2.4$  includes these eigenvalues for all operating conditions  $\mathbf{q} \in Q$ . The open loop is ( $r = 2.4$ )-stable. In the design process, we move away from the open loop  $\mathbf{k} = \mathbf{0}$  in  $\mathbf{k}$ -space. The design direction should be such that  $r$  is reduced. For  $r = 1$ , Schur-stability is achieved, for  $r = 0.6$  a solution term  $(-0.2)^i$  is still admitted but no alternating terms that decay slower. For  $r = 0.5$ , all alternating terms are ruled out but the deadbeat solution is still admitted. A further improvement in the degree of stability is now achieved by pushing eigenvalues in the right half  $z$ -plane closer to the origin. The ideal deadbeat solution cannot be achieved simultaneously for a plant family, but it is a well-posed question to ask for the smallest radius  $r_{min}$  that can be achieved simultaneously by a controller of fixed structure.

*Remark 11.5*

If a strict contraction is desired, then the relationship between  $\tau_0$  and  $r$  may be changed to

$$\tau_0(1 - \tau_0) = \alpha r(1 - r), \quad (11.3.3)$$

with  $\alpha < 1$  instead of  $\alpha = 1$  in (11.3.2).  $\square$

## 11.4 Classical Stability Tests

The approaches for testing Hurwitz-stability of a polynomial family can easily be modified for testing Schur-stability of polynomial families:

$$P(z, \mathbf{q}) = \{ p(z, \mathbf{q}) = \sum_{i=0}^n a_i(\mathbf{q}) z^i \mid \mathbf{q} \in Q \}. \quad (11.4.1)$$

The root set calculation by gridding all parameter intervals is the same as for continuous time, only the interpretation is different because we are now interested in the root location relative to the unit circle. If we rely on a gridding approach for robustness analysis, then also the discretization (11.1.3) may be performed numerically on a  $\mathbf{q}$ -grid.

### Boundary Crossing

The boundary crossing idea for discrete-time systems was formulated by Jury and Pavlidis [117]. There are three boundaries:

- i) A real root boundary at  $z = 1$ , i.e.

$$p(1, \mathbf{q}) = 0. \quad (11.4.2)$$

ii) A real root boundary at  $z = -1$ , i.e.

$$p(-1, \mathbf{q}) = 0. \quad (11.4.3)$$

iii) A complex root boundary for a root on the upper half of the unit circle, i.e.

$$p(e^{j\omega T}, \mathbf{q}) = 0, \quad \omega T \in [0; \pi]. \quad (11.4.4)$$

The polynomial with real coefficients then also has a symmetric root on the lower half of the unit circle.

### Algebraic Problem Formulation

The algebraic problem formulation corresponding to Theorem 2.1 (Frazer, Duncan) is:

### Theorem 11.6 (Jury, Pavlidis)

The polynomial family  $P(z, Q) = \{ p(z, \mathbf{q}) \mid \mathbf{q} \in Q \}$  with  $p(z, \mathbf{q})$  continuous is Schur-stable, if and only if:

- i. There exists a  $\mathbf{q}^0 \in Q$  such that the polynomial  $p_0(z) = p(z, \mathbf{q}_0)$  is Schur-stable.
- ii.  $p(1, \mathbf{q}) \neq 0$ , for all  $\mathbf{q} \in Q$ .
- iii.  $p(-1, \mathbf{q}) \neq 0$ , for all  $\mathbf{q} \in Q$ .
- iv.  $\det \mathbf{S}(\mathbf{q}) \neq 0$ , for all  $\mathbf{q} \in Q$ , where  $\mathbf{S}(\mathbf{q}) = \mathbf{X}(\mathbf{q}) - \mathbf{Y}(\mathbf{q})$  and (omitting the dependency on  $\mathbf{q}$ )

$$\mathbf{X} = \begin{bmatrix} a_n & a_{n-1} & a_{n-2} & \cdots & a_2 \\ 0 & a_n & a_{n-1} & \cdots & a_3 \\ 0 & 0 & a_n & \cdots & a_4 \\ \vdots & \vdots & \vdots & & \vdots \\ 0 & 0 & 0 & \cdots & a_n \end{bmatrix}, \quad \mathbf{Y} = \begin{bmatrix} 0 & 0 & 0 & \cdots & a_0 \\ \vdots & \vdots & \vdots & & \vdots \\ 0 & 0 & a_0 & \cdots & a_{n-4} \\ 0 & a_0 & a_1 & \cdots & a_{n-3} \\ a_0 & a_1 & a_2 & \cdots & a_{n-2} \end{bmatrix}. \quad (11.4.5)$$

□

### Proof

In [117], the following counterpart to Orlando's formula was shown,

$$\det \mathbf{S} = a_n^{n-1} \prod_{i=1}^{n-1} \prod_{k=i+1}^n (1 - z_i z_k), \quad (11.4.6)$$

where  $z_i, z_k$  are roots of  $p(z)$ . Consider now a continuous variation of  $\mathbf{q}$  starting with  $\mathbf{q}^0$ , i.e. a stable polynomial. If a conjugate pair of roots  $z_i, z_k$  crosses the unit circle, then  $1 - z_i z_k = 0$  and  $\det \mathbf{S} = 0$ . The only other possibilities for the polynomial to become unstable are that a real root crosses the unit circle at  $z = 1$  (Condition 2) or  $z = -1$  (Condition 3). Then, Theorem 11.6 follows from the boundary crossing Theorem 4.1.

□

*Remark 11.7*

Complete tests for a polynomial to have all its roots inside the unit circle have been given by Schur [176], [177] and Cohn [67]. A simplified formulation for polynomials with real coefficients was given by Jury [116]. Since we always assume that we know a stable polynomial to start with and use the boundary crossing theorem, we do not need the complete set of algebraic inequalities. Here we only give the inequalities corresponding to Conditions 2, 3 and 4 of Theorem 11.6.

$$\begin{aligned} p(1) &> 0, \\ (-1)^n p(-1) &> 0, \\ \det S &> 0. \end{aligned} \quad (11.4.7)$$

□

*Example 11.8*

Consider the characteristic polynomial (11.2.2). Let  $T = 1$ ,  $Q = \{q, k \mid q \in [0.1; 2], k \in [0.1; 2]\}$ . Is this polynomial family Schur-stable?

$$\begin{aligned} p(z, q, k) &= a_0 + a_1 z + a_2 z^2, \\ a_0 &= qe^{-q} + k(1 - qe^{-q} - e^{-q}), \\ a_1 &= -q(1 + e^{-q}) - k(1 - q - e^{-q}), \\ a_2 &= q. \end{aligned}$$

- i. Let  $q = 1$ ,  $k = 1$ , then  $p_z(z, 1, 1) = (1 - e^{-1}) - z + z^2$  has roots inside the unit circle. The three stability boundaries are given by:
- ii.  $p(1, q, k) = kq(1 - e^{-q}) \neq 0$ .
- iii.  $p(-1, q, k) = 2q(1 + e^{-q}) + k[2(1 - e^{-q}) - q(1 + e^{-q})] \neq 0$ .
- iv.  $X = a_2$ ,  $Y = a_0$ ,  $S = a_2 - a_0 = q(1 - e^{-q}) - k(1 - qe^{-q} - e^{-q}) \neq 0$ .

Condition 2 yields the boundaries  $q = 0$  and  $k = 0$ , which are outside  $Q$ . Conditions 3 and 4 may be checked graphically by plotting the stability boundaries in the  $(q, k)$ -plane.

From Condition 3 follows the stability boundary at  $z = -1$ , with

$$k_{-1} = \frac{2q(1 + e^{-q})}{q(1 + e^{-q}) - 2(1 - e^{-q})}$$

From Condition 4 follows the complex root boundary at  $z = e^{j\omega T}$ , with

$$k_c = \frac{q(1 - e^{-q})}{1 - qe^{-q} - e^{-q}}, \quad \lim_{q \rightarrow 0} k_c = 2.$$

The stability boundaries  $k_{-1}$  and  $k_c$  are plotted in Figure 11.6 together with the boundaries  $k = 0$  and  $q = 0$  resulting from Condition 2. Figure 11.6 not only provides a test for the given  $Q$ -box, but the entire stable region is exhibited. For comparison, consider the continuous-time system (11.1.10) with feedback  $k$ . Its characteristic polynomial is  $qk + qs + s^2$ , it is stable for  $q > 0$ ,  $k > 0$ , i.e. in the entire first quadrant in Figure 11.6.

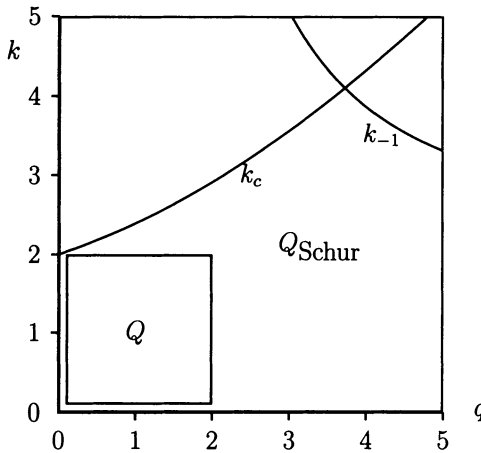


Figure 11.6. The stability boundaries do not intersect  $Q$ , and  $Q$  contains a stable point at  $q = 1, k = 1$ . Therefore, the polynomial family is robustly Schur-stable

The situation that sampling reduces stability regions is typical, however, it is possible to construct (somewhat exotic) examples for which sampling stabilizes [20]. Note that in the example the loop-gain  $k$  enters affinely into the characteristic polynomial. Therefore, it was easy to solve explicitly for the stability boundary  $k(q)$ . In general, it is not possible to test Conditions 3 and 4 of Theorem 11.6 without gridding  $q$ .  $\square$

An alternative algebraic formulation of stability criteria uses a bilinear transformation of the polynomial  $p(z)$  by

$$w := \frac{z-1}{z+1}, \quad z = \frac{1+w}{1-w}. \quad (11.4.8)$$

It maps the unit disk of the  $z$ -plane into the left half  $w$ -plane. Substituting  $z = (1+w)/(1-w)$  into  $p(z)$  of (11.4.1), a new polynomial  $p_w(w)$  is obtained as

$$\begin{aligned} p_w(w) &= (1-w)^n p\left(\frac{1+w}{1-w}\right) \\ &= \sum_{i=0}^n a_i (1+w)^i (1-w)^{n-i} \\ &= \sum_{i=0}^n b_i w^i. \end{aligned} \quad (11.4.9)$$

$p(z)$  is a Schur polynomial if and only if  $p_w(w)$  is a Hurwitz polynomial. Thus, results of Chapter 2 can be adapted to the discrete-time case. Of course, an exponential

dependency of  $a_i(\mathbf{q})$  is inherited by  $b_i(\mathbf{q})$  and the robustness analysis in terms of physical plant parameters  $\mathbf{q}$  remains a difficult problem.

*Remark 11.9*

In addition to, the two cases of  $a_i$ -intervals of  $p(z)$  and  $b_i$ -intervals of  $p_w(w)$  there is a further alternative by the  $\delta$ -transform [144], where

$$\delta = \frac{z - 1}{T}.$$

The transformed polynomial is

$$p_\delta(\delta) = p(\delta T + 1) = \sum_{i=0}^n a_i(\delta T + 1)^i = \sum_{i=0}^n c_i \delta^i.$$

The polynomial  $p(z)$  is Schur-stable if and only if  $p_\delta(\delta)$  has all its roots inside a circle centered at  $\delta = -1/T$  and passing through  $\delta = 0$ .  $\square$

*Example 11.10*

Consider again Example 11.8. The transformed polynomial is

$$\begin{aligned} p_w(w, q, k) &= b_0 + b_1 w + b_2 w^2, \\ b_0 &= a_0 + a_1 + a_2 = kq(1 - e^{-q}), \\ b_1 &= 2(a_2 + a_0) = 2[q(1 - e^{-q}) - k(1 - qe^{-q} - e^{-q})], \\ b_2 &= a_0 - a_1 + a_2 = 2q(1 + e^{-q}) + k[2(1 - e^{-q}) - q(1 + e^{-q})]. \end{aligned}$$

The boundaries for Hurwitz-stability, i.e.  $b_0 = 0, b_1 = 0, b_2 = 0$  are identical to the Schur-stability boundaries of Example 11.8 with the result plotted in Figure 11.6.  $\square$

The correspondence between the critical stability conditions of  $p(z, \mathbf{q})$  and  $p_w(w, \mathbf{q})$  is the following:

$$\begin{aligned} p(1, \mathbf{q}) &= 0 \iff b_0(\mathbf{q}) = 0, \\ p(-1, \mathbf{q}) &= 0 \iff b_n(\mathbf{q}) = 0, \\ \det \mathbf{S}(\mathbf{q}) &= 0 \iff \det \mathbf{H}_{n-1}(\mathbf{q}) = 0. \end{aligned} \tag{11.4.10}$$

The bilinear transformation also provides a set of relatively simple necessary stability conditions:

$$b_i(\mathbf{q}) > 0, \quad i = 0, 1, \dots, n. \tag{11.4.11}$$

The necessary condition (11.4.11), interpreted in terms of the original coefficients  $a_i$ , is closely related to the following result on the convex hull of the stable region in coefficient space [84].

*Theorem 11.11 (Fam, Meditch )*

Consider the stability region of

$$p(z) = a_0 + a_1 z + \dots + a_{n-1} z^{n-1} + z^n \quad (11.4.12)$$

in the space of coefficients  $a_0, a_1, \dots, a_{n-1}$ . Its convex hull is a polytope with  $n+1$  vertices corresponding to the polynomials

$$p_i(z) = (z+1)^i(z-1)^{n-i}, \quad i = 0, 1, \dots, n \quad (11.4.13)$$

□

It was shown in [4] that the above convex hull is formed by hyperplanes representing the necessary stability conditions  $b_i(a_0, a_1, \dots, a_{n-1}) > 0$ ,  $i = 0, 1, \dots, n$ .

*Example 11.12*

Necessary conditions for Schur-stability of a given polynomial are

$$p(z) = a_0 + a_1 z + a_2 z^2 + a_3 z^3 + z^4.$$

The corresponding vertex polynomials are

$$\begin{aligned} p_0 &= (1-w)^4 = 1 - 4w + 6w^2 - 4w^3 + w^4, \\ p_1 &= (1-w)^3(1+w) = 1 - 2w + 2w^3 - w^4, \\ p_2 &= (1-w)^2(1+w)^2 = 1 - 2w^2 + w^4, \\ p_3 &= (1-w)(1+w)^3 = 1 + 2w - 2w^3 - w^4, \\ p_4 &= (1+w)^4 = 1 + 4w + 6w^2 + 4w^3 + w^4. \end{aligned}$$

The transformed polynomial is

$$p_w(w) = \sum_{i=0}^4 a_i p_i(w) = \sum_{i=0}^4 b_i w^i.$$

Necessary conditions for Schur-stability of  $p(z)$  are

$$\begin{aligned} b_0 &= a_0 + a_1 + a_2 + a_3 + 1 > 0, \\ b_1 &= 2(-2a_0 - a_1 - a_3 + 2) > 0, \\ b_2 &= 2(3a_0 - a_2 + 3) > 0, \\ b_3 &= 2(-2a_0 + a_1 - a_3 + 2) > 0, \\ b_4 &= a_0 - a_1 + a_2 - a_3 + 1 > 0. \end{aligned}$$

These five linear inequalities correspond to five three-dimensional hyperplanes in the four-dimensional space with coordinates  $a_0, a_1, a_2, a_3$ . The hyperplanes form the convex hull of the stability region.

The five inequalities can be combined as

$$|a_1 + a_3| - (1 + a_0) < a_2 < 3(1 + a_0),$$

$$|a_1 - a_3| < 2(1 - a_0).$$

□

Necessary stability conditions have only limited value in robustness analysis, because we have to be pessimistic in analysis. For design, however, ( $\mathbf{q}$  replaced by the undetermined controller coefficients  $\mathbf{k}$ ), necessary stability conditions are useful because they yield a finite region in  $\mathbf{k}$ -space where possible solutions must be located.

#### Frequency Domain Problem Formulation

In frequency domain problem formulations, we have to substitute  $s = j\omega$ , i.e.  $z = e^{j\omega T}$ . Then, an initially stable polynomial  $p(z, \mathbf{q})$  will become unstable by variation of  $\mathbf{q}$  whenever we have simultaneously

$$\begin{aligned} \operatorname{Re} p(e^{j\omega T}, \mathbf{q}) &= 0, \\ \operatorname{Im} p(e^{j\omega T}, \mathbf{q}) &= 0 \end{aligned} \quad (11.4.14)$$

for some  $\omega T \in [0; \pi]$ . For  $\omega T = 0$  or  $\omega T = \pi$ , the second condition of (11.4.14) is always satisfied and there remains only the first condition  $p(1, \mathbf{q}) = 0$  or  $p(-1, \mathbf{q}) = 0$ .

#### Parameter Space Approach

In the parameter space approach for two uncertain parameters  $\mathbf{q} = [q_1 \ q_2]$ , we try to eliminate  $q_1$  or  $q_2$  from the two equations (11.4.14). This was possible up to polynomial coefficient functions as shown in Chapter 4. This approach is no more feasible if  $q_1$  and  $q_2$  enter exponentially.

The parameter space approach will be used as a design tool in  $\mathbf{k}$ -space. For single-input plants, the controller can always be assumed in a form such that the undetermined controller parameters in  $\mathbf{k}$  enter affinely into the coefficients of  $p(z, \mathbf{k})$ . In the multi-input case, the controller structure can be assumed such that the coefficient functions are multilinear. For such design considerations, it is useful to have some idea of the shape of stability regions in the space of coefficients  $a_i$ . We will treat the examples of polynomials with degree  $n = 2$  and  $n = 3$ .

#### Example 11.13

$$p(z) = a_0 + a_1 z + z^2$$

The polynomial is Schur-stable for  $a_0 = 0, a_1 = 0$ . Find the stable neighborhood of this point in the coefficient plane.

By (11.4.2) and (11.4.3), the real root boundaries result from

$$\begin{aligned} p(1) &= a_0 + a_1 + 1 = 0, \\ p(-1) &= a_0 - a_1 + 1 = 0. \end{aligned}$$

These two straight lines are plotted in the  $(a_1, a_2)$ -plane of Figure 11.7. By (11.4.4), the complex root boundary is

$$p(e^{j\omega T}) = a_0 + a_1 e^{j\omega T} + e^{j2\omega T}, \quad \omega T \in [0; \pi]$$

It is more convenient, however, to parameterize the unit circle in the plane  $z = \tau + j\eta$  by the real part  $\tau$  instead of the phase angle  $\omega T$ . On the unit circle,  $\tau$  and  $\eta$  are connected by  $\tau^2 + \eta^2 = 1$ ,  $\tau \in [-1; 1]$ , and a polynomial with a pair of conjugate roots on the unit circle has the form

$$(z - \tau - j\eta)(z - \tau + j\eta) = z^2 - 2\tau z + 1, \quad \tau \in [-1; 1].$$

By comparison with the second order polynomial, the complex root boundary is obtained as

$$a_0 = 1, \quad a_1 = -2\tau, \quad \tau \in [-1; 1].$$

This line segment  $c$  is also shown in Figure 11.7. Point 0 in Figure 11.7 is common to

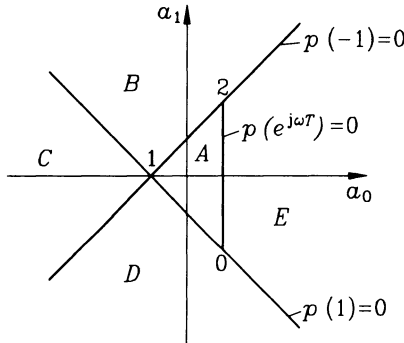


Figure 11.7. Partition of the polynomial coefficient plane for  $n = 2$

$p(e^{j\omega T}) = 0$  and  $p(1) = 0$ . A double root arises here for  $z = 1$ , i.e.

$$p_0(z) = (z - 1)^2 = z^2 - 2z + 1,$$

and correspondingly,

$$\begin{aligned} p_1(z) &= (z - 1)(z + 1) = z^2 - 1, \\ p_2(z) &= (z + 1)^2 = z^2 + 2z + 1. \end{aligned}$$

The two straight lines  $p(1) = 0$  and  $p(-1) = 0$ , and the complex root boundary  $p(e^{j\omega T}) = 0$  partition the coefficient plane into the following regions (EV = eigenvalue, UC = unit circle):

- A: Both EV's in the UC.
- B: One EV in the UC, one to the left.
- C: One EV to the left, one to the right of the UC.

D: One EV in the UC, one to the right.

E: Both EV's outside the UC, either as a complex pair or both to the left, or both to the right. (Note that these cases can be transferred into each other by continuous motion of the eigenvalues across the branching points of a root locus without crossing the unit circle.)

We are mainly interested in the stability region A, which is completely determined by the vertices of the triangle 012.  $\square$

#### *Example 11.14*

The polynomial

$$p(z) = a_0 + a_1 z + a_2 z^2 + z^3$$

has real root boundaries

$$\begin{aligned} p(1) &= a_0 + a_1 + a_2 + 1 = 0, \\ p(-1) &= a_0 - a_1 + a_2 - 1 = 0. \end{aligned}$$

In the space of coefficients  $a_0, a_1, a_2$  the linear equation  $p(1) = 0$  describes a plane; in Figure 11.8 it is the plane containing the points 0, 1 and 2. The plane  $p(-1) = 0$  contains the points 1, 2 and 3.

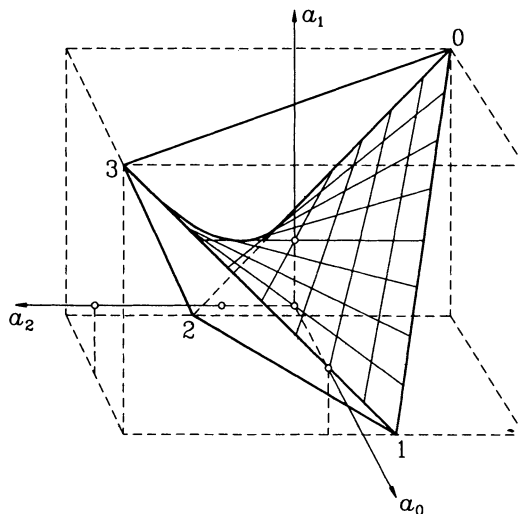


Figure 11.8. Stability region in the polynomial coefficient space for  $n = 3$

The polynomial  $p(z) = (z^2 - 2\tau z + 1)(z + r) = z^3 + (r - 2\tau)z^2 + (1 - 2r\tau)z + r$  has a conjugate pair of roots on the unit circle for an arbitrary real  $r$  and  $\tau \in [-1; 1]$ . Thus,

the complex root boundary is

$$\begin{aligned} a_0 &= r, \\ a_1 &= 1 - 2r\tau, \\ a_2 &= r - 2\tau. \end{aligned} \quad \tau \in [-1; 1],$$

The boundary is bilinear in  $r$  and  $\tau$ , i.e. for constant  $r$  it is a family of straight line segments beginning with  $\tau = -1$  on edge 23 and ending with  $\tau = 1$  on edge 01. For constant  $\tau \in [-1; 1]$  it is a family of straight lines through the edges 02 and 13. The relevant part of the stability boundary is the line segment for  $r \in [-1; 1]$ .

The corners of the stability region correspond to the four polynomials with zeros in  $\{-1, 1\}$ , i.e.

$$\begin{aligned} p_0(z) &= (z - 1)^3 &= -1 + 3z - 3z^2 + z^3, \\ p_1(z) &= (z + 1)(z - 1)^2 &= 1 - z - z^2 + z^3, \\ p_2(z) &= (z + 1)^2(z - 1) &= -1 - z + z^2 + z^3, \\ p_3(z) &= (z + 1)^3 &= 1 + 3z + 3z^2 + z^3. \end{aligned}$$

If the coefficients move along an edge from the corner  $i$  to the corner  $i + 1$ , then a real root migrates from  $z = 1$  to  $z = -1$  and the other roots remain at  $z = -1$  or  $z = 1$ . If the coefficients move along an edge from corner  $i$  to the corner  $i + 2$ , then a conjugate pair moves along the unit circle from  $z = 1$  to  $z = -1$  and the remaining real eigenvalue is located at  $z = 1$  or  $z = -1$ .

The complex boundary is the saddle surface visualized in Figure 11.8. It is a ruled surface that can easily be plotted by subdividing edge 02 and edge 13 into the same number of equal segments and connecting the corresponding points. The same procedure applies to edges 01 and 23. The stable region is the one that contains the origin, in Figure 11.8, below the saddle surface. Theorem 11.11 says for this example that the tetrahedron 0123 is the convex hull of the stability region.

We will refer to Figure 11.8 several times in order to visualize various concepts for the case  $n = 3$ .  $\square$

If the polynomial coefficients are functions of uncertain parameters  $\mathbf{q}$ , then the boundary representation Theorem 4.1 provides a systematic way of generating the equations for mapping stability boundaries into the space of parameters  $\mathbf{q}$ .

Let us apply Theorem 4.1 to the unit circle

$$\begin{bmatrix} d_0 & d_1 & d_2 & \dots & d_n \\ 0 & d_0 & d_1 & \dots & d_{n-1} \end{bmatrix} \mathbf{a}(\mathbf{q}) = \begin{bmatrix} 0 \\ 0 \end{bmatrix}. \quad (11.4.15)$$

This general expression may be simplified [23] for the unit circle parameterized by the real part of  $z = \tau + j\eta$ , i.e.  $\tau \in [-1; 1]$ ,  $\tau^2 + \eta^2 = 1$ . Then

$$\begin{aligned} d_0 &= 1, \\ d_1 &= 2\tau, \\ d_{i+1} &= 2\tau d_i - d_{i-1}, \quad i = 1, 2, \dots, n - 1. \end{aligned}$$

Premultiplying (11.4.15) by

$$s = \begin{bmatrix} 0 & 1 \\ -1 & 2\tau \end{bmatrix} \quad (11.4.16)$$

yields

$$\begin{bmatrix} 0 & d_0 & d_1 & d_2 & \dots & d_{n-1} \\ -d_0 & 0 & d_0 & d_1 & \dots & d_{n-2} \end{bmatrix} \mathbf{a}(\mathbf{q}) \stackrel{!}{=} \begin{bmatrix} 0 \\ 0 \end{bmatrix}. \quad (11.4.17)$$

The term  $d_n$  with the highest power of  $\tau$  has been removed. This reduction procedure may be continued  $n/2$  times for  $n$  even and  $(n+1)/2$  times for  $n$  odd. The resulting equations are for  $n$  even:

$$\begin{bmatrix} -d_{\frac{n}{2}-2} & \dots & -d_0 & 0 & d_0 & d_1 & \dots & d_{\frac{n}{2}} \\ -d_{\frac{n}{2}-1} & \dots & -d_1 & -d_0 & 0 & d_0 & \dots & d_{\frac{n}{2}-1} \end{bmatrix} \mathbf{a}(\mathbf{q}) = \begin{bmatrix} 0 \\ 0 \end{bmatrix}, \quad (11.4.18)$$

and for  $n$  odd:

$$\begin{bmatrix} -d_{\frac{n+1}{2}-2} & \dots & -d_0 & 0 & d_0 & d_1 & \dots & d_{\frac{n+1}{2}-1} \\ -d_{\frac{n+1}{2}-1} & \dots & -d_1 & -d_0 & 0 & d_0 & \dots & d_{\frac{n+1}{2}-2} \end{bmatrix} \mathbf{a}(\mathbf{q}) = \begin{bmatrix} 0 \\ 0 \end{bmatrix}. \quad (11.4.19)$$

In (11.4.18) and (11.4.19), the highest degree polynomials in  $\tau$  have been reduced to about half the degree arising in (11.4.15).

### Example 11.15

Let

$$\begin{aligned} p(z, q_1, q_2) = & (-0.825 + 0.225q_1 + 0.1q_2) + (0.895 + 0.025q_1 + 0.09q_2)z \\ & + (-2.475 + 0.675q_1 + 0.3q_2)z^2 + z^3. \end{aligned}$$

The real root boundaries  $p(1, q_1, q_2) = 0$  and  $p(-1, q_1, q_2) = 0$  yield two straight lines in the  $(q_1, q_2)$ -plane of Figure 11.9. The complex root boundary is described by

$$\begin{bmatrix} -d_0 & 0 & d_0 & d_1 \\ -d_1 & -d_0 & 0 & d_0 \end{bmatrix} \mathbf{a}(\mathbf{q}) = \begin{bmatrix} 0 \\ 0 \end{bmatrix},$$

$$\begin{bmatrix} -1 & 0 & 1 & 2\tau \\ -2\tau & -1 & 0 & 1 \end{bmatrix} \mathbf{a}(\mathbf{q}) = \begin{bmatrix} 0 \\ 0 \end{bmatrix}.$$

For the example

$$\mathbf{a}(\mathbf{q}) = \begin{bmatrix} a_0(\mathbf{q}) \\ a_1(\mathbf{q}) \\ a_2(\mathbf{q}) \\ 1 \end{bmatrix} = \begin{bmatrix} -0.825 \\ 0.895 \\ -2.475 \\ 1 \end{bmatrix} + \begin{bmatrix} 0.225 & 0.1 \\ 0.025 & 0.09 \\ 0.675 & 0.3 \\ 0 & 0 \end{bmatrix} \begin{bmatrix} q_1 \\ q_2 \end{bmatrix},$$

the resulting equations

$$\begin{bmatrix} -1.65 + 2\tau \\ 0.105 + 1.65\tau \end{bmatrix} + \begin{bmatrix} 0.45 & 0.2 \\ -0.025 - 0.45\tau & -0.09 - 0.2\tau \end{bmatrix} \begin{bmatrix} q_1 \\ q_2 \end{bmatrix} = \begin{bmatrix} 0 \\ 0 \end{bmatrix}$$

can be solved for

$$\begin{bmatrix} q_1 \\ q_2 \end{bmatrix} = \begin{bmatrix} 3.592 \\ 0.169 \end{bmatrix} + \begin{bmatrix} -5.070 \\ 1.408 \end{bmatrix} \tau + \begin{bmatrix} -11.268 \\ 25.352 \end{bmatrix} \tau^2, \quad \tau \in [-1; 1].$$

The complex boundary is also plotted in Figure 11.9. This figure is a cross-section through an affine image of the stability region of Figure 11.8.  $\square$

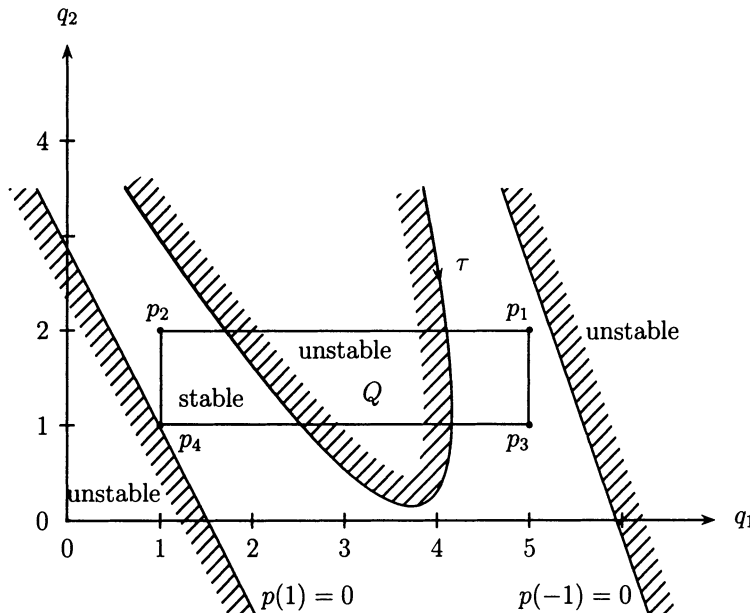


Figure 11.9. The vertices of the operating domain  $Q$  are stable, but  $Q$  is not robustly stable

For  $n \geq 4$ , we cannot visualize the stability region but some conclusions are obvious:

- i. The stability region is finite and simply connected. It is contractable to the origin of the coefficient space corresponding to the polynomial  $p(z) = z^n$ .
- ii. The stability region is bounded by two hyperplanes corresponding to  $p(1) = 0$  and  $p(-1) = 0$  and by a complex root boundary surface.
- iii. The stability region for  $n \geq 3$  is non-convex.
- iv. The convex hull of the stability region is a polytope whose vertices correspond to the  $n + 1$  polynomials

$$p_i(z) = (z + 1)^i(z - 1)^{n-i}, \quad i = 0, 1, \dots, n;$$

see Theorem 11.11.

- v. The edges with a vertex number difference of 1 or 2 are part of the stability boundary. Edges with a vertex number difference  $m > 2$  are outside of the stability region. A motion along these edges corresponds to a motion of a complex conjugate root pair along the root locus of  $(z - 1)^m + K(z + 1)^m = 0$ , which consists of circles passing through  $z = 1$  and  $z = -1$  whose tangents intersect at  $180^\circ/m$ .

*Remark 11.16*

A sufficient stability condition is due to Cohn [67]. The polynomial

$$p(z) = a_0 + a_1 z + \dots + a_{n-1} z^{n-1} + z^n$$

is stable if

$$\sum_{i=0}^{n-1} |a_i| < 1. \quad (11.4.20)$$

For  $n = 3$ , this is the octahedron shown in Figure 11.10. The point  $A$  with coordinates

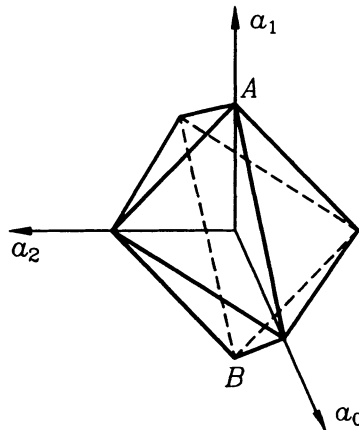


Figure 11.10. Sufficient stability condition  $|a_0| + |a_1| + |a_2| < 1$  for  $n = 3$

$[0 \ 1 \ 0]$  is the saddle point, see Figure 11.8. The point  $B$  with coordinates  $[0 \ -1 \ 0]$  is the center of edge 12 of Figure 11.8. The illustration for  $n = 3$  shows the conservativeness of the sufficient condition.  $\square$

## 11.5 Edge Test

The proof of the edge theorem [43] applies to the unit circle as well. Thus, the crucial condition is that the polynomial coefficients depend affinely on the uncertain parameters  $\mathbf{q}$ . For this case, it suffices to check the edges of the  $Q$ -box. If this testing set is Schur-stable, then the entire  $Q$ -box is Schur-stable.

The following Schur-stability test for a single edge was given in [14].

*Theorem 11.17 (Ackermann, Barmish)*

Let  $\mathbf{S}_b$  and  $\mathbf{S}_c$  be the stability testing matrices (11.4.5) of two polynomials

$$\begin{aligned} p_b(z) &= b_0 + b_1 z + \dots + b_n z^n, \\ p_c(z) &= c_0 + c_1 z + \dots + c_n z^n, \end{aligned}$$

respectively. The convex combination of the two polynomials

$$p(z, q) = (1 - q)p_b(z) + qp_c(z), \quad q \in [0; 1], \quad (11.5.1)$$

is Schur-stable, if and only if:

- i.  $p_b(z)$  is Schur-stable.
- ii.  $\text{sign } p_b(1) = \text{sign } p_c(1)$ .
- iii.  $\text{sign } p_b(-1) = \text{sign } p_c(-1)$ .
- iv. The matrix  $\mathbf{S}_b^{-1}\mathbf{S}_c$  has no non-positive real eigenvalues.

□

The proof follows closely the proof of Theorem 8.20.

### *Example 11.18*

Consider Example 11.15 with the uncertainty rectangle  $Q = \{\mathbf{q} \mid q_1 \in [1; 5], q_2 \in [1; 2]\}$ . Figure 11.9 shows the rectangle (and the stability boundaries).

The four extreme polynomials are

$$\begin{aligned} p_1(z) &= p(z, 5, 2), & p_3(z) &= p(z, 5, 1), \\ p_2(z) &= p(z, 1, 2), & p_4(z) &= p(z, 1, 1), \end{aligned}$$

and it is easily verified that their zeros are inside the unit circle. The four matrices  $\mathbf{S}_i = \mathbf{S}(p_i)$  are

$$\mathbf{S}_1 = \begin{bmatrix} 1 & 1 \\ -0.5 & -0.2 \end{bmatrix}, \quad \mathbf{S}_3 = \begin{bmatrix} 1 & 0.8 \\ -0.4 & -0.11 \end{bmatrix},$$

$$\mathbf{S}_2 = \begin{bmatrix} 1 & -0.8 \\ 0.4 & -0.1 \end{bmatrix}, \quad \mathbf{S}_4 = \begin{bmatrix} 1 & -1 \\ 0.5 & -0.01 \end{bmatrix},$$

Only two of the  $\mathbf{S}_i$  must be inverted to obtain  $\mathbf{S}_i\mathbf{S}_j^{-1}$  for the four edges.

- i. Edge  $p_1p_2$

$$\mathbf{S}_1\mathbf{S}_2^{-1} = \frac{1}{0.22} \begin{bmatrix} -0.5 & 1.8 \\ 0.13 & -0.6 \end{bmatrix}$$

with eigenvalues  $\lambda_1 = -0.289$  and  $\lambda_2 = -4.711$ .

ii. Edge  $p_4p_2$

$$\mathbf{S}_4 \mathbf{S}_2^{-1} = \frac{1}{0.22} \begin{bmatrix} 0.3 & -0.2 \\ -0.046 & -0.399 \end{bmatrix}$$

with eigenvalues  $\lambda_1 = 2.079$  and  $\lambda_2 = 1.098$ .

iii. Edge  $p_1p_3$

$$\mathbf{S}_1 \mathbf{S}_3^{-1} = \frac{1}{0.21} \begin{bmatrix} 0.29 & 0.2 \\ -0.025 & 0.2 \end{bmatrix}$$

with eigenvalues  $\lambda_{1,2} = 1.167 \pm j0.260$ .

iv. Edge  $p_4p_3$

$$\mathbf{S}_4 \mathbf{S}_3^{-1} = \frac{1}{0.21} \begin{bmatrix} -0.51 & -1.8 \\ -0.059 & -0.41 \end{bmatrix}$$

with eigenvalues  $\lambda_1 = -0.621$  and  $\lambda_2 = -3.760$ .

The edges  $p_4p_2$  and  $p_1p_3$  do not yield negative real eigenvalues, i.e. they are Schur-stable. Edges  $p_1p_2$  and  $p_4p_3$ , however, have negative real eigenvalues. Thus, the  $Q$ -box is not robustly Schur-stable.  $\square$

*Remark 11.19*

For small sampling intervals  $T$ , the control system of Figure 11.1 with  $c_z(z) = k$  behaves very similarly to its continuous-time counterpart without sample and hold element. Therefore, an interesting question is: if the continuous system has a characteristic polynomial with affine coefficient functions such that an edge result holds, then it can be conjectured that an edge result also holds for the sampled-data system with sufficiently small  $T$ . Indeed, this conjecture was proven in [112]. It is still an open question whether robust sampled-data stability for affine continuous plants can be deduced from edges.  $\square$

## 11.6 Construction of Value Sets

Presently, there are no results available on tree-structures in characteristic polynomials of sampled-data systems. In [112], an example with affine continuous plant is considered. The value set  $p(e^{j\omega T}, q)$  of the sampled system is bounded not only by images of the edges of  $Q$ , but also by images of interior points of  $Q$ . Thus, the construction of value sets for sampled-data systems is a difficult problem.

## 11.7 Real Radius of Stability

The problem of finding the real radius of stability of a sampled-data control system in the space of plant parameters is extremely difficult. For controller parameters entering affinely into the coefficients, the results of Chapters 10 can be used directly. Chapter 4 shows the modification for general  $\Gamma$ -stability regions, which can be applied for the unit circle by using the simplified boundary representations in (11.4.18) or (11.4.19).

## 11.8 Single-loop Feedback Structures

In Chapter 5, we have discussed the use of a Nyquist value set for continuous-time plants. The zero exclusion from the value set of the characteristic polynomial is thereby replaced by the exclusion of the critical point  $-1$  from the Nyquist value set. We will now translate this result to the discrete-time case.

Consider the single-loop sampled-data control system of Figure 11.1 with the open-loop frequency response

$$h_0(e^{j\omega T}, \mathbf{q}) = c_z(e^{j\omega T})h_z(e^{j\omega T}, \mathbf{q}). \quad (11.8.1)$$

The discrete-time frequency response has the following properties:

- i. It is periodic in  $\omega T$  with period  $2\pi$ .
- ii. It is symmetric with respect to the real axis, i.e.

$$\begin{aligned} \operatorname{Re} h_0(e^{j\omega T}, \mathbf{q}) &= \operatorname{Re} h_0(e^{-j\omega T}, \mathbf{q}), \\ \operatorname{Im} h_0(e^{j\omega T}, \mathbf{q}) &= -\operatorname{Im} h_0(e^{-j\omega T}, \mathbf{q}). \end{aligned} \quad (11.8.2)$$

- iii. For  $\omega T = \pi$ ,

$$h_0(e^{j2\pi}, \mathbf{q}) = h_0(-1, \mathbf{q}) \quad (11.8.3)$$

is real, i.e.

$$h_0(-1, \mathbf{q}) = -1 \quad (11.8.4)$$

yields the real root boundary for  $z = -1$ .

- iv.

$$h_z(1, \mathbf{q}) = g_s(0, \mathbf{q}) \quad (11.8.5)$$

(see [20]). Thus,

$$h_0(1, \mathbf{q}) = c_z(1)h_z(1, \mathbf{q}) = c_z(1)g_s(0, \mathbf{q}). \quad (11.8.6)$$

From 1. and 2., it follows that it suffices to sweep  $\omega T$  from zero to  $\pi$ .

The four conditions of Theorem 11.6 have their counterparts in terms of the open-loop frequency response as summarized in:

*Theorem 11.20*

A single-loop sampled-data feedback system with open-loop discrete frequency response  $h_0(e^{j\omega T}, \mathbf{q})$  is Schur-stable for all  $\mathbf{q} \in Q$ , if and only if:

- i. There exists a  $\mathbf{q}^0 \in Q$  such that the loop is Schur-stable.
- ii.  $h_0(1, \mathbf{q}) \neq -1$  for all  $\mathbf{q} \in Q$ .
- iii.  $h_0(-1, \mathbf{q}) \neq -1$  for all  $\mathbf{q} \in Q$ .
- iv.  $h_0(e^{j\omega T}, \mathbf{q}) \neq -1$  for all  $\mathbf{q} \in Q$ . and all  $\omega \in [0; \pi]$

□

Condition 1 is easily tested for an arbitrarily picked  $\mathbf{q}^0 \in Q$ . Condition 2 is relatively simple; in view of (11.8.5),  $\mathbf{q}$  does not enter exponentially. Conditions 3 and 4, however, contain exponential terms in  $\mathbf{q}$  and are therefore difficult to test unless we are willing to grid  $Q$ .

An alternate formulation of Conditions 3 and 4 is given by the Poisson sum form of the  $z$ -transfer function, see (11.1.9). For  $z = -1$ , i.e.  $\omega T = \pi$ , this sum may be simplified as follows:

$$\begin{aligned}
 h_z(-1, \mathbf{q}) &= 2 \sum_{m=-\infty}^{\infty} \frac{g_s[j(1+2m)\pi/T, \mathbf{q}]}{j(1+2m)\pi} \\
 &= 2 \sum_{m=0}^{\infty} \frac{g_s[j(1+2m)\pi/T, \mathbf{q}]}{j(1+2m)\pi} + 2 \sum_{i=0}^{\infty} \frac{g_s[-j(1+2i)\pi/T, \mathbf{q}]}{-j(1+2i)\pi} \\
 &= 2 \sum_{m=0}^{\infty} \left( \frac{g_s[j(1+2m)\pi/T, \mathbf{q}]}{j(1+2m)\pi} + \frac{g_s[-j(1+2m)\pi/T, \mathbf{q}]}{-j(1+2m)\pi} \right) \\
 &= 4 \sum_{m=0}^{\infty} \operatorname{Re} \frac{g_s[j(1+2m)\pi/T, \mathbf{q}]}{j(1+2m)\pi}.
 \end{aligned} \tag{11.8.7}$$

Thus, Theorem 11.20 may be reformulated in terms of the continuous-time transfer function  $g_s(s, \mathbf{q})$ .

*Theorem 11.21*

The single-loop sampled-data feedback system with continuous plant  $g_s(s, \mathbf{q})$ , sampler, hold and discrete compensator  $c_z(z)$  (see Figure 11.1) is stable for all  $\mathbf{q} \in Q$ , if and only if:

- i. There exists a  $\mathbf{q}^0 \in Q$  such that the loop is Schur-stable.
- ii.  $c_z(1)g_s(0, \mathbf{q}) \neq -1$  for all  $\mathbf{q} \in Q$ .
- iii.  $c_z(-1) 4 \sum_{m=0}^{\infty} \operatorname{Re} \frac{g_s[j(1+2m)\pi/T, \mathbf{q}]}{j(1+2m)\pi} \neq -1$  for all  $\mathbf{q} \in Q$ . (11.8.8)

iv. For all  $\mathbf{q} \in Q$  and all  $\omega \in [0; \pi]$ ,

$$c_z(e^{j\omega T})(1 - e^{j\omega T}) \sum_{m=-\infty}^{\infty} \frac{g_s(s + jm2\pi/T, \mathbf{q})}{sT + jm2\pi} \neq -1. \quad (11.8.9)$$

□

The advantage of the formulation of Theorem 11.21 is that for a proper plant  $g_s(s, \mathbf{q})$ , the infinite series can be calculated with any desired accuracy by a finite number of terms and  $\mathbf{q}$  enters into each term only with the same complexity as in the continuous-time case.

Many plants  $g_s(s)$  have a low-pass characteristic with relative degree larger than one. The convergence of the series (11.8.8) and (11.8.9) is enhanced by the  $1/s$  term from the hold element. In this case, the sum converges rapidly and the dominant effect of sampling is described by the term  $m = 0$ , i.e. for the

*real root boundary* at  $z = -1$ ,

$$h_z(-1, \mathbf{q}) \approx 4 \operatorname{Re} \frac{g_s(j\pi/T, \mathbf{q})}{j\pi}, \quad (11.8.10)$$

*complex root boundary* at  $z = e^{j\omega T}$ ,

$$h_z(e^{j\omega T}, \mathbf{q}) \approx \frac{1 - e^{-j\omega T}}{j\omega T} g_s(j\omega, \mathbf{q}). \quad (11.8.11)$$

Note that the factor  $(1 - e^{-j\omega T})/j\omega T$  is the frequency response of the hold element divided by  $T$ . It may also be written as

$$\begin{aligned} \frac{1 - e^{-j\omega T}}{j\omega T} &= \frac{e^{j\omega T/2} - e^{-j\omega T/2}}{j\omega T} \cdot e^{-j\omega T/2} \\ &= \frac{\sin \omega T/2}{\omega T/2} \cdot e^{-j\omega T/2}. \end{aligned} \quad (11.8.12)$$

For the calculation of the complex root boundary, the essential effect comes from the term  $e^{-j\omega T/2}$ , i.e. a phase lag equal to that of a dead time of half a sampling interval. The gain factor is one for  $\omega T = 0$  and decreases with increasing  $\omega T$ .

The approximation (11.8.11) is very good for small sampling intervals  $T$ , i.e. large frequency intervals  $2\pi/T$  at which values of the frequency response  $g_s(j\omega, \mathbf{q})/\omega$  are taken in the sum (11.8.9). With increasing  $T$ , the quality of approximation deteriorates. Then, however, at some sampling interval the type of oscillation illustrated by Figure 11.3 takes over, which is indicated by Condition (11.8.10). For such sampling intervals, the approximation is good, again because it includes a second term of (11.8.9).

### Example 11.22

Consider Example 11.1 with  $T = 1$  again. The approximate boundary equations are for  $z = -1$ :

$$4 \operatorname{Re} \frac{k}{(j\pi)^2(1 + j\pi/q)} = -1,$$

and for  $z = e^{j\omega T}$  from (11.1.12):

$$\frac{-(1 - e^{-j\omega})k}{(\omega + m2\pi)^2[1 + j(\omega + m2\pi)/q]} = -1.$$

The approximate boundaries (dotted) are shown in Figure 11.11; the exact boundaries (solid lines) are from Figure 11.6. The approximation is good for small  $q$ . Note that a variable  $T$  would appear in a term  $qT$ , thus, small  $q$  has an effect like small  $T$ . For larger  $q$ , the approximation of the complex root boundary  $k_c$  for  $z = e^{j\omega T}$  gets worse. A good approximation is then achieved for larger  $q$ , where the stability boundary  $k_{-1}$  for  $z = -1$  takes over.  $\square$

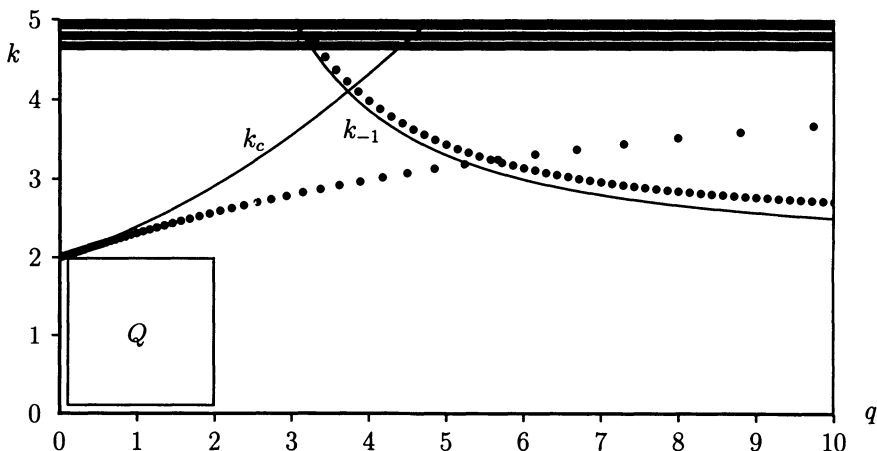


Figure 11.11. Approximation of Figure 10.6 by truncated Poisson series

### Example 11.23

For the automatic bus steering Example 4.20 and (6.10.13), the compensator

$$c(s) = 25^3 \frac{0.15s^2 + 0.7s + 0.6}{(s^2 + 25s + 25^2)(s + 25)}$$

was discretized by the Tustin approximation (11.0.1) with a sampling interval  $T = 10$  [ms], yielding

$$c_z(z) = 9.3464 \frac{(z - 0.988986)(z - 0.965028)(z + 1)}{(z - 0.7788)(z^2 - 1.7238z + 0.7788)}.$$

The resulting stability boundaries are shown in Figure 11.12. The solid line is the  $\Gamma$ -

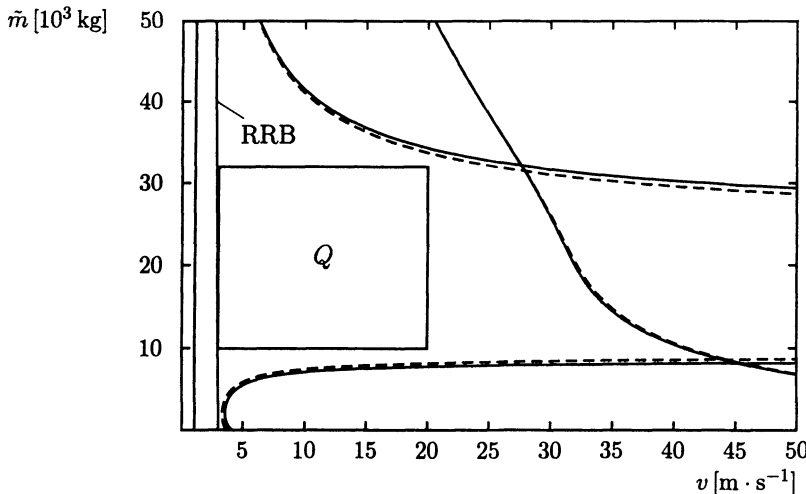


Figure 11.12. Continuous time (solid) and approximated discrete time (dashed)  $\Gamma$ -stability boundaries in the  $(v, \tilde{m})$ -plane

stability boundary  $\partial\Gamma = \{\sigma + j\omega \mid \omega^2 = 25\sigma^2 - 49/16, \sigma \leq -0.25\}$  for the continuous system. The dashed line is the approximated  $\Gamma$ -stability boundary for the system with discretized compensator  $c_z(z)$ . The accuracy of the approximation was tested by finding the roots of some polynomials on both sides nearby the approximate boundary. The agreement was excellent such that the dashed line is also the exact  $\Gamma$ -stability boundary for the discrete-time system. This effect is not surprising because the continuous-time plant has a relative degree three, i.e. the Poisson series converges like  $1/\omega^4$  and the sampling interval of  $T = 10$  [ms] used for the controller implementation is small for this plant. In this example, the  $\Gamma$ -stable region is not much reduced by the compensator discretization.  $\square$

## 11.9 Circle Stability

In Section 11.3, we have discussed eigenvalue specifications for sampled-data control systems. A conclusion was that circles centered on the real axis are useful regions of  $\Gamma$ -stability for sampled-data systems. In this section, we show how the results obtained for Schur-stability can be generalized to  $\Gamma$ -stability for a circle with real center  $\tau_0$  and radius  $r$ , see Figure 11.13.

*Definition 11.24*

We call a polynomial *circle stable* if all its roots are located in a circle with given real center and radius.  $\square$

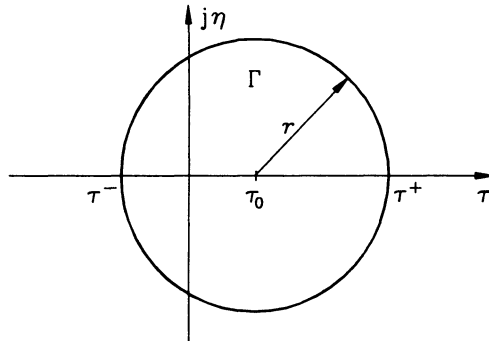


Figure 11.13. Circle stability

Circle stability is specified by two parameters, e.g. center  $\tau_0$  and radius  $r$ , or alternatively,

$$\begin{aligned}\tau^- &:= \tau_0 - r, \\ \tau^+ &:= \tau_0 + r.\end{aligned}\quad (11.9.1)$$

The circle of Figure 11.13 can be mapped onto the unit circle by an affine transformation

$$\tilde{z} := (z - \tau_0)/r, \quad z = r\tilde{z} + \tau_0. \quad (11.9.2)$$

Thus, a polynomial  $p(z) = a_0 + a_1z + \dots + a_nz^n$  is circle stable if and only if the polynomial

$$\begin{aligned}\tilde{p}(\tilde{z}) &= p(r\tilde{z} + \tau_0) \\ &= \sum_{i=0}^n a_i(r\tilde{z} + \tau_0)^i \\ &= \sum_{i=0}^n \tilde{a}_i \tilde{z}^i\end{aligned}\quad (11.9.3)$$

is Schur-stable.

The affine transformation (11.9.2) can be directly combined with the bilinear transformation (11.4.7)

$$w = \frac{\tilde{z} - 1}{\tilde{z} + 1} = \frac{z - \tau_0 - r}{z - \tau_0 + r}, \quad z = r \frac{1 + w}{1 - w} + \tau_0 \quad (11.9.4)$$

or, written in terms of the parameters  $\tau^-, \tau^+$ ,

$$w = \frac{z - \tau^+}{z - \tau^-}, \quad z = \frac{\tau^+ - \tau^- w}{1 - w}. \quad (11.9.5)$$

A polynomial  $p(z) = a_0 + a_1z + \dots + a_nz^n$  is circle stable if and only if the polynomial

$$\begin{aligned} p_w(w) &= (1-w)^n p\left(\frac{\tau^+ - \tau^- w}{1-w}\right) \\ &= \sum_{i=0}^n a_i (\tau^+ - \tau^- w)^i (1-w)^{n-i} \\ &= \sum_{i=0}^n b_i w^i \end{aligned} \quad (11.9.6)$$

is Hurwitz-stable.

Again, the necessary stability conditions  $b_i > 0$ ,  $i = 0, 1, \dots, n$  describe the convex hull of the stability region in the space of coefficients  $a_i$ .

### Example 11.25

The zeros of the polynomial  $p(z) = a_0 + a_1z + a_2z^2 + z^3$  should lie inside the circle with center  $\tau_0 = 0.4$  and radius  $r = 0.4$ , i.e.  $\tau^- = 0$ ,  $\tau^+ = 0.8$ .

$$\begin{aligned} p_w(w) &= \sum_{i=0}^3 a_i 0.8^i (1-w)^{3-i} = \sum_{i=0}^3 b_i w^i, \\ b_0 &= p(0.8) = a_0 + 0.8a_1 + 0.64a_2 + 0.512, \\ b_1 &= -(3a_0 + 1.6a_1 + 0.64a_2), \\ b_2 &= 3a_0 + 0.8a_1, \\ b_3 &= -a_0. \end{aligned} \quad (11.9.7)$$

The convex hull of the stability region is described by the inequalities  $b_i > 0$ ; the critical conditions contributing to the boundary of the stable region are  $b_0 > 0$ ,  $b_3 > 0$  and  $b_1 b_2 - b_0 b_3 > 0$ .  $\square$

The modified form of Theorem 11.11 can be shown by barycentric coordinates [4]. The result is:

### Theorem 11.26

Consider the circle stability region of

$$p(z) = a_0 + a_1z + \dots + a_{n-1}z^{n-1} + z^n \quad (11.9.8)$$

in the space of coefficients  $a_0, a_1, \dots, a_n$ . Its convex hull is a polytope with  $n+1$  vertices corresponding to the polynomials

$$p_i(z) = (z - \tau^-)^i (z - \tau^+)^{n-i}, \quad i = 0, 1, 2, \dots, n. \quad (11.9.9)$$

$\square$

A boundary representation (9.2.15) for frequency domain approaches is obtained by substitution of

$$\eta^2 + (\tau - \tau_0)^2 = r^2, \quad \text{i.e. } \eta^2 + \tau^2 = r^2 + 2\tau_0\tau - \tau_0^2 \quad (11.9.10)$$

into (9.2.16):

$$\begin{aligned} d_0 &= 1, \\ d_1 &= 2\tau, \\ d_{i+1} &= 2\tau d_i - (r^2 + 2\tau_0\tau - \tau_0^2) d_{i-1}, \end{aligned} \quad (11.9.11)$$

and (9.2.15) yields the boundary description.

### Example 11.27

Consider again Example 11.25 with  $\tau_0 = 0.4$ ,  $r = 0.4$ :

$$\begin{aligned} d_0 &= 1, \\ d_1 &= 2\tau, \\ d_2 &= 4\tau^2 - 0.8\tau, \\ d_3 &= 4\tau^3 - 3.2\tau^2. \end{aligned}$$

The coefficients  $a_i$  of a third degree polynomial with roots on the circle of radius  $r = 0.4$ , centered at  $\tau_0 = 0.4$ , satisfy

$$\begin{aligned} \begin{bmatrix} d_0 & d_1 & d_2 & d_3 \\ 0 & d_0 & d_1 & d_2 \end{bmatrix} \begin{bmatrix} a_0 \\ a_1 \\ a_2 \\ 1 \end{bmatrix} &= \begin{bmatrix} 0 \\ 0 \end{bmatrix}, \\ \begin{bmatrix} 1 & 2\tau & 4\tau^2 - 0.8\tau & 4\tau^3 - 3.2\tau^2 \\ 0 & 1 & 2\tau & 4\tau^2 - 0.8\tau \end{bmatrix} \begin{bmatrix} a_0 \\ a_1 \\ a_2 \\ 1 \end{bmatrix} &= \begin{bmatrix} 0 \\ 0 \end{bmatrix}, \quad \tau \in [0; 0.8]. \end{aligned}$$

The cubic term in  $\tau$  may be eliminated by a left multiplication of the above equations by

$$\begin{bmatrix} 1 & -\tau \\ 0 & 1 \end{bmatrix},$$

yielding

$$\begin{bmatrix} 1 & \tau & 2\tau^2 - 0.8\tau & -2.4\tau^2 \\ 0 & 1 & 2\tau & 4\tau^2 - 0.8\tau \end{bmatrix} \begin{bmatrix} a_0 \\ a_1 \\ a_2 \\ 1 \end{bmatrix} = \begin{bmatrix} 0 \\ 0 \end{bmatrix}.$$

□

# A Polynomials and Polynomial Equations

This appendix summarizes some results from classical algebra concerning univariate or multivariate polynomials. Only those properties of polynomials are mentioned that are important for understanding and applying the methods of robust control in this book. More details can be found in standard textbooks like [51] and [93].

## Introduction

The parameter space method [15] has as its basis the closed-loop characteristic polynomial  $p(s, \mathbf{q}, \mathbf{k})$ , where  $\mathbf{q}$  are the uncertain plant parameters, and  $\mathbf{k}$  are the controller parameters. The aim of the control design is to find the controller parameters  $\mathbf{k}$  such that the roots of the uncertain polynomial (the parameters  $\mathbf{q}$  vary in a given operating domain) are located in a prescribed region  $\Gamma$  of the  $s$ -plane. Fixing all but two parameters, the feasible region in the parameter plane is represented. The parameter space method can also be used in an analysis step. In this case, a test can be done in the plant parameter plane to determine if the entire operating domain is  $\Gamma$ -stable.

In both analysis and design, the basic equation is  $p(s, x, y) = 0$ , where  $x, y$  are parameters and  $s$  varies on the boundary  $\partial\Gamma$  of the region  $\Gamma$ . Substituting  $s = u(\alpha) + j v(\alpha) \in \partial\Gamma$  in the uncertain polynomial and separating into real and imaginary parts leads to the system of polynomial equations

$$\operatorname{Re} p(x, y, \alpha) = 0, \quad \operatorname{Im} p(x, y, \alpha) = 0, \quad (\text{A.1})$$

which has to be solved for varying  $\alpha$ . The solutions represent parameter combinations that lead to a polynomial with a root or a root pair on the boundary  $\partial\Gamma$ . So, after we have mapped the boundary  $\partial\Gamma$  into the parameter plane, the next step is to find the active boundaries that are the points (or boundaries) that contribute to the boundary of the  $\Gamma$ -stable area.

The complexity of the system of equations (A.1) depends on how the parameters appear in the characteristic polynomial. We distinguish three types of dependence with increasing complexity: affine, bilinear and polynomial dependence.

In the following, we discuss methods that can be used to solve the system (A.1) and related problems. To aid in this discussion, we first introduce some definitions and theorems from the theory of algebraic curves. We then present procedures for solving various systems like (A.1) and discuss the applications in which the procedures are useful. We demonstrate the methods presented using simple examples.

## Algebraic Curves

If  $f(x, y)$  is a bivariate polynomial in  $x, y$ :

$$f(x, y) = \sum_{i,j \geq 0}' a_{ij} x^i y^j \quad (\text{A.2})$$

(the prime denotes that the sum is finite) with real coefficients  $a_{ij}$ , then the set  $\{(x, y) \in \mathbb{R}^2 : f(x, y) = 0\}$  is called an *algebraic curve*. The *degree* of  $f$  is the highest sum of the exponents, and is equal to the number of common points with a straight line. We call

$$f(x, y) = 0 \quad (\text{A.3})$$

the *implicit* representation of the curve. Curves may have also an *explicit* representation

$$x = f(\alpha), \quad y = g(\alpha), \quad (\text{A.4})$$

where  $x(\alpha)$  and  $y(\alpha)$  are rational functions of the real parameter  $\alpha$ . Equivalent is the representation

$$x = \frac{n_1(\alpha)}{d_1(\alpha)}, \quad y = \frac{n_2(\alpha)}{d_2(\alpha)}, \quad (\text{A.5})$$

with  $n_i(\alpha), d_i(\alpha), i = 1, 2$ , polynomials in  $\alpha$ . These curves are called *rational* curves. Nyquist or Popov plots are trivial examples of rational curves. The root loci have, in general, no parametric representation.

## Elimination Theory. The Resultant

In this section, we follow the representation used in [121]. More details of the algebraic theory can be found in classical textbooks like [42], [54] or [194]. For the theory of curves, see [59].

Consider the two polynomials

$$\left. \begin{aligned} f(y) &= a_n y^n + a_{n-1} y^{n-1} + a_{n-2} y^{n-2} + \cdots + a_0 \\ g(y) &= b_m y^m + b_{m-1} y^{m-1} + b_{m-2} y^{m-2} + \cdots + b_0, \end{aligned} \right\}, \quad (\text{A.6})$$

( $a_n \neq 0, b_m \neq 0$ ), whose coefficients  $a_i, b_i$  are real numbers.

The theory of the resultant originates in the following:

### Problem

Give a necessary and sufficient condition on the coefficients of (A.6), such that  $f(y) = 0$  and  $g(y) = 0$  have a common root.  $\square$

### Theorem 1.1

$f$  and  $g$  have a common root, if and only if the determinant of the matrix  $\mathbf{R}$ , in (A.8) is zero.

$\square$

This determinant is called the *resultant*<sup>1</sup> of  $f$  and  $g$  with respect to  $y$ , i.e.

$$\text{Res}(f, g, y) = \det \mathbf{R}. \quad (\text{A.7})$$

Assume now that  $f$  and  $g$  have a common root, then the degree of the greatest common divisor of  $f$  and  $g$  ( $\gcd(f, g)$ ) is at least 1. For finding this greatest common divisor, an additional definition is given.

### Definition 1.2

The matrix  $\mathbf{R}_1$  of dimension  $m + n - 2$ , obtained by deleting the first and the last rows and the first and the last columns in the Matrix  $\mathbf{R}$ , is called *the first inner of  $\mathbf{R}$* . Continuing on the deletion process, we obtain the inners  $\mathbf{R}_2, \mathbf{R}_3, \dots$  of dimension  $m+n-4, m+n-6, \dots$  respectively. The determinants of inners are called *subresultants*.

□

### Example 1.3

For  $n = 4, m = 3$  we have the matrix  $\mathbf{R}$  and 3 inners:

$$\mathbf{R} = \begin{bmatrix} a_4 & a_3 & a_2 & a_1 & a_0 & 0 & 0 \\ 0 & a_4 & a_3 & a_2 & a_1 & a_0 & 0 \\ 0 & 0 & a_4 & a_3 & a_2 & a_1 & a_0 \\ 0 & 0 & 0 & b_3 & b_2 & b_1 & b_0 \\ 0 & 0 & b_3 & b_2 & b_1 & b_0 & 0 \\ 0 & b_3 & b_2 & b_1 & b_0 & 0 & 0 \\ b_3 & b_2 & b_1 & b_0 & 0 & 0 & 0 \end{bmatrix}, \quad (\text{A.8})$$

$$\mathbf{R}_1 = \begin{bmatrix} a_4 & a_3 & a_2 & a_1 & a_0 \\ 0 & a_4 & a_3 & a_2 & a_1 \\ 0 & 0 & b_3 & b_2 & b_1 \\ 0 & b_3 & b_2 & b_1 & b_0 \\ b_3 & b_2 & b_1 & b_0 & 0 \end{bmatrix},$$

$$\mathbf{R}_2 = \begin{bmatrix} a_4 & a_3 & a_2 \\ 0 & b_3 & b_2 \\ b_3 & b_2 & b_1 \end{bmatrix},$$

---

<sup>1</sup>In the literature the matrix is often defined in a slightly different manner, the rows of the  $b_i$  are exchanged, so only the sign of the resultant may change depending on the number of exchanges.

$$\mathbf{R}_3 = b_3.$$

□

*Theorem 1.4*

If  $\det \mathbf{R} = \det \mathbf{R}_1 = \dots = \det \mathbf{R}_{k-1} = 0$  and  $\det \mathbf{R}_k \neq 0$ , then the degree of  $\gcd(f, g)$  is  $k$ . In this case,  $\gcd(f, g)$  equals the determinant of the matrix obtained from  $\mathbf{R}_k$  by replacing the last column in it by the column

$$\begin{aligned} & [y^{m-k-1}f(y), y^{m-k-2}f(y), \dots, \\ & f(y), g(y), yg(y), \dots, y^{n-k-1}g(y)]'. \end{aligned} \quad (\text{A.9})$$

□

$$\left( \begin{array}{c} (\text{m rows}) \\ \mathbf{R} \\ (\text{n rows}) \end{array} \right) = \left[ \begin{array}{ccccccccc} a_n & a_{n-1} & a_{n-2} & \cdots & a_1 & a_0 & 0 & 0 & \cdots & 0 & 0 & 0 \\ 0 & a_n & a_{n-1} & \cdots & a_1 & a_0 & 0 & 0 & \cdots & 0 & 0 & 0 \\ \cdot & \cdots & \cdot & \cdot & \cdot \\ 0 & 0 & 0 & \cdot & \cdot & \cdot & \cdot & \cdot & \cdot & a_1 & a_0 & 0 \\ 0 & 0 & 0 & \cdot & \cdot & \cdot & \cdot & \cdot & \cdot & b_1 & b_0 & 0 \\ \cdot & \cdot \\ 0 & b_m & b_{m-1} & \cdots & b_1 & b_0 & 0 & 0 & \cdots & 0 & 0 & 0 \\ b_m & b_{m-1} & b_{m-2} & \cdots & b_1 & b_0 & 0 & 0 & \cdots & 0 & 0 & 0 \end{array} \right]. \quad (\text{A.10})$$

*Example 1.5*

Suppose in Example 1.3 that  $k = \deg(\gcd(f, g)) = 1$ , then

$$\gcd(f, g) = \det \begin{bmatrix} a_4 & a_3 & a_2 & a_1 & yf(y) \\ 0 & a_4 & a_3 & a_2 & f(y) \\ 0 & 0 & b_3 & b_2 & g(y) \\ 0 & b_3 & b_2 & b_1 & yg(y) \\ b_3 & b_2 & b_1 & b_0 & y^2g(y) \end{bmatrix}.$$

Using the fact that  $\gcd(f, g)$  is linear in  $y$ ,  $\gcd(f, g) = Ay + B$ , all quadratic and higher

terms in  $y$  must vanish so we can simplify the determinant:

$$\gcd(f, g) = \det \begin{bmatrix} a_4 & a_3 & a_2 & a_1 & a_0 y \\ 0 & a_4 & a_3 & a_2 & a_1 y + a_0 \\ 0 & 0 & b_3 & b_2 & b_1 y + b_0 \\ 0 & b_3 & b_2 & b_1 & b_0 y \\ b_3 & b_2 & b_1 & b_0 & 0 \end{bmatrix}.$$

Thus,  $\gcd(f, g) = Ay + B$ , where  $A = \det \mathbf{R}_1$  and

$$\mathbf{B} = \det \begin{bmatrix} a_4 & a_3 & a_2 & a_1 & 0 \\ 0 & a_4 & a_3 & a_2 & a_0 \\ 0 & 0 & b_3 & b_2 & b_0 \\ 0 & b_3 & b_2 & b_1 & 0 \\ b_3 & b_2 & b_1 & b_0 & 0 \end{bmatrix}.$$

For  $k = 1$  in Theorem 1.4 we have  $\square$

### Corollary

If  $f$  and  $g$  have a single common root  $y_s$  ( $\det \mathbf{R} = 0$ ,  $\det \mathbf{R}_1 \neq 0$ ), then

$$y_s = -\det \tilde{\mathbf{R}}_1 / \det \mathbf{R}_1, \quad (\text{A.11})$$

where  $\tilde{\mathbf{R}}_1$  equals the matrix obtained from  $\mathbf{R}_1$  by replacing the last column in it by the column  $\underbrace{[0, \dots, 0]}_{m-2}, a_0, b_0, \underbrace{[0, \dots, 0]}_{n-2}^T$ .  $\square$

### Application

Let  $p(s)$  be any real polynomial. If we set  $s = j\omega$ , we can write

$$\begin{aligned} p(j\omega) &= a_0 - a_2\omega^2 + a_4\omega^4 + \dots \\ &\quad + j\omega(a_1 - a_3\omega^2 + a_5\omega^4 \dots) \\ &= p_{\text{even}} + j\omega p_{\text{odd}}. \end{aligned}$$

Setting  $\Omega = \omega^2$ , we can rewrite these polynomials as

$$\begin{aligned} p_{\text{even}}(\Omega) &= a_0 - a_2\Omega + a_4\Omega^2 \dots, \\ p_{\text{odd}}(\Omega) &= a_1 - a_3\Omega + a_5\Omega^2 \dots. \end{aligned}$$

The resultant of the polynomials  $p_{\text{odd}}(\Omega)$  and  $p_{\text{even}}(\Omega)$  with respect to  $\Omega$  is the determinant of the well-known Hurwitz matrix. Apart from the sign of some entries,  $R$  is the Hurwitz matrix (1.6.2).

### Example 1.6

For  $n = 4$ , we have  $f = a_0 - a_2\Omega + a_4\Omega^2$  and  $g = a_1 - a_3\Omega$ , the matrix  $R$  is

$$R = \begin{bmatrix} a_4 & -a_2 & a_0 \\ 0 & -a_3 & a_1 \\ -a_3 & a_1 & 0 \end{bmatrix}.$$

□

### The Discriminant

A special case of the resultant is the *discriminant*  $D_f$ . The second polynomial  $g$  is the derivative of the first polynomial  $f$ , i.e.

$$D_f := \frac{1}{a_0} \text{Res}(f, f', y). \quad (\text{A.12})$$

Let  $y_i$ ,  $i = 1 \dots n$ , the roots of  $f(y) = 0$ . Another definition of the discriminant is

$$D_f = (-1)^{\frac{n(n-1)}{2}} a_0^{2n-2} \prod_{i=1}^n \prod_{k=1}^n (y_i - y_k)^2 \quad (i \neq k). \quad (\text{A.13})$$

### Theorem 1.7

The equation  $D_f = 0$  is a necessary and sufficient condition that  $f(y)$  has a root of multiplicity of at least 2.

□

### Application

The breakaway points (real) and saddle points (complex) of the root locus can be determined by computing the discriminant and finding the zeros.

### Example 1.8

Let  $p(s) = (s+2)(s+1)(s-1) + k = s^3 + 2s^2 - s - 2 + k$ , then  $p'(s) = 3s^2 + 4s - 1$  and

$$D_p = \det \begin{bmatrix} 1 & 2 & -1 & -2+k & 0 \\ 0 & 1 & 2 & -1 & -2+k \\ 0 & 0 & 3 & 4 & -1 \\ 0 & 3 & 4 & -1 & 0 \\ 3 & 4 & -1 & 0 & 0 \end{bmatrix}$$

$$= 27k^2 - 40k - 36 = 0.$$

The two solutions are  $k_{1,2} = (20 \pm 14\sqrt{7})/27$  and lead to a double root at  $s_{1,2} = (-2 \pm \sqrt{7})/3$ .

□

### Intersection Points of Algebraic Curves

Consider now a system of two polynomial equations

$$f(x, y) = 0, \quad g(x, y) = 0 \quad (\text{A.14})$$

with real coefficients. We assume that  $f$  and  $g$  have no common factor, and that both polynomials are irreducible over the rational numbers. Each equation can be seen as a curve. So the points  $(x, y)$  for which  $f(x, y) = 0$  and  $g(x, y) = 0$  are the intersection points of the two curves.

We can see  $f(x, y)$  and  $g(x, y)$  as polynomials in one of the variables, say  $y$ , where the coefficients  $a_i, b_i$  of (A.14) are now polynomials in  $x$ .

Using Theorem 1.1, the resultant is no longer a number but a polynomial in  $x$ . So we have eliminated the variable  $y$ . The first component  $x^*$  of the intersection point  $(x^*, y^*)$  is then a root of the resultant. The other component is determined by the  $\gcd(f, g) = 0$ , where  $x^*$  is substituted for  $x$ :

$$\gcd\left(f(x^*, y), g(x^*, y)\right) = 0 \quad (\text{A.15})$$

### Theorem of Bézout

Let  $n_f = \deg(f)$ ,  $n_g = \deg(g)$ . Then, the number of intersection points (real and/or complex) of  $f(x, y) = 0$  and  $g(x, y) = 0$  is  $n_f n_g$ .  $\square$

### Remark 1.9

If the degree of the resultant  $\text{Res}(f, g, y) = h(x)$  is not  $n_f n_g$ , then

- i. Some roots are at infinity, and/or
- ii. More than one component  $y^*$  belongs to one component  $x^*$ , and/or
- iii. The multiplicity of one or more intersection points is greater than 1.

$\square$

### Application

Given an explicit representation of a curve

$$x = \frac{n_1(\alpha)}{d_1(\alpha)}, \quad y = \frac{n_2(\alpha)}{d_2(\alpha)},$$

we can eliminate the parameter  $\alpha$  using the resultant method:

$$f(x, y) = \text{Res}(d_1(\alpha)x - n_1(\alpha), d_2(\alpha)y - n_2(\alpha), \alpha) = 0.$$

The inverse process, that is to find a parametric representation given an explicit representation, is only possible for rational curves.

## The Intersection of Two Polynomial Families

Consider now a system of two parametric polynomial families

$$f(x, y, \alpha) = 0, g(x, y, \alpha) = 0, \alpha \in [\alpha^-, \alpha^+] \quad (\text{A.16})$$

For fixed  $\alpha$ , we have the situation of the preceding section. For varying  $\alpha$ , the solution pairs  $(x^*, y^*)$  generate a new curve consisting of one or more (real or complex) branches. The parameter-free equation  $F(x, y) = 0$  of this curve can be generated by elimination of  $\alpha$ :

$$F(x, y) = \text{Res}(f, g, \alpha) = 0. \quad (\text{A.17})$$

But the restriction to an interval of the parameter  $\alpha$  gets lost, so  $F(x, y) = 0$  has “more” points than the parametric representation. Therefore, we eliminate  $y$  rather than  $\alpha$ .

The procedure for solving (A.16) is the following:

First, compute the resultant of  $f$  and  $g$  with respect to  $y$ :

$$h(x, \alpha) = \text{Res}\left(f(x, y, \alpha), g(x, y, \alpha), y\right). \quad (\text{A.18})$$

Then, grid  $\alpha$ . For  $\alpha = \alpha^*$ , determine the roots  $x^*$  of  $h(x, \alpha^*) = 0$ . For the corresponding value(s)  $x^*$ , again the greatest common divisor has to be determined:

$$\text{gcd}\left(f(x^*, y, \alpha^*), g(x^*, y, \alpha^*)\right). \quad (\text{A.19})$$

Varying  $\alpha$ , the number of real roots can change (i.e. branches of the curve can terminate or arise). This happens when two roots coincide on the real axis and go into the complex plane (or vice versa).

The condition for double roots in this case is:

$$D_{h(x, \alpha)} = \text{Res}(h(x, \alpha), \frac{\partial h(x, \alpha)}{\partial x}, x) = k(\alpha) = 0. \quad (\text{A.20})$$

The real zeros of  $k(\alpha) = 0$  divide the range of  $\alpha$  into intervals where the number of real roots  $x^*$  are constant. These numbers are only different in the neighborhood of a zero of  $k(\alpha) = 0$ , if the sign of the discriminant changes.

### Application

Solving (A.16) is the main task of the parameter space method.  $x, y$  are the uncertain plant parameters and/or controller parameters. Varying  $\alpha$  corresponds to the movement on the boundary of the desired pole regions. If the dependence on  $x, y$  is affine, the equations (A.16) can be solved easily (the equations are linear in  $x, y$ ) and we arrive at the explicit representation (A.4). Also, the solution of the bilinear case (the equations (A.16) are bilinear in  $x, y$ ) can be given in a closed form. According to the theorem of Bézout, we should have four intersections points. Two points are at infinity, since both curves are, in general, hyperbolas with asymptotes parallel to the coordinate axes. So, the final equation (the univariate polynomial) has degree two. An algebraic argument for this fact is the following: we can linearly combine both equations such that the resulting equation is linear in  $x$  and  $y$ . Solving for  $x$  and substituting in one of the basic equations gives a quadratic equation in  $y$ . Examples can be found in [159].

### The Envelope

Given a one-parameter family of algebraic curves,

$$f(x, y, \alpha) = 0. \quad (\text{A.21})$$

An *envelope* is a curve that touches each member of the one-parameter family and is touched at each of its points by some curve of the family. If the envelope exists (for example, concentric circles have no envelope), then the defining equations are

$$f(x, y, \alpha) = 0, \quad \frac{\partial f}{\partial \alpha}(x, y, \alpha) = 0. \quad (\text{A.22})$$

Again, the parameter  $\alpha$  has to be eliminated, this leads to the implicit equation:

$$F(x, y) = D_f = 0. \quad (\text{A.23})$$

The notion of the envelope has still another meaning. It is also used for the extremal curves or hull of a family of curves. Its equation can not be generated by means of the discriminant.

#### Example 1.10

Let  $f(x, y, \alpha) = (x - \alpha)^2 + y^2 - 1 = 0$ , a family of circles with center on the  $x$ -axis and radius 1. The derivative with respect to  $\alpha$  is  $f' = 2(x - \alpha)(-1)$ . Substituting the solution  $\alpha = x$  in  $f(x, y, \alpha) = 0$  gives the envelope  $y = \pm 1$ .  $\square$

#### Application

Algebraic constraints or bounds on transfer functions (sensitivity function, complementary sensitivity function) are often formulated as inequalities  $f(x, y, \omega) > 0$  for each frequency [159]. Instead of gridding  $\omega$  and plotting  $f(x, y, \omega) = 0$ , the envelope (if it exists) could be computed.

#### Example 1.11

The data for an uncertain transfer function used in this example are from [48]. For each frequency  $\omega$ , we have a requirement  $f(x, y, \omega) > 0$ . The feasible region (necessary but not sufficient) (Figure A.1) for  $x$  and  $y$  lies outside the ellipsoidal areas (dotted lines). Instead of plotting all these areas, we compute the equation of the envelope  $D_f = F(x, y) = 0$ . Because we have only the implicit representation, we must grid  $x$  and/or  $y$  to get a pointwise plot (diamonds) of the envelope.  $\square$

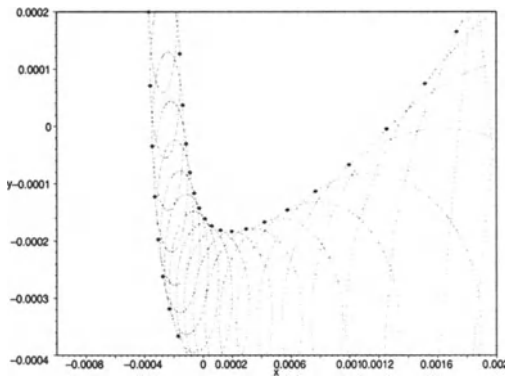


Figure A.1. Requirements for different frequencies and the corresponding envelope

### *Singular Points*

#### *Definition 1.12*

A point  $(x, y)$  on a curve  $f(x, y) = 0$  is called *singular* if both partial derivatives vanish. In this case, we have three polynomial equations

$$f(x, y) = 0, \quad f_x(x, y) = 0, \quad f_y(x, y) = 0. \quad (\text{A.24})$$

If higher partial derivatives also vanish, we speak of a higher singularity.

There are three types of (normal) singularities depending on the sign of the expression

$$D = f_{xx}f_{yy} - f_{xy}^2 \quad (\text{A.25})$$

(also a discriminant). If  $D > 0$ , we have a double point (node); the curve intersects itself. If  $D = 0$ , we have a cusp and for  $D < 0$  we have an isolated point. In its vicinity there are no further (real) points.

The resultant method is also useful for finding the singularities.

If the curve is defined in parametric form:

$$x = f(\alpha), \quad y = g(\alpha) \quad (\text{A.26})$$

( $f, g$  rational functions), then the intersection points (double points) can be found by solving the following system:

$$f(\alpha_1) = f(\alpha_2), \quad g(\alpha_1) = g(\alpha_2), \quad (\text{A.27})$$

which has the trivial solution  $\alpha_1 = \alpha_2$ . So, instead we should solve the reduced system

$$\text{Num}\left(\frac{f(\alpha_1) - f(\alpha_2)}{\alpha_1 - \alpha_2}\right) = 0, \quad (\text{A.28})$$

$$\text{Num} \left( \frac{g(\alpha_1) - g(\alpha_2)}{\alpha_1 - \alpha_2} \right) = 0. \quad (\text{A.29})$$

□

### Application

Determining the  $\Gamma$ -stable region (not only the complex root boundary) requires the knowledge of the intersection points of a curve with itself (see [159]).

### Application

An algebraic curve is rational if

$$(n-1)(n-2) = \sum r_i(r_i-1) \quad (\text{A.30})$$

( $r_i$  are the multiplicities of the singular points). Only rational curves have a parametric representation. Finding it, starting from the implicit representation, needs the knowledge of all singular points and additionally  $n-3$  simple points.

### Special System of Equations

Consider the following system of equations:

$$\frac{N(x, y, \alpha)}{D(x, y, \alpha)} = 0, \quad \frac{\partial}{\partial \alpha} \frac{N(x, y, \alpha)}{D(x, y, \alpha)} = 0 \quad (\text{A.31})$$

( $N, D$  polynomials). The first equation is called the *point condition*, the second *tangent condition*.

### Lemma

The system

$$N(x, y, \alpha) = 0, \quad \frac{\partial}{\partial \alpha} N(x, y, \alpha) = 0 \quad (\text{A.32})$$

is equivalent to (A.31).

### Proof

From  $N/D = 0$  follows  $N = 0$ . Therefore,  $(N/D)' = \frac{DN' - D'N}{D^2} = \frac{N'}{D} = 0$  is equivalent to  $N' = 0$ .

### Application

The conditions that the Nyquist curve (or any curve) touches another curve (for example, a circle around the critical point  $-1$ ) leads to a system like (A.32). Further

examples can be found in [63].

### *Application*

Computing the stability radius [15] also leads to a system of type (A.32).

### *Double Tangent and Popov-line*

Find the double tangent of a curve  $x = f(\alpha)$ ,  $y = g(\alpha)$ .

The tangent  $t$  at a point  $\alpha = \alpha^*$  is

$$t : \quad x_t = f(\alpha^*) + \lambda \frac{\partial f}{\partial \alpha} \Big|_{\alpha=\alpha^*}, \quad y_t = g(\alpha^*) + \lambda \frac{\partial g}{\partial \alpha} \Big|_{\alpha=\alpha^*}. \quad (\text{A.33})$$

These equations are substituted in the parameter-free representation

$$F(x, y) \Big|_{x=x_t, y=y_t} = F(\alpha^*, \lambda) = 0. \quad (\text{A.34})$$

Since the tangent  $t$  touches  $F$ ,  $\lambda = 0$  is a double root. To touch the curve once more, we have the condition that  $F(\alpha^*, \lambda)/\lambda^2$  has a double root. So again, the discriminant with respect to  $\lambda$  yields the corresponding polynomial whose roots are the values for  $\alpha$ , which give the touching points.

### *Application*

The Popov-line is either the tangent at an intersection point of the Popov plot with the real axis or a double tangent to the Popov plot.

### *Example 1.13*

Let  $g(s) = (0.01s + 1)/(s^5 + 5s^4 + 10s^3 + 41s^2 + 11s + 1)$ . We want to determine the double tangent which is also the Popov-line. Since the real part and the imaginary part of the Popov plot are always quadratic functions of  $\omega$ , we can replace  $\omega^2$  by  $\alpha$ . The degree of the parametric representation, as well as the degree of the implicit representation in  $\alpha$ , is five, the degree of the denominator polynomial of  $g(s)$ . The parameter values for the touching points are  $\alpha_1 = 0.0766$  and  $\alpha_2 = 8.23$ , resulting from the discriminant polynomial which has degree 118. The Popov-line intersects the real axis at  $-1/k = -0.136$  and leads to the sector with  $k = 7.36$  (Figure A.2). □

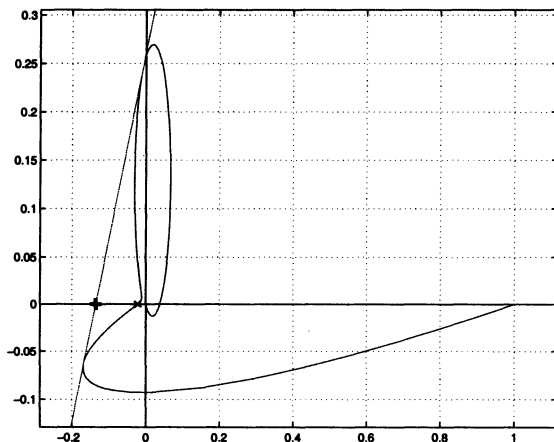


Figure A.2. Popov plot and Popov-line

# B PARADISE: Parametric Robustness Analysis and Design Interactive Software Environment

This appendix gives a brief introduction to the PARADISE toolbox.

It is not our intention to describe a specific set of features or a certain version of this toolbox. Moreover, the concept and basic usage of this toolbox is explained such that the reader is able to repeat the case studies in Chapters 6 and 7 and to try his or her own design. The latest version of PARADISE is available at <http://www.robotic.dlr.de/control/paradise>. More details and examples can be found at this site and in the comprehensive toolbox manual [152].

## *Concept*

PARADISE is a MATLAB-based toolbox that implements parametric robust control methods. The aim was to design a user-friendly toolbox with graphical user interfaces (GUI), which hides all calculations from the user as much as possible. Rather than doing tedious calculations, the user should concentrate on analyzing the graphical results. PARADISE uses both symbolical and numerical code to get the benefits from both worlds.

## *Architecture*

The architecture of the CACSD (Computer-aided Control System Design) toolbox PARADISE is driven by the following objectives: user friendliness, code maintenance, code efficiency and reusability of code. For this reason the toolbox was split into several modules. The modularity allows the realization of these objectives.

A basic partition of any interactive CACSD toolbox is the subdivision into interactive and computational modules. Figure B.1 shows the coarse structure of PARADISE. The individual modules will be discussed in subsequent sections.

## *Interactive Modules*

In order to achieve maximal user friendliness, the user can choose between numer-

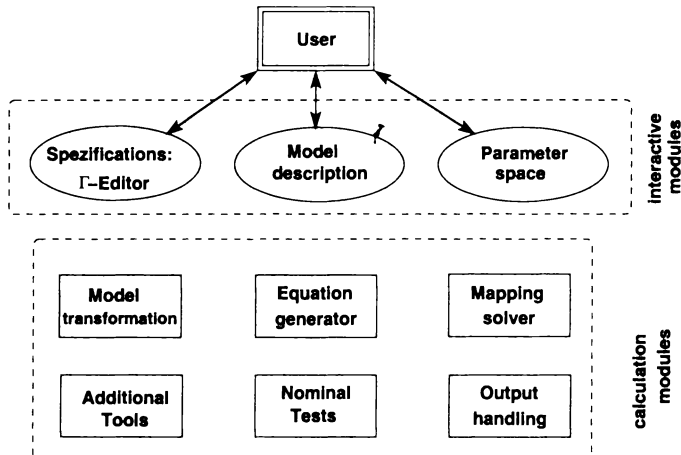


Figure B.1. Modular design of the toolbox

ous possibilites to interact with the toolbox. Apart from the GUIs, the toolbox can be controlled from the command-line or batch-file driven. Data can be imported using files, e.g. SIMULINK models, or by direct exchange of MATLAB workspace variables. The main interactive modules will be described in more detail in section “Working with the toolbox”.

### *Calculation Modules*

The *model transformation* module has two purposes; it analyses a given SIMULINK model to determine the inputs and outputs of the model and generates a symbolic model of the system. Additionally, this module is used to find the characteristic polynomial for eigenvalue specifications and to transform systems from state space into transfer function format.

The general mapping equations for specifications presented in this book are given by two polynomial equations with three real parameters  $q_1, q_2, \alpha$ :

$$\begin{aligned} p_1(q_1, q_2, \alpha) &= 0, \\ p_2(q_1, q_2, \alpha) &= 0, \end{aligned} \tag{B.1}$$

where  $\alpha$  is an artificial parameter stemming from the specification with  $\alpha \in [\alpha^-; \alpha^+]$ . Note: parameters  $q_1, q_2$  might be uncertain plant or controller parameters. The mapping equations (B.1) are generated by the *equation generator* module using the system description and the user-defined specifications.

The generic problem is now to find all curves  $q_1(\alpha), q_2(\alpha)$  that satisfy (B.1). These curves form the boundaries in a parameter plane. The curves are determined by the *mapping solver* module.

In order to get short execution times, the *mapping solver* module first classifies the polynomials  $p_1, p_2$  with respect to the parameter dependence for  $q_1, q_2$  in affine, bilinear

and polynomial. For each class, there exists a special code, which is run automatically such that the user needs not to choose the appropriate method. Furthermore, the modular design of the toolbox allows incorporation of code for special cases easily, e.g. PID-controllers [22].

Generating the mapping equations (B.1) and finding all solution branches hereof requires numerical and symbolical methods. The Extended Symbolic Math Toolbox adds the symbolic mathematics of the MAPLE symbolic engine to the powerful numeric capabilites of MATLAB. All symbolic computations in PARADISE are done using this toolbox.

## *Working with the Toolbox*

### *Input*

The first step to solve a parametric robust control problem involves the definition of the plant with the used controller structure, determination of the operating range and specification of the control requirements.

A parametric plant model can be imported into PARADISE using a parametric state space description provided as a text-file. Apart from the user-generated symbolic plant description, PARADISE can work with parametric SIMULINK models. These are ordinary SIMULINK models, where the model parameters are entered as strings instead of numerical values. PARADISE analyzes the given block interconnection and generates a parametric state space representation. PARADISE can also work with the multi-model formulation described in Section 2.6, or if no continuous parameter dependence is available like in the aircraft example of Section 7.2.

After the model description has been imported, all parameters existing in the model are determined. The user can now classify these parameters into controller, variable or constant parameters. Subsequently, the numerical values for controller and constant parameters and the numerical ranges for variable parameters have to be entered. A special parameter specification GUI therefore is available.

The control-related specifications can be entered using special GUIs. As an example, we consider the  $\Gamma$ -editor, which is used to define  $\Gamma$ -specifications. The  $\Gamma$ -region is formed by choosing different basic elements that form the boundary of the  $\Gamma$ -region. There is a library of basic elements, e.g. real part limitation or hyperbola, all of which are conic sections. The geometrical parameters of all basic elements can be entered either graphically using the GUI or by entering the numerical values. All basic elements can be logically combined through logical union or intersection such that almost any region can be described using basic elements. Figure B.2 shows the  $\Gamma$ -editor.

### *Design and Analysis*

The main purpose of PARADISE is to map specifications into a parameter plane. Through mapping given specifications into a parameter plane, the user can easily do a robustness analysis. The specifications can be mapped into planes of given parameters or the user can define his own parameter planes. Actually, there is special support for

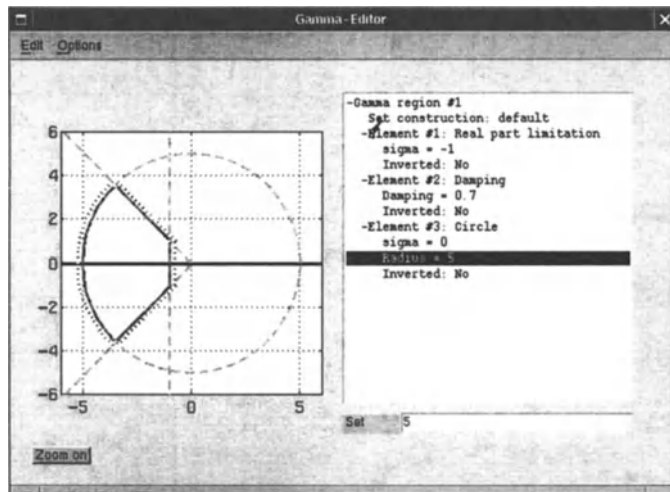


Figure B.2.  $\Gamma$ -Editor

invariance planes, which allows successive pole-shifting, see Section 2.4.

Another possibility to verify a control design is to display the resulting closed-loop poles directly in the  $\Gamma$ -editor.

After specifying the plant model and the parameters, a robust design of a control system is done iteratively by performing the following steps:

- i. Define the specifications.
- ii. Choose an appropriate parameter plane.
- iii. Map the current specifications into parameter plane.
- iv. Check if specifications are fulfilled or tune parameters such that specifications are achieved/improved. (Maybe go back to step 1. and relax specifications).
- v. Go back to step 2. until specifications are robust fulfilled.

### *Output*

All results of the analysis and design steps are displayed graphically to facilitate the interpretation. There are interfaces to save and export the data in appropriate formats, e.g. MATLAB variables.

# Bibliography

- [1] J. Ackermann, “Der Entwurf linearer Regelungssysteme im Zustandsraum (State space design of linear control systems),” *Regelungstechnik*, vol. 20, pp. 297–300, 1972.
- [2] J. Ackermann, “Parameter space design of robust control systems,” *IEEE Trans. on Automatic Control*, vol. 25, pp. 1058–1072, 1980.
- [3] J. Ackermann, “Robustness against sensor failures,” *Automatica*, vol. 20, pp. 211–215, 1984.
- [4] J. Ackermann, *Sampled-data control systems: analysis and synthesis, robust system design*. Berlin: Springer, 1985.
- [5] J. Ackermann, “Verfahren zum Lenken von Straßenfahrzeugen mit Vorder- und Hinterradlenkung I (Method of steering road vehicles having both front-wheel steering and rear-wheel steering I).” German Patent P 4028320, European Patent 0474130, US Patent 5375057, Japanese Patent 3158347, Priority Sept. 6, 1990.
- [6] J. Ackermann, “Does it suffice to check a subset of multilinear parameters in robustness analysis?,” *IEEE Trans. on Automatic Control*, vol. 37, pp. 487–488, 1992.
- [7] J. Ackermann, “Verfahren zum Lenken von Straßenfahrzeugen mit Vorder- und Hinterradlenkung II (Method of steering road vehicles having both front-wheel steering and rear-wheel steering II).” German Patent P 4206654, European Patent 0559114, US Patent 5515275, Japanese Patent 3210471, Priority March 3, 1992.
- [8] J. Ackermann, “Verfahren zum Lenken von Straßenfahrzeugen mit Vorderradlenkung (Method of correcting steering of a road driven vehicle).” German Patent 4307420, European Patent 0614795, US Patent 54 28 536, Japanese Patent Application 6-59841, Priority March 9, 1993.
- [9] J. Ackermann, “Verfahren zur Lenkunterstützung eines Fahrers eines Straßenfahrzeugs (Method of correcting steering of a road driven vehicle).” German Patent P 19650691, European Patent 97121452.3-2206, US Patent 5925083, Priority Dec. 12, 1996.
- [10] J. Ackermann, “Yaw disturbance attenuation by robust decoupling of car steering,” in *Proc. 13th IFAC World Congress*, vol. Q, (San Francisco), pp. 1–6, 1996.
- [11] J. Ackermann, “Robust control prevents car skidding,” *IEEE Control Systems Magazine*, pp. 23–31, June 1997. Bode Prize Lecture 1996.

- [12] J. Ackermann, "Verfahren zur Vorgabe einer gewünschten geschwindigkeits - abhängigen Gierdämpfung bei der Fahrzeuglenkung (Method of assignment of a desired velocity-dependent yaw damping for vehicle steering)." German Patent Application 10206730.9, Priority Feb. 18, 2002.
- [13] J. Ackermann, *Pole placement control*. UNESCO, 2002 (to appear). Encyclopedia of Life Support Systems.
- [14] J. Ackermann and B. Barmish, "Robust Schur stability of a polytope of polynomials," *IEEE Trans. on Automatic Control*, vol. 33, pp. 984–986, 1988.
- [15] J. Ackermann, A. Bartlett, D. Kaesbauer, W. Sienel, and R. Steinhauser, *Robust control: Systems with uncertain physical parameters*. London: Springer, 1993.
- [16] J. Ackermann and T. Bünte, "Robust prevention of limit cycles for robustly decoupled car steering dynamics," *Kybernetika*, vol. 35, no. 1, pp. 105–116, 1999.
- [17] J. Ackermann, T. Bünte, J. Dietrich, B. Gombert, and B. Willberg, "Aktuator zum Korrigieren eines über das Lenkrad eines Fahrzeugs an die Räder einer gelenkten Achse eingegebenen Lenkwinkels (Actuator for generating an additional steering angle for road vehicles)." German Patent 19750585, European Patent 0916568, US Patent 6343671, Priority Nov. 17, 1997.
- [18] J. Ackermann, T. Bünte, W. Sienel, H. Jeebe, and K. Naab, "Driving safety by robust steering control," in *Proc. Int. Symposium on Advanced Vehicle Control*, (Aachen, Germany), June 1996.
- [19] J. Ackermann, J. Guldner, W. Sienel, R. Steinhauser, and V. I. Utkin, "Linear and nonlinear control design for automatic steering," *IEEE Trans. on Control Systems Technology, Special Issue on Automotive Control Systems*, vol. 3, no. 1, pp. 132–143, 1995.
- [20] J. Ackermann and H. Hu, "Robustness of sampled-data control systems with uncertain physical plant parameters," *Automatica*, vol. 27, pp. 705–710, 1991.
- [21] J. Ackermann, H. Hu, and D. Kaesbauer, "Robustness analysis: a case study," *IEEE Trans. on Automatic Control*, vol. 35, pp. 352–356, 1990.
- [22] J. Ackermann and D. Kaesbauer, "Design of robust PID controllers," in *Proc. European Control Conference*, (Porto), 2001.
- [23] J. Ackermann, D. Kaesbauer, and R. Münch, "Robust  $\Gamma$ -stability analysis in a plant parameter space," *Automatica*, vol. 27, pp. 75–85, 1991.
- [24] J. Ackermann, D. Kaesbauer, and W. Sienel, "Design by search," in *Proc. First IFAC Symposium on Design Methods of Control Systems*, vol. 1, (Zürich), pp. 181–186, 1991.
- [25] J. Ackermann and D. Odenthal, "Robust steering control for active rollover avoidance of vehicles with elevated center of gravity," in *Proc. International Conference on Advances in Vehicle Control and Safety*, (Amiens, France), pp. 118–123, July 1998.
- [26] J. Ackermann and D. Odenthal, "Damping of vehicle roll dynamics by gain scheduled active steering," in *Proc. European Control Conference*, (Karlsruhe, Germany), 1999.
- [27] J. Ackermann and W. Sienel, "Computer-aided robustness analysis for characteristic polynomials with polynomial parameter dependence," in *Proc. IEEE Conf. Decision and Control*, (Tampa), pp. 1934–1935, 1989.

- [28] J. Ackermann and W. Sienel, "Robust control for automatic steering," in *Proc. American Control Conference*, (San Diego), pp. 795–800, 1990.
- [29] J. Ackermann and W. Sienel, "What is a 'large' number of parameters in robust systems," in *Proc. IEEE Conf. Decision and Control*, (Honolulu), pp. 3496–3497, 1990.
- [30] J. Ackermann and W. Sienel, "On the computation of value sets for robust stability analysis," in *Proc. First European Control Conference*, (Grenoble), pp. 2318–2327, 1991.
- [31] J. Ackermann and W. Sienel, "Robust yaw damping of cars with front and rear wheel steering," *IEEE Trans. on Control Systems Technology*, vol. 1, no. 1, pp. 15–20, 1993.
- [32] J. Ackermann and S. Türk, "A common controller for a family of plant models," in *Proc. 21st IEEE Conf. Decision and Control*, (Orlando), pp. 240–244, 1982.
- [33] B. Aksun Güvenç, T. Bünte, D. Odenthal, and L. Güvenç, "Robust two degree of freedom vehicle steering controller design," in *Proc. American Control Conference*, (Arlington, VA, USA), June 2001.
- [34] B. Aksun Güvenç and L. Güvenç, "Robust two degree-of-freedom add-on controller design for automatic steering," *IEEE Trans. on Control Systems Technology*, vol. 10, no. 1, pp. 137–148, 2002.
- [35] R. W. Allen, H. T. Szostak, D. H. Klyde, T. J. Rosenthal, and K. J. Owens, "Vehicle dynamic stability and rollover," tech. rep., Systems Technology, Inc., Hawthorne, CA, 1992. U.S.-D.O.T., NHTSA.
- [36] J. Anagnos, C. Desoer, and R. Minichelli, "Generalized Nyquist test for robust stability: Frequency domain generalizations of Kharitonov's theorem," in *Robustness in Identification and Control* (M. Milanese, R. Tempo, and A. Vicino, eds.), pp. 79–96, New York: Plenum Press, 1989.
- [37] K. Åström and B. Wittenmark, *Computer controlled systems*. Englewood Cliffs, N.J.: Prentice-Hall, 1984.
- [38] G. Balas, J. Doyle, K. Glover, A. Packard, and R. Smith, *The  $\mu$  analysis and synthesis toolbox*. The MathWorks, Inc., 1998.
- [39] B. Barmish, "New tools for robustness analysis," in *Proc. IEEE Conf. Decision and Control*, (Austin), pp. 1–6, 1988.
- [40] B. Barmish, "A generalization of Kharitonov's four-polynomial concept for robust stability problems with linearly dependent coefficient perturbations," *IEEE Trans. on Automatic Control*, vol. 34, no. 2, pp. 157–165, 1989.
- [41] B. Barmish, *New tools for robustness of linear systems*. New York: MacMillan, 1994.
- [42] S. Barnett, *Polynomials and Linear Control Systems*. New York: M. Dekker, 1983.
- [43] A. Bartlett, C. Hollot, and Huang-Lin, "Root locations of an entire polytope of polynomials: it suffices to check the edges," *Mathematics of Control, Signals and Systems*, vol. 1, pp. 61–71, 1988.
- [44] R. Bass and I. Gura, "High order system design via state-space considerations," in *Joint Automatic Control Conference*, pp. 311–318, 1965. Preprints.

- [45] R. Bass and P. Mendelson, "Aspects of general control theory," Final report 2754, AFOSR, 1962.
- [46] S. Bennani, C. Magni, and J. Terlouw, *Robust Flight Control*. London: Springer, 1997.
- [47] R. Berger, J. Hess, and D. Anderson, "Compatibility of maneuver load control and relaxed static stability applied to military aircraft," AFFDL-TR-73-33, Air Force Flight Dynamics Laboratory, 1973.
- [48] V. Besson and A. T. Shenton, "An interactive parameter space method for robust performance in mixed sensitivity problems," *IEEE Trans. on Automatic Control*, vol. 44, pp. 1272–1276, June 1999.
- [49] S. Bialas, "A necessary and sufficient condition for the stability of convex combinations of stable polynomials or matrices," *Bulletin of the Polish Academy of Sciences*, vol. 33, pp. 473–480, 1985.
- [50] M. Biehler, "Sur une classe d'équations algébriques dont toutes les racines sont réelles," *J. Reine Angewandte Mathematik*, vol. 87, pp. 350–352, 1879.
- [51] G. Birkhoff and S. M. Lane, *A survey of modern algebra*. New York: The MacMillan Company, 1965.
- [52] P. Blue and S. Banda, "D-K iteration with optimal scales for systems with time-varying and time-invariant uncertainties," in *Proc. American Control Conference*, 1997.
- [53] P. Blue, L. Güvenç, and D. Odenthal, "Large envelope flight control satisfying  $H_\infty$  robustness and performance specifications," in *Proc. American Control Conference*, (Arlington, VA, USA), June 2001.
- [54] M. Bocher, *Introduction to Higher Algebra*. New York: Dover, 1964.
- [55] H. Bode, *Network analysis and feedback amplifier design*. New York: D. van Nostrand Company, Inc., 1945.
- [56] S. Boyd, V. Balakrishnan, and P. Kabamba, "A bisection method for computing the  $H_\infty$  norm of a transfer matrix and related problems," *Mathematics of Control, Signals and Systems*, vol. 2, pp. 207–219, 1989.
- [57] S. Boyd and C. Barratt, *Linear Controller Design: Limits of Performance*. Prentice-Hall, 1991.
- [58] S. Boyd, L. E. Ghaoui, E. Feron, and V. Balakrishnan, *Linear Matrix Inequalities in System and Control Theory*. SIAM studies in applied mathematics, 1994.
- [59] E. Brieskorn and H. Knörrer, *Plane Algebraic Curves*. Basel, Boston, Stuttgart: Birkhäuser Verlag, 1986.
- [60] R. Brockhaus, *Flugregelung*. Berlin: Springer, 1994.
- [61] I. N. Bronstein and K. A. Semendjajew, *Taschenbuch der Mathematik*. Thun und Frankfurt/Main: Harri Deutsch Verlag, 1987.
- [62] T. Bünte, *Beiträge zur robusten Lenkregelung von Personenkraftwagen (Contributions to robust car steering control)*. Ph.D. thesis, RWTH Aachen, 1998. VDI Fortschritt-Bericht, Reihe 12, Nr. 366, VDI-Verlag, Düsseldorf, 1998.
- [63] T. Bünte, "Mapping of Nyquist/Popov Theta-stability margins into parameter space," in *Proc. 3rd IFAC Symposium on Robust Control Design*, (Prague, Czech Republic), 2000.

- [64] T. Bünte, "Die Anwendung des Parameterraumverfahrens auf Ortskurvenkriterien (Application of the parameter space method to frequency loci criteria)," *Automatisierungstechnik*, vol. 49, pp. 547–556, December 2001.
- [65] T. Bünte, D. Odenthal, B. Aksun Güvenç, and L. Güvenç, "Robust vehicle steering control design based on the disturbance observer," in *Proc. 3rd IFAC Workshop on Advances in Automotive Control*, (Karlsruhe), pp. 107–116, 2001.
- [66] F. Cellier, *Continuous system modelling*. New York: Springer, 1991.
- [67] A. Cohn, "Über die Anzahl der Wurzeln einer algebraischen Gleichung in einem Kreise," *Mathematische Zeitschrift*, vol. 14, pp. 110–148, 1922.
- [68] L. Cremer, "Ein neues Verfahren zur Beurteilung der Stabilität linearer Regelungssysteme," *ZAMM*, p. 161, 1947.
- [69] W. Darenberg, "Automatische Spurführung von Kraftfahrzeugen," *Automobil-Industrie*, pp. 155–159, 1987.
- [70] S. Dasgupta, "Perspectives on Kharitonov's theorem: a view from the imaginary axis," tech. rep., Dept. Elect. Comp. Eng., University of Iowa, Iowa City, 1987.
- [71] A. Datta, M. Ho, and S. Bhattacharyya, *Structure and synthesis of PID controllers*. London: Springer, 2000.
- [72] M. Debes, E. Herb, R. Müller, G. Sokoll, and A. Straub, "Dynamische Stabilitäts Control DSC der Baureihe 7 von BMW - Teil 1/2," *Automobiltechnische Zeitschrift*, vol. 99, no. 3/4, pp. 134–140, 208–213, 1997.
- [73] R. deGaston and M. Safonov, "Exact calculation of the multiloop stability margin," *IEEE Trans. on Automatic Control*, vol. 33, pp. 156–171, 1988.
- [74] E. Dickmanns, "Entwicklungsschritte zur Erhöhung von Sicherheit und Komfort durch sehende Autos," *Automatisierungstechnik*, vol. 44, pp. 243–251, 1996.
- [75] T. Djajaferis, "Stabilization of systems with real parameter variations," in *Proc. IEEE Conf. Decision and Control*, (Tampa), pp. 1870–1871, 1989.
- [76] E. Donges, R. Aufhammer, P. Fehrer, and T. Seidenfuß, "Funktion und Sicherheitskonzept der Aktiven Hinterachs kinematik von BMW," *Automobiltechnische Zeitschrift*, vol. 10, pp. 580–587, 1990.
- [77] E. Donges and K. Naab, "Regelsysteme zur Fahrzeugführung und -stabilisierung in der Automobiltechnik," *Automatisierungstechnik*, vol. 44, pp. 226–236, Mai 1996.
- [78] J. Doyle and G. Stein, "Multivariable feedback design: concepts for a classical modern synthesis," *IEEE Trans. on Automatic Control*, vol. 26, no. 1, pp. 4–16, 1981.
- [79] J. C. Doyle, B. A. Francis, and A. R. Tannenbaum, *Feedback control theory*. New York: MacMillan Publishing Company, 1992.
- [80] H. Duda, *Fliegbarkeitskriterien bei begrenzter Stellgeschwindigkeit*. Ph.D. thesis, Technische Universität Braunschweig, April 1997. Forschungsbericht 97-15, Deutsche Forschungsanstalt für Luft- und Raumfahrt e.V., Köln.
- [81] B. Etkin, *Dynamics of atmospheric flight*. New York: Wiley, 1972.
- [82] B. Etkin and L. Reid, *Dynamics of Flight*. New York: John Wiley and Sons, Inc., 1995.
- [83] S. Faedo, "Un nuovo problema di stabilità per le equazioni algebriche a coefficienti reali," *Ann. Scuola Norm. Super Pisa, Sci. Fis. Mat.*, vol. 7, pp. 53–63, 1953.

- [84] A. Fam and J. Meditch, "A canonical parameter space for linear system design," *IEEE Trans. on Automatic Control*, vol. 23, pp. 454–458, 1978.
- [85] C. Favre, "Modern flight control system a pilot partner towards better safety," in *Proc. of the 2nd International Symposium on Aerospace, Science and Technology, ISASTI 96*, (Jakarta), pp. 472–481, 1996.
- [86] B. Francis, *A course in  $H_\infty$  control theory*. New-York: Springer, 1987.
- [87] G. Franklin and J. Powell, *Digital control*. Reading, Massachusetts: Addison-Wesley, 1980.
- [88] S. Franklin and J. Ackermann, "Robust flight control: a design example," *AIAA J. Guidance and Control*, vol. 4, pp. 597–605, 1981.
- [89] R. Frazer and W. Duncan, "On the criteria for the stability of small motions," in *Proc. Royal Society A*, vol. 124, pp. 642–654, 1929.
- [90] J. S. Freudenberg and D. P. Looze, "Right half plane poles and zeros and design tradeoffs in feedback systems," *IEEE Trans. on Automatic Control*, vol. 30, no. 6, pp. 555–565, 1985.
- [91] F. Frühauß and R. Rutz, "Innovisia – eine aktive Federung für den Reisebus," *Automatisierungstechnik*, vol. 46, pp. 120–127, 1998.
- [92] M. Fu, "Polytopes of polynomials with zeros in a prescribed region: New criteria and algorithms," *Systems and Control Letters*, vol. 15, pp. 125–145, 1990.
- [93] W. Fulton, *Algebraic Curves*. Reading, Massachusetts: Addison-Wesley, 1989.
- [94] F. Gantmacher, *The theory of matrices*. New York: Chelsea, 1959.
- [95] A. Gelb and W. Vander Velde, *Multiple-Input Describing Functions and Nonlinear System Design*. New York: MacGraw-Hill, 1968.
- [96] S. Germann and R. Isermann, "Determination of the centre of gravity height of a vehicle with parameter estimation," in *IFAC Symposium on System Identification*, (Copenhagen), 1994.
- [97] E. Gilbert, "Controllability and observability in multivariable control systems," *SIAM Journal of Control and Optimization*, pp. 128–151, 1963.
- [98] G. Grübel, D. Joos, D. Käsbauer, and R. Hillgren, "Robust back-up stabilization for artificial-stability aircraft," in *Proc. 14th ICAS Congress*, (Toulouse), 1984.
- [99] J. Guldner, W. Sienel, H. Tan, J. Ackermann, S. Patwardhan, and T. Bünte, "Robust automatic steering control for look-down reference systems with front and rear sensors," *IEEE Trans. on Control Systems Technology*, vol. 7, no. 1, pp. 2–11, 1999.
- [100] L. Güvenç, "Closed loop pneumatic position control using discrete time model regulation," in *Proc. American Control Conference*, pp. 4273–4277, 1999.
- [101] L. Güvenç, T. Bünte, B. Aksun Güvenç, and D. Odenthal, "Regelung des dynamischen Verhaltens eines Fahrzeugs um eine definierte Achse (Control of the dynamic behavior of a vehicle around a defined axis)." German Patent Application 10061966.5, European Patent Application 01129567.2, Priority Dec. 13, 2000.
- [102] L. Güvenç and K. Srinivasan, "Friction compensation and evaluation for a force control application," *J. of Mechanical Systems and Signal Processing*, vol. 8, no. 6, pp. 623–638, 1994.

- [103] C. Halfmann, H. Holzmann, R. Schwarz, and M. Würtenberger, "Identifikation der Wankdynamik eines Kraftfahrzeugs mit Parameterschätzverfahren und Neuronalen Netzen," *Automatisierungstechnik*, vol. 46, no. 9, pp. 420–425, 1998.
- [104] M. Hautus, "Controllability and observability condition of linear autonomous systems," *Proc. Kon. Ned. Akad. Wetensch.*, vol. 72, no. ser. A, pp. 443–448, 1969.
- [105] M. Hautus, "Controllability and stabilizability of sampled systems," *IEEE Trans. on Automatic Control*, no. 17, pp. 528–531, 1972.
- [106] F. Hecker, S. Hummel, O. Jundt, K.-D. Leimbach, I. Faye, and H. Schramm, "Vehicle dynamics control for commercial vehicles," *SAE*, no. 973284, 1997.
- [107] C. Hermite, "Sur le nombre des racines d'une équation algébrique comprise entre des limites données," *J. Reine Angewandte Mathematik*, vol. 52, pp. 39–51, 1852. English translation *Int. Journal of Control*, 1977.
- [108] M. Ho, A. Datta, and S. Bhattacharyya, "Design of P, PI and PID controller for interval plants," in *Proc. American Control Conference*, (Philadelphia), pp. 2496–2501, 1998.
- [109] Honeywell Technology Center, "Application of multivariable control theory to aircraft control laws, Final Report: Multivariable Control Design Guidelines," May 1996. WL-TR-96-3099.
- [110] H. Hopkins, "Delivered with feeling," *Flight International 20*, pp. 31–34, 1991.
- [111] I. Horowitz, *Synthesis of feedback systems*. New York: Academic Press, 1963.
- [112] H. Hu, C. Hollot, R. Tempo, and J. Ackermann, "Absence of extreme-point results in sampled-data control systems," in *Proc. First European Control Conference*, (Grenoble), pp. 1356–1359, 1991.
- [113] A. Hurwitz, "Über die Bedingungen, unter welchen eine Gleichung nur Wurzeln mit negativen reellen Teilen besitzt," *Mathematische Annalen*, vol. 46, pp. 273–284, 1895.
- [114] Joint Aviation Authority, "Joint aviation requirements JAR-25 large aeroplanes," 1994. pp. 1-C-8-10.
- [115] C. Jung and W. Hirschberg, *EUROMOTOR Seminar: Understanding human monitoring and assessment, TNO Delft, November 20-21, 1997*, ch. Payload monitoring as one basis for commercial vehicles dynamics. Amsterdam: Swets & Zeitlinger, 1998.
- [116] E. Jury, *Theory and application of the z-transform method*. New York: John Wiley, 1964.
- [117] E. Jury and T. Pavlidis, "Stability and aperiodicity constraints for systems design," *IEEE Trans. on Circuit Theory*, vol. 10, pp. 137–141, 1963.
- [118] D. Kaesbauer, "On robust stability of polynomials with polynomial parameter dependency: two/three parameter case," *Automatica*, vol. 29, no. 1, pp. 215–217, 1993.
- [119] D. Kaesbauer and J. Ackermann, "The distance from stability or gamma-stability boundaries," in *Proc. 11th IFAC Congress*, (Tallinn), pp. 130–134, 1990.
- [120] T. Kailath, *Linear systems*. Englewood Cliffs, N.J.: Prentice-Hall, 1980.

- [121] E. Kalinina and A. Uteshev, "Determination of the number of roots of a polynomial lying in a given algebraic domain," *accepted for Linear Algebra and Its Applications*, 2000.
- [122] R. Kalman, "On the general theory of control systems," in *First IFAC Congress*, (Moscow), pp. 481–492, 1960.
- [123] R. Kalman, "Mathematical description of linear dynamical systems," *SIAM Journal of Control and Optimization*, pp. 152–192, 1963.
- [124] C. Kempf and S. Kobayashi, "Disturbance observer and feedforward design for a high-speed direct-drive positioning table," *IEEE Trans. on Control Systems Technology*, vol. 7, no. 5, pp. 513–526, 1999.
- [125] V. Kharitonov, "Asymptotic stability of an equilibrium position of a family of systems of linear differential equations," *Differential Equations*, vol. 14, no. 3, pp. 26–35, 1979.
- [126] D. Konik, R. Bartz, F. Bärnthol, H. Bruns, and M. Wimmer, "Dynamic Drive – the new active roll stabilization system from BMW Group – system description and functional improvements," in *Proceedings of AVEC 2000, 5th Int'l Symposium on Advanced Vehicle Control*, (Ann Arbor, Michigan), June 2000.
- [127] M. Kordt and J. Ackermann, "Robust design of a structural dynamic engine out controller for a large transport aircraft," *AIAA Journal of Guidance, Control and Dynamics* 24 (2), pp. 305–314, 2001.
- [128] G. Kreisselmeier, "Struktur mit zwei Freiheitsgraden (two-degree of freedom controller structure)," *Automatisierungstechnik*, vol. 47, pp. 266–269, 1999.
- [129] A. Lambregts, "Integrated system design for flight and propulsion control using total energy principles," in *AIAA Aircraft design, systems and technology meeting*, (Texas), 1983. paper no. AIAA-83-2561.
- [130] D. Lazard, "System of algebraic equations (algorithms and complexity)," in *Symposium on symbolic and algebraic computation*, (Bonn), 1991.
- [131] A. Leonhard, "Neues Verfahren zur Stabilitätsuntersuchung," *Archiv für Elektrotechnik*, vol. 38, pp. 17–28, 1944.
- [132] A. Liénard and A. Chipart, "On the sign of the real part of the roots of an algebraic equation," *J. Math. Pures et Appl.*, vol. 10, pp. 291–346, 1914.
- [133] R. C. Lin, D. Cebon, and D. J. Cole, "Optimal roll control of a single-unit lorry," in *Proc. IMechE*, vol. 210, Part D, pp. 45–55, 1996.
- [134] W. Linvill, "Sampled-data control systems studied through comparison of sampling with amplitude modulation," *AIEE Transactions*, vol. 70, pp. 1779–1788, 1951.
- [135] T. D. Lomax, "Structural loads analysis for commercial transport aircraft: Theory and practice," *AIAA, Education Series*, pp. 42–45, 143–160, 1995.
- [136] L. MacColl, *Fundamental theory of servomechanisms*, pp. 88–101. New York: Van Nostrand, 1945.
- [137] J. M. Maciejowski, *Multivariable Feedback Design*. Electronic Systems Engineering Series, Addison-Wesley, 1989.
- [138] M. Mansour, "On Robust Stability of Linear Systems," in *Systems and Control Letters*, (North Holland), 1993.

- [139] A. Markazie and N. Hori, "A new method with guaranteed stability for discretization of continuous-time control systems," in *Proc. American Control Conference*, (Chicago), pp. 1397–1402, 1992.
- [140] D. McLean, *Automatic Flight Control System*. London: Prentice Hall International Ltd., 1990.
- [141] D. McLean, "An automatic engine-out recovery system," in *Proc. of Intern. Aviation Safety Conf., IASC 97*, (Amsterdam), pp. 763–776, 1997.
- [142] D. McRuer, I. Ashkenas, and D. Graham, *Aircraft dynamics and automatic control*. Princeton: Princeton University Press, 1973.
- [143] S. Mehring, U. Franke, and A. Suissa, "Optische Spurhaltung - Eine Unterstützung des Fahrers bei der Lenkaufgabe," *Automatisierungstechnik*, vol. 44, pp. 238–242, 1996.
- [144] R. Middleton and G. Goodwin, *Digital control and estimation*. Englewood Cliffs, N.J.: Prentice-Hall, 1990.
- [145] A. Mikhailov, "Method of harmonic analysis in control theory," *Avtomatika i Telemekhanika*, vol. 3, pp. 27–81, 1938.
- [146] "Flying qualities of piloted airplanes." MIL-F-8785 B (ASG), August 1969.
- [147] "Flying qualities of piloted airplanes." MIL-STD-1797A, 1990.
- [148] J. Minor, A. Thurling, and E. Ohmit, "VISTA – a 21st century UAV testbed," in *Proc. 32nd Society of Flight Test Engineers Symposium*, 2001.
- [149] D. Mitrovic, "Graphical analysis and synthesis of feedback control systems," *Trans. AIEE*, vol. 77, no. 2, pp. 476–503, 1958.
- [150] M. Mitschke, *Dynamik der Kraftfahrzeuge*, vol. C. Berlin: Springer, 1990.
- [151] M. Muhler, "Mapping MIMO control system specifications into parameter space," *submitted to IEEE Conference on Decision and Control*, 2002.
- [152] M. Muhler, D. Odenthal, and W. Sienel, *PARADISE User's Manual*. Deutsches Zentrum für Luft und Raumfahrt e. V., DLR Oberpfaffenhofen, 2001. [www.robotic.dlr.de/control/paradise](http://www.robotic.dlr.de/control/paradise).
- [153] A. Müller, W. Achenbach, E. Schindler, T. Wohland, and F.-W. Mohn, "Das neue Fahrsicherheitssystem Electronic Stability Program von Mercedes Benz," *Automobiltechnische Zeitschrift 96*, vol. 11, pp. 656–670, 1994.
- [154] R. Münch, "Reglerauslegung und Robustheitsanalyse für einen spurgeführten Bus," Tech. Rep. IB 515-86-14, DLR, Oberpfaffenhofen, Germany, 1986.
- [155] N. Munro and M. T. Solyemez, "Fast calculation of stabilizing PID controllers for uncertain parameter systems," in *Proc. 3rd IFAC Symposium on Robust Control Design*, (Prague, Czech Republic), 2000.
- [156] Y. Neimark, "On the root distribution of polynomials," *Dokl. Akad. Nauk.*, vol. 58, pp. 357–360, 1947.
- [157] H. Nyquist, "Regeneration theory," *Bell Systems Technical Journal*, p. 126, 1932.
- [158] D. Odenthal, *Ein robustes Fahrdynamik-Regelungskonzept für die Kippvermeidung von Kraftfahrzeugen (A robust vehicle dynamics control concept for rollover avoidance)*. Ph.D. thesis, TU München, 2002. VDI Fortschritt-Bericht, Reihe 12, VDI-Verlag, Düsseldorf, 2002.

- [159] D. Odenthal and P. Blue, "Mapping of frequency response magnitude specifications into parameter space," in *Proc. 3rd IFAC Symposium on Robust Control Design*, (Prague, Czech Republic), 2000.
- [160] D. Odenthal and T. Bünte, "Verfahren zur Reduktion der Kippgefahr von Straßenfahrzeugen (Method of rollover avoidance for road vehicles)." German Patent P 19918597 C2, European Patent Application, Priority April 23, 1999.
- [161] D. Odenthal, T. Bünte, and J. Ackermann, "Nonlinear steering and braking control for vehicle rollover avoidance," in *Proc. European Control Conference*, (Karlsruhe, Germany), 1999.
- [162] D. Odenthal, T. Bünte, and R. Koeppe, "Regelung von Systemen mit kinästhetischer Kopplung (Control of systems with kinesthetic coupling)." German Patent Application 10216247.6, Priority April 12, 2002.
- [163] K. Ohnishi, "A new servo method in mechatronics," *Trans. Japanese Soc. Electr. Eng.*, vol. 107-D, pp. 83–86, 1987.
- [164] L. Orlando, "Sul problema di Hurwitz relativo alle parti reali delle radici di un'equazione algebrica," *Mathematische Annalen*, vol. 71, pp. 233–245, 1911.
- [165] M. Otter, "Objektorientierte Modellierung physikalischer Systeme," *Automatisierungstechnik*, vol. 47, 17 parts from 1/1999 to 12/2000. Series "Theorie für den Anwender".
- [166] L. Palkovics, A. Semsey, and E. Gerum, "Roll-over prevention systems for commercial vehicles – additional sensorless function of the electronic brake system," *Vehicle System Dynamics*, vol. 32, pp. 285–297, 1999.
- [167] E. Panier, M. Fan, and A. Tits, "On the robust stability of polynomials with no cross-coupling between the perturbations in the coefficients of even and odd powers," *Systems and Control Letters*, vol. 12, pp. 291–299, 1989.
- [168] V. Popov, "Absolute stability of nonlinear systems of automatic control," *Autom. & Rem. Control*, vol. 22, pp. 857–875, 1962.
- [169] F. Preparata and M. Shamos, *Computational geometry*. New York: Springer, 1985.
- [170] P. Putz and M. Wozny, "A new computer graphics approach to parameter space design of control systems," *IEEE Trans. on Automatic Control*, vol. 32, pp. 294–302, 1987.
- [171] J. Raisch, *Mehrgrößenregelung im Frequenzbereich*. München: Oldenbourg Verlag, 1994.
- [172] P. Riekert and T. Schunck, "Zur Fahrmechanik des gummibereiften Kraftfahrzeugs," *Ingenieur Archiv*, vol. 11, pp. 210–224, 1940.
- [173] J. Rissanen, "Control system synthesis by analogue computer based on the generalized linear feedback concept," in *Proc. Int. Seminar on Analog Computation*, (Brussels, Belgium), Nov. 1960.
- [174] E. Routh, *A treatise on the stability of a given state of motion*. London: MacMillan, 1877.
- [175] R. Saeks and J. Murray, "Fractional representation, algebraic geometry, and the simultaneous stabilization problem," *IEEE Trans. on Automatic Control*, vol. 27, pp. 895–903, 1982.

- [176] I. Schur, "Über Potenzreihen, die im Inneren des Einheitskreises beschränkt sind," *Journal für Mathematik*, vol. 147, pp. 205–232, 1917.
- [177] I. Schur, "Über Potenzreihen, die im Inneren des Einheitskreises beschränkt sind," *Journal für Mathematik*, vol. 148, pp. 122–145, 1918.
- [178] I. Schwamm, "Analytische und simulative Untersuchungen zur Verbesserung der robusten Lenkregelung," Tech. Rep. IB 515-97-14, DLR, Oberpfaffenhofen, Germany, 1997. Betreuer J. Ackermann und T. Bünte.
- [179] L. Segel, "Theoretical prediction and experimental substantiation of the response of the automobile to steering control," in *IMechE*, pp. 310–330, 1956–1957.
- [180] A. Sideris and R. deGaston, "Multivariable stability margin calculation with uncertain correlated parameters," in *Proc. IEEE Conf. Decision and Control*, (Athens), pp. 766–771, 1986.
- [181] A. Sideris and R. S. Peña, "Fast computation of the multivariable stability margin for real interrelated uncertain parameters," *IEEE Trans. on Automatic Control*, vol. 34, pp. 1272–1276, 1989.
- [182] W. Sienel, "Algorithms for tree structured decomposition," in *Proc. IEEE Conf. Decision and Control*, (Tucson), pp. 739–740, 1992.
- [183] W. Sienel, *Analyse und Entwurf von robusten Regelungssystemen durch Konstruktion von komplexen Wertemengen (Analysis and design of robust control systems by construction of complex value sets)*. Ph.D. thesis, Technische Universität München, 1994. VDI Fortschritt-Bericht, Reihe 8, Nr. 476, VDI-Verlag, Düsseldorf, 1995.
- [184] W. Sienel, "Robust decoupling for active car steering holds for arbitrary dynamic tire characteristics," in *Proc. Third European Control Conference*, (Rome), pp. 744–748, 1995.
- [185] O. Smith, *Feedback Control Systems*. New York: McGraw-Hill, 1958.
- [186] C. Soh, C. Berger, and K. Dabke, "On the stability properties of polynomials with perturbed coefficients," *IEEE Trans. on Automatic Control*, vol. 30, pp. 1033–1036, 1985.
- [187] K. Sondergeld, "A generalization of the Routh-Hurwitz stability criteria and an application to a problem in robust controller design," *IEEE Trans. on Automatic Control*, vol. 28, pp. 965–970, 1983.
- [188] M. Spillman, P. Blue, L. Lee, and S. Banda, "A robust gain scheduling example using linear parameter varying feedback," in *Proc. 13th IFAC World Congress*, (San Francisco), 1996.
- [189] B. Stevens and F. Lewis, *Aircraft control and simulation*. New York: Wiley, 1992.
- [190] M. Stieber, *Das Konzept des Tandemreglers zur automatischen Spurführung nicht schienengebundener Fahrzeuge*. MAN, Internal Report B 094002-EDS-005, 1980.
- [191] Y. Tsyplkin and B. Polyak, "Frequency domain criteria for  $l^p$ -robust stability of continuous linear systems," *IEEE Trans. on Automatic Control*, vol. 36, no. 12, pp. 1464–1469, 1991.
- [192] Y. Tsyplkin and B. Polyak, "Frequency domain criteria for robust stability of polytope of polynomials," in *Control of uncertain dynamic systems* (S. Bhattacharyya and L. Keel, eds.), pp. 491–499, CRC Press, 1991.

- [193] T. Umeno and Y. Hori, "Robust speed control of DC servomotors using modern two degrees-of-freedom controller design," *IEEE Trans. Ind. Electron.*, vol. 38, no. 5, pp. 363–368, 1991.
- [194] J. Uspensky, *Theory of Equations*. New York: McGraw-Hill, 1948.
- [195] A. v. Zanten, R. Erhardt, and G. Pfaff, "FDR - die Fahrdynamikregelung von Bosch," *Automobiltechnische Zeitschrift*, vol. 96, pp. 674–689, 1994.
- [196] P. Varaiya, "Smart cars on smart roads: Problems of control," *IEEE Trans. on Automatic Control*, vol. 38, pp. 195–207, 1993.
- [197] A. Vicino, A. Tesi, and M. Milanese, "An algorithm for nonconservative stability bounds computation for systems with nonlinearly correlated parametric uncertainties," *IEEE Trans. on Automatic Control*, vol. 35, pp. 835–841, 1990.
- [198] M. Vidyasagar, *Nonlinear systems analysis*. Englewood Cliffs, N.J.: Prentice-Hall, 1978.
- [199] I. Vishnegradsky, "Sur la théorie générale des régulateurs," *Compt. Rend. Acad. Sci.*, vol. 83, pp. 318–321, 1876.
- [200] D. Šiljak, *Nonlinear systems: the parameter analysis and design*. New York: Wiley, 1969.
- [201] E. Walach and E. Zeheb, "Generalized zero sets of multiparameter polynomials and feedback stabilization," *IEEE Trans. on Circuits and Systems*, vol. 29, pp. 15–23, 1982.
- [202] L. Zadeh and C. Desoer, *Linear system theory: the state space approach*. New York: MacGraw-Hill, 1963.
- [203] K. Zhou, J. Doyle, and K. Glover, *Robust and optimal control*. Upper Saddle River, NJ: Prentice-Hall, 1996.
- [204] A. Zomotor, *Fahrwerktechnik: Fahrverhalten*. Würzburg: Vogel-Verlag, 1987.

# Index

- $\mathcal{B}$ -specifications, 231
- $\mathcal{B}$ -stability, 131, 149, 152, 230
- $\delta$ -transform, 429
- $\Gamma$ -editor, 463
- $\Gamma$ -stability, 43, 59, 66, 67, 230, 256, 356
- $\Theta$ -stability, 104, 107, 117
- $\Theta$ -stability margin, 222
- $\mu$ -split braking test, 173, 192
- $\mu$ -synthesis, 328, 331
- absolute stability, 114, 261
- accelerometer, 13, 189, 206, 286
- accelerometer feedback, 210
- Ackermann angle, 201
- Ackermann steering, 201
- Ackermann's formula, 37
- Ackermann, J., 38, 82, 186, 211, 216, 438
- active boundary, 32, 52, 71, 448
- actuator, 16, 27, 60, 173, 223, 279, 303, 422
- actuator constraints, 22, 141, 215
- actuator model, 253
- actuator uncertainties, 278
- additive perturbation, 27, 143
- admissible solution set, 36, 308
- affine coefficients, 349, 400, 404, 428, 437, 448
- affine polynomial family, 351
- affine transformation, 445
- aircraft dynamics, 286
- algebraic curves, 448, 449
- algebraic problem formulation, 98, 426
- analytical modelling, 2
- Anderson, B.D.O., 344
- anti-aliasing filter, 60, 421
- approximation, 419
- automatic car steering, 180, 181, 272
- bandwidth, 60, 68, 143, 314, 325
- Barmish, B.R., 335, 438
- barycentric coordinates, 353
- Bhattacharyya, S., 48
- Bialas, S., 353
- bicycle model, 180
- bilinear coefficient, 98, 358, 363, 434, 448
- bilinear transformation, 95, 428, 445
- bisection, 364, 370, 391
- Bode magnitude plot, 133, 165
- Bode's integral theorem, 148, 230
- boundary crossing, 67, 425
- boundary crossing theorem, 29, 34, 36, 67, 339, 405, 426
- boundary representation theorem, 434
- Boyd, S., 166
- braking, 171, 173, 261, 268
- branching point, 73
- Butterworth pole configuration, 87, 280
- calculation modules, 462
- cancellation, 9, 60, 64, 292
- cancellation in the argument of the function, 292
- canonical form, 10
- cascade structure, 210
- Cauchy's principle of the argument, 334
- Cayley-Hamilton theorem, 38, 39
- center of eigenvalues, 60
- characteristic polynomial family, 7, 14, 201, 207, 374
- characteristic velocity, 199
- Chapart, A., 21
- chord approximation, 364, 380

- circle, 94, 424  
 circle stability, 444  
 coefficient function, 84, 431, 437  
 Cohn, A., 427  
 color coding, 37, 76  
 compensator, 56, 65  
 complementary sensitivity function, 26,  
     136, 147, 224  
 complex root boundary (CRB), 29, 34,  
     50, 69, 82, 426  
 complexity, 365, 378, 410, 442  
 computer algebra, 416  
 computer animation, 371  
 concurrent engineering, 2, 36  
 conformal mapping, 95  
 conic section boundaries, 81, 96, 119  
 construction of value sets, 370  
 contact force, 171  
 continued fractions, 24  
 contour algorithm, 374  
 contractable, 436  
 control architecture, 323  
 controllability, 10, 12, 37, 74, 172, 197,  
     204, 252, 276, 420  
 controllability Gramian, 161  
 controller discretization, 417  
 controller structure, 23, 215, 290, 294,  
     307  
 convex, 73  
 convex hull, 352, 436, 446  
 convex hull of the stable region, 429, 431  
 convex hull of the value set, 367  
 convex polygons, 48, 92  
 coordinate transformation, 94  
 cornering stiffness, 192  
 corrective angle, 184  
 corrective rudder deflection, 297  
 corrective slip angle, 185  
 corrective steering angle, 206  
 crane, 2, 9  
 Cremer, L., 335  
 critical  $\Theta$ -stability condition, 122  
 critical frequency, 410  
 critical stability conditions, 29  
 crossing the imaginary axis, 29, 32  
 Curtis, 335  
 curvature, 200, 273  
 damping, 60, 61, 65, 68, 88, 202, 212,  
     305, 421  
 dead time, 25, 442  
 deadbeat solution, 421, 425  
 decoupled lateral subsystem, 188  
 decoupled yaw subsystem, 188  
 decoupling point, 178, 196, 291  
 describing function, 107, 108, 218  
 design, 75, 358, 431, 448  
 design process, 59  
 Desoer mapping theorem, 367, 393  
 Desoer, C., 335  
 digital controller, 417  
 dilation factor, 395  
 direct rollover avoidance, 241  
 direct transmission, 133 -  
 discontinuity in the distance function,  
     407  
 discrete-time frequency response, 440  
 discriminant, 88, 453  
 disjoint solution sets, 86  
 displacement, 275  
 distance, 405, 407  
 disturbance attenuation, 26, 138, 147,  
     177, 209, 228, 230  
 disturbance observer, 223, 227, 323  
 disturbance torque, 173, 177, 247, 289  
 DLR plate experiment, 391  
 domain splitting algorithms, 369  
 dominant poles, 60, 64, 87  
 double cancellation, 215  
 double root, 69, 73, 88, 167, 432  
 double tangent Popov-line, 459  
 driver, 180  
 driver assistant systems, 173, 181  
 driver reaction time, 173  
 driving tests, 218  
 dual locus method, 107, 220  
 Duncan, W., 29, 335  
 dynamic model uncertainty, 27  
 dynamic order of the controllers, 279  
 edge polynomial family, 350

- edge theorem, 349, 352, 393, 437  
 eigenvalue, 18, 41, 74, 203, 305, 358, 419  
 eigenvalue regions, 24  
 eigenvalue specifications, 68, 105  
 eigenvalue tracing, 73  
 electric RLC network, 371  
 engine out, 286  
 envelope, 456  
 equation generator, 462  
 even-odd decoupling, 349  
 existence of robust controllers, 74  
 exponential parameter dependence, 419  
 exponential parameter dependency, 421, 429  
 extended state space model, 274  
 fading integrator, 213, 221  
 Faedo, S., 342  
 Fam, A., 430  
 family of Popov plots, 388  
 fault detection, 312  
 fault tolerance, 310  
 feasible transfer function, 25, 139  
 feedback of the yaw rate, 289  
 feedback perturbation, 27, 143  
 feedback structure, 12, 75, 185  
 fictitious boundary, 32, 33, 123  
 finite plant family, 54  
 finite test, 356  
 fixed eigenvalues, 37, 40  
 flight conditions, 305  
 four wheel steering, 180  
 Fourier series, 108  
 fragility, 71  
 Frazer, R., 29, 335  
 frequency band, 369  
 frequency domain criteria, 76, 104  
 frequency endpoint condition, 122, 128  
 frequency loci specifications, 104, 121  
 frequency range, 375  
 frequency response, 27  
 frequency response magnitude, 104, 132  
 friction coefficient, 195, 198  
 Fu, M., 352  
 gain, 159  
 gain-reduction margin, 316  
 gain-scheduled controller, 76, 77, 225, 318, 331  
 generalized frequency, 80  
 generalized singular frequencies, 90  
 generation of mapping equations, 37  
 geometric approach, 405  
 Gilbert, E., 10  
 graphical frequency domain criteria, 396  
 graphical user interfaces, 37, 461  
 graphical warning on closeness to instability, 364  
 gray-tone coding, 168  
 gridding, 66, 72, 78, 100, 338, 358, 364, 371, 374, 392, 428  
 gyro, 286  
 gyro or accelerometer faults, 314  
 $H_2$ -norm, 160  
 $H_\infty$  design specifications, 318, 328  
 $H_\infty$ -norm, 132, 147, 165, 331  
 Hamiltonian matrix, 166  
 handling, 212, 288, 293, 322  
 harmonic linearization, 108  
 Hautus, M., 74  
 Hermite, C., 19  
 Hermite-Biehler theorem, 48, 334  
 hold element, 417  
 Hollot, C., 349  
 Huang, L., 349  
 Hurwitz determinant, 19, 326, 392  
 Hurwitz, A., 19  
 hyperbola, 68, 76, 280, 357  
 hyperplanes, 59, 405  
 ideal mass distribution, 198  
 immediate reaction, 212  
 indirect rollover avoidance, 241  
 infinite locus magnitude condition, 122, 128  
 infinite root boundary (IRB), 29, 50  
 inner bound, 370  
 input sensitivity function, 136  
 input-output modelling, 2  
 interactive modules, 461  
 interlacing property, 337

- internal  $\Gamma$ -stability, 60  
 internal stability, 26, 137  
 intersection of sets, 76, 86, 95, 129, 154,  
     258, 463  
 intersection points of algebraic curves,  
     454  
 interval plants, 348  
 interval polynomials, 341, 396  
 invariance plane, 40, 464  
 inverse Laplace transform, 62  
 inversion of a complex set, 382  
 isolated unstable point, 362, 364  
  
 Jacobian, 98, 362, 363, 366, 379  
 Joint-Aviation-Requirements, 288  
 junctions, 119  
 Jury, E.I., 344, 425, 427  
  
 Kaesbauer, D., 82  
 Kalman, R., 10, 37  
 Kamm circle, 171  
 Kharitonov's theorem, 341, 393, 398  
 Kharitonov, V., 342  
  
 lane keeping, 243  
 lane reference, 272  
 Laplace transform, 208, 373  
 largest stable box, 404  
 largest stable hypersphere, 404  
 lateral acceleration, 200, 291  
 lateral subsystem, 209  
 lateral tire forces, 174, 192  
 lean controller structure, 24, 215, 281  
 Leonhard, A., 335  
 Leverrier-Faddejew algorithm, 7, 15, 16  
 Liénard, A., 21  
 Liénard-Chipart conditions, 32  
 limit cycle avoidance, 220  
 limit cycles, 107, 215, 217, 237  
 linear-quadratic-regulator, 161  
 linearization, 3, 241, 247, 273  
 load alleviation, 287, 297  
 logarithmic spiral, 423  
 longitudinal dynamics, 319  
 low-pass filtered differentiation, 22  
 low-pass properties, 108, 220  
  
 Mansour, M., 344, 398  
 mapping solver, 462  
 Mason's formula, 384  
 mass-spring-damper elements, 371  
 MATLAB, 462, 463  
 measurement noise, 22  
 Meditch, J., 430  
 Mikhailov plot, 334, 344  
 Mikhailov set, 340  
 Mikhailov, A., 335, 396  
 MIMO systems, 16, 158, 431  
 Mitrović, D., 36  
 model reference, 25, 138  
 modular toolbox, 461  
 momentary pole, 182  
 monic polynomial, 6, 16, 18  
 multi-model approach, 151, 418  
 multilinear coefficient functions, 15, 16,  
     336, 359, 362, 431  
 multiplication of value sets, 378  
 multiplicative perturbation, 27, 141, 147  
 multiplicity, 419  
 multivariate polynomials, 448  
 Munro, N., 48  
  
 natural frequency, 61, 202, 212, 305, 421  
 necessary condition, 370  
 Neimark, Y., 36  
 noise rejection, 138, 148, 228  
 nominal performance, 326  
 nominal plant model, 27  
 nominal polynomial, 87  
 non-active boundary, 32  
 non-linear, 14, 297  
 non-linear coefficient functions, 96, 98,  
     362, 370, 371, 393  
 non-linear simulation, 290, 318, 331  
 non-linear transformation, 96  
 non-minimum phase zeros, 25, 64  
 non-observable, 9, 13, 41, 177, 186, 289  
 non-parametric uncertainty, 27  
 normal vector, 405  
 norms, 160  
 number of edges, 353, 358  
 numeric optimization methods, 36  
 Nyquist plot, 48, 105, 117, 121

- Nyquist value set, 440  
 Nyquist, H., 140, 145, 165, 335, 382  
 Nyquist-stability margin, 140
- observability, 10, 12, 13, 74, 205, 252,  
 277, 420  
 observer, 191  
 octahedron, 437  
 Olbrot, A., 349  
 one-to-one correspondence of the eigen-  
 values, 73, 308  
 operating domain, 6, 12, 249  
 order of the controller, 14  
 Orlando's formula, 31, 426  
 orthogonal, 405  
 orthogonalization procedure, 406  
 oscillations, 61  
 output feedback, 14, 66  
 output sensitivity function, 137  
 overbounding, 348  
 overshoot, 60, 61, 66  
 oversteering, 202
- Panier, E., 349  
 paper-and-pencil graphic methods, 36  
**PARADISE**, 461  
 parallel accelerometers, 314  
 parallel gyros, 314  
 parallelepiped, 350  
 parameter space approach, 33, 36, 37,  
 48, 67, 76, 78, 107, 266  
 parameter space control design, 229, 325  
 parametric state space representation,  
 463  
 parpolygon, 352, 356  
 partition of the uncertainties, 380  
 path tracking, 210, 279  
 Pavlidis, T., 425  
 performance, 318  
 performance weight, 326  
 phase angle, 27, 61, 191, 336  
 phase margin, 159, 176, 177, 219, 442  
 PID-control, 47, 78, 92, 101  
 pitch, 286  
 pitch-rate, 319  
 planar model, 290
- plant disturbance, 6, 26  
 plant family, 75  
 point condition, 122, 123, 153  
 Poisson sum form, 441  
 pole placement, 37, 67, 74  
 pole placement matrix, 39, 41  
 pole region assignment, 68  
 Polyak, B., 397, 400  
 polynomial coefficient, 359  
 polynomial dependence, 100, 121, 358,  
 362  
 polynomial equations, 448  
 polynomial family, 27, 334, 349, 395  
 polytope, 352, 430  
 Popov criterion, 113, 191, 224, 237  
 Popov plot, 115  
 Popov value sets, 382  
 Popov-line, 115, 130, 237  
 Popov-sector, 115  
 prefilter, 65, 186, 212, 290, 309  
 product decomposable, 381  
 projected  $\Gamma$ -stability boundaries, 78
- rank, 57  
 rate limited, 111, 218  
 rate sensor, 13, 279  
 reaction time, 286, 288, 299  
 real radius of stability, 440  
 real root boundary (RRB), 69  
 real root boundary (RRB), 29, 34, 49,  
 100, 422, 425  
 realizability, 26, 48  
 rear-wheel steering, 210  
 reduced number of uncertain parame-  
 ters, 196  
 reduced order observer, 14  
 reduction procedure, 435  
 reference path, 273  
 regulator transfer function, 135  
 relative degree, 8, 25, 60, 133, 147, 213,  
 324, 420, 442  
 representative operating conditions, 36,  
 54, 55, 418  
 required control input, 138  
 resultant method, 30, 81, 100, 103  
 road curvature, 279

- robot in free motion, 371  
 robust controllability, 12  
 robust controller design, 150  
 robust limit cycle avoidance, 218  
 robust observability, 12  
 robust performance, 146  
 robust pitch stabilization, 286  
 robust stability, 144, 326  
 robust stability analysis, 418, 431, 448, 463  
 robust unilateral decoupling, 180, 185, 286, 293  
 robustness analysis, 55, 72, 150, 334  
 roll damping, 254, 256  
 roll motion, 286, 289, 290  
 rollover avoidance, 238, 261  
 rollover coefficient, 239  
 root finding algorithm, 66  
 root locus, 9, 60, 73, 203, 280, 356  
 root set, 7, 49, 66, 392, 425  
 Routh, E., 19  
 ruled surface, 434  
  
 sampled-data control system, 417  
 sampling interval, 417, 420, 421  
 saturation, 110, 171, 221  
 scaling, 61, 404, 420  
 Schur, I., 427  
 Schur-stability, 421, 425, 426, 437  
 sensitivity analysis, 233, 260  
 sensitivity function, 26, 136, 147, 255  
 sensor, 13, 16, 27, 307  
 sensor coordinates, 303, 311  
 sensor dynamics, 141  
 sensor fault, 286, 311  
 sensor noise, 25, 26, 325  
 sensors, 312  
 separation, 14, 180  
 sequential pole shifting, 37, 40, 78  
 set operations, 378  
 shear forces, 293  
 short-period longitudinal mode, 65, 73, 286, 303, 318, 319  
 side forces, 181  
 side wind test, 192  
 sideslip angle, 174, 273, 290, 301  
  
 Siljak, D., 36, 88  
 simply connected, 436  
 simulation, 234, 270, 283, 286, 297  
 SIMULINK, 462  
 simultaneous stabilizers, 48  
 simultaneously  $\Gamma$ -stabilized, 71  
 simultaneously stabilized, 75  
 single-track model, 180, 192, 243  
 singular frequency, 44, 49, 98, 100, 360, 401  
 singular points, 457  
 singular value, 165, 168  
 singularity of value sets, 360  
 skidding avoidance, 174, 215  
 slices, 78  
 sluggish responses, 60  
 small-gain theorem, 145, 165  
 smallest destabilizing perturbation, 395, 410  
 specifications, 68, 132  
 stability, 172, 191, 202, 250  
 stability analysis, 22  
 stability profile, 389, 392, 393  
 stability radius, 395, 408  
 stability regions, 428  
 stabilizing feedback, 13  
 stable neighborhood, 29  
 stable test point, 51  
 state space model, 1, 4, 14, 195, 207, 248, 296, 304  
 stationary cornering, 199  
 stationary flight, 286  
 steady state behavior, 64, 133, 139, 199, 224  
 steer-by-wire, 174, 192, 224  
 steering, 171, 256, 261  
 steering actuator model, 224  
 step response, 59, 65  
 stepwise change, 172  
 stepwise design procedure, 16, 40  
 strict contraction, 425  
 strictly proper controller transfer function, 421  
 structural dynamics, 288, 293, 305  
 structural robustness, 190, 210

- structured singular value, 329
- subpolynomial, 24, 56, 381
- subpolytopes, 412
- subsystem, 60, 191
- sufficient condition, 370
- sum decomposable, 381
- symbolic computer programs, 37
- system performance, 36
  
- tangent condition, 122, 126, 153, 411, 458
- theorem of Bézout, 414, 454
- time scaling, 61
- time-domain specifications, 59, 68
- tire side force, 175
- tire slip angle, 174
- tires, 171
- tomographic rendering, 48, 52, 78
- trace of a matrix, 8
- track-guided bus, 44, 102, 414
- tracking, 138, 148
- trackwidth, 174
- transfer function, 25, 203, 224, 314, 384
- transfer function matrix, 1, 8, 249
- transformed PID parameters, 95
- transition frequency, 143, 351
- transparency of controller structure, 14, 24, 74, 210, 215, 281
- transparent design, 331
- trapezoidal rule for integration, 418
- tree-structure, 362, 370, 393, 439
- tree-structured decomposition, 380, 382
- tree-structured value set, 370
- Tsyplkin, Y., 397, 400
- Tsyplkin-Polyak loci, 396
- tuning parameters, 14
- Tustin approximation, 417
- two-mass systems, 24
  
- uncertain aerodynamics, 289
- uncertainty, 3, 146, 321
- uncertainty structure, 27
- uncertainty weight, 326
- undecomposable, 381
- underbounding, 348
- understeering, 202
  
- unilateral decoupling, 177, 289
- union of sets, 86, 463
- unit circle, 421, 434
- unmodelled uncertainties, 27
- unstable island, 98
- unstructured uncertainty, 27, 141, 321
  
- value set, 334, 335, 339, 363, 393
- variance, 160
- vehicle sideslip angle, 180
- vertex polynomial, 350, 430
- Vicino, A., 410
- Vishnegradsky, I., 36
  
- weighted sensitivity, 224
- weighting function, 141
- wheelbase, 173, 180
  
- yaw angle, 180, 273, 286
- yaw damping at high velocities, 215
- yaw disturbance torque, 287
- yaw motion, 65
- yaw rate, 174, 180, 200, 288, 290, 291
- yaw rate feedback, 278, 284
- yaw rate reference, 206
- yaw rate sensor, 206
- yaw subsystem, 209
  
- $z$ -transfer function, 417
- Zadeh, L., 335
- zero exclusion, 334, 335, 340, 352, 370, 393